Titre: Title:	Modélisation des écoulements diphasiques : amortissement, forces interfaciales et turbulence diphasique.
Auteur: Author:	Cédric Béguin
Date:	2010
Type:	Mémoire ou thèse / Dissertation or Thesis
Référence: Citation:	Béguin, C. (2010). Modélisation des écoulements diphasiques : amortissement, forces interfaciales et turbulence diphasique. [Thèse de doctorat, École Polytechnique de Montréal]. PolyPublie. https://publications.polymtl.ca/494/

URL de PolyPublie: PolyPublie URL:	https://publications.polymtl.ca/494/
Directeurs de recherche: Advisors:	Michel Pettigrew, & Njuki Mureithi
Programme: Program:	Génie mécanique

UNIVERSITÉ DE MONTRÉAL

MODÉLISATION DES ÉCOULEMENTS DIPHASIQUES : AMORTISSEMENT, FORCES INTERFACIALES ET TURBULENCE DIPHASIQUE

CÉDRIC BÉGUIN
DÉPARTEMENT DE GÉNIE MÉCANIQUE
ÉCOLE POLYTECHNIQUE DE MONTRÉAL

THÈSE PRÉSENTÉE EN VUE DE L'OBTENTION
DU DIPLÔME DE PHILOSOPHIÆ DOCTOR
(GÉNIE MÉCANIQUE)
DÉCEMBRE 2010

UNIVERSITÉ DE MONTRÉAL

ÉCOLE POLYTECHNIQUE DE MONTRÉAL

Cette thèse intitulée :

MODÉLISATION DES ÉCOULEMENTS DIPHASIQUES :
AMORTISSEMENT, FORCES INTERFACIALES ET TURBULENCE DIPHASIQUE

présentée par : BÉGUIN, Cédric
en vue de l'obtention du diplôme de : Philosophiæ Doctor
a été dûment acceptée par le jury d'examen constitué de :

M. GARON, André, Ph.D., président.
M. PETTIGREW, Michel, Post grad. dipl, membre et directeur de recherche.
M. MUREITHI, Njuki, Ph.D., membre et codirecteur de recherche.
M. TEYSSEDOU, Alberto, Ph.D., membre.
M. BALIGA, Bantwal Rabindranath, Ph.D., membre.

À notre futur fils,

REMERCIEMENTS

Je tiens tout d'abord à remercier très sincèrement mes directeurs de recherche, Messieurs Michel Pettigrew et Njuki Mureithi : Michel Pettigrew, pour ses encouragements, sa grande expérience et sa généreuse disponibilité ; pour sa connaissance approfondie des écoulements diphasiques et ses nombreux commentaires constructifs M. Njuki Mureithi .

Je remercie également avec gratitude celle que j'appellerai officieusement ma troisième directrice de recherche, Annie Ross. Sa patience, son enthousiasme et surtout ses conseils pleins de bon sens ont été d'une utilité inestimable. Je tiens également à remercier Stéphane Étienne et Emmanuel de Langre qui m'ont donné la chance de profiter de leurs expertises.

Je remercie aussi sincèrement Thierry Lafrance et Bénédict Besner pour leur savoir-faire et leur généreuse aide. Ensuite, je tiens donc à remercier très chaleureusement tous les étudiant(e)s du laboratoire. Je pense à Jean-François, Joël, Romain, François, Thomas, Eddy, Mathieu, Hubert, Isabelle, Arnaud, Claude et bien d'autres. Tous ont su m'apporter leur soutien, leurs bonnes idées et bien sûr leur amitié tout au long de ce doctorat.

Enfin, je tiens à remercier aussi beaucoup tous mes ami(e)s pour leur soutien, leur curiosité, leur amitié et leur support moral. Même si je ne vous cite pas un par un, le cœur y est.

Dernièrement, je remercie Jasmine, ma femme pour tout son appui et les encouragements qu'elle m'a apportés tout au long de ce doctorat. Et surtout pour le cadeau que nous attendons en février.

RÉSUMÉ

Les écoulements diphasiques sont très courants dans l'industrie. Ce type d'écoulement est une source potentielle de vibration dans la tuyauterie. De tels écoulements peuvent induire des vibrations entraînant de la fatigue ou de l'usure prématurée des tuyaux. Les bris de composants de tuyauterie sont critiques et doivent être évités en particulier dans l'industrie nucléaire. Les écoulements diphasiques peuvent s'organiser dans des configurations d'écoulement très différentes et produire par conséquent de forces très variables sur la structure. À titre d'exemple, on observe une augmentation significative de l'amortissement dans les tuyaux contenant un écoulement diphasique par rapport à ceux contenant un écoulement monophasique. Cet amortissement est appelé l'amortissement diphasique. Deux articles de revues scientifiques, constituant la première partie de cette thèse, y sont consacrés. Le taux de vide (le rapport du volume de gaz par rapport au volume total) est un paramètre clé des phénomènes diphasiques et en particulier de l'amortissement diphasique. L'influence du taux de vide sur les forces d'interface et les écoulements autour de quelques bulles est donc primordiale à étudier.

Dans un premier temps, un travail technique a été réalisé pour créer des instruments de mesure du taux de vide.

Dans un deuxième temps, une étude sur la structure de l'écoulement autour des bulles a été réalisée. Elle constitue la dernière partie de cette thèse avec un article de revue scientifique en deux parties. Cette étude aux petites échelles est un bon moyen de comprendre les phénomènes d'écoulement diphasique dans leur globalité.

La première partie de cette thèse est consacrée à l'amortissement diphasique. Cet amortissement est considéré comme une solution pour améliorer la durée de vie des structures, car il constitue un élément dominant de l'amortissement total dans la tuyauterie transportant des écoulements diphasiques. Cependant, les mécanismes responsables de l'amortissement diphasique ne sont pas encore bien compris et il n'existe pas de modèle pratique disponible pour prévoir cet amortissement.

L'amortissement diphasique est de la plus haute importance pour prédire la fatigue et l'usure par frottement et par conséquent prévoir la durée de vie des structures entourées d'écoulement diphasique. Cet amortissement est également crucial pour prédire la vitesse critique pour l'instabilité fluidélastique en écoulement transverse. Toutefois, en écoulement transverse, les forces liées à l'amortissement diphasique sont accompagnées d'autres forces importantes telles que la turbulence diphasique, l'amortissement visqueux, les forces quasi périodiques, etc. Une mesure correcte de l'amortissement diphasique en écoulement trans-

verse est donc complexe. Dans les écoulements internes, notamment dans un tube encastré encastré, tous les mécanismes d'amortissement autre que l'amortissement structural sont relativement faibles et permettent une mesure directe de l'amortissement diphasique. Des mesures d'amortissement diphasique ont été réalisées en écoulement interne. Néanmoins, les connaissances acquises en écoulement interne devraient également être utiles pour prédire l'amortissement diphasique en écoulement transverse. Les mesures d'amortissement diphasique ont été obtenues à partir des vibrations libres sur un tube en utilisant la technique de décrément logarithmique.

Un premier article, soumis dans le *Journal of Fluid and Structure*, présente nos premières conclusions. Des expériences ont été réalisées avec un tube vertical encastré à ses deux extrémités. Les premières expériences simulaient des "bulles de géométrie contrôlée" avec des billes de verre en sédimentation dans l'eau stagnante. Puis de l'air a été injecté dans l'alcool stagnant afin de générer un flux de bulles uniformes et mesurables. Les expériences nous ont amenés à conclure que l'amortissement diphasique est lié à la surface d'interface, et par conséquent à la configuration d'écoulement.

Dans les deux cas, l'amortissement diphasique est corrélé au nombre de bulles (ou sphères). L'amortissement diphasique est donc directement lié à la surface d'interface et, par conséquent, à la configuration d'écoulement. Des expériences complémentaires ont été effectuées avec des tubes dans lesquels circulait un mélange d'air et d'eau. Une série de photographies témoigne le fait qu'en écoulement à bulle, l'amortissement diphasique augmente pour un plus grand nombre de bulles. Il est maximal juste avant la transition de l'écoulement à bulles à l'écoulement bouchon. Au-delà de la transition, l'amortissement diminue. L'amortissement diphasique augmente avec le diamètre du tube.

Un premier modèle simple montre, qu'en raison de la différence de densité, les deux phases ont un mouvement relatif et que ce mouvement peut conduire à un amortissement visqueux. Une étude sur l'ordre de grandeur de l'énergie de tension superficielle démontre que l'amortissement diphasique ne peut pas être expliqué avec un amortissement engendré par la création de nouvelles surfaces d'interface. La tension de surface joue, cependant, un rôle dans la forme et la taille des bulles et par conséquent sur l'amortissement.

L'étape suivante consiste à confirmer les conclusions ci-dessus en utilisant différents mélanges de fluides. Le but est de réaliser des expériences en faisant varier la densité et la viscosité. Un article, soumis à l'*International Journal of Multiphase Flow*, résume les résultats et les conclusions obtenus, déjà présentés dans plusieurs articles de conférences FIV (*Flow Induced Vibrations*) et PVP (*Pressure Vessel and Piping*). Le but de ces études a été d'explorer les relations entre les propriétés physiques des deux phases et l'amortissement diphasique. Des expériences simples ont été réalisées dans un tube transparent encastré encastré. Des

fluides divers, tels que l'air, l'alcool, l'eau pure, l'eau sucrée, la glycérine et un perfluorocarbone, ont été combinés pour obtenir différents mélanges et déterminer l'effet de la tension de surface, la densité et la viscosité sur l'amortissement diphasique. Les expériences avec des tuyaux en PVC, laiton et polycarbonate ont également été comparées. De même que lors de la précédente série d'expériences, les amortissements diphasiques ont été mesurés à partir des vibrations libres du tube. Deux séries d'expériences avec la phase continue stagnantes et en mouvement ont été menées.

Sur la base de l'analyse dimensionnelle, nous avons obtenu un modèle semi-empirique pour l'amortissement diphasique dans les écoulements à bulles et bouchons. Le taux de vide et le nombre de Bond se sont révélés comme des paramètres importants. L'amortissement diphasique est expliqué par un transfert d'énergie cinétique du tube à la phase continue par l'intermédiaire du mouvement relatif entre la phase dispersée et la phase continue. Étonnamment, la viscosité des fluides semble n'avoir aucun effet significatif sur l'amortissement diphasique. Ce dernier est donc d'abord un effet d'inertie. L'augmentation de l'énergie cinétique de la phase continue s'accompagne d'un amortissement de la structure. En écoulement à bouchons, un certain amortissement visqueux est ajouté sans doute à cause du sillage oscillant des bulles de Taylor.

La tension de surface joue un rôle important dans la taille et la forme de bulles de gaz. Elle affecte donc la capacité des bulles à transférer de l'énergie cinétique à la phase continue. En écoulement à bulles, l'amortissement diphasique ne dépend pas beaucoup de la viscosité du fluide, l'énergie cinétique ajoutée dans le liquide est donc sans doute transportée avec l'écoulement. Des expériences mesurant la variation d'intensité de turbulence à la sortie du tube lorsque le tube vibre pourraient apporter la preuve de ce qui précède. De nouvelles hypothèses ont été proposées suggérant que l'impact entre les bulles ou entre les bulles et la structure soit un mécanisme envisageable pour apporter de l'énergie dans la phase continue.

Une plus grande différence de densité et un plus grand taux de vide conduisent à un plus grand amortissement diphasique, tant que le taux de vide est inférieur à une valeur critique correspondant à l'amortissement maximal. L'amortissement diphasique augmente assez linéairement avec le taux de vide jusqu'au taux de vide critique. Ce taux de vide critique correspond à un changement de comportement de l'amortissement et à une transition de configuration d'écoulement. La transition d'écoulement ne semble dépendre que de la vitesse homogène. Dans la gamme de tubes étudiés (11 mm$<$ D $<$25 mm), le diamètre du tube semble n'avoir aucun effet significatif sur cette transition d'écoulement. Le taux de vide, l'inertie et la tension de surface sont les principaux paramètres qui régissent l'amortissement diphasique. Ce second article propose une corrélation pour prédire l'écoulement diphasique en écoulement à bulles et bouchons.

Pour être en mesure de comprendre les mécanismes de transition en configuration d'écoulement et l'amortissement diphasique, la modélisation des forces d'interface et de l'écoulement autour d'une bulle est clairement apparue comme une nécessité. En effet, peu de travaux ont été consacrés pour comprendre le rôle du taux de vide sur les forces d'interface agissant sur une bulle ainsi que la structure de l'écoulement autour d'elle. Parallèlement à l'étude numérique et analytique sur l'écoulement autour des bulles, la conception d'un capteur capacitif a été amorcée. Cet instrument de mesure du taux de vide utilise la différence de propriété électrique de l'air et de l'eau. Il est un instrument utile pour étudier la variation spatiale et spectrale du taux de vide. En effet l'instabilité des ondes de taux de vide est une bonne candidate pour expliquer la transition de l'écoulement à bulles à écoulement bouchons.

L'influence du taux de vide sur l'écoulement autour des bulles et sur les forces d'interface est le moteur des ondes du taux de vide. L'étude expérimentale des ondes de taux de vide avec capteur de capacité serait un bon moyen de valider les connaissances acquises par les études analytiques et numériques.

Un article en deux parties soumis pour publication dans le *Journal of Fluid Mechanic* relate le résultat de nos investigations. La Partie I de cet article propose une relation entre le coefficient de traînée de bulles (ou gouttes) sphériques et le nombre de Reynolds Re, le taux de vide ε, les rapports de viscosité et de densité entre les deux phases ($\bar{\mu}$ et $\bar{\rho}$). Les relations proposées s'appliquent à tous les mélanges fluide-fluide. La limite sous laquelle les bulles restent sphériques a également été étudiée. Cette condition permet d'identifier la limite du modèle.

Le taux de glissement dans les écoulements à bulles reste en général très faible. Dans presque tous les cas pratiques d'écoulement à bulles, l'écoulement autour de la bulle peut être considéré comme un écoulement de Stokes. Le taux de vide ε a un effet majeur sur la traînée essentiellement par confinement. La relation proposée peut être utilisée pour construire un modèle d'écoulement à deux phases pour les écoulements à bulles ou annulaire. Ce travail propose une amélioration sur les relations de fermeture du coefficient de traînée (C_D) par rapport aux travaux antérieurs.

La principale conclusion est que l'écoulement de Stokes représente, de façon très précise, l'écoulement autour des bulles. L'écoulement est laminaire et par conséquent la turbulence ne peut être attribuée à de la turbulence classique. L'écoulement dans la phase continue peut être considéré comme un écoulement de film dans lequel la turbulence classique ne peut se développer. La turbulence diphasique est essentiellement due à des perturbations induites par le passage de bulles.

La Partie II propose un modèle pour la pseudo-turbulence (turbulence induite par les particules). Des relations entre le tenseur de Reynolds de la phase continue et dispersée et

le nombre de Reynolds Re, le taux de vide ε et le rapport de viscosité et de densité entre les deux phases ($\bar{\mu}$ et$\bar{\rho}$) sont proposées. Les relations proposées sont applicable à tous les mélanges fluide-fluide. Les implications sur la taille des bulles et les forces induites par la turbulence sur les bulles sont également étudiées. Un modèle simple est proposé faisant le lien entre les forces de turbulence sur les bulles et la prédiction de la taille des bulles. Il est montré que les forces conduisant à la rupture des bulles sont peu présentes dans le tuyau. Cela pourrait expliquer pourquoi la transition entre l'écoulement à bulles et l'écoulement bouchons est indépendante du diamètre du tube.

Cette thèse constitue une étude de l'amortissement diphasique ainsi que de l'influence du taux de vide sur les caractéristiques de l'écoulement et sur les forces induites. L'amortissement diphasique est le plus souvent un effet d'inertie apportant de l'énergie à la phase continue par l'intermédiaire d'un mouvement relatif entre les deux phases. Ce processus implique un impact majeur de la différence de densité et de la tension superficielle. L'étude de l'influence du taux de vide sur la force d'interface et la pseudo-turbulence nous mène à la conclusion de son importance capitale. Un très petit pourcentage de changement du taux de vide est suffisant pour complètement changer la nature de l'écoulement. Cela montre le danger d'identifier simplement des phénomènes d'écoulement monophasique pour comprendre les phénomènes en écoulement diphasique. En particulier, la nature de la turbulence dans l'écoulement diphasique s'est avérée être complètement différente de celle observée dans un écoulement monophasique.

L'auteur espère que cette thèse sera agréable à lire et contribuera un peu à une meilleure compréhension de certains phénomènes observés dans les écoulements diphasiques.

ABSTRACT

Two-phase flow is common in industry. This kind of flow is a potential source of vibration in piping systems. Such flow may induce vibration that can lead to premature fatigue or wear in piping. Failure of piping components is critical and must be avoided especially in the nuclear industry. Two-phase flow can reorganize itself into very different flow patterns, thus, generating very different kinds of forces on the structure . As an example, a significant increase in damping is observed in two-phase flow compared to single phase flow. This damping is naturally called two-phase damping. Two journal articles, constituting the first part of this thesis, are devoted to it. The void fraction (ratio of gas volume to total volume) constitutes one key parameter controlling two-phase flow phenomena and in particular two-phase damping. The influence of void fraction on interface forces and flow around a group of bubbles is therefore studied. First, technical work to develop void fraction measurement instruments was done. Second a closer look at flow structure around bubbles constitutes the last part of the thesis yielding a two-part journal paper. This study at a fundamental scale leads to insights into two-phase flow phenomena at the larger scale.

The first part of the thesis is devoted to two-phase damping. This damping is considered part of the solution against failure of piping, since it constitutes a dominant component of the total damping in piping conveying two-phase flow. However, the mechanisms responsible for two-phase damping are not well understood and no convenient models are available to predict this damping.

Two-phase damping is of the utmost importance to predict fatigue and fretting-wear and consequently predict the life of structures operating in two-phase flow. This damping is also crucial in the prediction of the critical velocity for fluidelastic instability in cross-flow. However, in cross-flow, two-phase damping is accompanied by other significant forces such as two-phase turbulence, viscous damping, quasi periodic forces, etc. A correct measure of two-phase damping is therefore complex. However, in internal flow, especially with clamped-clamped tubes two-phase damping and structural damping are the two only significant damping. This allows a direct measurement of two-phase damping. For this reason, damping experiments were first carried out with internal flow. Nevertheless, the knowledge acquired with internal flow should also be useful to predict two-phase damping in cross-flow as the general mechanism of two-phase damping should be the same. Experiments were performed with a vertical tube clamped at both ends. Two-phase damping ratios were obtained from free transverse vibration measurements on the tube using the log-decrement technique.

A first paper, published in Journal of Fluid and Structures, presents the first conclusions

reached. First, gas bubbles of controlled geometry were simulated with glass spheres let to settle in stagnant water. Second, air was injected in stagnant alcohol to generate a uniform and measurable bubble flow.

In both cases, the two-phase damping ratio is correlated to the number of bubbles (or spheres). Two-phase damping is therefore directly related to the interface surface area and, therefore, to flow pattern. Further experiments were carried out on tubes with internal two-phase air-water flow. A strong dependence of two-phase damping on flow parameters in bubbly flow regime was observed. A series of photographs confirms the fact that two-phase damping in bubbly flow increases for a larger number of bubbles, and for smaller bubbles. It is highest immediately prior to the transition from bubbly flow to slug flow regimes. Beyond the transition, damping decreases. It is also shown that two-phase damping increases with the tube diameter.

A first simple model shows that due to density difference the two phases have a relative motion and this motion can lead to viscous damping. A study on the magnitude of surface tension energy led to the conclusion that two-phase damping cannot be explained via creation of new interface surfaces. Surface tension plays, however, an important role in determining the shape and size of bubbles and consequently two-phase damping.

The next step was to confirm the aforementioned findings using different fluid mixtures by varying both density and viscosity. A paper submitted for publication in International Journal of Multiphase Flow summarizes the results and the conclusions obtained in several papers presented at FIV (*Flow Induced Vibration*) and PVP (*Pressure Vessels and Piping*) conferences. The purpose of these studies was to explore the relationships between two-phase damping and fluid properties. Simple experiments were carried out in a clear vertical clamped-clamped tube to verify the effects of fluid and pipe properties on two-phase damping. Various fluids, such as air, alcohol, pure water, sugared water, glycerol, and perfluorocarbon, were combined to obtain different controlled mixtures and to determine the effect of surface tension, density and viscosity on two-phase damping. Experiments with PVC, brass and polycarbonate tubes were also compared. Similarly to the previous set of experiments, two-phase damping ratio measurements were obtained from free transverse vibration of the tube. Two sets of experiments with stagnant and moving continuous phase were conducted.

Based on dimensional analysis, we obtained a semi-empirical model for two-phase damping in bubbly and slug flow. The void fraction and the Bond number were shown to be the dominant parameters in two-phase damping. Surprisingly the viscosity of the fluid constituting the continuous phase appears to have no significant effect on two-phase damping. Two-phase damping seems therefore to be primarily an inertial effect. Two-phase damping in bubbly flow is likely due to an increase of kinetic energy in the continuous phase due to

inertial effects of the relative motion of gas bubbles. This increase of kinetic energy leads to the damping of the structure. In slug flow, some viscous damping is added due to the oscillating wake of the Taylor bubbles.

Surface tension plays an important role in the size and shape of the gas bubbles. Consequently, it affects the ability of the bubbles to transfer kinetic energy into the continuous phase. In bubbly flow, two-phase damping does not depend strongly on fluid viscosity. This leads to the conclusion that the increase of kinetic energy in the liquid due to relative motion between phases is carried out of the tube by the flow. Experimental studies of turbulence intensity variation at the tube exit when the tube is vibrating should provide supporting evidence of the above findings. Some new hypotheses are proposed suggesting "impact" between bubbles or bubbles and structure leading to vibration of the bubble interface as a potential mechanism to transfer energy to the continuous phase.

The experiments leads to the conclusion that a greater density difference and higher void fraction leads to higher two-phase damping, up to a critical void fraction corresponding to the maximum damping. Two-phase damping increases fairly linearly with void fraction up to this critical void fraction. The critical void fraction is associated with a change of two-phase damping behavior corresponding to a flow pattern transition. The flow pattern transition seems to depend only on the homogeneous velocity. For intermediate diameter (10-25 mm), tube diameter seems to have no significant effect on this flow pattern transition. Void fraction, inertia and surface tension are the major governing parameters for two-phase damping. The second paper proposes a correlation to predict two-phase flow in bubbly and slug/churn flow.

To be able to understand both the mechanisms of two-phase flow pattern transition and two-phase damping, modelling the interface area and the flow around a bubble clearly becomes a necessity. Indeed not much has been done to understand the effect of void fraction on the interface forces acting on a bubble and the flow around it. In parallel to a numerical and analytical study on flow around bubbles, the design of a capacitance void fraction sensor was done. This instrument, using the difference of electrical properties between air and water, could be a useful instrument to study the spatial and spectral variation of void fraction. Indeed void wave instability has been shown to be the mechanism underlying the transition from bubbly flow to slug flow.

The influence of void fraction on flow around bubbles and the interface force drive the void waves. The experimental study of void waves using capacitance sensors would be a good way to validate the knowledge acquired from the analytical and numerical studies.

A two-part paper submitted for publication in the Journal of Fluid Mechanics is the results of our investigations on void fraction influence on flow around bubbles. Part I of the paper proposes a relation for the drag coefficient of spherical bubbles (or droplets) depending

on Reynolds number Re, void fraction ε, viscosity ratio $\bar{\mu}$ and density ratio $\bar{\rho}$. The proposed relation is shown to be useful for all fluid-fluid cases. The limiting conditions under which bubbles remain spherical are also studied. This sphericity limit marks the limit of this model.

Moreover, it is shown that the slip ratio is very small for bubbly flow. In almost all practical cases of bubbly flow, flow around a bubble can be considered as Stokes flow. The void fraction ε, has a major effect on the drag essentially through confinement. The proposed relation can be used to construct a two-phase flow model for bubbly or annular flows. This work proposes an improvement on the the closure relations for the drag coefficient (C_D) compared to previous works.

The main conclusion is that Stokes flow represents, very accurately, the flow around bubbles. The flow is consequently laminar and therefore two-phase turbulence cannot be attributed to classical turbulence. The flow in the continuous phase can be viewed as a film flow in which classical turbulence cannot develop. Two-phase turbulence, which is called pseudo turbulence, is essentially due to perturbations induced by bubble passage.

Part II of the paper proposes a model for pseudo turbulence (bubble induced turbulence) in two-phase flow. Relations for the Reynolds stress tensor for both the dispersed and the continuous phases are proposed depending on Reynolds number Re, void fraction ε and viscosity and density ratios ($\bar{\mu}, \bar{\rho}$). The proposed relations are useful for all fluid-fluid cases. The implications for bubble size and turbulence forces on bubbles are also studied. A simple model is proposed in this paper as a relation for turbulence forces on bubbles as well as a model to predict bubble size. It is shown that no significant breakup forces are present in pipes conveying two-phase flow. This could explain why the flow pattern transition from bubbly flow to slug flow is independent of tube diameter.

This PhD thesis consists of a study on two-phase damping and influence of void fraction on flow characteristics and on the induced forces. Two-phase damping was identified to be mostly an inertial effect bringing energy to the continuous phase due to a relative motion between phases. This process underlines the major impact of density difference and surface tension. The study on the influence of void fraction on interface force and pseudo turbulence leads to the conclusion of major importance. That only a few percentage of void fraction changes completely the nature of the flow. This shows the danger in identifying single-phase flow phenomena with two-phase flows. In particular, the nature of turbulence in two-phase flow is proved to be completely different from that observed in single-phase flow.

The author hope that this PhD thesis will be interesting to read and will contribute to give a slightly better understanding of some phenomena observed in two-phase flows.

TABLE DES MATIÈRES

LISTE DES TABLEAUX

LISTE DES FIGURES

LISTE DES SIGLES ET ABRÉVIATIONS

Indices

$_{2\phi}$: mélange diphasique

$_{l}$: liquide

$_{g}$: gaz

Exposant et autres annotations

^{i} : variable liée a l'interface

^{w} : variable liée a la paroi

$^{\rightarrow}$: vecteur

$^{=}$: tenseur

$\langle X \rangle$: valeur moyennée

$\bar{X}$: valeur sans dimension

X^{*} : petites perturbations ou correction

Propriétés Physique

t : temps (s)

T : température (^{o}K)

P : pression $(Pa : kg.m^{-1}.s^{-2}$ ou $N/m^{2})$

$\vec{g}$: vecteur gravité $(m.s^{-2})$

$\vec{v}$,$\vec{U}$: vecteur vitesse (m/s)

u, v, w : composante de la vitesse (m/s)

e : énergie interne $(J : kg.m^{2}.s^{-2})$

h : enthalpie $(J : kg.m^{2}.s^{-2})$

ρ : masse volumique (kg/m^{3})

γ : tension de surface $(kg.s^{-2}$ ou $N/m)$

μ : viscosité dynamique $(kg.m^{-1}.s^{-1})$

$\bar{\bar{T}}$: tenseur des contraintes

$\bar{\bar{\tau}}$: tenseur des contraintes visqueuses

Variables liées aux écoulements diphasiques

A	:	section de passage (m^2)
p	:	pas (m)
D	:	diamètre des tubes (m)
V	:	volume (m^3)
Q	:	débit volumique (m^3/s)
W	:	débit massique (kg/s)
ε	:	taux de vide : $V_g/(V_l + V_g)$
α	:	taux de vide local
β	:	titre volumique : $Q_g/(Q_l + Q_g)$
X	:	titre massique : $W_g/(W_l + W_g)$
S_r	:	taux de glissement u_g/u_l
χ	:	paramètre de Martinelli (ne pas confondre avec χ_k fonction indicatrice de phase)
$\vec{n_k^i}$	:	le vecteur normal à l'interface pointant à l'extérieur de la phase k
$[\![f_k]\!]$	:	$f_l + f_g$

CHAPITRE 1

INTRODUCTION

La mécanique des fluides et celle des solides ont été longtemps des sciences séparées. Pourtant, dans l'industrie comme dans la vie quotidienne les interactions fluides-structures sont omniprésentes. Le ronflement, l'emballement d'un tuyau d'arrosage soumis à un fort débit ou le martèlement d'un robinet ne sont que quelques exemples bien connus où l'écoulement d'un fluide en contact avec des éléments de structure entraîne un comportement vibratoire important. L'essentiel des problèmes de l'industrie aéronautique, navale, chimique et énergétique est directement lié aux interactions fluide-structure. Surtout au cours des cinquante dernières années, l'étude de ses interactions est devenue une science à part entière. Les vibrations dues aux écoulements peuvent parfois être utiles (dans un instrument de musique à vent, par exemple), mais elles sont considérées comme un problème à éviter dans la plupart des applications industrielles. La vibration excessive de systèmes de tuyauterie peut entraîner de l'usure prématurée due au frottement ou à la fatigue et même, plus rarement, la destruction complète d'éléments de structure.

Parmi les écoulements fluides, ceux mélangeant une ou plusieurs phases non miscibles intéressent particulièrement l'industrie. Prés de la moitié des systèmes de tuyauterie en milieu industriel opèrent dans des conditions d'écoulement diphasique Pettigrew et Taylor (1994). Dans plusieurs applications, l'utilisation de ces écoulements permet de meilleurs rendements thermiques et des échanges de chaleur plus efficaces. Les écoulements diphasiques se retrouvent dans une grande variété d'applications industrielles dans des domaines tels que la pétrochimie, la biochimie, la production d'électricité, l'aérospatiale, l'industrie des procédés, la microélectronique, etc. Au sein de l'industrie nucléaire, les écoulements diphasiques jouent un rôle de premier plan. Dans une centrale nucléaire à réacteur CANDU, par exemple, les générateurs de vapeur qui alimentent les turbines sont des composants qui comportent des milliers de tubes soumis à des écoulements diphasiques eau vapeur. Depuis le début des années 50, les écoulements diphasiques ont été étudiés de façon intensive : ébullition nucléique, condensation, transfert de chaleur, pertes de charge et la thermohydraulique des écoulements sont des sujets qui furent approfondis très tôt pour faire face aux nombreux défis à relever dans l'essor de l'industrie nucléaire.

Afin de mieux appréhender ces phénomènes, la chaire Interaction Fluide-Structure met en place des techniques expérimentales et théoriques pour mesurer et modéliser les caractéristiques de tels écoulements afin de mieux connaitre leurs effets sur les structures.

Cette thèse s'intéressera plus particulièrement à l'amortissement diphasique et la compréhension des phénomènes qui y sont reliés. L'amortissement diphasique est particulièrement dépendant du taux de vide (la proportion d'une phase par rapport à l'autre). L'influence du taux de vide sera étudiée. En particulier, ce dernier joue un rôle clé dans la configuration que choisit l'écoulement (l'organisation des deux phases dans l'espace et le temps). Afin de mieux comprendre son rôle, nous allons étudier les raisons qui peuvent modifier la dépendance spatiale et spectrale du taux de vide. En effet, les mesures de la densité spectrale ont montré que les écoulements possèdent un caractère périodique ; les fréquences pouvant être corrélées en fonction du flux volumétrique du liquide Jones et Prosperetti (1985). Le taux de vide est donc un paramètre très utile pour la compréhension et la caractérisation des écoulements diphasiques. On verra que sa variation locale est la source de modification profonde de l'écoulement. La modélisation de ce phénomène est donc d'une importance primordiale pour comprendre la physique de tels écoulements.

Les écoulements engendrant des vibrations peuvent être classés en trois catégories :

- Les écoulements internes (écoulement dans une tuyauterie)
- Les écoulements externes axiaux (écoulement autour d'un train, d'un fuselage d'avion ou de certains tuyaux d'un échangeur de chaleur)
- Les écoulements externes transverses (écoulement autour d'une cheminée, d'un faisceau de tubes, etc.)

Mon étude s'intéresse en particulier aux écoulements internes. Elle a trois objectifs principaux :

- Mettre au point de nouvelles techniques de mesure des écoulements diphasiques.
- Proposer des explications sur les mécanismes générant l'amortissement diphasique.
- Modéliser et comprendre le rôle de la turbulence et du taux de vide dans les écoulements diphasiques.

Ma thèse s'articulera autour de quatre articles de journaux. Deux sur l'amortissement diphasique et deux sur la modélisation des écoulements. Le premier chapitre donnera lieu à une revue de littérature. Le deuxième chapitre détaillera le travail accompli pour mettre au point des sondes à capacitance, lequel n'a pas encore fait l'objet d'aucune publication dans un journal. Les chapitres 4 et 5 seront consacrés aux deux articles de journaux consacrés à l'amortissement diphasique. Les chapitres 6 et 7 correspondront aux deux articles de journaux traitant de la modélisation des écoulements diphasiques et en particulier le rôle du taux de vide dans les forces interfaciales et la turbulence diphasique.

CHAPITRE 2

REVUE DE LITTÉRATURE

2.1 Mise en situation

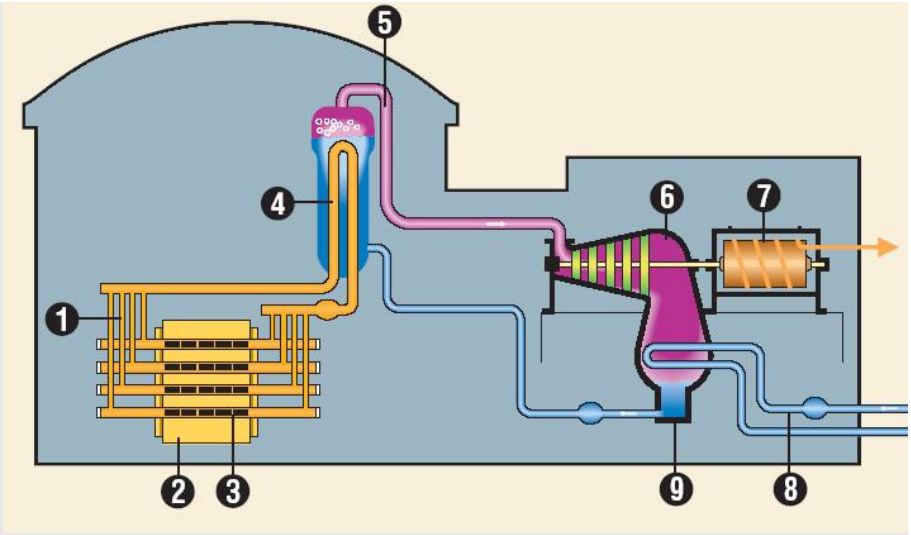

Figure 2.1 Schéma de fonctionnement d'un réacteur CANDU

Dans les centrales nucléaires, la production d'électricité s'effectue selon le processus suivant (cf. figure 2.1). L'eau lourde du circuit primaire de refroidissement (1) circule dans le réacteur (2) autour du combustible traité et assemblé sous forme de grappes (3). On crée ainsi les conditions favorables à la fission entretenue des noyaux d'uranium. À mesure que la réaction se produit, on récupère la chaleur intense dégagée par le combustible grâce à l'eau du circuit primaire. L'eau lourde chaude et pressurisée (environ 300^0C et 10 MPa) est transportée jusqu'aux générateurs de vapeur (4) qui transmettent la chaleur à l'eau ordinaire du circuit secondaire de refroidissement. L'eau de ce circuit secondaire se transforme en vapeur (5) qui actionne une turbine (6), fait tourner un alternateur (7) et produit ainsi de l'électricité. L'eau venant d'un fleuve ou de la mer (8) sert à refroidir la vapeur ; celle-ci est condensée (9). L'eau retourne aux générateurs de vapeur et le cycle recommence. Dans le cas où le refroidissement par l'eau du fleuve ou de la mer n'est pas suffisant, l'eau est envoyée dans une tour de refroidissement (cf. figure 2.2). Cette dernière est répartie sur une grille horizontale avant de s'écouler en gouttelettes vers le bas. Au contact du flux d'air ascendant (effet de cheminée naturelle), l'eau se refroidit. Une petite fraction de l'eau de refroidissement (1.5%)

s'évapore et s'échappe de la tour de refroidissement sous la forme d'un nuage de vapeur.

Figure 2.2 Tours de refroidissement

Le mélange diphasique du circuit primaire en provenance du cœur nucléaire circule dans le générateur de vapeur par des milliers de tubes en "U". À l'extérieur de ces tubes se trouve l'écoulement du circuit secondaire. Ainsi ces tubes sont soumis à des écoulements diphasiques internes et externes. Le bris d'un seul de ces tubes en raison de vibrations excessives pourrait avoir des conséquences néfastes. Une étude plus approfondie est requise pour mieux comprendre les mécanismes qui gouvernent les vibrations observées dans la tuyauterie soumise à des écoulements diphasiques internes et externes.

2.2 Définitions

Ce paragraphe introduit les notations et les définitions utilisées couramment et que j'utiliserai dans le reste du mémoire. Pour distinguer le gaz du liquide on utilise les indices 'g' pour le gaz et 'l' pour le liquide. Les variables peuvent être moyennées dans le temps ou dans l'espace. On notera : Le taux de vide local, noté α, est une moyenne temporelle. Il représente la proportion de temps où un point donné est en phase gazeuse.

$$\alpha(\vec{x}) = \frac{t_g(\vec{x})}{t_g(\vec{x}) + t_l(\vec{x})} \tag{2.1}$$

Le taux de vide, noté ε est une moyenne spatiale. Il représente la proportion de volume occupé par le gaz par rapport au volume de contrôle choisi.

$$\varepsilon = \frac{V_g}{V_g + V_l} \tag{2.2}$$

Dans le cas d'un tuyau on peut parler du taux de vide dans le volume de hauteur Δz suffisamment petit alors dans ce cas on peut exprimer ε comme

$$\varepsilon = \frac{A_g \Delta z}{A_g \Delta z + A_l \Delta z} = \frac{A_g}{A_g + A_l} \tag{2.3}$$

où A_g et A_l représentent respectivement la section occupée par le gaz et celle occupée par le liquide. On note $\bar{\varepsilon}$, le taux de vide moyenné dans le temps. Dans ce cas, on peut supposer que $\bar{\varepsilon}$ est aussi égal à la moyenne spatiale de α sur la section du tuyau considéré (on dit que l'écoulement est ergodique).

On définit le titre volumétrique noté β comme le rapport du débit volumétrique de gaz sur le débit total

$$\beta = \frac{Q_g}{Q_g + Q_l} = \frac{A_g u_g}{A_g u_g + A_l u_l} = \frac{A_g}{A_g + A_l \frac{u_l}{u_g}} \tag{2.4}$$

où Q représente le débit, u la vitesse moyenne sur la section de passage. On appelle taux de glissement le rapport $S = u_g/u_l$. On peut relier ε et β grâce aux taux de glissement.

$$\beta = \frac{\varepsilon}{\varepsilon + (1-\varepsilon)(1/S)} \tag{2.5}$$

ou

$$S\left(\frac{1}{\beta} - 1\right) = \frac{1}{\varepsilon} - 1 \tag{2.6}$$

On définit le titre massique de l'écoulement X comme le rapport du débit massique de gaz sur le débit total

$$X = \frac{W_g}{W_g + W_l} = \frac{\rho_g Q_g}{\rho_g Q_g + \rho_l Q_l} \tag{2.7}$$

De même, on peut passer de β à X grâce au rapport de densité des deux phases.

$$\frac{1}{X} - 1 = \left(\frac{1}{\beta} - 1\right)\frac{\rho_l}{\rho_g} = \left(\frac{1}{\varepsilon} - 1\right)\frac{1}{S}\frac{\rho_l}{\rho_g} \tag{2.8}$$

On définit les vitesses superficielles respectivement de la phase liquide, de la phase gazeuse et du mélange comme la vitesse moyenne qu'aurait une phase si elle occupait tout l'espace

de la conduite :

$$\begin{aligned} U_{gs} &= \frac{Q_g}{A_l + A_g} \quad (a) \\ U_{ls} &= \frac{Q_l}{A_l + A_g} \quad (b) \\ U_{2\phi} &= U_{gs} + U_{ls} \quad (c) \end{aligned} \tag{2.9}$$

De (a),(b),(c) et de la définition du taux de vide ε (équation (2.3)) et du titre volumique β (équation(2.4)) on déduit

$$\begin{aligned} U_{gs} &= \beta j_{2\phi} = \varepsilon u_g \\ U_{ls} &= (1-\beta) j_{2\phi} = (1-\varepsilon) u_l \\ U_{2\phi} &= \varepsilon u_g + (1-\varepsilon) u_l \end{aligned} \tag{2.10}$$

On définit la densité du mélange comme

$$\rho_{2\phi} = \varepsilon \rho_g + (1-\varepsilon)\rho_l \tag{2.11}$$

2.3 Caractéristiques des écoulements diphasiques

Plusieurs auteurs, dont Aloui (1994), rappellent que les écoulements diphasiques peuvent être classés selon les phases en présence (liquide, solide, gaz ou plasma (gaz ionisé)) les combinaisons possibles sont les suivantes :

- Mélange de deux liquides non miscibles (échangeurs à contact direct par exemple)
- Mélange solide liquide (transport de boue, etc.)
- Mélange gaz solide (transport pneumatique)
- Mélange gaz liquide (ébullition dans les réacteurs nucléaires)
- Mélange plasma solide (synthèse de nanoparticule)

Dans notre cas, nous nous intéresserons uniquement aux mélanges de fluides (gaz liquide ou deux liquides non miscibles) sans transfert de masse entre les deux fluides (ni réaction chimique ni changement de phase). Les écoulements diphasiques peuvent également être classés selon la distribution spatiale des interfaces. Les différentes organisations que peut prendre un écoulement diphasique sont appelées configurations d'écoulement.

2.3.1 Les configurations d'écoulement

Un écoulement diphasique est très complexe. Les deux phases ont des interfaces variables et déformables. L'organisation des deux phases a une importance critique pour déterminer les propriétés du mélange. Ainsi, le modèle par configuration d'écoulement tente de classifier

les écoulements en fonction de la configuration qu'adoptent les deux phases et de proposer des corrélations pour chaque configuration.

Deux interactions principales dirigent la configuration d'écoulement. Premièrement, les interactions des phases avec les parois des conduites à travers les forces de friction, deuxièmement, l'interaction des phases par l'intermédiaire des forces de tension de surface. L'observation a permis de classifier les écoulements selon différentes organisations. Dans le cas d'un écoulement interne de gaz et de liquide vertical concurrent (c'est-à-dire que les deux phases vont dans la même direction), les différentes organisations de l'écoulement sont généralement classées en cinq configurations d'écoulement présentées à la figure 2.3. Selon les auteurs, les définitions et le nombre de configurations peuvent légèrement varier. Différents classements présentés sous forme de carte seront présentés plus tard dans le document.

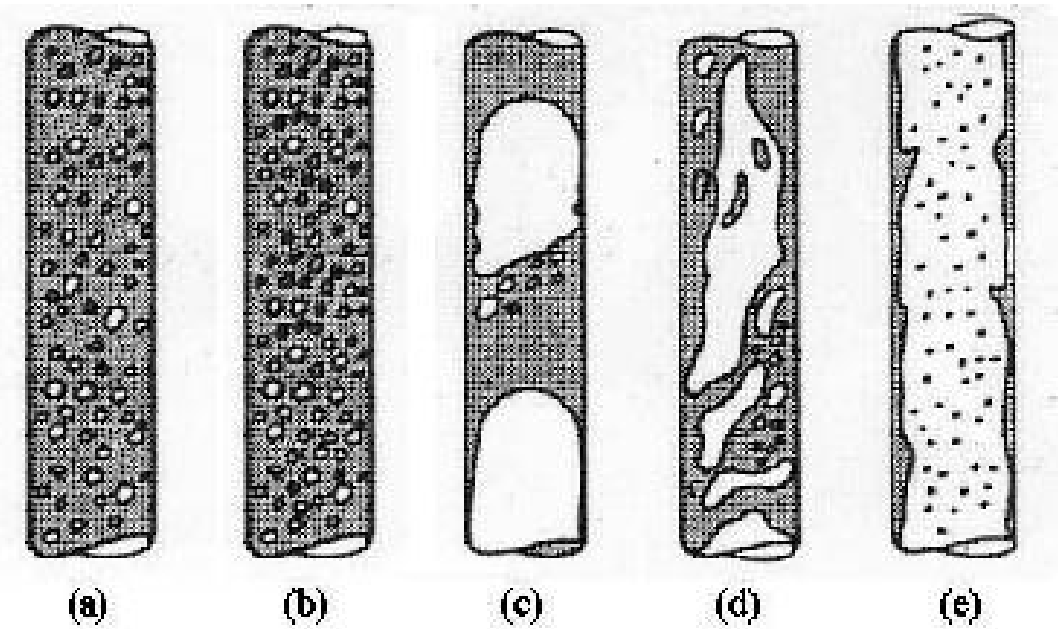

Figure 2.3 Configurations d'écoulements possibles pour une conduite circulaire et verticale : (a) écoulement à bulles dispersées, (b) écoulement à lit dense de bulles, (c) écoulement à bouchons, (d) écoulement agité et (e) écoulement annulaire

– (a) Régime à bulles séparées :
  La phase gazeuse de l'écoulement est repartie sous forme de bulles peu nombreuses et déformées car de tailles relativement élevées. Ce régime d'écoulement apparaît pour un mélange circulant à faible débit de gaz. Ainsi, l'écoulement vertical à bulles n'existe que pour de faibles vitesses superficielles de liquide (non-division des bulles), mais aussi pour de faibles vitesses superficielles de gaz afin de ne pas provoquer le phénomène de coalescence menant à la formation de poches d'air.

– (b) Régime à lit dense de bulles :
  En augmentant le débit de liquide, la phase gazeuse se divise sous l'effet des forces de turbulence. De fines bulles se dispersent dans le liquide qui constitue la phase continue. Le degré d'uniformité de la distribution de la phase gazeuse est notablement supérieur à celui observé dans un régime à bulles séparées (vitesse superficielle de liquide plus basse). La turbulence du mélange est suffisante pour que les bulles se fractionnent sans pouvoir se regrouper ensuite, le phénomène de coalescence est par conséquent supprimé. Il est alors envisageable de modéliser les fines bulles ainsi formées par des sphères rigides.
– (c) Régime à bouchons :
  En augmentant le débit de gaz, on atteint une valeur limite à partir de laquelle la phase gazeuse ne peut pas rester dispersée dans le liquide. La promiscuité est telle que la coalescence des bulles est forcée. Ce régime intervient d'autant plus rapidement que la turbulence du mélange est faible. Ainsi, un régime à bulles séparées évoluera plus facilement vers un régime à bouchons qu'un régime à lit dense de bulles. Une partie du gaz est présent sous la forme de poches, d'aspect cylindrique dont les extrémités supérieures sont de forme de calotte sphérique, de sections voisines de celle de la conduite. Ces poches de gaz, aussi appelées "Bulles de Taylor", impliquent l'existence de bouchons de liquide les séparant. Taitel *et al.* (1980) affirment que le film de liquide formé entre les bulles de Taylor et le tube s'écoule vers le bas de conduite c'est-à-dire dans le sens contraire de celui du mélange diphasique. Les bouchons sont composés de la phase liquide à l'intérieur de laquelle se trouve la partie restante du gaz non coalescée et encore sous forme de bulles de petite taille.
– (d) Régime agité :
  Le régime agité est assez similaire au régime à bouchons, il en constitue la continuité dans un schéma d'augmentation progressive de la proportion de gaz dans la conduite. Il est cependant bien plus chaotique et désordonné. Les poches de gaz deviennent plus étroites et se déforment de manière aléatoire. La concentration élevée de gaz dans les bouchons provoque une dislocation répétée des bulles de Taylor. Cette alternance de formations et d'effondrements des poches gazeuses induit un phénomène d'oscillations du mélange selon l'axe du tube. Le liquide s'accumule avant d'être de nouveau propulsé de manière ascendante par le gaz. Pour un mélange propulsé à un débit élevé, on observe une dispersion chaotique, mais néanmoins plus fine de la phase gazeuse dans la phase liquide. Le désordre accru de l'écoulement provoque un certain effacement de la séparation "grossière" des phases qui est caractéristique des écoulements à bouchons, donnant ainsi lieu à une structure plus homogène dans laquelle le mélange est plus intime.

– (e) Régime annulaire :

Lorsque la proportion et le débit de la phase gazeuse sont très élevés, le liquide ne peut plus être assimilé par l'écoulement et reste confiné aux parois de la conduite formant alors un anneau dont la face interne est ondulée par les turbulences. Le régime annulaire est ainsi caractérisé par la continuité de la phase gazeuse au cœur du tube et donc par une séparation quasi totale des phases. De fines gouttelettes sont cependant observées dans la colonne de gaz centrale.

Alors que les premiers travaux sur les écoulements diphasiques tendaient à modéliser ces écoulements comme des mélanges stationnaires, il est maintenant reconnu que toutes les configurations d'écoulement sont caractérisées par des structures périodiques (Azzopardi et Baker (2003)). Ces auteurs ont compilé les données provenant de dizaines de travaux sur les structures périodiques associées aux différentes configurations d'écoulement. Ils ont créé une banque de données contenant plus de 1250 points permettant d'identifier des tendances communes dans les fréquences caractéristiques associées aux écoulements diphasiques. Leur analyse mène à la conclusion que les propriétés fluctuantes des écoulements diphasiques, horizontaux et verticaux, pour toutes les configurations d'écoulement, peuvent être corrélées sur un graphique du nombre de Strouhal en fonction du paramètre de Lockhart-Martinelli et du titre massique. (cf. figure 2.4).

Ces propriétés fluctuantes ont été mises en évidence et exploitées par de nombreux chercheurs. Jones et Zuber (1975) et Cheng *et al.* (1998) ont suggéré d'utiliser la fonction de densité de probabilité (abréviation tirée de l'anglais : PDF) et la densité spectrale (PSD) des fluctuations du taux de vide comme indicateurs objectifs (et non qualitatifs) de la configuration d'écoulement. Tutu (1982) a employé une approche similaire, en utilisant les fluctuations de pression. Une revue détaillée des différentes techniques objectives utilisées pour déterminer la configuration d'écoulement est présentée par Han (1999).

Pour les écoulements à bulles, la PDF est caractérisée par un maximum prononcé pour les faibles taux de vide dû aux petites bulles dans l'écoulement. Pour les écoulements annulaires, les auteurs ont trouvé un maximum unique qui correspond à un taux de vide élevé. Les écoulements à bouchons sont caractérisés par la présence de deux maxima. Cette distribution de PDF à deux maxima correspond à un régime d'écoulement périodique. Vince et Lahey (1982) ont recommandé l'utilisation de la variance comme indicateur objectif de la configuration d'écoulement. Des études similaires de PDF pour la reconnaissance de configurations ont été menées par Merilo *et al.* (1977) (cf. figure 2.5), Das et Pattanayak (1994) et Costigan et Whalley (1996).

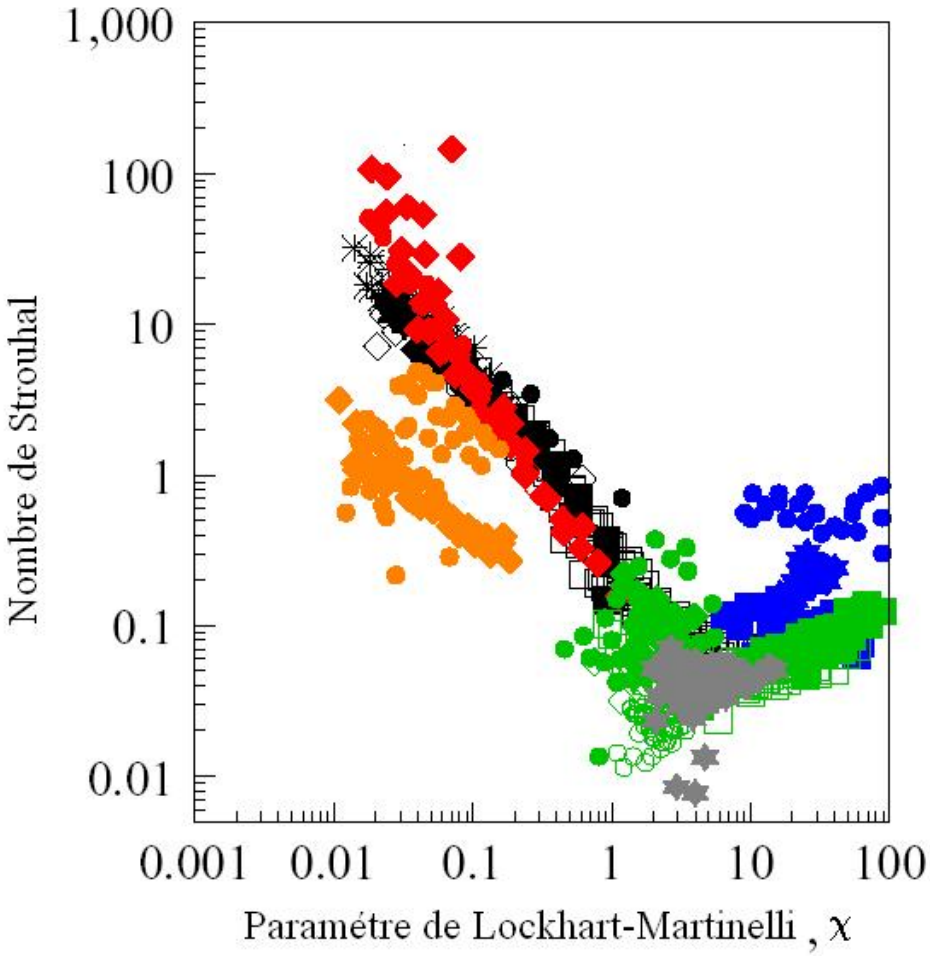

Figure 2.4 Graphique proposé par Azzopardi et Baker (2003)

2.3.2 Les cartes d'écoulement

Une carte d'écoulement est une représentation généralement 2D des domaines d'existence des configurations d'écoulement. Chaque auteur utilise des coordonnées différentes pour représenter une carte d'écoulement. Il n'existe pas de consensus sur le meilleur système ; la qualité de la carte d'écoulement dépend plutôt du choix des paramètres fixant les frontières des transitions. Cependant, les vitesses superficielles du gaz et du liquide sont fréquemment utilisées. En effet, ces deux grandeurs sont facilement mesurables en laboratoire. Les domaines d'existence dépendent a priori de la pression, de la température, du diamètre intérieur du tube, des viscosités et densités des deux phases, de la tension de surface, etc. Ainsi les frontières des domaines sont des fonctions des paramètres du problème. De ce fait, de nombreuses cartes existent selon les conditions d'écoulement (interne ascendant, descendant, concurrent, vertical, horizontal, en micro-gravité, etc.)

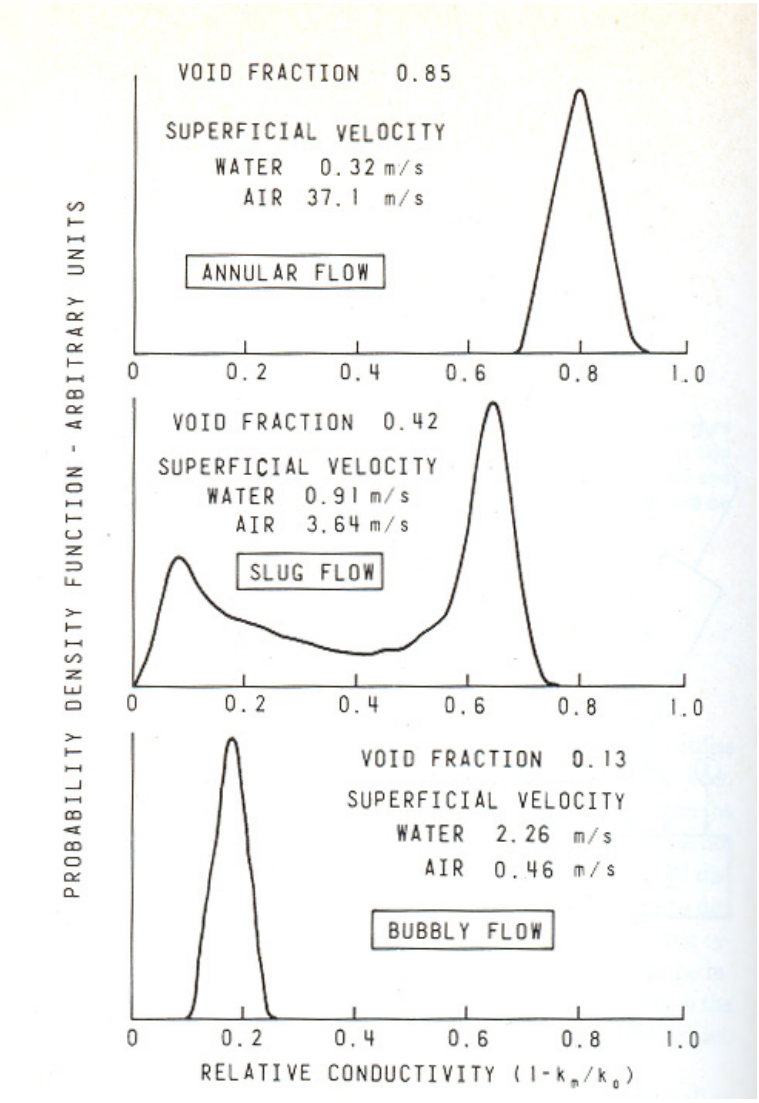

Figure 2.5 Fonction de densité de probabilité du mesure de la conductivité (quasi proportionnel au taux de vide) tiré de Merilo *et al.* (1977)

Plusieurs auteurs menèrent des études pour prédire les transitions de régimes sur un écoulement diphasique gaz-liquide. La première carte fut celle de Baker (1954) pour les écoulements diphasiques internes horizontaux. Dans le cas des écoulements ascendants en conduit vertical, trois principales publications sont reconnues pour leur qualité. La première fut émise par Hewitt et Robertson (1969) et reprise par Collier et Thome (1996), ensuite Taitel et Dukler (1976) et Mc Quillan (1985) ont proposé leurs travaux au début de la décennie suivante.

a) Carte de Hewitt et Robertson

La carte d'écoulement élaborée par Hewitt et Robertson (1969) est fréquemment reprise dans la littérature. La figure 2.6 donne un exemple de cette carte pour un écoulement vertical ascendant eau-air. Hewitt et Robertson (1969) utilisent comme système de coordonnées les pressions dynamiques du liquide et du gaz en coordonnées logarithmique. Les pressions dynamiques sont obtenues en multipliant la masse volumique du fluide par le carré de sa vitesse superficielle. Les cartes d'écoulement de Hewitt et Robertson (1969) sont majoritairement élaborées à partir de reconnaissances visuelles puis par corrélation des variables de l'écoulement diphasique.

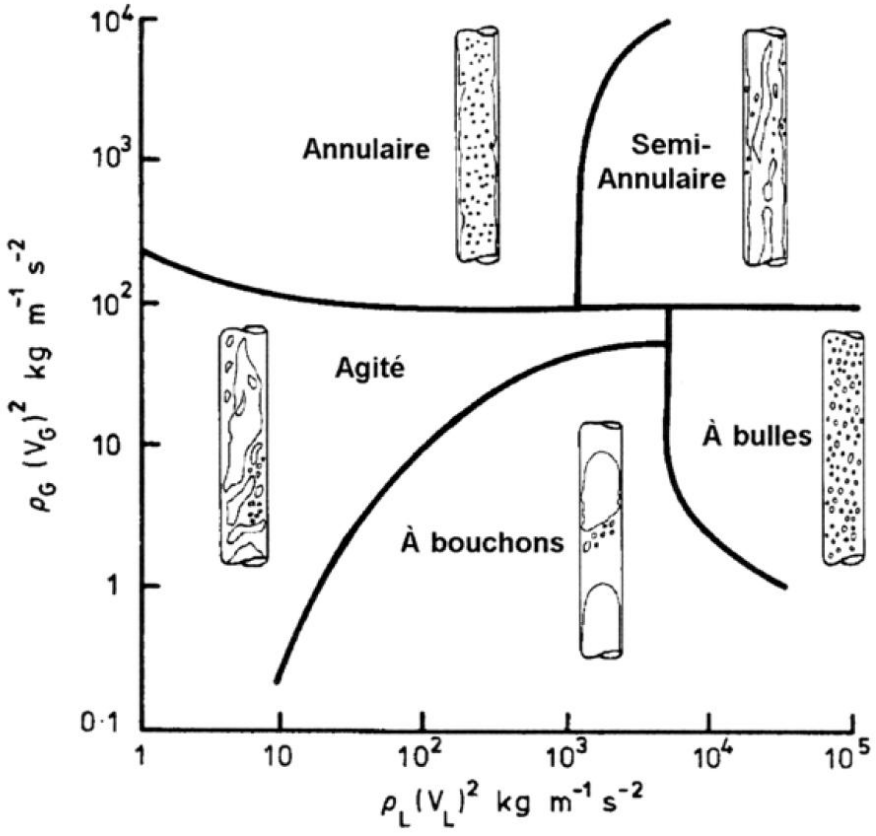

Figure 2.6 Carte d'écoulement de Hewitt et Robertson (tirée de Collier) pour un écoulement vertical ascendant eau-air

b) La carte de Taitel *et al.*

La représentation de Taitel *et al.* (1980) est peu répandue dans la littérature et ce pour des raisons mal définies car la qualité de leur carte d'écoulement est pourtant avérée. Celle-ci tient principalement à de solides fondements théoriques utilisant entre autres des calculs de dissipation d'énergie. La figure 2.7 montre une carte établie pour un écoulement ascendant dans une conduite de diamètre intérieur $D = 50mm$. Taitel *et al.* (1980) considèrent uniquement les vitesses superficielles comme coordonnées pour leur carte.

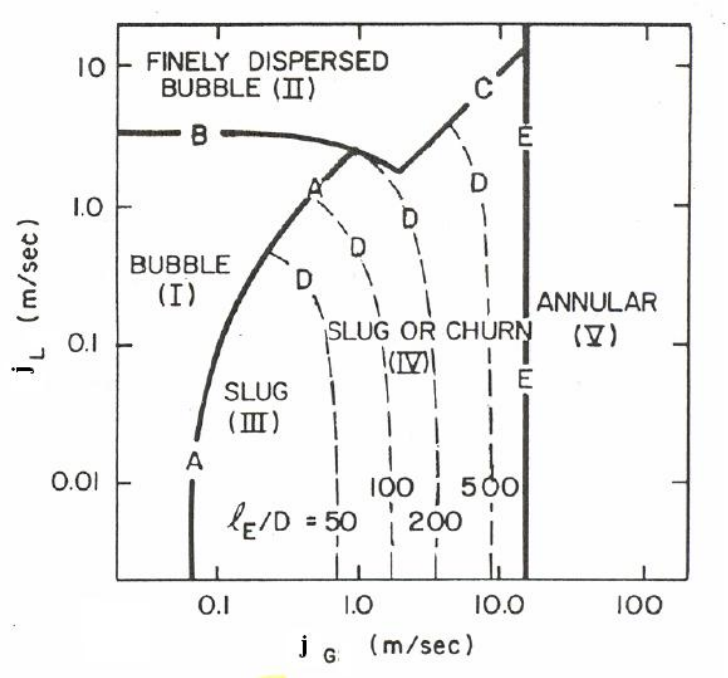

Figure 2.7 Carte d'écoulement de Taitel *et al.* (1980), écoulement ascendant eau-air ; $D = 50$ mm.

c) La carte de McQuillan

La représentation de Mc Quillan (1985) reprend certains concepts théoriques déjà employés par Taitel et al. et tente d'en ajouter certains autres venant d'observations basées sur des études en écoulement horizontal. Cette démarche mène à l'élaboration de cartes d'écoulements dont l'aspect semble proche des cartes créées par Taitel et al.. Un exemple de carte, pour un écoulement ascendant vertical eau-air dans un conduit de diamètre intérieur $D = 51$ mm, est montré sur la figure 2.8. Le système de coordonnées est identique à celui adopté par Taitel et al., c'est-à-dire la vitesse superficielle du liquide en ordonnée et la vitesse superficielle du gaz en abscisse. Les coordonnées sont également affichées sur deux échelles logarithmiques. Bien que l'apparence générale de la carte soit proche de celle de Taitel et al., des différences significatives dans la position (et dans le nombre) des frontières de transition existent.

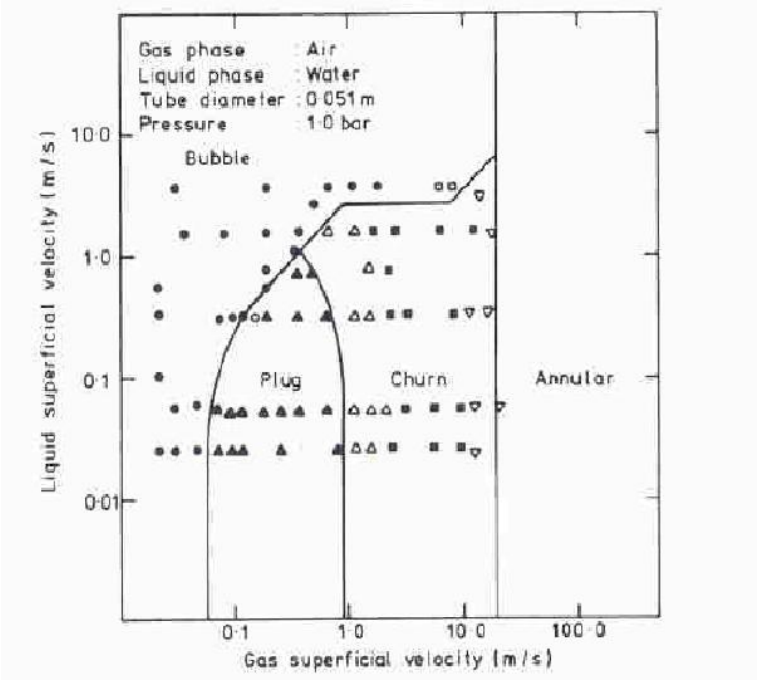

Figure 2.8 Carte d'écoulement de Mc Quillan (1985), écoulement ascendant-eau-air, D = 51 mm.

Pour les écoulements transverses on peut souligner quelques travaux : Grant et Murray (1972), Kondo et Nakajima (1980) ont identifié des régimes d'écoulement par observation visuelle d'écoulement diphasique air-eau transverse. Ils ont proposé des cartes d'écoulement, la plupart des auteurs s'entendent pour identifier trois régimes d'écoulement à bulles, bouchons et annulaire. L'écoulement à bouchons est parfois nommé écoulement intermittent, et l'écoulement annulaire écoulement à gouttelettes. Pettigrew *et al.* (1988) ont également reporté l'existence de ces régimes et les ont identifiés par observation visuelle corrélée aux phénomènes de vibrations induites par l'écoulement sur les tubes. Hahne *et al.* (1990) ont utilisé les mesures de taux de vide par fibre optique. Ulbrich et Mewes (1994) ont déterminé une carte d'écoulement par observations visuelles et mesure de perte de charge. Ueno *et al.* (1995) ont employé des capteurs pour mesurer le taux de vide local, la fréquence des bulles et la vitesse de l'interface. Jones et Zuber (1975) ont les premiers classifié les différents écoulements par la fonction de densité de probabilité du taux de vide. Comme pour les écoulements internes la fonction de densité de probabilité présente un pic à faible taux de vide pour les écoulements à bulles, deux pics pour les écoulements à bouchons ou intermittents et un pic à taux de vide élevé pour les écoulements annulaires.

a) La Carte de Pettigrew et Taylor (2003)

La carte des régimes d'écoulement présenté à la figure 2.9 par Pettigrew et Taylor (2003) a été élaborée à l'aide des données de Grant (1975). Elle est séparée en trois régions : écoulement à bulles, à gouttelettes (gouttelettes de liquide contenues dans un écoulement de gaz) et intermittent (description dans Pettigrew et Taylor (2003)).

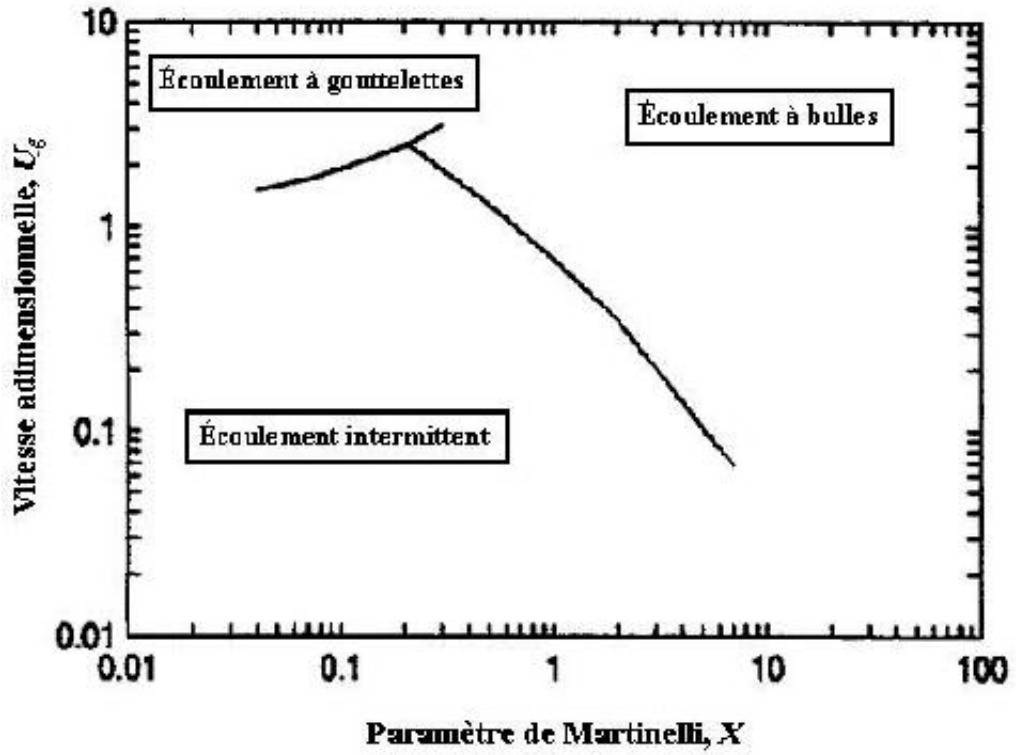

Figure 2.9 Carte de configurations d'écoulements verticaux pour un faisceau de tubes compact (Pettigrew et Taylor (2003))

Les écoulements à bulles et gouttelettes sont considérés comme des régimes continus tandis que le régime intermittent est hautement non stationnaire, ce qui affecte grandement la structure. Cette configuration doit donc être évitée. Les paramètres en abscisse et en ordonnée de la carte sont respectivement le paramètre de Martinelli (χ) et la vitesse adimensionnelle de la phase gazeuse ($\overline{U_g}$). Ces derniers sont définis de la façon suivante :

$$\chi = \left(\frac{1-\varepsilon}{\varepsilon}\right)^{0.9} \left(\frac{\rho_l}{\rho_g}\right)^{0.4} \left(\frac{\mu_l}{\mu_g}\right)^{0.1} \tag{2.12}$$

$$\overline{U_g} = \frac{W_{it}}{\left(d_e g \rho_g (\rho_l - \rho_g)\right)^{1/2}} \tag{2.13}$$

où $W_{it} = \rho_{2\phi} j_{2\phi}(p/(p-D))$ est le flux massique inter-tubes, $d_e = 2(p-D)$ est le diamètre hydraulique équivalent, p le pas et D le diamètre des tube (cf. figure 2.10).

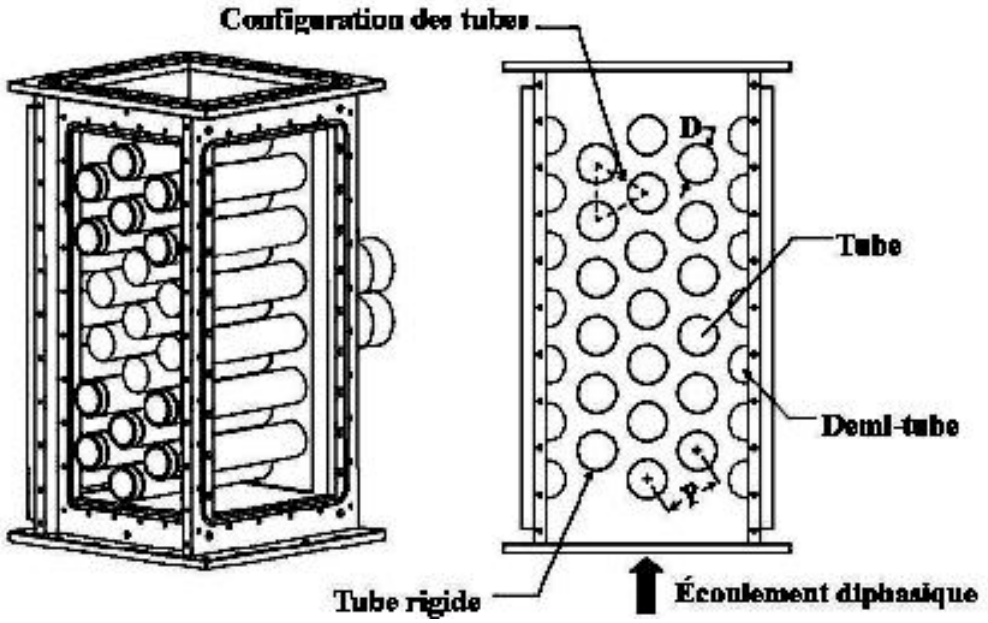

Figure 2.10 Paramètres géométriques et vue isométrique de la section d'essais.

b) La Carte de Noghrehkar et al.

La carte élaborée par Noghrekar *et al.* (1999) est présentée à la figure 2.11. Ils ont mesuré le taux de vide local à l'aide d'une sonde à résistivité. Ils ont caractérisé les différents écoulements en utilisant la fonction de densité de probabilité.

2.4 L'amortissement diphasique

Un tube flexible, soumis à une vibration, peut être amorti ou excité par le fluide qui y circule. Lorsqu'un mélange diphasique circule dans un tube, ce dernier est fortement amorti. L'amortissement sous écoulement diphasique est bien plus important que sous écoulement monophasique. Carlucci (1980) et Carlucci et Brown (1983) proposent de décomposer l'amortissement total d'un tube soumis à un écoulement en tenant compte des termes suivants :

- ζ_s : amortissement de la structure à vide ;
- ζ_v : amortissement visqueux ;
- ζ_f : amortissement causé par les forces fluide élastiques ;
- $\zeta_{2\phi}$: la composante dite diphasique de l'amortissement.

Ils proposent ainsi de définir l'amortissement total du tube par la somme de ses composantes,

$$\zeta_t = \zeta_s + \zeta_v + \zeta_f + \zeta_{2\phi} \tag{2.14}$$

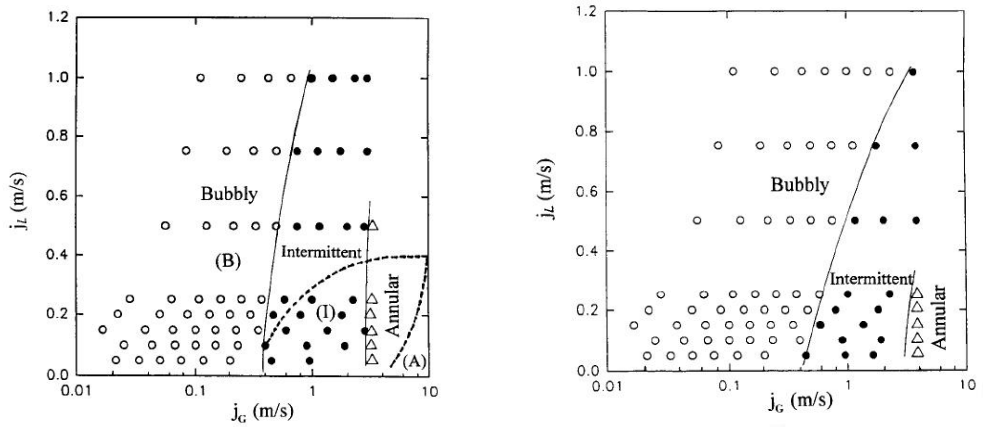

Figure 2.11 Carte tirée de Noghrekar *et al.* (1999) pour les écoulements transverses dans un faisceau de tubes en ligne (gauche) et triangle tourné (droite) en pointillé la carte de Ulbrich et Mewes (1994)

L'amortissement de la structure à vide ζ_s correspond à l'énergie dissipée par la structure du tube et, par conséquent, est indépendant de l'écoulement.

L'amortissement visqueux ζ_v représente la perte d'énergie au sein du fluide contraint de bouger par le mouvement du tube.

L'amortissement causé par les forces fluide élastiques ζ_f est dû à l'effet de vitesse du fluide (cf. Baj (1998)). Ceci s'interprète directement en calculant la différence entre les énergies cinétiques du fluide en sortie et en entrée du système et ce en tenant compte du déplacement du tube (cf. de Langre (2001)). Si le tube est encastré, son déplacement aux extrémités est nul et, par simple conservation de la masse, les énergies cinétiques du fluide en sortie et en entrée du système sont identiques, donc cette composante de l'amortissement est nulle. En revanche, à chaque fois que le mouvement du solide perturbera l'écoulement en augmentant l'énergie cinétique entre l'amont et l'aval, ce dernier aura un effet amortissant sur le mouvement du solide.

L'amortissement diphasique $\zeta_{2\phi}$ est introduit pour tenir compte que l'amortissement sous écoulement diphasique est plus important que celui calculé avec le modèle monophasique. La figure 2.12 extraite de Carlucci (1980) montre la répartition de chacun de ces termes dans la composition de l'amortissement total. On y remarque que l'amortissement diphasique $\zeta_{2\phi}$ est prépondérant et que son comportement est très différent de celui des autres composantes de l'amortissement. Les essais de Carlucci correspondent à un écoulement axial externe (confiné).

Pour un écoulement interne, les valeurs des diverses composantes de l'amortissement seront différentes. Cependant, les mécanismes d'amortissement étant les mêmes, l'allure de la

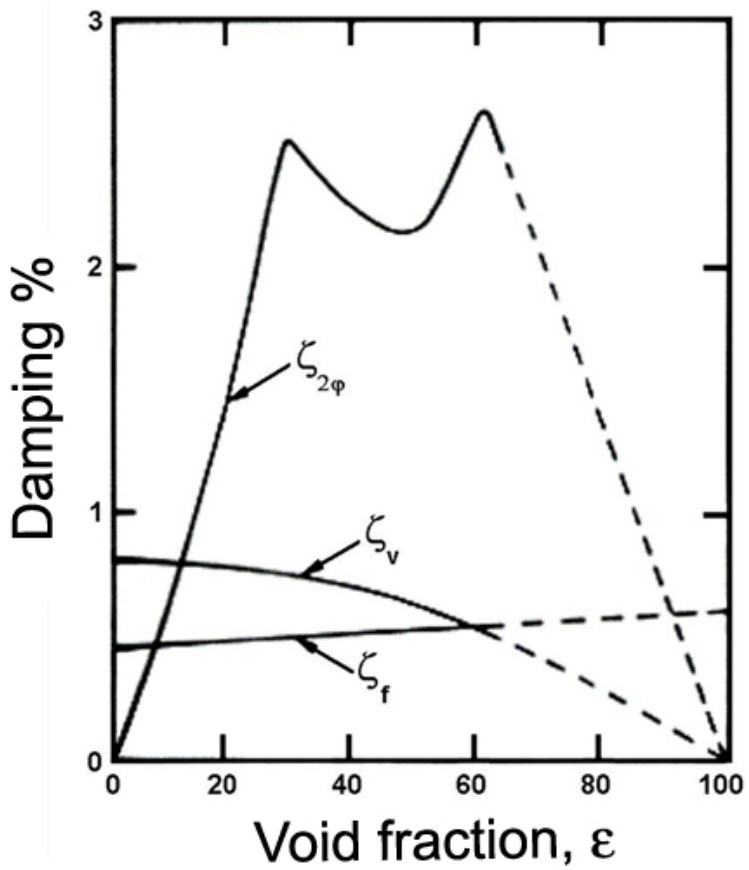

Figure 2.12 Évolution des différents composants de l'amortissement avec le taux de vide (cf. Carlucci (1980)).

courbe d'amortissement diphasique $\zeta_{2\phi}$, selon le taux de vide ε, reste semblable.

2.5 Les mesures de l'amortissement

Deux techniques principales sont utilisées pour mesurer l'amortissement d'une structure. La première, nommée décrément logarithmique, utilise la réponse impulsionnelle ou la réponse libre à un déplacement initial. Le mouvement de la structure X a alors la forme :

$$X = A_0 e^{-\zeta\omega_0 t} \cos\left(\sqrt{1-\zeta^2}\omega_0 t + \varphi\right) \tag{2.15}$$

Les maxima X_i de l'équation précédente vérifient :

$$ln\left(\frac{X_i}{A_0}\right) = -\zeta\omega_0 t_i \tag{2.16}$$

L'autre solution est de supposer que l'écoulement génère sur la structure une force aléatoire avec un contenu spectral neutre. La transformée de Fourier du déplacement du tube permet de mesurer la fonction de transfert H :

$$|H| = \frac{1}{\sqrt{\left(1 - \left(\frac{\omega}{\omega_0}\right)^2\right)^2 + 4\zeta^2 \left(\frac{\omega}{\omega_0}\right)^2}} \tag{2.17}$$

Les deux méthodes permettent de déduire l'amortissement ζ. Plus de détails sur l'amortissement diphasique et sa mesure sont présentés dans les articles des chapitres 4 et 5.

2.6 Les mesures du taux de vide

Les mesures du taux de vide sont importantes pour bien définir l'écoulement et le caractériser. En effet, comme exposé précédemment, la mesure du taux de vide et, en particulier, la fonction de densité de probabilité du taux de vide est un outil très largement utilisé pour classifier de façon objective les configurations d'écoulement. Il existe plusieurs techniques pour mesurer le taux de vide dont les plus populaires sont les sondes optiques, la gamma densitométrie et les sondes à capacitance.

2.6.1 Les sondes optiques

a) Principe

Le rôle des sondes optiques est de mesurer le taux de vide local, la vitesse de la phase gazeuse et la taille des bulles des écoulements diphasiques. Les sondes optiques sont composées d'une fibre optique raccordée à une diode laser. Le faisceau lumineux émis par le laser se propage à l'intérieur de la fibre. Il arrive au bout de la fibre et rentre en contact avec l'écoulement. En fonction du milieu rencontré (eau ou air), il sera réfléchi dans le sens inverse avec une certaine intensité lumineuse. En effet, l'indice de réfraction (rapport entre la vitesse de la lumière dans le vide et la vitesse de propagation dans un milieu donné) de l'eau est plus fort que l'indice de réfraction de l'air. Le signal retourne donc dans la fibre et est séparé du signal sortant. Il est transformé ensuite en courant puis en tension à l'aide d'une photodiode. La tension est alors amplifiée par un circuit électrique et peut être visualisée sur un oscilloscope. Le signal observé a une forme de créneau. Un fois, le signal amplifié et traité, il permet d'obtenir les vitesses, les tailles des bulles ainsi que les taux de vide pour une certaine durée d'acquisition. L'utilisation des sondes optiques pour la mesure du taux de vide a été décrite par Morris *et al.* (1987)

b) Conception des expériences

Les résultats obtenus vont dépendre du type de sonde utilisé. Il existe deux configurations : les sondes simples ou les sondes doubles. Les sondes simples sont constituées d'une seule fibre optique. Nous obtenons ainsi les informations moyennes telles que le taux de vide local et la taille moyenne des bulles grâce à la vitesse des phases. Les sondes doubles sont constituées de deux fibres optiques. Les deux pointes des fibres sont placées dans un même tube et ajustées avec un décalage axial d'une centaine de microns. Cette distance entre pointes est ensuite mesurée. Ce type de sonde permet donc de mesurer des vitesses locales, car une même bulle va passer sur les deux pointes dont on connaît l'écartement. On peut aisément trouver la taille des bulles ainsi que le taux de vide local.

Le but des fibres optiques est de transporter de la "lumière ". Une fibre optique est toujours composée de trois couches : le cœur, la gaine et la couche protectrice (cf. figure 2.13). Le signal est contenu à l'intérieur du cœur grâce à la gaine (différence d'indice de réfraction) et est protégé de l'extérieur par la troisième couche (protection thermique, chimique, mécanique)

Le signal émis dans la fibre va se propager au sein du cœur avec un certain angle. Quand le signal arrive à la limite entre le cœur et la gaine, il y a réflexion symétrique par rapport à la normale au point de contact. Pour que le signal soit totalement réfléchi dans le cœur, il est nécessaire que le cœur possède un indice plus fort que la gaine optique.

Cette différence d'indice est rendue possible grâce au dopage du cœur ou de la gaine. Par exemple, on peut augmenter l'indice du cœur en introduisant du germanium ou on peut doper la gaine en fluorine pour diminuer son indice. Une différence minime (quelques centièmes) d'indice de réfraction entre la gaine et le cœur permet d'obtenir le résultat souhaité. Il existe deux grandes familles dans les fibres optiques : les fibres monomodes et les fibres multimodes.

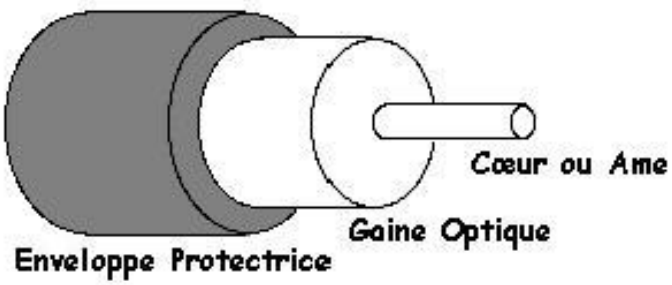

Figure 2.13 Différentes couches d'une fibre optique

Il existe deux sortes de fibres multimodes à saut et à gradient d'indice.

- Fibre à saut d'indice :

Elle est constituée d'un cœur et d'une gaine optique en verre ayant différents indices de réfraction. Deux faisceaux lumineux dans de telles fibres ne parcourent pas la même distance. Il y a donc une déformation du signal dans le temps. La fibre n'est efficace que sur de courtes distances.

- Fibre à gradient d'indice :

Le cœur de la fibre optique à gradient d'indice possède des couches de verre successives. Ces couches modifient graduellement l'indice de réfraction. Ainsi, l'indice de réfraction varie de façon parabolique avec la distance radiale, le maximum étant situé au niveau de l'axe. Les rayons guidés suivent une trajectoire d'allure sinusoïdale. La gaine, d'indice différent (inférieur) n'intervient pas directement, elle élimine uniquement les rayons trop inclinés. L'avantage essentiel de ce type de fibre, par rapport à la fibre multimode à saut d'indice, est de minimiser la dispersion du temps de propagation. Il y a donc une meilleure cohérence à la réception du signal.

La fibre monomode a le cœur si fin que le signal se propage suivant un seul mode en ligne droite. La dispersion du signal est quasiment nulle. Le signal est donc très peu déformé. Cette fibre est utilisée essentiellement pour les sites à distance. Le petit diamètre du cœur demande une grande puissance d'émission et les diodes laser sont relativement onéreuses.

2.6.2 La Gamma-densitométrie

Le principe de cette méthode est de calculer le taux d'absorption de rayons Gamma à travers l'écoulement. Ce principe nécessite des précautions en plus d'être relativement onéreux. L'utilisation de rayons Gamma pour la mesure du taux de vide a été décrite par Teyssedou *et al.* (1992)

2.6.3 Les sondes à capacitance

a) Principe

La capacitance et la conductance de deux électrodes dépendent de la nature de la matière entre les électrodes (le diélectrique). L'eau et l'air présentant des différences significatives de propriétés électriques, il est possible de déduire le taux de vide entre les deux électrodes en mesurant la capacitance et la conductance. Hewitt (1978) et Teyssedou *et al.* (1988) décrivaient les techniques de mesure du taux de vide par capacitance comme très prometteuses. Elles permettent une mesure quasi instantanée. Cette technique comporte cependant quelques désavantages soulignés par Das et Pattanayak (1994) et Duncan *et al.* (1993) : polarisation, écaillage, temps de démouillage des électrodes, changement de conductivité du liquide, sensibilité de la calibration à la configuration d'écoulement. Elkow et Rezkallah (1996) ajoutent les

effets non linéaires de bord et de géométrie ainsi que les bruits électromagnétiques extérieurs. Hewitt (1978) ainsi que la plupart des auteurs insistent donc sur la nécessité d'effectuer une calibration à l'aide d'une deuxième technique de mesure. En effet, chaque système de mesure conserve des effets impossibles à prévoir a priori. La mesure du taux de vide à l'aide des valves à fermeture rapide est la technique de calibration la plus populaire cf. Duncan *et al.* (1993), Elkow et Rezkallah (1996). La difficulté majeure des jauges à impédance reste leur sensibilité aux configurations d'écoulement.

b) Design des électrodes

Les travaux de Merilo *et al.* (1977) et Tollefsen et Hammer (1998) semblent donner des solutions pour limiter la dépendance de la mesure à la configuration de l'écoulement. Merilo *et al.* (1977) proposent de mesurer l'impédance moyenne d'une série de condensateurs disposés en cercle alimentés avec un déphasage. Ainsi, cela permet de créer un champ électrique en rotation (cf. figure 2.14) et d'éliminer une grande partie de la dépendance de la mesure de la configuration d'écoulement (cf. figure 2.15).

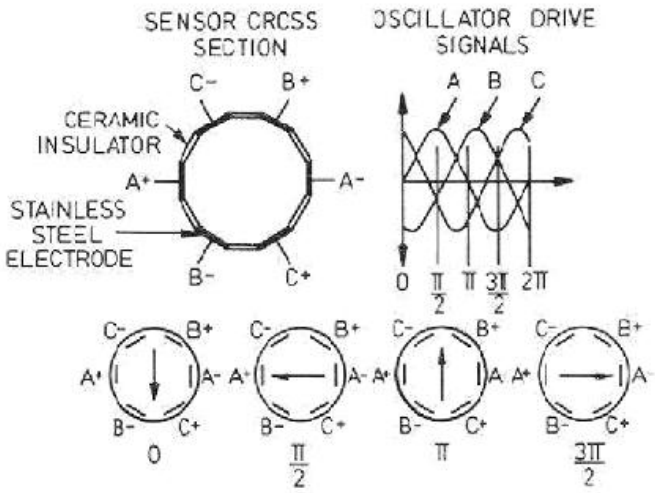

Figure 2.14 Champ électrique en rotation proposé par Merilo *et al.* (1977)

Tollefsen et Hammer (1998) obtiennent des résultats similaires avec des électrodes planes hélicoïdales (cf. figure 2.16), créant ainsi un champ électrostatique vrillé à 180^o. Leurs calculs laissent espérer des résultats équivalents (cf. figure 2.17).

Jaworek et Krupa (2004) conseillent de rendre la capacitance prédominante par rapport à la conductance qui est plus sensible à la température. Elkow et Rezkallah (1996) obtiennent une phase de -89^o pour une fréquence de 1 MHz. La capacitance est affectée par la pureté de l'eau, l'utilisation d'eau désionisée et distillée est préférable, afin d'éviter la corrosion et de

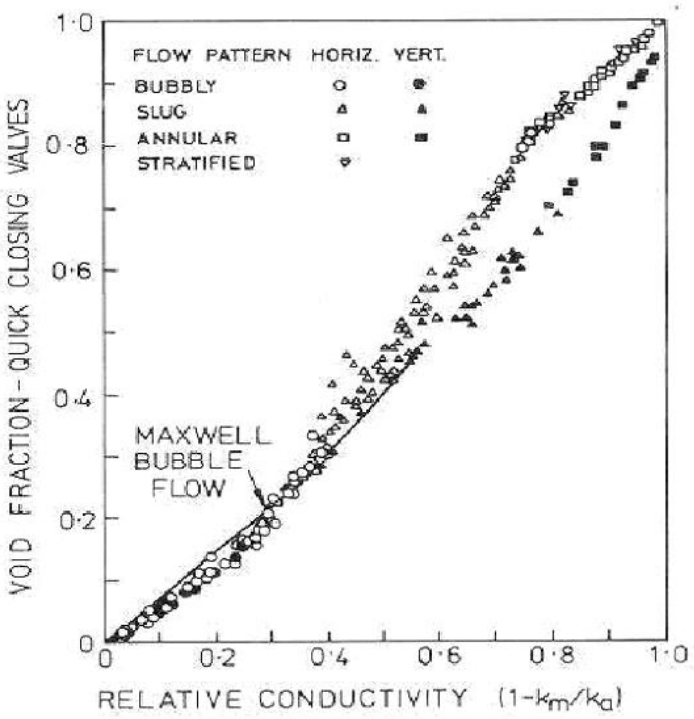

Figure 2.15 Résultat de la calibration de Merilo et al.

limiter l'effet de la conductance. L'effet de la température est important et il faut faire des étalonnages supplémentaires si on opère à d'autres températures. Scott *et al.* (1985) quant à eux effectuent une comparaison entre des électrodes à l'intérieur du tube et à l'extérieur. Ils soulignent l'effet non linéaire des électrodes posées à l'extérieur du tube.

Jaworek et Krupa (2004) ont mis au point une technique de mesure à haute fréquence (80 MHz),suivant les recommandations de Elkow et Rezkallah (1996); Tollefsen et Hammer (1998). L'auteur se propose d'éliminer la composante résistive à moins de 1% soit pour de l'eau une fréquence de 80 MHz et une phase de 82^o.

2.7 Modèles couramment utilisés

Les modèles couramment employés pour l'analyse des écoulements diphasiques consistent à formuler les équations classiques de conservation de la mécanique des fluides en supposant un des deux modèles suivants (Wallis (1969)).

1. Approche par moyennage des équations Navier-Stockes

   Ce modèle nécessite des relations de fermeture car le processus de moyennage introduit de nouvelles variables. Le modèle de fermeture le plus simple est le modèle homogène, le mélange diphasique étant considéré comme un seul fluide dont les propriétés physiques

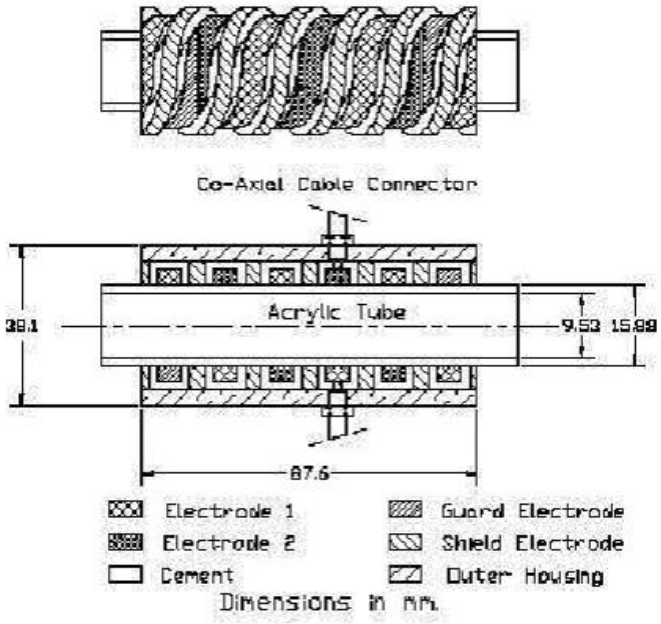

Figure 2.16 Design proposé par Tollefsen et Hammer (1998)

correspondent aux propriétés moyennes de chacune des phases.

2. Approche par configurations d'écoulement, où des corrélations sont formulées selon chaque configuration d'écoulement (cf. section 2.3.1)

2.7.1 Moyennage dans l'espace des équations de Navier-Stokes

La plupart des études théoriques s'appuient sur les équations de Navier-Stokes décrivant les deux fluides et moyennées dans l'espace. Les indices k=(g ou l) se rapportent respectivement au gaz ou au liquide, les exposants ^{i} et ^{w} indiquent que la variable est liée à l'interface gaz-liquide ou à la paroi. On notera avec un $\langle\rangle$, les variables moyennées. Le principe du moyennage dans l'espace des équations de Navier-Stokes est notamment exposé dans le cours de Teyssedou (2005)

Dans le cas où la gravité est la seule force massique, les équations de Navier-Stokes

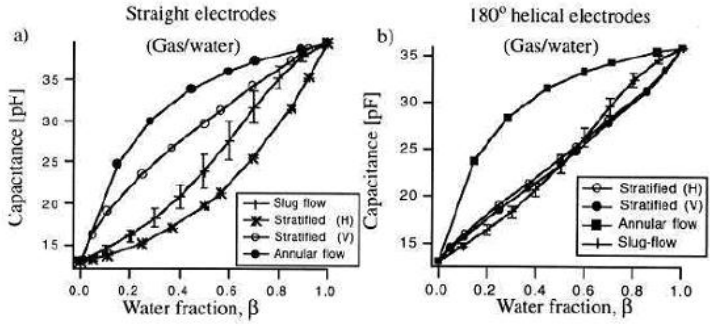

Figure 2.17 Calcul effectué par Tollefsen et Hammer (1998)

s'expriment :

- équation pour la conservation de la masse :

$$\frac{\partial \rho_k}{\partial t} + \nabla \cdot (\rho_k \vec{v_k}) = 0$$

- équation pour la conservation de la quantité de mouvement :

$$\frac{\partial \rho_k \vec{v_k}}{\partial t} + \nabla \cdot (\rho_k \vec{v_k} \otimes \vec{v_k}) = \rho_k \vec{g} - \nabla P_k + \nabla \cdot \bar{\bar{\tau}}_k$$

- équation pour l'énergie interne $e_k = C_p.T_k$:

$$\rho_k \frac{\partial e_k}{\partial t} + \rho_k (\nabla e_k . \vec{v_k}) = -P_k \nabla \cdot \vec{v_k} + \Phi_k - \nabla \cdot (-k_k \vec{\nabla} T_k) \qquad (2.18)$$

Le terme Φ_k représente la fonction de dissipation :

$$\Phi_k = -\frac{2}{3}\mu_k (\nabla \cdot \vec{v_k}) \bar{\bar{\mathbb{I}}} + \mu_k ([\nabla \vec{v_k}] + [\nabla \vec{v_k}]^t)) \odot \nabla \vec{v_k}$$

- équation d'état des gaz parfaits :

$$P_g = \rho_g R T_g$$

Le terme $-k_k \vec{\nabla} T_k$ représente le flux de chaleur par conduction où k_k désigne le coefficient de conduction du fluide (loi de Fourier). Le $\odot$ exprime le produit tensoriel contracté deux fois.

Enfin les conditions limites (On note $[\![f_k]\!] = f_g + f_l$) :

a) Pour le transfert de masse :

$$\begin{aligned} [\![\rho_k (\vec{v_k} - \vec{v^i}) . \vec{n_k^i}]\!] &= 0 \\ \rho_k (\vec{v_k} - \vec{v^i}) . \vec{n_k^i} &= \Gamma_k \end{aligned} \qquad (2.19)$$

Γ_k représente le flux massique qui se transforme de la phase 'k' vers l'autre phase (ex : vaporisation).

S'il n'y a pas de transfert de masse

$$\begin{aligned} & \rho_l (\vec{v_l} - \vec{v^i}) . \vec{n_l^i} = \rho_g (\vec{v_g} - \vec{v^i}) . \vec{n_g^i} = 0 \\ \text{ou} \quad & (\vec{v_l} - \vec{v_g}) . \vec{n_l^i} = 0 \end{aligned} \qquad (2.20)$$

b) Pour le transfert de la quantité de mouvement

$$[\![-P_k\vec{n_k^i} + (\bar{\bar{\tau}}_k + \bar{\bar{\tau}}_k^{Re}.\vec{n_k^i} - \rho\vec{v_k}(\vec{v_k} - \vec{v^i}).\vec{n_k^i}]\!] = \frac{2\gamma}{a}\vec{n_l^i} \tag{2.21}$$

avec γ, la tension de surface, et a le rayon local de la "bulle".

Nous introduisons la fonction χ_k indicatrice de phase :

$$\chi_k(\vec{x},t) = \begin{cases} 1, \text{ si la phase k est présente en } (\vec{x},t) \\ 0, \text{ sinon} \end{cases} \tag{2.22}$$

Les dérivées de χ_k sont donc nulles partout sauf aux interfaces. On distingue deux types d'interface : l'interface gaz-liquide notée avec l'exposant ^{i} et l'interface avec les parois notée avec l'exposant ^{w}. En supposant les parois immobiles, donc $\vec{v_k}\delta^w = 0$, nous obtenons :

$$\begin{aligned}
\frac{\partial\chi_k}{\partial t} &= -\vec{v^i}.\vec{n_k^i}\delta^i + 0 \\
\nabla\chi_k &= \vec{n_k^i}\delta^i + \vec{n_k^w}\delta^w \\
\vec{v_k}\nabla\chi_k &= \vec{v_k}\vec{n_k^i}\delta^i + 0 \\
\vec{v_k}\vec{v_k}\nabla\chi_k &= \vec{v_k}\vec{v_k}\vec{n_k^i}\delta^i + 0 \\
\bar{\bar{\tau}}_k^{Re}\nabla\chi_k = -\rho_k\vec{v_k'}\vec{v_k'}\nabla\chi_k &= \underbrace{-\rho_k\vec{v_k'}\vec{v_k'}\vec{n_k^i}\delta^i}_{\text{interface gaz-liquide}} + \underbrace{0}_{\text{interface à la paroi}}
\end{aligned} \tag{2.23}$$

Avec δ^i et δ^w les fonctions de Dirac respectivement non nulles à l'interface gaz-liquide et à la paroi.

Notons la moyenne dans l'espace

$$\langle\phi\rangle(\vec{x},t) = \frac{1}{L^3}\int_{x_1+L/2}^{x_1-L/2}\int_{x_2+L/2}^{x_2-L/2}\int_{x_3+L/2}^{x_3-L/2}\phi(\vec{x}',t)dx_3'dx_2'dx_1' \tag{2.24}$$

Afin d'intégrer sur un volume de contrôle indépendant de la présence des phases, on multiplie les équations de Navier-Stockes par χ_k. On effectue ensuite l'opération de moyenne dans l'espace. Certains auteurs utilisent la notation $\langle\phi\rangle^k = \langle\chi_k\phi\rangle$

$$\begin{aligned}
&\langle\chi_k\frac{\partial\rho_k}{\partial t}\rangle + \langle\chi_k\nabla\cdot(\rho_k\vec{v_k})\rangle = 0 \\
&\langle\chi_k\frac{\partial\rho_k\vec{v_k}}{\partial t}\rangle + \langle\chi_k\nabla\cdot(\rho_k\vec{v_k}\otimes\vec{v_k})\rangle = \langle\chi_k\rho_k\vec{g}\rangle - \langle\chi_k\nabla P_k\rangle + \langle\chi_k\nabla\cdot\bar{\bar{\tau}}_k\rangle
\end{aligned} \tag{2.25}$$

Remarquons que

$$\begin{array}{lcl}
\langle \chi_k \frac{\partial \rho_k}{\partial t} \rangle & = & \frac{\partial \langle \chi_k \rho_k \rangle}{\partial t} - \langle \rho_k \frac{\partial \chi_k}{\partial t} \rangle = \frac{\partial \langle \chi_k \rho_k \rangle}{\partial t} + \langle \rho_k \vec{v^i}.\vec{n_k^i}\delta^i \rangle \\
\langle \chi_k \frac{\partial \rho_k \vec{v_k}}{\partial t} \rangle & = & \frac{\partial \langle \chi_k \rho_k \vec{v_k} \rangle}{\partial t} - \langle \rho_k \vec{v_k} \frac{\partial \chi_k}{\partial t} \rangle = \frac{\partial \langle \chi_k \rho_k \rangle}{\partial t} + \langle \rho_k \vec{v_k} \vec{v^i} \vec{n_k^i} \delta^i \rangle \\
\langle \chi_k \nabla \cdot (\rho_k \vec{v_k}) \rangle & = & \nabla \cdot \langle \chi_k \rho_k \vec{v_k} \rangle - \langle \rho_k \vec{v_k}.\vec{n_k^i}\delta^i \rangle \\
\langle \chi_k \nabla \cdot (\rho_k \vec{v_k} \otimes \vec{v_k}) \rangle & = & \nabla \cdot \langle \chi_k \rho_k \vec{v_k} \otimes \vec{v_k} \rangle - \langle \rho_k \vec{v_k} \otimes \vec{v_k}.\vec{n_k^i}\delta^i \rangle \\
\langle P_k.\nabla \chi_k \rangle & = & \langle P_k.\vec{n_k^i}\delta^i \rangle + \langle P_k.\vec{n_k^w}\delta^w \rangle \\
\langle \bar{\bar{\tau}}_k.\nabla \chi_k \rangle & = & \langle \bar{\bar{\tau}}_k \vec{n_k^i}\delta^i \rangle + \langle \bar{\bar{\tau}}_k \vec{n_k^w}\delta^w \rangle \\
\langle \chi_k \rho_k \frac{\partial e_k}{\partial t} \rangle & = & \frac{\partial \langle \chi_k \rho_k e_k \rangle}{\partial t} - \langle \frac{\partial \chi_k \rho_k}{\partial t} e_k \rangle
\end{array} \tag{2.26}$$

Soit finalement :

$$\begin{array}{lcl}
\frac{\partial \langle \chi_k \rho_k \rangle}{\partial t} & + & \nabla \cdot \langle \chi_k \rho_k \vec{v_k} \rangle = \langle \rho_k (\vec{v_k} - \vec{v^i}).\vec{n_k^i}\delta^i \rangle \\
\frac{\partial \langle \chi_k \rho_k \vec{v_k} \rangle}{\partial t} & + & \nabla \cdot \langle \chi_k \rho_k \vec{v_k} \otimes \vec{v_k} \rangle = ... \\
& - & \nabla \langle \chi_k P_k \rangle + \langle \chi_k \rho_k \rangle \vec{g} + \nabla \cdot \langle \chi_k \bar{\bar{\tau}}_k \rangle + \langle (\rho_k \vec{v_k} (\vec{v_k} - \vec{v^i})).\vec{n_k^i}\delta^i \rangle \\
& + & \langle P_k.\vec{n_k^i}\delta^i \rangle - \langle \bar{\bar{\tau}}_k \vec{n_k^i}\delta^i \rangle + \langle P_k.\vec{n_k^w}\delta^w \rangle - \langle \bar{\bar{\tau}}_k \vec{n_k^w}\delta^w \rangle
\end{array} \tag{2.27}$$

Pour les conditions limites aux interfaces gaz-liquide, on effectue également une moyenne dans l'espace.
Transfert de masse :

$$[\![\langle \rho_k (\vec{v_k} - \vec{v^i}).\vec{n_k^i}\delta^i \rangle]\!] = 0 \tag{2.28}$$

Transfert de la quantité de mouvement :

$$[\![-\langle P_k.\vec{n_k^i}\delta_k^i \rangle + \langle \bar{\bar{\tau}}_k \vec{n_k^i}\delta^i \rangle - \langle \rho_k \vec{v_k} (\vec{v_k} - \vec{v^i}).\vec{n_k^i}\delta_k^i \rangle]\!] = \langle \frac{\gamma}{R} \vec{n_l^i} \rangle \tag{2.29}$$

Introduisons :

$$\begin{array}{lcl}
\varepsilon_k & = & \langle \chi_k \rangle \\
\langle \rho_k \rangle & = & \langle \chi_k \rho_k \rangle / \varepsilon_k \\
\langle \vec{v_k} \rangle & = & \langle \chi_k \rho_k \vec{v_k} \rangle / \varepsilon_k \rho_k \\
\varepsilon_k \bar{\bar{\tau}}_k^{Re} & = & \langle \rho_k \rangle \langle \vec{v_k} \rangle \otimes \langle \vec{v_k} \rangle - \langle \chi_k \rho_k \vec{v_k} \otimes \vec{v_k} \rangle \\
\langle P_k \rangle & = & \langle \chi_k P_k \rangle / \varepsilon_k \\
\langle \bar{\bar{\tau}}_k \rangle & = & \langle \chi_k \bar{\bar{\tau}}_k \rangle / \varepsilon_k \\
\vec{M}_k^i & = & \langle (\rho_k \vec{v_k} (\vec{v_k} - \vec{v^i})).\vec{n_k^i}\delta^i \rangle + \langle P_k \vec{n_k^i}\delta^i \rangle - \langle \bar{\bar{\tau}}_k.\vec{n_k^i}\delta^i \rangle \\
\vec{\tau}_k^w & = & \langle P_k \vec{n_k^w}\delta^w \rangle - \langle \bar{\bar{\tau}}_k.\vec{n_k^w}\delta^w \rangle \\
\Gamma_k & = & \langle \rho_k (\vec{v_k} - \vec{v^i}).\vec{n_k^i}\delta^i \rangle \\
\vec{\kappa} & = & \langle \frac{\gamma}{R} \vec{n_l^i} \rangle
\end{array} \tag{2.30}$$

Par simplification d'écriture, nous n'allons pas garder les notations $\langle - \rangle$, mais il ne faut pas oublier que les valeurs moyennes ne sont pas les valeurs réelles. En particulier nous n'avons pas de vitesse moyenne nulle à la paroi, car le volume de contrôle contient des zones avec des vitesse non nulles.

Conformément à la définition, ε_k cf. équation (2.3), correspond aux taux de vide dans le volume de contrôle. Par simple définition de la fonction indicatrice, nous avons :

$$\varepsilon_g + \varepsilon_l + \varepsilon_s = 1 \tag{2.31}$$

où ε_s est le pourcentage de structure dans le volume de contrôle. Si nous n'avons pas de structure dans le volume de contrôle :

$$\varepsilon = \varepsilon_g = 1 - \varepsilon_l \tag{2.32}$$

Les équations de Navier-Stokes moyennées dans l'espace peuvent alors s'écrire :

$$\begin{aligned} \frac{\partial \varepsilon_k \rho_k}{\partial t} + \nabla \cdot (\varepsilon_k \rho_k \vec{v}_k) &= \Gamma_k \\ \frac{\partial}{\partial t}(\varepsilon_k \rho_k \vec{v}_k) + \nabla \cdot (\varepsilon_k \rho_k \vec{v}_k \otimes \vec{v}_k) &= -\nabla(\varepsilon_k P_k) + \varepsilon_k \rho_k \vec{g} + \nabla \cdot (\varepsilon_k (\bar{\bar{\tau}}_k + \bar{\bar{\tau}}_k^{Re})) + \vec{M}_k^i + \vec{\tau}_k^w \end{aligned} \tag{2.33}$$

Pour les conditions limites,

$$\begin{aligned} [\![\Gamma_k]\!] &= 0 \\ [\![\vec{M}_k^i]\!] &= -\vec{\kappa} \end{aligned} \tag{2.34}$$

S'il n'y a pas de transfert de masse :

$$\Gamma_l = \Gamma_g = 0 \tag{2.35}$$

Si l'écoulement est incompressible

$$\rho_k = \langle \chi_k \rho_k \rangle / \varepsilon_k = \rho_k = Cte \tag{2.36}$$

2.7.2 Relations de fermeture

Si on introduit les conditions limites dans les équations, nous avons pour une zone sans structure :

$$\begin{aligned}
\frac{\partial \varepsilon\rho_g}{\partial t} + \nabla\cdot(\varepsilon\rho_g\vec{v}_g) &= -\Gamma_l \\
\frac{\partial (1-\varepsilon)\rho_l}{\partial t} + \nabla\cdot((1-\varepsilon)\rho_l\vec{v}_l) &= \Gamma_l \\
\\
\frac{\partial}{\partial t}(\varepsilon\rho_g\vec{v}_g) + \nabla\cdot(\varepsilon\rho_g\vec{v}_g\otimes\vec{v}_g) &= -\nabla(\varepsilon P_g) + \varepsilon\rho_g\vec{g} + \nabla\cdot(\varepsilon(\bar{\bar{\tau}}_g + \tau_g^{\bar{\bar{Re}}})) - \vec{M}_l^i + \vec{\kappa} \\
\frac{\partial}{\partial t}((1-\varepsilon)\rho_l\vec{v}_l) + \nabla\cdot((1-\varepsilon)\rho_l\vec{v}_l\otimes\vec{v}_l) &= -\nabla((1-\varepsilon)P_l) + (1-\varepsilon)\rho_l\vec{g} \\
&\quad +\nabla\cdot((1-\varepsilon)(\bar{\bar{\tau}}_l + \tau_l^{\bar{\bar{Re}}})) + \vec{M}_l^i
\end{aligned} \tag{2.37}$$

soit 8 équations, mais beaucoup plus d'inconnues $\varepsilon, \vec{v}_g, \vec{v}_l, P_g, P_l, \bar{\bar{\tau}}_g, \tau_g^{\bar{\bar{Re}}}, \bar{\bar{\tau}}_l, \tau_l^{\bar{\bar{Re}}}, \kappa$ et $\vec{M}_l^i$. Il est donc nécessaire de proposer des relations supplémentaires dites de fermeture.

L'équation dite du mélange est la somme des équations pour la quantité de mouvement :

$$\begin{aligned}
\frac{\partial \varepsilon_g\rho_g + \varepsilon_l\rho_l}{\partial t} + \nabla\cdot(\varepsilon_g\rho_g\vec{v}_g + \varepsilon_l\rho_l\vec{v}_l) &= 0 \\
\frac{\partial}{\partial t}(\varepsilon_g\rho_g\vec{v}_g + \varepsilon_l\rho_l\vec{v}_l) + \nabla\cdot(\varepsilon_g\rho_g\vec{v}_g\otimes\vec{v}_g + \varepsilon_l\rho_l\vec{v}_l\otimes\vec{v}_l) &= -\nabla(\varepsilon_g P_g + \varepsilon_l P_l) + \vec{\kappa} \\
&\quad +(\varepsilon_g\rho_g + \varepsilon_l\rho_l)\vec{g} \\
&\quad +\nabla\cdot(\varepsilon_g(\bar{\bar{\tau}}_g + \tau_g^{\bar{\bar{Re}}})) \\
&\quad +\nabla\cdot(\varepsilon_l(\bar{\bar{\tau}}_l + \tau_l^{\bar{\bar{Re}}}))
\end{aligned} \tag{2.38}$$

Il est bien évident que les modèles de fermeture sont difficiles à vérifier d'autant que les écoulements diphasiques sont hautement turbulents. Dans quelques cas simples, on peut effectuer le calcul analytique des relations de fermeture grâce à quelques approximations souvent d'ordre géométriques. Sinon, il est nécessaire de proposer des modèles de fermeture semi-empiriques.

2.7.3 Modèle homogène

Le modèle homogène consiste à utiliser l'équation du mélange (2.38), en faisant l'hypothèse que $\vec{u}_l = \vec{u}_g$. Nous avons donc d'après la définition des vitesses superficielles (2.10).

$$\begin{aligned}
\vec{v_{2\phi}} = \vec{u}_l = \vec{u}_g \\
\beta = \varepsilon
\end{aligned} \tag{2.39}$$

C'est pour cela que la vitesse superficielle du mélange est parfois appelée vitesse homogène. Nous obtenons finalement les équations

$$\begin{cases} \text{- équation de continuité :} \\ \dfrac{\partial \rho_{2\phi}}{\partial t} + \nabla \cdot \rho_{2\phi} \vec{v}_{2\phi} = 0 \\ \\ \text{- équation de la conservation de la quantité de mouvement :} \\ \dfrac{\partial \rho_{2\phi} \vec{v}_{2\phi}}{\partial t} + \nabla \cdot \rho_{2\phi} \vec{v}_{2\phi} \otimes \vec{v}_{2\phi} = -\nabla P_{2\phi} + \rho_{2\phi} \vec{g} + \nabla \cdot \bar{\bar{\tau}}_{2\phi} + \vec{\kappa} + \nabla \cdot \bar{\bar{\tau}}^{Re}_{2\phi} \end{cases} \tag{2.40}$$

avec

$$\begin{aligned} \rho_{2\phi} &= \langle \chi_g \rho_g + \chi_l \rho_l \rangle = \varepsilon \langle \rho_g \rangle + (1-\varepsilon) \langle \rho_l \rangle \\ \vec{v}_{2\phi} &= \langle \chi_g \rho_g \vec{v}_g + \chi_l \rho_l \vec{v}_l \rangle / \rho_{2\phi} = (\varepsilon \langle \rho_g \rangle \langle \vec{v}_g \rangle + (1-\varepsilon) \langle \rho_l \rangle \langle \vec{v}_l \rangle) / \rho_{2\phi} \\ P_{2\phi} &= \langle \chi_g P_g + \chi_l P_l \rangle = \varepsilon P_g + (1-\varepsilon) P_l \\ \nabla \cdot (\bar{\bar{\tau}}_{2\phi}) &= \nabla \cdot (\varepsilon \langle \bar{\bar{\tau}}_g \rangle + (1-\varepsilon) \langle \bar{\bar{\tau}}_l \rangle) \\ \nabla \cdot \bar{\bar{\tau}}^{Re}_{2\phi} &= -\nabla \cdot \langle \chi_g \rho_g \vec{v}_g \vec{v}_g + \chi_l \rho_l \vec{v}_l \vec{v}_l \rangle + \nabla \cdot \rho_{2\phi} \vec{v}_{2\phi} \vec{v}_{2\phi} \end{aligned} \tag{2.41}$$

Finalement, les équations correspondent aux équations d'un fluide équivalent dont les propriétés sont les propriétés moyennes des deux phases pondérées par le taux de vide. Plus de détails sont apportés sur ce genre de modélisation dans les articles présentés aux chapitres 6 et 7.

2.8 Les forces interfaciales $\vec{M}_l^i$

Park *et al.* (1998),Song et Ishii (2001),Leon-Becerril et Liné (2001) et Espinosa-Paredes (2001) sont quelques-uns des auteurs à avoir proposé des relations de fermeture. Suivant une proposition de Ishii (1975), tous ces auteurs décomposent les forces interfaciales $\vec{M}_l^i$ en injectant les valeurs moyennes à l'interface du tenseur des contraintes visqueuses $\bar{\bar{\tau}}_l^i$, du tenseur des contraintes turbulentes (nommé aussi tenseur de Reynolds) $\bar{\bar{\tau}}^{Re}_{li}$ et de la pression P_l^i :

$$M_l^i = M_l^{i(m)} + P_l^i \nabla \varepsilon - (\bar{\bar{\tau}}_l^i - \bar{\bar{\tau}}^{Re}_{li}) \nabla \varepsilon \tag{2.42}$$

avec

$$M_l^{i(m)} = \langle (P_l - P_l^i) \nabla \chi_l \rangle - \langle (\bar{\bar{\tau}}_l - \bar{\bar{\tau}}_l^i) \nabla \chi_l \rangle - \langle (\bar{\bar{\tau}}^{Re}_l - \bar{\bar{\tau}}^{Re}_{li}) \nabla \chi_l \rangle \tag{2.43}$$

L'introduction de ces valeurs me semble peu judicieuse et complique à mon sens inutilement le problème. D'autant que nous avons par définition :

$$M_l^i = \langle P_l \nabla \chi_l \rangle - \langle (\bar{\bar{\tau}}_l + \bar{\bar{\tau}}^{Re}_l) \nabla \chi_l \rangle \tag{2.44}$$

Sachant que par définition $\varepsilon = \langle \chi_g \rangle$ cela suppose entre autres :

$$P_l^i \nabla \langle \chi_l \rangle = \langle P_l^i \nabla \chi_l \rangle \tag{2.45}$$

Ce qui n'est pas nécessairement vrai et la relation de fermeture pour P_l^i est loin d'être évidente.

Voici un exemple de modélisation des forces interfaciales par Park *et al.* (1998) déduite à partir d'un écoulement potentiel autour d'une bulle en considérant son expansion possible, puis en y ajoutant les forces de traînée et de portance. Le fait d'ajouter les termes de traînées alors que les forces de pression déduites par l'écoulement potentiel ont déjà calculées, me font penser que les forces de pression sont comptées deux fois.

Les forces interfaciales dans le modèle de Park *et al.* (1998) s'écrivent en 3D :

$$\begin{aligned} M_l^{\vec{i}(m)} &= C_{vm}\varepsilon\rho_l a_{\vec{vm}} + \varepsilon\rho_l \vec{v}_r.\left[C_1.(\nabla \vec{v}_l{}^T - \nabla \vec{v}_l) + C_2.\nabla \vec{v}_r{}^T + C_3.\nabla(\vec{v}_r{}^T + \vec{v}_r)\right] \\ &+C_4\rho_l \vec{v}_r\left(\left(\tfrac{\partial}{\partial t} + \vec{u}_g\right)\varepsilon + \varepsilon\nabla\cdot\vec{v}_g\right) + C_5\varepsilon\rho_l(\nabla\cdot\vec{v}_r)\vec{v}_r + C_6\rho_l(\vec{v}_r\nabla\varepsilon)\vec{v}_r \\ &+C_7\rho_l(\vec{v}_r.\vec{v}_r)\nabla\varepsilon + C_L\rho_l\varepsilon\vec{v}_r \times \nabla \times \vec{v}_l \\ &+C_D\tfrac{3}{8a}\rho_l\varepsilon|\vec{v}_r|\vec{v}_r \end{aligned} \tag{2.46}$$

Avec $\vec{v}_r = \vec{v}_g - \vec{v}_l$ la vitesse relative entre les phases, a le rayon de la "bulle". Les coefficients sont :

$$\begin{aligned} C_{vm} &= \frac{1}{2} \\ C_1 &= \frac{1}{4} & C_2 &= \frac{5}{4} \\ C_3 &= -\frac{9}{20} & C_4 &= \frac{1}{2} \\ C_5 &= -\frac{9}{20} & C_6 &= -\frac{2}{5} \\ C_7 &= \frac{3}{10} & C_L &= 0.01 - 0.5 \\ C_D &= \tfrac{4}{3}\left(\tfrac{\Delta\rho g a^2}{\gamma(1-\varepsilon)}\right)^{1/2} \text{ ou } & C_D &= 24\frac{1+0.1Re_b^{0.75}}{Re_b} \end{aligned} \tag{2.47}$$

Re_b est le nombre de Reynolds de la "bulle" :

$$\begin{aligned} Re_b &= \frac{2\rho_l v_r a}{\mu_l}(1-\varepsilon)^{2.5\mu^*} \\ \mu^* &= \tfrac{\mu_g + 0.4\mu_l}{\mu_g + \mu_l}, \end{aligned} \tag{2.48}$$

et a_{vm} l'accélération relative entre les phases.

$$a_{vm} = \left(\frac{\partial}{\partial t} + \vec{u_g}\right)\vec{u_g} - \left(\frac{\partial}{\partial t} + \vec{u_l}\right)\vec{u_l} \tag{2.49}$$

Voici son équivalent en une dimension et sa comparaison avec d'autres relations de fermeture :

$$\begin{aligned} M_l^{i(m)} &= (1-\varepsilon)^{n+1}\left[C_{vm}\varepsilon\rho_l a_{vm} + C_{m1}\varepsilon\rho_l u_r \tfrac{\partial u_r}{\partial z} + C_{m2}\rho_l u_r^2 \tfrac{\partial \varepsilon}{\partial z}\right] \\ &\quad + C_D \tfrac{3}{8a}\rho_l \varepsilon u_r^2 \end{aligned} \tag{2.50}$$

Les coefficients n, C_{m1} et C_{m2} sont présentés au tableau 2.1, en notant $C'_{vm} = \partial C_{vm}/\partial\varepsilon$. Les forces de portance sont bien entendues nulles dans un modèle à une dimension. C_{vm} est le coefficient de masse ajoutée, il est présenté dans la section suivante.

2.8.1 La masse ajoutée

Le coefficient de masse ajoutée C_{vm} a été étudié par de nombreux auteurs. Leurs corrélations ou modèles sont présentés sur le tableau 2.2 : Z est le facteur de correction de la sphéricité donné par Milne-Thomson (1968)

$$Z = -2\frac{\chi^2 cos^{-1}(\chi^{-1}) - \chi^2(\chi^2-1)^{1/2}}{\chi^2 cos^{-1}(\chi^{-1}) - (\chi^2-1)^{1/2}} \tag{2.51}$$

Et χ le coefficient de sphéricité, pour un ellipsoïde $\chi = a/b$ où a et b sont les deux diamètres de l'ellipse génératrice. En particulier, pour une sphère ($a = b$), le coefficient de sphéricité est égal à 1 ($\chi = 1$).

Auteur	n	C_{m1}	C_{m2}
Park *et al.* (1998)	−1	$-\frac{1}{10}$	$-\frac{1}{10}$
Voinov (1973)	−1	0	0
Biesheuvel et Gorissen (1990)	0	$\varepsilon(C_{vm} - (1-\varepsilon)C'_{vm})$	$\varepsilon(C_{vm} + \varepsilon C'_{vm})$
Pauchon et Smereka (1992)	1	$\varepsilon(1-\varepsilon)(2C_{vm} - (1-\varepsilon)C'_{vm})$	$\varepsilon(C_{vm}(1-2\varepsilon) + (1-\varepsilon)\varepsilon C'_{vm})$

Tableau 2.1 Coefficient pour le modele 1D des forces interfaciales (cf. Eq. 2.50).

Auteur	Hypothèses	C_{vm}
Voinov (1973) Nigmatulin (1979)	Bulles sphériques isolées écoulement potentiel	$\frac{1}{2}$
Zuber (1964)	Bulles sphériques non-isolées écoulement potentiel	$\frac{1}{2}\frac{1+2\varepsilon}{1-\varepsilon} \simeq \frac{1}{2} + 1.5\varepsilon$
Van Wijngaarden (1976)	Bulles sphériques non-isolées écoulement potentiel	$\frac{1}{2} + 1.39\varepsilon$
Van Wijngaarden (1991)	Bulles ellipsoïdales non-isolées écoulement potentiel	$\frac{1}{2}\left[1 + \left(1 + \frac{2}{Z}\right)\varepsilon\right]$
Mokeyev (1977)	Corrélation empirique	$\frac{1}{2} + 2.1\varepsilon$

Tableau 2.2 Modèle pour le coefficient de masse ajoutée C_{vm}

2.8.2 La force de portance

Auton (1987) propose un coefficient de portance pour une sphère C_L = 0.5. Une autre étude est aussi présentée dans les articles reproduits aux chapitres 6 et 7

2.8.3 Force de traînée

La formulation traditionnelle de la traînée

$$\vec{M}_l^{i(d)} = \frac{3}{8}\varepsilon\rho_l\frac{C_D}{a}|\vec{v}_r|\vec{v}_r \tag{2.52}$$

Avec C_D le coefficient de traînée dont les modèles sont présentés au tableau 2.3. D'autres modèles et corrélations sont présentés dans l'article reproduit au chapitre 7, dont c'est le sujet principal.

2.8.4 Les contraintes turbulentes interfaciales moyennes $\bar{\bar{\tau}}_{ki}^{Re}$

Tous les auteurs proposent des relations du type :

$$\begin{aligned} \bar{\bar{\tau}}_{ki}^{Re} &= -\rho_k\left[C_{ik1}\vec{v}_r \otimes \vec{v}_r + C_{ik2}(\vec{v}_r.\vec{v}_r)\bar{\bar{I}}\right] && \text{Pour le modèle 3D} \\ \tau_{ki}^{Re} &= -C_{ik}\rho_k u_r^2 && \text{Pour le modèle 1D} \end{aligned} \tag{2.53}$$

Auteur(s)	Condition	C_D
Ishii et Zuber (1979)	Régime de Stoke	$\frac{24}{Re_b}$
	Régime de Visqueux	$\frac{24(1+0.1Re_b^{3/4})}{Re_b}$
Harmathy (1960)	Particules déformées	$\frac{4}{3}\sqrt{\frac{\Delta\rho g a^2}{\gamma(1-\varepsilon)}}$

Tableau 2.3 Coefficient de trainée d'une bulle

Park *et al.* (1998) proposent :

$$\begin{aligned} C_{ig1} &= 0, \quad C_{ig2} = 0, \quad C_{il1} = \tfrac{1}{20}, \quad C_{il2} = \tfrac{3}{20} && \text{Pour le modèle 3D} \\ C_{ig} &= 0, \qquad\qquad C_{il} = \tfrac{1}{5} && \text{Pour le modèle 1D} \end{aligned} \tag{2.54}$$

2.8.5 La pression moyenne à l'interface

Tous les auteurs proposent des relations du type :

$$\begin{aligned} \Delta P_g^i = P_g - P_l^i &= C_{pg}\rho_l v_r^2 \\ \Delta P_l^i = P_l - P_l^i &= C_{pl}\rho_l v_r^2 \\ \text{Bien entendu } P_l - P_g &= (C_{pl} - C_{pg})\rho_l v_r^2 \end{aligned} \tag{2.55}$$

où les coefficients C_{pg} et C_{pl} sont présentés au tableau 2.4. Concrètement tous ces auteurs

Auteur(s)	Condition	C_{pg}	C_{pl}
Approche classique	Bulle sphérique isolée	0	$\frac{1}{4}$
Leon-Becerril (2001)	Bulle sphérique non isolée	0	$\frac{1+\varepsilon}{4(1-\varepsilon)}$
Park *et al.* (1998)		0	$\frac{\varepsilon}{4}$
Drew et Lahey (1983)		0	0

Tableau 2.4 Coefficients des forces de pression sur une bulle

considèrent la pression du gaz comme étant la pression moyenne du liquide à l'interface. Par ailleurs, Drew et Lahey (1983) affirment que cette différence de pression est déjà contenue dans la force de trainée ($C_{pg} = C_{pl} = 0$), ce qui me semble l'évidence même. Cette affirmation me pousse à conclure que l'introduction des valeurs moyennes à l'interface de la pression P_k^i, des tenseurs des contraintes $\overline{\overline{\tau}}_k^i$ et $\overline{\overline{\tau}}_{ki}^{Re}$ est inutile.

2.8.6 La force d'Archimède

La modélisation des forces interfaciales exposée jusqu'à présent est une revue de la littérature des auteurs précédemment cités. Très curieusement, aucun auteur ne mentionne clairement le rôle de la force d'Archimède dans les forces d'interface. Celle-ci est en réalité prise en compte par l'intermédiaire des pressions moyennes à l'interface. Dans le cas où on décide de se passer de cet artifice, il est nécessaire d'ajouter la force d'Archimède à M_l^i.

$$M_l^{i(\vec{arch})} = \varepsilon \Delta\rho \vec{g} \tag{2.56}$$

2.8.7 La tension de surface κ

L'effet de la tension de surface apparaît dans la condition de saut des contraintes normales à l'interface gaz-liquide. Park *et al.* (1998) introduisent son effet à travers un tenseur de contraintes surfaciques. C'est d'ailleurs la différence majeure entre le modèle de Park *et al.* (1998) et Pauchon et Banerjee (1986b).

$$M_l^i + M_g^i = \nabla \cdot \left\{ \varepsilon \left[\gamma_s + (P_g^i - P_l^i) \bar{\bar{I}} \right] \right\} \tag{2.57}$$

avec

$$\gamma_s = \rho_l \left[-\frac{9}{20} \vec{v_r} \otimes \vec{v_r} + \frac{3}{20} (\vec{v_r}.\vec{v_r}) \right] \tag{2.58}$$

2.9 Les forces à la paroi

La modélisation des forces à la paroi, et donc l'influence de l'écoulement diphasique sur la structure est de la première importance, mais encore peu d'auteurs s'y sont intéressés. La raison principale est que les chercheurs qui modélisent les écoulements diphasique proviennent beaucoup de la chimie et tentent de modéliser des chambres à bulles où l'interaction fluide-structure est minimale et de faible importance. Ce n'est pas le cas dans l'industrie nucléaire. La compréhension des forces induites par la turbulence diphasique, l'amortissement diphasique, les forces périodiques, l'instabilité fluide élastique en diphasique est encore peu avancée. Plus de travaux, en revanche, ont été faits concernant la perte de charge diphasique.

2.9.1 Forces de pression à la paroi

Si le tube est immobile, les forces de pression ne travaillent pas :

$$P_k^w = 0 \tag{2.59}$$

2.9.2 Contrainte pariétale

Pour les écoulements internes, tous les auteurs proposent une formulation du type :

$$\tau_k^w = -\frac{4\rho_k f_k^w \vec{v_k}^2}{2D} \tag{2.60}$$

Leon-Becerril et Liné (2001) utilisent la loi de Blasius pour un écoulement monophasique.

$$\begin{array}{rcl} f_l^w & = & \frac{0.079}{Re^{1/4}} \\ f_g^w & = & 0 \end{array} \tag{2.61}$$

avec $Re = \dfrac{\rho_l v_l D}{\mu_l}$

2.10 Tenseur de Reynolds, turbulence et pseudo-turbulence

Les auteurs décomposent la turbulence comme la somme de deux contributions : la turbulence classique et la turbulence induite par les bulles (aussi communément appelée pseudo-turbulence). La turbulence est définie par la différence entre la moyenne du carré des vitesse avec la moyenne des vitesses au carré. La turbulence classique peut être modélisée par exemple par une viscosité turbulente. Tous les auteurs proposent pour la pseudo-turbulence une formulation du type :

$$\begin{array}{rcll} \bar{\bar{\tau}}_k^{Re} & = & \rho_k \left[-C_{rk1}\rho_k \vec{v}_r \otimes \vec{v}_r - C_{rk2}(\vec{v}_r.\vec{v}_r)\bar{\bar{I}} \right] & \text{pour le modèle 3D} \\ \bar{\bar{\tau}}_k^{Re} & = & -C_{rk}\rho_k(\vec{v}_r.\vec{v}_r)^2 & \text{pour le modèle 1D} \end{array} \tag{2.62}$$

Les coefficient C_{rk} sont présentés à la table 2.5. Pauchon et Banerjee (1986a),Leon-Becerril (2001) proposent des modèles 1D de bulles non isolées. l'article du chapitre 7 présente une discussion sur cette modélisation.

Auteur(s)		C_{rl1}	C_{rl2}
	1D	C_{rl}	
Biesheuvel et Van Wijngaarden (1984)	3D	$\frac{1}{20}\varepsilon$	$\frac{3}{20}\varepsilon$
	1D	$\frac{1}{5}\varepsilon$	
Park *et al.* (1998)	3D	$\frac{1}{20}\frac{\varepsilon}{1-\varepsilon}$	$\frac{3}{20}\frac{\varepsilon}{1-\varepsilon}$
	1D	$\frac{1}{5}\frac{\varepsilon}{1-\varepsilon}$	
Pauchon et Banerjee (1986a)	1D	$\frac{1+5\varepsilon(1-\varepsilon)}{5(1-\varepsilon)^2}$	
Leon-Becerril (2001)	1D	$\frac{1}{5}\frac{1}{(1-\varepsilon)^2}$	

Tableau 2.5 Coefficient pour modeliser la pseudo turbulence

2.11 Résolution des équations

Si on introduit la décomposition proposée par Ishii (1975) (cf. Eq. 2.42) dans les équations (2.37) nous avons :

$$\begin{aligned}
\tfrac{\partial \varepsilon\rho_g}{\partial t} + \nabla\cdot(\varepsilon\rho_g\vec{v}_g) &= -\Gamma_l && (a)\\
\tfrac{\partial (1-\varepsilon)\rho_l}{\partial t} + \nabla\cdot((1-\varepsilon)\rho_l\vec{v}_l) &= \Gamma_l && (b)\\
\tfrac{\partial}{\partial t}(\varepsilon\rho_g\vec{v}_g) + \nabla\cdot(\varepsilon\rho_g\vec{v_g}\otimes\vec{v_g}) &= -\nabla(\varepsilon P_g) + \varepsilon\rho_g\vec{g} + \nabla\cdot(\varepsilon(\bar{\bar{\tau}}_g + \bar{\bar{\tau}}_g^{Re})) - \vec{M}_l^{i(m)} \\
&\quad + P_l^i\nabla\varepsilon - (\bar{\bar{\tau}}_l^i + \bar{\bar{\tau}}_{li}^{Re})\nabla\varepsilon + \vec{\kappa} && (c)\\
\tfrac{\partial}{\partial t}((1-\varepsilon)\rho_l\vec{v}_l) + \nabla\cdot((1-\varepsilon)\rho_l\vec{v}_l\otimes\vec{v}_l) &= -\nabla((1-\varepsilon)P_l) + (1-\varepsilon)\rho_l\vec{g} \\
&\quad + \nabla\cdot((1-\varepsilon)(\bar{\bar{\tau}}_g + \bar{\bar{\tau}}_g^{Re})) + \vec{M}_l^{i(m)} \\
&\quad - P_l^i\nabla\varepsilon + (\bar{\bar{\tau}}_l^i + \bar{\bar{\tau}}_{li}^{Re})\nabla\varepsilon && (d)
\end{aligned} \tag{2.63}$$

Dans le cas 3D, nous avons 8 équations et les relations de fermeture sont exprimées à partir des inconnues ε,P_l,$\vec{u}_l$,$\vec{u_g}$, les équations précédentes sont donc résolues sous la forme :

$$[A]\frac{\partial\vec{\Phi}}{\partial t} + [B]\frac{\partial\vec{\Phi}}{\partial x} + [C]\frac{\partial\vec{\Phi}}{\partial y} + [D]\frac{\partial\vec{\Phi}}{\partial z} = \vec{E} \tag{2.64}$$

Avec

$$\vec{\Phi} = \begin{pmatrix} \varepsilon \\ u_{gx} \\ u_{gy} \\ u_{gz} \\ u_{lx} \\ u_{ly} \\ u_{lz} \\ P_l \end{pmatrix} \tag{2.65}$$

L'étude des valeurs propres en introduisant les modèles de fermeture permet de vérifier si le problème est bien posé.

2.12 Équation d'onde pour le taux de vide

Pour un écoulement incompressible 1D sans transfert de masse, nous avons :

$$\begin{aligned}
\tfrac{\partial \varepsilon_g}{\partial t} + \varepsilon_g \tfrac{\partial u_g}{\partial z} + u_g \tfrac{\partial \varepsilon_g}{\partial z} &= 0 && (a)\\
\tfrac{\partial \varepsilon_l}{\partial t} + \varepsilon_l \tfrac{\partial u_l}{\partial z} + u_l \tfrac{\partial \varepsilon_l}{\partial z} &= 0 && (b)\\
\rho_g \tfrac{\partial}{\partial t}(\varepsilon_g v_g) + \rho_g \tfrac{\partial}{\partial z}.(\varepsilon_g u_g^2) &= -\varepsilon_g \tfrac{\partial P_g}{\partial z} + \Delta P_g^i \tfrac{\partial \varepsilon_g}{\partial z} - \kappa + \varepsilon_g \rho_g g \\
&\quad + \tfrac{\partial}{\partial z}.(\varepsilon_g \tau_g + \tau_g^{Re}) + \kappa \\
&\quad - (\tau_l^i + \tau_{li}^{Re}).\tfrac{\partial \varepsilon_g}{\partial z} - \vec{M}_l^i + P_g^w \tfrac{\partial \varepsilon_g}{\partial z} + \vec{\tau}_g^w && (c)\\
\rho_l \tfrac{\partial}{\partial t}(\varepsilon_l u_l) + \rho_l \tfrac{\partial}{\partial z}.(\varepsilon_l u_l^2) &= -\varepsilon_l \tfrac{\partial P_l}{\partial z} + \Delta P_l^i \nabla \tfrac{\partial \varepsilon_l}{\partial z} + \varepsilon_l \rho_l g \\
&\quad + \tfrac{\partial}{\partial z}.(\varepsilon_l(\tau_l + \tau_l^{Re})) \\
&\quad - (\tau_l^i + \tau_{li}^{Re}).\tfrac{\partial \varepsilon_l}{\partial z} + \vec{M}_l^i + P_l^w.\tfrac{\partial \varepsilon_l}{\partial z} + \vec{\tau}_l^w && (d)
\end{aligned} \tag{2.66}$$

Classiquement nous utilisons la méthode des perturbations.

$$\begin{aligned}
\varepsilon_g &= \varepsilon_0 + \varepsilon' \\
\varepsilon_1 &= 1 - \varepsilon_g \\
u_g &= u_{g0} + u_g' \\
u_l &= u_{l0} + u_l'
\end{aligned} \tag{2.67}$$

$\varepsilon_0, u_{g0}, u_{l0}$ sont les solutions stables stationnaires des équations du mouvement. Deux hypothèses sont alors possible :

- $\varepsilon_0, u_{g0}, u_{l0}$ constant
  Justifié pour des écoulements à bulles dans des tuyaux.
- $\varepsilon_0, u_{g0}, u_{l0}$ non constant.

La première hypothèse permet dans le cas 1D de construire une équation d'onde unique pour ε', les équations de conservation de la masse permettant de supprimer les composantes u'_l et u'_g. Entre autres, Park *et al.* (1998), Leon-Becerril (2001) ont réalisé des études théoriques des ondes de taux de vide.

2.13 Études expérimentales sur les ondes de taux de vide

2.13.1 Ondes forcées

À faible taux de vide, toutes les ondes sont amorties et l'amortissement augmente avec la fréquence. Une fréquence de coupure semble exister autour de 3-4 Hz. Les ondes sont fortement amorties au-delà de cette fréquence. La cohérence des ondes faiblement amorties est proche de 1. La cohérence chute très rapidement quand l'amortissement augmente. La vitesse des ondes est indépendante de leur fréquence, les ondes sont donc non dispersives. La vitesse des ondes se situe entre la vitesse du mélange ($u_{2\phi}$) et la vitesse des bulles (u_g).

À taux de vide plus élevé, un mode plus rapide apparaît sa vitesse augmente avec le taux de vide dont la vitesse est supérieure à celle des bulles. Ces ondes sont amorties à haute fréquence, mais amplifiées aux basses fréquence où elles semblent associées aux premiers rassemblements de bulles. Les ondes amplifiées sont très cohérentes.

2.13.2 Ondes naturelles

Le spectre de densité de puissance en écoulement à bulles présente un pic autour de 3 Hz. L'augmentation du taux de vide conduit a un spectre plus étroit et le pic descend en fréquence jusqu'à environ 1 Hz.

À faible taux de vide, les ondes sont amorties et elles ont une faible cohérence. La vitesse des ondes est constante le long de la section et indépendante de la fréquence.

Aux taux de vide plus élevés, la vitesse et la cohérence des ondes tendent à augmenter juste avant que les ondes deviennent instables.

Dans un système très visqueux (huile-air), il existe deux modes d'onde. La vitesse des ondes les plus rapides correspond à la vitesse des conglomérats de bulles.

2.13.3 Exemple d'études expérimentales

Auteurs	Diamètre du tuyau (mm)	Longueur du tuyau (m)	Diamètre des bulles (mm)	u_L (m/s)
Cheng *et al.* (1998)	28.9	4.1		0-1.25
	150	10.5		0-0.65
Sun *et al.* (2002)	112.5	12	3.3-3.5	0.01-0.15
Cheng *et al.* (2002)	28.9	4.1	3-4.4	0.356

Les premières études de Cheng *et al.* (1998) ont associé, dans le cas de tubes de faible diamètre, la corrélation entre une instabilité des ondes de taux de vide avec la transition bulle-bouchons. Dans le cas de tubes larges (150 mm de diamètre), ils n'observent pas de transition mais plutôt une transition graduelle d'un écoulement à bulles vers un écoulement agité. Ils observent cependant des ondes de taux de vide instables (facteur de gain supérieur à 1).

Sun *et al.* (2002) ont mené une étude expérimentale en écoulement interne pour des tubes assez larges, soit de 112.5 mm de diamètre. Ils apportent quelques éclaircissements sur les premières expériences réalisées par Cheng *et al.* (1998). Sun *et al.* (2002) détectent une instabilité des ondes de taux de vide conduisant à un écoulement à bouchons pour des vitesses d'écoulement faibles. Dans le cas de vitesses d'écoulement plus élevées, ils observent une transition graduelle de l'écoulement à bulles à l'écoulement agité.

Cheng *et al.* (2002) se sont intéressés, plus spécifiquement, à l'influence de la taille des bulles sur la transition bulles-bouchons ainsi que sur les ondes de taux de vide.

Ils arrivent aux conclusions suivantes :

(1) La taille initiale des bulles a un effet important sur la transition de configuration. A flux de liquide constant, le taux de vide critique auquel la transition a lieu décroit avec l'augmentation de la taille des bulles.

(2) La taille des bulles affectent également l'instabilité des ondes de taux de vide. À flux de liquide constant, le taux de vide critique auquel le facteur de gain devient supérieur à 1 et le gradient de vitesse des ondes de taux de vide est négatif décroit également avec l'augmentation de la taille des bulles.

Cependant seulement pour une taille de bulles de 4.5 mm, ces trois effets se produisent simultanément (transition bulle-bouchons, facteur de gain supérieur à un, diminution de la vitesse des ondes de taux de vide).

(3) Étant donné l'influence notoire de la taille des bulles, un modèle de la transition se doit de la considérer.

Les résultats théoriques des ondes de taux de vide correspondent qualitativement aux observations expérimentales, mais pas encore quantitativement. La raison principale est la

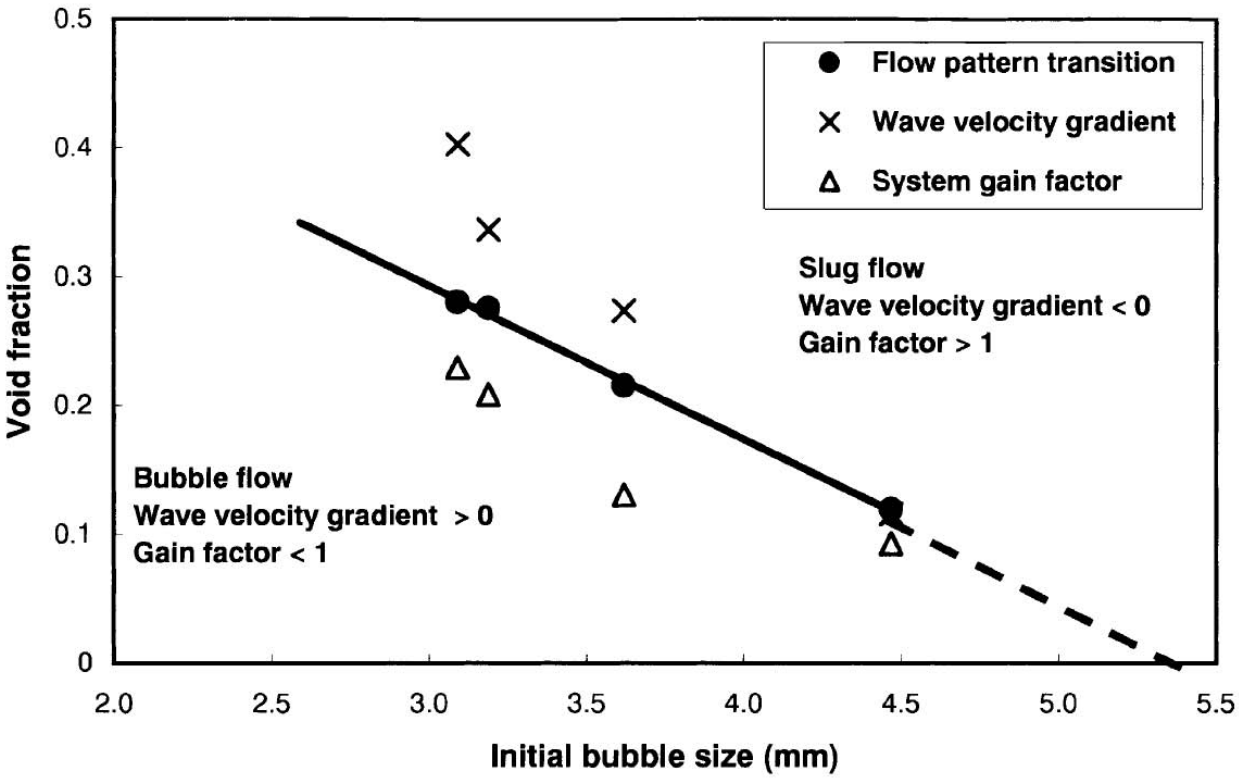

Figure 2.18 Taux de vide critiques pour différents diamètres de bulles - Cheng *et al.* (2002)

faible connaissance de l'influence du taux de vide sur les différents paramètres de l'équation comme la portance, la trainée et la masse ajoutée des bulles. Par ailleurs, il n'y a pas de consensus sur la modélisation des pressions moyennes à l'interface. Il est nécessaire de réaliser un travail théorique, numérique et expérimental sur l'évaluation des forces interfaciales sur les bulles pour améliorer nos connaissances dans ce domaine. Ce questionnement est traité dans les articles présentés aux chapitres 6 et 7.

CHAPITRE 3

DÉMARCHE GÉNÉRALE, MÉTHODES EXPÉRIMENTALES ET SONDES À CAPACITANCE

Ce chapitre sera consacré à la description de la démarche générale de la recherche pour mettre en perspective et faire le lien entre les différents articles. De plus, nous ferons une revue des méthodes expérimentales disponibles au laboratoire, ainsi qu'un aperçu du travail technique réalisé pour la conception des sondes à capacitance.

3.1 Démarche générale

Les écoulements diphasiques sont une source potentielle de vibration dans la tuyauterie pouvant induire de la fatigue ou de l'usure prématurée des tuyaux. On observe cependant une augmentation significative de l'amortissement dans les tuyaux contenant un écoulement diphasique par rapport à ceux contenant un écoulement monophasique. Les deux articles de journaux présentés aux chapitres 4 et 5, constituant la première partie de cette thèse, sont consacrés à l'amortissement diphasique. Les mécanismes responsables de l'amortissement diphasique ne sont pas encore bien compris. Afin de les comprendre, nous avons étudié l'influence de différents paramètres sur l'amortissement diphasique tout en faisant des hypothèses sur des mécanismes physiques permettant d'expliquer les variations de l'amortissement diphasique en fonction des différents paramètres. Les mesures d'amortissement diphasique ont été réalisées en écoulement interne, car elles permettent une mesure directe de l'amortissement diphasique. En effet, dans les écoulements internes, notamment dans un tube encastré encastré, tous les mécanismes d'amortissement autre que l'amortissement structural sont relativement faibles.

Le premier article publié dans le *Journal of Fluids and Structures* est consacré principalement à l'influence du diamètre et de la configuration d'écoulement sur l'amortissement diphasique. Pour cela, nous voulions contrôler le plus possible les caractéristiques de l'écoulement. Les premières expériences simulaient des "bulles de géométrie contrôlée" avec des billes de verre en sédimentation dans l'eau stagnante. Puis, de l'air a été injecté dans l'alcool stagnant afin de générer un flux de bulles uniformes et mesurables. Les expériences nous ont amenés à conclure que dans les deux cas, l'amortissement diphasique est corrélé au nombre de bulles (ou sphères). En d'autres mots, l'amortissement diphasique est lié à la surface d'interface et, par conséquent, à la configuration d'écoulement. Cependant, une étude sur l'ordre

de grandeur de l'énergie de tension superficielle démontre que l'amortissement diphasique ne peut pas être expliqué avec un amortissement engendré par la création de nouvelles surfaces d'interface. La tension de surface joue, cependant, un rôle dans la forme et la taille des bulles et, par conséquent, sur l'amortissement.

Des expériences complémentaires ont été effectuées avec des tubes dans lesquels circulait un mélange d'air et d'eau. Une série de photographies témoigne du fait qu'en écoulement à bulles, l'amortissement diphasique augmente, et est maximal juste avant la transition de l'écoulement à bulles à l'écoulement à bouchons. Au-delà de la transition, l'amortissement diminue. L'amortissement diphasique augmente avec le diamètre du tube.

Un premier modèle simple montre, en raison de la différence de densité, que les deux phases ont un mouvement relatif et que ce mouvement peut conduire à un amortissement visqueux. L'étape suivante consistait à confirmer cette hypothèse en utilisant différents mélanges de fluides.

Le but est de réaliser des expériences en faisant varier la densité et la viscosité. Un article soumis à l'*International Journal of Multiphase Flow* résume les résultats et les conclusions obtenus et déjà présentés dans plusieurs articles aux conférences FIV (*Flow Induced Vibrations*) et PVP (*Pressure Vessel and Piping*). Ces études explorent les relations entre les propriétés physiques des deux phases et l'amortissement diphasique. Des expériences simples ont été réalisées dans un tube transparent encastré encastré avec divers fluides, tels que l'air, l'alcool, l'eau pure, l'eau sucrée, la glycérine et un perfluorocarbone. Les résultats des expériences avec des tuyaux en PVC, laiton et polycarbonate ont été également comparées. De même que lors de la précédente série d'expériences, l'amortissement diphasique a été mesuré à partir des vibrations libres du tube. Deux séries d'expériences avec la phase continue stagnante et en mouvement ont été menées.

Sur la base de l'analyse dimensionnelle, nous avons obtenu un modèle semi-empirique pour l'amortissement diphasique dans les écoulements à bulles et à bouchons. Le taux de vide et le nombre de Bond se sont révélés comme des paramètres importants. L'amortissement diphasique est expliqué par un transfert d'énergie cinétique du tube à la phase continue par l'intermédiaire du mouvement relatif entre la phase dispersée et la phase continue. Étonnamment, la viscosité des fluides semble n'avoir aucun effet significatif sur l'amortissement diphasique. Ce dernier est donc d'abord un effet d'inertie. L'augmentation de l'énergie cinétique de la phase continue s'accompagne d'un amortissement de la structure. Cependant, en écoulement à bouchons, un certain amortissement visqueux est ajouté sans doute à cause du sillage oscillant des bulles de Taylor.

La tension de surface joue un rôle important dans la taille et la forme des bulles de gaz. Elle affecte donc la capacité des bulles à transférer de l'énergie cinétique à la phase continue. En

écoulement à bulles, puisque l'amortissement diphasique ne dépend pas significativement de la viscosité du fluide, l'énergie cinétique ajoutée dans le liquide est donc sans doute transportée avec l'écoulement. De nouvelles hypothèses ont été proposées. La première suggère que la traînée des bulles soumises à une excitation périodique soit principalement une traînée de forme indépendante de la viscosité du liquide. La deuxième suggère que l'impact entre les bulles ou entre les bulles et la structure soit un mécanisme possible pour apporter de l'énergie dans la phase continue. L'impact d'une goutte sur un solide est un phénomène purement inertiel ce qui est sans doute aussi le cas des bulles. Des expériences mesurant la variation d'intensité de turbulence à la sortie du tube lorsque le tube vibre pourraient apporter la preuve de ce qui précède. D'autres expériences filmant la vibration des bulles lors de l'excitation du tube nous apporteraient aussi des éclaircissements sur les mécanismes en jeu.

Pour être en mesure de comprendre les mécanismes de transition en configuration d'écoulement et l'amortissement diphasique, la modélisation des forces d'interface et de l'écoulement autour d'une bulle est clairement apparue comme une nécessité. Le taux de vide est un paramètre clé et pourtant peu de travaux ont été consacrés pour comprendre son rôle. Effectivement, l'effet du taux de vide sur les forces d'interface agissant sur une bulle est le moteur des ondes de taux de vide. La nature de la structure de l'écoulement autour d'une bulle n'est pas encore clairement définie. En plus d'une étude numérique et analytique sur l'écoulement autour des bulles, la conception du capteur capacitif a été amorcée. Cet instrument de mesure du taux de vide utilise la différence de propriété électrique de l'air et de l'eau. Il est un instrument utile pour étudier la variation spatiale et spectrale du taux de vide. En effet, l'instabilité des ondes de taux de vide est une bonne candidate pour expliquer la transition de l'écoulement à bulles vers l'écoulement à bouchons.

L'influence du taux de vide sur l'écoulement autour des bulles et sur les forces d'interface sont le moteur des ondes de taux de vide. L'étude expérimentale des ondes de taux de vide avec capteur de capacité serait un bon moyen de valider les connaissances acquises par les études analytiques et numériques.

L'étude de l'effet du taux de vide sur les forces d'interface et la structure de l'écoulement constitue la dernière partie de cette thèse avec un article de journal en deux parties. Cette étude aux petites échelles est un bon moyen de comprendre les phénomènes d'écoulement diphasique dans leur globalité. Un article en deux parties soumis pour publication dans le *Journal of Fluid Mechanic* est le résultat de ces investigations. La Partie I de cet article propose une relation pour le coefficient de traînée de bulles (ou gouttes) sphériques en fonction du nombre de Reynolds Re, du taux de vide ε, du rapport de viscosité et de densité entre les deux phases ($\bar{\mu}$ et $\bar{\rho}$). Les relations proposées sont utiles pour tous les mélanges fluide-fluide. La limite sous laquelle les bulles restent sphériques a également été étudiée. Cette condition

permet d'identifier la limite du modèle.

Le taux de glissement dans les écoulements à bulles reste en général très faible. Dans presque tous les cas pratiques d'écoulements à bulles, l'écoulement autour de la bulle peut être considéré comme un écoulement de Stokes. Le taux de vide ε, a un effet majeur sur la traînée essentiellement par confinement. La relation proposée peut être utilisée pour construire un modèle d'écoulement à deux phases pour les écoulements à bulles ou annulaire. Ce travail propose une amélioration sur les relations de fermeture du coefficient de traînée (C_D) par rapport aux travaux antérieurs.

La principale conclusion est que l'écoulement de Stokes représente, de façon très précise, l'écoulement autour des bulles. L'écoulement est laminaire et par conséquent la turbulence ne peut être attribuée à de la turbulence classique. L'écoulement dans la phase continue peut être considéré comme un écoulement de film dans lequel la turbulence classique ne peut se développer. La turbulence diphasique est essentiellement due à des perturbations induites par le passage de bulles.

La Partie II propose un modèle pour la pseudo-turbulence (turbulence induite par les particules). Des relations entre le tenseur de Reynolds de la phase continue et dispersée et le nombre de Reynolds Re, le taux de vide ε et les rapports de viscosité et de densité entre les deux phases ($\bar{\mu}$ et $\bar{\rho}$) sont avancées. Les relations proposées sont applicables à tous les mélanges fluide-fluide. Les implications pour la taille des bulles et les forces induites par la turbulence sur les bulles sont également étudiées. Un modèle simple est proposé faisant le lien entre les forces de turbulence sur les bulles et la prédiction de la taille des bulles. Il est montré que les forces conduisant à la fragmentation des bulles sont peu présentes dans le tuyau. Cela pourrait expliquer que la transition d'un écoulement à bulles à un écoulement à bouchons soit indépendante du diamètre du tube.

En résumé, cette thèse constitue une étude de l'amortissement diphasique et de l'influence du taux de vide sur les caractéristiques de l'écoulement et les forces induites. L'amortissement diphasique est le plus souvent un effet d'inertie apportant de l'énergie à la phase continue par l'intermédiaire d'un mouvement relatif entre les deux phases. Ce mécanisme implique que la différence de densité et la tension superficielle jouent un rôle majeur. L'étude de l'influence du taux de vide sur la force d'interface et la pseudo-turbulence nous mène à conclure également qu'il constitue un paramètre de première importance. Un très petit pourcentage de changement du taux de vide est suffisant pour complètement changer la nature de l'écoulement. Cela montre le danger d'identifier simplement des phénomènes d'écoulement monophasique pour comprendre les phénomènes en écoulement diphasique. En particulier, la nature de la turbulence dans l'écoulement diphasique s'est avérée être complètement différente de celle observée dans un écoulement monophasique.

3.2 Méthode expérimentale

Le laboratoire est déjà muni de différents instruments pour générer et mesurer les écoulements diphasiques. La partie suivante de ce chapitre est consacrée à décrire l'ensemble des outils disponibles au laboratoire. Nous exposerons également les travaux préliminaires effectués afin de concevoir des sondes à capacitance.

3.2.1 Boucle diphasique

Le laboratoire possède quatre boucles diphasiques. Elles sont toutes conçues sur le même principe. Une boucle diphasique typique installée au laboratoire permet de créer des mélanges eau-air. La plus grosse boucle est représentée schématiquement à la figure 3.1.

Les éléments principaux d'une boucle diphasique sont les suivants :

- Un bassin permet de recueillir le mélange diphasique après son passage dans la section d'essais. L'air s'échappe dans l'atmosphère et le volume d'eau circule à nouveau par les pompes.
- Les pompes électriques permettent de faire circuler l'eau dans la boucle.
- L'air utilisé pour les mélanges provient du service d'air comprimé de l'École disponible au laboratoire.
- Le mélangeur est l'élément où se rencontrent les écoulements d'air et d'eau. Il est inséré à l'entrée de la section d'essais.
- Un débitmètre à eau permet de mesurer le débit de l'eau
- Des débitmètres et/ou rotamètres à air permettent la mesure du débit d'air à l'entrée du mélangeur.
- Éventuellement, des manomètres sont utilisés pour déterminer la pression locale à l'entrée de la section d'essais.

3.2.2 Les mélangeurs

Les mélangeurs dans les plus grandes boucles d'essais sont composés d'un treillis complexe. Dans les plus petites boucles d'essais, ils sont composés d'une simple grille et d'une entrée d'air en opposition à l'écoulement de l'eau. Jusqu'à présent, l'effet des mélangeurs n'a pas réellement été étudié hormis l'impression visuelle d'avoir un mélange eau/air homogène. L'article présenté au chapitre 7 présente un modèle pour prévoir la taille des bulles en fonction des caractéristiques du mélangeur.

Un mélangeur peut être décrit comme un milieu poreux. Ils sont alors définis par les trois quantités suivantes (cf. Morancais *et al.* (1999)) :

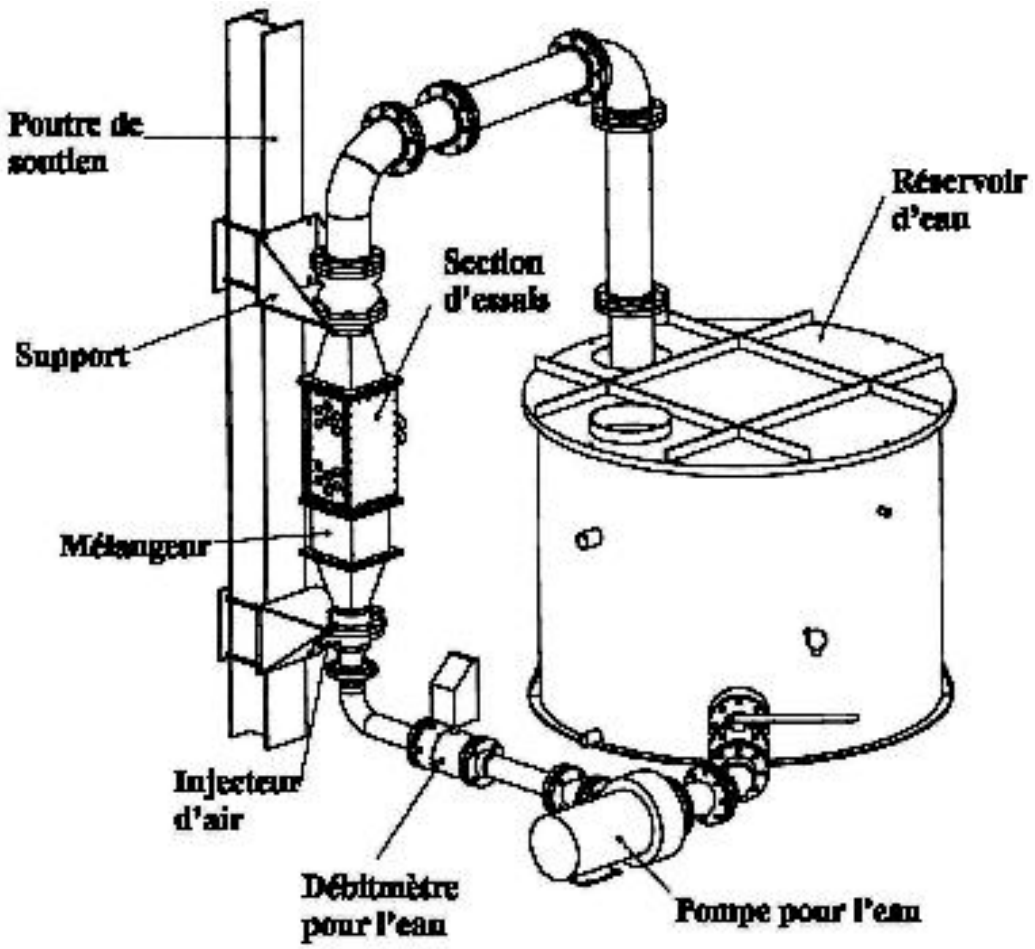

Figure 3.1 Boucle diphasique

- T, la tortuosité qui représente à quel point le fluide doit changer de direction lors de sa traversée du milieu poreux,
- d_p, la taille typique des pores dans le mélangeur et
- Φ la porosité qui représente la proportion du volume de vide (ou des pores) sur le volume total du milieu.

L'expression mathématique la plus simple pour évaluer la tortuosité T est le rapport de la longueur totale du parcours que l'écoulement doit prendre pour passer à travers le mélangeur (L) sur la dimension du mélangeur (H) :

$$T = \frac{L}{H} \tag{3.1}$$

La tortuosité et la porosité permettent de déterminer la vitesse typique dans le mélangeur. En effet, par conservation de la masse, sachant que le fluide circule à une vitesse U_p à travers une section évaluée par le rapport entre le volume des pores V_p sur leur longueur totale L, nous déduisons :

$$\begin{aligned} U_{2\phi}\frac{V_t}{H} &= U_p\frac{V_p}{L} \\ U_p &= \frac{U_{2\phi}T}{\Phi} \end{aligned} \tag{3.2}$$

où $U_{2\phi}$ est la vitesse homogène avant le mélangeur.

Comiti et Maurice (1989) considèrent que la chute de pression dans un milieu poreux est la somme de deux termes :

- un premier proportionnel à la vitesse du fluide représentant la perte visqueuse sur la paroi des pores.
- un deuxième proportionnel au carré de la vitesse due à la perte d'énergie cinétique causée par les changements de direction.

Le terme de résistance visqueuse peut être évalué par l'équation de Poiseuille avec une vitesse moyenne U_p dans les pores.

$$\Delta P_{\mathrm{V}} = \frac{32}{d_b^2}\mu_{2\phi}U_pL \tag{3.3}$$

L'effet des nombreux changements de direction peut être déduit par le facteur de frottement de la formule de Nikuradse. Il suffit de faire l'hypothèse que la rugosité est du même ordre de grandeur que le diamètre des pores ce qui conduit à $f = 0.1936$:

$$\Delta P_{\mathrm{C}} = \frac{2f}{d_b}\rho_{2\phi}U_p^2L = \frac{0.3872}{d_b}\rho_{2\phi}U_p^2L \tag{3.4}$$

Nous obtenons finalement l'équation suivante :

$$\frac{\Delta P}{H}\frac{d_b^2}{\mu_{2\phi}U_p} = 32T + 0.3872TRe_p \tag{3.5}$$

où $Re_p = \rho_{2\phi}U_p d_p/\mu_{2\phi}$ est le nombre de Reynolds dans les pores. Les équations (3.2) et (3.5) sont utilisées pour déduire la valeur de la taille des pores : d_p et de la tortuosité T, à partir des mesures de perte de charge et de porosité.

L'équation (3.5) présente la même tendance que la corrélation empirique proposée par Ergun (1952) pour des mélangeurs composés de sable et de particules de coke, valide pour une grande plage de nombre de Reynolds ($1 < Re_p < 2500$) :

$$\frac{\Delta P}{H}\frac{d_p^2}{\mu_{2\phi}U_p} = 150\left(\frac{1-\Phi}{\Phi}\right)^2 + 1.75\frac{1-\Phi}{\Phi^2}Re_p \tag{3.6}$$

Grâce aux équations (3.5) et (3.6), nous pouvons calculer une tortuosité $T = 1.44$ et une porosité $\Phi = 60\%$. Ces valeurs sont en accord avec le type de mélangeur utilisé par Ergun (1952).

Das *et al.* (2005) ont proposé un modèle pour prédire la taille maximum des gouttes a_{max}, à la sortie d'un mélangeur traversé par un écoulement diphasique liquide-liquide :

$$\begin{gathered}\text{À faible nombre de Reynolds } Re_p < 20 \\ \frac{a_{max}}{d_p} = \frac{0.38}{Ca_p} \qquad (a) \\ \text{À haut nombre de Reynolds } Re_p > 20 \\ \frac{a_{max}}{d_p} = \frac{0.33}{We_p^{0.33}} \qquad (b)\end{gathered} \tag{3.7}$$

où $Ca_p = \mu_{2\phi}U_p/\gamma$ est le nombre capillaire dans les pores et $We_p = \rho_{2\phi}U_p^2 d_p/\gamma$ le nombre de Weber dans les pores. On peut supposer que ce modèle reste valable pour un mélange gaz-liquide et prévoit adéquatement les tailles des bulles d'air générer par le mélangeur.

Comme montré précédemment, la vitesse dans les pores est proportionnelle à la vitesse homogène $U_{2\phi}$ (cf. Eq.(3.2)). La première équation (3.7 (a)) conduit à une dépendance de la taille des bulles proportionnelle à $1/U_{2\phi}$. La seconde équation (3.7 (b)) conduit à une dépendance de la taille des bulles proportionnelle à $1/U_{2\phi}^{2/3}$. Les résultats de Das *et al.* (2005) pour un taux de vide de 20% ($\varepsilon = 20\%$) sont présentés aux figures 3.2 et 3.3.

Ce modèle présente des tendances similaires à celles proposées par Hinze (1955) (Taille de bulle proportionnelle à $1/U_{2\phi}^{1.1}$). La différence est expliquée par le fait que dans les mélangeurs, la turbulence n'a pas le temps de se développer complètement. Dans le mélangeur, la

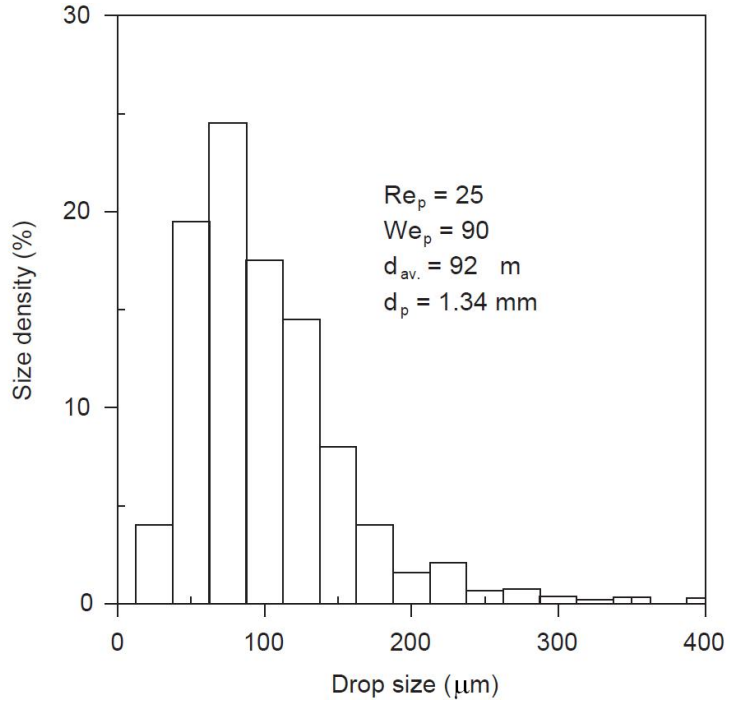

Figure 3.2 Distribution typique de taille de gouttes observée par Das *et al.* (2005) (similaire à une distribution de Rayleigh).

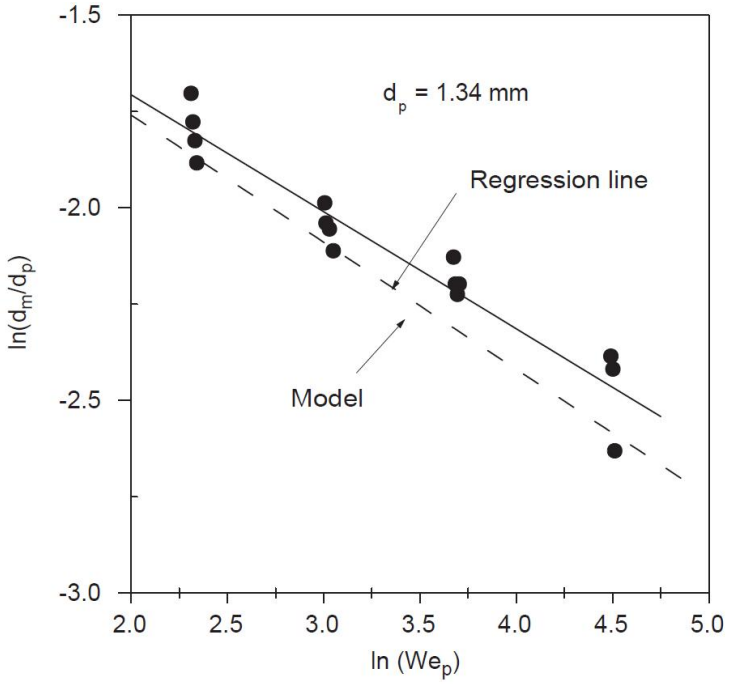

Figure 3.3 Taille maximale des gouttes vs le nombre de Weber (cf. équation (7.80 (b)) (tiré de Das *et al.* (2005)).

turbulence liée au cisaillement est dominante et contrôle la taille des bulles. Pour de grandes vitesses d'écoulement, le mélangeur va créer des taille de bulles plus petites. De petites bulles sont quasiment solides et réduisent considérablement la coalescence, ce qui permet de maintenir des écoulements à bulle pour de plus grands taux de vide.

Dans nos expériences, le mélangeur était composé de grilles de porosité élevée. soit Φ = 0.95. À partir de la définition de la vitesse dans les pores (cf. Eq. (3.2)), l'équation (3.5) peut se réécrire :

$$\frac{\Delta P}{H}\frac{1}{U_{2\phi}} = \frac{32T^2\mu_{2\phi}}{\Phi d_b^2} + 0.3872\frac{\rho_{2\phi}T^3}{d_b\Phi^2}U_{2\phi} \tag{3.8}$$

Nos mesures de perte de charge sont présentées à la Figure 3.4. Ces mesures nous ont permis de caractériser notre mélangeur :

- Tortuosité : T = 1.26
- Diamètre des pores : d_p = 0.42 mm
- Porosité : Φ = 0.95

Ces paramètres et le modèle présenté à l'équation (7.80) nous permettent de déduire la taille des bulles que nous générons.

3.2.3 Les sondes optiques

a) Utilisation

Le laboratoire a opté pour les fibres multimodes, elles sont utilisées depuis plusieurs années. Le processus d'obtention de cônes au bout des fibres est maintenant parfaitement maîtrisé. Les sondes optiques comprennent deux parties, d'une part le système de déplacement des fibres optiques, d'autre part la fibre elle-même. Le système de déplacement (cf. figure 3.5) est constitué principalement de quatre ensembles : le fourreau (1), le piston (2), la tête micrométrique (3), le support des fibres optiques (4). Les fibres optiques sont placées à l'intérieur d'un fin tube rigide (4) qui leur sert de support. Nous utilisons au laboratoire des sondes doubles (cf. figure 3.6) puisqu'elles permettent l'obtention de résultats plus intéressants.

b) Étalonnage

Pour étalonner les fibres optiques, nous nous appuyons sur des données photographiques. La photographie nous apporte une information sur la forme des bulles. Pour l'étalonnage, nous utilisons des vitesses peu élevées de l'air dans de l'eau stagnante. On obtient alors des vitesses de l'ordre de 0.25 m/s, ce qui est tout à fait raisonnable. Les essais ont été possibles grâce à un stroboscope. La méthode opératoire a consisté à régler la lampe stroboscopique à 125 Hz pour un temps de pose de 1/60 de secondes. Ainsi la coïncidence de la lampe et de l'appareil photographique, permet de superposer sur la même image, deux fois les mêmes

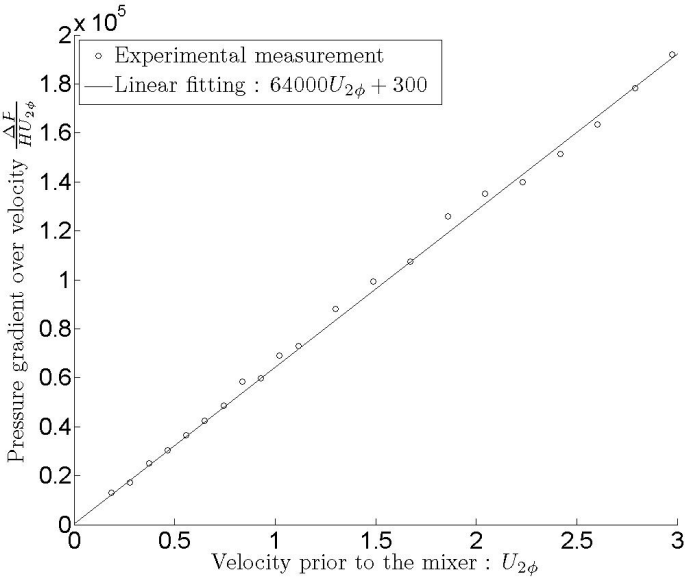

Figure 3.4 Mesure de la chute de pression dans le mélangeur.

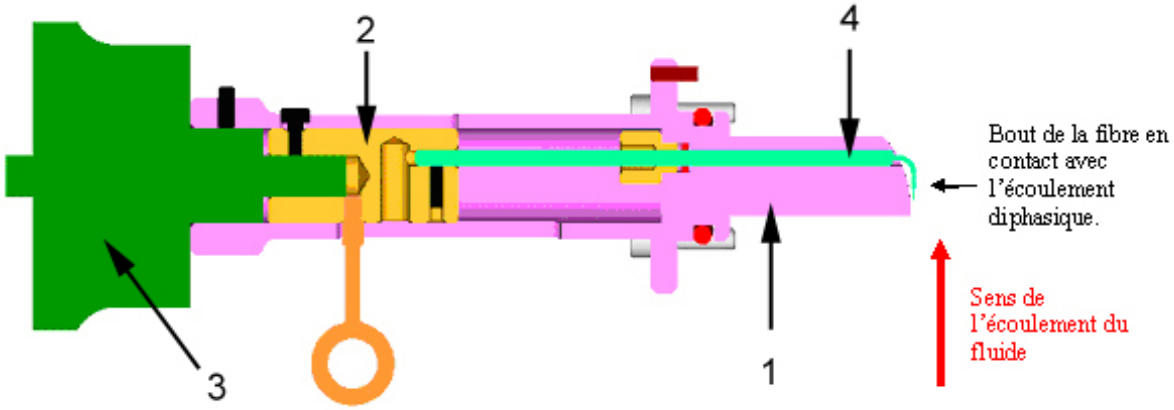

Figure 3.5 Vue en coupe du système de déplacement des fibres tirée du rapport de **?**

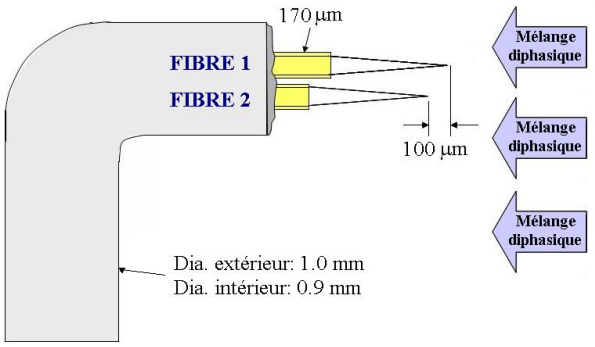

Figure 3.6 Schéma d'une sonde double

bulles. On peut ainsi obtenir, en plus du diamètre des bulles leurs vitesses (cf. photographie 3.7). L'erreur sur la vitesse est de l'ordre de 4 % ce qui est largement acceptable.

3.3 Les sondes à capacitance

Cet outil n'est pas encore disponible au laboratoire. Mon premier travail a été de montrer la faisabilité d'utiliser un tel système au laboratoire. Dans un premier temps, nous avons retenu un design, semblable à celui de Merilo *et al.* (1977), avec deux paires d'électrodes et un déphasage de $\pi/2$ (design (b) figure 3.8). Cela permet d'obtenir un champ électrique rotatif et de limiter la dépendance de la mesure à la configuration d'écoulement.

3.3.1 Conditions d'utilisation

La première conception électrique constituait à monter en série une bobine avec les électrodes que l'on peut représenter schématiquement par une capacité et une résistance variable (cf. figure 3.9). La capacité et la résistance peuvent être évaluées en première approximation par :

$$\begin{aligned} C &= \varepsilon_0 \varepsilon_r \frac{S}{e} \\ R &= \frac{e}{\gamma S} \end{aligned} \tag{3.9}$$

Où

- S est la surface en vis à vis des feuilles métalliques (en m^2)
- e est l'épaisseur du diélectrique (en m)
- ε_0 est la permittivité du vide (en F/m)
- ε_r est la permittivité ou constante diélectrique du milieu (sans dimension)
- γ est la conductivité en $(\Omega.m)^{-1}$

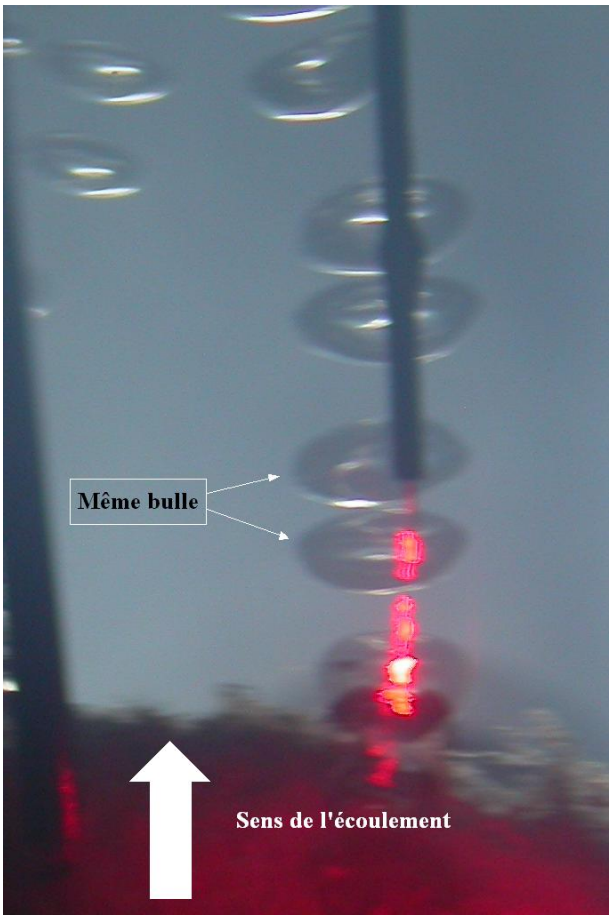

Figure 3.7 Photographie avec deux images superposées grâce aux flashs d'un stroboscope

ε_0 est égal à $8,85.10^{-12}$ F/m. Pour le vide ε_r est égal à 1. L'air sec a une permittivité très proche de celle du vide. L'eau pure a une permittivité relative de 78,5 à 25 ^{o}C. L'eau distillée a une conductivité de 10^{-9}. À partir du schéma électrique équivalent (cf. figure 3.9), il est facile de déterminer la fonction de transfert. La réponse dépend donc de R et C qui dépendent du diélectrique par l'intermédiaire de ε_r et γ. ε_r et γ dépendent à la fois du taux de vide (ε) et de la configuration des deux phases (C_o).

$$\text{En notant} \frac{1}{Z_e(C_o,\varepsilon)} = \frac{1}{R(C_o,\varepsilon)} + jC(C_o,\varepsilon)\omega$$
$$H(\omega,\varepsilon,C_o) = \left|\frac{Z_e(C_o,\varepsilon)}{Z_e(C_o,\varepsilon)+jL\omega}\right| = \left|\frac{1}{1+jL\omega/Z_e(C_o,\varepsilon)}\right| = \left|\frac{1}{1+j\frac{L}{R(C_o,\varepsilon)}\omega - LC(C_o,\epsilon)\omega^2}\right| \quad (3.10)$$
$$\text{où } j^2 = -1$$

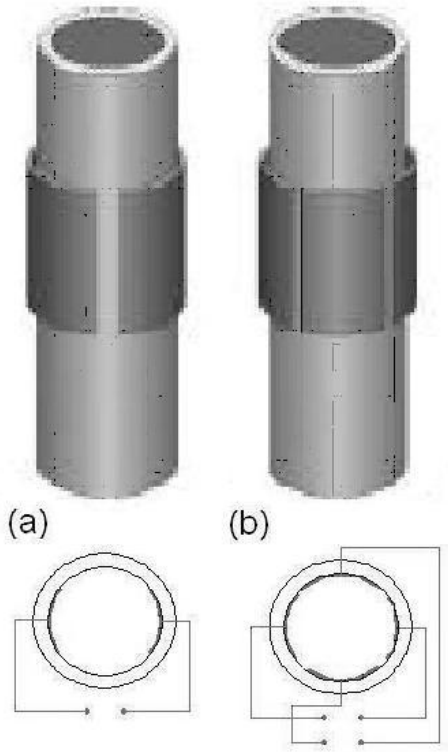

Figure 3.8 Conception des électrodes

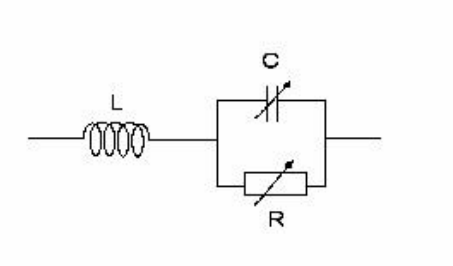

Figure 3.9 Schéma électrique équivalent des électrodes

En notant $\omega_0 = 1/\sqrt{LC}$ et $\zeta/\omega_0 = R/(2L)$ nous avons

$$H(\omega, \varepsilon, C_o) = \frac{1}{\sqrt{\left(1 - \left(\frac{\omega}{\omega_0}\right)^2\right)^2 + (2\zeta\frac{\omega}{\omega_0})^2}} \tag{3.11}$$

C'est une fonction de transfert classique d'un filtre passe-bas qui possède une fréquence de résonance ou de coupure.

– si $\zeta < 1/\sqrt{2}$ c'est-à-dire $R^2C < 2L$, la fréquence de résonance est :

$$\omega_n = \omega_0\sqrt{1 - 2\zeta^2} \tag{3.12}$$

– si $\zeta > 1/\sqrt{2}$, la fréquence de coupure $H(\omega_c) = 1/\sqrt{2}$ est :

$$\omega_c = \omega_0\sqrt{(1 - 2\zeta^2) + \sqrt{1 + (1 - 2\zeta^2)^2}} \tag{3.13}$$

L'idéalisation des électrodes (une résistance et un condensateur en parallèle) semble conforme aux fonctions de transfert expérimentales (figure 3.10). Dans l'exemple d'une paire d'électrodes simple nous avons trouvé par ajustement des fonctions de transfert expérimentales, les coefficients suivants

pour l'eau :

$\omega_{ol} = 2.64\ 10^6$, $\zeta_l = 0.9$, $\omega_{cl} = 1.21\ 10^6$

et pour l'air :

$\omega_{og} = 5.28\ 10^6$, $\zeta_g = 0.31$, $\omega_{ng} = 4.75\ 10^6$.

Pour faire une mesure du taux de vide de l'écoulement, nous alimentons le circuit avec une fréquence fixe choisie entre les deux fréquences caractéristiques. En considérant en première approximation que :

$$\begin{aligned} \omega_o(\varepsilon, C_0) &= \varepsilon\omega_{ng} + (1-\varepsilon)\omega_{cl} \\ \zeta(\varepsilon, C_0) &= \varepsilon\zeta_g + (1-\varepsilon)\zeta_l \end{aligned} \tag{3.14}$$

Les réponses attendues sont représentées sur la figure 3.10 du trait plein au pointillé foncé

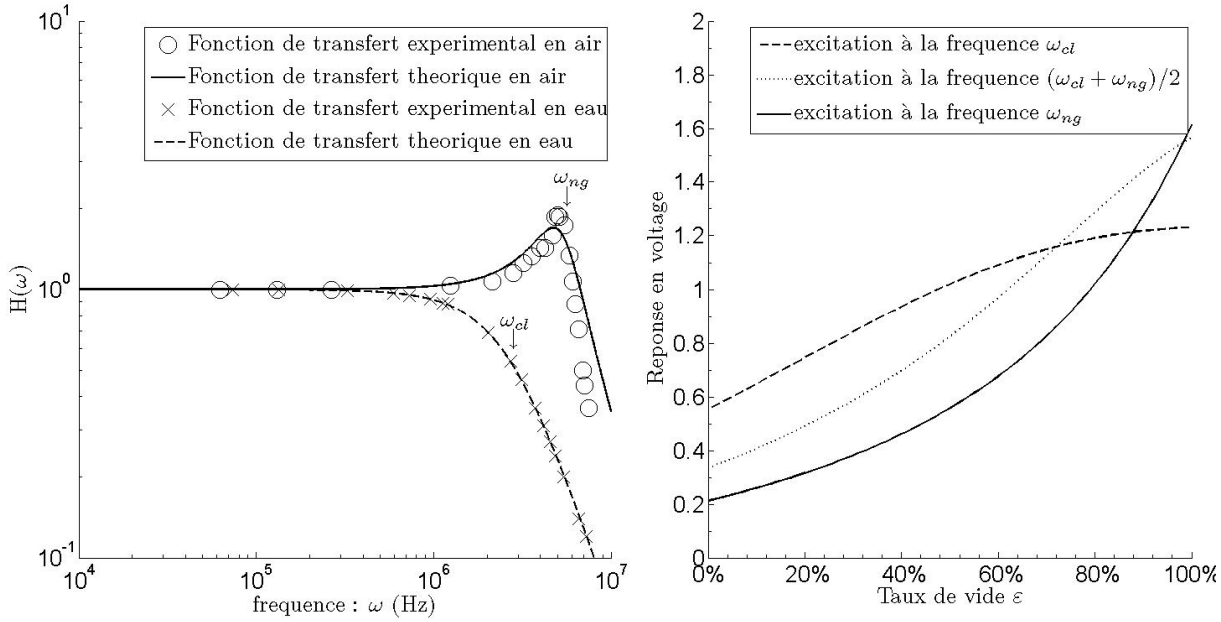

Figure 3.10 Fonction de transfert (gauche) et réponse pour différentes fréquences (droite)

respectivement $\omega = \omega_{cl}; (\omega_{cl} + \omega_{ng})/2; \omega_{ng}$. On remarque que l'on obtient une réponse quasi-linéaire pour une fréquence entre les deux fréquences caractéristiques. Bien entendu une calibration est nécessaire, mais le choix de la fréquence $(\omega_{cl} + \omega_{ng})/2$ permet d'obtenir une réponse quasi linéaire. La vérification expérimentale permet de conclure qu'effectivement le choix de cette fréquence donne une réponse correcte.

3.3.2 Fabrication

Après plusieurs essais, le processus de fabrication présenté à la figure 3.11 a été choisi. Les électrodes sont fabriquées en collant avec de l'époxy deux feuilles métalliques vis-à-vis. La connexion électrique est faite avec une soudure noyée dans l'époxy.

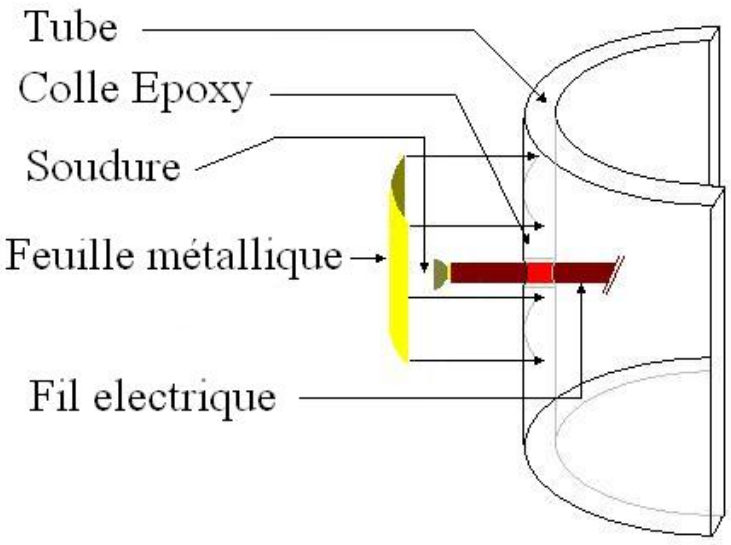

Figure 3.11 Montage d'une électrode sur un tube transverse

3.3.3 Méthodes d'étalonnage

Afin de pouvoir étalonner les électrodes, il faut un moyen précis de mesurer le taux de vide.

a) Étalonnage statique

La première série de mesures est effectuée de façon statique. Un volume d'eau préalablement mesuré est retenu entre les électrodes grâce à deux bouchons en plastique (cf. figure 3.12). Cette méthode permet d'étalonner le taux de vide avec une précision supérieure à 1%. Le système est ensuite agité et soumis à toutes les positions possibles ; l'eau et l'air étant emprisonnés entre les bouchons, le taux de vide ne varie pas, seulement la configuration des deux phases. L'enregistrement de la tension nous donne un minimum et un maximum que l'on peut considérer comme la marge d'erreur de mesure du taux de vide grâce aux électrodes. Nous présentons les résultats de cet étalonnage à la figure 3.13. Nous remarquons tout de suite la très forte dépendance de la mesure par les électrodes à la configuration d'écoulement. Utiliser deux paires d'électrodes diminue cependant cette dépendance. Il est donc primordial de faire un étalonnage pour chaque configuration d'écoulement.

b) Étalonnage dynamique

Une deuxième série de mesures est effectuée de façon dynamique en évaluant le taux de vide grâce à la mesure du titre volumique et à l'évaluation du taux de glissement (modèle de Thom (1968)). La boucle d'essai utilisée est présentée à la figure 3.14. Nous avons exploré les configurations d'écoulement à bulles, agité et à bouchons (cf. figure 3.15). Cette série

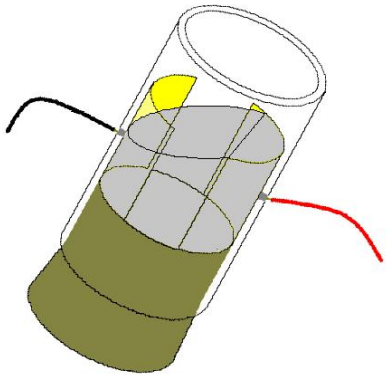

Figure 3.12 Principe de la calibration statique

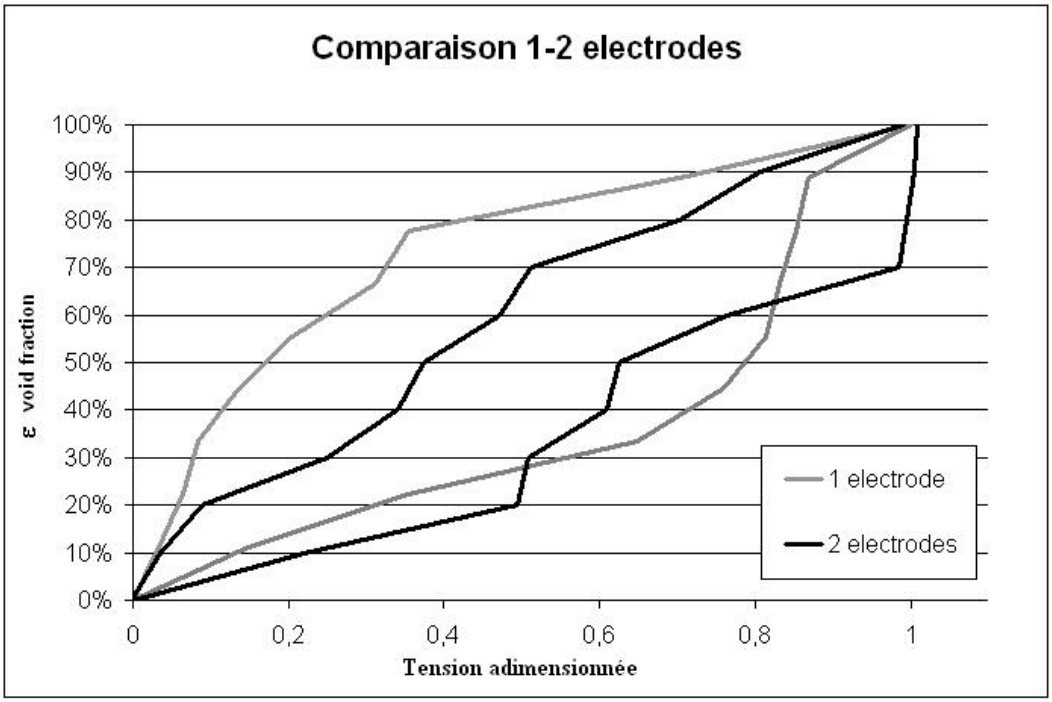

Figure 3.13 Plus grande et plus faible tension enregistrées dans un étalonnage statique

d'expériences a montré la faisabilité du principe de mesure avec les électrodes.

Une autre série d'expériences a été réalisée avec une phase continue stagnante. Cette série permettait une bonne caractérisation de la configuration d'écoulement et du taux de vide. Une première expérience consistait à faire sédimenter des billes de verre dans de l'eau stagnante. La deuxième série d'expériences consistait à générer des bulles à partir de minuscule orifice (0.3 mm) et les laisser monter dans de l'alcool stagnant. Les deux expériences nous ont permis de mesurer à la fois le taux de vide, la vitesse de la phase gazeuse (ou des billes), la surface d'interface et la configuration d'écoulement avec une très bonne précision. Nous avons illustré, à la figure 3.16, l'erreur absolue sur la mesure du taux de vide pour du gaz s'élevant dans de l'alcool stagnant. Les sondes optiques peuvent être aussi utilisées dans un processus d'étalonnage. L'étape suivante est la conception et l'étalonnage d'électrodes pour les écoulements transverses qui présente un défi plus important.

3.4 Caractérisation des configurations d'écoulement

Nous avons mis en rapport les données sur l'écoulement diphasique et les mesures d'amortissement de la structure. Les expériences en liquide stagnant permettent une excellente visualisation de l'écoulement (cf. figure 3.17).

Nous avons montré le lien étroit entre configuration d'écoulement et comportement dynamique de la structure. Comme illustré à la figure 3.18 nous pouvons voir le lien étroit entre la configuration d'écoulement et l'amortissement diphasique. La mesure des propriétés mécaniques de la structure peut donc être une technique de caractérisation des écoulements diphasiques. De façon générale, une transition de régime d'écoulement entraine généralement des changements dans les propriétés des forces induites par l'écoulement.

Ce travail nous a amenés à proposer une révision de la carte de Taitel *et al.* (1980) sur la transition entre les écoulements à bulles et les écoulements à bouchons ou agité, comme présenté dans l'article du chapitre 5.

3.5 Modèle théorique : résolution des équations de Laplace

Dans le cas des écoulements transverses, la géométrie est beaucoup plus complexe. La position et la forme des électrodes nous laissent moins de liberté. Afin de proposer une conception optimale des électrodes et connaître les limites attendues de la mesure, les équations de Laplace pour l'électrostatique ont été résolues afin de prévoir le champ électrique généré par une paire d'électrodes et en déduire la capacité.

Les équations de Laplace pour l'électrostatique sont résolues grâce au potentiel défini

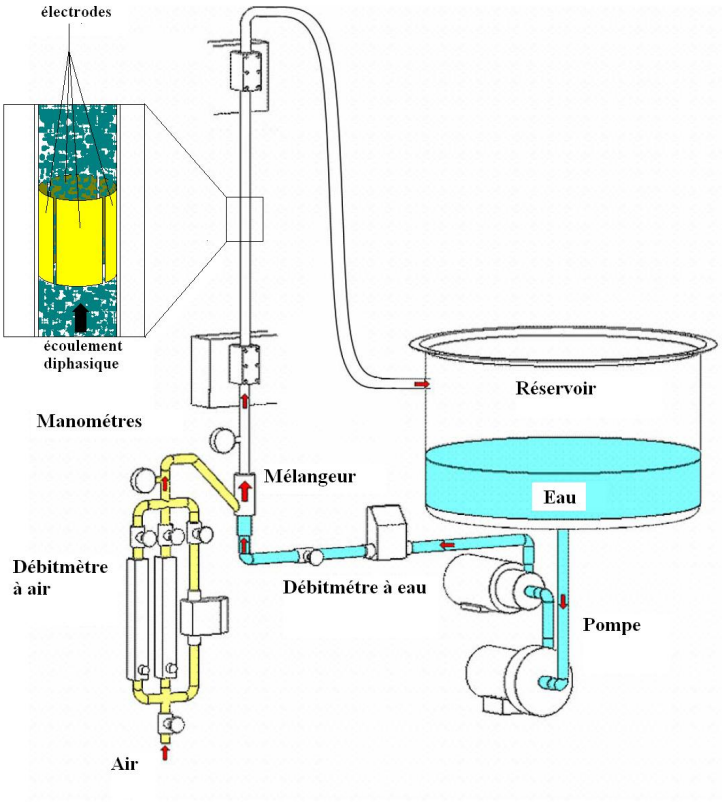

Figure 3.14 Principe de l'étalonnage dynamique

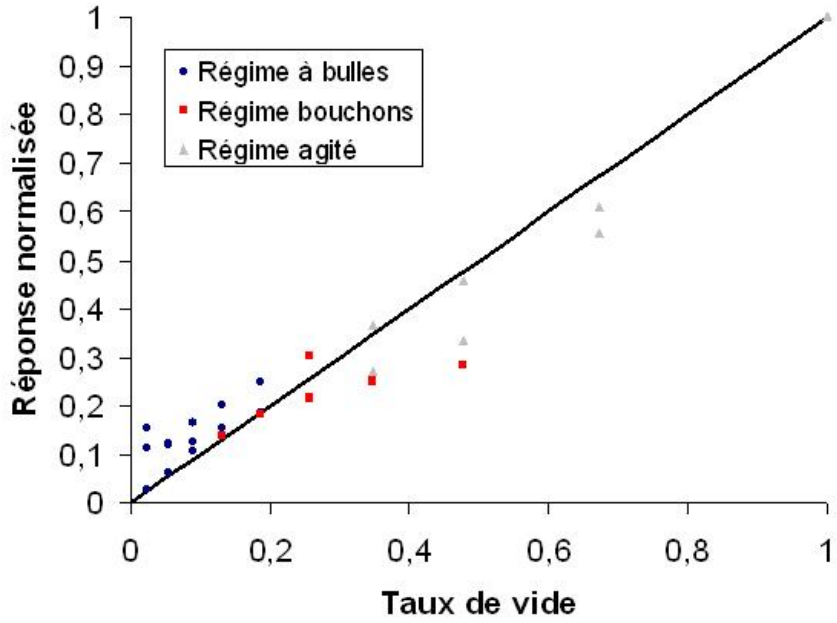

Figure 3.15 Étalonnage dynamique

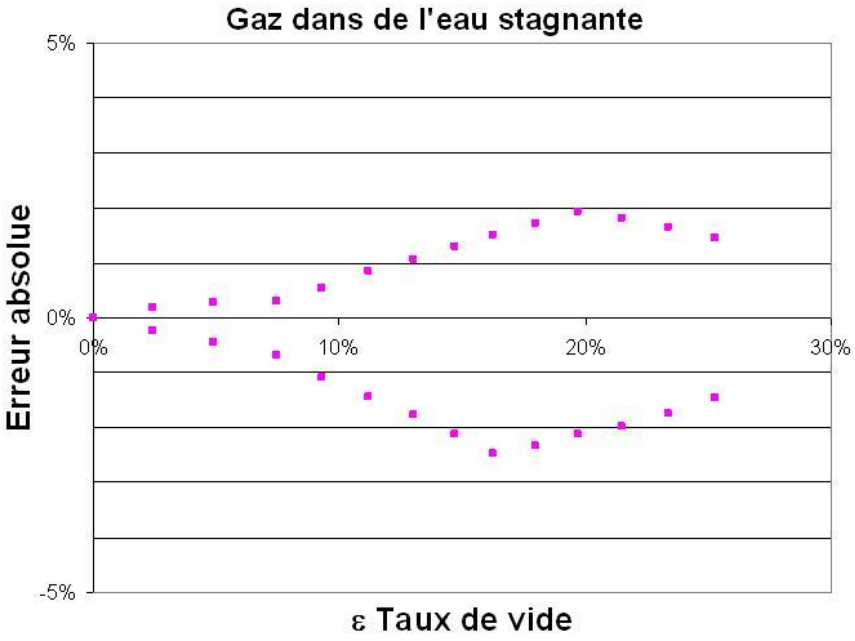

Figure 3.16 Mesure du taux de vide par mesure de la vitesse, débit du gaz et mesure directe des volumes et compilation statistique pour évaluer l'erreur absolue de la mesure

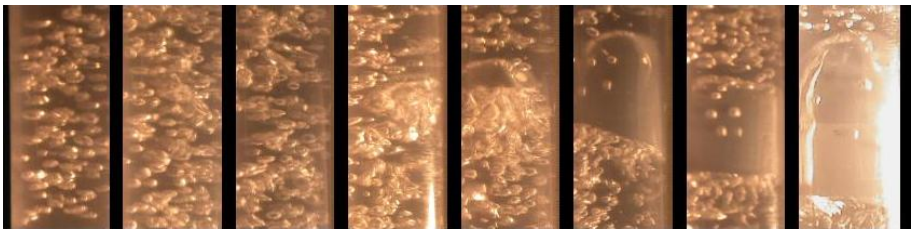

Figure 3.17 Visualisation de la transition dans un liquide stagnant

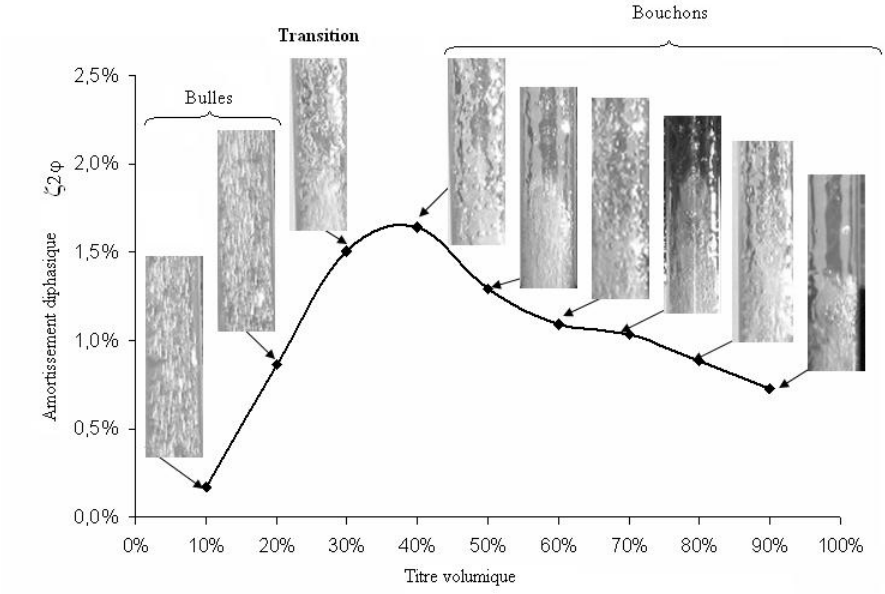

Figure 3.18 Lien entre configurations d'écoulement et amortissement diphasique

comme

$$\vec{E} = -\nabla V \tag{3.15}$$

Nous posons sur les électrodes $V = 1$ (Volt) en dehors V doit vérifier :

$$\Delta V = 0 \tag{3.16}$$

À chaque changement de milieu air-eau, eau-tube, air-tube, le champ électrique doit vérifier le saut de composante normal :

$$\vec{n}_{12} \cdot \left[\varepsilon_2 \vec{E}_2 - \varepsilon_1 \vec{E}_1\right] = 0 \tag{3.17}$$

Soit en 2D sans charge surfacique :

$$\vec{n}_{12}. \left[\varepsilon_1 \left(-\frac{\partial V_1}{\partial x}\vec{e_x} - \frac{\partial V_1}{\partial y}\vec{e_y}\right) - \varepsilon_2 \left(-\frac{\partial V_2}{\partial x}\vec{e_x} - \frac{\partial V_2}{\partial y}\vec{e_y}\right)\right] = 0 \tag{3.18}$$

3.5.1 Méthode de résolution

Les équations ont été résolues par une méthode de différences finies programmée sur MATLAB. La résolution est faite de façon monolithique en une seule itération. Elle consiste à trouver la valeur du potentiel en chaque nœud. La résolution nécessite donc l'inversion d'une matrice (N x N) où N est le nombre de nœuds. Le tableau 3.1 présente l'étude de convergence spatiale. La capacité prévue ne dépend plus du nombre de nœuds à partir 3000 nœuds. Les calculs ont été effectués avec 3240 nœuds, soit un maillage 36x90.

3.5.2 Étude de cas

Les différentes géométries étudiées sont présentées à la figure 3.19. En trait plein noir épais sont représentés les tubes, en traits pointillés le volume de contrôle et en trait gris épais les électrodes. Le volume de contrôle sert à définir le taux de vide qui est le rapport entre le volume d'air sur le volume total de fluide dans ledit volume de contrôle.

Pour chaque géométrie, l'influence de la configuration des deux phases a été étudiée. Pour cela, nous avons simulé la présence d'une goutte d'eau dans l'air dont le centre se situe entre les deux électrodes et de diamètre variable. Nous avons fait de même avec une bulle d'air dans l'eau. Les capacités prévues numériquement sont présentées en fonction du taux de vide calculé sur le volume de contrôle. La taille du volume de contrôle a été choisie de façon à ce que les capacités prévues pour une goutte et une bulle à un même taux de vide soient les plus proches possible. L'écart entre les deux courbes nous donne une bonne indication de la sensibilité à la configuration d'écoulement. Les résultats sont présentés à la figure 3.20.

C (pF)	N_x	N_y	Nombre total de nœud
2.9	43	109	4687
2.9	40	102	4080
2.9	**36**	**90**	**3240**
2.9	34	87	2958
3.1	31	79	2449
3.3	28	72	2016
3.3	24	60	1440
3.7	21	51	1071
4.5	15	36	540
6.6	9	24	216

Tableau 3.1 Étude de convergence spatiale pour la résolution des équations de Laplace

La figure nous montre que, dans les cas des écoulements transverses, la géométrie ne permet pas d'éliminer aussi facilement la dépendance à la configuration d'écoulement. Plus les électrodes sont petites et proches l'une de l'autre, plus elles permettent une mesure du taux de vide sur un petit volume. En revanche, de petites électrodes produisent de plus petites variations de valeurs de la capacité. Comme nous pouvons le constater, la variation de la capacité n'est pas du tout linéaire avec le taux de vide. Il est même possible de constater des valeurs de capacité plus grandes pour des taux de vide plus grands, contrairement à la logique. Cela correspond au moment où le champ électrique peut passer uniquement par l'eau entre les deux tubes. Cela conduit à une augmentation soudaine de la capacité par rapport à une configuration où le champs électrique doit passer successivement d'une phase à l'autre. Cet effet semble d'autant plus important que les électrodes sont petites. Nous sommes donc confrontés à un dilemme : augmenter la taille des électrodes et mesurer le taux de vide sur un grand volume ou réduire la taille des électrodes et voir apparaitre des artéfacts de mesure liés à la configuration d'écoulement.

Cette étude succincte nous montre que pour les écoulements transverses, les sondes optiques restent un moyen plus fiable d'avoir une mesure du taux de vide. Cela tient en partie au fait que la géométrie en écoulement transverse nous empêche d'installer une électrode de garde autour du dispositif de mesure. En revanche, les sondes à capacitance restent un moyen très valable pour étudier les variations spectrales et spatiales de l'écoulement. Nous pouvons remarquer, cependant, que pour les taux de vide élevés où le champ électrique n'a pas le choix de passer à travers l'air, des mesures adéquates du taux de vide sont possibles.

3.6 Mesure de la capacité par charge-décharge

Comme nous l'avons vu au chapitre précédent, étant donné les caractéristiques électriques de l'air et de l'eau, si nous voulons privilégier une mesure de la capacité par rapport à la résistance. Les mesures doivent être effectuées à de très hautes fréquences (50-100 MHz : radiofréquence). Dans le cas où les électrodes ne sont pas placées directement en contact avec l'écoulement, la partie résistive liée à la présence de la structure impose une mesure uniquement de la partie capacitive. Les circuits électriques, excités à des radiofréquences, sont particulièrement sensibles à l'environnement extérieur. Les essais expérimentaux ont été peu concluant entraînant des mesures avec un bruit de l'ordre de la variation de capacité entre un dispositif de mesure plongée dans l'eau ou dans l'air.

Avec l'aide du soutien technique du génie électrique de Polytechnique, nous avons alors envisagé une mesure par charge décharge à partir d'une puce électronique. Afin de mesurer la capacitance, les électrodes et un condensateur de référence sont reliés à une résistance, formant un filtre passe-bas. Les électrodes et le condensateur de référence doivent avoir une capacité du même ordre de grandeur, afin de minimiser l'erreur de mesure.

Les condensateurs sont chargés à la tension d'alimentation V_{Cap} et ensuite déchargés à travers la résistance. Le temps de décharge à un niveau de déclenchement V_{trig} arbitraire est mesuré avec précision grâce à un TDC (Time-to-Digital Converter), (cf. figure 3.21). Le temps de décharge de la capacité de référence et celui des électrodes sont comparés. Ce processus de mesure est répété dans le temps. La fréquence de charge-décharge et la résistance doivent être choisies adéquatement en fonction de la plage de variation de la capacité des électrodes de mesure. La fréquence de charge-décharge est programmée grâce à un microcontrôleur.

Une fois le circuit électrique conçu, le bruit avait la même intensité qu'avec les mesures avec un filtre constitué d'électrodes excitées aux radiofréquences. Nous avons donc miniaturisé le circuit électrique sur un PCB pour réduire le bruit, sans succès notable. Le PCB a alors été placé dans un boîtier pour l'isoler des perturbations extérieures, cela entraîne un changement dans la plage de mesure des capacités nécessitant la reprogrammation du microcontrôleur. Malheureusement, cela n'a pas été possible.

3.7 Futurs développements

La méthode de mesure est prometteuse mais il est nécessaire de réduire le bruit à un niveau raisonnable. Pour cela, deux possibilités sont envisagées. La première est la plus simple, elle consiste en la programmation du micro-contrôleur pour permettre des mesures avec le circuit isolé des perturbations extérieures.

La deuxième étape est la conception d'une mesure comparative pour "mesurer" en temps

réel le bruit et le retirer de la mesure.

Une fois le bruit réduit à un niveau acceptable, une série d'expériences sera nécessaire afin d'effectuer l'étalonnage des sondes. Ces expériences impliqueront des mesures avec liquide stagnant et des mesures de taux de vide par des sondes optiques.

Des sondes correctement étalonnées seront alors un bel outil pour étudier les ondes de taux de vide en comparaison avec les ondes prévues par un modèle numérique utilisant les relations de fermeture présentées dans les articles des chapitres 6 et 7.

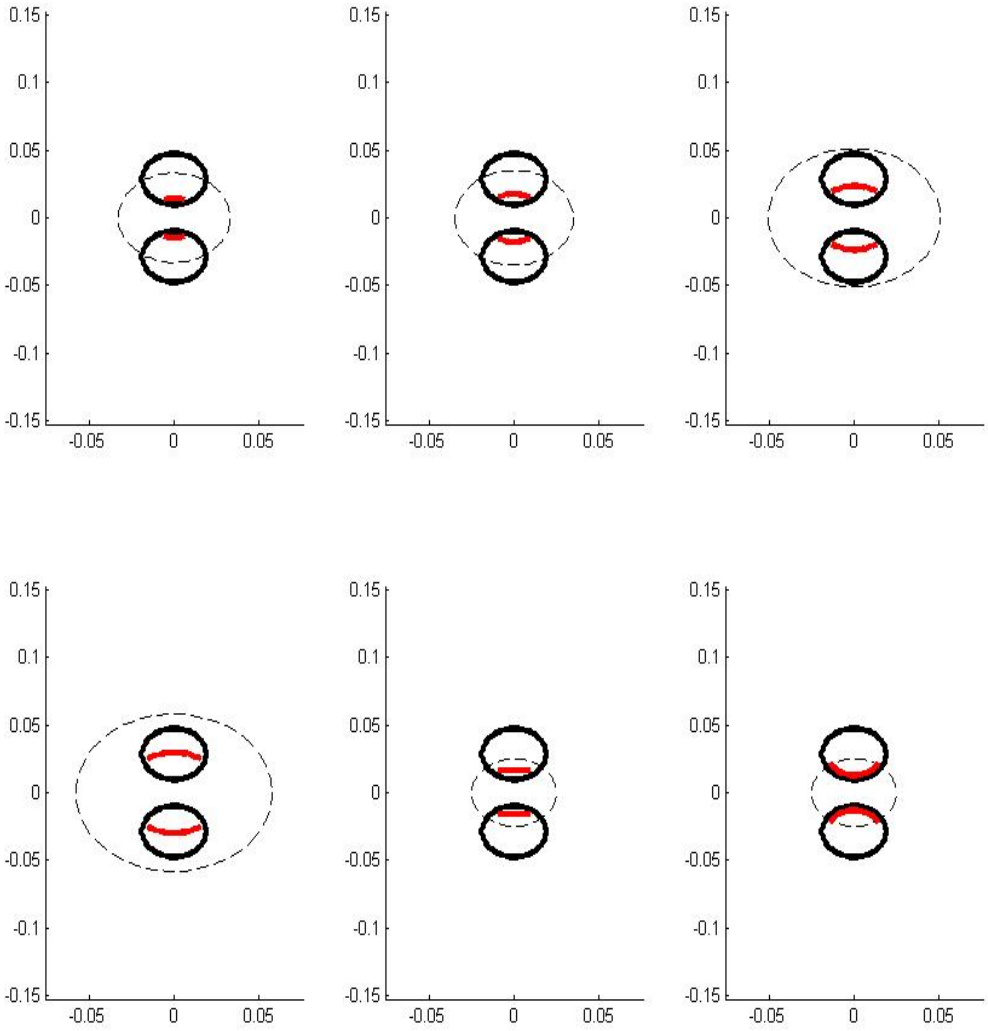

Figure 3.19 Les différentes géométries d'électrodes étudiées, (x et y en m)

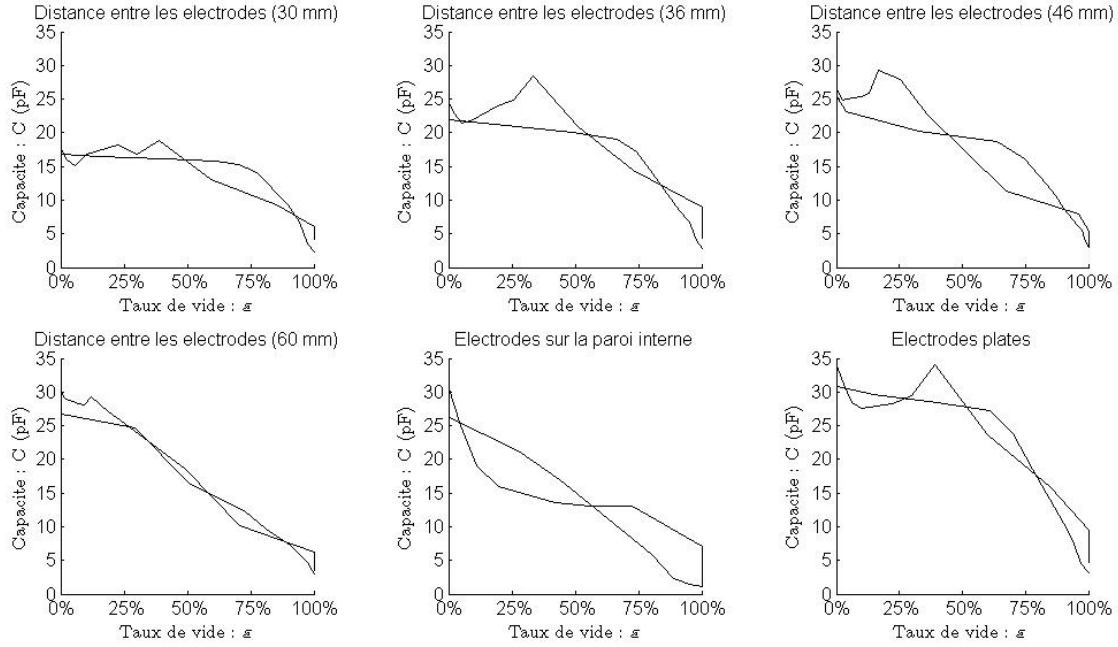

Figure 3.20 Capacités prévues pour les différentes géométries étudiées

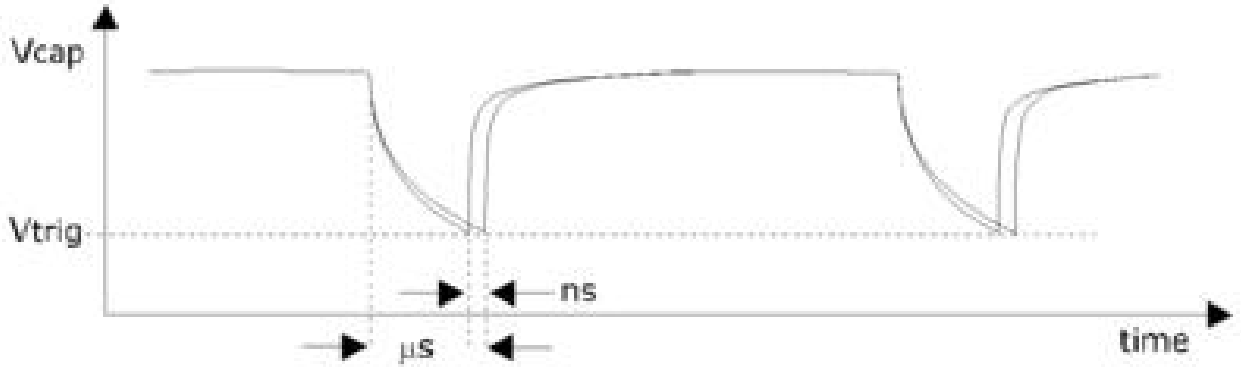

Figure 3.21 Principe de mesure par charge décharge

CHAPITRE 4

TWO-PHASE DAMPING AND INTERFACE SURFACE AREA IN TUBES WITH VERTICAL INTERNAL FLOW

Ce premier article publié dans le *Journal of Fluids and Structures* est consacré principalement à l'influence du diamètre et de la configuration d'écoulement sur l'amortissement diphasique. Pour cela, nous voulions contrôler le plus possible les caractéristiques de l'écoulement. Les premières expériences simulaient des "bulles de géométrie contrôlée" avec des billes de verre en sédimentation dans l'eau stagnante. Puis de l'air a été injecté dans l'alcool stagnant afin de générer un flux de bulles uniformes et mesurables. Des expériences complémentaires ont été effectuées avec des tubes dans lesquels circulait un mélange d'air et d'eau. Une série de photographies ont permis de relier amortissement diphasique et configurations d'écoulement.

C. Béguin, F. Anscutter, A. Ross, N.W. Mureithi & M. J. Pettigrew
BWC/AECL/NSERC Chair of Fluid-Structure Interaction
Department of Mechanical Engineering,École Polytechnique,
P.O.Box 6079, succ.Centre-Ville, Montréal, Quebec, Canada H3C3A7

Abstract

Two-phase flow is common in the nuclear industry. It is a potential source of vibration in piping systems. In this paper, two-phase damping in bubbly flow regime is related to the interface surface area and, therefore, to flow configuration. Experiments were performed with a vertical tube clamped at both ends. First, gas bubbles of controlled geometry were simulated with glass spheres let to settle in stagnant water. Second, air was injected in stagnant alcohol to generate a uniform and measurable bubble flow. In both cases, the two-phase damping ratio is correlated to the number of bubbles (or spheres). Two-phase damping is directly related to the interface surface area, based on a spherical bubble model. Further experiments were carried out on tubes with internal two-phase air-water flows. A strong dependence of two-phase damping on flow parameters in bubbly flow regime is observed. A series of photographs attests to the fact that two-phase damping in bubbly flow increases for a larger number of bubbles, and for smaller bubbles. It is highest immediately prior to the transition from bubbly flow to slug or churn flow regimes. Beyond the transition, damping decreases. It is also shown that two-phase damping increases with the tube diameter.

Keywords *: internal two-phase flow, two-phase damping, flow regime, interface surface area, tube diameter*

4.1 Introduction

In the nuclear industry, heat exchangers and piping elements are often subjected to two-phase flows. Flow-induced vibration can lead to structural degradation, process malfunction, and component failure. Two-phase damping can significantly contribute to reducing vibration and thus, to prevent premature fatigue or wear. Therefore, it is desirable to identify some of the parameters that govern two-phase damping in pipes with internal two-phase flow. In the present paper, we propose to correlate two-phase damping with the interface surface area. The first damping experiments on a tube subjected to two-phase flow were performed some 25 years ago. Carlucci (1980) carried out a series of tests on tubes subjected to an axially confined air-water two-phase flow. His results showed that damping in two-phase flow strongly depends on void fraction, but no significant relation was found with fluid mixture velocity. Many researchers have since contributed to the knowledge of two-phase damping. Recently, Gravelle *et al.* (2007) shed new light on the parameters that govern two-phase damping in vertical tubes with internal air-water two-phase flows. The experiments showed that damping is affected by void fraction, flow velocity, and flow regime. The authors suggested that the interface surface area, which depends on the flow regime, may be a dominant factor. This paper is intended to prove the validity of this hypothesis by means of simple experiments. In addition, tube diameter is also investigated as an important parameter affecting damping.

Nomenclature

Variables:

A: surface area (m2)
B_i : various constants
b_i: integration constants
c: damping coefficient (Ns/m)
d: bubble diameter (mm)
D: tube diameter (mm)
E: Young's modulus (GPa)
E_γ: surface energy (J)
E_{damp}: energy dissipated by damping (J)
F : force (N)
f_n: natural frequency (Hz)
f: friction factor
g: gravitational acceleration (m/s^2)
I: tube second moment of area (mm^4)
I_i, K_i: Modified Bessel function
k: stiffness (N/m)
l: inter-bubble distance (m)
L: tube length (m)
m: mass per unit length (kg/m)
M: reduced mass
N: number of bubbles per unit length of tube
P: fluid pressure (Pa)
Q: volume flow rate (m^3/s)
r, θ cylindrical coordinate
S: interface surface area (m^2)
S_r: slip ratio between phases
U_R : reduced velocity
W: mass flow rate (kg/s)
X: lateral bubble position inside tube (m)
Y: lateral tube displacement (m)
U: superficial velocity (m/s)
V: volume of fluid (m^3)

β: volumetric quality
ΔL: unit length of tube (m)
ε: void fraction
ζ: damping ratio (%)
ρ: mass density (kg/m^3)
γ: surface tension (N/m)
τ: power dissipation per unit mass in turbulent pipe flow (W/kg)
μ: viscosity (Pas)
ν : kinematic viscosity (m2/s)

Indices:
b: bubble, or sphere
o: outer
f: flow-dependent
g: gas
i: inner
l: liquid
s: structural
v: viscous
t: total
2ϕ: two-phase

Other symbols are defined in the text.

4.2 Two-phase flow considerations

4.2.1 Basic definitions

The proportion of gas in a two-phase gas-liquid mixture is characterized either by the void fraction ε or by the volumetric quality β (Collier and Thome (1996). In one unit length ΔL of a two-phase mixture inside a tube, void fraction and volumetric quality are defined as:

$$\varepsilon = \frac{V_g}{V_g + V_l} = \frac{A_g \Delta L}{A_g \Delta L + A_l \Delta L} = \frac{A_g}{A_g + A_l} \tag{4.1}$$

and

$$\beta = \frac{Q_g}{Q_g + Q_l} = \frac{A_g \Delta L U_g}{A_g \Delta L U_g + A_l \Delta L U_l} = \frac{A_g}{A_g + A_l \dfrac{U_l}{U_g}} = \frac{A_g}{A_g + A_l S_r} \tag{4.2}$$

where V_g and V_l are the volumes of the gas and liquid phases in the mixture, Ag and Al are the areas of each phase in the tube section, Q_g and Q_l are the volume flow rates, U_g and U_l are the velocities of each phase. Each proportion is related to the other through the slip ratio between phases, $S_r = U_g/U_l$.

4.2.2 Damping in two-phase flow

When a single phase fluid flows through a transversely vibrating tube, the transverse motion $x(\xi, t)$ of the tube can be damped by the fluid motion (ξ is the axial position along the tube, and t is the time). The equation of motion of such system is as follows (de Langre (2001)):

$$(MU_R^2 - 1)\frac{\partial^2 x}{\partial \xi^2} + 2MU_R\frac{\partial x}{\partial \overline{t}}\xi + (M+1)\frac{\partial^2 x}{\partial t^2} = 0 \tag{4.3}$$

The dimensionless mass of the fluid is given by $M = \rho\pi D^2/(4m)$, where m is the mass per unit length of the tube. The reduced velocity of the fluid is given using the velocity of the transverse wave in the tube itself: $U_R = U/\sqrt{T/m}$, where T is the tension in the tube.

In the second term of Eq. (4.3), the axial velocity U_R of the fluid mass inside the transversely vibrating tube causes a Coriolis type force due to the rotation $\partial x/\partial \xi$ of the tube. This force is proportional to the transverse velocity $\partial x/\partial t$ of the tube: it thus acts as a damping element on the tube. It can be shown from Eq. (4.3) that for low flow velocities, flow-dependent damping is positive: the vibration of the tube is reduced and kinetic energy is either transferred to the fluid flow, or dissipated (de Langre (2001)). Carlucci and Brown (1983) have reported that damping in two-phase flows is much greater than it is in single-phase flows. Thus, the concept of two-phase damping was introduced to allow for this difference. Damping in two-phase flows therefore includes the following components:

- ζ_s : structural damping;
- ζ_v : viscous damping;
- ζ_f : flow dependent damping; and
- $\zeta_{2\phi}$: two-phase damping.

Fig. 4.1 shows the contribution of each component to the total damping ratio for confined annular air-water axial flow. Structural damping depends on the tube material and supports; it is not shown in this figure. Two-phase damping $\zeta_{2\phi}$ is preponderant and strongly depends on void fraction. Carlucci et al. suggested that Coriolis forces in Eq. (5.19) should be written as :

$$2MU_R\frac{\partial x}{\partial \overline{t}}\xi + \underbrace{\left(\frac{\partial M}{\partial t} + U_R\frac{\partial M}{\partial \xi}\right)\frac{\partial x}{\partial t}}_{\text{Two-phase random Coriolis}} .$$

This effect causes a detuning mechanism that could explain Two-phase damping, but this

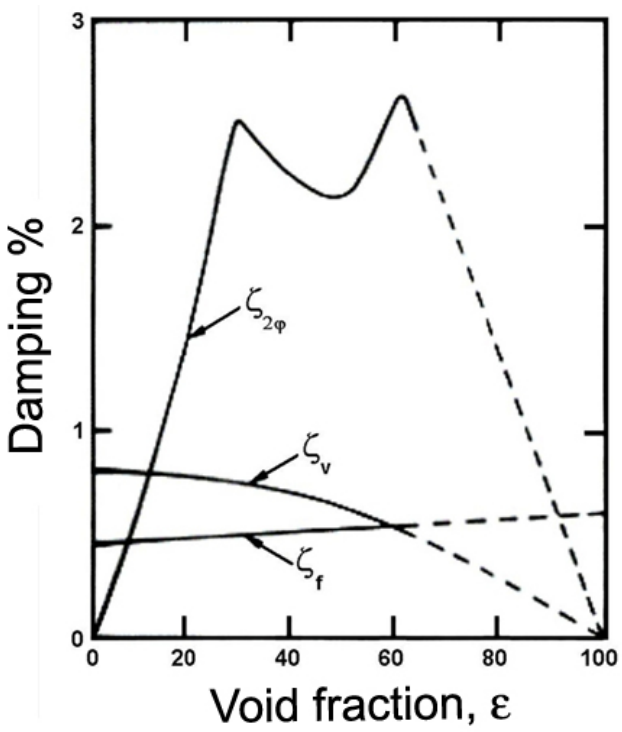

Figure 4.1 Components of total damping in two-phase flow (Carlucci (1980))

model does not explain the void fraction dependency. Hara and Kohgo (1993) considered a bubbly flow forced to oscillate due to a vibrating structure. The motion of bubble in liquid is governed by added mass and fluid viscosity. The energy dissipation in Hara and Kohgo model is due to the liquid viscosity acting between the vibrating gas columns and liquid. However, Carlucci's and Hara's tests were performed with an axially confined external flow, the various damping mechanisms in an internal flow are expected to be the same. The geometric configuration is different, but the motion of the tube and the dependence of two-phase damping on void fraction should exhibit similar trends. Carlucci and Brown (1983) suggested that the total damping ratio ζ_t should be given by the sum of the various damping components:

$$\zeta_t = \zeta_s + \zeta_v + \zeta_f + \zeta_{2\phi} \tag{4.4}$$

Carlucci found two-phase damping to be a dominant component in the 30% to 80% void fraction range, as in Fig.1. However, in the tests described hereafter, we found that the viscous component ζ_v and the flow-dependent component ζ_f were small with respect to the two-phase component$\zeta_{2\phi}$ in the entire range of void fractions. ζ_s was measured with stagnant water and stagnant air. Total damping was measured at 0% and 100% void fractions (where $\zeta_{2\phi} = 0$), for various flow velocities. For each condition, the difference between total damping and

structural damping was not significant; thus, the sum of viscous and flow-dependent damping was found to be negligible in our single-phase experiments, at the flow rates considered. Fig. 1 shows that both viscous and flow-dependent components are monotonic functions of void fraction. Therefore, these two components (ζ_v and ζ_f) were considered to be negligible for all void fractions from 0% to 100%. Finally, the measured structural damping ratio ζ_s ranges between 0.6% and 0.7%, which is much less than the two-phase damping ratios reported in the following sections, hence $\zeta_v + \zeta_f << \zeta_s < \zeta_{2\phi}$. Thus, viscous damping and flow-dependent damping were ignored and the two-phase component $\zeta_{2\phi}$ was calculated as:

$$\zeta_{2\phi} = \zeta_t - \zeta_s \tag{4.5}$$

4.2.3 Two-phase flow regimes

Two-phase flow analysis is formulated from the classic fluid mechanics conservation law. Our discussion will be focused on the homogeneous flow model. In this model, the two-phase mixture is considered as a single fluid whose physical properties correspond to the averaged properties of the phases (Wallis (1969)). The homogeneous model assumes that velocity is the same for both phases, so $S_r = 1$, and $\varepsilon = \beta$.

In two-phase flow, the configuration of the deformable interface between phases is of critical importance to determine mixture properties. Each phase interacts with the tube wall through friction forces, and with the other phase through interfacial forces. The flow structure in gas-liquid vertical flow is commonly categorized into the following flow regimes:

(a) Bubbly flow: At low flow rates, the gas phase is dispersed in relatively large deformable bubbles.

(b) Finely dispersed bubble flow: By increasing the liquid flow rate, the large bubbles break up due to turbulent forces. The small bubbles disperse in the liquid, and coalescence is inhibited by the turbulence.

(c) Slug flow: By increasing the gas flow rate, bubbles agglomerate. Part of the gas phase is arranged in bubbly water slugs and Taylor bubbles. The photographs in Fig. 4.2 show the transition from bubbly to slug flow for a given flow velocity when the void fraction is increased from 6% to 29%.

(d) Churn flow: Churn flow is similar to slug flow. When the gas flow rate of slug flow is increased, slugs become smaller, distorted, and unstable. The flow is more random. Some authors report that slug/churn flow transition is not easy to discern, and instead introduce stable and unstable slug flows (Costigan and Whalley (1996)). For the sake of simplicity in this paper, both slug and churn flow regimes are referred to as slug/churn regime.

(e) Annular flow: At high gas flow rates, the liquid phase forms a layer along the tube

wall. The gas fills the center of the tube.

4.3 Two-phase damping mechanism in bubbly flow

The proposed flow pattern identification technique is based on previous observations according to which two-phase damping is maximum immediately prior to the transition from bubbly to slug/churn flow (Gravelle *et al.* (2007)). As shown below, the surface energy variations of the bubbles do not contribute significantly to two-phase damping. In bubbly flow, it is proposed that viscous dissipation is responsible for two-phase damping, and that it is proportional to the interface surface area.

4.3.1 Estimate of surface energy dissipation

The interface surface area is written as:

$$S = \sum_{k=1}^{N} S_{b,k} = \sum_{k=1}^{N} \pi d_{b,k}^2 = N\pi\langle d_b^2\rangle \tag{4.6}$$

where $S_{b,k}$ and $d_{b,k}$ are the surface area and diameter of the k^{th} bubble, $\langle d_b^2\rangle$ is the average squared diameter of the bubbles, and N is the number of bubbles. In addition:

$$N = \frac{V_g}{\langle V_b\rangle} = \frac{\varepsilon\pi\left(\frac{D_i}{2}\right)^2 L}{\frac{\pi}{6}\langle d_b^3\rangle} \tag{4.7}$$

So

$$S = \frac{3\pi\varepsilon D_i^2 L\langle d_b^2\rangle}{2\langle d_b^3\rangle} \tag{4.8}$$

where L and D_i are the length and inside diameter of the tube. Riverin and Pettigrew (2004) suggested that bubble diameters follow a Rayleigh distribution law in this case:

$$\frac{\langle d_b^2\rangle}{\langle d_b^3\rangle} = \frac{B_1}{\langle d_b\rangle} = \frac{B_2}{d_{max}} \tag{4.9}$$

where B_1 and B_2 are constants and d_{max} is the maximum bubbles diameter. The surface energy is related to the surface tension γ:

$$E_\gamma = \gamma S = \frac{\gamma 3\pi\varepsilon B_2 D_i^2 L}{2d_{max}} \tag{4.10}$$

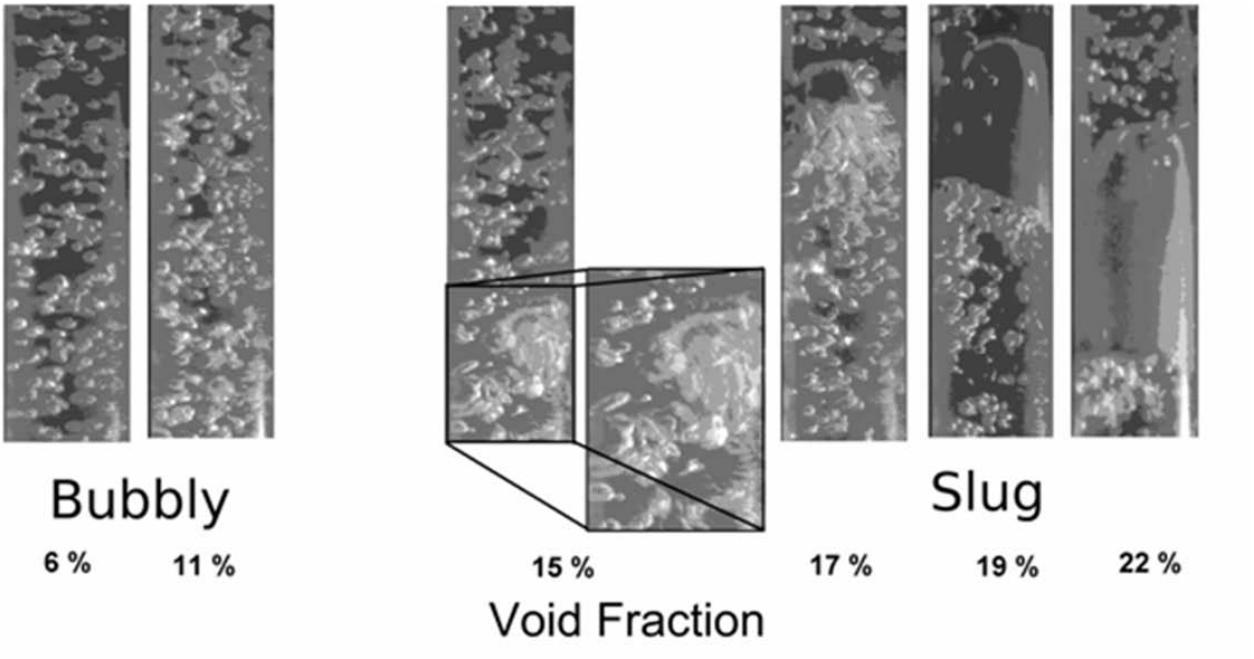

Figure 4.2 Illustration of transition between bubbly flow and slug flow

The bubble diameter suggested by Hinze (1955) for a bubbly flow is:

$$d_{max} = 1.14\left(\frac{\gamma}{\rho_l}\right)^{3/5}\tau^{-2/5} \tag{4.11}$$

where the power dissipation per unit mass in turbulent pipe flow, τ, is given as (Taitel *et al.* (1980)):

$$\tau = \left|\frac{\partial P}{\partial L}\right|\frac{U_{2\phi}}{\rho_{2\phi}} = \left|\frac{2f}{D_i}\rho_{2\phi}U_{2\phi}^2\right|\frac{U_{2\phi}}{\rho_{2\phi}} \tag{4.12}$$

where $U_{2\phi}$ and $\rho_{2\phi}$ are the homogeneous velocity and density of the two-phase flow, and P is the pressure in the fluid. The friction factor f is (Hinze (1955)) :

$$f = 0.046\left(\frac{U_{2\phi}D_i}{\nu_l}\right)^{-1/5} \tag{4.13}$$

Finally, from Eqs. (4.9) to (4.12), the maximum surface energy in a 1m long bubbly air-water flow can be estimated:

$$E_\gamma = \gamma S = 1.6B_2\gamma^{0.4}\rho_l^{0.6}U_{2\phi}^{1.12}D_i^{1.52}\nu_l^{0.08}\varepsilon \tag{4.14}$$

where $B_2 = \dfrac{d_{max}\langle d_b^2 \rangle}{\langle d_b^3 \rangle}$.

It should be noticed that

- Bubbly flow is the pattern having the greatest surface energy.
- By choosing conservative values $B_2 = 2$, $\gamma = 0.076 N/m^2$, $\rho_l = 1000 kg/m^3$, $\nu_l = 10^{-6}$, $U_{2\phi} < 5m/s$, $D_i = 0.021m$ and $\varepsilon < 1$ the maximum surface energy in bubbly flow is estimated to be $E_\gamma < 0.38J$. It should be noted that based on a Rayleigh distribution of the bubble diameter, and defining d_{max} as the 99^{th} percentile, parameter B_2 should not exceed 1.61; thus $B_2 = 2$ is a conservative value.

We conclude that E_γ is certainly inferior than to 0.4 Joules in all cases. As shown below, this value is equivalent to the energy dissipated in one second by the free vibration of the tube with a 0.2% damping ratio. The equivalent stiffness, $k_t = 2660 N/m$, and natural frequency, $f = 21.7$ Hz, of the tube were measured experimentally. The initial transverse displacement of the tube was $x(0) = 2.510^{-2}m$. The strain energy E_d lost in the first one second of free vibration (~ 22 oscillations) with a damping ratio of 0.2% is:

$$\begin{gathered} E_d = \tfrac{1}{2}k_t(x(0))^2 - \tfrac{1}{2}k_t(x(1))^2 = \tfrac{1}{2}k_t(x(0))^2\left(1 - \left(e^{-2\pi 21.70.002}\right)^2\right) \\ E_d = 0.35J \end{gathered} \tag{4.15}$$

Therefore, even if the total interfacial surface doubled within one second during the motion of the tube, it could only explain a 0.2% damping ratio. It will be seen in the next sections that a damping ratio of 0.2% is small compared to the overall two-phase damping. Therefore, even a maximum and extreme change of surface energy in a very short time would not be sufficient to explain the observed two-phase damping. Thus, surface energy variations in bubbly flow seem to play a minor role in two-phase flow damping.

Even during transition from bubbly to slug/churn flow, the surface energy drop may not exceed 0.4 Joules. Thus, dissipation of surface energy during the transition is not sufficient to explain two-phase flow damping. However surface energy governs the flow pattern which may play a major role in two-phase damping. Consequently, another hypothesis is examined below to explain two-phase flow damping.

4.3.2 Two-phase viscous damping mechanism

The hypothesis that two-phase damping is a form of viscous damping in the liquid phase was first introduced by Carlucci and Brown (1983). Damping mechanisms and parameters have been reviewed by Hara (1985) and by Pettigrew and Taylor (2004). In this section, we will show that this hypothesis is realistic, and that two-phase damping is related to the den-

sities of each phase. Indeed, a transverse excitation of the tube induces a relative transverse velocity between the two phases, causing shear dissipation in the liquid. The mechanism can be considered as a coupled problem. Due to the oscillations of the tube, a forced excitation is generated on the gas phase through the liquid. To illustrate the phenomenon, a simple model of a two-phase fluid inside a tube is shown in Fig. 4.3. In this model, the tube of radius R_o is allowed to move along the Y axis. The gas phase is represented as a single, non deformable gas cylinder of radius R_i, parallel to the tube axis and allowed to move along the X axis only. Absolute coordinates X and Y are collinear. No axial flow or other axial phenomena are considered; thus, the masses of liquid and gas are constant in an elementary length of the fluid filled tube. The two-dimensional equations of motion in the plane of the cross-section are:

$$m_s\ddot{Y} + c_s\dot{Y} + k_sY = F_s \tag{4.16}$$

$$m_g\ddot{X} = F_g \tag{4.17}$$

where m_g, m_s are the masses of the gas and tube elements; c_s and k_s are the equivalent damping coefficient and rigidity of the tube. The resulting forces F_s and F_g exerted by the liquid on the tube element and gas element will now be determined. The in-plane movement of the liquid is considered in the r, θ coordinate system originating at the center of the tube section. The tube is chosen as the reference frame. A two-dimensional approach is proposed where the velocity of the liquid inside the elementary control volume is written as $\vec{U} = u_r\vec{e_r} + u_\theta\vec{e_\theta}$. The liquid (water) is considered incompressible. The Navier-Stokes equations for the liquid phase include inertial terms due to the motion of the reference frame $(\rho_l\ddot{Y})$:

$$\begin{aligned}
&\frac{\partial u_r}{\partial r} + \frac{u_r}{r} - \frac{1}{r}\frac{\partial u_\theta}{\partial \theta} = 0 && (a)\\
&\frac{\partial u_r}{\partial t} + u_r\frac{\partial u_r}{\partial r} + \frac{u_\theta}{r}\frac{\partial u_r}{\partial \theta} - \frac{u_\theta^2}{r} = -\frac{1}{\rho_l}\frac{\partial P}{\partial r} + \ldots\\
&\qquad \ldots\nu_l\left(\frac{\partial^2 u_r}{\partial r^2} + \frac{1}{r^2}\frac{\partial^2 u_r}{\partial \theta^2} + \frac{1}{r}\frac{\partial u_r}{\partial r} - \frac{u_r}{r^2} - \frac{2}{r^2}\frac{\partial u_\theta}{\partial \theta}\right) - \ddot{Y}\cos\theta && (b)\\
&\frac{\partial u_\theta}{\partial t} + u_r\frac{\partial u_\theta}{\partial r} + \frac{u_\theta}{r}\frac{\partial u_\theta}{\partial \theta} - \frac{u_r u_\theta}{r} = -\frac{1}{\rho_l}\frac{\partial P}{\partial \theta} + \ldots\\
&\qquad \ldots\nu_l\left(\frac{\partial^2 u_\theta}{\partial r^2} + \frac{1}{r^2}\frac{\partial^2 u_\theta}{\partial \theta^2} + \frac{1}{r}\frac{\partial u_\theta}{\partial r} - \frac{u_\theta}{r^2} + \frac{2}{r^2}\frac{\partial u_r}{\partial \theta}\right) - \ddot{Y}\sin\theta && (c)
\end{aligned} \tag{4.18}$$

Momentum equations (4.18) (b)) and (4.18) (c)) are combined using $\frac{1}{r}\frac{\partial}{\partial r}(r(c)) - \frac{\partial}{\partial \theta}((b))$ to give the vorticity equation :

$$\frac{\partial \omega}{\partial t} + u_r\frac{\partial \omega}{\partial r} + \frac{u_\theta}{r}\frac{\partial \omega}{\partial \theta} + \omega\left(\frac{\partial u_r}{\partial r} + \frac{u_r}{r} + \frac{1}{r}\frac{\partial u_\theta}{\partial \theta}\right) = \nu_l\nabla^2\omega \tag{4.19}$$

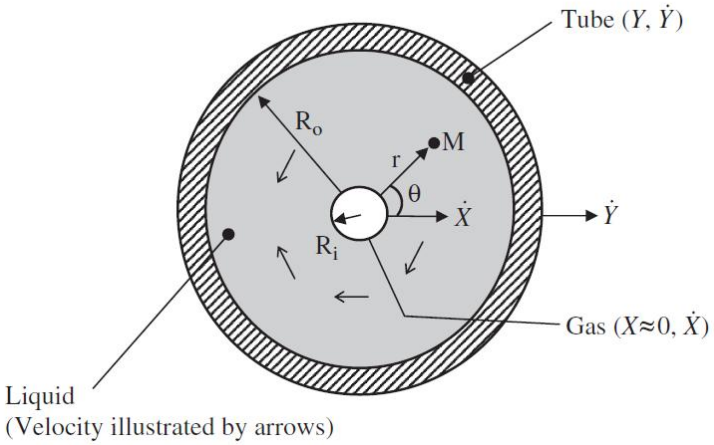

Figure 4.3 Cross section of a tube filled with liquid and a single cylindrical gas bubble. M is a point at coordinates (r, θ).

where $\omega = \frac{1}{r}\left(\frac{\partial(ru_\theta)}{\partial r} - \frac{\partial u_r}{\partial \theta}\right)$ is the magnitude of the vorticity. Noting that the fourth term of the left hand side is zero due to continuity, and by introducing the stream function

$$\begin{aligned} u_r &= -\frac{1}{r}\frac{\partial \Psi}{\partial \theta} \\ u_\theta &= \frac{\partial \Psi}{\partial r} \\ \|rot\ \vec{V}\| &= \nabla^2 \Psi \end{aligned} \tag{4.20}$$

the vorticity equations becomes:

$$\frac{\partial(\nabla^2\Psi)}{\partial t} - \frac{1}{r}\frac{\partial \Psi}{\partial \theta}\frac{\partial(\nabla^2\Psi)}{\partial r} + \frac{1}{r}\frac{\partial \Psi}{\partial r}\frac{\partial(\nabla^2\Psi)}{\partial \theta} = \nu_l \nabla^4 \Psi \tag{4.21}$$

It is assumed that momentum is conserved in the in-plane direction perpendicular to the motion of the tube. It is also assumed that the motion of the gas phase is small compared to that of the liquid phase, with respect to the moving reference frame. Therefore,

$$\frac{\partial(\nabla^2\Psi)}{\partial t} = \nu_l \nabla^4 \Psi \tag{4.22}$$

This equation was previously solved by Chen (1987) in a similar case, the only difference come from the inertial forces due to frame's motion. Inertial forces are non-rotational and conduct to the sane vorticity equation, however they changes of course expressions of forces F_g and F_s. Knowing that the position of the gas phase in the tube referential is $X - Y$, the

above homogeneous equation allows the exact solution:

$$\begin{aligned} \Psi &= (\dot{X} - \dot{Y})G(r)\sin\theta \\ G(r) &= \tfrac{b_1}{r} + b_2 r + b_3 I_1(\lambda_0 r) + b_4 K_1(\lambda_0 r) \end{aligned} \tag{4.23}$$

Therefore,

$$\begin{aligned} u_r &= (\dot{Y} - \dot{X})\frac{G(r)}{r}\cos\theta \\ u_\theta &= (\dot{X} - \dot{Y})G'(r)\sin\theta \end{aligned} \tag{4.24}$$

where $\lambda_0^2 = \frac{i\Omega}{\nu_l}$, Ω is the complex frequency of the motion, and $G'(r) = \frac{\partial G}{\partial r}$. Integration constants b_i are dependent on the boundary conditions:

$$\begin{aligned} &u_r(R_i,\theta) = (\dot{Y} - \dot{X})\cos\theta \\ &u_r(R_o,\theta) = 0 \\ &u_r = (\dot{X} - \dot{Y})\sin\theta \\ &u_\theta(R_o,\theta) = 0 \end{aligned} \quad \Leftrightarrow \quad \begin{aligned} &G(R_i) = -R_i \\ &G(R_o) = 0 \\ &G'(R_i) = -1 \\ &G'(R_o) = 0 \end{aligned} \tag{4.25}$$

The stress vector on the circumferential faces of a liquid element is

$$\bar{\bar{\sigma}}(r) = \left(-P + 2\mu_l \frac{\partial u_r}{\partial r}\right)\vec{e_r} + \mu_l \left(r\frac{\partial \frac{u_r}{r}}{\partial r} + \frac{1}{r}\frac{\partial u_\theta}{\partial \theta}\right)\vec{e_r} \tag{4.26}$$

The resulting forces on the gas cylinder (F_g) and on the tube (F_s) in the X direction are

$$\begin{aligned} F_g &= \int \bar{\bar{\sigma}}(R_i).\vec{e_x} r d\theta \\ F_s &= \int \bar{\bar{\sigma}}(R_o).\vec{e_x} r d\theta \end{aligned} \tag{4.27}$$

Thus, the resulting force exerted in the X direction by an annular element of the liquid is

$$F_x(r) = \int_0^{2\pi} \left[\left(-P + 2\mu_l \frac{\partial u_r}{\partial r}\right)\cos\theta + \mu_l \left(r\frac{\partial \frac{u_r}{r}}{\partial r} + \frac{1}{r}\frac{\partial u_\theta}{\partial \theta}\right)\sin\theta\right] r d\theta \tag{4.28}$$

Using Eqs. 4.25 and (4.28), the force exerted by the liquid on the gas cylinder (F_g) and on the tube (F_s) are obtained as follows:

$$\begin{aligned} F_g &= \rho_l \pi R_i^2 \left[(2b_2 + 3)\ddot{X} - (2b_2 + 2)\ddot{Y}\right] - 2\mu_l \pi(\dot{X} - \dot{Y}) \\ F_s &= \rho_l \pi R_o^2 \left[-2b_2\ddot{X} + (2b_2 + 1)\ddot{Y}\right] \end{aligned} \tag{4.29}$$

Finaly, Eqs. (4.16) and (4.17)

$$\begin{aligned} m_s\ddot{Y} + c_s\dot{Y} + k_sY &= \rho_l\pi R_o^2\left[-2b_2\ddot{X} + (2b_2+1)\ddot{Y}\right] \\ m_g\ddot{X} &= \rho_l\pi R_i^2\left[(2b_2+3)\ddot{X} - (2b_2+2)\ddot{Y}\right] - 2\mu_l\pi(\dot{X}-\dot{Y}) \end{aligned} \tag{4.30}$$

where

$$\begin{aligned} 2b_2 &= b_r - \frac{b_i}{i\Omega}\text{with}(b_r, b_i) \in \mathbb{R}^2 \\ 2b_2\ddot{X} &= b_r\ddot{X} + b_i\dot{X} \end{aligned} \tag{4.31}$$

The final equations of motion are :

$$\begin{aligned} m_s\ddot{Y} + c_s\dot{Y} + k_sY &= \rho_l\pi R_o^2\left[-b_r\ddot{X} + (b_r+1)\ddot{Y} - b_i(\dot{X}-\dot{Y})\right] \\ m_g\ddot{X} &= \rho_l\pi R_i^2\left[(b_r+3)\ddot{X} - (b_r+2)\ddot{Y} + \left(b_i - \tfrac{2\nu_l}{R_i^2}\right)\pi(\dot{X}-\dot{Y})\right] \end{aligned} \tag{4.32}$$

If there is no relative displacement between the liquid and gas phases ($X = Y$), then

$$\begin{aligned} m_s\ddot{Y} + c_s\dot{Y} + k_sY &= -\rho_l\pi R_o^2\ddot{Y} \\ m_g\ddot{Y} &= \rho_l\pi R_i^2\ddot{Y} \end{aligned} \tag{4.33}$$

In this case, a non trivial solution ($\ddot{Y} \neq 0$) is obviously not possible unless the mass of the gas phase (m_g) is $\rho_l\pi R_i^2$, which requires that $\rho_g = \rho_l$. This leads us to conclude that unless both phases have the same density, there exists a relative transverse displacement $Y - X \neq 0$ between the liquid and the gas phase. In addition, the relative transverse velocity between phases leads to two-phase damping through the terms $\rho_l\pi R_i^2\left(b_i - \frac{2\nu_l}{R_i^2}\right)\pi(\dot{X}-\dot{Y})$ and $\rho_l\pi R_o^2 b_i(\dot{X}-\dot{Y})$. This basic model shows that transverse motion of the tube comes with viscous dissipation due to the relative motion of the liquid and gas phases. This dissipation is the result of the difference in the densities of each phase. Moreover, it should be noted that a larger bubble yields a greater dissipation from the tube.

From a physical point of view, the foregoing results can be interpreted as follows. A transverse displacement of the tube causes a pressure differential in the liquid around the gas bubble, causing the bubble to move relative to the tube. The liquid thus circulates locally around the bubble, and viscous friction is initiated which causes damping in the fluid-structure system.

4.3.3 Relation between two-phase viscous damping and interface surface area

From the above simple model, it was shown that a force excitation is generated on the gas phase through the liquid. A more complete model would show that liquid flows around each bubble and induces forces that depend on the boundary conditions of the liquid

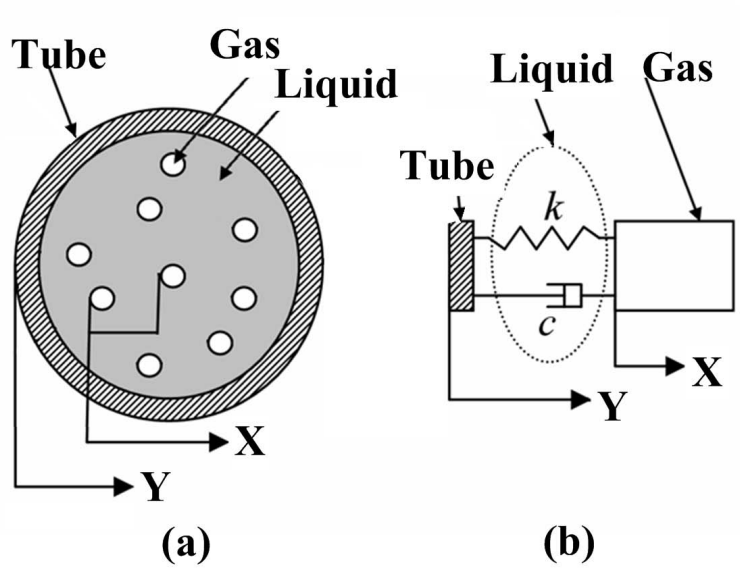

Figure 4.4 Illustration of viscous damping mechanism in two-phase flow:(a) tube cross-section and (b) one degree of freedom model.

$(X, Y, \dot{X}, \dot{Y}, , \ddot{X}, \ddot{Y}, U_{2\Phi}$. The above simple model has yielded equations of the form [ref. Eq. (4.32)]:

$$\begin{aligned} m_s\ddot{Y} + c_s\dot{Y} + k_sY &= m_{sg}\ddot{X} + m_{ss}\ddot{Y} + c_{sg}(\dot{X} - \dot{Y}) \\ m_g\ddot{X} &= m_{gg}\ddot{X} + c_{gs}(\dot{X} - \dot{Y}) \end{aligned} \tag{4.34}$$

A more complete model would probably lead to:

$$\begin{aligned} m_s\ddot{Y} + c_s\dot{Y} + k_sY &= m_{sg}\ddot{X} + m_{ss}\ddot{Y} + c_{sg}(\dot{X} - \dot{Y}) + k_{sg}X + k_{ss}Y \\ m_g\ddot{X} &= m_{gg}\ddot{X} + c_{gs}(\dot{X} - \dot{Y}) + k_{gg}X + k_{gs}Y \end{aligned} \tag{4.35}$$

This system is represented as a simple equivalent mechanism illustred in Fig. 4.4, where the forces of the liquid on the gas are shown as spring and damper forces. These forces are calculated using a surface integral on the liquid/gas interface. As a result, the viscous damping ratio ζ is expected to be proportional to the interface surface area. Finally, the gas is set in motion relative to the tube, due to these forces. Assuming that $\dot{X} = \lambda\dot{Y}$, where λ is probably related to the relative densities of the phases and the mixture velocity $U_{2\phi}$, the energy dissipation in the liquid during one oscillation cycle is:

$$E_{damp} = \int c(\dot{Y} - \dot{X})dY = \int c(1-\lambda)\dot{Y}dY = \int c_{2\phi}\dot{Y}dY = \tag{4.36}$$

The relative transverse velocity between phases is responsible for the viscous dissipation:

$$\zeta_{2\phi} = g(S)f(U_{2\phi}) = B_3 S f(U_{2\phi}) \tag{4.37}$$

where B_3 is a constant. The proportionality between two-phase damping and interface surface area comes from Gravelle *et al.* (2007) observations. It seems to be valid for bubbly flow only, whereas the damping mechanism may be different in other flow regimes. In the following sections, the relation was verified in bubbly flow through two simple experiments in which both the damping ratio and the interface surface area were measured precisely. Other parameters such as the bubble distribution pattern, bubble interaction and liquid turbulence may also play a major role in governing two-phase damping, but this study was focused on one parameter: the interface surface area.

4.4 Evaluation of two-phase damping

Each experiment was performed on a vertical, clamped-clamped cylindrical tube. Three PVC tubes of similar effective lengths, but different internal diameters (21.2 mm, 15.5 mm and 11.7 mm) were used. Test tube properties are given in Table 4.1.

The tubes were subjected to internal flows (described later), and were set to vibrate. The tubes were deflected with a transverse displacement of 10mm at mid-length, and released using a quick-release device. The resulting transverse vibration was measured using strain gauges (Gravelle *et al.* (2007)).

At first, damping was determined using both the logarithmic decrement and the random vibration techniques. Both methods were found to give the same results, as expected. Since it was faster and simpler, and because of suitable test conditions, the logarithmic decrement technique was then used for most tests.

4.5 Experiments with rigid spheres in water

4.5.1 Apparatus and procedure

This is one of two experiments used to verify the dependence of two-phase damping on the interface surface area. Small glass spheres of controlled diameter were let to settle in stagnant water. The glass spheres represent gas bubbles. The use of spheres to model bubbly flow is justified by the fact that below a certain diameter near the capillary length (order of one mm) bubbles can be regarded as spheres. Bubble deformation can be ignored, because surface energy dissipation is negligible, as shown previously. Clearly, glass spheres do not coalesce, thus only bubbly flow can be simulated in this experiment. The two-phase flow has a very low

Property	Tube #1	Tube #2	Tube #3
Length, L (m)	1.48	1.55	1.58
Inner diameter, D_i (mm)	21.2	15.5	11.7
Outer diameter, D_o (mm)	26.8	21.3	17.0
PVC Young's modulus E (GPa)	2.4	2.4	2.4
PVC density, rs (kg/m3)	1380	1380	1380
Second moment of area of tube section I (m^4)	1.54×10^{-8}	7.27×10^{-9}	3.18×10^{-9}
Tube mass, m (kg)	0.458	0.250	0.186
Theoretical frequency, fn (Hz)	21.7	16.04	12.37
Structural damping, ζ_s (%) 0.7	0.65	0.6	

Table 4.1 Characteristics of test tubes

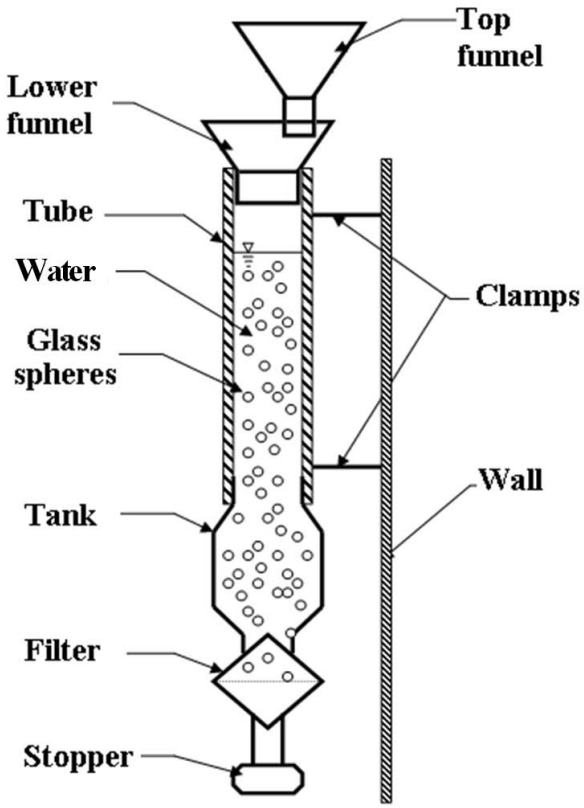

Figure 4.5 Schematic representation of the test rig for glass–water experiments

homogeneous velocity. The low velocity of the spheres allows for a good visual observation of the flow.

The test rig shown in Fig. 4.5 consisted of six parts. Two funnels were laid out on top of each other, the lower funnel being directly attached to a vertical PVC tube. A tank, a filter and a plug were fitted at the bottom of the tube. The 21.2 mm diameter tube was supported by two clamps on a rigid wall. The glass spheres used have a diameter of 0.85 mm ±0.1%. They were released from the top funnel to the lower one. The top funnel was not centered and the outlet diameter of the second funnel was identical to the diameter of the tube. Thus the spheres spread evenly through the tube section. The spheres fell through the stagnant water in the tube, while damping measurements were performed. The spheres were stopped by the filter and collected inside the tank. At the end of each experiment, the plug was removed, the water was evacuated, and the spheres were retrieved from the tank.

Void fraction (the proportion of spheres in the water) was controlled by varying the outlet diameter of the top funnel. The interface surface area S was calculated using Eq. (4.6). The number of spheres N was determined as follows:

$$N = \frac{W_b}{\rho_b U_b \left(\frac{\pi}{6} d_b^3\right)} \tag{4.38}$$

An empirical relation was developed to relate the granular mass flow rate W_b to the outlet diameter of the funnel. The mass of glass spheres flowing down the funnel in a given time was measured, and the mass flow rate was calculated. This was done for various funnel diameters, and the results are shown in Fig. 4.6.

The mass density ρ_b of the spheres was also determined experimentally. A beaker partially filled with a given volume of water (V_1) was weighed, giving m_1. Glass spheres were then added, as in Fig.4.7, and the resulting mass (m_2) and volume (V_2) were measured. The density of the glass spheres was then calculated:

$$\rho_b = \frac{m_2 - m_1}{V_2 - V_1} \tag{4.39}$$

The sphere velocity U_b was determined by measuring the sedimentation time of glass spheres through a given length of water inside the tube. A few spheres were painted in red in order to be tracked easily. This was done for various funnel diameters, and results are given in Fig. 4.8. The velocities of a single unpainted and a single red sphere were compared to verify that the influence of paint is negligible. The single sphere velocity is approximately 0.07 m/s; it is shown as a straight horizontal line on Fig. 4.8, with dashed lines showing the error range.

Finally, the interface surface area S and void fraction ε were evaluated. Resulting values spread within ±5% around the average values, as shown in Fig. 4.9. When void fraction

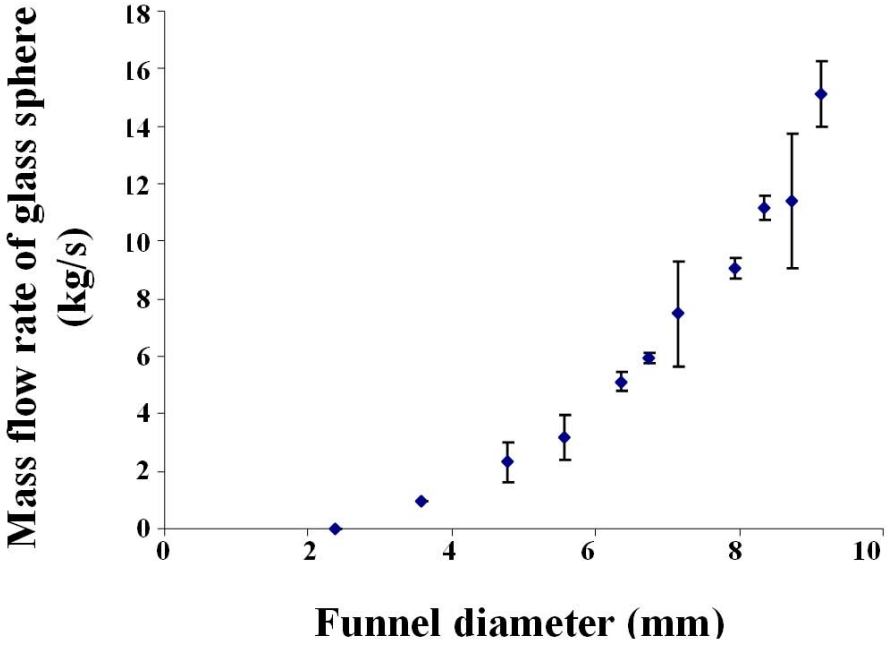

Figure 4.6 Mass flow rate with respect to funnel diameter

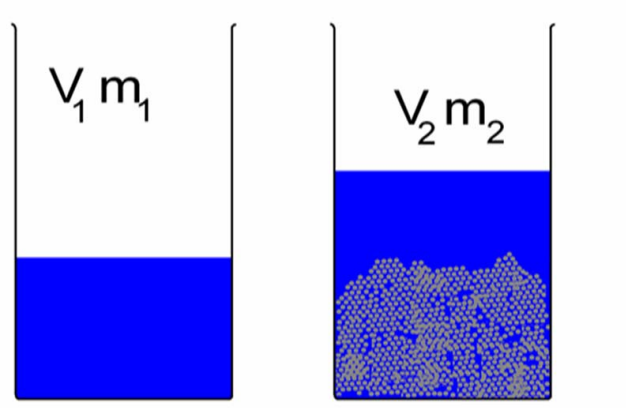

Figure 4.7 Empirical determination of glass spheres mass density ρ_b.

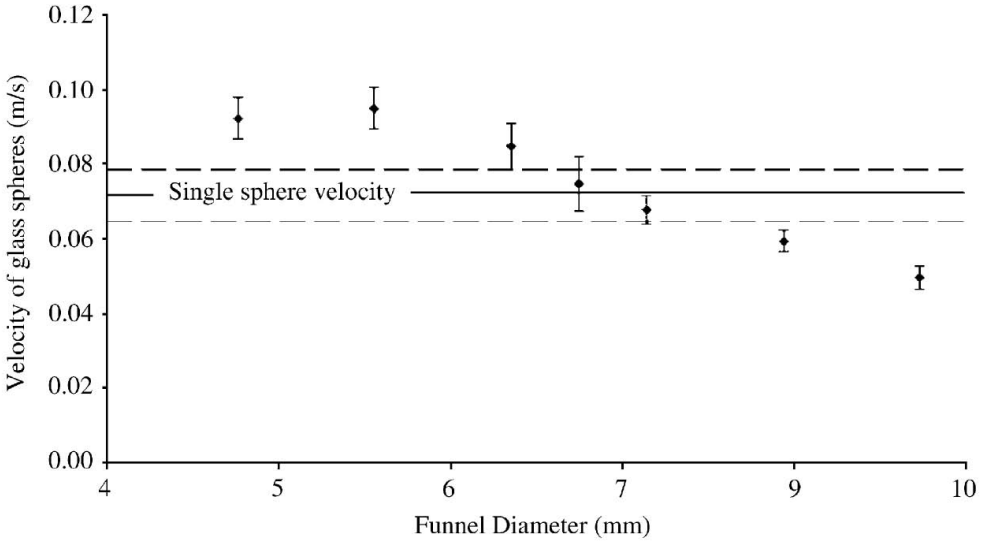

Figure 4.8 Sedimentation velocity of glass spheres with respect to funnel diameter.

exceeded 35%, the glass spheres tended to cluster at the top of the water column. Thus, the experiments were limited to the following void fractions: 2%, 4%, 5%, 8%, 15%, 19%, 32% and 34% ($\varepsilon = 34\%$ requires a flow of 23 000 spheres per second).

4.5.2 Results

For each void fraction, two-phase damping was measured three times. Fig. 4.10 shows that the results of the different tests are repeatable. For any given void fraction, the variation absolute empirical error of two-phase damping is less than within ±0.2%.

The interface surface area was calculated as described above, and is represented by the straight full line. For void fractions up to 15%, two-phase damping is directly related to interfacial surface area. At 15%, a transition was observed in the behaviour of the glass spheres. The spheres started interacting with each other, due to their high concentration in the water. The motions of the spheres were no longer independent. Shear forces in the water were reduced, resulting in lower two-phase damping, as seen in Fig. 4.10. It should be noted from Figs. 4.8 and 4.9 that a 7 mm funnel diameter corresponds to both a void fraction of approximately 15% and a sphere velocity equal to that of a single sphere. For void fractions less than 15%, the sphere velocity is greater than the sedimentation velocity of a single sphere; for void fraction above 15%, the sphere velocity is lower than that of a single sphere. Two preliminary conclusions are put forward:

– First, the transition from bubbly flow to slug/churn flow was observed around $\varepsilon = 15\%$ in stagnant water. A strong interaction was detected between the glass spheres at void

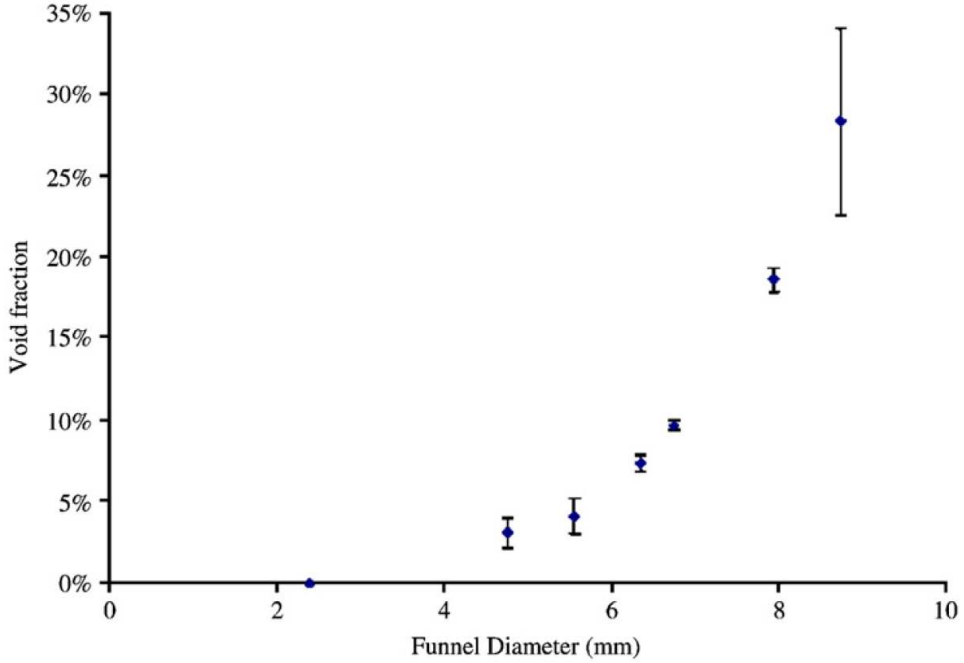

Figure 4.9 Void fraction with respect to funnel diameter.

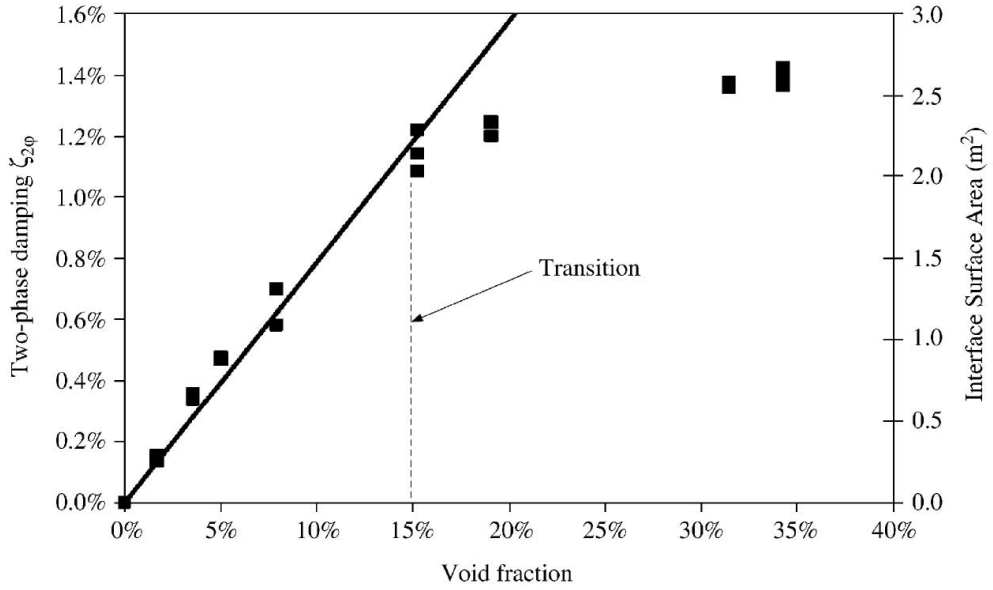

Figure 4.10 Two-phase damping ratio in glass spheres–water mixture (■ : two-phase damping; - : interface surface area).

fractions above 15%. Spheres occupying more than 15% of the total volume attempt to group together and move slower than an isolated sphere. If such interaction existed between bubbles in air-water mixtures, it would lead to the coalescence of air bubbles.

– Second, below ε = 15% ("bubbly" flow) the motions of glass spheres seem to be independent of each other. Therefore, the contribution of glass spheres (or bubbles) to the two-phase damping is linear with the number of spheres. Hence, two-phase damping may be directly related to the interface surface area.

4.6 Experiments with air in alcohol (static)

In the previous experiment, the correlation between two-phase damping and interface surface area was shown for void fractions up to 15% only. This second experiment is used to confirm that the interface surface area is a fundamental parameter in two-phase damping for all void fractions.

The experiment consists in creating a network of air bubbles at the bottom of the tube. Two-phase damping is measured while the bubbles rise to the surface of stagnant alcohol, the properties of which are given in Table 4.2. The number and size of the air bubbles are regulated. Homogeneity of the bubble flow is maintained, and so is the void fraction. Thus, the interface surface of the bubbles can be calculated and correlated with two-phase damping for all void fractions.

4.6.1 Apparatus and procedure

This experiment was carried out in the same clamped-clamped tube as in the previous experiment (21.2 mm diameter). An air injector is mounted at the bottom of the tube, and a reservoir is mounted at the top, as shown in Fig. 4.11.

The air injector is made of three parts, shown in an exploded view in Fig. 4.11. The main part is a perforated plate holding three needles of 10 mm length and 0.3 mm inside diameter. Premature coalescence of the bubbles close to the plate is avoided by placing the needles 10 mm apart, in a triangular pattern on the plate. The lower and upper parts of the air injector assembly are connected together to form two sealed chambers separated by the plate-and-needle unit. Air flows from the lower part to the upper part through the needles, and continues inside the tube.

The open reservoir at the top of the tube is used to contain any overflow of the alcohol/air mixture from the tube during the experiments. This happens for large void fractions.

A micro flow meter is positioned upstream of the plate-and-needle unit to guarantee that the air flow is sufficiently low to prevent premature coalescence of the bubbles.

4.6.2 Bubble size

The diameter of the bubbles is predicted, in order to determine the appropriate needle hole. The following model is considered in Fig. 4.12, where the bubble reaches its full diameter db before it detaches from the needle. By isolating the bubble from its surrounding medium (alcohol) and by making a quasi-static assumption, the bubble is subjected exclusively to two forces: buoyancy (or Archimedes) force F_A and the capillary force F_γ which retains the bubble to the needle:

$$F_\gamma = \gamma \pi D_h \cos\theta = \gamma \pi D_h \frac{D_h}{d_b} \tag{4.40}$$

and

$$F_A = (\rho_l - \rho_g) g \frac{\pi}{6} d_b^3 \tag{4.41}$$

In the above equations, D_h is the diameter of the needle hole, and g is the gravitational acceleration. The bubble sets off when buoyancy overcomes the capillary force, yielding the equation:

$$d_b^4 = \frac{6 D_h \gamma}{(\rho_l - \rho_g) g} \tag{4.42}$$

The critical bubble diameter before coalescence is given by the maximum diameter for which a bubble can be regarded as a rigid sphere (Brodkey (1967))

$$d_{max}^2 = \frac{0.4\gamma}{(\rho_l - \rho_g) g} \tag{4.43}$$

The combination of (4.41) and (4.41) gives the diameter of the needle hole:

$$D_h = \frac{0.4^2}{6} \frac{\gamma}{(\rho_l - \rho_g) g} \tag{4.44}$$

Therefore, the critical bubble diameter is 1.7 mm in water and 1.0 mm in alcohol. The needle diameter that satisfies the critical bubble diameter is 0.26 mm for alcohol and 0.45 mm for water. The needles used have 0.3 mm internal diameter. The size of the bubbles produced

Property	Alcohol	Water
Temperature, T (^{o}C)	20	20
Density of liquid, ρ_l (kg/m^3)	860	1000
Density of the air, ρ_g (kg/m^3)	1.18	1.18
Surface tension, γ (N/m)	0.022	0.074
Density ratio, ρ_l/ρ_g	728.8	847.5

Table 4.2 Properties of alcohol and water

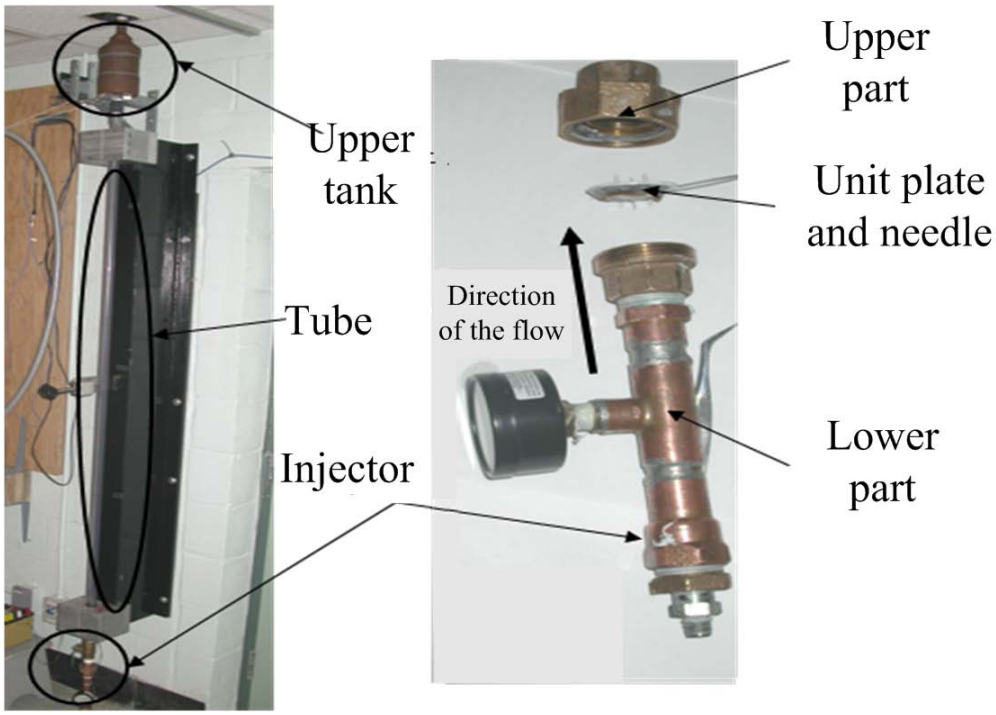

Figure 4.11 Photographs of the test rig for air–alcohol experiments.

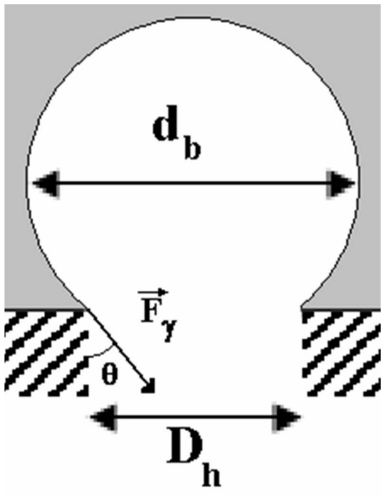

Figure 4.12 Model for air bubble.

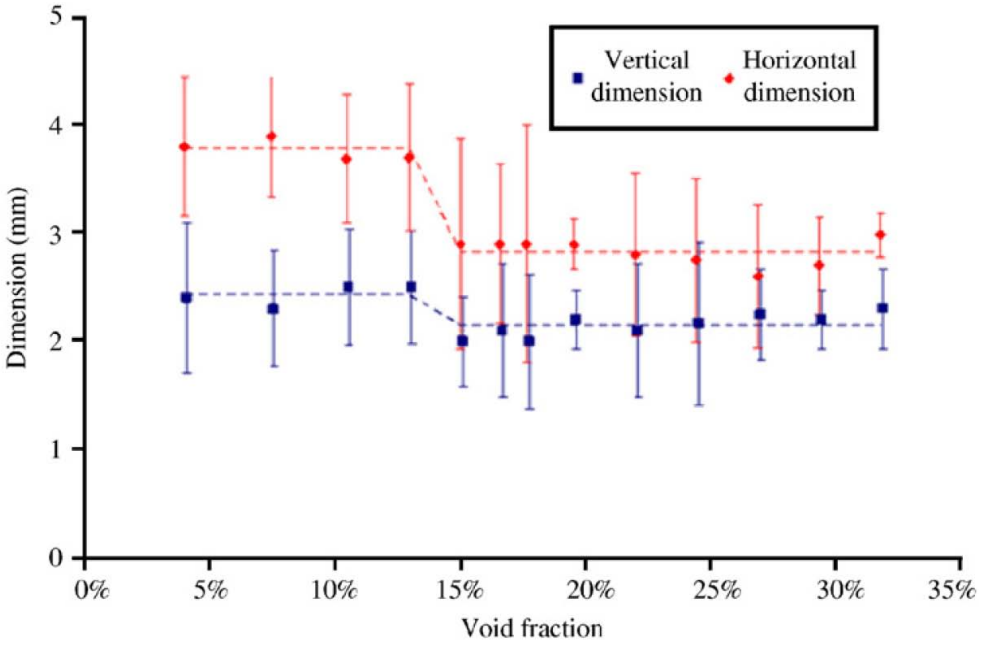

Figure 4.13 Bubble dimensions with respect to void fraction in air–stagnant alcohol(■: vertical dimension; ◆: horizontal dimension).

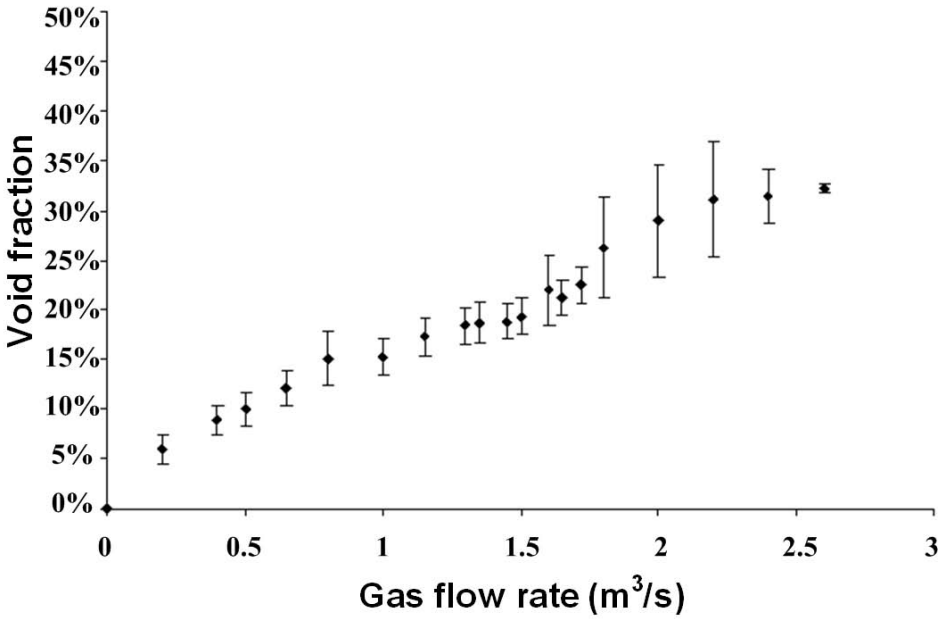

Figure 4.14 Void fraction in air–stagnant alcohol with respect to gas volume flow rate.

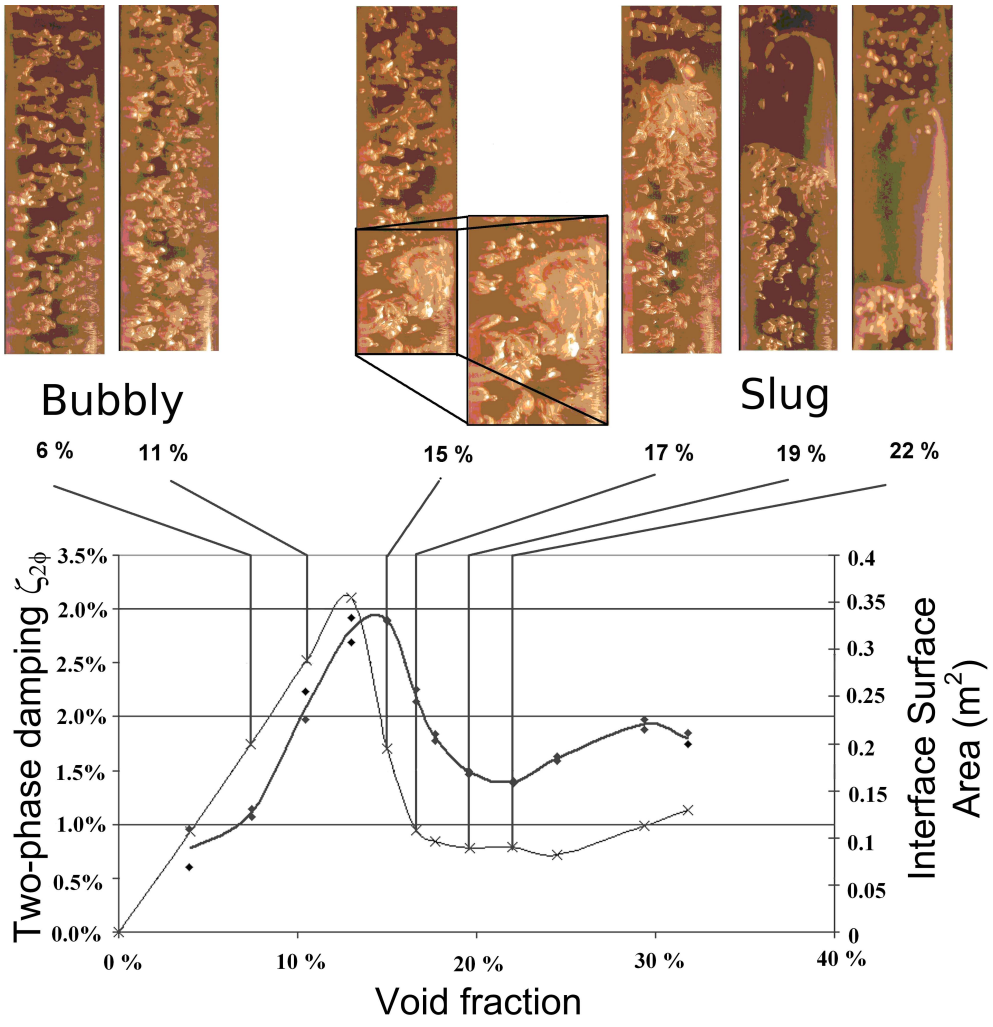

Figure 4.15 Damping ratio and interface surface area in air–alcohol mixtures(◆: two-phase damping; ×: interface surface area).

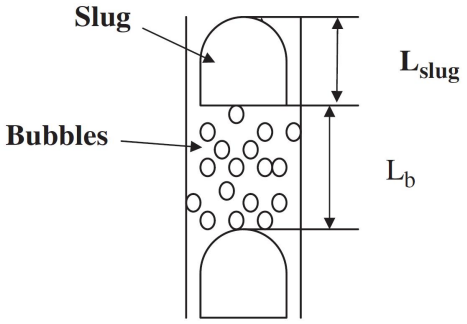

Figure 4.16 Illustration of slug flow.

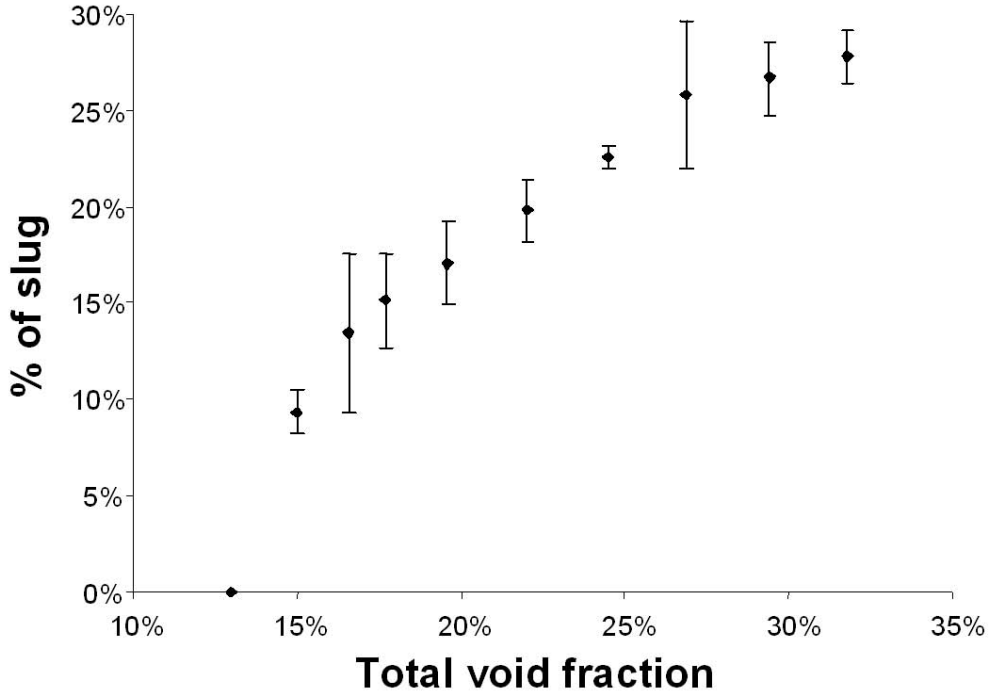

Figure 4.17 Relative slug length with respect to total void fraction (100% is total tube length).

during the experiments was measured, and the use of the 0.3 mm needles was validated. Both alcohol and water could be used, but it was observed that the air-liquid mixture is more homogeneous with alcohol, possibly because the needles provide closer bubble packing in alcohol. During the experiments, the size of the bubbles was measured from photographs. Fig. 13 shows the measured bubble sizes with respect to void fraction. For all void fractions, the horizontal dimension (◆) is greater than the vertical dimension (■) of the bubbles. Except for a drop (which is significant on the horizontal dimension) near a 15% void fraction, both dimensions are relatively constant. Void fraction was determined from the difference between the mixture level inside the tube during the injection and the liquid level prior to the injection. As shown in Fig. 4.14, void fraction is fairly linear with gas flow rate, and resulting values spread within ±5% around the average values. The mean values were used to calculate the interface surface area in the mixture.

4.6.3 Results

Two-phase damping was measured twice for various void fractions ranging from 3% to 33%. The data points are given in Fig. 4.15, showing that the tests are repeatable.

The trend through the data points is shown as a thick line, and the interface surface area

is shown as a thin line (x). For bubbly flow (low void fractions), the interface surface area is calculated using Eq. (4.8), and considering each bubble as an ellipsoid. The interface surface area in slug/churn flow was evaluated from the following model :

$$S = S_{bubbles} + S_{slugs} = 2\pi N' \left(a^2 + b^2 \frac{e}{\tan e} \right) + N_{slug}(2\pi D_i^2 + \pi D_i L_{slug}), \tag{4.45}$$

where a and b are the minor and major axes of the ellipsoid and $e = arcos(a/b)$; N_{slug} is the number of slugs in the tube, and L_{slug} is the average slug length, as shown in Fig.4.16. The number of bubbles N' is calculated using Eq. (4.7) and considering bubbly flow between slugs. Fig. 4.17 shows the ratio of slug length to tube length with respect to void fraction. The error bars do not correspond to measurement error which is very low but to the heterogeneity of bubble size. We can see that this heterogeneity is relatively small.

$$N' = \frac{\varepsilon' \pi \left(\frac{D_i}{2} \right)^2 \left(\frac{L_b}{L_{slug}} \right) L}{V_b} \tag{4.46}$$

L_b/L_{slug} is the average length between each liquid slug over the average length of gas slugs (see Fig. (4.16) measured from photographs. Fig. 4.17 shows the measured total length of slugs over the length of the picture that could be expressed as:

$$\left(\frac{L_{slug}}{L_b + L_{slug}} \right) = \frac{1}{\frac{L_b}{L_{slug}} + 1} \tag{4.47}$$

The bubble volume V_b is calculated from the measured horizontal and vertical dimensions of the bubbles, considering them as ellipsoids. We deduce ε' (void fraction between slugs) from the total void fraction and average lengths L_b and L_{slug}:

$$\varepsilon = \frac{V_b + V_{slug}}{V_t} = \frac{L_b \varepsilon' + L_{slug}}{L_b + L_{slug}} \tag{4.48}$$

The photographs at the top of Fig. 4.15 were taken during the experiments. They clearly show that the flow is bubbly for void fractions up to 15%, and slug/churn for void fractions above 23%. According to the photographs, the bubbles begin to interact at a void fraction of approximately 15%, which would mark the beginning of the transition from bubbly flow to slug/churn flow. A close up of the photo at 15% void fraction was added to show this interaction clearly.

As in the previous experiment, there is a remarkably good correlation between the interface surface area and the two-phase damping ratio. However, the relationship between the two parameters is somewhat different below and above ε = 15%. The constant of proportionality that relates the two-phase damping ratio to the interface surface area is higher

in slug/churn flow ($\varepsilon > 15\%$) than it is in bubbly flow ($\varepsilon < 15\%$). Apparently, there is an additional damping mechanism in slug/churn flow which is also related to the interface surface area. It is possible that considerable energy dissipation occurs in the wake of the slugs which are moving transversally due to the motion of the tube.

4.7 Discussion

The two experiments described above show that two-phase damping is directly proportional to the interface surface area. The constant of proportionality is different for bubbly flow than for slug/churn flow. Also, in the air-alcohol mixture, the damping ratio increases quasi-linearly with void fraction in bubbly flow. Both the damping ratio and the interface surface area fall abruptly when the void fraction reaches the transition point from bubbly to slug/churn flow. If this trend also exists in other two-phase flows, measuring the damping ratio could be used as a technique for detecting this transition. Experiments were also performed on tubes subjected to internal air-water two-phase flows, as described below. In stagnant liquid ($u_{gs} << 1$) both experiments show that the transition from bubbly to slug/churn flow occurs near 15% void fraction. Experimental observations suggest that the transition from bubbly to slug/churn flow is related to the confinement of gas bubbles. When the distance between bubbles (or spheres) is too small, they start interacting. In the case of rigid spheres, the spheres and the liquid between them move together. As a result, less viscous friction occurs and less energy is dissipated than if the spheres moved independently. In the case of gas bubbles the interaction leads to coalescence and lower energy dissipation. Although the diameter is not the same for glass spheres (0.85 mm) and bubbles (1.0 mm), the transition occurs at almost the same void fraction in both cases (around $\varepsilon = 15\%$). The distance between spheres (or bubbles) was calculated assuming homogeneous packing of the gas phase, in order to determine its relationship with the transition void fraction. We use the following notation: l is the distance between spheres and d is the sphere diameter (the center-to-center distance between the spheres is $(l + d)$. Different hypothesis can be made

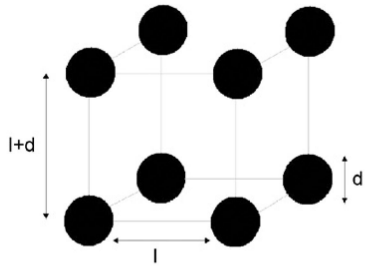

Figure 4.18 Cubic bubble arrangement.

concerning the arrangement of the spheres in the flow. A cubic arrangement, a triangular prism arrangement and a pyramidal lattice arrangement are considered below.

4.7.1 Cubic arrangement

A cubic arrangement is shown in Fig. 4.18. Each cube is delimited by 8 bubbles; one eight of each bubble in contained in each cube. The void fraction in one cube is calculated as the volume ratio of the gas phase over the liquid phase:

$$\varepsilon = \frac{8 \times \frac{1}{8} \times V_{sphere}}{V_{cube}} = \frac{8 \times \frac{1}{8} \times \frac{\pi}{6} d^3}{(l+d)^3} \tag{4.49}$$

Consequently, the ratio of the distance between bubbles to the bubble diameter is:

$$\frac{l}{d} = \left(\frac{\pi}{6\varepsilon}\right)^{1/3} - 1 \tag{4.50}$$

4.7.2 Triangular prism arrangement

A triangular prism arrangement is shown in Fig. 4.19. The height (x) and area (A) of an equilateral triangle of length $(l+d)$ are:

$$\begin{gathered} x^2 + \left(\frac{l+d}{2}\right)^2 = (l+d)^2 \\ x = \frac{\sqrt{3}}{2}(l+d) \end{gathered} \tag{4.51}$$

and

$$A = \frac{x(l+d)}{2} = \frac{\sqrt{3}}{4}(l+d)^2 \tag{4.52}$$

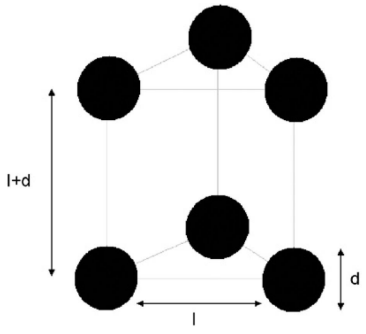

Figure 4.19 Triangular prism bubble arrangement.

Each prism is delimited by 6 bubbles; one twelfth of each bubble in contained in each prism. The void fraction in one prism is:

$$\varepsilon = \frac{6 \times \frac{1}{12} \times V_{sphere}}{V_{prisme}} = \frac{6 \times \frac{1}{12} \times \frac{\pi}{6} d^3}{\frac{\sqrt{3}}{4}(l+d)^3} \tag{4.53}$$

Consequently, the ratio of the distance between bubbles to the bubble diameter is:

$$\frac{l}{d} = \left(\frac{\pi}{3\sqrt{3}\varepsilon}\right)^{1/3} - 1 \tag{4.54}$$

4.7.3 Pyramidal arrangement

A pyramidal arrangement is shown in Fig. 4.20. This is the most compact arrangement that can be achieved. Simple calculations can be carried out by using a hexagonal prism pattern. The height of one prism is $2z$, with z being the height of one triangular pyramid.

$$\begin{gathered} z^2 + \left(\frac{2}{3}x\right)^2 = (l+d)^2 \\ z = \frac{\sqrt{6}}{3}(l+d) \end{gathered} \tag{4.55}$$

The area of the equilateral triangle at the base of each pyramid is A, calculated as in section 4.7.2. The base of one prism is composed of the bases of 6 pyramids, so the volume of the prism is:

$$V_{total} = 6A \times 2z = 6\frac{\sqrt{3}}{4}\frac{2\sqrt{6}}{3}(l+d)^3 = 3\sqrt{2}(l+d)^3 \tag{4.56}$$

Each prism is delimited by 12 bubbles; one sixth of these bubbles in contained in each cube. In addition, the prism contains 2 half bubbles (one at the top and one at the bottom of the prism) and 3 complete bubbles inside the prism. The void fraction in one prism is:

$$\varepsilon = \frac{\left(12 \times \frac{1}{6} + 2 \times \frac{1}{2} + 3\right) \times V_{sphere}}{V_{total}} = \frac{6 \times \frac{\pi}{6} d^3}{3\sqrt{2}(l+d)^3} \tag{4.57}$$

$$\frac{3\sqrt{2}}{\pi}\varepsilon = \frac{1}{\left(1 + \frac{l}{d}\right)^3} \tag{4.58}$$

Consequently, the ratio of the distance between bubbles to the bubble diameter is:

$$\frac{l}{d} = \left(\frac{\pi}{3\sqrt{2}\varepsilon}\right)^{1/3} - 1 \tag{4.59}$$

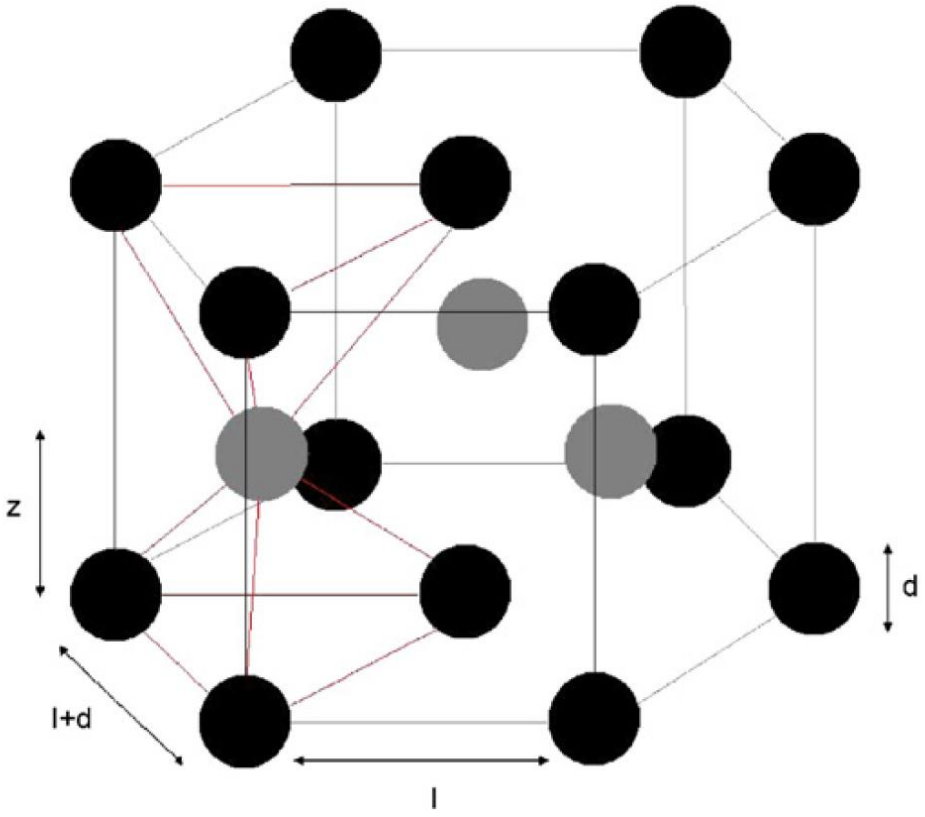

Figure 4.20 Pyramidal bubble arrangement (the most compact arrangement).

4.7.4 Transition void fraction

The general expression for any of the above arrangements can be expressed as:

where constant B depends on the arrangement. Fig. 4.21 shows the evolution of ratio l/d with respect to void fraction, for each of the three arrangements. It can be seen that ratio l/d depends largely on void fraction, and not so much on the selected arrangement. Finally, assuming the transition occurs at void fraction ε = 15%, the ratio of the distance between bubbles to the bubble diameter at transition would be:

$$\frac{l}{d} = B\left(\frac{1}{\varepsilon}\right)^{1/3} - 1 \tag{4.60}$$

where constant B depends on the arrangement. Fig. 4.21 shows the evolution of ratio l/d with respect to void fraction, for each of the three arrangements. It can be seen that ratio l/d depends largely on void fraction, and not so much on the selected arrangement. Finally, assuming the transition occurs at void fraction ε = 15%, the ratio of the distance between bubbles to the bubble diameter at transition would be:

$$\begin{aligned} &\tfrac{l}{d} \simeq 0.52 \quad \text{for the cubic lattice} \\ &\tfrac{l}{d} \simeq 0.59 \quad \text{for the triangular lattice} \\ &\tfrac{l}{d} \simeq 0.7 \quad \text{for the pyramidal lattice} \end{aligned} \tag{4.61}$$

In the most general case:

$$\varepsilon = B^3 \frac{\langle d^3 \rangle}{(\langle l \rangle + \langle d \rangle)^3} \tag{4.62}$$

From this calculation, it can be concluded that at 15% void fraction, the typical distance between bubbles is somewhere between one bubble radius and one bubble diameter. Krishna and van Baten (1999) have shown from simulations that air bubbles having a diameter less than 9 mm rise in water with a transverse oscillatory motion (Fig. 4.22). The typical amplitude of this oscillation is in the order of one bubble radius to one bubble diameter. This oscillatory motion could induce lateral contact between bubbles, and could possibly explain the occurrence of a transition between bubbles and slug flow in stagnant liquid where turbulence is minimal.

4.8 Experiment with air-water two-phase flow

4.8.1 Apparatus and procedure

In this experiment, water and air are supplied at normal ambient pressure and temperature. Damping measurements are performed while the pre-measured mixture is injected at

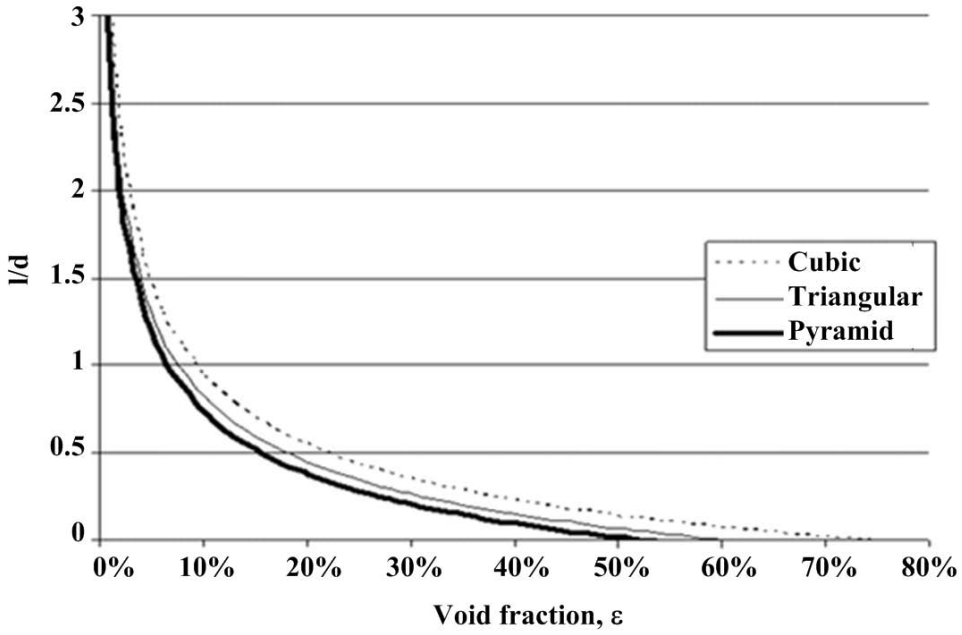

Figure 4.21 Bubble distance to diameter ratio (l/d) with respect to void fraction for various bubble arrangements.

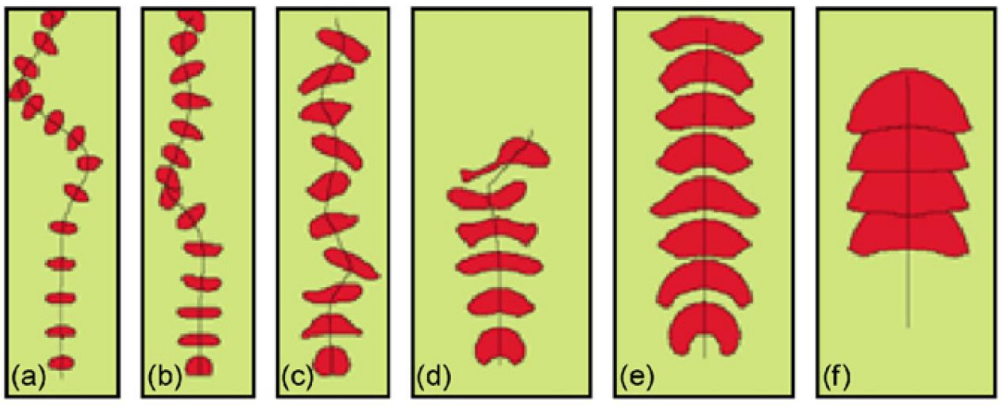

Figure 4.22 Two-dimensional simulations of the rise trajectories of air bubbles in water (Krishna and van Baten (1999)). The bubble sizes are: (a) 4 mm, (b) 5 mm, (c) 7 mm, (d) 9 mm, (e) 12 mm, and (f) 20 mm.

the bottom of the vertical tube, as shown in Fig. 4.23. The tests have two purposes. One is to establish the behaviour of two-phase damping with respect to the internal diameter of the tube, and to confirm the effect of confinement on bubble coalescence. The second purpose is to confirm the validity of the method suggested above, by which flow regime transitions could be detected from damping measurements. The tests were carried out on all three PVC tubes (Table 4.1), for volumetric quality β ranging from 0% to 90%. For simplicity and consistency, flow conditions are given in terms of the homogeneous parameter. Homogeneous flow velocities ranged from 1 m/s to 5 m/s for the 21.2 mm tube, from 1m/s to 9m/s for the 15.5 mm tube and from 2 m/s to 11 m/s for the 11.7 mm tube. A full description of the test loop is given in Gravelle *et al.* (2007). For each test configuration, photographs were taken to determine the flow regime and possible bubble interactions.

4.9 Results and discussion

4.9.1 Effect of void fraction

The measurement results are presented in Figs. 4.24, 4.25 and 4.26 for the 21.2mm, the 15.5mm, and the 11.7mm diameter tubes, respectively. Once again, the distinctive behaviour of two-phase damping with void fraction can be observed. For each tube and flow velocity, damping increases gradually, reaches a maximum, and decreases thereafter as void fraction increases. This is in agreement with previous studies on two-phase damping (Carlucci (1980)). Two-phase damping $\zeta_{2\phi}$ evolves quasi-linearly with void fraction from 0% up to a critical value of ε in conformity with Eq. (4.37). The critical void fraction corresponds to the transition between bubbly and slug/churn flow, and increases with homogeneous flow velocity. It seems that the proportionality between the interface surface area and two-phase damping ratio is valid for bubbly two-phase flows. For void fractions beyond the critical value, two-phase damping decreases, and is no longer proportional to void fraction. The sudden change of behaviour seems to result from a transition in flow regime.

4.9.2 Effect of tube diameter

In bubbly flow, bubbles are considered spherical. For a given void fraction, the number of bubbles, thus the interface surface area, increases with tube diameter. However, the size of the bubbles also increases with the tube diameter, thus contributing to a smaller interface surface area. According to Eq. (4.14), the combined effects of the number and size of the bubbles is that interface surface area increases with the tube diameter:$S \sim D_i^{1.52}$. Hence a greater damping ratio is expected in larger tubes. The tube diameters given in Table 4.1 are sufficiently different to provide a good experimental assessment of the influence of tube

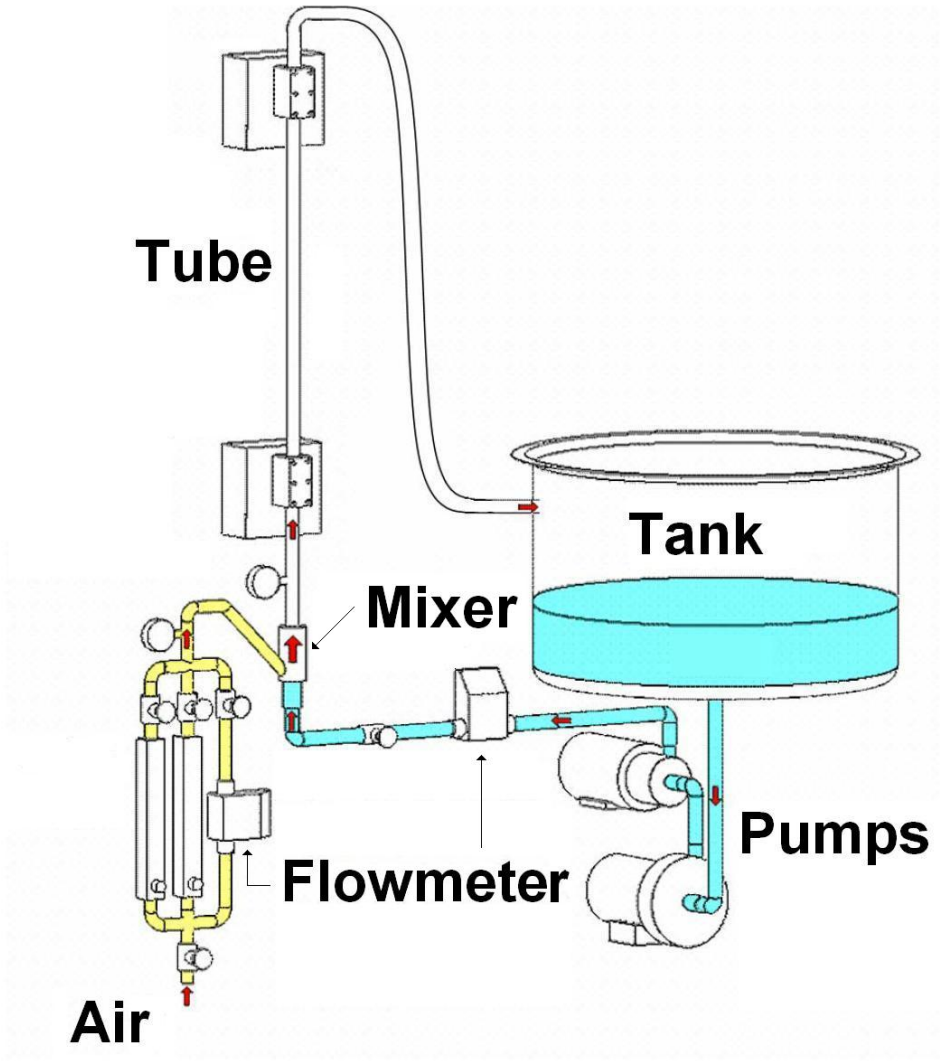

Figure 4.23 Test loop for two-phase flow experiments.

diameter on two-phase damping. The results are compared for the different diameters in Figs. 24 to 26. All three plots show a similar pattern: the critical void fraction (where maximum damping is observed) increases with flow velocity. Thus, the qualitative damping behaviour does not depend on tube diameter.

However, all damping values decrease for smaller diameter tubes, as shown in Figs. 4.24 to 4.26. This is observed not only in bubbly flow but also in slug flow. Using the average two-phase damping values for each tube in bubbly flow, we have compared the evolution of damping with that of interface surface area ($S \sim D_i^{1.52}$), relative to the tube diameter. The diameter ratio between the 11.7 and 21.2 mm tubes is 55%, and the interface surface area for the 11.7 mm tube is estimated at 40% that for the largest tube. For the 15.5 mm tube, the diameter ratio is 73%, and the estimated interface surface area ratio is 62%. For the 21.1 mm tube, both the diameter ratio and the interface surface area ratio are 100%. The ratios of interface surface areas are plotted in Fig.4.27 with respect to tube diameter. Also reported in Fig. 27 are the ratios of damping values for the three tubes. The damping values for the 11.7 mm tubes are 36% those for the 21.2mm tube. For the 15.5 mm tube, damping values are 65% those for the 21.2 mm tube. Therefore, based on these tubes, the relationship between damping ratio and tube diameter is similar to the aforementioned relationship between interface surface area and tube diameter, thus: $\zeta_{2\phi} \sim D_i^{1.52}$. Therefore, it can be stated that the damping ratio is proportional to the interface surface area, and to the tube diameter, in the approximate proportion: $S \sim \zeta_{2\phi} \sim D_i^{1.52}$.

The above experimental observations are valid only for bubbly flow. The influence of internal diameter D_i on two-phase damping is due essentially to the relationship between interface surface area and tube diameter. Actually, smaller tubes bring a greater confinement of the two-phase flow; the major impact is a smaller interface surface area, resulting in a lower damping ratio. Moreover, for a given homogeneous flow velocity, confinement in the two smaller tubes contributes to maintain a lower interface surface area. The results must therefore be examined in terms of flow regime.

4.9.3 Effect of flow regime

For each test configuration, photographs of the two-phase mixture were taken to determine the flow regime and possible bubble interactions. For each different tube and flow velocity, the photos show the behaviour of flow regime with void fraction, which is correlated with the behaviour of two-phase damping. Typical trends for each tube are presented in Figs. 4.28 to 4.30, for a flow velocity of 3m/s. The flow regimes observed are identified on the figures. In all test configurations, the flow regime varies from either bubbly or finely dispersed bubbles (at low void fractions) to slug/churn flow (at high void fractions). As mentioned previously,

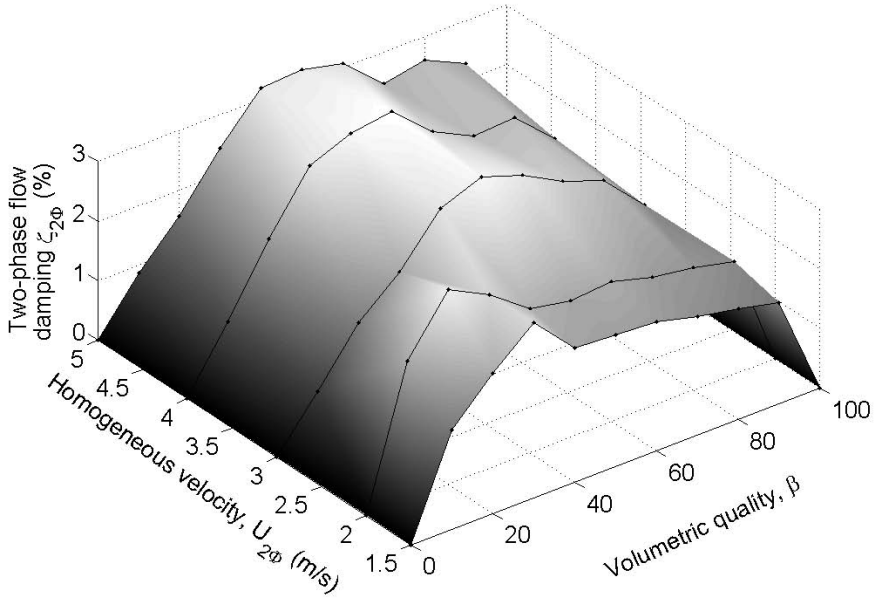

Figure 4.24 Behaviour of the two-phase damping ratio versus volumetric quality and homogeneous velocity, D_i=21.2 mm.

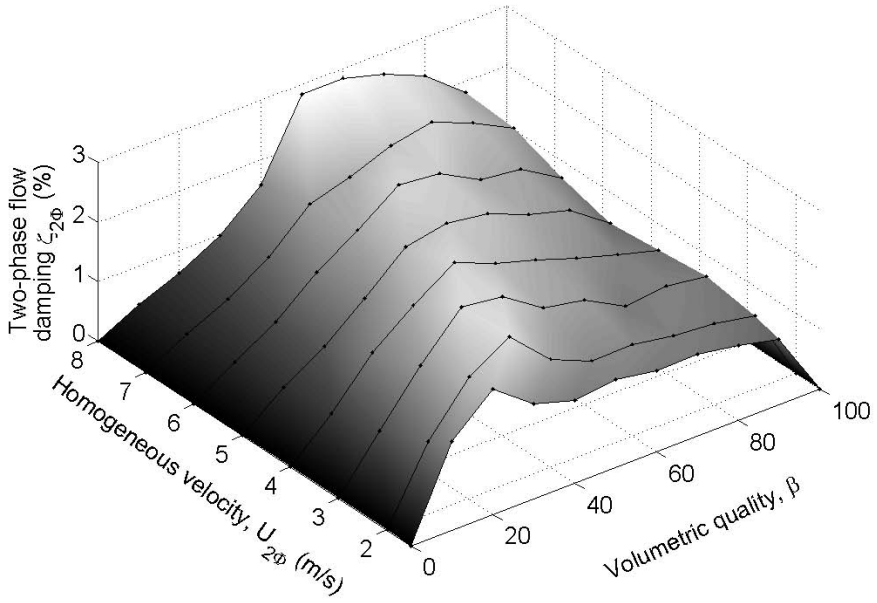

Figure 4.25 Behaviour of the two-phase damping ratio versus volumetric quality and homogeneous velocity, D_i=15.5 mm.

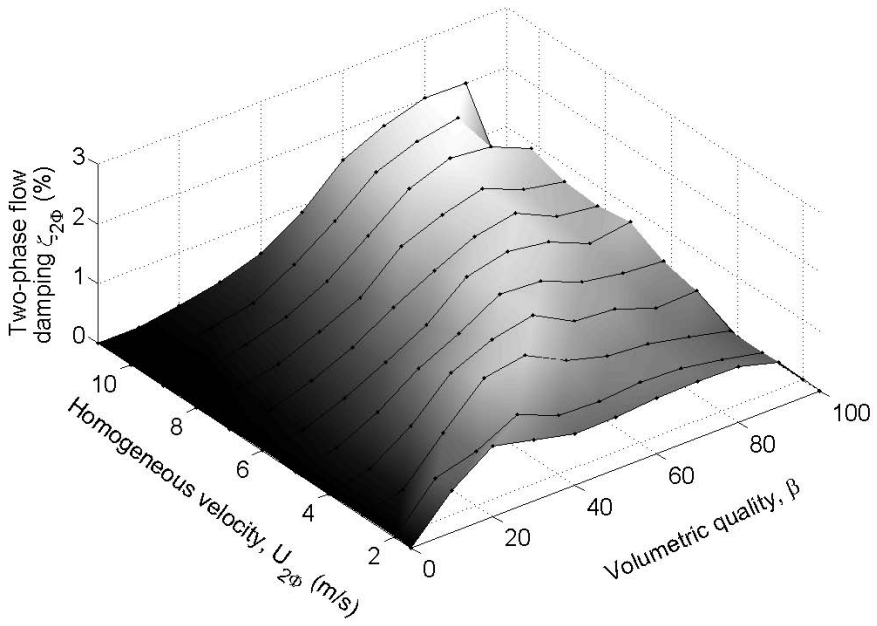

Figure 4.26 Behaviour of the two-phase damping ratio versus volumetric quality and homogeneous velocity, D_i=11.7 mm.

the shapes of the two-phase damping curves are reasonably similar. The damping values, however, are lower for smaller tubes. In the bubbly flow regimes, two-phase damping increases almost linearly with void fraction, as mentioned before. Photographs clearly show that the overall number of bubbles becomes more significant and the bubbles become smaller as the void fraction and two-phase damping increase. This observation is useful to confirm the dependence of two-phase damping on the interface surface area. In the slug/churn regime, damping decreases with a further increase in void fraction. Slugs contain large volumes of air for a small interface surface area. The number and the size of the slugs increase with void fraction, thereby reducing the interface surface area. Again, two-phase damping and interface surface area are correlated. The maximum two-phase damping value observed for any given tube and flow velocity consistently occurs very close to the transition between bubbly flow and slug/churn flow. The maximum two-phase damping and the flow regime transition occur at a lower void fraction for smaller tubes (around 50% for the 21.2mm tube and around 25% for the two smaller tubes). Thus, the measurement of two-phase damping could very well be used for detecting the transition in air-water flow patterns. This conclusion will be confirmed using two-phase flow maps and pictures.

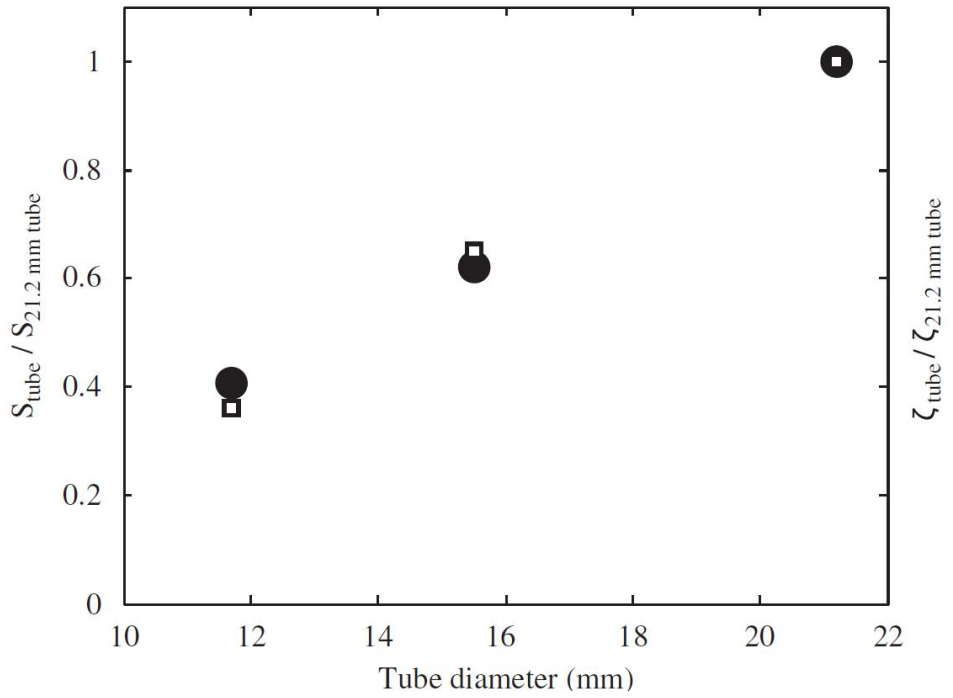

Figure 4.27 Comparison of interface surface area and two-phase damping with respect to tube diameter(■: ratio of interface surface area; •: ratio of damping values).

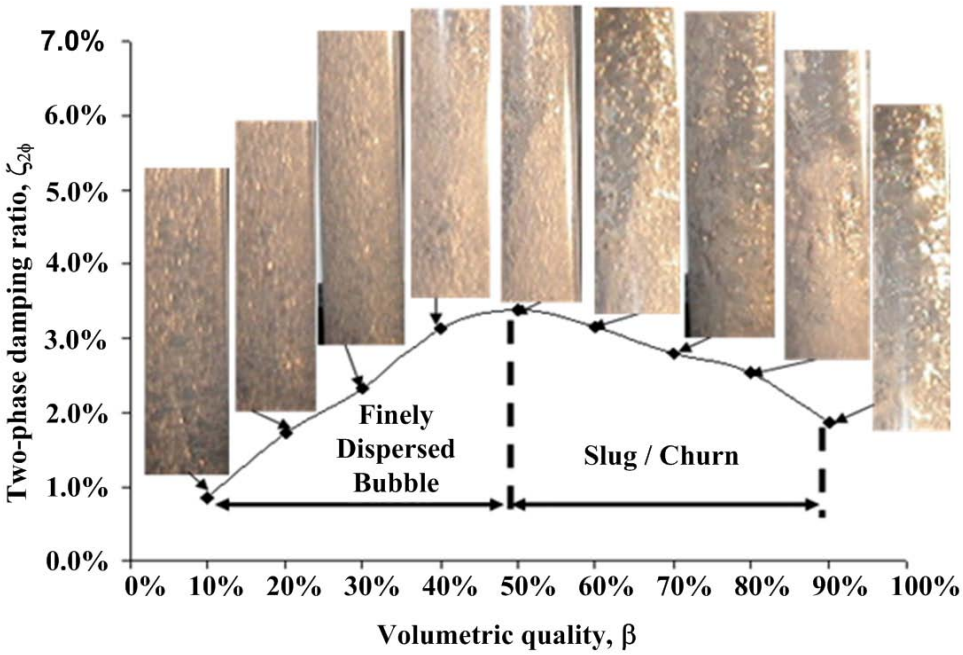

Figure 4.28 Correlation between two-phase damping ratio and flow pattern, D_i = 21.2 mm (3 m/s).

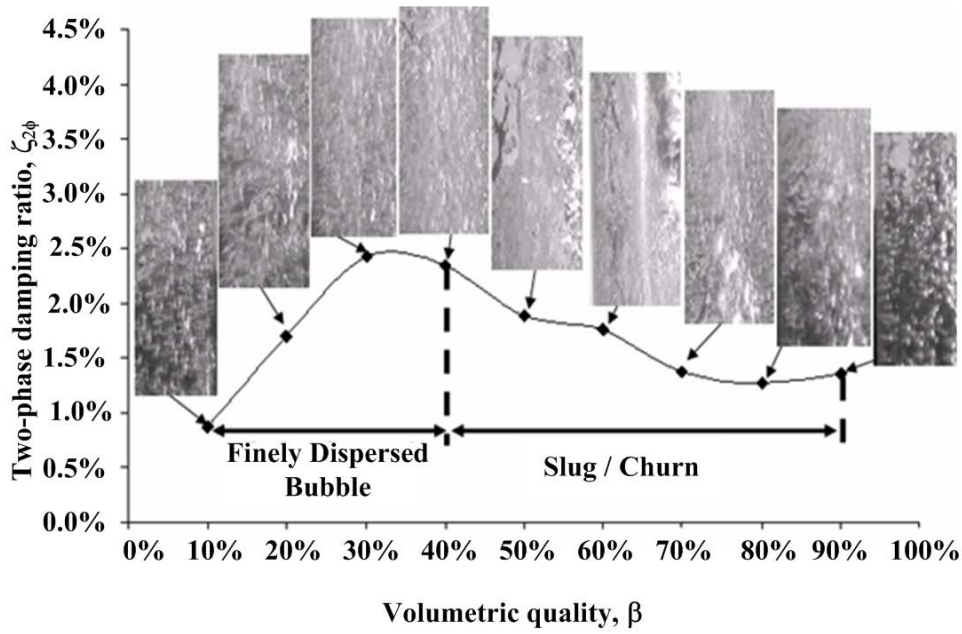

Figure 4.29 Correlation between two-phase damping ratio and flow pattern, D_i = 15.5 mm (3 m/s).

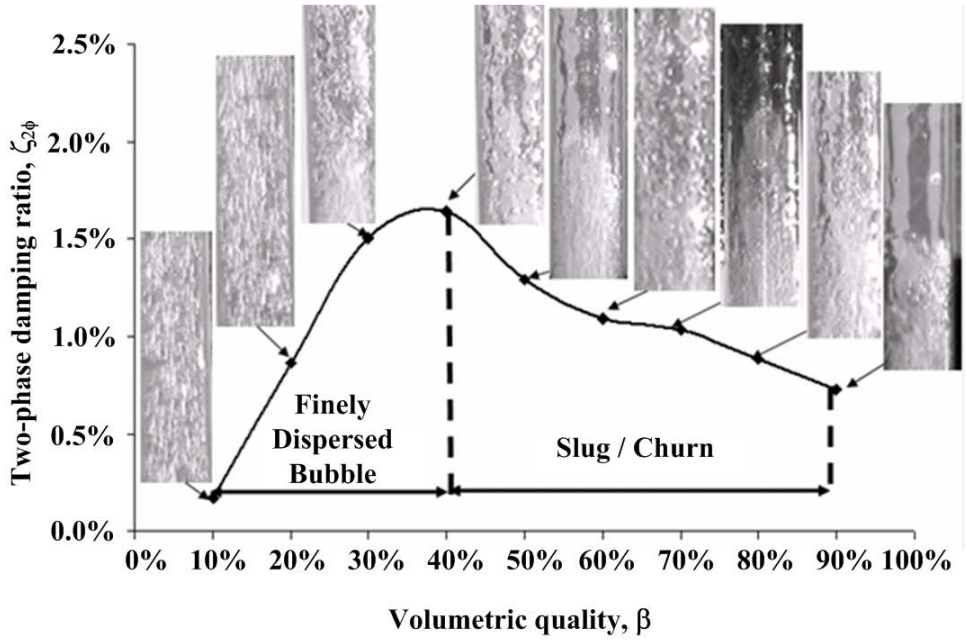

Figure 4.30 Correlation between two-phase damping ratio and flow pattern, D_i = 11.7 mm (3 m/s).

4.10 Conclusion

The purpose of this study was to understand the relation between two-phase damping, interface surface area and flow regime in two-phase flows. The results show that:

- Maximum two-phase damping consistently occurs immediately prior to the transition from bubbly flow to slug/churn flow at a given flow velocity. It decreases rapidly for higher void fractions (as does the interface surface area). Thus, the transition could be detected from two-phase damping measurements.
- The transition from bubbly to slug flow was found to occur near 15% void fraction in stagnant liquid, for two slightly different bubble sizes, for both air-alcohol and glass sphere-water mixtures. The ratio of the distance between bubbles with respect to the bubble diameter may be an important parameter for transition in stagnant liquid.
- Two-phase damping is lower for smaller diameter tubes. Both the interface surface area and two-phase damping are proportional to $D_i^{3/2}$, where D_i is the internal tube diameter. Thus, two-phase damping is proportional to interface surface area between phases.
- Two-phase damping is proportional to the interface surface area, both in bubbly and slug/churn flows. However, the constant of proportionality is different in bubbly flow and slug/churn flow. Damping is higher in slug/churn flow than in bubbly flow for the same interface surface area. We presume that dissipation in the wake of the slug creates the additional damping.

Acknowledgements

This work was supported by the Natural Sciences and Engineering Research Council of Canada (NSERC) through the BWC/AECL/NSERC Industrial Research Chair in Fluid-Structure Interaction. Authors wish to thanks E. De Langre for his advice and help.

References

BRODKEY, R. (1967). *The Phenomena of Fluid Motions*. Addison-Wesley Press.

CARLUCCI, L. (1980). Damping and hydrodynamic mass of a cylinder in two-phase flow. *ASME Journal of Mechanical Design*, 102, 597–602.

CARLUCCI, L. and BROWN, J. (1983). Experimental studies of damping and hydrodynamic mass of a cylinder in confined two-phase flow. *ASME Journal of Vibration, Acoustics, Stress, and Reliability in Design*, 105, 83–89.

CHEN, S. (1987). *Flow-induced Vibration of Cylindrical Structures.* Hemisphere Publishing,New York,.

COLLIER, J. and THOME, J. (1996). *Convective boiling and condensation*. Clarendon Press, Oxford University Press, troisième édition.

COSTIGAN, G. and WHALLEY, P. (1996). Slug flow regime identification from dynamic void fraction measurement in vertical air-water flows. *International Journal of Multiphase Flow*, 23, 263–282.

DE LANGRE, E. (2001). *Fluides et solides*. Edition de l'École Polytechnique, Paris.

GRAVELLE, A., ROSS, A., PETTIGREW, M. and MUREITHI, N. (2007). Damping of tubes due to internal two-phase flow. *Journal of Fluids and Structures*, 23, 447.

HARA, F. (1985). Review of damping of two-phase flows. *ASME, Pressure Vessels and Piping Division (Publication) PVP*, 256, 87–101.

HARA, F. and KOHGO, O. (1993). A theory for a vibrating circular rod damping in two-phase bubbly fluid. *Transactions JSME*, 51, 143–148.

HINZE, J. (1955). Fundamentals of hydrodynamic mechanism of splitting in dispersion processes. *Chemical Engineering Progress*, 1, 289–295.

KRISHNA, R. and VAN BATEN, J. (1999). Simulating the motion of gas bubbles in a liquid. *Nature*, 398, 208.

PETTIGREW, M. and TAYLOR, C. (2004). Damping of heat exchanger tubes in two-phase flow: Review and design guidelines. *ASME Journal of Pressure Vessel Technology*, 126, 523.

RIVERIN, J. and PETTIGREW, M. (2004). Fluctuating forces in piping elements subjected to internal two-phase flow. *8th International Conference on Flow-Induced Vibrations*. École Polytechnique, Paris, France, 327.

TAITEL, Y., BORNEA, D. and A.E., D. (1980). Modelling flow pattern transitions for steady upward gas-liquid flow in vertical tubes. *AIChE Journal*, 26, 345–354.

WALLIS, G. (1969). *One-dimensional two-phase flow*. Mathematical approaches in Hydrodynamics, New York, McGraw-Hill édition.

CHAPITRE 5

INFLUENCE OF DENSITY, VISCOSITY AND SURFACE TENSION ON TWO-PHASE DAMPING

Le premier modèle simple proposé dans l'article précédent a montré, qu'en raison de la différence de densité, les deux phases ont un mouvement relatif et que ce mouvement peut conduire à un amortissement visqueux. L'étape suivante consiste à confirmer cette hypothèse en utilisant différents mélanges de fluides.

Le but est de réaliser des expériences en faisant varier la densité et la viscosité. Cet article, soumis à l'*International Journal of Multiphase Flow*, résume les résultats et les conclusions obtenus et déjà présentés dans plusieurs articles aux conférences FIV (*Flow Induced Vibrations*) et PVP (*Pressure Vessel and Piping*). Ces études explorent les relations entre les propriétés physiques des deux phases et l'amortissement diphasique. Des expériences simples ont été réalisées dans un tube transparent encastré encastré avec divers fluides tels que l'air, l'alcool, l'eau pure, l'eau sucrée, la glycérine et un perfluorocarbone. De même que lors de la précédente série d'expériences, l'amortissement diphasique a été mesuré à partir des vibrations libres du tube. Deux séries d'expériences avec la phase continue stagnante et en mouvement ont été menées.

C. Béguin, A. Ross, N.W. Mureithi & M. J. Pettigrew
Department of Mechanical Engineering,École Polytechnique,
P.O.Box 6079, succ.Centre-Ville, Montréal, Quebec, Canada H3C3A7

Abstract

Internal two-phase flow is common in piping systems. Such flow may induce vibration that can lead to premature fatigue or wear of pipes. In the nuclear industry in particular, it is critically important to avoid failure of piping components. Two-phase damping is considered part of the solution, since it constitutes a dominant component of the total damping in piping with internal flow. However, the energy dissipation mechanisms in two-phase flow are yet to be fully understood.

The purpose of this paper is to explore the relationships between two-phase damping and fluid properties. Simple experiments were carried out in a clear vertical clamped-clamped tube to verify the effects of fluid and pipe properties on two-phase damping. Various fluids, such

as air, alcohol, pure water, sugared water, glycerol, and perfluorocarbon, were combined to obtain different controlled mixtures and to determine the effect of surface tension, density and viscosity on two-phase damping. Experiments with PVC, brass and polycarbonate tube are also compared to understand the effect of structure properties. Two-phase damping ratios were obtained from free transverse vibration measurements on the tube. Experiments with both stagnant and moving continuous phase were conducted.

Based on dimensional analysis, a semi-empirical model for two-phase damping in bubbly and slug flow has been developed. The void fraction and the Bond number are shown to be major parameters for two-phase damping. Two-phase damping is described as a kinetic energy transfer from the tube to the continuous phase thanks to the relative motion between the dispersed phase and the continuous phase.

Keyword *Two-phase damping, flow pattern , internal two-phase flow, mixture properties, density, viscosity, surface tension*

Nomenclature

Variables

A Section (m^2)
a Characteristic bubble radius (m)
b_i, c_i, d_i Constants
D Internal tube diameter (m)
g Gravity (9.81 m/s^2)
L Length (m)
Q Volume flow rate (m^3/s)
U Velocity (m/s)
V Volume (m^3)
ε Void fraction
β Volumetric quality
ρ Density (kg/m^3)
γ Surface tension (N/m)
ζ Damping ratio
μ Dynamic viscosity ($kg.m^{-1}.s^{-1}$)

Subscript

$_b$ Bubble
$_c$ Critical
$_f$ Flow dependent

$_g$ Gas or lighter fluid
$_{gs}$ Superficial gas (velocity)
$_l$ Liquid or heavier fluid
$_{ls}$ Superficial liquid (velocity)
$_s$ Structural
$_v$ Viscous
$_t$ Total
$_{2\phi}$Two-phase

Introduction

In the nuclear and chemical process industries, many piping elements operate with two-phase flows (Pettigrew and Taylor (2004)). Flow induced vibration can lead to structural degradation, process malfunction, and component failure. Two-phase damping can significantly contribute to reducing vibration and thus, to prevent premature fatigue or wear. It is therefore desirable to identify some of the parameters that govern two-phase damping in pipes carrying internal two-phase flow.

The first damping experiments in two-phase flow were performed about 30 years ago by Carlucci (1980) on a series of tubes subjected to an axially confined air-water two-phase flow. His results showed that damping in two-phase flow strongly depends on void fraction; no significant relation was found with frequency or fluid mixture velocity. Many researchers have since contributed to the knowledge of two-phase damping. In the present paper, the effect on two-phase damping of density, viscosity, surface tension, velocity and bubble diameter is investigated. Several two-phase mixtures are studied and compared.

5.1 Two-phase flow considerations

In two-phase flow, the following terms must be defined :

- Void fraction (ε)

Void fraction is typically used to characterize the proportion of gas in a two-phase gas-liquid mixture (Collier and Thome (1996)). However, some of the present experiments were conducted with two liquids, and a non-traditional void fraction definition was used defining the lighter fluid as the "gas" even if it is a liquid:

$$\varepsilon = \frac{V_g}{V_g + V_l} \tag{5.1}$$

where V are the volumes of the phases in the mixture and the subscript "g" is used for the lighter fluid and "l" for the heavier fluid. For simplicity "gas" will henceforth refer to the lighter fluid and "liquid" to the heavier fluid.

• Volumetric flow quality (β)

Volumetric flow quality is defined as the ratio of the volumetric flow rates by Collier and Thome (1996) as:

$$\beta = \frac{Q_g}{Q_g + Q_l} \tag{5.2}$$

For a length ΔL of a two-phase mixture inside a tube, void fraction and volumetric quality can be expressed as:

$$\begin{aligned} \varepsilon &= \frac{V_g}{V_g+V_l} = \frac{A_g \Delta L}{A_g \Delta L + A_l \Delta L} = \frac{A_g}{A_g+A_l} \\ \beta &= \frac{Q_g}{Q_g+Q_l} = \frac{A_g U_g}{A_g U_g + A_l U_l} = \frac{\varepsilon}{\varepsilon+(1-\varepsilon)S_r} \end{aligned} \tag{5.3}$$

A_g and A_l are the cross sectional areas occupied by each phase in the tube section, Q_g and Q_l are the volume flow rates, and U_g and U_l are the velocities of each phase. Void fraction and volumetric quality are related to each other through the slip ratio, $S_r = U_l/U_g$. We choose to use the homogeneous model where both phases have approximately the same velocity $S_r \simeq 1$, in this case $\beta \simeq \varepsilon$.

• The superficial velocities of the phases (U_{gs}, U_{ls}) and the homogeneous velocity ($U_{2\phi}$) are defined as :

$$\begin{aligned} U_{gs} &= \frac{Q_g}{A} = \frac{A_g U_g}{A} = \varepsilon U_g = \beta U_{2\phi} \\ U_{ls} &= \frac{Q_l}{A} = (1-\varepsilon) U_l = (1-\beta) U_{2\phi} \\ U_{2\phi} &= \frac{Q_g+Q_l}{A} = U_{gs} + U_{gl} \end{aligned} \tag{5.4}$$

• The two-phase density and viscosity ($\rho_{2\phi}$, $\mu_{2\phi}$) are defined by Taylor (1932) as:

$$\begin{aligned} \rho_{2\phi} &= \varepsilon \rho_g + (1-\varepsilon)\rho_l \\ \mu_{2\phi} &= \mu_l \left[1 + \varepsilon \left(\frac{\mu_l + 2.5\mu_g}{\mu_l + \mu_g} \right) \right] \end{aligned} \tag{5.5}$$

5.2 Damping in two-phase flow

Tube motion affects internal flow and allows energy transfer from the tube to the fluid and vice versa. If the fluid gains energy, the tube motion is damped; conversely if the fluid looses energy, the tube becomes unstable.

Energy transfer is directly related to the initial energy in the fluid and, in particular, kinetic energy. Damping depends a priori on flow rates. Carlucci's experiments and theory show that energy transfer (damping) in two-phase flows is greater than in single-phase flows. Thus, the concept of two-phase damping was introduced to allow for this difference

by Carlucci (1980). The total damping in two-phase flows therefore includes the components of structural (ζ_s), viscous (ζ_v), flow dependent (ζ_f) and two-phase damping ($\zeta_{2\phi}$). Figure 5.1

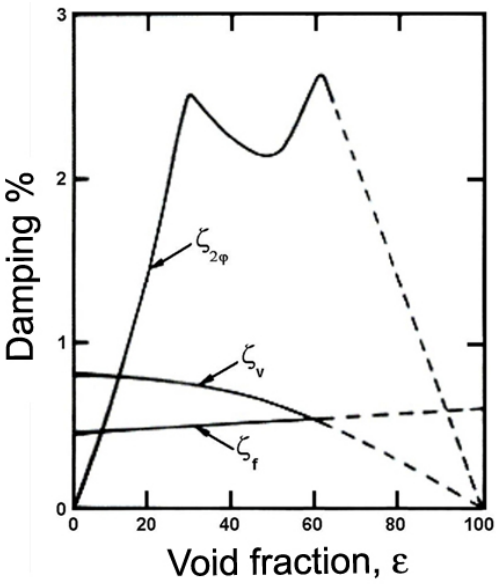

Figure 5.1 Components of Damping ratio in two-phase flow, Carlucci (1980)

shows the contributions of each component to the total damping ratio for confined annular air-water axial flow. Structural damping depends on the tube material and supports; it is not shown on this figure. Two-phase damping is preponderant and strongly depends on void fraction. Although tests by Carlucci (1980) were performed with an axially confined external flow, the various damping mechanisms in an internal flow are expected to be the same. The geometric configuration is different, but the motion of the tube and the dependence of two-phase damping on void fraction exhibit trends similar to internal flow. Carlucci (1980) suggested that the total damping ratio ζ_t should be given by the sum of the various damping components:

$$\zeta_t = \zeta_s + \zeta_v + \zeta_f + \zeta_{2\phi} \tag{5.6}$$

In our experiments, the test tube is clamped-clamped, consequently $\zeta_f = 0$. Damping measurements with internal monophasic flow (each fluid was tested) at comparable velocities showed that $\zeta_v << \zeta_s$. The structural damping ζ_s was measured with stagnant water and stagnant air. Total damping was measured at 0% and 100% void fractions (where $\zeta_{2\phi} = 0$), for various flow velocities. For each condition, the difference between total damping and structural damping was not significant; thus, the viscous damping was found to be negligible in our single-phase experiments, at the flow rates considered. Finally, the measured structural damping ratio ζ_s ranges between 0.5% and 0.8%, which is much less than the two-phase

damping ratios reported in the following sections, hence $\zeta_v + \zeta_f << \zeta_s < \zeta_{2\phi}$. Thus, Eqn. (5.6) becomes :

$$\zeta_t \simeq \zeta_s + \zeta_{2\phi} \tag{5.7}$$

and two-phase damping is simply deduced from: $\zeta_t - \zeta_s$.

The actual most probable explanation of two-phase damping is that the transverse vibration of the tube causes the bubbles to move relative to the tube due to density difference. The liquid thus circulates locally around the bubble. The resulting increase of kinetic energy in the continuous phase (liquid) leads to the damping of the structure. Surface tension plays an important role in the size and shape of the gas bubbles and consequently their added masses (related to the kinetic energy in the continuous phase). It is not clear if this increase of kinetic energy in the liquid is damped by liquid viscosity or carried out of the tubes by the flow. This study will try to respond to this question.

5.3 Fluids parameters

A list of parameters that could play a role in determining two-phase damping is:

Fluid Mixtures	ρ_l	μ_l	ρ_g	μ_g	γ
		10^{-3}		10^{-6}	10^{-3}
	kg/m^3	Pa.s	kg/m^3	Pa.s	N/m
HFE-7100/Water	1520	0.6	1000	1000	72
Alcohol/Air	786	2	1.2	18	22
Water/Air	1000	1	1.2	18	72
HFE-7100/Air	1520	0.6	1.2	18	17
Sugared water/Air	1200	7.7	1.2	18	77
(Glycerol+water)/Air	1200	73	1.2	18	65

Table 5.1 Mixture Properties

$\mu_l, \mu_g,$	liquid and gas viscosity, respectively
$\rho_l, \rho_g,$	liquid and gas density, respectively
$a,$	typical dimension of bubbles ($a^3 = \frac{3<V_b>}{4\pi}$) where $< V_b >$ is the average volume of bubbles
$D,$	internal diameter of the tube
$g,$	acceleration due to gravity
$\gamma,$	surface tension between liquid and gas
$\varepsilon,$	void fraction
$U_b,$	bubble velocity relative to the liquid ($U_g - U_l$)
$U_{2\phi}$	homogeneous velocity

We consider that slug and churn flows are mixed flows of bubbles and (deformed or not) Taylor bubbles, respectively of typical dimensions a and D. These are the only typical lengths selected. Gravelle *et al.* (2007) have already shown that two-phase damping does not depend on tube properties except for the internal diameter. This is why we do not include tube stiffness, structural damping, or any other typical length dimension of the tube. In order to explore the effect of the parameters listed above on two-phase damping, several two-phase mixtures presented in Table 5.1 are studied. Bubble size a and velocities U_b were not measured during the experiments but as physical properties of the fluid internal diameter, homogeneous velocity and void fraction completely defined the flow conditions. Bubble size a and velocities U_b are consequently complex function of the previous quantities. We will seek a correlation for two-phase damping without considering bubble radius a and bubble velocity U_b.

5.4 Experiments with a heavier stagnant liquid

The purpose of the experiments is to measure two-phase damping for mixtures having different densities, viscosities and surface tensions. Because two-phase damping may differ in solid-fluid mixtures and fluid-fluid mixtures, all experiments were conducted with fluid-fluid mixtures.

Non-miscible fluids with various properties were selected (Table 5.1). Different mixtures were made using air bubbles in stagnant alcohol, water, sugared water and perfluorocarbon (HFE-7100) or water droplets in perfluorocarbon (HFE-7100). To generate a uniform and measurable bubbly flow, the test section shown in Figure 5.2 was used. The setup was composed of a transparent vertical clamped-clamped PVC tube filled with a stagnant liquid (i.e. alcohol, water, sugared water or HFE-7100). The second fluid was injected through a perforated flanged plate at the bottom of the tube. The second fluid was lighter than the

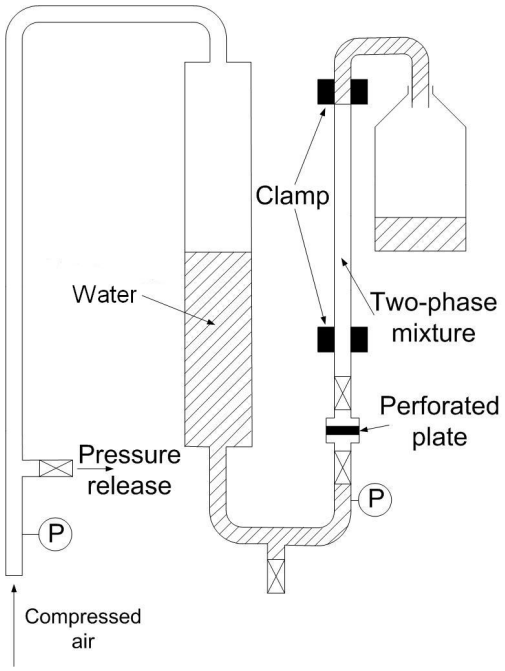

Figure 5.2 Test section for heavier stagnant liquid

stagnant fluid, causing the injected bubbles to rise.

Table 5.2 presents the dimensions of the oscillating tube. For experiments with water "bubbles", compressed air was used to push the water through the holes of the perforated plate to generate the bubbles. When air was used as the lighter fluid, the experiments were similar except that compressed air was injected directly through the perforated plate. The size of the holes was chosen to provide a bubble radius around 1.4 mm in all mixtures.

The void fraction was regulated by controlling the number of lighter fluid "bubbles" which depends on the compressed air pressure, and the number and the diameter of the holes. Void fraction was measured using two different methods. It was first measured by comparing the volume of the stagnant heavier liquid and that of the two-phase mixture. It was also evaluated from flow rate and bubble velocity measurements using:

$$\varepsilon = \frac{4Q_g/U_g}{\pi D^2} \tag{5.8}$$

Length	2.13 m
Internal Diameter	0.0238 m
Internal Volume	3.79 L

Table 5.2 Tube dimensions

where Q_g is the flow rate of lighter fluid, U_g is the bubble velocity and D is the tube internal diameter. The two methods gave very similar results. The bubble diameter was measured using a photographic technique. The bubble velocity was measured with a stopwatch, since the typical velocities in stagnant liquid are slow enough for a direct measurement.

Damping was measured using the logarithmic decrement technique with an initial transverse displacement of the tube. Two-phase damping was obtained from Eqn. (5.7).

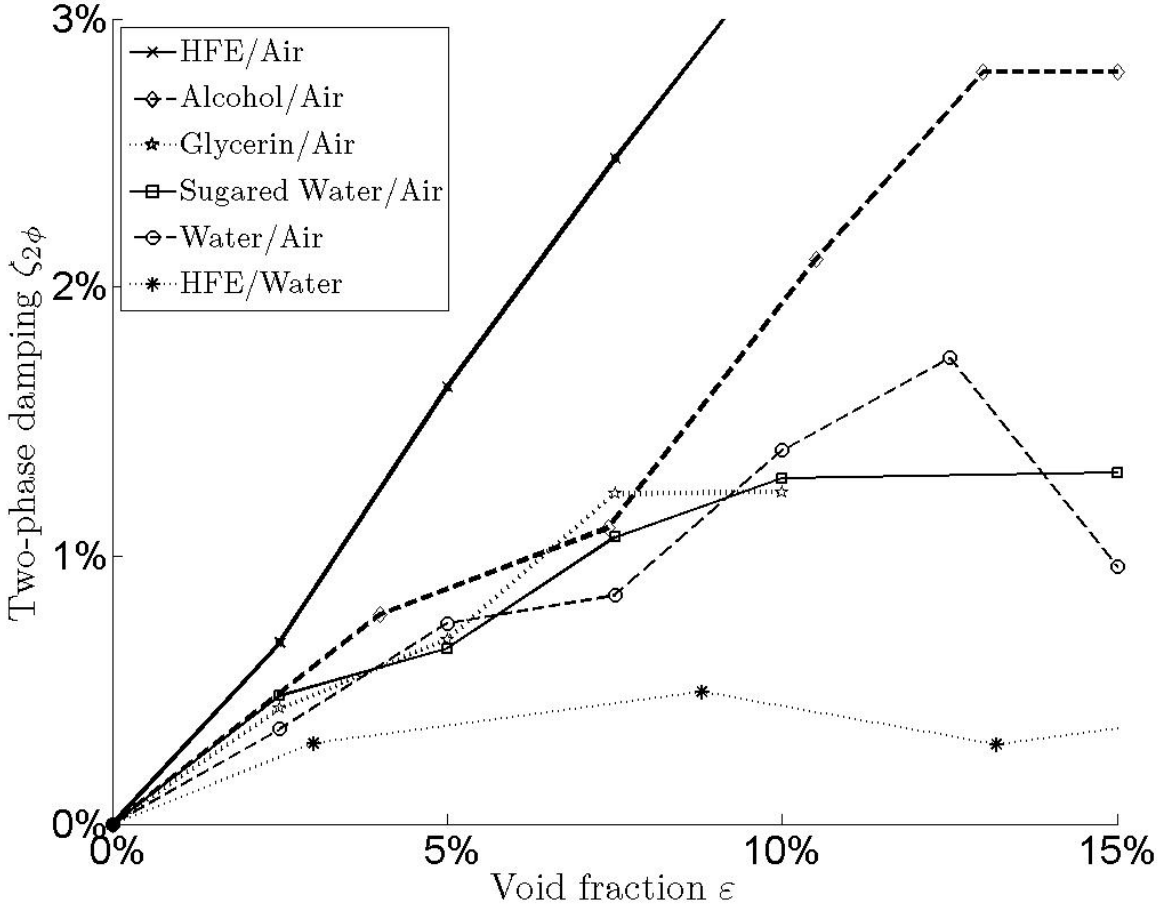

Figure 5.3 Two-phase damping vs. void fraction and density difference with heavier stagnant fluid

In figure 5.3, two-phase damping is presented with respect to average void fraction. As usually observed in two-phase damping experiments, void fraction has a major impact. Two-phase damping increases fairly linearly with void fraction until a critical void fraction is reached. Experiments with low void fraction correspond mostly to bubbly flow. With higher void fraction, the first slug appears and two-phase damping increases at a slower rate or decreases with void fraction. The flow pattern transition was usually observed around a

critical void fraction 15% ($\varepsilon_c = 15\%$).

However, in the particular case of HFE-air experiment, slugs appear at very low void fraction (less that 5%) and seem to have no impact on the two-phase damping behavior. Due to the great density difference and low viscosity of the liquid, the slugs are very distorted and we could consider the flow as churn flow. Anscutter *et al.* (2006) have previously suggested that two-phase damping is strongly correlated with flow pattern, and maximum damping could be used to detect flow regime transition. They suggested that the maximum two-phase damping occurs at the transition from bubbly flow to slug/churn flow. The present experiments seem to indicate that it occurs at the transition from bubbly or churn flow to slug flow.

Two-phase damping does not depend strongly on fluid viscosity as suggested by the two-phase damping measured for sugared water and glycerin+water. Indeed sugared water and glycerin+water have the same density difference but the viscosity of glycerin+water is ten times that of sugared water; surprisingly the two mixtures have nearly the same two-phase damping, as can be seen in Figure (5.3). For simplicity the glycerin/water blend is sometimes called only by its major component, i.e., glycerin.

Due to the type of experiment, it was not possible to obtain high void fraction, and critical void fraction was not reached for all mixtures so we cannot conclude about maximum two-phase damping. In the case where transition was observed, critical void fraction occurred between 10% and 15%.

According to Table 5.1, we can defined the capillary length of each mixture :

$$L_c = \sqrt{\frac{\gamma}{\Delta\rho g}} \tag{5.9}$$

Two-phase damping seems to be inversely proportional to the capillary length. Consequently, the major dimensionless parameters that will probably have a significant role in two-phase damping are the void fraction ε, and the Bond number, $Bo = \Delta\rho g D^2/\gamma$. The Bond number is also known as the Eötvös number. The term Eötvös number is more frequently used in Europe, while Bond number is commonly used in other parts of the world. However as underlined by a study of energy magnitude, two-phase damping cannot be the result of dissipation through energy needed for creation of surface (cf. Anscutter *et al.* (2006)). If surface tension plays a role in two-phase damping, it must be through a different mechanism.

The transverse vibration of the tube causes the bubbles to move relative to the tube due to density difference. The liquid thus circulates locally around the bubbles. The resulting increase of kinetic energy in the continuous phase (liquid) creates added mass for the bubbles and leads to the damping of the structure. Surface tension plays a great role in the size and

shape of the gas bubbles and consequently in determining their added masses (related to kinetic energy in the continuous phase).

5.5 Experiments with two-phase flow

5.5.1 Present experiments

In addition to the experiments in stagnant liquid, tests were carried out with three different mixtures (Sugared water/air, (Glycerin+water)/air and Water/air) supplied at normal ambient pressure and temperature. Damping measurements were performed while the premeasured mixture was injected at the bottom of the vertical tube, as shown in Fig. 5.4. Damping was measured using the logarithmic decrement technique with an initial transverse displacement of the tube. For each test configuration, photographs were taken to determine the flow regime. The tests were performed at different homogeneous velocities, namely 1, 2, 3 and 4 m/s.

In Figure 5.5, two-phase damping is shown with respect to homogeneous velocity and volumetric quality of the flowing mixtures. For low volumetric qualities corresponding to bubbly flow, the two-phase damping ratio increases linearly with volumetric quality, as previously noticed by Béguin *et al.* (2008). In bubbly flow, higher velocity leads to lower two-phase damping. Higher velocity also causes the transition from bubbly flow to churn or slug flow where two-phase damping is maximum at higher void fractions. Béguin *et al.* (2008) have already shown that the critical void fraction does not depend on tube diameter in the range of $11mm < D < 23mm$. The present experiments show that the critical void fraction, corresponding to the maximum two-phase damping and to the transition from bubbly flow to slug flow, does not depend on fluid densities or viscosities.

5.5.2 Previous experiments

In addition to the aforementioned results, we also take into account the previous results obtained with the same experimental apparatus. Table 5.3 shows the characteristics of the test performed by a) Gravelle *et al.* (2007), b) Anscutter *et al.* (2006), c) Béguin *et al.* (2008), d) present data already presented in a conference paper by Béguin *et al.* (2009). Volumetric quality increment are shown in brackets $[x\%]$. Gravelle *et al.* (2007) have concluded that tube properties and in particular its natural frequencies do not have significant impact on two-phase damping. Indeed they did not observe any difference between Brass, PVC and Polycarbonate tubes having similar internal diameter but significantly different natural frequencies.

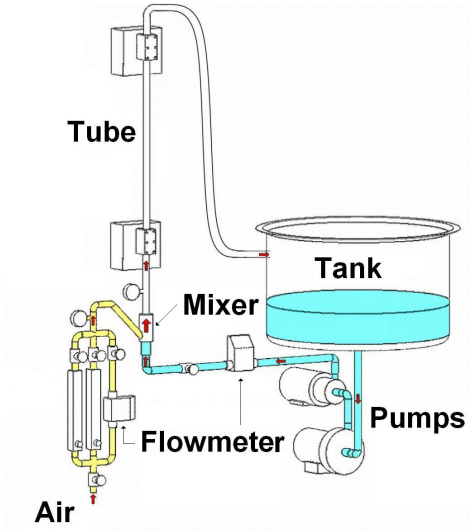

Figure 5.4 Test section with two-phase flow

Test	Tube Material	Mixture used	D_i (mm)	$\beta(\%)$ $[x\%]$	$U_{2\phi}$ (m/s)
a □	Brass, PVC Polycarbonate	Air-water	18, 19 and 21	0-100 [10%]	1.5-6
b ◯	PVC	Air-water	11, 15 and 21	0-100 [10%]	1.5-11
c ◇	PVC	Air-water	9, 13 18, 24	0-100 [5%]	1-5
d ★	PVC	All mixtures presented in table 5.1	24	0-100 usually [10%]	0-5

Table 5.3 Test characteristics

The measurement results of Anscutter et al. are presented in Figures 5.6 for three different tube diameters. Once again, the distinctive behaviour of two-phase damping with void fraction can be observed. For each tube and flow velocity, damping increases gradually, reaches a maximum, and decreases thereafter while void fraction increases. Two-phase damping evolves quasi-linearly with void fraction from 0% up to a critical value of ε_c. The critical void fraction corresponds to the transition between bubbly and churn flow, and varies with homogeneous flow velocity. For void fractions beyond the critical value, two-phase damping decreases. The sudden change of behaviour seems to result from a transition in flow regime.

The tube diameters are sufficiently different to provide a good experimental assessment of the influence of tube diameter on two-phase damping. All three plots in Figure 5.6 show

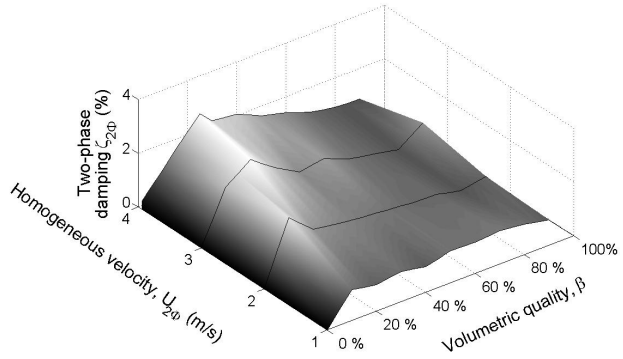

(a) *Water*

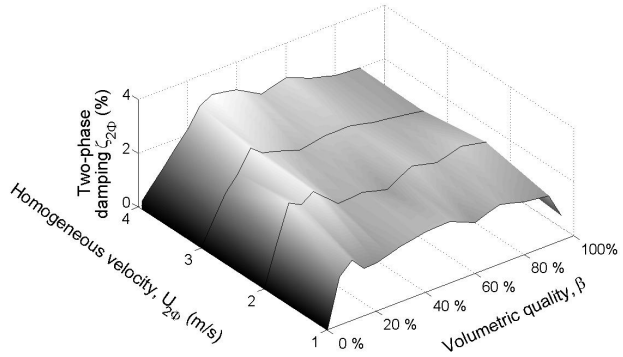

(b) *Sugared water*

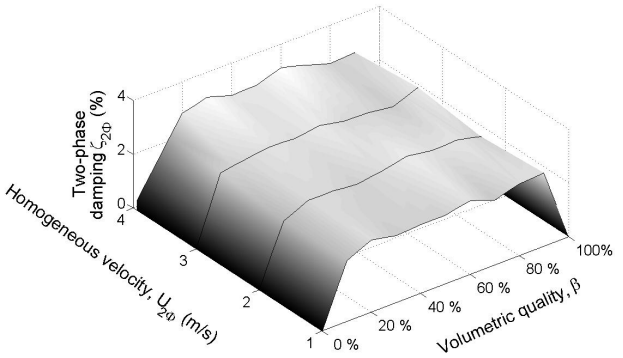

(c) *Glycerin*

Figure 5.5 Two-phase damping vs. volumetric quality and homogeneous velocity

a similar pattern: the critical void fraction (where maximum damping is observed) increases with flow velocity. Thus, the qualitative damping behaviour does not depend on tube diameter. However, all damping values decrease for smaller diameter tubes. Average two-phase damping ratio measurements for the 15 mm and 11 mm tubes are respectively 35% and 65% those for the 21 mm tube. Anscutter *et al.* (2006) have shown that the influence of internal diameter D on two-phase damping is due essentially to the relationship between interface surface area and tube diameter. Actually, smaller tubes introduce a greater confinement of the two-phase flow; the major impact is a smaller interface surface area, resulting in a lower damping ratio.

Clearly, at a given void fraction and flow pattern, two-phase damping decreases for higher homogeneous flow velocities. However a higher flow velocity leads to bubbly flow being maintained for higher void fraction.

We assume that the critical void fraction depends only on inertia and surface tension. Due to the limited number of experiments with different surface tensions, the relationship proposed by Béguin *et al.* (2008) is used:

$$\varepsilon_c = 0.15 + 0.065 U_{2\phi} \tag{5.10}$$

Considering the low slip ratio observed in bubbly flow, the homogeneous model $\varepsilon = \beta$ is assumed. Bubbly or churn flow occurs for void fractions less than ε_c, and slug flow exists for void fractions greater than ε_c. In Figure 5.7, the maximum damping ratio which is associated with flow pattern change is plotted for all experiments presented in Table 5.3. The solid line represents equation (5.10), and dashed line represents ±10% error bound corresponding to the usual step used in the experiments. The large majority of the experiments are well represented by equation 5.10. The different symbols used corresponds to the different set of experiment as presented in Table 5.3.

This relation leads to a rethinking of the transition from bubbly flow to slug flow. Taitel *et al.* (1980) have proposed a transition for low homogeneous velocity for a void fraction of $\varepsilon = 25\%$ and a transition at $\varepsilon = 50\%$ for higher homogeneous velocity. They have, however, conducted experiments with homogeneous velocity only up to 5 m/s. In the present set of experiments we reach velocities up to 11 m/s. Figure 5.8 illustrates the new transition A' deduced from equation 5.10 on the map of Taitel *et al.* (1980) for a tube diameter of 11 mm. Figure 5.8 presents also the corresponding experimental points where two-phase damping were measured.

The photographs at the top of Figure 5.9 were taken during experiments conducted by Anscutter *et al.* (2006). They clearly show that the flow is bubbly for void fractions up to

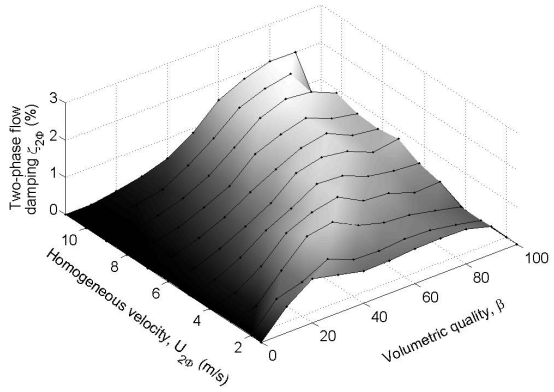

(a) *Internal diameter of* $D = 11$ *mm*

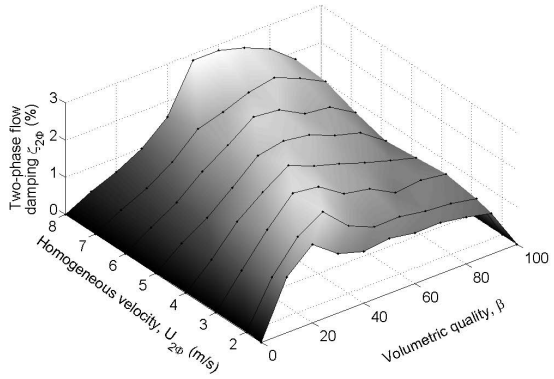

(b) *Internal diameter of* $D = 15$ *mm*

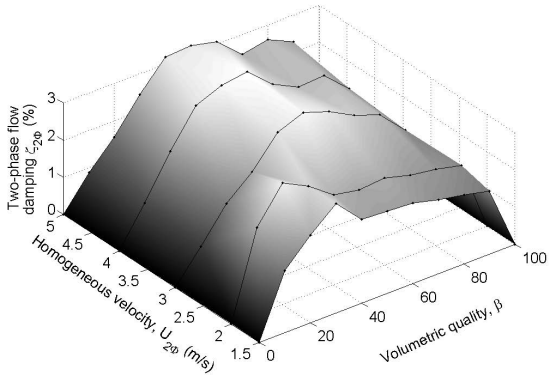

(c) *Internal diameter of* $D = 21$ *mm*

Figure 5.6 Two-phase damping vs. volumetric quality and homogeneous velocity from Anscutter *et al.* (2006).

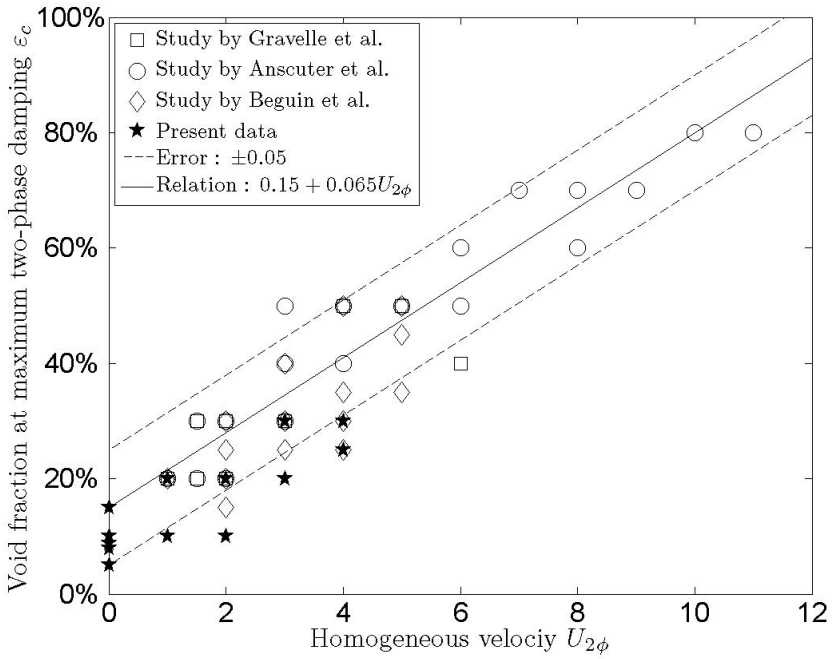

Figure 5.7 Void fraction observed at maximum two-phase damping vs. homogeneous velocity.

15%, and slug/churn for higher void fraction. According to the photographs, the bubbles begin to interact at a void fraction of approximately 15%, which would mark the beginning of the transition from bubbly flow to slug/churn flow. A close-up of the photo at 15% void fraction was added to show this interaction clearly. The authors show the remarkably good correlation between the interface surface area and the two-phase damping ratio. However, the relationship between the two parameters is somewhat different below and above $\varepsilon > 15\%$. The constant of proportionality that relates the two-phase damping ratio to the interface surface area is higher in slug/churn flow than it is in bubbly flow. Apparently, there is an additional damping mechanism in slug/churn flow, which is also related to the interface surface area. The explanation given by Anscutter *et al.* (2006) is that energy dissipation occurs in the slugs wake, which move transversely due to the motion of the tube.

5.6 Influence of different parameters

For each parameter, internal diameter, void fraction and homogeneous velocity, we search a correlation with a set of test data with all other parameters fixed. As an example, to determine the effect of internal diameter, the series of tests with the same mixture, volumetric qualities, homogeneous velocity and flow pattern are selected. As shown in the previous section, bubbly flows corresponds to the region between zero void fraction $\varepsilon = 0$ to maximum

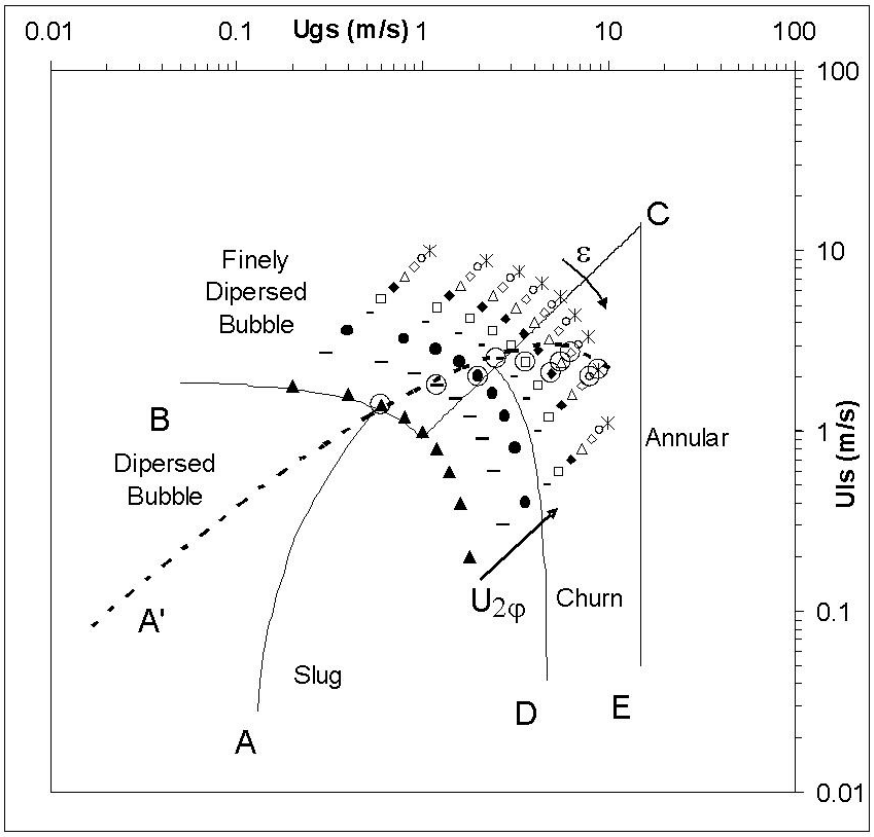

Figure 5.8 Superimposition of experimental points on air-water flow pattern map for D~ 11 mm from Anscutter *et al.* (2006). Symbols represent flow condition where two-phase damping were measured. ◯ corresponds to maximal damping observed for a each constant homogeneous velocity.

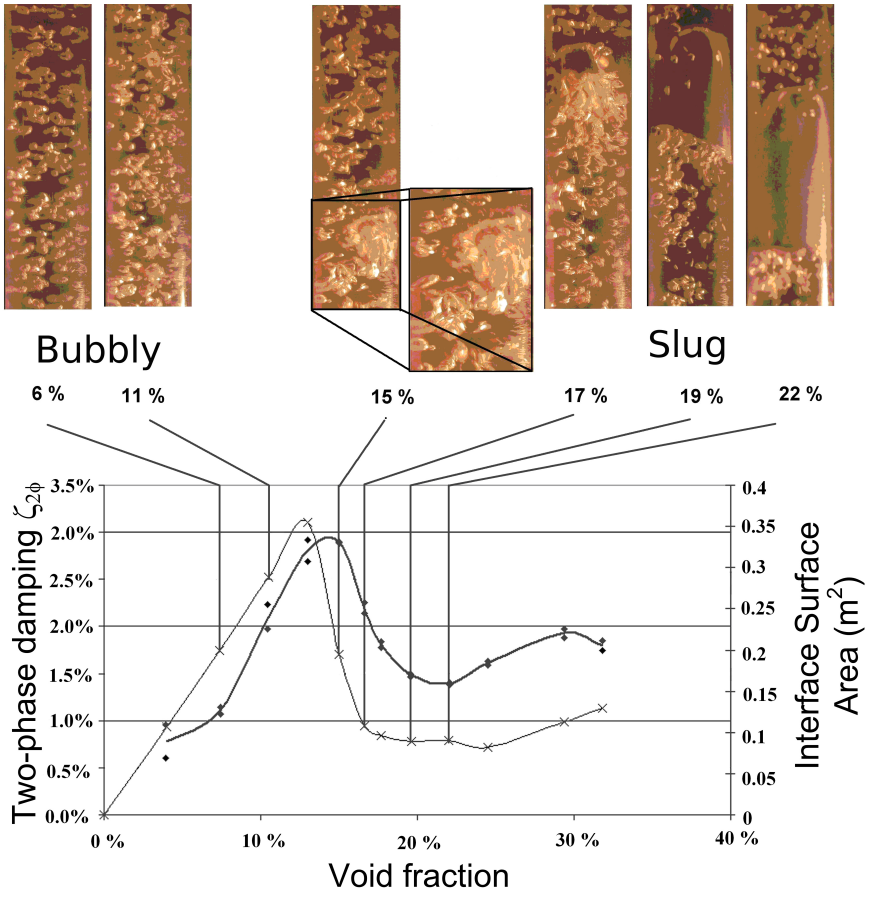

Figure 5.9 Damping ratio and interface surface area in air/alcohol mixtures (◇: two-phase damping; × interface surface area). from Anscutter *et al.* (2006)

two-phase damping. For each series we seek a correlation of the form $\zeta_{2\phi} = A.D^n$. The factor A and exponent n will a priori depend on all other parameters and will be functions of $\mu_l, \mu_g, \rho_l, \rho_g, \gamma, U_{2\phi}$ and β. This is why a correlation is done for each $\mu_l, \mu_g, \rho_l, \rho_g, \gamma, U_{2\phi}$ and β constant.

5.6.1 Effect of internal diameter on two-phase damping

The two-phase damping should tend to zero when the internal diameter tends to zero, so we seek a correlation $\zeta_{2\phi} = A.D^n$ with $n > 0$. All correlations for different sets of parameters show a value n that does not vary much and is around 1.2. Two-phase damping seems to vary with $D^{1.2}$. These results are obtained from different series of test carried out by four different groups of experimenters. This result is in agreement with the previous correlation proposed by Anscutter *et al.* (2006) based only on their results:

$$\zeta_{2\phi} = 3.3\varepsilon D^{1.52} U_{2\phi}^{-1.2} \left(\frac{\rho_l}{\gamma}\right)^{3/5} \nu_l^{2/25} \tag{5.11}$$

In Figure 5.10 the agreement with the correlation $AD^{1.2}$ is presented for all data. The values are presented with different symbols corresponding to the different groups of experimenters. The power of the internal diameter corresponds roughly to the dependence of the total surface area with the tube diameter. Indeed the larger the diameter the more bubbles we will have ($\sim D^2$). However, larger tubes are also associated with larger bubbles corresponding to less total interface area for the same void fraction explaining a final power somewhat less than 2.

5.6.2 Effect of void fraction on two-phase damping

As previously underlined, for bubbly flow we assumed homogeneous model leading to equivalence between volumetric quality and void fraction $\beta = \varepsilon$. By definition, two-phase damping tends to zero when the void fraction tends to zero, hence we seek a correlation $\zeta_{2\phi} = A.\beta^n$ with $n > 0$. All correlation for different sets of parameters show a value n that does not vary much and is around 1. Two-phase damping seems to vary linearly with β for bubbly flow. Again, these results are obtained from different series of tests carried out by four different groups of experimenters. In agreement with the previous remarks, the two-phase damping in bubbly flow depends linearly on volumetric quality (supposed to be equal to the void fraction):

$$\zeta_{2\phi} \simeq A\beta \tag{5.12}$$

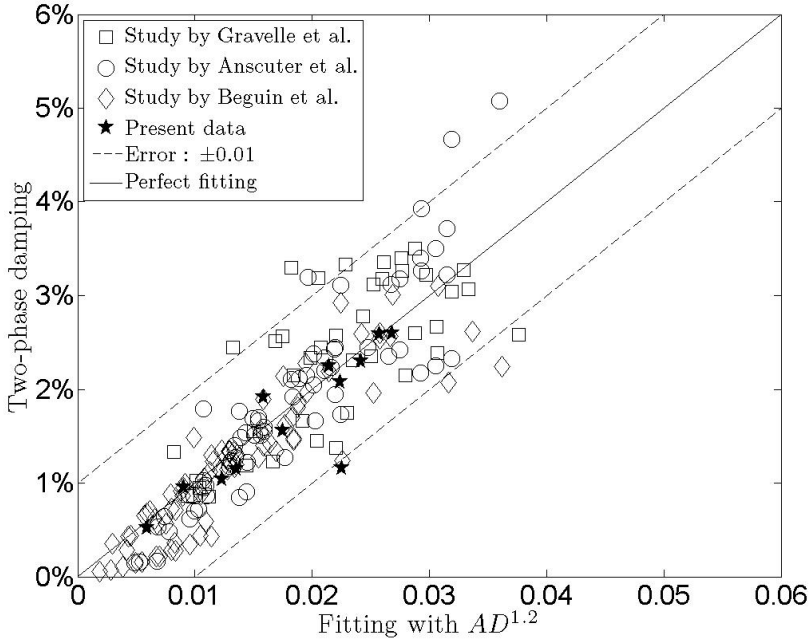

Figure 5.10 Comparison between correlation ($\simeq A.D^{1.2}$) and two-phase damping measurement for bubbly flow.

Figure 5.11 shows the agreement between the correlation $\zeta_{2\phi} = A\beta$ and measurements for all the data. The values are presented with different symbols corresponding to different mixtures. The linear character of two-phase damping with void fraction in bubbly flow seems not to depend on the physical characteristics of the two fluids constituting of the mixture. The linear trends with void fraction correspond exactly to the trends of the total surface area or mass of the "bubbles". Figure 5.12 shows the same agreement but presenting only the present data. This figure allows us to see more clearly that for all mixtures the linear trends between two-phase damping and void fraction is valid.

5.6.3 Effect of homogeneous velocity on two-phase damping

Two-phase damping should not tend to zero when the homogeneous velocity tends to zero. In fact we still should have a two-phase damping at zero homogeneous velocity. de Langre et al. suggest to use two-phase damping at zero homogeneous velocity in Connor's equation to predict fluid-elastic instability in two-phase cross-flow. For this reason, we seek a correlation $\zeta_{2\phi} = A.e^{nU_{2\phi}}$. All correlations for different sets of parameters show a value of the factor n that vary. The variation of n is, however, not large, and we do not have a sufficient number of experiments with variation of only homogeneous velocity to understand the dependence on n. The average of n is therefore chosen to obtain a correlation $n \sim -0.2$. This trend is in

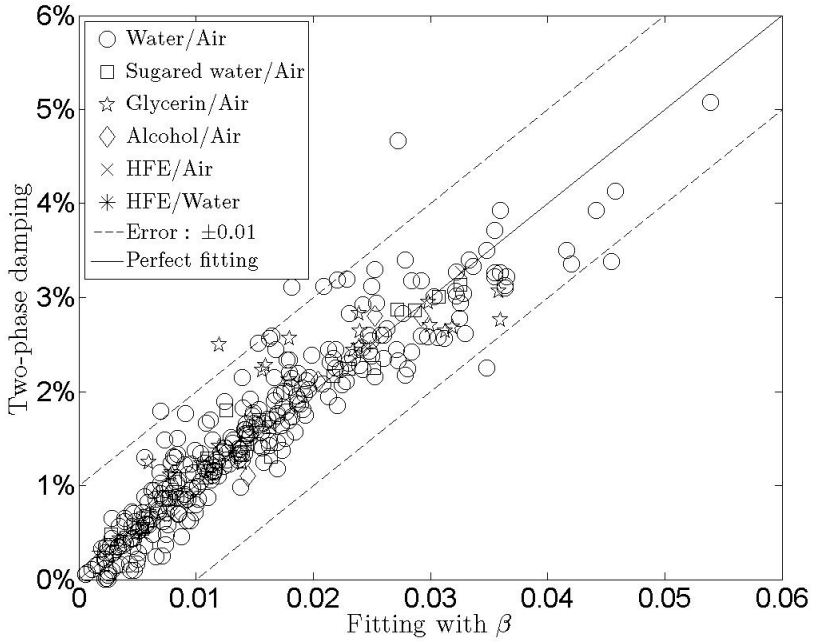

Figure 5.11 Comparison between correlation ($\simeq A.\beta$) and two-phase damping measurement for bubbly flow (all data presented).

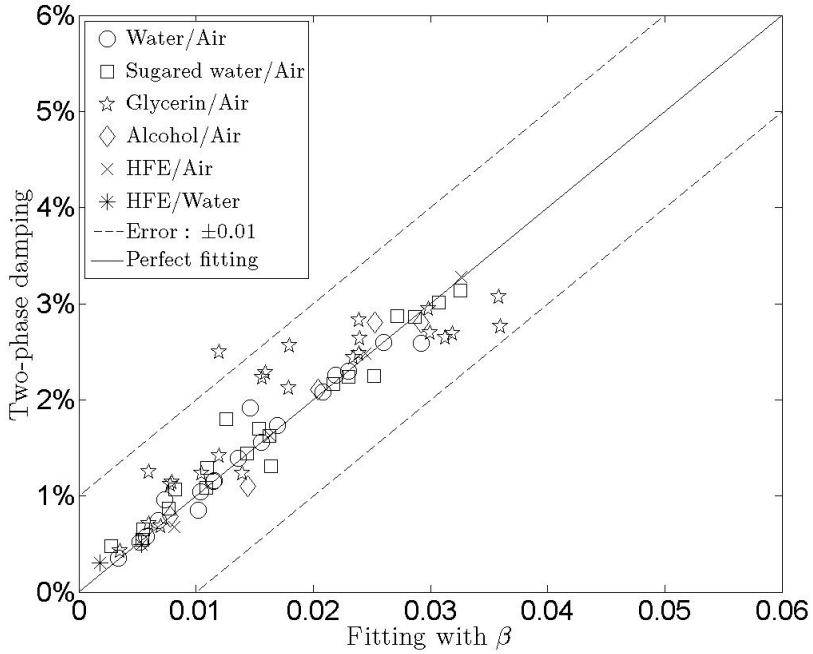

Figure 5.12 Comparison between correlation ($\simeq A.\beta$) and two-phase damping measurement for bubbly flow (only present data).

accordance with observed results of a slight diminution of two-phase damping in bubbly flow for a given mixture, void fraction and tube.

In Figure 5.13, the agreement between the correlation $\zeta_{2\phi} \simeq A.e^{-0.2U_{2\phi}}$ and two-phase damping measurements is presented for all data. The values are presented with different symbols corresponding to the different mixtures. The diminution of two-phase damping with homogeneous velocity can be explained in terms of a decrease in the bubbles ability to transfer energy into the continuous phase as homogeneous velocity increases. Figure 5.14 shows the same agreement but presenting only current data. This figure allows us to see more clearly the relatively good agreement between two-phase damping and homogeneous velocity correlation for all mixture.

5.6.4 Effect on physical properties of fluids on two-phase damping

Contrary to void fraction, homogeneous velocity and tube diameter, it is far more complicated to vary only one fluid parameters over a wide range without changing other physical properties. However, the choice of sugared water and a water-glycerin blend with proper concentration makes it possible to have two fluids with almost the same density and surface tension but different viscosities. The water-glycerin blend has ten times the viscosity of sugared water. Sugared water itself has ten times the viscosity of pure water for a density increase of only 20%. As underlined in the previous section, these two mixtures have almost the same two-phase damping. This leads to the conclusion that the viscosity of the continuous phase has no significant effect on two-phase damping. On the other hand the density difference seems to have a great effect on two-phase damping.

From the previous section we reach the conclusion that two-phase damping should vary as:

$$\zeta_{2\phi} = A.\beta D^{1.2} e^{-BU_{2\phi}} \tag{5.13}$$

Note that the factors A and B are not dimensionless. These factors will depend on the physical properties. According to previous considerations (cf. section 5.6.3) B does not vary much from one experiment to another. B has the inverse dimensions of a velocity. As viscosity is shown to have no significant effect, B probably depends only on surface tension γ, gravity g and fluid densities ρ_l and ρ_g. From these quantities, the velocity of distorted bubbles proposed by Harmathy (1960) is an excellent candidate :

$$U_0 = \left(\frac{\Delta\rho g\gamma}{\rho_l^2} \right)^{1/4} \tag{5.14}$$

The factor A should be related to a length and as density difference and surface tension

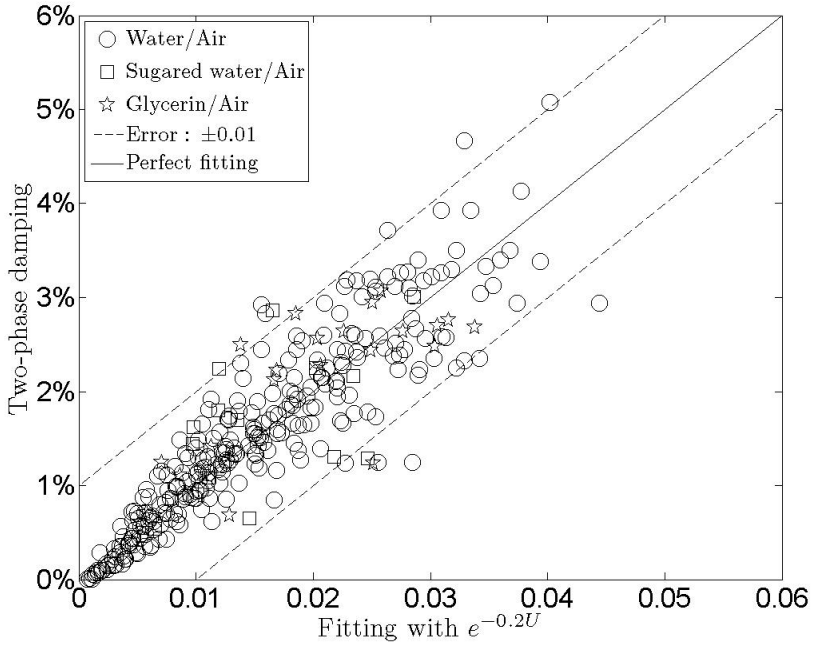

Figure 5.13 Comparison between correlation ($\simeq A.e^{-0.2U_{2\phi}}$) and two-phase damping measurement for bubbly flow (all data presented).

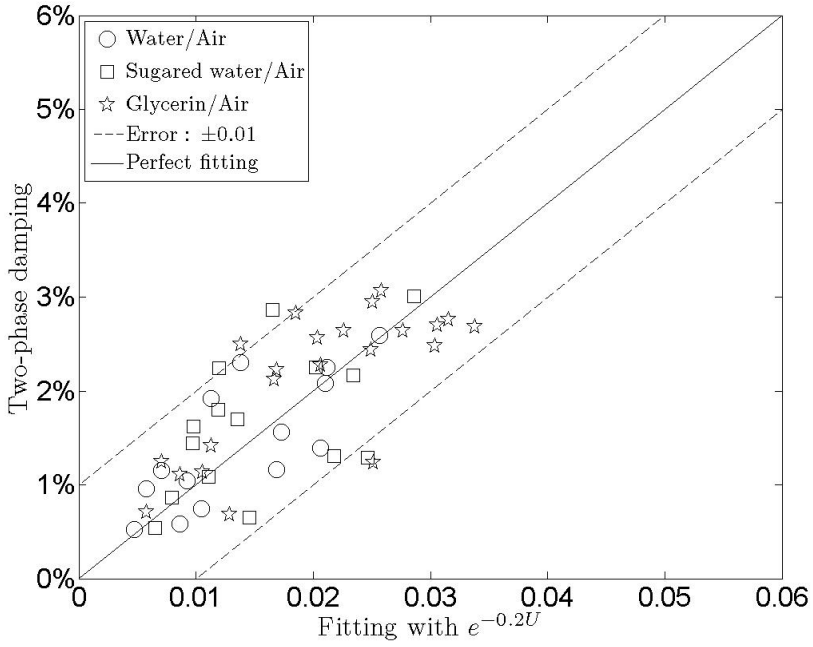

Figure 5.14 Comparison between correlation ($\simeq A.e^{-0.2U_{2\phi}}$) and two-phase damping measurement for bubbly flow (only present data).

seem to play an important role, the capillary length is a good candidate:

$$L_c = \sqrt{\frac{\gamma}{\Delta\rho g}} \tag{5.15}$$

We proposed therefore to seek a relation of the form :

$$\zeta_{2\phi} = A\beta\left(\frac{\Delta\rho g D^2}{\gamma}\right)^{0.6} e^{-B\frac{U_{2\phi}}{U_0}} \tag{5.16}$$

This time A and B are dimensionless number. More experiments should now be conducted with a large range of U_0 and in particular with a greater variation of γ to validate this. The ratio of tube diameter to capillary length define the Bond number so finally the relation becomes:

$$\zeta_{2\phi} = 0.0115\beta Bo^{0.6} e^{-0.02\frac{U_{2\phi}}{U_0}} \tag{5.17}$$

Similar work on two-phase damping for slug flow (for void fractions higher than those corresponding to the maximum damping) was also done. For such a relation we used the fact that two-phase damping tends to zero when the volumetric quality tends to 1. We sought, for this reason, a relation of the form $(1-\beta)^n$; this led to:

$$\zeta_{2\phi} = 0.004(1-\beta)^{1/4} Bo^{0.4} e^{0.01\frac{U_{2\phi}}{U_0}} \tag{5.18}$$

The results of this correlation are presented in Figure 5.15. However, a difference is noted between sugared water and glycerin/water blends. In slug flow glycerin/water blend has a higher two-phase damping which indicated the presence of a viscous effect not captured by the proposed correlation. The viscous effect comes probably from the oscillating liquid film flow present between the Taylor bubbles and the tube. To be able to understand this effect, specific experiments need to be carry out using small diameter tube and more different two-phase mixtures. In small tubes, pure slug flow can be achieved, with no bubbles present in the liquid between the Taylor bubbles. The results of the correlation (Eq. 5.18) are presented in Figure 5.15.

5.6.5 Physical Interpretation of two-phase damping

The first assumption to explain two-phase damping was proposed by Carlucci (1980). When a single phase fluid flows through a transversely vibrating tube, the transverse motion $x(\xi, t)$ of the tube can be damped by the fluid motion (ξ is the axial position along the tube,

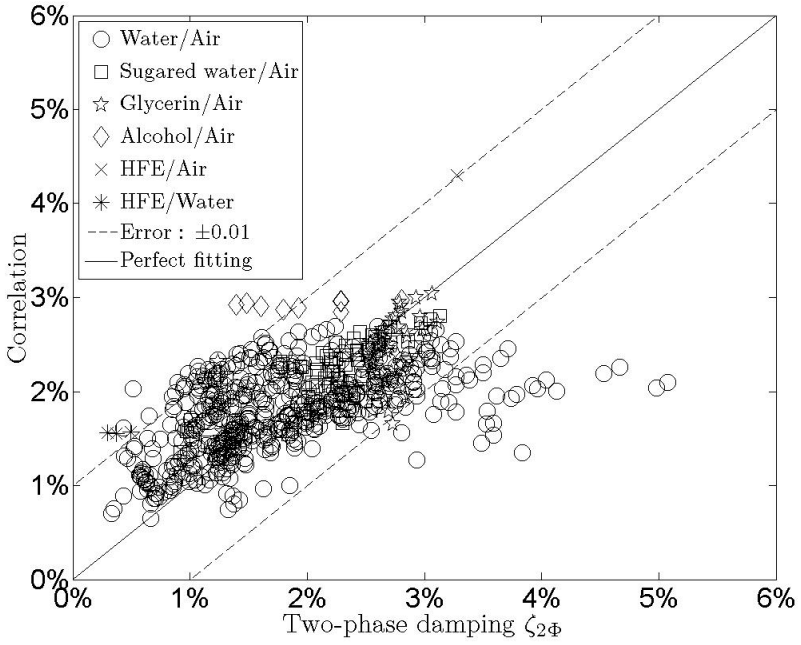

Figure 5.15 Comparison between correlation (5.18) and two-phase damping measurement in slug flow (all data presented).

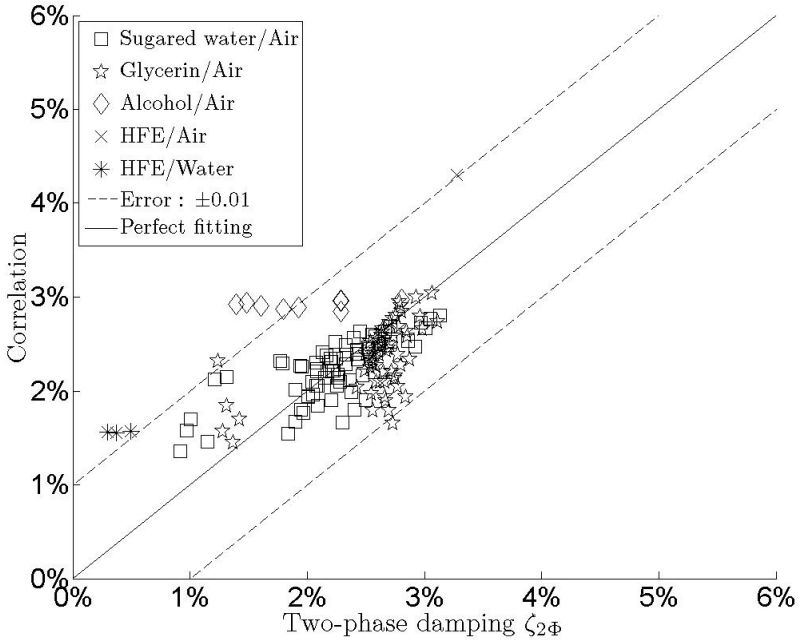

Figure 5.16 Comparison between correlation (5.18) and two-phase damping measurement in slug flow for mixture other than water/air.

and t is the time). The equation of motion of such system is as follows de Langre (2001):

$$(MU_R^2 - 1)\frac{\partial^2 x}{\partial \xi^2} + 2MU_R\frac{\partial^2 x}{\partial \xi \partial t} + (M+1)\frac{\partial^2 x}{\partial t^2} = 0 \tag{5.19}$$

The dimensionless mass of the fluid is given by $M = \rho\pi D^2/(4m)$, where m is the mass per unit length of the tube. The reduced velocity of the fluid is given using the velocity of the transverse wave in the tube itself: $U_R = U/\sqrt{T/m}$, where T is the tension in the tube.

In the second term of Eq. (5.19), the axial velocity U_R of the fluid mass inside the transversely vibrating tube causes a Coriolis type force due to the rotation $\partial x/\partial \xi$ of the tube. This force is proportional to the transverse velocity $\partial x/\partial t$ of the tube: it thus acts as a damping element on the tube. Carlucci et al. suggested that Coriolis forces in Eq. (5.19) should be written in two-phase flow as :

$$2MU_R\frac{\partial^2 x}{\partial \xi \partial t} \quad \underbrace{+\left(\frac{\partial M}{\partial t} + U_R\frac{\partial M}{\partial \xi}\right)\frac{\partial x}{\partial t}}_{\text{Two-phase random Coriolis}} \tag{5.20}$$

This effect, due to mass change, causes a detuning mechanism that could explain two-phase damping, but this model does not explain the void fraction dependency. Hara and Kohgo (1993) considered a bubbly flow forced to oscillate due to a vibrating structure. The motion of bubbles in liquid is governed by added mass and fluid viscosity. The energy dissipation in Hara and Kohgo's model is due to the liquid viscosity acting between the vibrating gas columns and liquid. Carlucci's and Hara's tests were performed with an axially confined external flow. Béguin *et al.* (2008) have proposed similar mechanism to that of Hara and Kohgo for internal flow . They proposed a simple model of a two-phase fluid inside a tube shown in Figure 5.17. In this model, the tube of radius $R_o = D/2$ is allowed to move along the Y axis. The gas phase is represented as a single, non deformable gas cylinder of radius R_i, parallel to the tube axis and allowed to move along the X axis only. Absolute coordinates X and Y are collinear. No axial flow or other axial phenomena are considered; thus, the masses of liquid and gas are constant in an elementary length of the fluid filled tube. The two-dimensional equations of motion in the plane of the cross-section are:

$$\begin{aligned} m_s\ddot{Y} + c_s\dot{Y} + k_s Y &= F_s \\ \rho_g \pi R_i^2 \ddot{X} &= F_g \end{aligned} \tag{5.21}$$

where $\rho_g$is the density of the gas, and tube elements; m_s,c_s and k_s are the equivalent mass, damping coefficient and rigidity of the tube. The resulting forces F_s and F_g exerted by the liquid on the tube element and gas element are determined by integrating the stress tensor

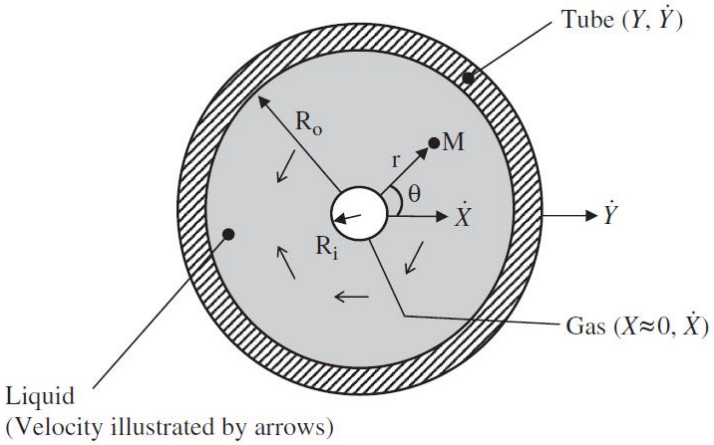

Figure 5.17 Geometry of the problem solve by Béguin *et al.* (2008).

$\bar{\bar{T}}$. Stokes equation for the fluid was solved based on a previous solution by Chen (1987).

$$\begin{aligned} F_s &= \oint_{r=R_o} \bar{\bar{T}}\vec{n}_s dl \\ F_g &= \oint_{r=R_i} \bar{\bar{T}}\vec{n}_l dl \end{aligned} \tag{5.22}$$

They finally arrive at the equation :

$$\begin{aligned} (m_s + \rho_l \pi R_o^2)\ddot{Y} + c_s\dot{Y} + k_s Y &= \rho_l \pi R_o^2 \left[b_r \left(\ddot{Y} - \ddot{X} \right) - b_i \left(\dot{Y} - \dot{X} \right) \right] \\ \Delta\rho\pi R_i^2 \ddot{X} + \rho_l \pi R_i^2 (b_r + 2) \left(\ddot{X} - \ddot{Y} \right) + \left(b_i - \frac{2\nu_l}{R_i^2} \right) (\dot{X} - \dot{Y}) &= 0 \end{aligned} \tag{5.23}$$

Where b_r and b_i are integration constant depending on ν_l in a complex way. This equation shows a coupled system where we can identify added mass on tube, and density difference on bubble inertia. Coupled viscous damping and inertial effects related to relative motion between the phases are also present. The actual form of the equation (5.23) does not explain a two-phase damping independent of tube frequency and liquid viscosity as the experiments shows.

Two assumptions are able to explain this fact: a form drag independent of viscosity and/or stiffness term due to surface tension.

a) Form drag

We suggested to add a form drag (also referred to as pressure drag) effect to the bubble motion equation. A bubble is not a slender body. In this region of parameter, it is possible that in oscillating flow the form drag is a lot higher than the friction drag and is independent of bubble Reynolds number therefore to liquid viscosity. This is the case for a deformed

bubble where the drag coefficient given by Harmathy (1960) is independent of the bubble Reynolds number. In the case of two-phase damping, contrarily to Harmathy's experience, we are in the presence of an oscillating liquid velocities. Measurement of drag of a bubble in oscillating velocity fields should provide supporting evidence of the above assumptions. Farris *et al.* (2004) have studied the motion of bubbles in a sinusoidally oscillating liquid in microgravity. Their experiments show that the amplitude ratio AR between bubbles and cell oscillation reached an asymptote as the excitation frequency rises. The cut-off frequency corresponds to the excitation frequency where the amplitude ratio AR reaches an asymptote. The cut-off frequency is shown to increase with higher viscosity. It is plausible that viscosity should be more important at low frequencies because it affects the steady drag and history forces but not the added mass force. However Farris et al. experiments were performed at low frequencies (up to 3 Hz). Maybe in all practical cases of piping structure, the natural frequency of the tube are higher that the cut-off frequency.

b) Stiffness effect due to surface tension

We suggested to add a stiffness effect to the bubble motion equation. The stiffness of bubble motion is related to surface tension. Indeed, noting drop radius a the contact time of water drop impact has been studied and shown to scale as $\sqrt{\rho_l a^3/\gamma}$ (Clanet *et al.* (2004)). Richard and Quéré (2000) explained that this variation, which is independent of the impact velocity U_0, can be understood by considering (globally) the rebound as an oscillation: the drop is a spring of stiffness γ and mass $\rho_l a^3$, which oscillates with a constant frequency of $\omega_b = \sqrt{\gamma/(\rho_l a^3)}$. The restitution coefficient of impact was found to be significantly lower than one. Energy dissipation is explained by drop oscillation after the lift-off, whereas it was just in translation before the impact. Thus, a part of the translational kinetic energy is transferred into internal modes of vibration during the shock. The oscillations are damped against time, because of the liquid viscosity, however, viscous dissipation could be neglected during the very short time of impact (of order 1 ms), leading to the impact being approximated by a pure inertial effect. The damping during impact is illustrated in Figure 5.18.

The non-dependence of two-phase damping with liquid viscosity can also be explained by the large ratio observed between typical frequency of the structure and frequency of the bubbles. The frequencies of the bubble oscillation ($\omega_b \sim \sqrt{\gamma/(\Delta\rho a^3)}$ are in the order of (200 – 1000 Hz) compared to the structure frequencies ($\omega_s \sim 20 - 70$ Hz). Considering the transfer function of the bubble exited to the structural frequency, where the damping ζ_b is related to drag of the bubbles and directly to the viscosity of the liquid.

$$H(\omega_s) = \frac{1}{\sqrt{\left(1 - \left(\frac{\omega_s}{\omega_b}\right)^2\right)^2 + \left(2\zeta_b \frac{\omega_s}{\omega_b}\right)^2}} \tag{5.24}$$

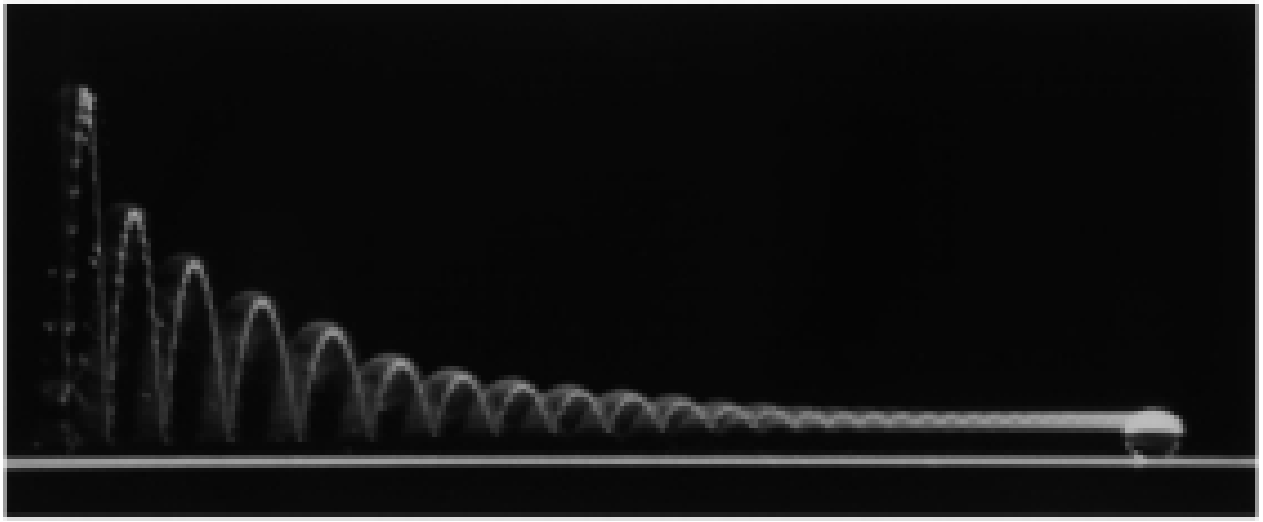

Figure 5.18 Water drop falling on a super-hydrophobic surface The drop in motion is illuminated by a continuous lamp which reflects on it, producing a line of light. The plane is slightly tilted, which allows us to reveal the whole trajectory of the drop by taking a photograph with a long-time exposure. The vertical scale of the whole picture is 1 cm and the drop diameter 1 mm. A long series of full rebounds is observed. The elasticity is limited by the vibration of the drop after each shock. These vibrations can directly be observed (modulation of the line of light) together with their damping (because of the liquid viscosity) along each parabolic arch. The drop finally stops on the solid (Richard and Quéré (2000)).

Because $\omega_b >> \omega_s$ the transfer function $H(\omega_s)$ will not vary for a very large range of viscosity of the liquid (affecting ζ_b). This could explain why two-phase damping does not depend on fluid viscosity. Impact between bubbles or bubbles and structure or excitation by oscillating velocities of the liquid leading to vibration of interface. This vibration of interface can be a potential mechanism to transfer energy to the continuous phase without involving a viscous effect. The increase of kinetic energy in the continuous phase will then be carried out of the tube by the flow or damped by viscous effect but in time scales quite longer that the time scale of tube vibration. Two-phase damping will be a transfer of energy at low frequency (structure natural frequency) to liquid turbulence at high frequency (bubble frequency) through impact forces.

Experimental studies of turbulence intensity variation at the tube exit when the tube is vibrating should provide supporting evidence of the above assumptions.

Conclusion

The purpose of this paper is to understand the fundamental mechanisms of two-phase damping and to try to explain the respective role of viscosity, density and surface tension in the damping phenomenon. An empirical model was developed for this purpose. The main conclusions are:

• Two-phase damping in bubbly flow is likely due to an increase of kinetic energy in the continuous phase due to inertial effect of gas bubbles. The increase of kinetic energy leads to damping of the structure. In slug flow, some viscous damping is added due to the presence of Taylor bubbles.

• Surface tension plays an important role in the size and shape of gas bubbles and consequently in their ability to transfer kinetic energy into the continuous phase. However it does not create damping by creating new interface surfaces.

• In bubbly flow, two-phase damping does not depend strongly on fluid viscosity. This leads to conclude that the increase of kinetic energy in the liquid due to relative motion between phases is carried out with the flow. Experimental studies of turbulence intensity variation at the tube exit when the tube is vibrating should provide supporting evidence of the above assumptions.

• Greater density difference and void fraction lead to greater two phase-damping, up to a critical void fraction corresponding to the maximum damping. Two-phase damping increases fairly linearly with void fraction up to this critical void fraction.

• The critical void fraction associated with a change of two-phase damping behavior seems to correspond to flow pattern transition. However in some rare cases, we observed the

creation of deformed slugs without impact on the two-phase damping behavior.

• Void fraction, inertia and surface tension are the major governing parameters for two-phase damping.

Acknowledgement

The experiments reported were performed with the valuable and much appreciated assistance of A. Raouhani, J. Wehbe, F. Anscutter and C. Loranger. Previous experiments from Gravelle *et al.* (2007) were also used. We wish to thank all these experimenters to let us used their results (almost 960 two-phase damping ratios were measured for 8 different tube diameters and 5 different two-phase mixtures)

References

ANSCUTTER, F., BÉGUIN, C., ROSS, A., PETTIGREW, M. and MUREITHI, N. (2006). Two-phase damping and interface surface area in tubes with internal flow. *ASME PVP2006*. 11.

BÉGUIN, C., ROSS, A., PETTIGREW, M. and MUREITHI, N. (2008). Relationship between vibration behavior and two-phase flow regime transition for piping with internal flow. *9th International Conference on Flow-Induced Vibrations*. Institute of Thermomechanics, Academy of Sciences of Czech Republic, Prague, Czech Republic, 619.

BÉGUIN, C., WEHBE, J., ROSS, A., PETTIGREW, M. and MUREITHI, N. (2009). Influence of viscosity, density and surface tension on two-phase damping. *Proceedings of ASME 2009 Pressure Vessels & Piping Conference*. ASME, Prague, Czech Republic, PVP2009 77423.

CARLUCCI, L. (1980). Damping and hydrodynamic mass of a cylinder in two-phase flow. *ASME Journal of Mechanical Design*, 102, 597–602.

CHEN, S. (1987). *Flow-induced Vibration of Cylindrical Structures.* Hemisphere Publishing,New York,.

CLANET, C., BÉGUIN, C., RICHARD, D. and QUÉRÉ, D. (2004). Maximal deformation of an impacting drop. *Journal of Fluid Mechanics*, 517, 199–208.

COLLIER, J. and THOME, J. (1996). *Convective boiling and condensation*. Clarendon Press, Oxford University Press, troisième édition.

DE LANGRE, E. (2001). *Fluides et solides*. Edition de l'École Polytechnique, Paris.

FARRIS, S. C., BUGG, J. D. and GABRIEL, K. S. (2004). The motion of bubbles in a sinusoidally oscillating liquid in microgravity. *Microgravity Science and Technology*, 15, 28–35.

GRAVELLE, A., ROSS, A., PETTIGREW, M. and MUREITHI, N. (2007). Damping of tubes due to internal two-phase flow. *Journal of Fluids and Structures*, 23, 447.

HARA, F. and KOHGO, O. (1993). A theory for a vibrating circular rod damping in two-phase bubbly fluid. *Transactions JSME*, 51, 143–148.

HARMATHY, T. (1960). Velocity of large drops and bubbles in media of infinite or restricted extend. *AIChE Journal*, 6, 281.

PETTIGREW, M. and TAYLOR, C. (2004). Damping of heat exchanger tubes in two-phase flow: Review and design guidelines. *ASME Journal of Pressure Vessel Technology*, 126, 523.

RICHARD, D. and QUÉRÉ, D. (2000). Bouncing water drops. *Europhysics Letters*, 50, 769–775.

TAITEL, Y., BORNEA, D. and A.E., D. (1980). Modelling flow pattern transitions for steady upward gas-liquid flow in vertical tubes. *AIChE Journal*, 26, 345–354.

TAYLOR, G. (1932). The viscosity of a fluid containing small drops of another fluid. *Proceedings of the Royal Society of London, Containing Papers of a Mathematical and Physical Character*. vol. 138, 41.

CHAPITRE 6

A MODEL FOR BUBBLY TWO-PHASE FLOW - PART I DRAG COEFFICIENT

Pour être en mesure de comprendre les mécanismes de transition en configuration d'écoulement et l'amortissement diphasique, la modélisation des forces d'interface et de l'écoulement autour d'une bulle est clairement apparue comme une nécessité. En effet, peu de travaux ont été consacrés pour comprendre le rôle du taux de vide sur les forces d'interface agissant sur une bulle et ainsi que la structure de l'écoulement autour d'elle.

L'influence du taux de vide sur l'écoulement autour des bulles et sur les forces d'interface est le moteur des ondes de taux de vide. Par ailleurs, les forces d'interface constituent une donnée indispensable dans la modélisation des écoulements diphasiques par moyennage des équations de Navier-Stokes. Cette modélisation est une façon de résoudre numériquement un écoulement diphasique avec des ressources informatiques raisonnables. La limite sous laquelle les bulles restent sphériques a également été étudiée. Cette condition permet de déterminer la limite du modèle proposé.

Cet article est la première partie d'un article en deux parties soumis pour publication dans le *Journal of Fluid Mechanics*. Il est le résultat de nos investigations sur le coefficient de traînée de bulles (ou gouttes) sphériques en fonction du nombre de Reynolds Re, du taux de vide ε, du rapport de viscosité et de densité entre les deux phases ($\bar{\mu}$ et $\bar{\rho}$).

C. Béguin[1], S. Étienne[2], N.W. Mureithi[1] & M. J. Pettigrew[1]

[1] BWC/AECL/NSERC Chair of Fluid-Structure Interaction

[2] Canada research chair in analysis, characterization and optimization of complex flows,

Department of Mechanical Engineering,École Polytechnique,

P.O.Box 6079, succ.Centre-Ville, Montréal, Quebec, Canada H3C3A7

Abstract

This paper proposes a relation for the drag coefficient of spherical bubbles (or droplets) depending on Reynolds number Re, void fraction ε , viscosity ratio $\bar{\mu}$ and density ratio $\bar{\rho}$. The proposed relations are useful for all fluid-fluid cases. The limiting conditions under which bubbles remain spherical are also studied.

Moreover, it is shown that the slip ratio is very small for bubbly flow. In almost all practical cases of bubbly flow, the flow around a bubble can be considered as Stokes flow.

The void fraction, ε, has a major effect on the drag essentially through confinement. The proposed relation can be used to construct a two-phase flow model for bubbly or annular flows. This work proposes an improvement on the the closure relations for the drag coefficient (C_D) compared to previous works.

The main conclusion is that Stokes flow represents, very accurately, the flow around bubbles. The flow is consequently laminar and therefore two-phase turbulence cannot be attributed to classical turbulence. The flow in the continuous phase can be viewed as a film flow in which classical turbulence cannot develop. Two-phase turbulence is essentially due perturbations induced by bubble passage.

Nomenclature

Variables :

a: bubble/drop radius (m)
B_i, C_i, D_i: integration constants
f: force (N)
g: gravitational acceleration (m/s^2)
l: inter-bubble distance (m)
P: fluid pressure (Pa)
Q: volume flow rate (m^3/s)
U, u, v: velocity (m/s)
V: volume of fluid (m^3)
ρ: mass density (kg/m^3)
γ: surface tension (N/m)
μ: viscosity (Pa.s)
r, θ, ϕ : spherical coordinate

Subscripts :

$_i$: at the liquid/gas interface
$_w$: at the wall interface
$_k$: phase k
$_l$: liquid/continuous phase
$_g$: gas/dispersed phase
$_{2\phi}$: two-phase
$_{ls}$: superficial liquid (velocity)
$_{gs}$: superficial gas (velocity)

$_{r,\ \theta,\ \phi}$: spherical coordinates

Dimensionless numbers :
$Re = \dfrac{2\rho_l U_b a}{\mu_l}$: Reynolds number
$Mo = \dfrac{\mu_l^4 \Delta\rho g}{\rho_l^2 \gamma^3}$: Morton Number
$Bo = \dfrac{4\Delta\rho g a^2}{\gamma}$: Bond Number
$\bar{\rho} = \dfrac{\rho_g}{\rho_l}$: Density ratio
$\bar{\mu} = \dfrac{\mu_g}{\mu_l}$: Viscosity ratio
β: volumetric quality
ε: void fraction
C_D: Drag coefficient
C_L: Lift coefficient
C_M: Added mass coefficient

Superscripts :
$\langle X \rangle$: space averaged variable
$\bar{X}$: dimensionless number
X^*: correctional term

Other symbols are defined in the text.

Introduction

In the nuclear and chemical process industries, 50% of components and piping elements operate with two-phase flows, see, *e.g.* Pettigrew and Taylor (2004). Flow-induced vibrations can lead to structural degradation, process malfunction and component failure. Two-phase flow can create significant damping or vibration excitation forces. In order to evaluate the forces induced by two-phase flow and prevent premature fatigue or wear it is desirable to identify the parameters that govern the flow. In the present paper, we propose to investigate some of these parameters.

In two-phase flow, the state of the deformable interface between the phases is of critical importance in determining mixture properties. Each phase interacts with the tube wall through friction forces, and with the other phase through interfacial forces. The resulting

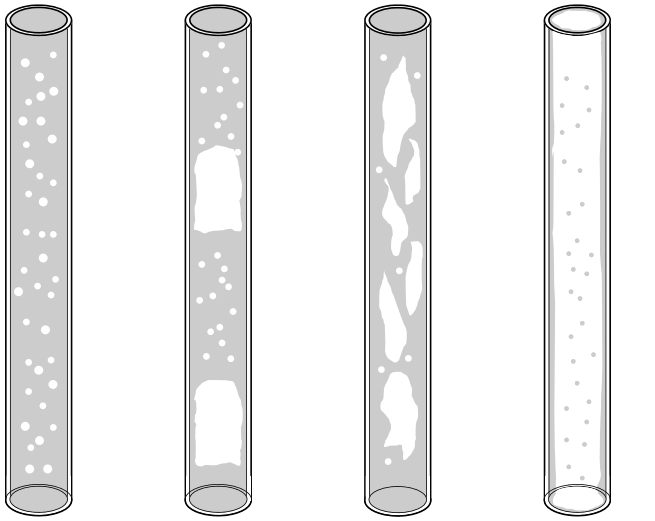

Figure 6.1 Flow patterns in internal two-phase flow

flow pattern is mainly governed by the respective liquid and gas flow rates. The flow structure in gas-liquid vertical flow is commonly categorized into the following flow regimes (cf. Figure 6.1):

- (a) Bubbly flow: At low void fraction, the gas phase is dispersed in relatively large deformable bubbles.On increasing the liquid flow rate, the large bubbles break up due to turbulence. The resulting small bubbles disperse in the liquid, and their coalescence is inhibited by the turbulence. Because the bubbles are small, surface tension forces are stronger than drag forces and the bubbles remain spherical.
- (b) Slug flow: On increasing the gas flow rate, bubbles approach and coalesce. Part of the gas phase forms into slugs called Taylor bubbles.
- (c) Churn flow: Churn flow is similar to slug flow. In a slug flow pattern, when the gas flow rate is increased, the slugs become smaller, distorted, and unstable. The flow is more chaotic.
- (d) Annular flow: At high gas flow rates, the liquid phase forms an annulus along the wall. The gas fills the central region of the tube. The gas flow in the central region has enough energy to lift and carry along small liquid droplets. This fact was used by Taitel *et al.* (1980) to determine flow pattern boundaries in a flow regime map.

In the present work, the forces on a spherical inclusion of one phase in the other are determined. This information is essential to completely characterize finely dispersed bubbly flows, where gas bubbles are present in a continuous liquid phase. It is also useful to model annular flow, where liquid inclusions (droplets) are present in a continuous gas phase.

Much information can be gained and fundamental modelling achieved from these forces for the following approach.

Firstly, the dispersed phase velocity is deduced from the total drag force on the bubble (or droplet). In classical experiments, both the flow rates of gas and liquid are measured. The actual void fraction is then deduced from the ratio of flow rates and the dispersed phase velocity. The dispersed phase velocity deduced here can be used to determine the actual void fraction.

Secondly, the limit at which the bubble (or droplet) remains spherical shaped is deduced by comparing the tangential distribution of forces on the bubble (or droplet) compared to the surface tension forces.

Thirdly, it is shown that the gas velocity variation leads to void fraction variation generating waves. The stability of the void waves can be used to determine the two-phase flow patterns.

Finally, the averaging procedure of the Navier-Stokes equations, a classical way to model two-phase flow, is revisited, see *e.g.* Ishii and Zuber (1979); Park *et al.* (1998); Leon-Becerril

and Liné (2001). In the averaging process new terms appear which must be determined by closure relations. It is shown that some of these terms are forces on the bubbles.

Most studies on drag forces neglect the effect of void fraction, considering that bubble forces are identical to forces on a bubble in an infinite liquid domain (Taitel *et al.* (1980)). However, the terminal bubble velocity (relative to the continuous phase velocity) is quite small and Stokes flow around the bubble represents the most commonly encountered condition, as will be shown. In the Stokes flow approximation, the variation in the boundary condition propagates deep into the whole domain. This makes it essential to consider the effect of surrounding bubbles.

This paper will explore the effect of drag on spherical bubbles (or droplets). For simplicity, spherical bubbles (or droplets) corresponding to the dispersed phase will be named "gas" or "bubbles" and the continuous phase "liquid" with the respective subscripts g and l. A priori, the drag coefficient (C_D) depends on fluid viscosity (μ_l,μ_g), fluid density (ρ_l,ρ_g), bubble size (radius : a), void fraction (ε - ratio of gas volume to total volume) and bubble velocity (U_b). Assuming there are no other parameters involved such as the presence of impurities and according to the Buckingham-π theorem, the drag coefficient (C_D) is a function of four independent dimensionless numbers. We choose:

- $\bar{\mu} = \dfrac{\mu_g}{\mu_l}$
- $\bar{\rho} = \dfrac{\rho_g}{\rho_l}$
- $Re = \dfrac{2\rho_l U_b a}{\mu_l}$
- ε

In the present work, a general expression for the drag coefficient $C_D = F(\bar{\mu}, \bar{\rho}, Re, \varepsilon)$ is sought. This present paper is the first part of an upcoming paper on pseudo two-phase turbulence and bubble size Béguin *et al.* (submitted in 2010). Previous studies, Moore (1963), Mei *et al.* (1994) and Taylor and Acrivos (1964) have proposed relations for an infinite liquid medium, meaning that $C_D = F(\bar{\mu}, \bar{\rho}, Re, \varepsilon = 0)$. Some authors such as Ishii and Zuber (1979) have, however, considered the void fraction effect on bubble velocity. Other authors have also proposed a slip ratio model related to void fraction, which in effect models the influence of void fraction on fluid velocity, hence $C_D = F(\varepsilon)$, see *e.g.* Feenstra *et al.* (2000).

The goal of the present work is to find a general relation $C_D = F(\bar{\mu}, \bar{\rho}, Re, \varepsilon)$. Our results will be compared with previous studies. The paper is divided into four sections. In the first section, we will define two-phase parameters and present a brief literature review of two-phase flow models. We will also present some new results directly deduced from the literature. In Section 2, analytical solutions for Stokes and Euler flows are presented. In Section 3, a numerical experiment is presented. The results lead to a proposal for a general relation of

the drag coefficient for a cloud of spherical bubbles. This section explores also the limit at which the bubbles/droplets depart from sphericity. The main results are summarized in the conclusion section.

6.1 Two-phase flow considerations

This first section introduces basic definitions and concepts specific to two-phase flow as well as a brief literature review. The review leads us to propose some new relations more useful to the specific problem of developing a general formulation for the drag coefficient and the terminal velocity of a bubble within a cloud of surrounding bubbles.

6.1.1 Basic definitions

The proportion of gas in a two-phase gas-liquid mixture is characterized either by the void fraction ε or by the volumetric quality β [Collier and Thome (1996)]. The two-phase mixture void fraction and volumetric flow quality in a tube section of length ΔL are defined as:

$$\begin{aligned} \varepsilon &= \frac{V_g}{V_g + V_l} = \frac{A_g \Delta L}{A_g \Delta L + A_l \Delta L} = \frac{A_g}{A_g + A_l} \\ \beta &= \frac{Q_g}{Q_g + Q_l} = \frac{A_g U_g}{A_g U_g + A_l U_l} = \frac{A_g}{A_g + A_l \frac{U_l}{U_g}} = \frac{\varepsilon}{\varepsilon + (1-\varepsilon) S_r} \end{aligned} \tag{6.1}$$

where V_g and V_l are the volumes of the gas and liquid phases in the mixture, A_g and A_l are the cross sectional areas of each phase in the tube cross section, Q_g and Q_l are the volume flow rates, and U_g and U_l the average phase velocities. The void fraction and volumetric quality are related through the slip ratio, $S_r = U_l/U_g$. The superficial velocities of the phases (U_{gs}, U_{ls}) and the total superficial velocity also named sometimes the homogeneous velocity ($U_{2\phi}$) are defined as :

$$\begin{aligned} U_{gs} &= \frac{Q_g}{A} = \frac{A_g U_g}{A} = \varepsilon U_g = \beta U_{2\phi} \\ U_{ls} &= \frac{Q_l}{A} = (1-\varepsilon) U_l = (1-\beta) U_{2\phi} \\ U_{2\phi} &= \frac{Q_g + Q_l}{A} = U_{gs} + U_{ls} \end{aligned} \tag{6.2}$$

The difference between the gas and liquid velocities denoted as $U_b = U_g - U_l$, represents the velocity of bubbles relative to the liquid (typical magnitude around 0.25 m/s). The higher the homogeneous velocity, the smaller is the difference between ε and β. Indeed with greater homogeneous velocity, gravity effects which govern U_b become relatively smaller (cf. equation (6.3)). The homogeneous model corresponds to no relative velocity between phases, $U_b = 0$,

leading to $\varepsilon = \beta$. In this case, the homogeneous velocity corresponds to the phase velocities ($U_{2\phi} = U_l = U_g$).

Using equations (6.1) and (6.2), Anscutter *et al.* (2006) deduced a slip ratio model and the following relation between volumetric quality and void fraction :

$$\begin{aligned} \beta &= \varepsilon + \varepsilon(1-\varepsilon)\frac{U_b}{U_{2\phi}} \\ \varepsilon &= \frac{1}{2}\left[1 + \frac{U_{2\phi}}{U_b} - \sqrt{\left(\frac{U_{2\phi}}{U_b}+1\right)^2 - 4\beta\frac{U_{2\phi}}{U_b}}\right] \end{aligned} \tag{6.3}$$

6.1.2 Bubble shape and velocity

The bubble terminal velocity is determined by the equilibrium between the buoyancy force on the bubble ($\Delta\rho g a^3$) and the drag force on the bubble :

$$\begin{aligned} \frac{1}{2}C_D\rho_l\pi a^2 U_b^2 &= \frac{4}{3}\pi\Delta\rho g a^3 \\ U_b^2 &= \frac{8}{3}\frac{\Delta\rho g a}{C_D\rho_l} \\ U_b &= \frac{1}{3}\frac{16}{C_D Re}\frac{\Delta\rho g a^2}{\mu_l} \end{aligned} \tag{6.4}$$

where $\Delta\rho = \rho_l - \rho_g$ represents the density difference. As a reasonable qualitative prediction, when bubbles are small (small Bond number $Bo = 4\Delta\rho g a^2/\gamma << 1$), they are spherical and their velocities depend only on the density, gravity, bubble size and liquid viscosity. The Bond number is also known as the Eötvös number. The term Eötvös number is more frequently used in Europe, while Bond number is commonly used in other parts of the world. For spherical bubbles, C_D is inversely proportional to Reynolds number, as proposed by Mei *et al.* (1994):

$$C_D = \frac{16}{Re}\left[1 + \frac{2}{\frac{16}{Re} + \frac{3.315}{\sqrt{Re}} + 1}\right] \tag{6.5}$$

Because the bubble Reynolds number Re, is defined using the bubble velocity, deriving a simple analytical solution for the bubble velocity from equations (6.4) and (6.5) is not feasible. We propose the following new relation, which we refer to as the "simplified Mei et al.

formulation". This relation leads to an analytical solution for equation (6.4) :

$$C_D = \frac{16}{Re}\left[1 + \frac{2}{1 + \frac{100}{3Re}}\right] \tag{6.6}$$

The two relations (6.6) and (6.5) are compared in Figure 6.2. From equations (6.4) and (6.6) we can express the bubble velocity using the following new formula :

$$\frac{U_b}{U_0} = \frac{1}{18}\left[1 - \frac{100}{A} + \sqrt{1 + \frac{1000}{A} + \left(\frac{100}{A}\right)^2}\right] \tag{6.7}$$

where U_0 is a typical bubble velocity expressed as $U_0 = \Delta\rho g a^2/\mu_l$ and A is a new dimensionless number which does not depend on the bubble velocity :

$$A = \frac{2\rho_l U_0 a}{\mu_l} = \frac{2\rho_l \Delta\rho g a^3}{\mu_l^2} \tag{6.8}$$

The Stokes approximation leads to $U_b/U_0 = 1/3$ while the Euler approximation leads to $U_b/U_0 = 1/9$ as illustrated in Figure 6.3.

Large bubbles ($Bo = 4\Delta\rho g a^2/\gamma >> 1$) are no longer spherical and do not rise along a straight path. The bubbles are usually cap or skirt shaped and their velocity U_b no longer depends on bubble size but only on the density difference, gravity and surface tension, as proposed by Harmathy (1960). Harmathy proposed the following relations for C_D and U_b.

$$\begin{aligned} C_D &= 0.57\sqrt{Bo} = 1.14\sqrt{\frac{\Delta\rho g a^2}{\gamma}} \\ U_b &= 1.53\left(\frac{\Delta\rho g\gamma}{\rho_l^2}\right)^{1/4} \end{aligned} \tag{6.9}$$

Zuber and Hench (1962) have proposed a correction with void fraction as follows :

$$\begin{aligned} C_D &= 0.57\sqrt{\frac{Bo}{1-\varepsilon}} \\ U_b &= 1.53(1-\varepsilon)^{1/2}\left(\frac{\Delta\rho g\gamma}{\rho_l^2}\right)^{1/4} \end{aligned} \tag{6.10}$$

From equations (6.6) and (6.9), we can deduce the limit where the bubbles are no longer

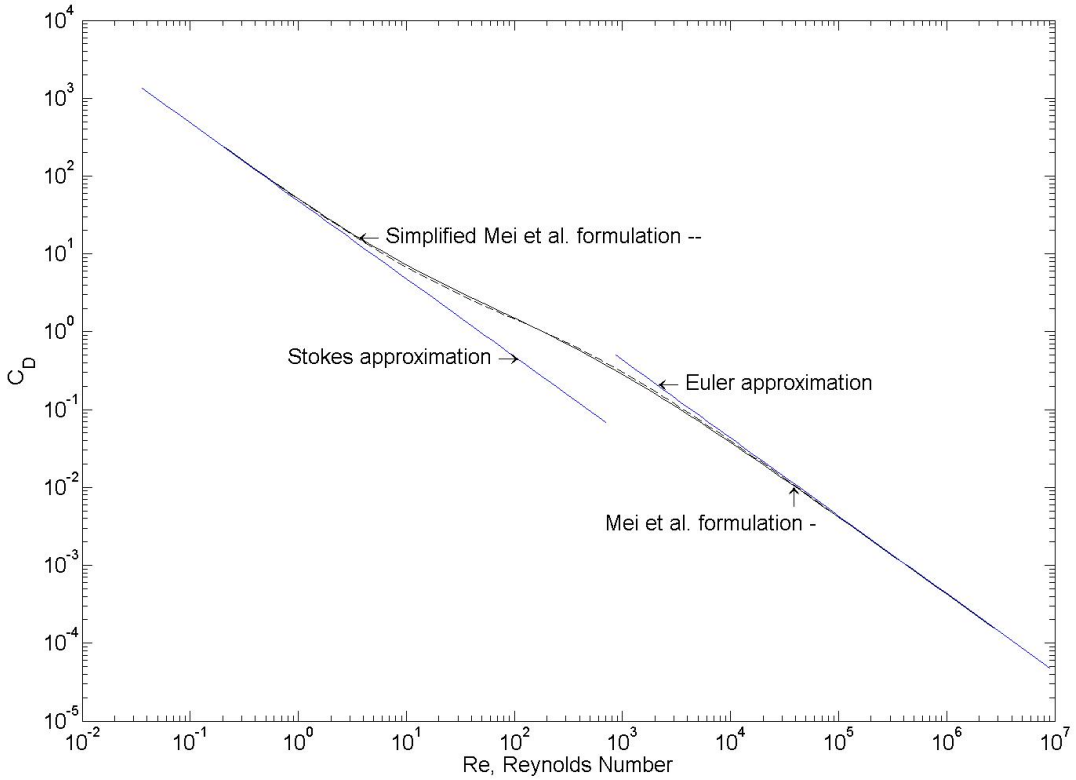

Figure 6.2 Spherical bubble drag coefficient in an infinite stagnant fluid domain vs Reynolds number defined by equation (6.5) and (6.6).

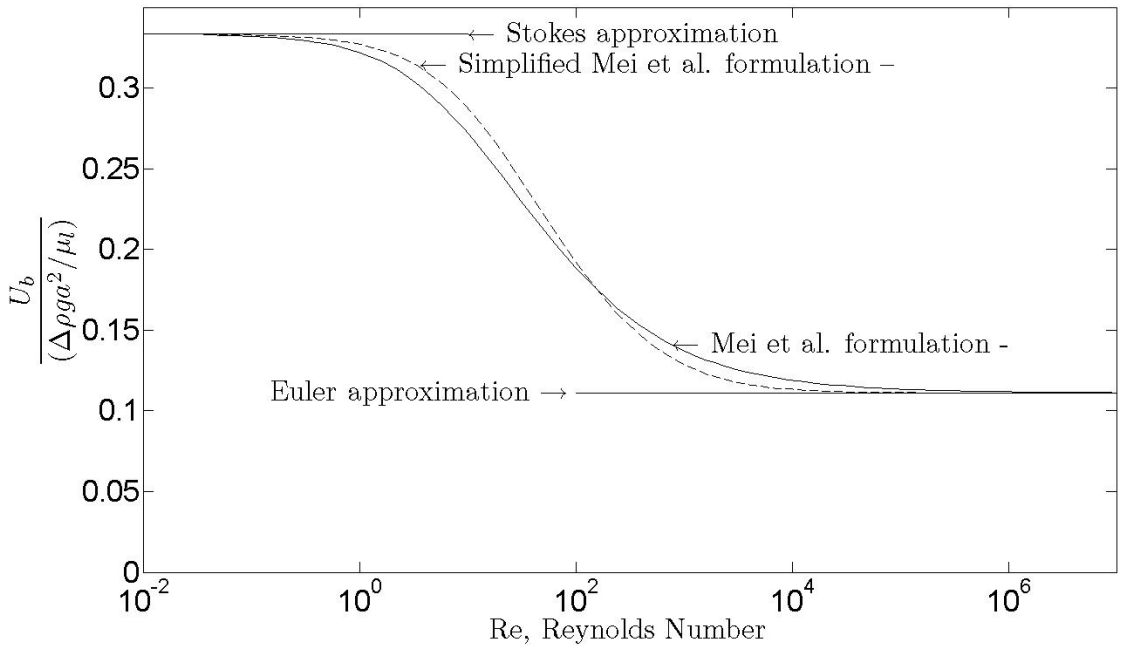

Figure 6.3 Spherical bubble velocity in an infinite stagnant fluid domain vs Reynolds number deduced from equation (6.4) and (6.6).

spherical by equating the two proposed expression for U_b :

$$\begin{aligned} 1.53\left(\frac{\Delta\rho g\gamma}{\rho_l^2}\right)^{1/4} &= \frac{1}{18}\left[1-\frac{100}{A}+\sqrt{1+\frac{1000}{A}+\left(\frac{100}{A}\right)^2}\right]\frac{\Delta\rho g a^2}{\mu_l} \\ \frac{\gamma\mu_l^4}{\rho_l^2\Delta\rho^3 g^3 a^8} &= \left[\frac{1}{27.53}\left(1-\frac{100}{A}+\sqrt{1+\frac{1000}{A}+\left(\frac{100}{A}\right)^2}\right)\right]^4 \\ \frac{Mo}{Bo^4} &= \left[\frac{1}{110.12}\left(1-\frac{100}{A}+\sqrt{1+\frac{1000}{A}+\left(\frac{100}{A}\right)^2}\right)\right]^4 \end{aligned} \tag{6.11}$$

where Mo is the Morton number, which can be expressed using the previous dimensionless numbers :

$$Mo = \frac{\mu_l^4\,\Delta\rho g}{\rho_l^2\gamma^3} = \frac{1}{16}\frac{Bo^3}{A^2} \tag{6.12}$$

The equation above means that the Morton number (Mo) and the Bond number (Bo) characterize the shape of bubbles or droplets moving in a surrounding fluid, as previously underlined by Bhaga and Weber (1981). Equation (6.11) is proposed as a new boundary for the transition from spherical to capped/skirted bubbles. This boundary is shown in Figure 6.4 where it is compared to the boundary proposed by Bhaga and Weber (1981). The proposed boundary between capped/skirted and spherical bubbles corresponds to ellipsoidal bubbles. In particular, this means that we are able to express the dimensionless velocity U_b/U_0 using the other dimensionless numbers :

$$\begin{aligned} &\text{Spherical bubble, if } Bo < \frac{110.12\,Mo^{1/4}}{1-\frac{100}{A}+\sqrt{1+\frac{1000}{A}+\left(\frac{100}{A}\right)^2}} \\ &U_b = \frac{1}{18}\left[1-\frac{100}{A}+\sqrt{1+\frac{1000}{A}+\left(\frac{100}{A}\right)^2}\right]\frac{\Delta\rho g a^2}{\mu_l} \\ &\text{Capped or skirted bubble, if } Bo > \frac{110.12\,Mo^{1/4}}{1-\frac{100}{A}+\sqrt{1+\frac{1000}{A}+\left(\frac{100}{A}\right)^2}} \\ &U_b = 1.53\left[\frac{\Delta\rho g\gamma}{\rho_l^2}\right]^{1/4} = 6.12\left[\frac{Mo^{1/4}}{Bo}\right]\frac{\Delta\rho g a^2}{\mu_l} \end{aligned} \tag{6.13}$$

However, the relations do not take into account the dependence of the drag coefficient (C_D) on the density ratio ($\bar{\rho}$),the viscosity ratio ($\bar{\mu}$) or the void fraction (ε).

For low Reynolds numbers, Taylor and Acrivos (1964) have proposed a relation that takes

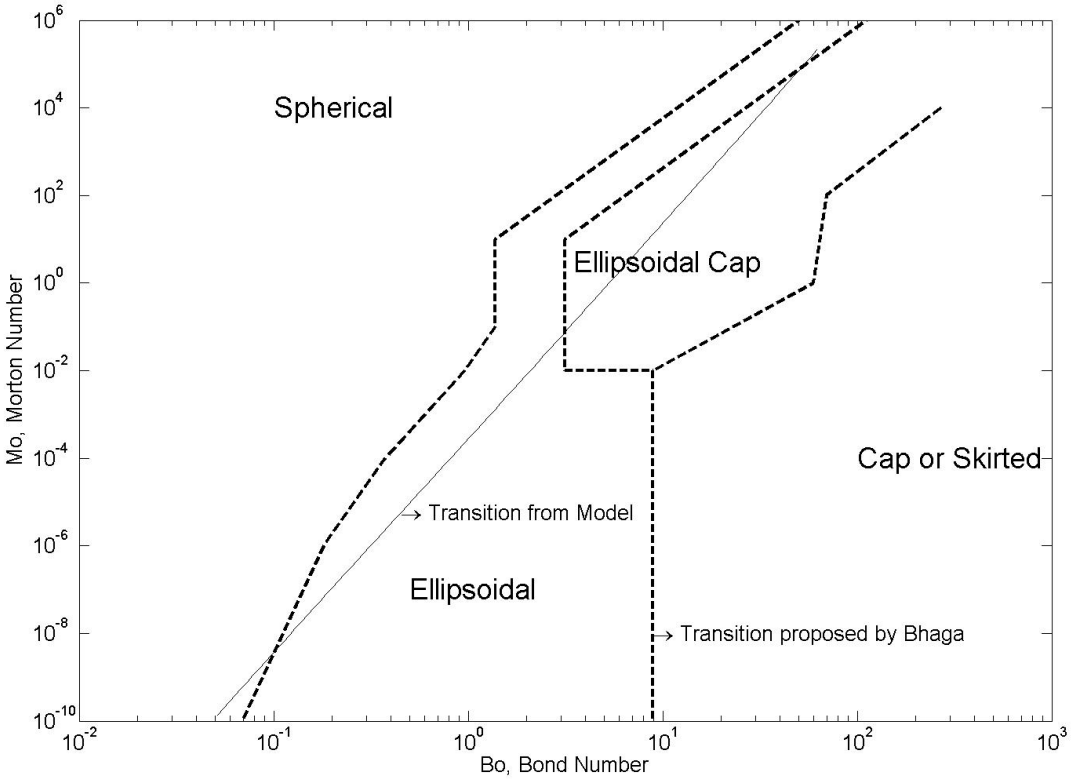

Figure 6.4 Map of bubble shape alone in an infinite liquid domain (ε = 0) as a function of Morton and Bond numbers proposed by Bhaga and Weber (1981) and the proposed newly transition (cf. Eq. 6.11).

into account the viscosity ratio ($\bar{\mu}$) dependence for a bubble in an infinite liquid domain ($\varepsilon = 0$), meaning no surrounding bubbles. The relation is :

$$C_D = \frac{16}{Re}\frac{2+3\bar{\mu}}{2+2\bar{\mu}}\left[1 + \frac{1}{8}\frac{2+3\bar{\mu}}{2+2\bar{\mu}}Re + \frac{1}{40}\left(\frac{2+3\bar{\mu}}{2+2\bar{\mu}}\right)^2 Re^2 \ln Re\right] \tag{6.14}$$

This equation gives the correct drag coefficient for a solid sphere at the limit $\bar{\mu} \to \infty$. Equation (6.14) corrects the fact that Stokes flows do not accurately take into account convective terms which become predominant far away from the bubble. The first correction term corresponds, when $\bar{\mu} \to \infty$, to the equation proposed by (Oseen (1910)).

$$C_D = \frac{24}{Re}\left(1 + \frac{3}{16}Re\right) \tag{6.15}$$

The drag coefficient for a solid sphere is also given by the following correlation of Clift *et al.* (1978) for $Re < 3.7 \times 10^5$:

$$C_D = \frac{24}{Re}\left[1 + 0.15Re^{0.687} + \frac{0.0175}{1 + \frac{42500}{Re^{1.16}}}\right] \tag{6.16}$$

Ishii and Zuber (1979) have proposed a relation for a droplet or small bubble at low Reynolds numbers which includes void fraction dependence

$$C_D = \frac{24}{Re}\left(\frac{1}{1-\varepsilon}\right)^{\frac{2+5\bar{\mu}}{2+2\bar{\mu}}} \tag{6.17}$$

Zuber and Hench (1962) have also proposed a similar relation which, however, does not take into account the viscosity ratio as :

$$C_D = \frac{24}{Re}\left(\frac{1}{1-\varepsilon}\right)^2 \tag{6.18}$$

Zuber and Hench (1962), Ishii and Zuber (1979) and Taylor and Acrivos (1964) are in agreement for $\bar{\mu} >> 1$ and $\varepsilon = 0$. It is known that very small bubbles, probably due to impurity, usually behave as solid particles (equivalent to $\bar{\mu} >> 1$).

6.1.3 Averaged Navier-Stokes equations

As underlined in the introduction, the averaging procedure of the Navier-Stokes equations is a classical way to model two-phase flow, see *e.g.* Ishii and Zuber (1979); Park *et al.* (1998);

Leon-Becerril and Liné (2001). In the averaging process, new terms appear which must be determined by closure relations. We will shown that some of these terms are forces on the bubbles and propose some closure relation. Concretely to model and comprehend the phenomena observed in two-phase flow, a general understanding on interface forces and flow around one bubble is required. In particular the effect of void fraction on interface forces has an utmost importance. When we have a local variation of void fraction we need to know if forces are going to damp or amplify this variation and hence affect the flow pattern. Void fraction variation and flow pattern are known to be the major cause on severe fluid structure interaction in two-phase flow.

One of the averaging procedures of the Navier-Stokes equations uses spatial averaging. It allows to obtain the solution of the two-phase flow without solving for each phase and inclusions, which would require a resolution of the interface location. Averaging the Navier-Stokes equations makes it possible to numerically solve two-phase flow with a reasonable amount of resources.

In the case for where gravity is the only body force, the Navier-Stokes equations for each phase k (k: liquid or gas) are:

$$\begin{aligned} &\frac{\partial \rho_k}{\partial t} + \nabla \cdot (\rho_k \vec{v_k}) = 0 \\ &\frac{\partial \rho_k \vec{v_k}}{\partial t} + \nabla \cdot (\rho_k \vec{v_k} \vec{v_k}) = \rho_k \vec{g} - \nabla P_k + \mu_k \Delta \vec{v_k} \end{aligned} \tag{6.19}$$

with the following boundary conditions (where ^{i} represents the liquid-gas interface):
a) Mass transfer:

$$[\![\rho_k (\vec{v_k} - \vec{v^i}).\vec{n_k^i}]\!] = 0 \tag{6.20}$$

Without mass transfer, the previous condition becomes:

$$\begin{aligned} &\rho_l (\vec{v_l} - \vec{v^i}).\vec{n_l^i} = \rho_g (\vec{v_g} - \vec{v^i}).\vec{n_g^i} = 0 \\ \text{Or} \quad &(\vec{v_l} - \vec{v_g}).\vec{n_l^i} = 0 \end{aligned} \tag{6.21}$$

b) Momentum transfer:

$$[\![P_k \vec{n_k^i} + \bar{\bar{\tau}}_k.\vec{n_k^i} - \rho_k \vec{v_k} (\vec{v_k} - \vec{v^i}).\vec{n_k^i}]\!] = \frac{2\gamma}{a} \vec{n_l^i} \tag{6.22}$$

c) Wall condition:

$$\vec{v_k} = 0 \tag{6.23}$$

In order to integrate the equations independently of phase location, the following phase

indicator function χ_k is introduced.

$$\chi_k(\vec{x},t) = \begin{cases} 1, \text{ if phase } k \text{ is at position } (\vec{x},t) \\ 0, \text{ if not} \end{cases} \tag{6.24}$$

The derivatives of the function χ_k is zero everywhere except at the interface location. The gas-liquid interface is denoted by the superscript ^{i}. The derivative of the indicator function are:

$$\begin{array}{rcl} \dfrac{\partial \chi_k}{\partial t} & = & -\vec{v^i}.\vec{n_k^i}\delta^i \\ \nabla \chi_k & = & \vec{n_k^i}\delta^i \end{array} \tag{6.25}$$

where δ^i is the Dirac delta function which is non zero at the gas-liquid interface.

The averaging procedure for the quantity φ is defined as[1] :

$$\langle\varphi\rangle(\vec{x},t) = \frac{1}{L^3}\int_{x^*=x-L/2}^{x+L/2}\int_{y^*=y-L/2}^{y+L/2}\int_{z^*=z-L/2}^{z+L/2}\varphi(\vec{x}^*,t)dx^*dy^*dz^* \tag{6.26}$$

The function χ_k is introduced prior to averaging. The averaging procedure of the Navier-Stokes equations is thus:

$$\begin{array}{l} \left\langle \chi_k \dfrac{\partial \rho_k}{\partial t} \right\rangle + \left\langle \chi_k \nabla\cdot(\rho_k \vec{v_k}) \right\rangle = 0 \\ \left\langle \chi_k \dfrac{\partial \rho_k \vec{v_k}}{\partial t} \right\rangle + \left\langle \chi_k \nabla\cdot(\rho_k \vec{v_k}\vec{v_k}) \right\rangle = \left\langle \chi_k \rho_k \vec{g} \right\rangle - \left\langle \chi_k \nabla P_k \right\rangle + \left\langle \chi_k \nabla\cdot\bar{\bar{\tau}}_k \right\rangle \end{array} \tag{6.27}$$

Noting that:

$$\begin{array}{rcl} \left\langle \chi_k \dfrac{\partial \rho_k}{\partial t} \right\rangle & = & \dfrac{\partial \langle \chi_k \rho_k \rangle}{\partial t} - \left\langle \rho_k \dfrac{\partial \chi_k}{\partial t} \right\rangle = \dfrac{\partial \langle \chi_k \rho_k \rangle}{\partial t} + \left\langle \rho_k \vec{v^i}.\vec{n_k^i}\delta^i \right\rangle \\ \left\langle \chi_k \dfrac{\partial \rho_k \vec{v_k}}{\partial t} \right\rangle & = & \dfrac{\partial \langle \chi_k \rho_k \vec{v_k} \rangle}{\partial t} - \left\langle \rho_k \vec{v_k} \dfrac{\partial \chi_k}{\partial t} \right\rangle = \dfrac{\partial \langle \chi_k \rho_k \vec{v_k} \rangle}{\partial t} + \left\langle \rho_k \vec{v_k} (\vec{v^i}.\vec{n_k^i})\delta^i \right\rangle \\ \left\langle \chi_k \nabla\cdot(\rho_k \vec{v_k}) \right\rangle & = & \nabla\cdot\left\langle \chi_k \rho_k \vec{v_k} \right\rangle - \left\langle \rho_k \vec{v_k}.\vec{n_k^i}\delta^i \right\rangle \\ \left\langle \chi_k \nabla\cdot(\rho_k \vec{v_k}\vec{v_k}) \right\rangle & = & \nabla\cdot\left\langle \chi_k \rho_k \vec{v_k}\vec{v_k} \right\rangle - \left\langle \rho_k \vec{v_k}\vec{v_k}.\vec{n_k^i}\delta^i \right\rangle \\ \left\langle \chi_k \nabla P_k \right\rangle & = & \nabla\langle \chi_k P_k \rangle - \left\langle P_k.\vec{n_k^i}\delta^i \right\rangle \\ \left\langle \chi_k \nabla\cdot\bar{\bar{\tau}}_k \right\rangle & = & \nabla\cdot\left\langle \chi_k.\bar{\bar{\tau}}_k \right\rangle - \left\langle \bar{\bar{\tau}}_k \vec{n_k^i}\delta^i \right\rangle \end{array} \tag{6.28}$$

1. Note that some authors use the notation $\langle\varphi\rangle^k = \langle\chi_k\varphi\rangle$

The final averaged equations are:

$$\begin{aligned}
\frac{\partial\langle\chi_k\rho_k\rangle}{\partial t} + \nabla\cdot\langle\chi_k\rho_k\vec{v}_k\rangle &= \langle\rho_k(\vec{v}_k - \vec{v^i}).\vec{n_k^i}\delta^i\rangle \\
\frac{\partial\langle\chi_k\rho_k\vec{v}_k\rangle}{\partial t} + \nabla\cdot\langle\chi_k\rho_k\vec{v}_k\vec{v}_k\rangle &= -\nabla\langle\chi_k P_k\rangle + \langle\chi_k\rho_k\rangle\vec{g} \\
&\quad +\nabla\cdot\langle\chi_k\bar{\bar{\tau}}_k\rangle + \langle(\rho_k\tilde{\vec{v}}_k(\tilde{\vec{v}}_k - \vec{v^i})).\vec{n_k^i}\delta^i\rangle \\
&\quad +\langle P_k.\vec{n_k^i}\delta^i\rangle - \langle\bar{\bar{\tau}}_k\vec{n_k^i}\delta^i\rangle
\end{aligned} \tag{6.29}$$

The same averaging procedure is done for the boundary conditions, yielding, for mass transfer:

$$[\![\langle\rho_k(\vec{v}_k - \vec{v^i}).\vec{n_k^i}\delta^i\rangle]\!] = 0 \tag{6.30}$$

and for momentum transfer :

$$[\![-\langle P_k.\vec{n_k^i}\delta_k^i + \bar{\bar{\tau}}_k\vec{n_k^i}\delta^i - \rho_k\vec{v}_k(\vec{v}_k - \vec{v^i}).\vec{n_k^i}\delta_k^i\rangle]\!] = \langle\frac{2\gamma}{a}\vec{n_l^i}\rangle \tag{6.31}$$

To resolve the liquid and gas equations, the following averaged quantities are defined:

$$
\begin{aligned}
& \text{Void fraction} \\
\varepsilon &= \langle \chi_g \rangle \\
1-\varepsilon &= \langle \chi_l \rangle \\
& \text{Average densities} \\
\langle \rho_g \rangle &= \langle \chi_g \rho_g \rangle / \varepsilon \\
\langle \rho_l \rangle &= \langle \chi_l \rho_l \rangle / (1-\varepsilon) \\
& \text{Average velocities} \\
\langle \vec{v}_g \rangle &= \frac{\langle \chi_g \rho_g \vec{v}_g \rangle}{\varepsilon \langle \rho_g \rangle} \\
\langle \vec{v}_l \rangle &= \frac{\langle \chi_l \rho_l \vec{v}_l \rangle}{(1-\varepsilon)\langle \rho_l \rangle} \\
& \text{Average pressures} \\
P_g &= \langle \chi_g P_g \rangle / \varepsilon \\
P_l &= \langle \chi_l P_l \rangle / (1-\varepsilon) \\
& \text{Average viscous tensors} \\
\nabla \cdot (\varepsilon \langle \bar{\bar{\tau}}_g \rangle) &= \nabla \cdot \langle \chi_g \bar{\bar{\tau}}_g \rangle \\
\nabla \cdot ((1-\varepsilon) \langle \bar{\bar{\tau}}_l \rangle) &= \nabla \cdot \langle \chi_l \bar{\bar{\tau}}_l \rangle \\
& \text{Average force at interface location} \\
\vec{M}_g^i &= \langle (\rho_g \vec{v}_g (\vec{v}_g - \vec{v^i})) . \vec{n}_g^i \delta^i \rangle + \langle P_g . \vec{n}_g^i \delta^i \rangle - \langle \bar{\bar{\tau}}_g \vec{n}_g^i \delta^i \rangle \\
\vec{M}_l^i &= \langle (\rho_l \vec{v}_l (\vec{v}_l - \vec{v^i})) . \vec{n}_l^i \delta^i \rangle + \langle P_l . \vec{n}_l^i \delta^i \rangle - \langle \bar{\bar{\tau}}_l \vec{n}_l^i \delta^i \rangle \\
& \text{Turbulence tensor} \\
\nabla \cdot \left(\varepsilon \bar{\bar{\tau}}_g^{Re} \right) &= -\nabla \cdot \langle \chi_g \rho_g \vec{v}_g \vec{v}_g \rangle + \nabla \cdot \varepsilon \langle \rho_g \rangle \langle \vec{v}_g \rangle \langle \vec{v}_g \rangle \\
\nabla \cdot \left((1-\varepsilon) \bar{\bar{\tau}}_l^{Re} \right) &= -\nabla \cdot \langle \chi_l \rho_l \vec{v}_l \vec{v}_l \rangle + \nabla \cdot (1-\varepsilon) \langle \rho_l \rangle \langle \vec{v}_l \rangle \langle \vec{v}_l \rangle \\
& \text{Mass transfer} \\
\Gamma_g &= \langle \rho_g (\vec{v}_g - \vec{v^i}) . \vec{n}_g^i \delta^i \rangle \\
\Gamma_l &= \langle \rho_l (\vec{v}_l - \vec{v^i}) . \vec{n}_l^i \delta^i \rangle \\
& \text{Surface tension effect} \\
\vec{\kappa} &= \langle \frac{2\gamma}{a} \vec{n}_l^i \rangle
\end{aligned}
\tag{6.32}
$$

With these defined quantities, the averaged gas equations are:

$$\begin{aligned}
\frac{\partial}{\partial t}\left(\varepsilon\langle\rho_g\rangle\right) + \nabla\cdot\left(\varepsilon\langle\rho_g\rangle\langle\vec{v}_g\rangle\right) = &\quad \Gamma_g \\
\frac{\partial}{\partial t}\left(\varepsilon\langle\rho_g\rangle\langle\vec{v}_g\rangle\right) + \nabla\cdot\left(\varepsilon\langle\rho_g\rangle\langle\vec{v}_g\rangle\otimes\langle\vec{v}_g\rangle\right) = &\quad -\nabla(\varepsilon P_g) + \varepsilon\langle\rho_g\rangle\vec{g} \\
&\quad +\nabla\cdot\left(\varepsilon\langle\bar{\bar{\tau}}_g\rangle\right) + \vec{M}_g^i + \nabla\cdot\left(\varepsilon\tau_g^{\bar{\bar{Re}}}\right)
\end{aligned} \tag{6.33}$$

while for the liquid phase, the equations are:

$$\begin{aligned}
\frac{\partial}{\partial t}\left((1-\varepsilon)\langle\rho_l\rangle\right) + \nabla\cdot\left((1-\varepsilon)\langle\rho_l\rangle\langle\vec{v}_l\rangle\right) = &\quad \Gamma_l \\
\frac{\partial}{\partial t}\left((1-\varepsilon)\langle\rho_l\rangle\langle\vec{v}_l\rangle\right) + \nabla\cdot\left((1-\varepsilon)\langle\rho_l\rangle\langle\vec{v}_l\rangle\otimes\langle\vec{v}_l\rangle\right) = &\quad -\nabla((1-\varepsilon)P_l) + (1-\varepsilon)\langle\rho_l\rangle\vec{g} \\
&\quad +\nabla\cdot\left((1-\varepsilon)\langle\bar{\bar{\tau}}_l\rangle\right) + \vec{M}_l^i \\
&\quad +\nabla\cdot\left((1-\varepsilon)\tau_l^{\bar{\bar{Re}}}\right)
\end{aligned} \tag{6.34}$$

Finally, the equations for the boundary conditions at the interface location are:

$$\begin{aligned}
[\![\Gamma_k]\!] = &\quad 0 \\
[\![\vec{M}_k^i]\!] = &\quad \vec{\kappa}
\end{aligned} \tag{6.35}$$

These equations need closure relations and in particular the average force on the interface, $\vec{M}_k^i$.

The explicit determination of the interface forces can be avoided by considering the mixture equations instead of the separate phase equations. Summing the gas and liquid phase equations (6.33,6.34) and applying the boundary conditions at the interface, (see Eq.(6.35) the following averaged mixture equations are obtained. This equations make possible to avoid modelling the interface condition.

$$\begin{aligned}
&\frac{\partial}{\partial t}\left[\varepsilon\langle\rho_g\rangle + (1-\varepsilon)\langle\rho_l\rangle\right] + \nabla\cdot\left(\varepsilon\langle\rho_g\rangle\langle\vec{v}_g\rangle + (1-\varepsilon)\langle\rho_l\rangle\langle\vec{v}_l\rangle\right) = 0 \\
&\frac{\partial}{\partial t}\left[\varepsilon\langle\rho_g\rangle\langle\vec{v}_g\rangle + (1-\varepsilon)\langle\rho_l\rangle\langle\vec{v}_l\rangle\right] + \nabla\cdot\varepsilon\langle\rho_g\rangle\langle\vec{v}_g\rangle\langle\vec{v}_g\rangle + (1-\varepsilon)\langle\rho_l\rangle\langle\vec{v}_l\rangle\langle\vec{v}_l\rangle = \ldots \\
&-\nabla(\varepsilon P_g + (1-\varepsilon)P_l) + (\varepsilon\langle\rho_g\rangle + (1-\varepsilon)\langle\rho_l\rangle)\vec{g}\ldots \\
&+\nabla\cdot\left(\varepsilon\langle\bar{\bar{\tau}}_g\rangle + (1-\varepsilon)\langle\bar{\bar{\tau}}_l\rangle\right) + \nabla\cdot\left[\varepsilon\tau_g^{\bar{\bar{Re}}} + (1-\varepsilon)\tau_l^{\bar{\bar{Re}}}\right] + \vec{\kappa}
\end{aligned} \tag{6.36}$$

Defining the average mixture density, velocity, pressure, viscous tensor and Reynolds tensor, respectively as:

$$\begin{aligned}
\rho_{2\phi} &= \langle \chi_g \rho_g + \chi_l \rho_l \rangle = \varepsilon \langle \rho_g \rangle + (1-\varepsilon)\langle \rho_l \rangle \\
\vec{v}_{2\phi} &= \langle \chi_g \rho_g \vec{v}_g + \chi_l \rho_l \vec{v}_l \rangle / \rho_{2\phi} = (\varepsilon \langle \rho_g \rangle \langle \vec{v}_g \rangle + (1-\varepsilon)\langle \rho_l \rangle \langle \vec{v}_l \rangle)/\rho_{2\phi} \\
P_{2\phi} &= \langle \chi_g P_g + \chi_l P_l \rangle = \varepsilon P_g + (1-\varepsilon) P_l \\
\nabla \cdot (\bar{\bar{\tau}}_{2\phi}) &= \nabla \cdot (\varepsilon \langle \bar{\bar{\tau}}_g \rangle + (1-\varepsilon)\langle \bar{\bar{\tau}}_l \rangle) \\
\nabla \cdot \bar{\bar{\tau}}^{Re}_{2\phi} &= -\nabla \cdot \langle \chi_g \rho_g \vec{v}_g \vec{v}_g + \chi_l \rho_l \vec{v}_l \vec{v}_l \rangle + \nabla \cdot \rho_{2\phi} \vec{v}_{2\phi} \vec{v}_{2\phi}
\end{aligned} \tag{6.37}$$

leads to the following form of the mixture equations:

$$\begin{aligned}
&\frac{\partial \rho_{2\phi}}{\partial t} + \nabla \cdot \rho_{2\phi} \vec{v}_{2\phi} = 0 \\
&\frac{\partial \rho_{2\phi} \vec{v}_{2\phi}}{\partial t} + \nabla \cdot \rho_{2\phi} \vec{v}_{2\phi} \vec{v}_{2\phi} = -\nabla P_{2\phi} + \rho_{2\phi} \vec{g} + \nabla \cdot \bar{\bar{\tau}}_{2\phi} + \vec{\kappa} + \nabla \cdot \bar{\bar{\tau}}^{Re}_{2\phi}
\end{aligned} \tag{6.38}$$

While these equations need fewer closure relations, since the interface boundary conditions do not need to be modelled, we however loose information such as void fraction variation which cannot be captured by this equation. We still need some albeit fewer closure relations to be able to solve the mixture equations. In particular a closure relation for the viscous tensor involving the relative velocity between phases is proposed as:

$$\begin{aligned}
\nabla \cdot \bar{\bar{\tau}}_{2\phi} &= \nabla \cdot \langle \chi_g \bar{\bar{\tau}}_g + \chi_l \bar{\bar{\tau}}_l \rangle \\
&= \nabla \cdot \langle \chi_g \mu_g \nabla \vec{v}_g + \chi_l \mu_l \nabla \vec{v}_l \rangle \\
&= \Delta \langle \chi_g \mu_g \vec{v}_g + \chi_l \mu_l \vec{v}_g \rangle + \nabla \cdot \left\langle \mu_g \vec{v}^{\,i}_g \otimes \vec{n}^{\,i}_g + \mu_l \vec{v}^{\,i}_l \otimes \vec{n}^{\,i}_l \right\rangle
\end{aligned} \tag{6.39}$$

The first term on the right hand side of the previous equation can be rewritten as:

$$\langle \chi_g \mu_g \vec{v}_g + \chi_l \mu_l \vec{v}_g \rangle = \underbrace{(\varepsilon \mu_g + (1-\varepsilon)\mu_l)}_{\mu_{2\phi}} \vec{v}_{2\phi} + \underbrace{\frac{\varepsilon(1-\varepsilon)(\mu_g \rho_l - \mu_l \rho_g)}{\rho_{2\phi}}}_{\mu_r} \underbrace{(\langle \vec{v}_g \rangle - \langle \vec{v}_l \rangle)}_{\vec{U}_b} \tag{6.40}$$

In previous equation (6.40), the following important quantities appear $\mu_{2\phi}$, the averaged two-phase viscosity weighted by void fraction, μ_r a kind of harmonic averaged viscosity weighted by mass of each phase and $\vec{U}_b$ the relative motion of each phase. Since at the interface we have $\vec{n}^{\,i}_l = -\vec{n}^{\,i}_g$ and $\vec{v}^{\,i}_g = \vec{v}^{\,i}_l$, the second term on the right hand side of equation (6.39) corresponding to viscous loss due to bubble deformation can be rewritten as :

$$\nabla \cdot \left\langle \mu_g \vec{v}^{\,i}_g \otimes \vec{n}^{\,i}_g + \mu_l \vec{v}^{\,i}_l \otimes \vec{n}^{\,i}_l \right\rangle = \nabla \cdot \left\langle (\mu_l - \mu_g) \vec{v}^{\,i}_l \otimes \vec{n}^{\,i}_l \right\rangle \tag{6.41}$$

Note that this closure relation does not assume anything because it involves only a mathematical reformulation. Finally, we have:

$$\nabla \cdot \bar{\bar{\tau}}_{2\phi} = \Delta(\mu_{2\phi}\vec{v}_{2\phi}) + \underbrace{\Delta(\mu_r \vec{U}_b)}_{\substack{\text{viscous loss} \\ \text{due to slip ratio}}} + \underbrace{\nabla \cdot \left\langle (\mu_l - \mu_g)\vec{v}_l^i \otimes \vec{n}_l^i \right\rangle}_{\substack{\text{viscous loss} \\ \text{due to bubble deformation}}} \tag{6.42}$$

In order to model two-phase viscous effects in the mixture equations, we need to be able to formulate $\vec{U}_b$. This relative velocity can be deduced using the average forces at the gas-liquid interface. Only considering $\mu_{2\phi}$ in mixture equation correspond to assuming small viscous loss due to slip ratio and bubble deformation.

Moreover it is noted that the averaged velocity weighted by the mass of each phase $\vec{v}_{2\phi}$ is more useful and more representative of physical phenomenon than the homogeneous velocity usually used, which is the averaged velocity weighted by volume of each phase (cf. Eq. 6.2).

In the case, we wants to resolve equations of both phases, interface forces are needed. To obtain the interface forces, we consider a control volume containing N bubbles. Interface forces M_g^i can be evaluated by summing the individual forces on the n^{th} bubble : $\vec{f_{g_n}^i}$

$$\vec{M}_g^i = \frac{1}{V_0}\sum_{n=1}^{N} \vec{f_{g_n}^i} = \frac{N}{V_0}\langle \vec{f}_g^i \rangle \tag{6.43}$$

The number of bubbles is determined from the volume occupied by the gas which is N times the average volume occupied by one bubble :

$$V_G = \varepsilon V_0 = N\frac{4}{3}\pi\langle a^3 \rangle \tag{6.44}$$

This gives :

$$\vec{M}_g^i = \frac{3\varepsilon}{4\pi\langle a^3 \rangle}\langle \vec{f}_g^i \rangle \tag{6.45}$$

where the average for $\langle \vec{f}_g^i \rangle$ and its various component can be modelled as :

$$\begin{aligned} \langle \vec{f}_g^i \rangle = & \left\langle C_M \tfrac{4}{3}\pi\rho_l a^3 \tfrac{D\vec{U}_b}{Dt} \right\rangle && \text{Added mass} \\ & + \left\langle \pi \tfrac{1}{2}\rho_l a^2 C_D |\vec{U}_b| \vec{U}_b \right\rangle && \text{Drag force} \\ & + \left\langle \tfrac{1}{2}\pi\rho_l a^2 C_L \vec{U}_b \times \nabla \times \vec{U}_b \right\rangle && \text{Lift Force} \\ & + \left\langle \tfrac{4}{3}\pi\Delta\rho a^3 \vec{g} \right\rangle && \text{Buoyancy} \\ & + \left\langle \vec{f_{turb}^i} \right\rangle && \text{interface force due to turbulence} \end{aligned} \tag{6.46}$$

The explicit form for the interface forces becomes

$$\vec{M}_g^i = \varepsilon \left(\rho_l \frac{\left\langle C_M a^3 \frac{D\vec{U}_b}{Dt} \right\rangle}{\langle a^3 \rangle} + \frac{3}{8}\rho_l \frac{\left\langle a^2 C_D |\vec{U}_b| \vec{U}_b \right\rangle}{\langle a^3 \rangle} + \frac{3}{8}\rho_l \frac{\left\langle a^2 C_L \vec{U}_b \times \nabla \times \vec{U}_l \right\rangle}{\langle a^3 \rangle} \right) + \varepsilon \Delta\rho \vec{g} + \varepsilon \frac{\left\langle \vec{f^i_{turb}} \right\rangle}{\langle a^3 \rangle} \tag{6.47}$$

A complete set of the closure relations needs also a model for C_M, C_L. Several values of added mass have presented by previous authors and summarize in table 6.1 where Z is the sphericity correction factor given by Milne-Thomson (1968)

$$Z = -2\frac{\chi^2 cos^{-1}(\chi^{-1}) - \chi^2(\chi^2-1)^{1/2}}{\chi^2 cos^{-1}(\chi^{-1}) - (\chi^2-1)^{1/2}} \tag{6.48}$$

And χ the sphericity coefficient defined for an ellipsoid as $\chi = a/b$ where a and b are the two diameter or the generatrix ellipse. *Note : for a sphere (a = b)* $\chi = 1$.. For the lift coefficient we can mention the work of Auton (1987) proposing a lift coefficient of $C_L = 0.5$. Little work consider void fraction effect on lift coefficient. We can mention the work of Beyerlein *et al.* (1985) leading to:

$$C_L = \frac{1.65 \times 10^{-3}}{\varepsilon^{0.78}} \tag{6.49}$$

The previous equation does not agrees with Auton (1987)'s work for void fraction tends to zero. This show the complexity to have good model of interface forces depending on void fraction.

A closure relation for turbulence and a distribution law for bubble size will be presented in the part II of this article. The present work will focus on modelling the drag coefficient (C_D) of spherical inclusions only.

6.2 Spherical Flow Field Solution

This section attends to presents an analytical results for drag coefficient taken into account the void fraction.The analytical results for a simple model representing one bubble in a bubbly flow are exposed. In order to model the effect of void fraction, in the bubble reference frame, we consider the stationary solution for a gas bubble of radius (a) centered in a liquid sphere of radius (l) (see Figure 6.5). The void fraction which is the ratio of gas to total volume can easily be calculated in this case as $\varepsilon = a^3/l^3$. We consider an incompressible fluid flow

Author	Assumption	C_M
Voinov (1973) Nigmatulin (1979)	Spherical bubble in an infinite liquid domain with a potential flow	$\frac{1}{2}$
Zuber (1964)	Non isolated spherical bubbles with a potential flow	$\frac{1}{2}\frac{1+2\varepsilon}{1-\varepsilon} \simeq \frac{1}{2} + 1.5\varepsilon$
Van Wijngaarden (1976)	Non isolated spherical bubbles with a potential flow	$\frac{1}{2} + 1.39\varepsilon$
Van Wijngaarden (1991)	Non isolated Ellipsoidal bubbles with a potential flow	$\frac{1}{2}\left[1 + \left(1 + \frac{2}{Z}\right)\varepsilon\right]$
Mokeyev (1977)	Empirical correlation	$\frac{1}{2} + 2.1\varepsilon$

Table 6.1 Models for added mass coefficient C_M

governed by:

$$\begin{aligned} \nabla \cdot \vec{u_g} &= 0 && (a) \\ \rho_g \vec{u_g} \nabla \vec{u_g} &= -\nabla P_g + \mu_g \Delta \vec{u_g} && (b) \end{aligned} \tag{6.50}$$

and

$$\begin{aligned} \nabla \cdot \vec{u_l} &= 0 && (a) \\ \rho_l \vec{u_l} \nabla \vec{u_l} &= -\nabla P_l + \mu_l \Delta \vec{u_l} && (b) \end{aligned} \tag{6.51}$$

The actual pressures would include a hydrostatic pressure component and would thus be $P_l + \rho_l g z$ and $P_g + \rho_g g z$. However, the effect of the hydrostatic pressure results in the well known buoyancy force $\frac{4}{3}\Delta\rho g \pi a^3$. Thus the hydrostatic pressure component effects are already taken into account and do not have to be include explicitly. We consider the following boundary conditions :

$r = l = \dfrac{a}{\varepsilon^{1/3}}$:

$$u_{rl} = -U_b(1-\varepsilon)\cos(\theta) \tag{1}$$

$$u_{\theta l} = U_b(1-\varepsilon)\sin(\theta) \tag{2}$$

$r = 0$: The condition of existence of a physical solution impose that u_{rg} and $u_{\theta g}$ have a finite value (3)

$r = a$:

$$u_{\theta l} = u_{\theta g} \tag{4}$$

$$\mu_l \left(r \frac{\partial}{\partial r}\left(\frac{u_{\theta l}}{r}\right) + \frac{1}{r}\frac{\partial u_{rl}}{\partial \theta} \right) = \mu_g \left(r \frac{\partial}{\partial r}\left(\frac{u_{\theta g}}{r}\right) + \frac{1}{r}\frac{\partial u_{rg}}{\partial \theta} \right) \tag{5}$$

$$P_l + \rho_l g a \cos\theta - 2\mu_l \frac{\partial u_{rl}}{\partial r} = P_g + \rho_g g a \cos\theta - 2\mu_g \frac{\partial u_{rg}}{\partial r} - \frac{2\gamma}{a} \tag{6}$$

(6.52)

Conditions (1) and (2) are chosen in order to have $\langle u_l \rangle = U_b$. This is important for the closure relation for space averaged Navier-stokes equation. Indeed, the proposed correct closure relations model is expressed using unknown factors of the averaged Navier-stokes equations. Some of the unknown factors are the average liquid and gas velocities. Since the problem is solved in the bubble frame we have $\langle u_g \rangle = 0$. In this case, U_b is not necessarily the actual relative velocity of the bubbles but rather is the velocity easily obtained from the unknown factors of averaged Navier-Stokes equation.

□ **Proof :**

Considering the problem symmetry and incompressibility, the liquid flow is described by the 2D stream vector: $\vec{\psi} = \psi \vec{e_\varphi}$. Choosing the form $\psi = F(r,\theta)/(r\sin\theta)$ for the stream function,

the resulting radial and tangential liquid velocity component are :

$$\begin{aligned} \vec{u_l} &= \nabla \wedge \vec{\psi} \\ u_{rl} &= \frac{1}{r\sin\theta}\frac{\partial}{\partial\theta}\left(\sin\theta\psi\right) = \frac{1}{r^2\sin\theta}\frac{\partial F}{\partial\theta} \\ u_{\theta l} &= -\frac{1}{r}\frac{\partial}{\partial r}\left(r\psi\right) = -\frac{1}{r\sin\theta}\frac{\partial F}{\partial r} \end{aligned} \tag{6.53}$$

Consequently, using outside boundary conditions,

$$\begin{aligned} u_{rl}\mid_{r=l} &= -U_b(1-\varepsilon)\cos(\theta) = \frac{1}{l^2\sin\theta}\left.\frac{\partial F}{\partial\theta}\right|_{r=l} \\ F\mid_{r=l} &= \frac{U_b l^2(1-\varepsilon)}{2}\sin^2\theta + F_0 \end{aligned} \tag{6.54}$$

Using boundary conditions at bubble/liquid interface location,

$$\begin{aligned} u_{rl}\mid_{r=a} &= 0 = \frac{1}{a^2\sin\theta}\left.\frac{\partial F}{\partial\theta}\right|_{r=a} \\ F\mid_{r=a} &= F_1 \end{aligned} \tag{6.55}$$

Finally using symmetry along axes,

$$\begin{aligned} u_{\theta l}\mid_{\theta=0} &= 0 \\ F\mid_{\theta=0} &= F_1 = F_0 = 0 \end{aligned} \tag{6.56}$$

We deduce values of stream function on outside boundary and at bubble/liquid interface location,

$$\begin{aligned} F\mid_{r=l} &= \frac{U_b l^2(1-\varepsilon)}{2}\sin^2\theta \\ F\mid_{r=a} &= 0 \end{aligned} \tag{6.57}$$

We therefore calculated averaged velocity as:

$$\begin{aligned} \langle\vec{u_l}\rangle &= \frac{\langle\chi_l\rho_l\vec{u_l}\rangle}{(1-\varepsilon)\langle\rho_l\rangle} \\ &= \frac{3}{4\pi l^3(1-\varepsilon)}\int_{r=a}^{l}\int_{\theta=0}^{\pi}\int_{\varphi=0}^{2\pi}\vec{u_l}dV \\ &= \frac{3}{4\pi l^3(1-\varepsilon)}\int_{r=a}^{l}\int_{\theta=0}^{\pi}\int_{\varphi=0}^{2\pi}\nabla\wedge\vec{\psi}dV \\ &= \frac{3}{4\pi l^3(1-\varepsilon)}\left[\int_{\theta=0}^{\pi}\int_{\varphi=0}^{2\pi}\vec{dS}\wedge\vec{\psi}\mid_{r=l} + \int_{\theta=0}^{\pi}\int_{\varphi=0}^{2\pi}\vec{dS}\wedge\vec{\psi}\mid_{r=a}\right] \\ &= \frac{3}{4}U_b\int_{\theta=0}^{\pi}\sin^3\theta d\theta\vec{e_z} \\ &= U_b\vec{e_z} \end{aligned} \tag{6.58}$$

□

The case $l \to \infty$ ($\varepsilon \to 0$) corresponds to the case of a single bubble in an infinite liquid volume. The influence of neighboring bubbles is set through the distance l, which represents the average half distance between the bubbles and its neighbors. Condition (6) in equation (6.52) is never valid because the assumption of a spherical bubble was made. This condition is replaced by $u_{rl} = u_{rg} = 0$. However, the condition (6) is used to verify the validity of the spherical shape assumption. Surface tension contributes to maintain spherical shape against other forces. Condition (6) is used to evaluate if surface tension forces are strong enough to overcome forces that could deform the bubble. We are able to solve this problem analytically only for Stokes or Euler flow. In the case of Euler flow, the analytical solution of the equations cannot satisfy all boundary conditions. Conditions (1) and (2) are therefore replaced by $\langle u_l \rangle = U_b$. As explained before, this is important for closure relation in the space averaged Navier-stokes equations as the considered velocities are averaged velocities.

Because, a Navier-Stokes solution for flow inside the bubble is found, we have to solve only two cases, external Stokes flow ($Re << 1$) and external Euler Flow ($Re >> 1$).

6.2.1 Internal solution

For the internal flow, we will demonstrate the existence of a Navier-Stokes solution, but in order to understand the role of the convective and Stokes component, we start by solving Stokes equations. We have:

$$\begin{aligned} \nabla \cdot \vec{u_g} &= 0 && (a) \\ 0 &= -\nabla P_g + \mu_g \Delta \vec{u_g} && (b) \end{aligned} \tag{6.59}$$

Considering incompressibility, symmetry and using spherical coordinates (r,θ,ϕ), assuming that velocity is the product of functions of r and θ, we can derive the velocity from

$$\begin{aligned} u_{rg} &= \frac{2}{r^2} G(r) \cos(\theta) \\ u_{\theta g} &= -\frac{1}{r} G'(r) \sin(\theta) \end{aligned} \tag{6.60}$$

Equation (6.60) ensures that the mass conservation equation (6.59-a) is satisfied. In order to eliminate pressure, the stationary Stokes vorticity equation is used -*rotation of equation*

(6.59)-(b)-:

$$\begin{aligned} 0 &= \nabla \wedge (\Delta \vec{u}) = \Delta(\nabla \wedge \vec{u}) \\ 0 &= \Delta\left[\sin(\theta)\left(\frac{2G(r)}{r^3} - \frac{G''(r)}{r}\right)\vec{e_\varphi}\right] \\ 0 &= \frac{\sin(\theta)}{r^3}\left(-r^4 G''''(r) + 4r^2 G''(r) - 8rG'(r) + 8G(r)\right) \end{aligned} \tag{6.61}$$

Searching for a solution : $G(r) = Br^n$, we finally obtains,

$$\begin{aligned} u_{rg} &= 2\left(B_0 r^2 + B_1 + \tfrac{B_2}{r} + \tfrac{B_3}{r^3}\right)\cos(\theta) \\ u_{\theta g} &= -\left(4B_0 r^2 + 2B_1 + \tfrac{B_2}{r} - \tfrac{B_3}{r^3}\right)\sin(\theta) \end{aligned} \tag{6.62}$$

Applying the boundary conditions $u_{rg}\big|_{r=a} = 0$ and with the condition for finite velocity for $r \to 0$, we have:

$$\begin{aligned} u_{rg} &= 2B_0(r^2 - a^2)\cos\theta \\ u_{\theta g} &= -2B_0(2r^2 - a^2)\sin\theta \end{aligned} \tag{6.63}$$

From the θ component of the momentum equation we deduce :

$$P_g = 20B_0\mu_g r\cos\theta + B_4 \tag{6.64}$$

We can also use the Stokes flow field for the bubble but deduce pressure from the Navier-Stokes equation. In this case we seek a solution of the form :$P_g = 20B_0\mu_g r\cos\theta + P^*$ and proved that Stokes flow field is in fact a Navier-Stokes solution.

Using the velocity field 6.63 and the θ component of the momentum equations allows to deduce the additional pressure term,

$$P^* = \rho_g B_0^2\left[(4r^4 - 6a^2r^2)\sin^2\theta + F(r)\right] \tag{6.65}$$

The r component of the momentum equations leads to:

$$\begin{aligned} \frac{\partial P^*}{\partial r} &= -\rho_g\left(u_{rg}\frac{\partial u_{rg}}{\partial r} + \frac{u_{\theta g}}{r}\frac{\partial u_{rg}}{\partial \theta} - \frac{u_{\theta g}^2}{r}\right) \\ &= \rho_g B_0^2\left[-(8r^3 - 8a^2 r) + (16r^3 - 12a^2 r)\sin^2\theta\right] \end{aligned} \tag{6.66}$$

From the two previous equations, we deduce the following solution for the Navier-Stokes

equations (also known as the Hill vortex solution):

$$\begin{aligned} u_{rg} &= 2B_0(r^2-a^2)\cos(\theta) \\ u_{\theta g} &= -2B_0(2r^2-a^2)\sin(\theta) \\ P_g &= \underbrace{20B_0\mu_g r\cos\theta}_{\text{Stokes component}} + \underbrace{\rho_g B_0^2\left[(4r^4-6a^2r^2)\sin^2\theta - 2r^4 + 4a^2r^2 + B_1\right]}_{\text{Euler or convective component}} \end{aligned} \tag{6.67}$$

We conclude that the difference between Stokes and Navier-Stokes solution lies in the pressure component due to the convective terms.

6.2.2 External Flow

External Stokes Flow ($Re << 1$)

In the case of external Stokes flow, we have :

$$\begin{aligned} \nabla\cdot\vec{u}_l &= 0 \qquad (a) \\ 0 &= -\nabla P_l + \mu_l\Delta\vec{u}_l \quad (b) \end{aligned} \tag{6.68}$$

Considering incompressibility and symmetry and using spherical coordinates (r,θ,ϕ), we can derive the velocity as

$$\begin{aligned} u_{rl} &= \frac{2}{r^2}G(r)\cos(\theta) \\ u_{\theta l} &= -\frac{1}{r}G'(r)\sin(\theta) \end{aligned} \tag{6.69}$$

and similarly to the internal solution (cf. Eq. (6.62)), we deduce from the vorticity equation :

$$\begin{aligned} u_{rl} &= 2\left(C_0r^2 + C_1 + \tfrac{C_2}{r} + \tfrac{C_3}{r^3}\right)\cos\theta \\ u_{\theta l} &= -\left(4C_0r^2 + 2C_1 + \tfrac{C_2}{r} - \tfrac{C_3}{r^3}\right)\sin\theta \end{aligned} \tag{6.70}$$

From the θ component of the momentum equation we deduce,

$$P_l = \mu_l\left[20C_0r + \tfrac{2C_2}{r^2}\right]\cos\theta + C_4 \tag{6.71}$$

Applying the boundary condition at the interface location ($u_{rl}\,|_{r=a} = 0$), we get

$$\begin{aligned} u_{rl} &= 2\left(C_0\left(r^2-a^2\right) + C_2\left(\tfrac{1}{r}-\tfrac{1}{a}\right) + C_3\left(\tfrac{1}{r^3}-\tfrac{1}{a^3}\right)\right)\cos(\theta) \\ u_{\theta l} &= -\left(2C_0\left(2r^2-a^2\right) + C_2\left(\tfrac{1}{r}-\tfrac{2}{a}\right) - C_3\left(\tfrac{1}{r^3}+\tfrac{2}{a^3}\right)\right)\sin(\theta) \\ P_l &= \mu_l\left(20C_0r + \tfrac{2C_2}{r^2}\right)\cos(\theta) + C_4 \end{aligned} \tag{6.72}$$

Satisfying the remaining boundary conditions (cf. eq. (6.52)) leads to

$$\begin{aligned}
a^2 B_0 &= -\frac{U_b}{2}\frac{1-\varepsilon}{F(\varepsilon)}(2-5\varepsilon+3\varepsilon^{5/3}) \\
a^2 C_0 &= \frac{U_b}{2}\frac{1-\varepsilon}{F(\varepsilon)}(2\varepsilon+3\bar{\mu}(\varepsilon-\varepsilon^{5/3})) \\
\frac{C_2}{a} &= U_b\frac{1-\varepsilon}{F(\varepsilon)}(2+3\varepsilon^{5/3}+3\bar{\mu}(1-\varepsilon^{5/3})) \\
\frac{C_3}{a^3} &= -U_b\frac{1-\varepsilon}{F(\varepsilon)}(\varepsilon+\bar{\mu}(1-\varepsilon)) \\
\text{With} & \\
F(\varepsilon) &= (1-\varepsilon^{1/3})^3\left((4+6\varepsilon^{1/3}+6\varepsilon^{2/3}+4\varepsilon)+\bar{\mu}(4+3\varepsilon^{1/3}-3\varepsilon^{2/3}-4\varepsilon)\right)
\end{aligned} \tag{6.73}$$

Using equation (6.72), the force on the bubble may be evaluated from surface stress integration:

$$\begin{aligned}
\vec{f} &= \int_{\varphi=0}^{2\pi}\int_{\theta=0}^{\pi}(-P_l\bar{\bar{1}}+\bar{\bar{\tau}}_l).\vec{n}a^2\sin(\theta)d\theta d\varphi \\
&= -8\pi\mu_l C_2\vec{e}_z
\end{aligned} \tag{6.74}$$

Introducing C_2 from equation (6.73), the following expression is obtained for the force on the bubble:

$$f = 4\pi\mu_l U_b a\left[\frac{1-\varepsilon}{(1-\varepsilon^{1/3})^3}\right]\left[\frac{4+6\varepsilon^{5/3}+6\bar{\mu}(1-\varepsilon^{5/3})}{(4+6\varepsilon^{1/3}+6\varepsilon^{2/3}+4\varepsilon)+\bar{\mu}(4+3\varepsilon^{1/3}-3\varepsilon^{2/3}-4\varepsilon)}\right] \tag{6.75}$$

In the limiting case of one bubble in an infinite liquid domain($\varepsilon = 0$), we have :

$$f = 4\pi\mu_l U_b a\frac{2+3\bar{\mu}}{2+2\bar{\mu}} \tag{6.76}$$

We can finally deduce the terminal velocity (U_b) of the bubble from the force balance between drag and buoyancy :

$$\begin{aligned}
f &= \tfrac{4}{3}\pi a^3\Delta\rho g \\
&= 4\pi\mu_l U_b a\left[\frac{1-\varepsilon}{(1-\varepsilon^{1/3})^3}\right]\left[\frac{4+6\varepsilon^{5/3}+6\bar{\mu}(1-\varepsilon^{5/3})}{(4+6\varepsilon^{1/3}+6\varepsilon^{2/3}+4\varepsilon)+\bar{\mu}(4+3\varepsilon^{1/3}-3\varepsilon^{2/3}-4\varepsilon)}\right]
\end{aligned} \tag{6.77}$$

We obtain,

$$U_b = \frac{1}{3}\frac{a^2\Delta\rho g}{\mu_l}\left[\frac{(1-\varepsilon^{1/3})^3}{1-\varepsilon}\right]\left[\frac{(4+6\varepsilon^{1/3}+6\varepsilon^{2/3}+4\varepsilon)+\bar{\mu}(4+3\varepsilon^{1/3}-3\varepsilon^{2/3}-4\varepsilon)}{4+6\varepsilon^{5/3}+6\bar{\mu}(1-\varepsilon^{5/3})}\right] \tag{6.78}$$

In the limiting case of one bubble in an infinite liquid domain ($\varepsilon = 0$), we have :

$$U_b = \frac{1}{3}\frac{\Delta\rho g a^2}{\mu_l}\frac{2+2\bar{\mu}}{2+3\bar{\mu}} \tag{6.79}$$

The drag coefficient C_D may also be determined by expressing the forces in the form :

$$\begin{aligned} f &= \tfrac{1}{2}C_D\rho_l\pi a^2 U_b^2 \\ &= 4\pi\mu_l U_b a\left[\frac{1-\varepsilon}{(1-\varepsilon^{1/3})^3}\right]\left[\frac{4+6\varepsilon^{5/3}+6\bar{\mu}(1-\varepsilon^{5/3})}{(4+6\varepsilon^{1/3}+6\varepsilon^{2/3}+4\varepsilon)+\bar{\mu}(4+3\varepsilon^{1/3}-3\varepsilon^{2/3}-4\varepsilon)}\right] \end{aligned} \tag{6.80}$$

Hence,

$$C_D = \frac{16}{Re}\left[\frac{1-\varepsilon}{(1-\varepsilon^{1/3})^3}\right]\left[\frac{4+6\varepsilon^{5/3}+6\bar{\mu}(1-\varepsilon^{5/3})}{(4+6\varepsilon^{1/3}+6\varepsilon^{2/3}+4\varepsilon)+\bar{\mu}(4+3\varepsilon^{1/3}-3\varepsilon^{2/3}-4\varepsilon)}\right] \tag{6.81}$$

In the limiting case of one bubble in an infinite liquid domain ($\varepsilon = 0$), the above expression reduces to

$$C_D = \frac{16}{Re}\frac{2+3\bar{\mu}}{2+2\bar{\mu}} \tag{6.82}$$

This result is in accordance with equation (6.14) proposed by Taylor and Acrivos (1964) for $\varepsilon = 0$. Equation (6.81) is a new result for the drag coefficient on a bubble in a two-phase mixture, assuming an external Stokes flow. Most importantly note that this results extends the expression for C_D to all values of the void fraction (ε).

Normal stress jump for Stokes flow

We consider next the normal stress jump described by the last boundary condition (cf. Eq. (6.52)-(6)) which is not considered in arriving at the solution of the previous section and is formally not satisfied since the bubble is not allowed to deform :

$$P_l - P_g - \Delta\rho g a\cos\theta - 2\mu_l\frac{\partial u_{rl}}{\partial r} + 2\mu_g\frac{\partial u_{rg}}{\partial r} = \frac{2\gamma}{a}C(\theta) \tag{6.83}$$

where $\Delta\rho = \rho_l - \rho_g$. The function $C(\theta)$ has been introduced to account for the curvature which variation is assumed to be small. As pressure is defined to within a constant, we choose to calculate the standard deviation (noted $std()$) of equation (6.83), and search the condition for which $std(C(\theta)) < 0.1$, corresponding to variation of the curvature below 10% . This condition will lead us to obtain the maximum radius for which the bubbles remain spherical, and to propose a validity range of this model in terms of density ratio $\bar{\rho}$, viscosity ratio $\bar{\mu}$, void fraction ε, Morton number Mo and Bond number Bo. The validity range is

expressed in terms of the Morton number rather than in terms of Reynolds number. Indeed, firstly only the Bond number depends on bubble size and therefore can be interpreted as a critical dimensionless bubble size. Secondly this allows to compare this model with the map of Bhaga and Weber (1981). For larger radii, bubbles become ellipsoidal or cap shaped and the drag coefficient no longer depends on Reynolds number as noted by Harmathy (1960). The standard deviation condition above leads to the inequality

$$std\left(P_l - P_g - \Delta\rho g a\cos\theta - 2\mu_l\frac{\partial u_{rl}}{\partial r} + 2\mu_g\frac{\partial u_{rg}}{\partial r}\right) < \frac{0.2\gamma}{a} \tag{6.84}$$

Using equation (6.4), we deduce :

$$\rho_g U_b^2 = \frac{\bar{\rho}}{72}\left(\frac{16}{C_D Re}\right)^2\sqrt{\frac{Bo^3}{Mo}}\Delta\rho g a \tag{6.85}$$

and

$$\frac{\mu_l U_b}{a} = \frac{1}{3}\frac{16}{C_D Re}\Delta\rho g a \tag{6.86}$$

The velocities and pressure equations (6.67), (6.72) and (6.73) are introduced in the previous equation and leading to the normal stress jump:

$$\begin{aligned}
std\left(P_l - P_g - \Delta\rho g a\cos\theta - 2\mu_l\tfrac{\partial u_{rl}}{\partial r} + 2\mu_g\tfrac{\partial u_{rg}}{\partial r}\right) &< \frac{0.2\gamma}{a}\\
std\left(\frac{\bar{\rho}}{144}\sqrt{\frac{Bo^3}{Mo}}\left(\frac{2-5\varepsilon+3\varepsilon^{5/3}}{4+6\varepsilon^{5/3}+\bar{\mu}(6-6\varepsilon^{5/3})}\right)^2\sin^2\theta\right) &< \frac{0.2\gamma}{\Delta\rho g a^2}\\
\frac{\bar{\rho}}{288}\sqrt{\frac{Bo^3}{2Mo}}\left(\frac{2-5\varepsilon+3\varepsilon^{5/3}}{4+6\varepsilon^{5/3}+\bar{\mu}(6-6\varepsilon^{5/3})}\right)^2 &< \frac{0.8}{Bo}\\
\sqrt{Bo} < \left(\frac{1300}{\bar{\rho}}\right)^{1/5}\left(\frac{2+3\varepsilon^{5/3}+\bar{\mu}(3-3\varepsilon^{5/3})}{2-5\varepsilon+3\varepsilon^{5/3}}\right)^{2/5} Mo^{1/10}&
\end{aligned} \tag{6.87}$$

The component of the normal stress jump coming from Stokes flow is exactly equal to the hydrostatic effect. Only pressure stemming from convective terms is responsible for a non-uniform normal stress jump and thus for non-spherical bubbles. As the liquid flow is assumed to be in the Stokes flow regime, this analytical model of the normal stress jump will not be as general as the drag coefficient model. It will be valid only if the convective term in the internal pressure is higher than the convective term contribution to the outer pressure which is not modelled. So the normal stress jump condition obtained above will be valid for $\bar{\rho} >> 1$ and $Re << 1$. As in Stokes flow, contrary to the normal stress jump the drag coefficient is not zero, the only condition required for the drag coefficient model to be valid is $Re << 1$.

External Euler flow without boundary layer correction ($Re >> 1$)

The case of external Euler flow is considered next. In this case, we have :

$$\begin{aligned} \nabla \cdot \vec{u}_l &= 0 \qquad (a) \\ \rho \vec{u}_l \nabla \vec{u}_l &= -\nabla P_l \quad (b) \end{aligned} \tag{6.88}$$

The actual pressure contains the hydrostatic pressure and is thus equal to $P_l + \rho_l g z$. This component is, however, not taken into account as explained in the beginning of this section. Similarly to the approach taken for the Stokes flow solution, the stationary Euler vorticity equation (*the rotation of equation (6.88)-(b)*) is used :

$$\begin{aligned} \nabla \vec{u}_l . (\nabla \wedge \vec{u}_l) &= 0 \\ \frac{1}{r^2}\left[\left(\frac{\partial}{\partial r}(r u_{\theta l}) - \frac{\partial u_{rl}}{\partial \theta}\right)\left(\frac{u_{\theta l}}{\tan\theta} + u_r\right)\right]\vec{e_\varphi} &= 0 \\ \left(-G'' + \frac{2G}{r^2}\right)\sin(\theta)\left(-\frac{G'}{r} + \frac{2G}{r^2}\right)\cos(\theta) &= 0 \end{aligned} \tag{6.89}$$

Searching for a solution of the form $G(r) = Br^n$ shows that n will satisfy

$$(n+1)(n-2)^2 = 0 \tag{6.90}$$

Finally, the following radial and tangential velocities are obtained.

$$\begin{aligned} u_{rl} &= \left(2C_0 + \frac{2C_1}{r^3}\right)\cos(\theta) \\ u_{\theta l} &= \left(-2C_0 + \frac{C_1}{r^3}\right)\sin(\theta) \end{aligned} \tag{6.91}$$

With the boundary condition : $u_{rl}\,|_{r=a} = 0$ we deduce

$$\begin{aligned} u_{rl} &= 2C_0\left(1 - \frac{a^3}{r^3}\right)\cos\theta \\ u_{\theta l} &= -2C_0\left(1 + \frac{a^3}{2r^3}\right)\sin\theta \end{aligned} \tag{6.92}$$

We cannot satisfy both the boundary conditions (6.52-(1) and (2)). We choose to respect only the condition $\langle u_l \rangle = U_b$, since it is a central condition for the averaged Navier-Stokes equations.

$$\begin{aligned} U_b &= -\langle \vec{u}_l . \vec{e_z} \rangle \\ &= -2C_0 \end{aligned} \tag{6.93}$$

Therefore we can write

$$\begin{aligned} u_{rl} &= -U_b\left(1-\tfrac{a^3}{r^3}\right)\cos\theta \\ u_{\theta l} &= U_b\left(1+\tfrac{a^3}{2r^3}\right)\sin\theta \end{aligned} \tag{6.94}$$

Satisfying solely the condition $\langle u_l\rangle = U_b$ instead of $\vec{u_l}\,|_{r=l} - U_b(1-\varepsilon)\vec{e_z}$, leads to following radial and tangential velocities for $r = l$:

$$\begin{aligned} u_{rl}\,|_{r=l} &= -U_b(1-\varepsilon)\cos\theta \\ u_{\theta l}\,|_{r=l} &= U_b\left(1+\frac{\varepsilon}{2}\right)\sin\theta \end{aligned} \tag{6.95}$$

This differs from a pure parallel flow boundary condition, and the difference grows as void fraction increases.

As previously,to deduce the pressure, the θ-momentum equation :

$$\frac{\partial P_l}{\partial\theta} = -\rho_l\left[r u_{rl}\frac{\partial u_{\theta l}}{\partial r} + u_{\theta l}\frac{\partial u_{\theta l}}{\partial\theta} + u_{rl}u_{\theta l}\right] \tag{6.96}$$

is integrating yielding

$$P_l = -\rho_l U_b^2\left[\left(\frac{3a^3}{2r^3}-\frac{3a^6}{8r^6}\right)\sin^2\theta + F(r)\right] \tag{6.97}$$

From the r component of the momentum equation, we have :

$$\begin{aligned} \frac{\partial P_l}{\partial r} &= -\rho_l\left(u_{rl}\frac{\partial u_{rl}}{\partial r} + \frac{u_{\theta l}}{r}\frac{\partial u_{rl}}{\partial\theta} - \frac{u_{\theta l}^2}{r}\right) \\ &= -\rho_l U_b^2\left[\left(\frac{3a^3}{r^4}-\frac{3a^6}{r^7}\right) - \left(\frac{9a^3}{2r^4}-\frac{9a^6}{4r^7}\right)\sin^2\theta\right] \end{aligned} \tag{6.98}$$

We finally obtain on integrating,

$$P_l = -\rho_l U_b^2\left[\left(\frac{3a^3}{2r^3}-\frac{3a^6}{8r^6}\right)\sin^2\theta - \frac{a^3}{r^3} + \frac{a^6}{2r^6} + C_1\right] \tag{6.99}$$

The tangential stress component does not vanish on $r = a$, because a boundary layer exists (non Euler flow). If we neglect this boundary layer, the force on the bubble can only be deduced through the total dissipation in the liquid domain which needs to be equal to the power of the drag forces (see Batchelor (1971)). With the velocity potential (Φ) and q^2 =

$|\nabla\Phi|^2 = u_{rl}^2 + u_{\theta l}^2$, the dissipated power balance is

$$\begin{aligned} U_b f &= -\mu_l \int \frac{\partial \Phi}{\partial x_i \partial x_j}\frac{\partial \Phi}{\partial x_i \partial x_j} dV \\ &= -\mu_l \int \frac{\partial^2 q^2}{\partial x_i \partial x_j} dV = \mu_l \int \vec{n}.\nabla q^2 dA \\ &= -2\pi\mu_l \int_0^\pi \frac{\partial q^2}{\partial r}_{r=a} a^2 \sin(\theta) d\theta + 2\pi\mu_l \int_0^\pi \frac{\partial q^2}{\partial r}_{r=l} l^2 \sin(\theta) d\theta \\ &= -2\pi\mu_l a U_b^2 \left(-6 + 6\varepsilon^2 \tfrac{l}{a}\right) \\ f &= 12\pi\mu_l a U_b (1-\varepsilon^{5/3}) \end{aligned} \tag{6.100}$$

We can finally deduce the velocity of the bubble from the balance between drag and buoyancy forces:

$$\begin{aligned} 12\pi a\mu_l U_b(1-\varepsilon^{5/3}) &= \frac{4}{3}\pi\Delta\rho g a^3 \\ U_b &= \frac{1}{9}\frac{\Delta\rho g a^2}{\mu_l}\frac{1}{1-\varepsilon^{5/3}} \end{aligned} \tag{6.101}$$

And the drag coefficient C_D :

$$\begin{aligned} f &= \tfrac{1}{2} C_D \rho_l \pi a^2 U_b^2 \\ C_D &= \frac{48}{Re}(1-\varepsilon^{5/3}) \end{aligned} \tag{6.102}$$

This relation is in accordance, for $Re >> 1$ and $\varepsilon = 0$, with the new relation Eq. (6.6) we have proposed. Using the same approach but for the different boundary conditions below

$$\begin{aligned} u_{rl}\,|_{r=l} &= -U_b \cos\theta \\ u_{\theta l}\,|_{r=l} &= U_b \frac{1+\frac{\varepsilon}{2}}{1-\varepsilon} \sin\theta \end{aligned} \tag{6.103}$$

Kendoush (2001) has obtained :

$$C_D = \frac{48}{Re}\left(\frac{1}{1-\varepsilon^2}\right) \tag{6.104}$$

The boundary condition (6.103) are not appropriate to be used for a closure relation for the averaged Navier-Stokes equations. Indeed their resulting averaged liquid velocities does not correspond to the relative velocities between phase U_b. A difficult question remains : in equation (6.100) do we need to integrate until $r = l$ or $r \to \infty$? We think that integrating up to $r = l$, is more appropriate, since after this distance the dissipation is due to other bubbles. Although Kendoush (2001) claims it needs to be done until $r \to \infty$.

External Euler flow with boundary layer correction ($Re >> 1$)

Moore (1963) proposed a boundary layer correction for $\varepsilon = 0$ and found :

$$C_D = \frac{48}{Re}\left[1 - \frac{2.2}{\sqrt{Re}} + 0(Re^{-5/6})\right] \tag{6.105}$$

Following the same procedure as Moore a new boundary layer correction is derived. This correction is valid only for $\bar{\mu} << Re$. The boundary layer correction is (cf. Appendix 6.5):

$$\begin{aligned}
u^*_{rl} &= \frac{U_b}{Re}\frac{4\chi(\theta)}{3}\left[\tau F(\tau) - \left(1 - \frac{\cos\theta}{2}\right)(6 + 9\bar{\mu})\ \mathrm{erf}(\tau)\right] \\
u^*_{\theta l} &= U_b\sqrt{\frac{2\chi(\theta)}{Re}}F(\tau)\sin\theta \\
&\text{with :} \\
\tau &= \sqrt{\frac{Re}{8\chi(\theta)}}\left(\frac{r}{a} - 1\right) \\
F(\tau) &= -(6 + 9\bar{\mu})\left[\frac{1}{\sqrt{\pi}}e^{-\tau^2} - \tau\,(1 - \ \mathrm{erf}(\tau))\right] \\
\chi(\theta) &= \frac{1}{18}\left(\frac{\cos(3\theta) - 9\cos\theta + 8}{\sin^4\theta}\right)
\end{aligned} \tag{6.106}$$

The corresponding corrected drag coefficient is :

$$C_D = \frac{48}{Re}\left[1 - \varepsilon^{5/3} - \frac{5.35(1 + 1.5\bar{\mu}) - 3.44(1 + 1.5\bar{\mu})^2}{\sqrt{Re}}\right] \tag{6.107}$$

For $\varepsilon = \bar{\mu} = 0$:

$$C_D = \frac{48}{Re}\left[1 - \frac{1.9}{\sqrt{Re}}\right] \tag{6.108}$$

This result is in accordance with Moore (1963) for $\varepsilon = \bar{\mu} = 0$ except for the factor 1.9 instead of 2.2. We probably do not have the same integral resolution. This new relation extends the drag formulation for $\varepsilon \neq 0$ and $\bar{\mu} \neq 0$. In the case of Euler flow, we neglect the pressure influence on the interface. For the procedure followed by Moore, some assumption about the pressure needed to be made. This leads to an incorrect value of the pressure field especially at the interface. That's why the drag coefficient is evaluated through the total dissipation in all the liquid domain including boundary layer and wake. Bur for the same reason, the normal stress jump calculation does not lead to satisfactory results. Thus, for high Reynolds number, we were not able to determine analytically, the limit at which the transition between spherical and non spherical bubbles occurs.

6.3 Numerical Solutions

In order to confirm and even improve the new relation we have proposed for the drag coefficient (C_D), numerical experiments have been carried out by varying Reynolds number Re (from 0.01 to 300), void fraction ε (from 10^{-6} to 0.6), viscosity ratio $\bar{\mu}$ (from 0.02 to 50) and density ratio $\bar{\rho}$ (from 10^{-3} to 10^{3}).

6.3.1 Numerical Solution Strategy

Figure 6.5 shows the geometry of the problem solved both numerically and analytically. Figure 6.6 shows the geometry of a more realistic case of a five bubble train. This problem was solved with two types of boundary conditions, one with $u = U_b(1-\varepsilon), v = 0$ for $r = l$ named later on the "Dirichlet case" and one with $u =$ "$Free$", $v = 0$ for $r = l$ named later on the "Neumann case". Both cases have for inlet and outlet condition : $u = U_b(1-\varepsilon), v = 0$. A finite element code was used to solve the incompressible Navier-Stokes equations in an axisymmetric frame of reference (the central axis of rotation is noted by a dash-dot line). A Taylor-Hood element was selected for both domains (external flow and flow within the bubble). The fluid velocity is discretized using 6-node quadratic elements, while fluid pressure is discretized by piecewise linear continuous functions. The mixed method is used in which the pressure is a Lagrange multiplier.

The tangential condition is satisfied via another Lagrange multiplier which enforces the non-penetration of fluid across the bubble boundary. An interface allows matching of the inner bubble boundary velocity to the outer bubble boundary velocity (Eq. (6.52)-4). Conversely, continuity of interface tangential loads is also enforced (Eq. (6.52)-5).

Dirichlet boundary conditions are imposed on the outer boundary of the domain. This means that the pressure needs to be set at only one point in the fluid domain. Symmetry conditions are imposed on all axial boundaries (dash-dot line). Finally, for all cases, we extract the total drag by integrating reactions on the outer boundary of the bubble.

Linearization of the flow equations accounts for all implicit dependencies to ensure quadratic convergence of Newton's method (Etienne and Pelletier (2005)). The resulting sparse matrix system is solved using the PARDISO software, (Schenk and Gärtner (2004, 2006)).

A convergence study has been performed to ensure that the results with sufficient numerical precision. Simulations were performed for a representative case corresponding to $\varepsilon = 20\%$ for a multi-bubble configuration, with $Re = 100$, $\bar{\mu} = 0.02$ and $\bar{\rho} = 10^{-3}$, Dirichlet condition of $u = U_b(1-\varepsilon), v = 0$. The results, in terms of drag coefficient values, are summarized in Table 6.2. From this table we deduced that taking a bubble train of 5 bubbles and 24662 nodes is sufficient to ensure accuracy to 3 or 4 significant digits while keeping the computational

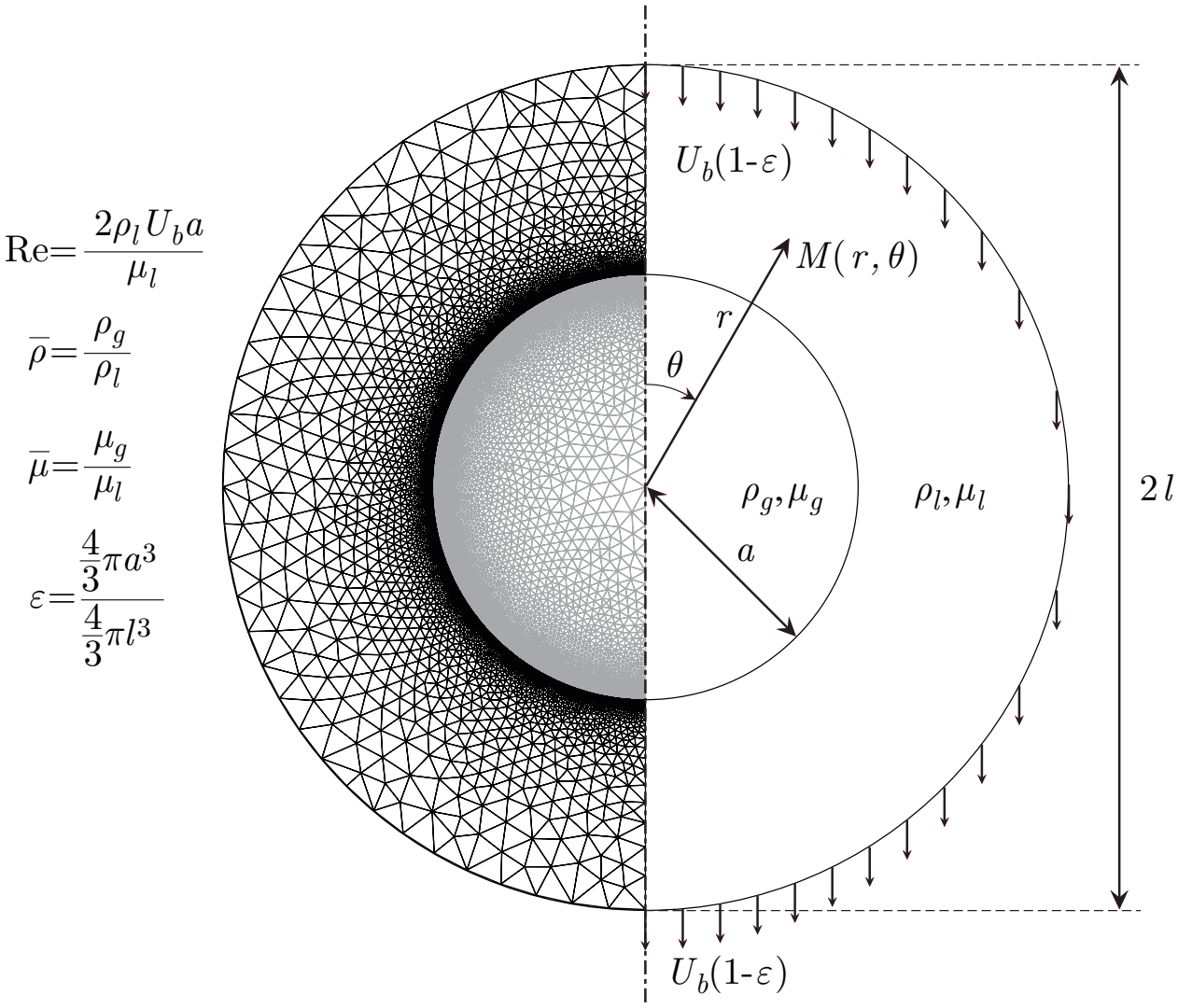

Figure 6.5 Geometry of the problem of a single bubble.

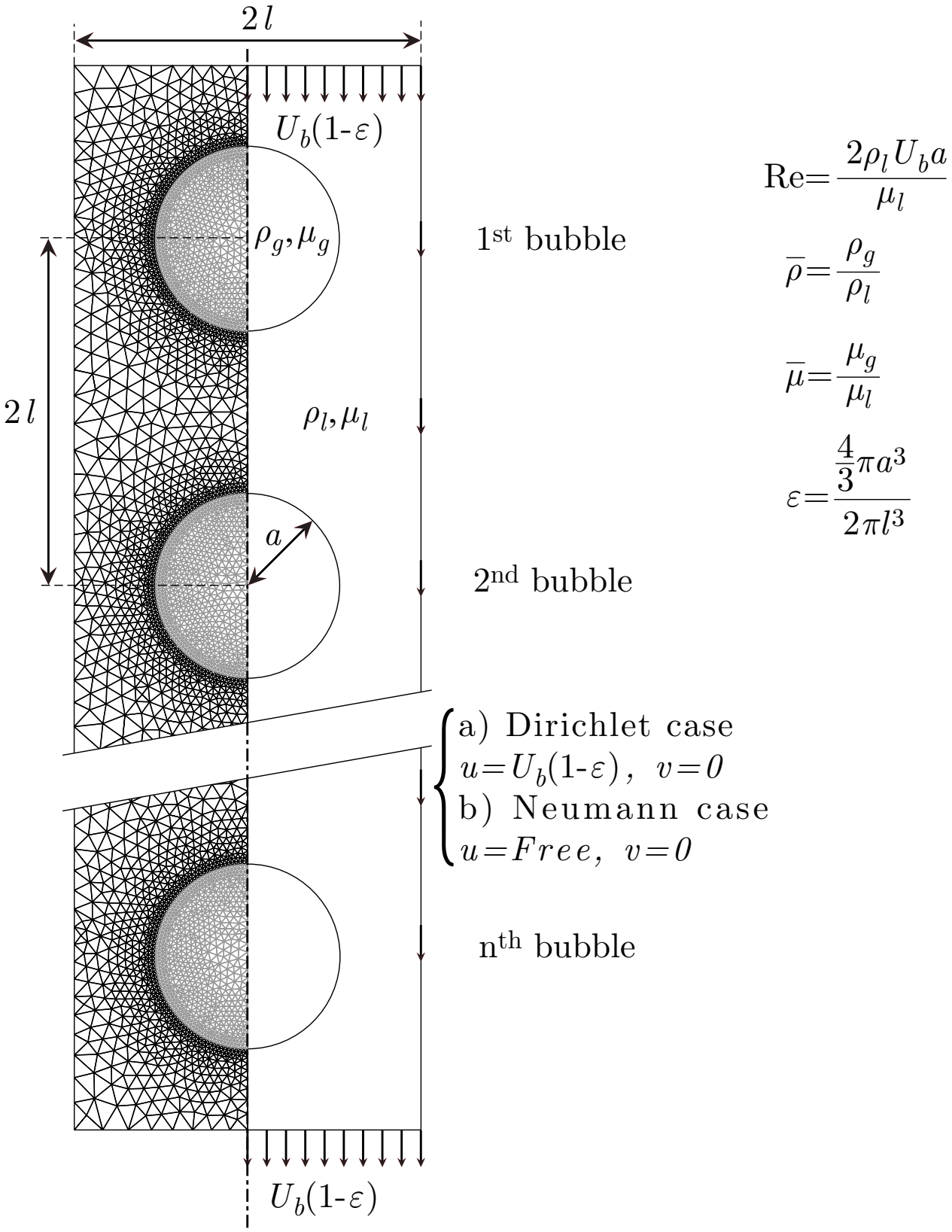

Figure 6.6 Geometry of the problem of a n bubbles train.

time reasonable.

6.3.2 Comparison with analytical results for the case of one bubble (cf. fig. 6.5)

The dimensionalization process allows us to choose $a = 0.5$, $U_b = 1$ and $\mu_l = 1$, which means:

$Re = \rho_l$, $\bar{\rho} = \rho_g/Re$, $\bar{\mu} = \mu_g$ and $\varepsilon = 0.5^3/l^3$.

We choose to obtain solutions for the following combinations of the parameters:

- $\bar{\rho} = 10^{-3}, 1, 10^3$
- $\bar{\mu} = 0.02, 0.1, 0.5, 2.5, 12.5, 50$
- $Re = 0.01, 0.1, 1, 10, 100, 300$
- $l = 0.59(60\%), 0.68(40\%), 0.79(25\%), 1(12.5\%), 2.5(0.8\%),$ $5(0.1\%), 10(0.0125\%), 50(0.0001\%)$

The corresponding void fraction (ε) is indicated inside the parenthesis.

The drag coefficient is inversely proportional to the Reynolds number while the terminal velocity varies according to the product of the drag coefficient and Reynolds number. For this reason we present the results of the dimensionless terminal velocity deduced by (Eq. 6.4).

Figure 6.7(a) shows a very good agreement between the dimensionless terminal velocity predicted by the numerical Navier-Stokes solutions and the relation of Mei *et al.* (1994). Except for $Re \geq 100$, the numerical results are slightly lower than Mei's model. However, note that the numerical results are presented for a viscosity ratio $\bar{\mu} = 0.02$ rather than the idealized solution of Mei *et al.* (1994) $\bar{\mu} = 0$.

Figure 6.7(b) shows a very good agreement between the dimensionless terminal velocity predicted by the numerical Navier-Stokes solution and the relation of Taylor and Acrivos

number of mesh nodes	drag coefficient
219	1.37657
2018	1.14649
6948	1.10445
24662	**1.10505**
94148	1.10516
188891	1.10517

number of bubbles	drag coefficient
1	1.22008
3	1.10543
5	**1.10505**
7	1.10496
9	1.10513
11	1.10503
13	1.10498

Table 6.2 Left: convergence with respect to the number of nodes, right: convergence with respect to the number of bubbles.

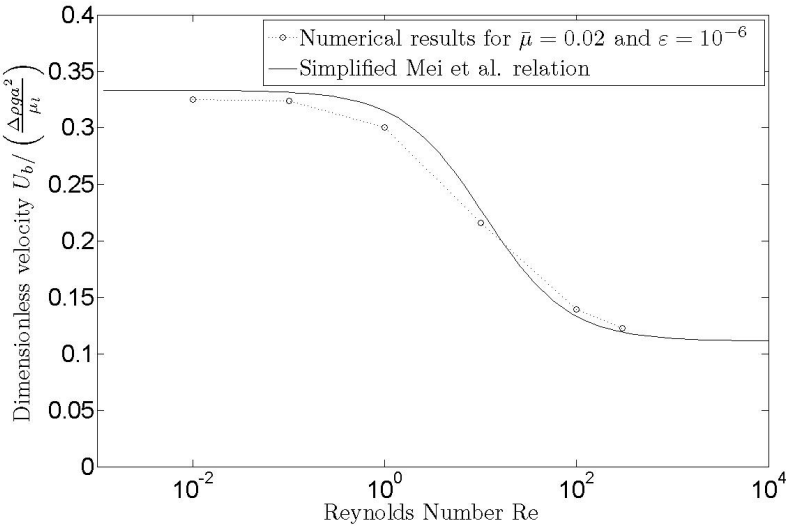

(a) Numerical results and the new model deduced from the formulation of Mei *et al.* (1994) (Eqn.6.7).

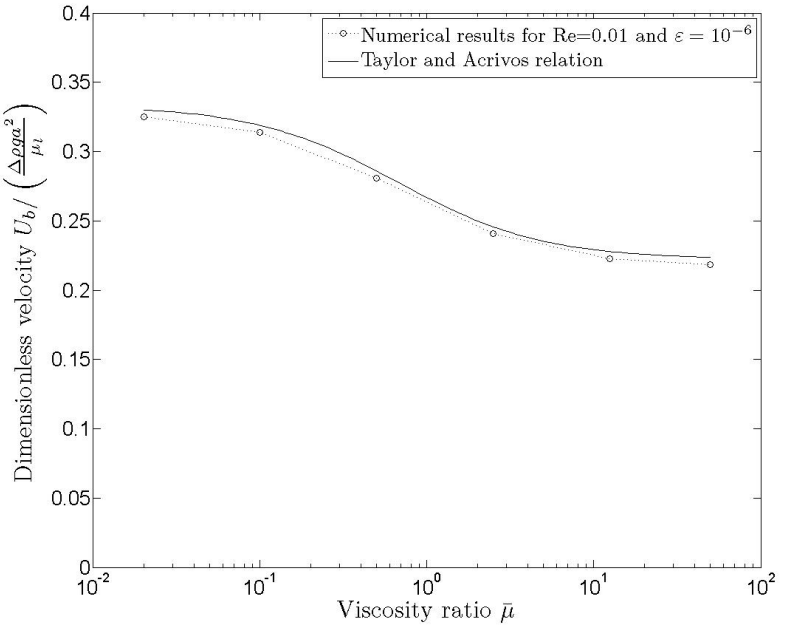

(b) Numerical results and the relation (Eqn.6.14) proposed by Taylor and Acrivos (1964).

Figure 6.7 Comparison of numerically predicted bubble velocities with models : case of one single bubble (cf. fig. 6.5).

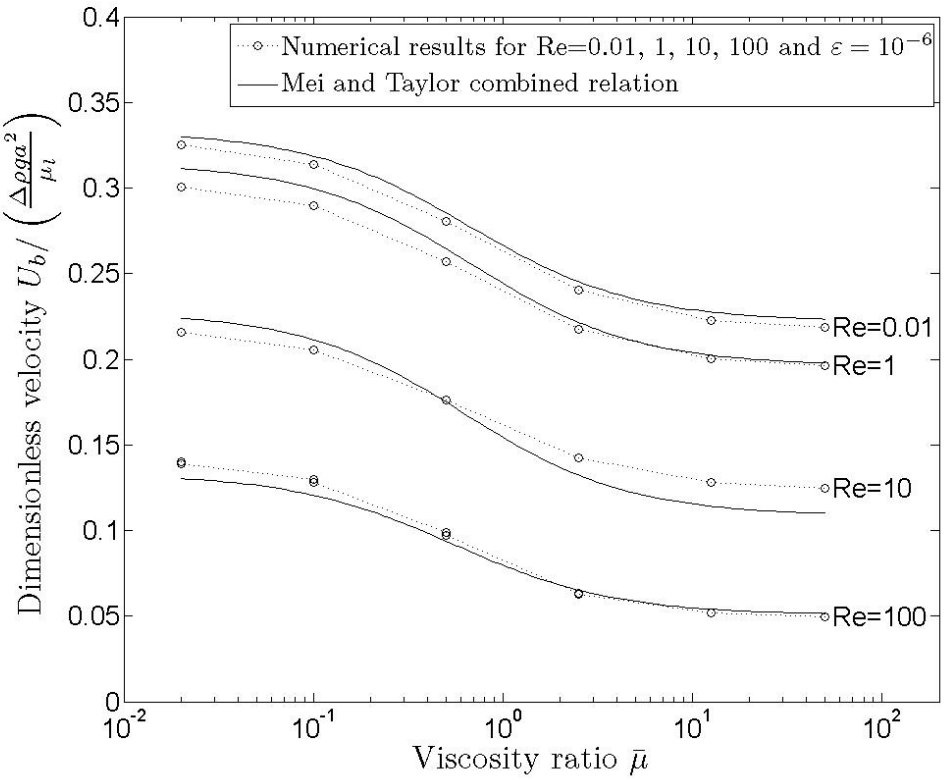

Figure 6.8 Comparison between numerically predicted terminal bubble velocity and the new relation (Eq. 6.109).

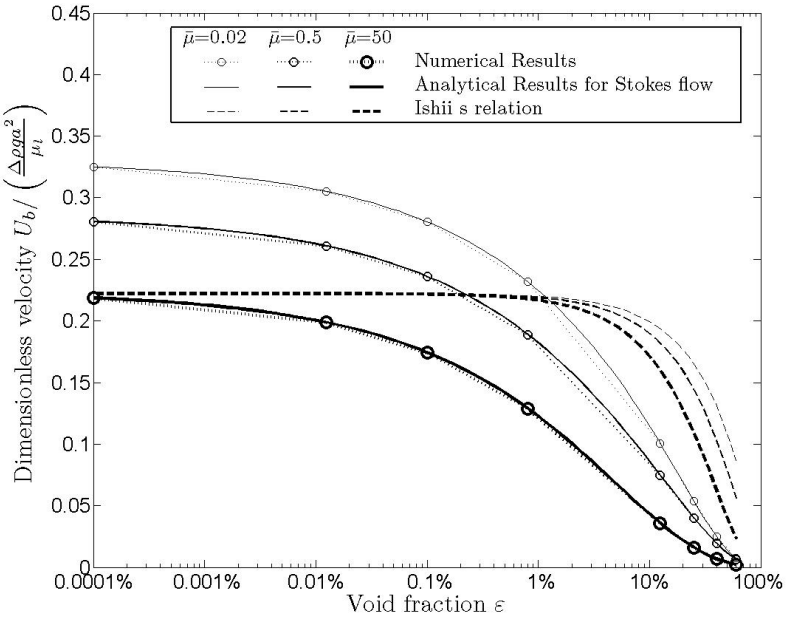

(a) Dimensionless terminal velocity vs void fraction for Re=0.01.

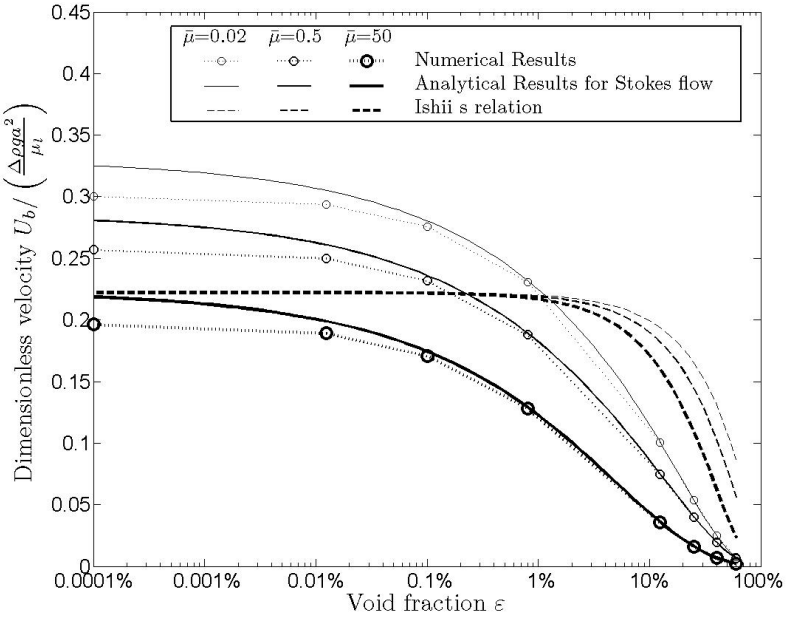

(b) Dimensionless terminal velocity vs void fraction for Re=1.

Figure 6.9 Numerical and analytical comparison of dimensionless velocity versus void fraction for (a) Re=0.01 (b) Re=1 (cf. Eq.(6.81) for analytical results and Eq. (6.17) for Ishii's relation).

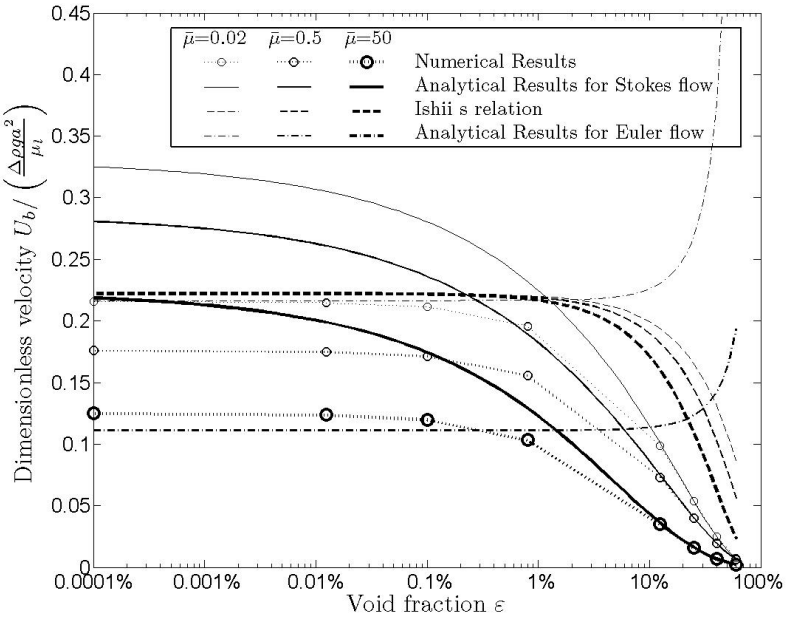

(a) Dimensionless terminal velocity vs void fraction for Re=10.

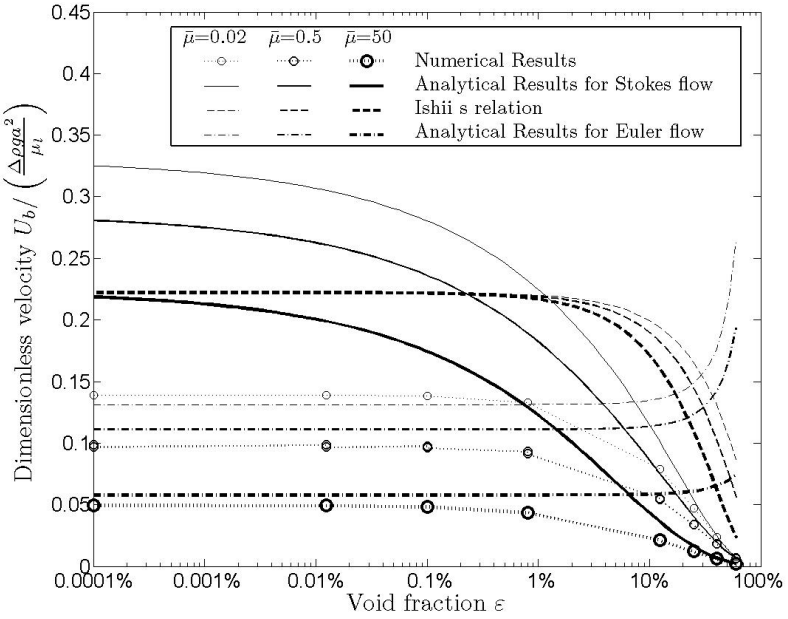

(b) Dimensionless terminal velocity vs void fraction for Re=100.

Figure 6.10 Comparison of numerical and analytical of dimensionless velocity versus void fraction for (a) Re=10 (b) Re=100 (cf. Eq. (6.81) -Stokes- and Eq. (6.107)-Euler- for analytical results and Eq. (6.17) for Ishii's relation).

(1964). The numerical results are slightly lower than the Taylor and Acrivos model prediction. However, note that numerical results are presented with a Reynolds numbers of $Re = 0.01$ rather than the idealized solution of $Re \to 0$.

Both results are obtained for a bubble surrounded by an outer infinite liquid domain. It is noted that a void fraction of $\varepsilon = 0.0001\%$ (or external boundary located at 100 times the radius of the bubble) was required to reach this spatial convergence. This means that even a very low void fraction already has a strong effect on the drag coefficient.

In order to be able to predict the influence of both the viscosity ratio ($\bar{\mu}$), and the Reynolds number (Re), we propose a new relation combining the Mei *et al.* (1994) model (Eq. 6.6) and the Taylor and Acrivos (1964) model (Eq. 6.14):

$$C_D = \frac{16}{Re}\left(1 + \frac{2\left(\dfrac{2+3\bar{\mu}}{2+2\bar{\mu}}\right)^2}{1+\dfrac{33}{Re}}\right)\frac{2+3\bar{\mu}}{2+2\bar{\mu}} \tag{6.109}$$

Comparison of this new relation with the numerical results (see Figure 6.8). A fairly good agreement is obtained between the terminal velocity of one bubble in an outer infinite liquid domain obtained from equation (6.109) and the from the Navier-Stokes simulations. Because equation (6.109) models the transition from Euler to Stokes flows, it follows the correction proposed by Oseen (1910). Oseen's correction takes into account the fact that convective terms become predominant far away from the bubble. Figure 6.11 presents the dimensionless velocity deduced from the new relation (6.109) for $\bar{\mu} \to \infty$ with the equations of Taylor and Acrivos (1964) (6.14) and Clift (6.16). The equation of Taylor and Acrivos (1964) proposes corrective terms in Stokes solution taking into account convective effect in the far field. Clift's relation is valid for a solid sphere up to $Re < 3.7 \times 10^5$ corresponding to the drag crisis due to the appearance of turbulence.

In order to evaluate the maximum Reynolds number for which Stokes assumption remains valid, computational results and analytical results are compared in Figures 6.9(a), 6.9(b), 6.10(a) and 6.10(b). A very good agreement with analytical results for Stokes flow is achieved for $Re < 10$. Similarly very good agreement with analytical results for Stokes flow is also achieved for all Reynolds number (0.01 to 300) in the case of void fractions higher than 10% ($\varepsilon > 0.1$). Moreover, the gas density is found to have almost no influence on the drag coefficient. Indeed no significant difference for $\bar{\rho} = 10^{-3}, 1$ and 10^3 can be seen. In each graph, the results for the three different density ratios are presented. They are so close that we are not able to distinguish the different points except for $Re = 100$ where we can see a small difference between $\bar{\rho} = 10^{-3}$ and $\bar{\rho} = 1$. Solution for $\bar{\rho} = 10^3$ have not converged for $Re \geq 100$.

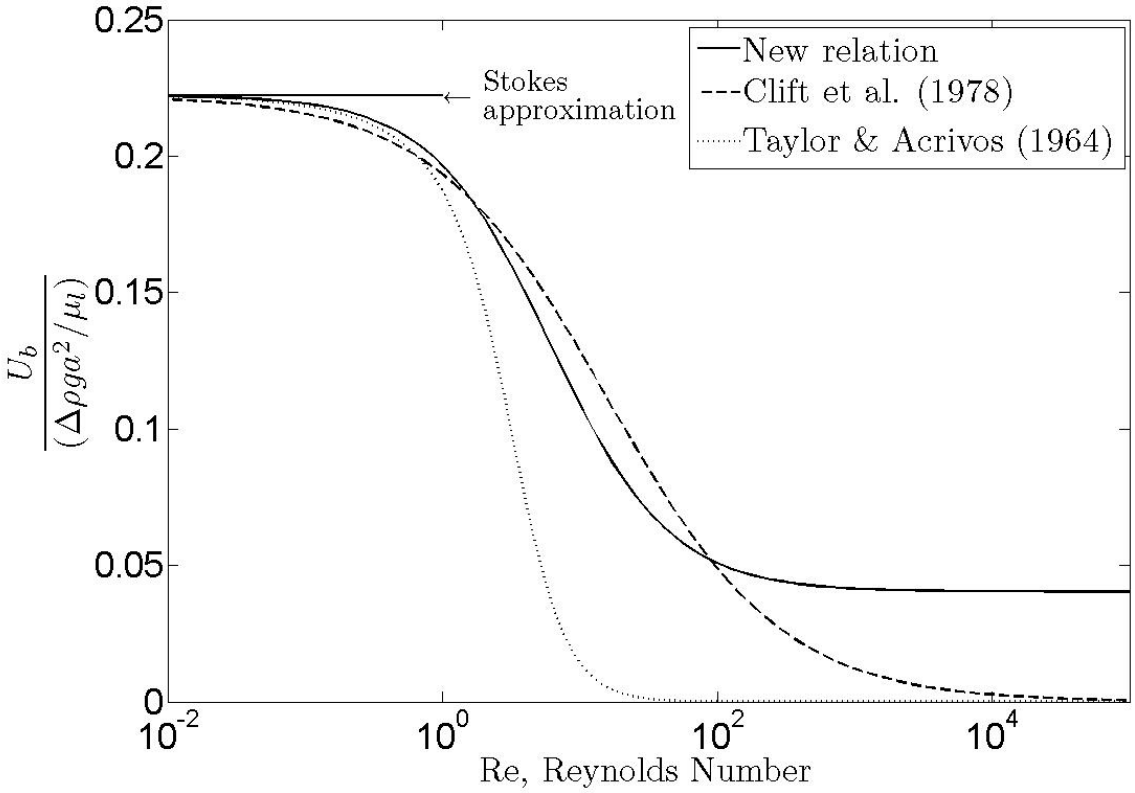

Figure 6.11 Comparison between predicted terminal solid sphere velocity from the new relation (Eq. 6.109) for $\bar{\mu} \to \infty$ with the equations of Taylor (6.14) and Clift (6.16).

This is due to the high Reynolds number inside the bubble. As an example for $Re = 100$, $\bar{\rho} = 10^3$ and $\bar{\mu} = 0.02$, the Reynolds number value inside the bubble Re_g is equal to 5 000 000. However, while the flow inside and outside of the bubble does not depend on gas density, the pressure field is strongly affected by $\bar{\rho}$ as predicted by equation (6.67) and illustrated on Figure 6.12. Although, the density ratio ($\bar{\rho}$) has almost no effect on the drag coefficient, it will, however, play a major role in the normal stress jump where the pressure difference intervenes. In other words, the density ratio is essential to verify the sphericity assumption validity.

As shown on Figure (6.10(b)), the new relation (6.107) is a good model for low void fractions and takes into account relatively well the influence of $\bar{\mu}$ while viscosity ratio remains small in front of Reynolds number ($\bar{\mu} << Re$) and for sufficient high Reynolds number $Re \geq 100$. At high Reynolds numbers flow ($Re \geq 100$), the influence of the void fraction is not important while $\varepsilon < 1\%$, which was not the case for low Reynolds number flow.

As underlined previously (cf. Eq. 6.95), Euler modeling is accurate only for low void fractions and small viscosity ratio in front of Reynolds number ($\bar{\mu} << Re$). This is why, the figure presenting results for $Re = 10$ does not show the analytical results for $\bar{\mu} = 50$.

As suggested by the results presented in Figures (6.9(a),6.9(b),6.10(a) and 6.10(b)), even at high Reynolds number, if the void fraction is higher than 10%, the Stokes flow is more representative of reality than Euler flow. When the flow is confined, viscous effects are generally more important than inertial effects. Even a low void fraction corresponds to a relatively small average distance between bubbles,consequently liquid flow is closer to liquid film flow between the bubbles rather than infinite liquid domain flow. This explains why the Stokes flow model is a better approach than the Euler flow model.

6.3.3 Numerical results of drag coefficient for more realistic cases

The agreement between numerical and analytical results gives confidence in the accuracy of both the numerical and the analytical calculations. Therefore, we can now study more realistic cases. The previous case allows us to obtain an analytical solution but does not take into account the wakes of surrounding bubbles. To investigate this, the problem presented on Figure 6.6 was solved. Several computations were done varying the number of bubbles in a bubble train. The bubbles are separated by a distance $2l$ inside a tube of radius l. As shown in Table 6.2, a train of five bubbles is sufficient to eliminate any variation of the C_D of the central bubble by adding more bubbles in the train. Solutions for a train of five bubbles were obtained for the following combinations of parameters :

- $\bar{\mu} = 0.02, 0.1, 0.5, 12.5, 25, 50$
- $Re = 0.01, 0.1, 1, 10, 100, 300$

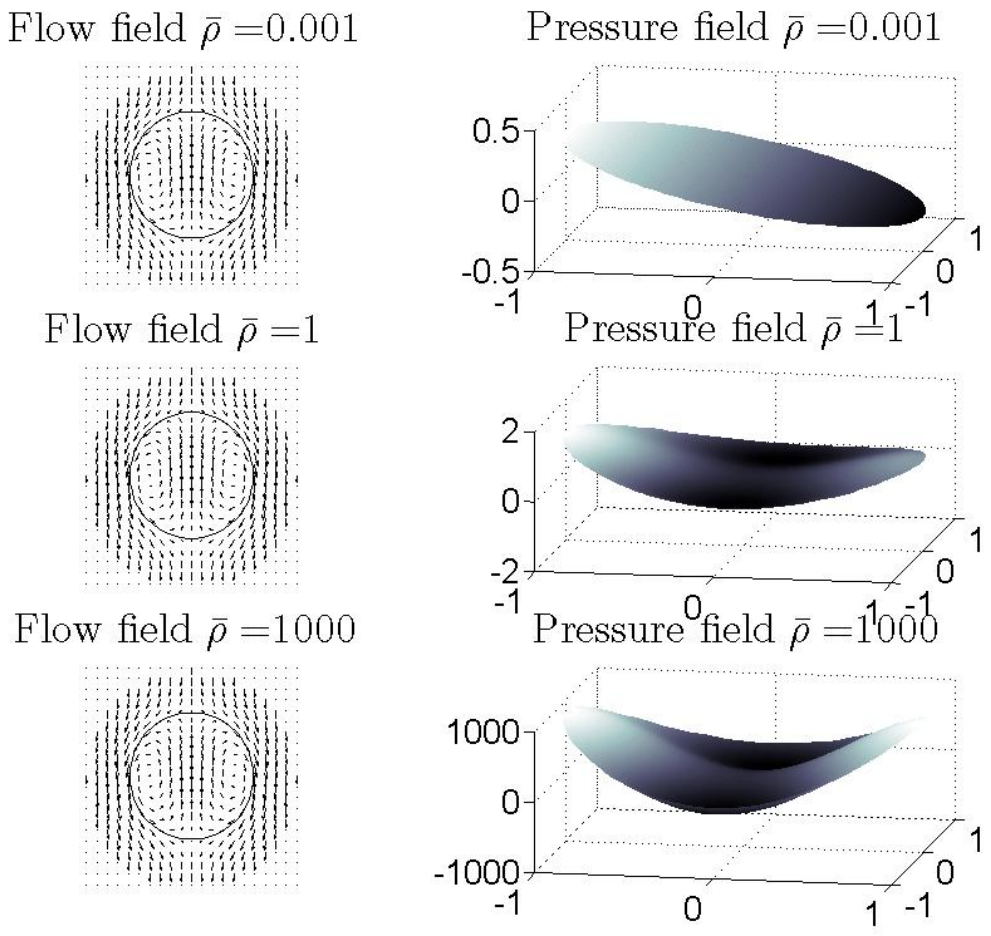

Figure 6.12 Flow field and Internal Pressure field for Re=1, $\bar{\mu}$ = 0.02 and ε = 0.2%.

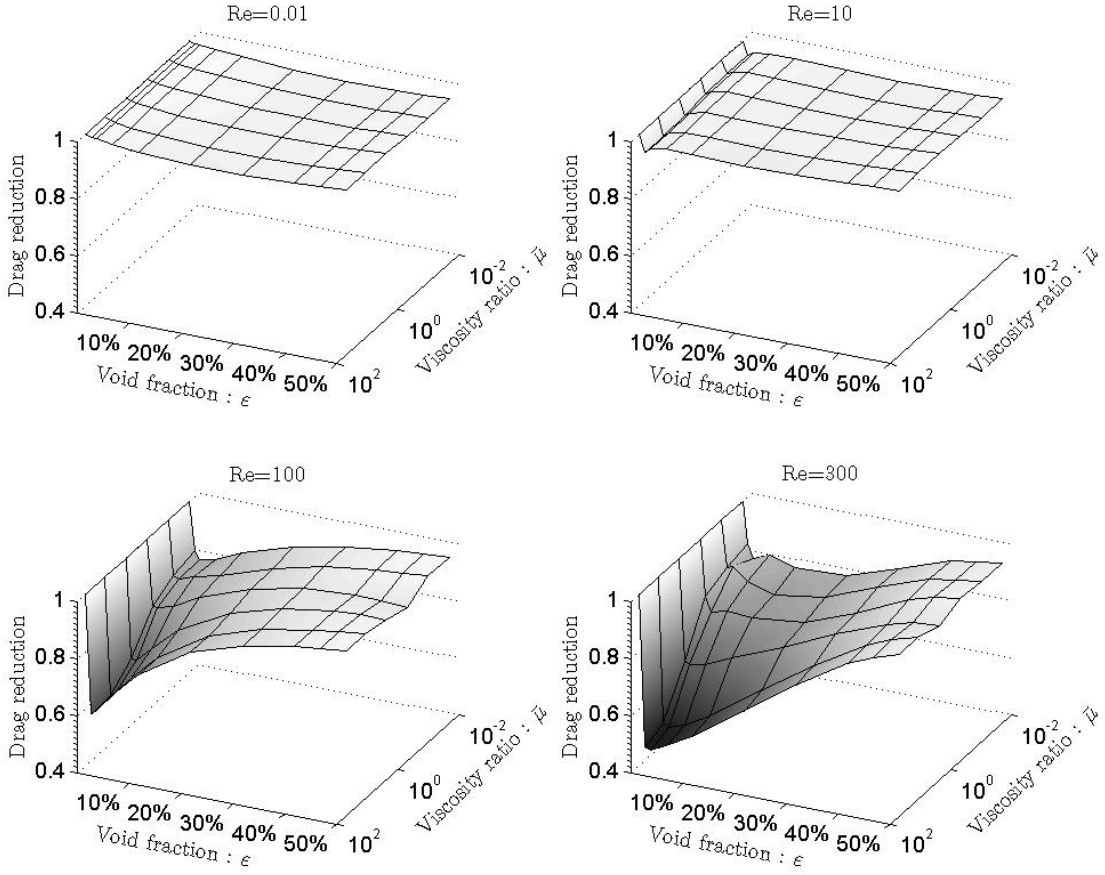

Figure 6.13 Relative reduction of drag coefficient $\frac{Cd_{train}}{Cd_{single}}$ due to wake vs. void fraction (ε) and viscosity ration ($\bar{\mu}$) for $Re = 0.01, 10, 100$ and 300, for Dirichlet case.

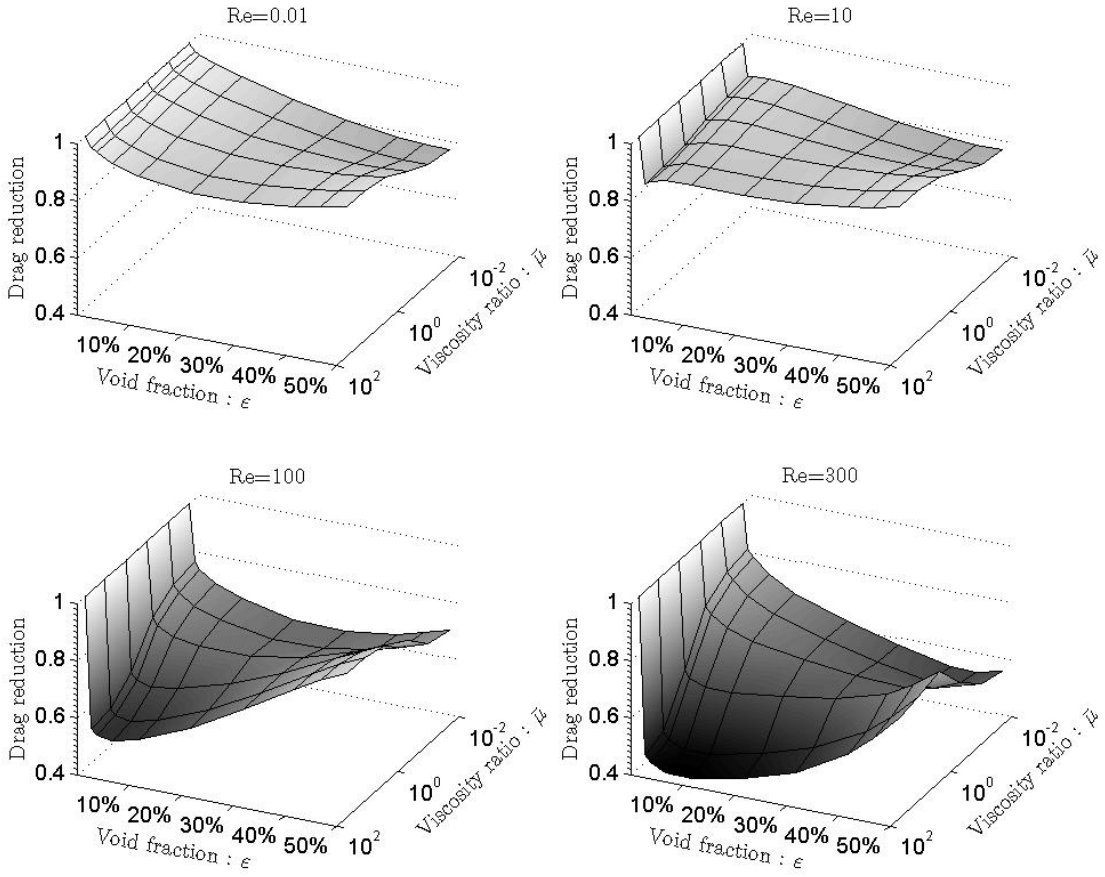

Figure 6.14 Relative reduction of drag coefficient due to wake $\frac{Cd_{train}}{Cd_{single}}$ vs. void fraction (ε) and viscosity ration ($\bar{\mu}$) for $Re = 0.01, 10, 100$ and 300, for Neumann case.

– $\varepsilon = 0, 0001\%, 1\%, 2\%, 5\%, 10\%, 20\%, 30\%, 40\%, 45\%, 50\%$

To evaluate the wake effect, numerical results of the drag coefficient obtained for a single bubble and that for the central bubble of a five bubble train were compared. As shown in Figure 6.13, the wake effect on the drag coefficient for the Dirichlet cases is fairly small except for high Reynolds numbers and high viscosity ratios.

Figure 6.14, presents results showing the wake effect on the drag coefficient for the Neumann cases. The effect is larger than for the Dirichlet case, but remains 30% below for Reynolds numbers lower than 10.

Since the effect of confinement is much larger that the wake effect, we conclude that the confinement is the main effect governing drag variation.

It follows that a model with one bubble will therefore represent reality quite well. Because the geometry of a single bubble in a cylinder allows a maximum void fraction of $\varepsilon_{max} = 2/3$ and one bubble in a sphere allows a maximum void fraction of $\varepsilon_{max} = 1$, we propose to change the analytical relation (6.81) by multiplying the void fraction by 1.5. The drag coefficient for the Dirichlet case is then estimated by:

$$\begin{aligned}
&C_D = \frac{16}{Re}\frac{1-1.5\varepsilon}{(1-(1.5\varepsilon)^{1/3})^3}\left[\frac{P_1(\varepsilon)+\bar{\mu}P_2(\varepsilon)}{P_3(\varepsilon)+\bar{\mu}P_4(\varepsilon)}\right] \\
&\text{with :} \\
&P_1(\varepsilon) = 4 + 6\times(1.5\varepsilon)^{5/3} \\
&P_2(\varepsilon) = 6 - 6\times(1.5\varepsilon)^{5/3} \\
&P_3(\varepsilon) = 4 + 6\times(1.5\varepsilon)^{1/3} + 6\times(1.5\varepsilon)^{2/3} + 4\times(1.5\varepsilon) \\
&P_4(\varepsilon) = 4 + 3\times(1.5\varepsilon)^{1/3} - 3\times(1.5\varepsilon)^{2/3} - 4\times(1.5\varepsilon)
\end{aligned} \tag{6.110}$$

Combining the above equation with the new relation (6.109), we arrive at the following newly proposed correlation :

$$C_D = \frac{16}{Re}\left(1 + \frac{2\left(\frac{2+3\bar{\mu}}{2+2\bar{\mu}}\right)^2}{1+\frac{Re_c}{Re}}\right)\frac{1-1.5\varepsilon}{(1-(1.5\varepsilon)^{1/3})^3}\frac{P_1(\varepsilon)+\bar{\mu}P_2(\varepsilon)}{P_3(\varepsilon)+\bar{\mu}P_4(\varepsilon)} \tag{6.111}$$

The transition from Stokes to Euler flows occurs at the critical Reynolds number Re_c. Because the transition depends on void fraction, and $Re_c = 33$ corresponds to transition at $\varepsilon = 0$, we seek a formula of the form: $Re_c = 33 + A\times(1.5\varepsilon)$ to account for void fraction dependence.

Optimization for the value of A, gives $A = 50000$. However, the maximum Reynolds number of the study was $Re = 300$. We can, therefore, only conclude that the transition

from Stokes to Euler flow occurs for values of Reynolds number larger than 300 for void fraction larger than 1%. The value of the drag coefficient from correlation (eq. (6.111)) gives a maximum error of 36% relative to numerical values and an average relative error of 16%. Figure 6.15 shows the agreement between the correlation (eq. (6.111)) and numerical results for the Dirichlet cases.

For the Neumann cases (free boundary condition), the effect of confinement is less important and we obtain a good correlation without multiplying the void fraction by 1.5. The proposed correlation in this case is :

$$
\begin{aligned}
&C_D = \frac{16}{Re}\left(1 + \frac{2\left(\dfrac{2+3\bar{\mu}}{2+2\bar{\mu}}\right)^2}{1+\dfrac{Re_c}{Re}}\right)\frac{1-\varepsilon}{(1-\varepsilon^{1/3})^3}\frac{P_1(\varepsilon)+\bar{\mu}P_2(\varepsilon)}{P_3(\varepsilon)+\bar{\mu}P_4(\varepsilon)}\\
&\text{with :}\\
&P_1(\varepsilon) = 4 + 6\varepsilon^{5/3}\\
&P_2(\varepsilon) = 6 - 6\varepsilon^{5/3}\\
&P_3(\varepsilon) = 4 + 6\varepsilon^{1/3} + 6\varepsilon^{2/3} + 4\varepsilon\\
&P_4(\varepsilon) = 4 + 3\varepsilon^{1/3} - 3\varepsilon^{2/3} - \varepsilon\\
&Re_c = 33 + 50000\varepsilon.
\end{aligned}
\tag{6.112}
$$

Figure 6.16 shows the agreement between correlation (Eq. (6.112)) and the numerical results for Neumann cases. As we can see the correlation is less accurate that in the Dirichlet cases. The error also increases with the void fraction. The results show the difficulty in estimating the effect of surrounding bubbles on the drag. The value of the drag coefficient from correlation (6.112) gives a maximal relative error of 47% compared to numerical values and an average relative error of 18%.

Figure 6.17 presents, respectively, the influence of Reynolds number (Re), void fraction (ε) and viscosity ratio ($\bar{\mu}$) on the terminal bubble velocity (U_b) in the Dirichlet cases. The drag coefficient rises dramatically with void fraction, essentially due to confinement and consequently to the terminal velocity decreases significantly. The previous comparison between one bubble and five bubbles leads to the conclusion that the wake influence is most of the time less than 10% of total drag. The drag coefficient rises with viscosity ratio. The value of $\bar{\mu} \sim 1$ corresponds to the transition between an approximately free surface condition and an essentially solid surface condition (no slip). The dimensionless terminal velocity decreases with Reynolds number. For void fractions $\varepsilon \geq 1\%$, the transition between Stokes and Euler flow occurs for $Re_c > 300$. For very low void fraction $Re_c \sim 33$ is the transition from Stokes to Euler flow. As the previous results suggest, gas density has effectively no effect on drag

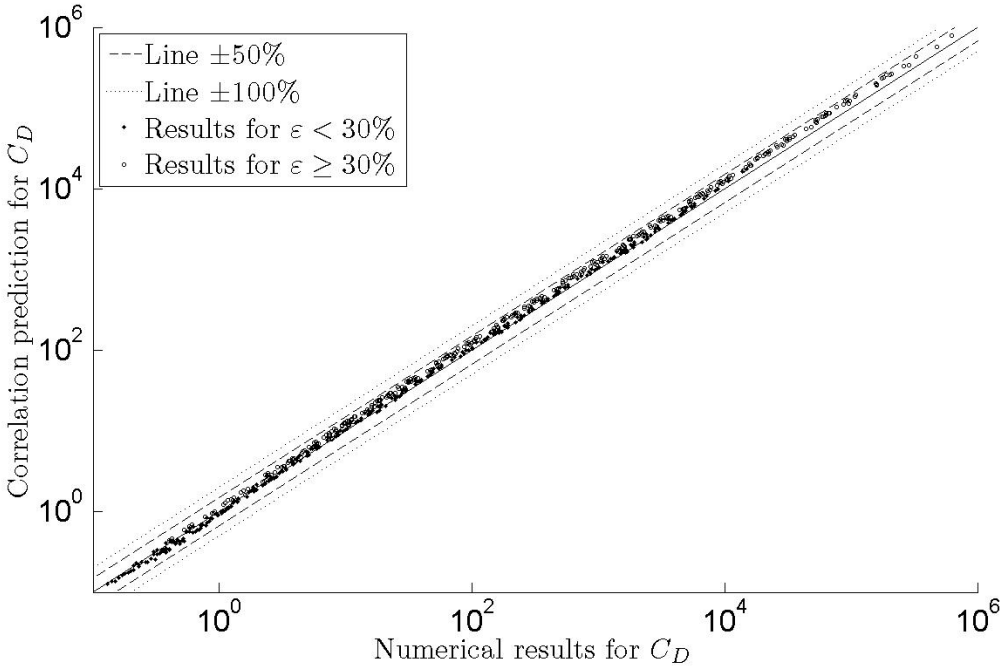

Figure 6.15 Comparison of the Correlation (eq. (6.111)) and numerical computation for the Dirichlet cases.

coefficient and consequently on the dimensionless terminal velocity.

6.3.4 Normal stress jump

As suggested in Section 6.2.2, the normal stress jump can be used to deduce the maximum possible radius of spherical bubbles. All figure from 6.18) to the maximum Bond number Bo where bubbles remains spherical 6.22 versus the Morton number Mo. The maximum Bond number is deduced for a standard deviation of the normal stress jump leading to a curvature variation less than 10%, (cf. Eq. 6.84). We made the assumption that the bubble have reach is terminal velocities deduced by the equilibrium between the numerically evaluated drag and buoyancy. All numerical results are indicated by symbols □, ◇,★ and ◯. Each symbols corresponds to a range of void fraction.

- □ indicate numerical results for $\varepsilon < 5\%$,
- ◇ indicate numerical results for $5\% \leq \varepsilon < 20\%$,
- ★ indicate numerical results for $20\% \leq \varepsilon < 40\%$,
- ◯ indicate numerical results for $\varepsilon \geq 40\%$.

All figures present also the boundary proposed by Bhaga and Weber (1981) for the transition between different bubbles shape. In case of results for bubble train we also plot the new

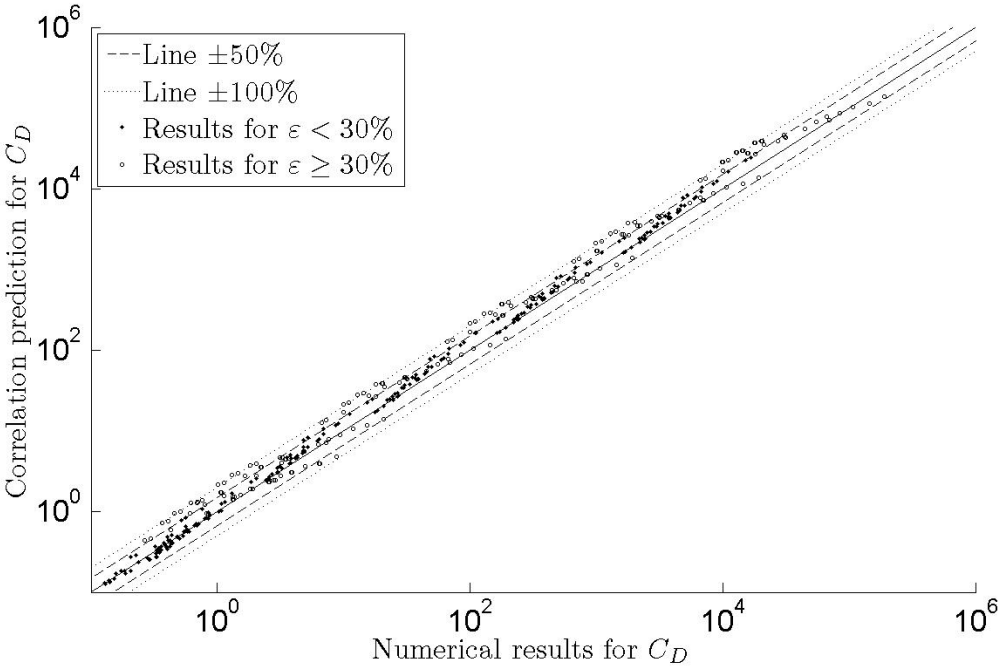

Figure 6.16 Comparison of the Correlation (eq. (6.112)) and numerical computation for the Neumann cases.

proposed transition presented below.

Figure 6.18 shows a very good agreement between numerical results indicated by symbols □, ◇,★ and ◯ and analytical results shown as curves, for all single bubble simulations for $\bar{\rho}$ = 1000 except for $\bar{\mu}$ = 50.

For other density ratios results ($\bar{\rho}$ = (10^{-3} and 1)), the analytical results do not agree with the numerical simulation results. Indeed, convective terms neglected for the the liquid flow have a stronger effect. Flow inside the bubble is obtained by solving the Navier-Stokes equations, while the outside flow is obtained by solving the Stokes equation. This means that the convective terms in the external flow are neglected. Since the normal stress jump due to Stokes flow is zero, only convective terms are responsible of for the jump. For this reason, the analytical solution is good only when bubble convective terms are dominant over outside convective terms. This corresponds to $\rho_g U_b^2 >> \rho_l U_b^2$, meaning $\bar{\rho} >> 1$. In the case where $\bar{\rho} \leq 1$, the main factors influencing the critical Bond number are the Morton number and the void fraction. The numerical results are in agreement with the boundary proposed by Bhaga and Weber (1981) for the transition from spherical to ellipsoidal bubbles.

For higher void fractions, the bubble train modelled with Neumann boundary conditions is more representative of the physics. As shown in Section 6.2.2, Stokes terms have no

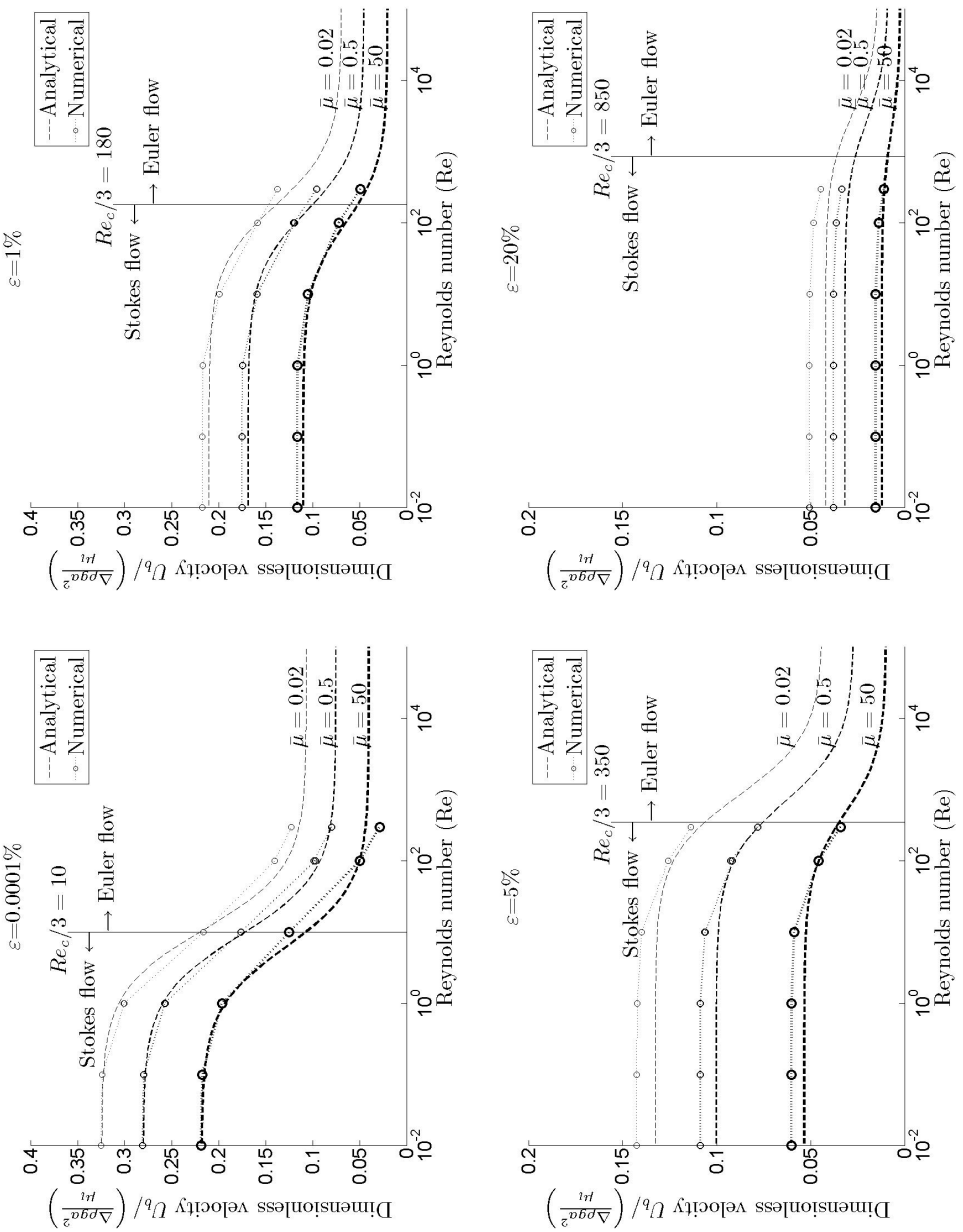

Figure 6.17 Numerical and Correlation (cf. Eq. (6.111)) comparison of dimensionless terminal velocity for different void fraction for Dirichlet case.

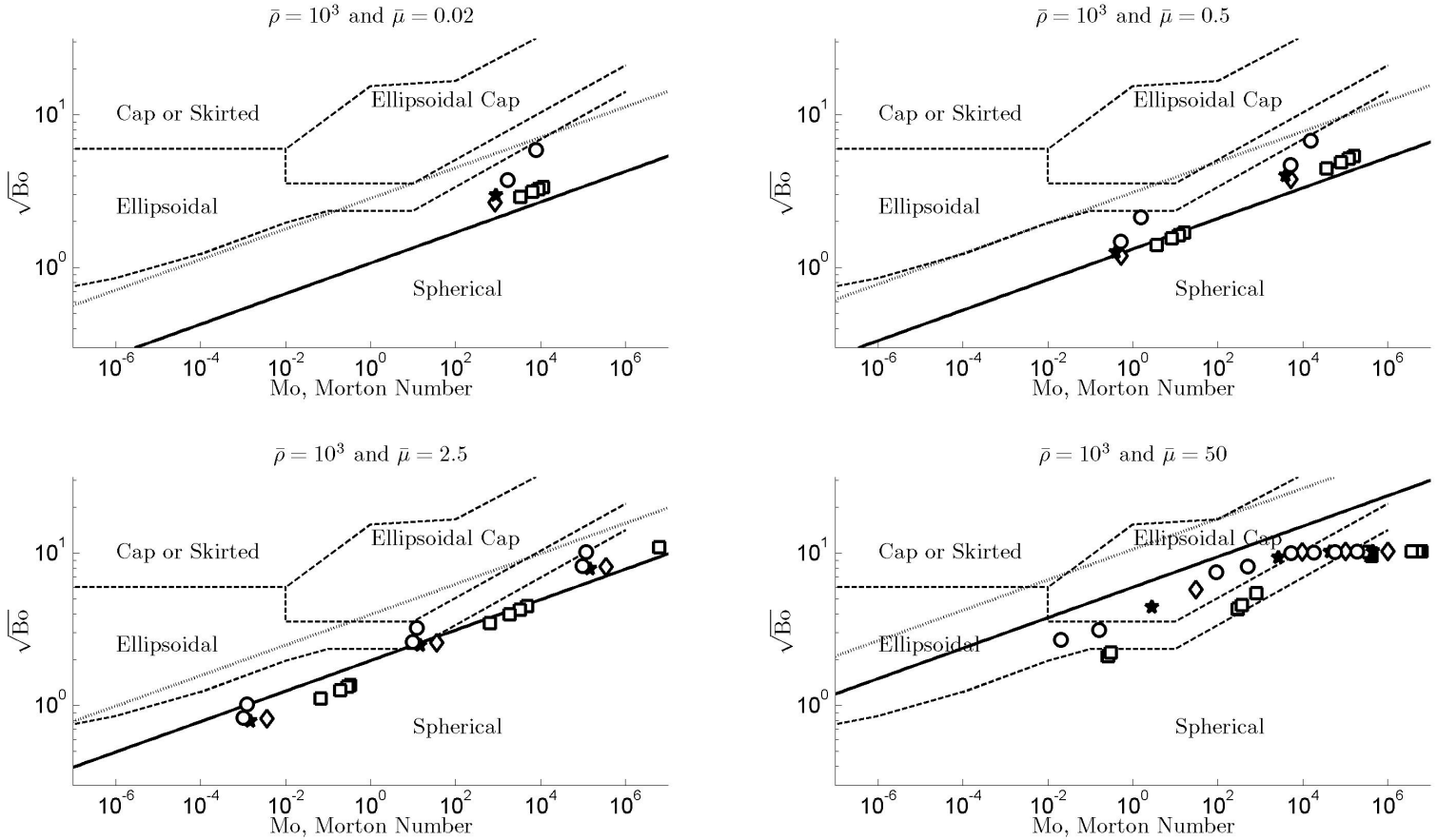

Figure 6.18 Maximum Bond number *Bo* where bubbles remains spherical for $\bar{\rho}$ =1000 vs. Morton number (*Mo*) and void fraction (ε) for different viscosity ratio ($\bar{\mu}$) for single bubble case. □ : Numerical results for ε < 5%, ◇ : Numerical results for 5% ≤ ε < 20% ★ : Numerical results for 20% ≤ ε < 40%, ◯ : Numerical results for ε ≥ 40% −− : Transition proposed by Bhaga, – : Transition correlation for ε = 0% cf. Eq. (6.113), ··· : Transition correlation for ε = 50% cf. Eq. (6.113)

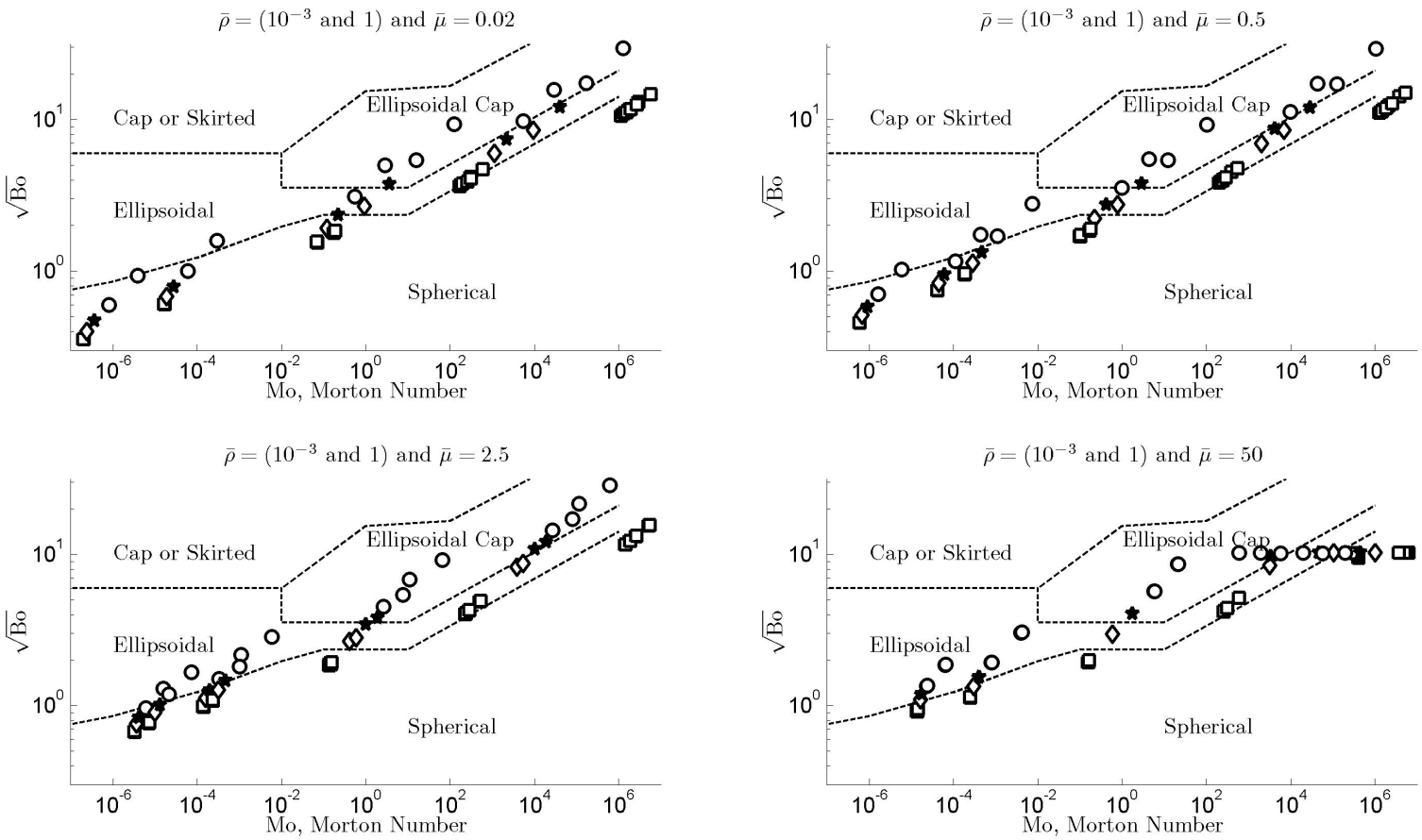

Figure 6.19 Maximum Bond number Bo where bubbles remains spherical for $\bar{\rho} \leq 1$ vs. Morton number (Mo) and void fraction (ε) for different viscosity ratio ($\bar{\mu}$) for single bubble case. □ : Numerical results for $\varepsilon < 5\%$, ◇ : Numerical results for $5\% \leq \varepsilon < 20\%$ ★ : Numerical results for $20\% \leq \varepsilon < 40\%$, ◯ : Numerical results for $\varepsilon \geq 40\%$ −− : Transition proposed by Bhagha.

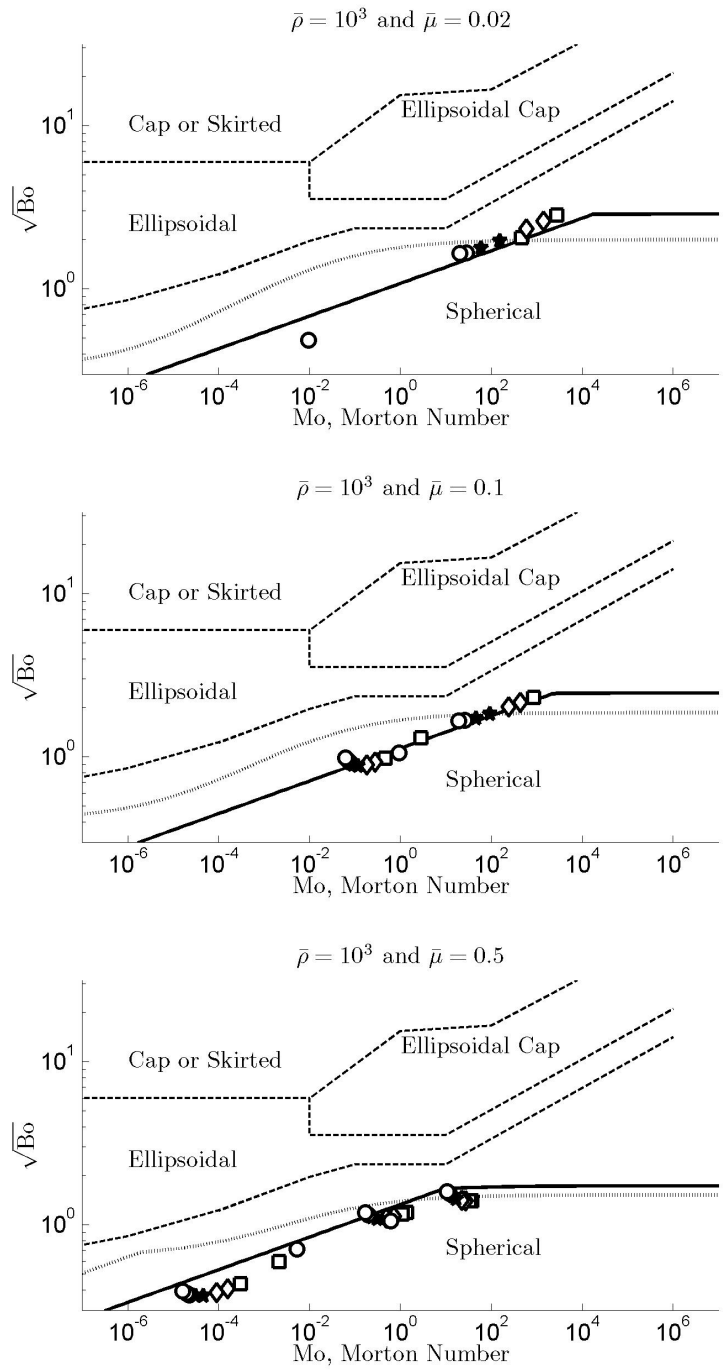

Figure 6.20 Maximum Bond number *Bo* where bubbles remains spherical for $\bar{\rho}$ =1000 vs. Morton number and void fraction for different viscosity ratio for bubble train (Neumann case) □ : Numerical results for $\varepsilon < 5\%$, ♢ : Numerical results for $5\% \leq \varepsilon < 20\%$ ★ : Numerical results for $20\% \leq \varepsilon < 40\%$, ◯ : Numerical results for $\varepsilon \geq 40\%$ −− : Transition proposed by Bhagha, − : Transition correlation for $\varepsilon = 0\%$ cf. Eq. (6.113), ··· : Transition correlation for $\varepsilon = 50\%$ cf. Eq. (6.113).

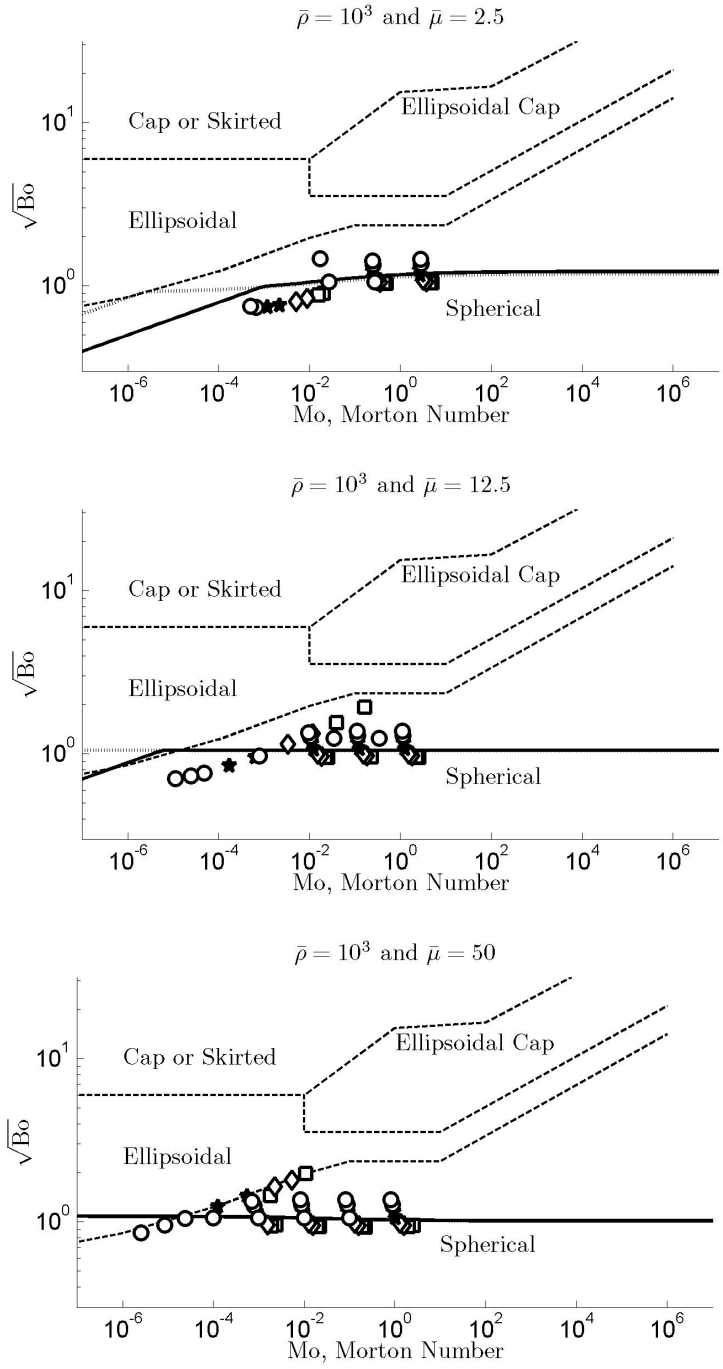

Figure 6.21 Maximum Bond number *Bo* where bubbles remains spherical for $\bar{\rho}$ =1000 vs. Morton number and void fraction for different viscosity ratio for bubble train (Neumann case) □ : Numerical results for $\varepsilon < 5\%$, ♢ : Numerical results for $5\% \leq \varepsilon < 20\%$ ★ : Numerical results for $20\% \leq \varepsilon < 40\%$, ◯ : Numerical results for $\varepsilon \geq 40\%$ −− : Transition proposed by Bhagha, − : Transition correlation for $\varepsilon = 0\%$ cf. Eq. (6.113), ··· : Transition correlation for $\varepsilon = 50\%$ cf. Eq. (6.113).

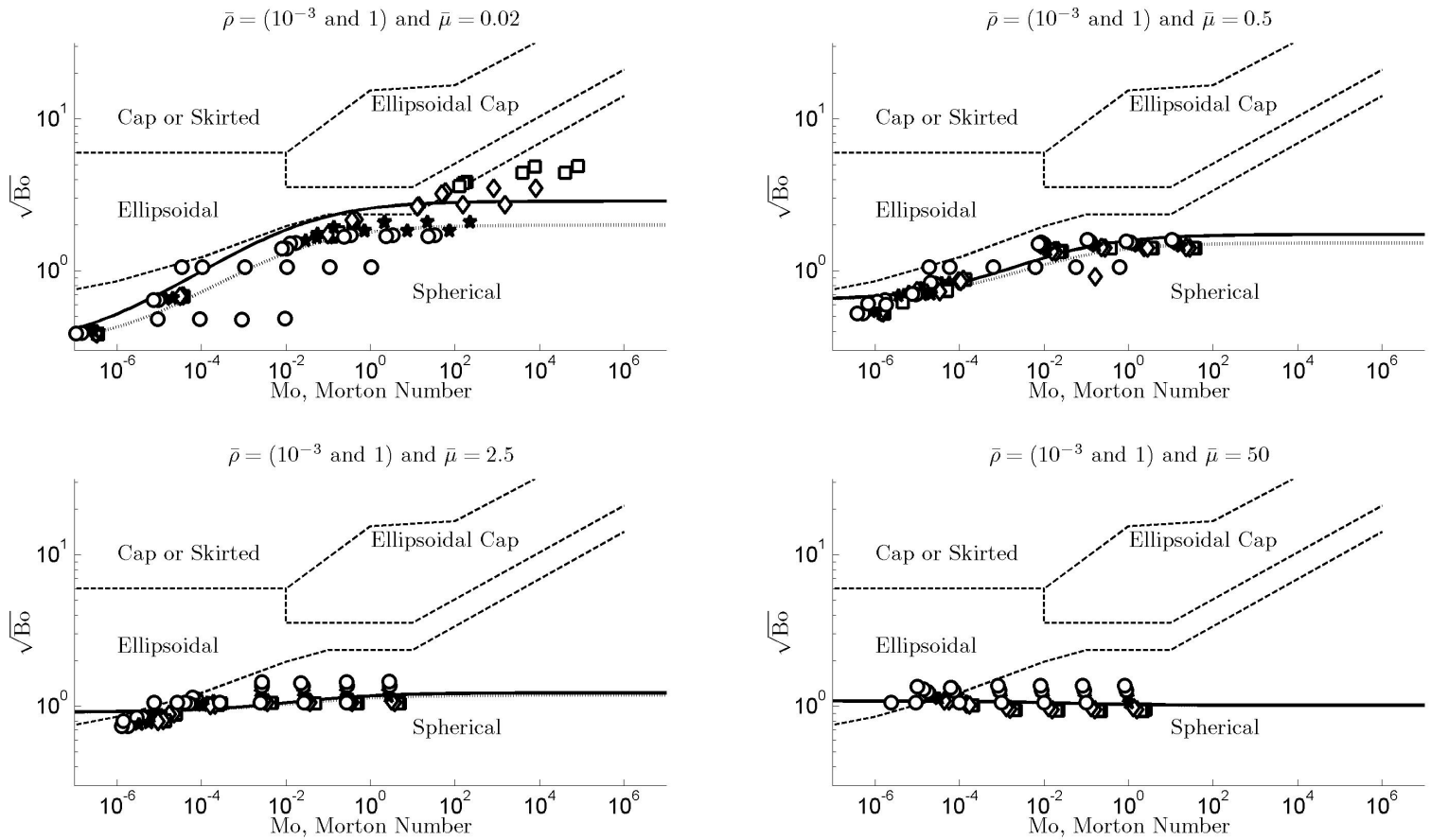

Figure 6.22 Maximum Bond number *Bo* where bubbles remains spherical for $\bar{\rho} \leq 1$ vs. Morton number and void fraction for different viscosity ratio for bubble train (Neumann case) □ : Numerical results for $\varepsilon < 5\%$, ◇ : Numerical results for $5\% \leq \varepsilon < 20\%$ ★ : Numerical results for $20\% \leq \varepsilon < 40\%$, ◯ : Numerical results for $\varepsilon \geq 40\%$ −− : Transition proposed by Bhagha, − : Transition correlation for $\varepsilon = 0\%$ cf. Eq. (6.113), ··· : Transition correlation for $\varepsilon = 50\%$ cf. Eq. (6.113).

destabilization effect on the spherical shape. The model presented before in equation (6.87) represents the destabilization effect by inner convective terms. This model does not take into account the outer convective terms. Therefore we have seek and found a correlation corresponding to destabilization by the outer convective terms. The new proposed relation is the minimum Bond number between these two destabilizations. Comparison between the correlation and numerical results are presented in Figures 6.20, 6.21 and 6.22

$$\begin{aligned}
&\text{Destabilization by inner convective terms cf. :Eq. (6.87)}\\
&\sqrt{Bo_g} = \left(\frac{1300}{\bar{\rho}}\right)^{1/5}\left(\frac{2+3\varepsilon^{5/3}+\bar{\mu}(3-3\varepsilon^{5/3})}{2-5\varepsilon+3\varepsilon^{5/3}}\right)^{2/5} Mo^{1/10}\\
&\text{Proposed correlation for destabilization by outer convective terms :}\\
&\sqrt{Bo_l} = \sqrt{\frac{\frac{1+12\bar{\mu}}{12+10\bar{\mu}} + 4Mo^{0.38}\frac{30+20\bar{\mu}}{3.2+8\varepsilon+20\bar{\mu}}}{1+4Mo^{0.38}}}\\
&\sqrt{Bo} = \min\left(\sqrt{Bo_g}, \sqrt{Bo_l}\right)
\end{aligned} \tag{6.113}$$

The destabilization effect due to inner flow is larger than the destabilization effect by outer flow only in the case where the density ratio is large enough ($\bar{\rho} = 1000$). We clearly see the transition in Figures 6.20 and 6.21. The destabilization by the inner flow (*e.g. convective terms*) is the straight line with a defendant in $Mo^{1/10}$. It correspond to the left part of the new proposed transition. For larger viscosity ratios, the destabilization by the outer flow overcomes the destabilization by the inner flow at smaller Morton number. Smaller viscosity ratios correspond to condition closer to free slip and consequently higher kinetic energy inside the bubbles. A higher internal kinetic energy explain why the destabilization effect due to inner flow have a stronger effect.

Surrounding bubbles has a strong effect on the normal stress jump. Indeed the comparison between the single bubble case and bubble train case shows that the wake of the preceding bubbles destabilize the spherical shape. The Bhaga and Weber (1981) transition is the transition for zero void fraction ($\varepsilon = 0$). The new proposed correlation was not able to reach Bhaga and Weber (1981) transition for ($\varepsilon = 0$) and consequently remains only true if the void fraction is greater that 1% ($\varepsilon > 0.01$).

6.4 Conclusion

This paper propose a relation for the drag coefficient of spherical bubbles or droplets for Reynold numbers, Re, less than 300, void fractions ε up to 50%, viscosity and density ratios

$(\bar{\mu}, \bar{\rho})$ between 10^{-3} and 10^{3}. For simplicity gas has been used to described the fluid in the dispersed phase. However, considering ratios of density and viscosity studied, liquid droplets are also taken into account in the new relations proposed in the paper. For practical cases, only solid spheres are able to reach Reynolds numbers consequently larger than 1 000 while remaining spherical. The proposed relations is then useful for all fluid-fluid cases.

The limit of a spherical shape can be deduced when the proposed drag coefficient is equal to the C_D for the non spherical bubbles proposed by Zuber and Hench (1962) or using the normal stress jump.

We have proposed a correction with void fraction as follow:

$$
\begin{aligned}
&\text{Spherical Bubble}\\
&C_D = \frac{16}{Re}\left(1 + \frac{2\left(\frac{2+3\bar{\mu}}{2+2\bar{\mu}}\right)^2}{1+\frac{Re_c}{Re}}\right)\frac{1-\varepsilon}{(1-\varepsilon^{1/3})^3}\frac{P_1(\varepsilon)+\bar{\mu}P_2(\varepsilon)}{P_3(\varepsilon)+\bar{\mu}P_4(\varepsilon)}\\
&\text{with :}\\
&P_1(\varepsilon) = 4 + 6\varepsilon^{5/3}\\
&P_2(\varepsilon) = 6 - 6\varepsilon^{5/3}\\
&P_3(\varepsilon) = 4 + 6\varepsilon^{1/3} + 6\varepsilon^{2/3} + 4\varepsilon\\
&P_4(\varepsilon) = 4 + 3\varepsilon^{1/3} - 3\varepsilon^{2/3} - 4\varepsilon\\
&\text{Cap or Skirted Bubble}\\
&C_D = 0.57\sqrt{\frac{Bo}{1-\varepsilon}}
\end{aligned}
\tag{6.114}
$$

More work remains to be done to evaluate the drag coefficient for larger bubbles. However, this relation shows that the slip ratio is very small for bubbly flow. Moreover, in almost all practical cases of bubbly flow, the flow around a bubble can be considered as Stokes flow. The void fraction, ε, has a major effect on the drag essentially through confinement. The proposed relation can be used to construct a two-phase flow model for bubbly flow.

C_D, C_L, turbulence, viscous terms, etc. all depend on Re, ε, Bo, Mo, $\bar{\rho}$, $\bar{\mu}$ and can be analytically modeled with Stokes flow. The classical two-phase flow model uses the well-known Ishii and Zuber (1979) and Harmathy (1960) relations. The present work proposes an improvement of the closure relation for the drag coefficient (C_D) compared to previous works. Previous work deduced forces on bubbles from potential flow, which as we have shown is not realistic. In Stokes flow the variation of forces due to void fraction have a much stronger effect than in Euler flow (previous model). The dependence on interface forces with void fraction has an utmost importance because they drive variation of void fraction. Void fraction variation and flow pattern are known to be the major cause on severe fluid structure

interaction in two-phase flow.

The limit for which bubbles (or droplets) can be considered spherical, based on the normal stress jump correlation, can be evaluated using the proposed relation for void fraction greater than 1%.

$$\begin{aligned}
&\text{Destabilization by inner convective terms :}\\
&\sqrt{Bo_g} = \left(\frac{1300}{\bar{\rho}}\right)^{1/5}\left(\frac{2+3\varepsilon^{5/3}+\bar{\mu}(3-3\varepsilon^{5/3})}{2-5\varepsilon+3\varepsilon^{5/3}}\right)^{2/5} Mo^{1/10}\\
&\text{Destabilization by outer convective terms :}\\
&\sqrt{Bo_l} = \sqrt{\frac{\dfrac{1+12\bar{\mu}}{12+10\bar{\mu}} + 4Mo^{0.38}\dfrac{30+20\bar{\mu}}{3.2+8\varepsilon+20\bar{\mu}}}{1+4Mo^{0.38}}}\\
&\sqrt{Bo} = \min\left(\sqrt{Bo_g}, \sqrt{Bo_l}\right)
\end{aligned} \tag{6.115}$$

For a single bubble in an infinite liquid domain and for $\bar{\rho} << 1000$, the transition proposed by Bhaga and Weber (1981) remains better. However, if $\bar{\rho} \geq 1000$, the transition proposed by the destabilization by inner convective terms is still very good.

As Stokes flows represents very accurately the flow around bubbles for void fraction higher than 1%, this flow is consequently laminar. One therefore arrives at the conclusion that two-phase turbulence cannot be attributed to classical turbulence as in single phase flow. The flow in the continuous phase should be effectively considered as a film flow in which classical turbulence cannot durably develop. Two-phase turbulence is then essentially due to bubble passage, and can be analytically modelled. Therefore a numerical model of space averaged two-phase flow, that implicitly takes into account turbulence effects can be realistically achieved.

6.5 Boundary layer and wake correction for Euler flow

6.5.1 Boundary layer correction

Following the approach of Moore (1963) and adding the influence of surrounding bubbles and internal flow, a complete solution is sought as:

$$\begin{aligned}
u_{rl} &= U_{rl} + u^*_{rl}\\
u_{\theta l} &= U_{\theta l} + u^*_{\theta l}\\
P_l &= P_{\infty l} + p^*_l
\end{aligned} \tag{6.116}$$

With $U_{rl}, U_{\theta l}$ and $P_{\infty l}$ solution of the Euler equation:

$$\begin{aligned} U_{rl} &= -U_b\left(1-\tfrac{a^3}{r^3}\right)\cos(\theta) \\ U_{\theta l} &= U_b\left(1+\tfrac{a^3}{2r^3}\right)\sin(\theta) \end{aligned} \tag{6.117}$$

The Navier-Stokes equations are:

$$\begin{aligned} \nabla\cdot\vec{u}_l &= 0 && (a) \\ \rho\vec{u}_l\nabla\vec{u}_l &= -\nabla P_l + \mu\Delta\vec{u}_l && (b) \end{aligned} \tag{6.118}$$

Introducing the solution form (6.116), we have

$$\begin{aligned} \nabla\cdot(\vec{U}_l+\vec{u}_l^*) &= 0 && (a) \\ \rho(\vec{U}_l+\vec{u}_l^*)\nabla(\vec{U}_l+\vec{u}_l^*) &= -\nabla(P_\infty+p_l^*)+\mu\Delta(\vec{U}_l+\vec{u}_l^*) && (b) \end{aligned} \tag{6.119}$$

which leads to the perturbation equations

$$\begin{aligned} \nabla\cdot\vec{u_l^*} &= 0 && (a) \\ \rho_l\vec{u_l^*}\nabla\vec{U}_l+\rho_l\vec{U}_l\nabla\vec{u_l^*}+\underbrace{\rho_l\vec{u_l^*}\nabla\vec{u_l^*}}_{\simeq 0 \text{ because } u_l^*<<U_l} &= -\nabla p_l^*+\mu_l\Delta(\vec{U}_l+\vec{u}_l^*) && (b) \end{aligned} \tag{6.120}$$

In terms of the radial and tangential velocity the equations are

$$\frac{\partial u_{rl}^*}{\partial r}+\frac{2u_{rl}^*}{r}+\frac{1}{r\sin(\theta)}\frac{\partial}{\partial\theta}(u_{\theta l}^*\sin\theta) = 0 \qquad (a)$$

$$\begin{aligned} \rho\left(\tfrac{U_{\theta l}}{r}\tfrac{\partial u_{rl}^*}{\partial\theta}+\tfrac{u_{\theta l}^*}{r}\tfrac{\partial U_{rl}}{\partial\theta}+U_{rl}\tfrac{\partial u_{rl}^*}{\partial r}+u_{rl}^*\tfrac{\partial U_{rl}}{\partial r}-2\tfrac{U_{\theta l}u_{\theta l}^*}{r}\right) &= -\tfrac{\partial p^*}{\partial r}+V_{rl}+V_{rl}^* && (b1) \\ \rho\left(\tfrac{U_{\theta l}}{r}\tfrac{\partial u_{\theta l}^*}{\partial\theta}+\tfrac{u_{\theta l}^*}{r}\tfrac{\partial U_{\theta l}}{\partial\theta}+U_{rl}\tfrac{\partial u_{\theta l}^*}{\partial r}+u_{rl}^*\tfrac{\partial U_{\theta l}}{\partial r}+\tfrac{U_{rl}u_{\theta l}^*}{r}+\tfrac{u_{rl}^*U_{\theta l}}{r}\right) &= -\tfrac{1}{r}\tfrac{\partial p^*}{\partial\theta}+V_{\theta l}+V_{\theta l}^* && (b2) \end{aligned} \tag{6.121}$$

where V_{rl},V_{rl}^*,$V_{\theta l}$,$V_{\theta l}^*$ are the following viscous terms given by :

$$\begin{aligned} V_{rl} &= \mu_l\left[\tfrac{1}{r^2}\tfrac{\partial}{\partial r}\left(r^2\tfrac{\partial U_{rl}}{\partial r}\right)+\tfrac{1}{r^2\sin\theta}\tfrac{\partial}{\partial\theta}\left(\sin\theta\tfrac{\partial U_{rl}}{\partial\theta}\right)-\tfrac{2}{r^2}U_{rl}-\tfrac{2}{r^2\sin\theta}\tfrac{\partial}{\partial\theta}\left(\sin\theta U_{\theta l}\right)\right] \\ V_{rl}^* &= \mu_l\left[\tfrac{1}{r^2}\tfrac{\partial}{\partial r}\left(r^2\tfrac{\partial u_{rl}^*}{\partial r}\right)+\tfrac{1}{r^2\sin\theta}\tfrac{\partial}{\partial\theta}\left(\sin\theta\tfrac{\partial u_{rl}^*}{\partial\theta}\right)-\tfrac{2}{r^2}u_{rl}^*-\tfrac{2}{r^2\sin\theta}\tfrac{\partial}{\partial\theta}\left(\sin\theta u_{\theta l}^*\right)\right] \\ V_{\theta l} &= \mu_l\left[\tfrac{1}{r^2}\tfrac{\partial}{\partial r}\left(r^2\tfrac{\partial U_{\theta l}}{\partial r}\right)+\tfrac{1}{r^2}\tfrac{\partial}{\partial\theta}\left(\tfrac{1}{\sin\theta}\tfrac{\partial\sin\theta U_{\theta l}}{\partial\theta}\right)+\tfrac{2}{r^2}\tfrac{\partial U_{rl}}{\partial\theta}\right] \\ V_{\theta l}^* &= \mu_l\left[\tfrac{1}{r^2}\tfrac{\partial}{\partial r}\left(r^2\tfrac{\partial u_{\theta l}^*}{\partial r}\right)+\tfrac{1}{r^2}\tfrac{\partial}{\partial\theta}\left(\tfrac{1}{\sin\theta}\tfrac{\partial\sin\theta u_{\theta l}^*}{\partial\theta}\right)+\tfrac{2}{r^2}\tfrac{\partial u_{rl}^*}{\partial\theta}\right] \end{aligned} \tag{6.122}$$

Defining δ as the typical dimensionless boundary layer thickness, where inertia is equivalent to viscous forces yields:

$$\delta^2 = \frac{\mu}{\rho U_b a} = \frac{2}{Re} \tag{6.123}$$

In order to have a not null perturbation, mass conservation equation (6.121-(a)) impose to have tangential and radial variation of the same magnitude yielding to $\sqrt{Re}u^*_{rl} \simeq u^*_{\theta l}$. Similarly to Moore work's, we express next the equations using :

$$\begin{aligned} r - a &= a\delta\bar{y} \\ dr &= a\delta d\bar{y} \\ U_{rl} &= U_b\delta\bar{U}_{rl} \\ U_{\theta l} &= U_b\bar{U}_{\theta l} \\ u^*_{rl} &= U_b\delta^2\bar{u}^*_{rl} \\ u^*_{\theta l} &= U_b\delta\bar{u}^*_{\theta l} \\ p^* &= \rho_l U_b^2\bar{p}^* \end{aligned} \tag{6.124}$$

Equation (6.121) therefore becomes:

$$\begin{aligned} \frac{\partial\bar{u}^*_{rl}}{\partial\bar{y}}\sin\theta + \frac{2\delta\bar{u}^*_{rl}\sin\theta}{\delta\bar{y}+1} + \frac{1}{\delta\bar{y}+1}\frac{\partial}{\partial\theta}(\bar{u}^*_{\theta l}\sin\theta) &= 0 && (a) \\ \frac{\delta\bar{U}_{\theta l}}{\delta\bar{y}+1}\frac{\partial\bar{u}^*_{rl}}{\partial\theta} + \frac{\delta\bar{u}^*_{\theta l}}{\delta\bar{y}+1}\frac{\partial\bar{U}_{rl}}{\partial\theta} + \delta\bar{U}_{rl}\frac{\partial\bar{u}^*_{rl}}{\partial\bar{y}} + \delta\bar{u}^*_{rl}\frac{\partial\bar{U}_{rl}}{\partial\bar{y}} - \frac{2\bar{U}_{\theta l}\bar{u}^*_{\theta l}}{\delta\bar{y}+1} &= -\frac{1}{\delta^2}\frac{\partial\bar{p}^*}{\partial\bar{y}} + \bar{V}_{rl} + \bar{V}^*_{rl} && (b1) \\ \frac{\bar{U}_{\theta l}}{\delta\bar{y}+1}\frac{\partial\bar{u}^*_{\theta l}}{\partial\theta} + \frac{\bar{u}^*_{\theta l}}{\delta\bar{y}+1}\frac{\partial\bar{U}_{\theta l}}{\partial\theta} + \bar{U}_{rl}\frac{\partial\bar{u}^*_{\theta l}}{\partial\bar{y}} + \bar{u}^*_{rl}\frac{\partial\bar{U}_{\theta l}}{\partial\bar{y}} + \frac{\delta\bar{U}_{rl}\bar{u}^*_{\theta l}}{\delta\bar{y}+1} + \frac{\delta\bar{u}^*_{rl}\bar{U}_{\theta l}}{\delta\bar{y}+1} &= -\frac{1}{\delta^2\bar{y}+\delta}\frac{\partial\bar{p}^*}{\partial\theta} + \bar{V}_{\theta l} + \bar{V}^*_{\theta l} && (b2) \end{aligned} \tag{6.125}$$

where the viscous terms $\bar{V}_{rl} = \dfrac{aV_{rl}}{\delta\rho U_b^2}$ and $\bar{V}_{\theta l} = \dfrac{aV_{\theta l}}{\delta\rho U_b^2}$, $\left(\dfrac{\mu}{\delta^2\rho U_b a} = 1\right)$ are given by :

$$\begin{aligned} \bar{V}_{rl} &= \frac{1}{(\delta\bar{y}+1)^2}\left[\frac{\partial}{\partial\bar{y}}\left((\delta\bar{y}+1)^2\frac{\partial\bar{U}_{rl}}{\partial\bar{y}}\right) + \frac{\delta^2}{\sin\theta}\frac{\partial}{\partial\theta}\left(\sin\theta\frac{\partial\bar{U}_{rl}}{\partial\theta}\right) - 2\delta^2\bar{U}_{rl} - \frac{2\delta}{\sin\theta}\frac{\partial}{\partial\theta}\left(\sin\theta\bar{U}_{\theta l}\right)\right] \\ \bar{V}^*_{rl} &= \frac{1}{(\delta\bar{y}+1)^2}\left[\delta\frac{\partial}{\partial\bar{y}}\left((\delta\bar{y}+1)^2\frac{\partial\bar{u}^*_{rl}}{\partial\bar{y}}\right) + \frac{\delta^3}{\sin\theta}\frac{\partial}{\partial\theta}\left(\sin\theta\frac{\partial\bar{u}^*_{rl}}{\partial\theta}\right) - 2\delta^3\frac{\bar{u}^*_{rl}}{\sqrt{Re}} - \frac{2\delta^2}{\sin\theta}\frac{\partial}{\partial\theta}\left(\sin\theta\bar{u}^*_{\theta l}\right)\right] \\ \bar{V}_{\theta l} &= \frac{1}{(\delta\bar{y}+1)^2}\left[\frac{\partial}{\partial\bar{y}}\left((\delta\bar{y}+1)^2\frac{\partial\bar{U}_{\theta l}}{\partial\bar{y}}\right) + \delta\frac{\partial}{\partial\theta}\left(\frac{1}{\sin\theta}\frac{\partial\sin\theta\bar{U}_{\theta l}}{\partial\theta}\right) + \delta^2\frac{\partial\bar{U}_{rl}}{\partial\theta}\right] \\ \bar{V}^*_{\theta l} &= \frac{1}{(\delta\bar{y}+1)^2}\left[\frac{\partial}{\partial\bar{y}}\left((\delta\bar{y}+1)^2\frac{\partial\bar{u}^*_{\theta l}}{\partial\bar{y}}\right) + \delta^2\frac{\partial}{\partial\theta}\left(\frac{1}{\sin\theta}\frac{\partial\sin\theta\bar{u}^*_{\theta l}}{\partial\theta}\right) + \delta^3\frac{\partial\bar{u}^*_{rl}}{\partial\theta}\right] \end{aligned} \tag{6.126}$$

From Euler solution, cf. equation (6.117), the magnitudes of the different dimensionless parameters are:

$$\begin{aligned}
\bar{y} &= \frac{r-a}{\delta a} && \simeq 1, \\
\bar{U}_{rl} &= -\frac{1}{\delta}\left(1-\frac{1}{(\delta\bar{y}+1)^3}\right)\cos\theta && \simeq -3\bar{y}\cos\theta \simeq 1, \\
\frac{\partial \bar{U}_{rl}}{\partial \bar{y}} &= -\frac{3}{(\delta\bar{y}+1)^4}\cos\theta && \simeq -3\cos\theta \simeq 1, \\
\frac{\partial^2 \bar{U}_{rl}}{\partial \bar{y}^2} &= -\frac{12\delta}{(\delta\bar{y}+1)^5}\cos\theta && \simeq -12\delta\cos\theta \simeq \delta, \\
\bar{U}_{\theta l} &= \left(1+\frac{1}{2(\delta\bar{y}+1)^3}\right)\sin\theta && \simeq \tfrac{3}{2}\sin\theta \simeq 1, \\
\frac{\partial \bar{U}_{\theta l}}{\partial \bar{y}} &= -\frac{3\delta}{2(\delta\bar{y}+1)^4}\sin\theta && \simeq -\tfrac{3\delta}{2}\sin\theta \simeq \delta, \\
\frac{\partial^2 \bar{U}_{\theta l}}{\partial \bar{y}^2} &= \frac{6\delta^2}{(\delta\bar{y}+1)^5}\sin\theta && \simeq 6\delta^2\sin\theta \simeq \delta^2 \\
\bar{u}^*_{rl} &\simeq 1 \\
\bar{u}^*_{\theta l} &\simeq 1
\end{aligned} \tag{6.127}$$

The magnitude of the pressure can be evaluate from the equation (6.125 -(b2)). When we reach the second a stagnation point ($\theta \to \pi$), we need to have $u^*_{\theta l} \simeq 0$. Equation (6.125 -(b2)) and each terms magnitude indicated under brace becomes:

$$\underbrace{\bar{u}^*_{rl}\left(\frac{\partial \bar{U}_{\theta l}}{\partial \bar{y}}+\frac{\delta \bar{U}_{\theta l}}{\delta\bar{y}+1}\right)}_{\delta} \simeq -\frac{1}{\delta^2\bar{y}+\delta}\frac{\partial \bar{p}^*}{\partial\theta}+\bar{V}_{\theta l}+\bar{V}^*_{\theta l} \tag{6.128}$$

With the viscous terms and its magnitude:

$$\bar{V}_{\theta l}+\bar{V}^*_{\theta l} \simeq \underbrace{\frac{\partial}{\partial\bar{y}}\left((\delta\bar{y}+1)^2\frac{\partial \bar{U}_{\theta l}}{\partial\bar{y}}\right)}_{\delta^2}+\underbrace{\delta\frac{\partial}{\partial\theta}\left(\frac{1}{\sin\theta}\frac{\partial \sin\theta \bar{U}_{\theta l}}{\partial\theta}\right)}_{\delta}+\underbrace{\delta^2\frac{\partial \bar{U}_{rl}}{\partial\theta}}_{\delta^2}+\underbrace{\delta^3\frac{\partial \bar{u}^*_{rl}}{\partial\theta}}_{\delta^3} \tag{6.129}$$

We can certainly deduce $-\dfrac{1}{\delta^2\bar{y}+\delta}\dfrac{\partial \bar{p}^*}{\partial\theta} \simeq \delta$. Considering $\delta << 1$,the foregoing order of magnitude analysis allow us to neglect some terms so the equation (6.125) becomes :

$$\begin{aligned}
\sin\theta\frac{\partial \bar{u}^*_{rl}}{\partial\bar{y}} + \frac{\partial}{\partial\theta}(\bar{u}^*_{\theta l}\sin\theta) &= 0 && (a)\\
-2\bar{U}_{\theta l}\bar{u}^*_{\theta l} &= \frac{1}{\delta^2}\frac{\partial \bar{p}^*}{\partial\bar{y}} && (b1)\\
\bar{U}_{\theta l}\frac{\partial \bar{u}^*_{\theta l}}{\partial\theta} + \bar{u}^*_{\theta l}\frac{\partial \bar{U}_{\theta l}}{\partial\theta} + \bar{U}_{rl}\frac{\partial \bar{u}^*_{\theta l}}{\partial\bar{y}} &= \frac{\partial^2 \bar{u}^*_{\theta l}}{\partial\bar{y}^2} && (b2)
\end{aligned} \tag{6.130}$$

Introducing $\bar{U}_{\theta l}$ and $\bar{U}_{rll}$,solution of averaged Euler flow (cf. Eq. (6.117)), we obtain:

$$\begin{aligned}
\sin\theta\frac{\partial \bar{u}^*_{rl}}{\partial\bar{y}} + \frac{\partial}{\partial\theta}(\bar{u}^*_{\theta l}\sin\theta) &= 0 && (a)\\
-6\bar{u}^*_{\theta l}\sin\theta &= Re\frac{\partial \bar{p}^*}{\partial\bar{y}} && (b1)\\
\frac{3}{2}\left[\frac{\partial \bar{u}^*_{\theta l}}{\partial\theta}\sin\theta + \bar{u}^*_{\theta l}\cos\theta - 2\bar{y}\frac{\partial \bar{u}^*_{\theta l}}{\partial\bar{y}}\cos\theta\right] &= \frac{\partial^2 \bar{u}^*_{\theta l}}{\partial\bar{y}^2} && (b2)
\end{aligned} \tag{6.131}$$

The previous equation (6.125)-(b2) can be rewritten as:

$$\frac{3}{2}\left[\frac{\partial \bar{u}^*_{\theta l}\sin\theta}{\partial\theta} - 2\bar{y}\frac{\partial \bar{u}^*_{\theta l}}{\partial\bar{y}}\cos\theta\right] = \frac{\partial^2 \bar{u}^*_{\theta l}}{\partial\bar{y}^2} \tag{6.132}$$

As suggested by Moore, we search for a solution in the form:

$$\bar{u}^*_{\theta l} = \chi(\theta)^{1/2}F(\tau)\sin\theta, \text{ with } \tau = \frac{\bar{y}}{2\chi(\theta)^{1/2}} \tag{6.133}$$

where χ will represent the boundary layer thickness. The various derivatives needed in equation (6.132) are

$$\begin{aligned}
\frac{\partial \bar{u}^*_{\theta l}\sin\theta}{\partial\theta} &= \frac{\chi'}{2\chi^{1/2}}F\sin^2\theta - \frac{\bar{y}\chi'}{4\chi}F'\sin^2\theta + 2\chi^{1/2}F\sin\theta\cos\theta\\
\frac{\partial \bar{u}^*_{\theta l}}{\partial\bar{y}} &= \frac{F'\sin\theta}{2}\\
\frac{\partial^2 \bar{u}^*_{\theta l}}{\partial\bar{y}^2} &= \frac{F''\sin\theta}{4\chi^{1/2}}
\end{aligned} \tag{6.134}$$

Finally, equation (6.132) becomes :

$$\begin{aligned}
\tfrac{3}{2}\left[\tfrac{\chi'}{2\chi^{1/2}}F\sin^2\theta - \tfrac{\bar{y}\chi'}{4\chi}F'\sin^2\theta + 2\chi^{1/2}F\sin\theta\cos\theta - \bar{y}F'\sin\theta\cos\theta\right] &= \tfrac{F''\sin\theta}{4\chi^{1/2}} \\
3\left[\left(\chi'\sin\theta + 4\chi\cos\theta\right)F - \left(\tfrac{\chi'}{2\chi^{1/2}}\sin\theta + 2\chi^{1/2}\cos\theta\right)\bar{y}F'\right] &= F'' \\
3\left(\chi'\sin\theta + 4\chi\cos\theta\right)\left[F - \tfrac{\bar{y}}{2\chi^{1/2}}F'\right] &= F''
\end{aligned} \tag{6.135}$$

The following function $F(\tau)$ can be shown to be a solution of equation (6.135) :

$$\begin{aligned}
F(\tau) &= \tfrac{D_1}{\sqrt{\pi}}e^{-\tau^2} + \tau\left(D_0 + D_1\ \mathrm{erf}(\tau)\right) \\
F - \tau F'(\tau) &= \tfrac{D_1}{\sqrt{\pi}}e^{-\tau^2} \\
F''(\tau) &= \tfrac{2D_1}{\sqrt{\pi}}e^{-\tau^2}
\end{aligned} \tag{6.136}$$

Introducing $F(\tau)$ above into equation (6.135) , we obtain the following equation for $\chi(\theta)$

$$\chi'\sin\theta + 4\chi\cos\theta = \frac{2}{3} \tag{6.137}$$

which can be integrated to give :

$$\chi(\theta) = \frac{1}{18}\left(\frac{\cos(3\theta) - 9\cos\theta + D_2}{\sin^4\theta}\right) \tag{6.138}$$

We can now deduce $\bar{u}^*_{rl}$ from the continuity equation (6.125)-(a) as detailed in the following

$$\begin{aligned}
\tfrac{\partial\bar{u}^*_{rl}}{\partial\bar{y}} &= -\tfrac{1}{\sin\theta}\tfrac{\partial}{\partial\theta}(\bar{u}^*_{\theta l}\sin\theta) \\
&= -\tfrac{\chi'}{2\chi^{1/2}}F\sin\theta + \tfrac{\bar{y}\chi'}{4\chi}F'\sin\theta - 2\chi^{1/2}F\cos\theta \\
&= -\tfrac{1}{2\chi^{1/2}}\left(\chi'\sin\theta + 4\chi\cos\theta\right)F + \tfrac{\bar{y}\chi'}{4\chi}F'\sin\theta \\
&= -\tfrac{2}{3\chi^{1/2}}\left[\tfrac{D_1}{\sqrt{\pi}}e^{-\frac{\bar{y}^2}{4\chi}} + \tfrac{\bar{y}}{2\chi^{1/2}}\left(D_0 + D_1\ \mathrm{erf}(\tfrac{\bar{y}}{2\chi^{1/2}})\right)\right] + \tfrac{\bar{y}\chi'}{4\chi}\left[D_0 + D_1\ \mathrm{erf}(\tfrac{\bar{y}}{2\chi^{1/2}})\right]\sin\theta \\
&= -\tfrac{2}{3\chi^{1/2}}\tfrac{D_1}{\sqrt{\pi}}e^{-\frac{\bar{y}^2}{4\chi}} + \bar{y}\tfrac{\chi'\sin\theta - \frac{4}{3}}{4\chi}\left(D_0 + D_1\ \mathrm{erf}(\tfrac{\bar{y}}{2\chi^{1/2}})\right) \\
&= -\tfrac{2\chi^{1/2}}{3}\left[\tfrac{\bar{y}}{2\chi^{1/2}}\cos\theta\left(D_0 + D_1\ \mathrm{erf}(\tfrac{\bar{y}}{2\chi^{1/2}})\right) + D_1\sqrt{\pi}e^{-\frac{\bar{y}^2}{4\chi}}\right]
\end{aligned} \tag{6.139}$$

Integrating the equation above one obtains

$$\begin{aligned}
\bar{u}^*_{rl} &= -\tfrac{2\chi}{3}\cos\theta\left[\left(\tfrac{\bar{y}^2}{4\chi} - \tfrac{1}{2} + \cos\theta\right)D_1\ \mathrm{erf}(\tfrac{\bar{y}}{2\chi^{1/2}}) + \tfrac{\bar{y}}{2\chi^{1/2}}\tfrac{D_1}{\sqrt{\pi}}e^{-\frac{\bar{y}^2}{4\chi}} + D_0\tfrac{\bar{y}^2}{4\chi}\right] + H(\theta) \\
&= -\tfrac{2\chi}{3}\left[\tau F(\tau)\cos\theta + \left(1 - \tfrac{\cos\theta}{2}\right)D_1\ \mathrm{erf}(\tau)\right] + H(\theta)
\end{aligned} \tag{6.140}$$

The boundary conditions are :

$$
\begin{aligned}
&r \to \infty \\
&\qquad u^*_{rl} \to 0 \qquad (1)\\
&\qquad u^*_{\theta l} \to 0 \qquad (2)\\
&r = a \\
&\qquad u_{rl} = u_{rg} = 0 \qquad (3)\\
&\qquad u_{\theta l} = u_{\theta g} \qquad (4)\\
&\qquad \mu_l \left(r \frac{\partial \left(\frac{u_{\theta l}}{r} \right)}{\partial r} + \frac{1}{r} \frac{\partial u_{rl}}{\partial \theta} \right) = \mu_g \left(r \frac{\partial \left(\frac{u_{\theta g}}{r} \right)}{\partial r} + \frac{1}{r} \frac{\partial u_{rg}}{\partial \theta} \right) \qquad (5)
\end{aligned}
\tag{6.141}
$$

Condition (6.141-(1)) leads to :

$$
\lim_{r \to \infty} u^*_{\theta l} = 0 \Rightarrow D_0 = -D_1 \text{ and } D_2 = 8 \tag{6.142}
$$

At the interface u_{rl} is null (cf. condition (6.141)-(3))

$$
u_{rl}(r = a) = 0 \Rightarrow H(\theta) = 0 \tag{6.143}
$$

At the interface location, tangential velocity are continuous (cf. condition (6.141)-(4))

$$
\begin{aligned}
&u_{\theta l} = u_{\theta g} \\
&\tfrac{3U_b}{2} \sin\theta + U_b \sqrt{\frac{2\chi}{Re}} F(0) \sin\theta = -2B_0 a^2 \sin(\theta) \\
&\tfrac{3}{2} + \sqrt{\frac{2\chi}{\pi Re}} D_1 = -\tfrac{2B_0 a^2}{U_b} \\
&\text{if } D_1 << \sqrt{\frac{Re}{\chi}} \Rightarrow B_0 a^2 = -\tfrac{3U_b}{4}
\end{aligned}
\tag{6.144}
$$

Continuity of the tangential stress at the interface location, (cf. condition (6.141)-(5)) gives :

$$
\begin{aligned}
\mu_l \frac{\partial \left(\frac{u_{\theta l}}{r} \right)}{\partial r} \Big|_{r=a} &= \mu_g \frac{\partial \left(\frac{u_{\theta g}}{r} \right)}{\partial r} \Big|_{r=a} \\
-\tfrac{3U_b}{a^2} - D_1 \tfrac{U_b}{2a^2} \left[1 + \sqrt{\frac{8\chi}{Re}} \right] &= -6\bar{\mu} B_0 = \bar{\mu} \tfrac{9U_b}{2a^2} \\
D_1 \left[1 + \sqrt{\frac{8\chi}{Re}} \right] &= -(6 + 9\bar{\mu}) \\
D_1 &= -(6 + 9\bar{\mu})
\end{aligned}
\tag{6.145}
$$

We have $D_1 << \sqrt{\frac{Re}{\chi}}$ only if $\bar{\mu} << \sqrt{\frac{Re}{\chi}}$.

Finally we have :

$$
\begin{aligned}
u_{rl} &= -U_b \left(1 - \tfrac{a^3}{r^3} \right) \cos(\theta) + u^*_{rl} \\
u_{\theta l} &= U_b \left(1 + \tfrac{a^3}{2r^3} \right) \sin(\theta) + u^*_{\theta l}
\end{aligned}
\tag{6.146}
$$

and the boundary layer correction is :

$$\begin{aligned} u^*_{\theta l} = &\quad U_b\sqrt{\frac{2}{Re}}\chi^{1/2}F(\tau)\sin\theta \\ u^*_{rl} = &\quad -\frac{U_b}{Re}\frac{4\chi}{3}\left[\tau F(\tau)\cos\theta - \left(1-\frac{\cos\theta}{2}\right)(6+9\bar{\mu})\ \mathrm{erf}(\tau)\right] \\ \text{with :}& \\ \tau = &\quad \sqrt{\frac{Re}{8\chi}}(\frac{r}{a}-1) \\ F(\tau) = &\quad -(6+9\bar{\mu})\left[\frac{1}{\sqrt{\pi}}e^{-\tau^2} - \tau\,(1-\ \mathrm{erf}(\tau))\right] \\ \chi(\theta) = &\quad \frac{1}{18}\frac{\cos(3\theta)-9\cos\theta+8}{\sin^4\theta} \end{aligned} \tag{6.147}$$

The boundary layer thickness tend to infty ($\chi \to \infty$) as $\theta \to \pi$, because the assumptions to construct the boundary layer are not anymore true. A Taylor expansion of χ around π leads to:

$$\chi \simeq \frac{1}{(\pi-\theta)^4} \tag{6.148}$$

So that $\sqrt{\frac{\chi}{Re}} << 1$, means :

$$\theta \leq \pi - Re^{-1/4} \tag{6.149}$$

This limit will be used when calculated the dissipation inside the boundary layer and will be the limit between boundary layer and wake correction.

6.5.2 Wake correction for Euler flow

As the boundary correction does not describe the flow around $\theta \simeq \pi$ in the wake, the flow is almost parallel. Using cylindrical coordinates (x is the distance to the central axis,

$x = r\sin\theta$,z is the altitude $z = r\cos\theta$,and φ the azimuthal coordinates), we have

$$\begin{aligned}
U_{xl} &= U_{rl}\sin\theta - U_{\theta l}\cos\theta \\
&= -U_b\cos\theta\sin\theta\left(\left(1-\frac{a^3}{r^3}\right)-\left(1+\frac{2a^3}{r^3}\right)\right) \\
&= U_b\frac{xz}{r^2}\frac{3a^3}{r^3} \\
&= U_b\frac{3a^3xz}{(x^2+z^2)^{5/2}} \\
U_{zl} &= U_{rl}\cos\theta - U_{\theta l}\sin\theta \\
&= U_b\left(\left(1-\frac{a^3}{r^3}\right)\cos^2\theta+\left(1+\frac{2a^3}{r^3}\right)\sin^2\theta\right) \\
&= -U_b\left(\left(1-\frac{a^3}{r^3}\right)\frac{z^2}{r^2}+\left(1+\frac{2a^3}{r^3}\right)\frac{x^2}{r^2}\right) \\
&= -U_b\frac{1}{r^5}\left(z^2(r^3+a^3)+x^2(r^3+2a^3)\right) \\
&= -U_b\left(1+\frac{a^3}{(x^2+z^2)^{3/2}}+\frac{a^3x^2}{(x^2+z^2)^{5/2}}\right)
\end{aligned} \tag{6.150}$$

A complete solution is sought in the form:

$$\begin{aligned}
u_{xl} &= U_{xl} + u^*_{xl} \\
u_{zl} &= U_{zl} + u^*_{zl} \\
P_l &= P_{\infty l} + p^*_l
\end{aligned} \tag{6.151}$$

with U_{xl}, U_{zl} and $P_{\infty l}$ being solution of the Euler equation.

Similarly to the process to obtain boundary layer correction, we obtain for the Navier-Stokes equations in the wake expressed in cylindrical coordinates:

$$\frac{\partial u^*_{xl}}{\partial x}+\frac{u^*_{xl}}{x}+\frac{\partial u^*_{zl}}{\partial z} = 0 \qquad (a)$$

$$\rho\left(U_{xl}\frac{\partial u^*_{xl}}{\partial x}+u^*_{xl}\frac{\partial U_{xl}}{\partial x}+U_{zl}\frac{\partial u^*_{xl}}{\partial z}+u^*_{xl}\frac{\partial U_{zl}}{\partial z}\right) = -\frac{\partial p^*_l}{\partial x}+V_{xl}+V^*_{xl} \qquad (b1)$$

$$\rho\left(U_{xl}\frac{\partial u^*_{zl}}{\partial z}+u^*_{xl}\frac{\partial U_{zl}}{\partial z}+U_{zl}\frac{\partial u^*_{zl}}{\partial z}+u^*_{zl}\frac{\partial U_{zl}}{\partial z}\right) = -\frac{\partial p^*_l}{\partial z}+V_{zl}+V^*_{zl} \qquad (b2)$$

(6.152)

with V_{xl},V^*_{xl},V_{zl},V^*_{zl} being the viscous terms :

$$\begin{aligned} V_{xl} &= \mu_l \left[\frac{\partial}{\partial x} \left(\frac{1}{x} \frac{\partial}{\partial x} (x U_{xl}) \right) + \frac{\partial^2 U_{xl}}{\partial z^2} \right] \\ V^*_{xl} &= \mu_l \left[\frac{\partial}{\partial x} \left(\frac{1}{x} \frac{\partial}{\partial x} (x u^*_{xl}) \right) + \frac{\partial^2 u^*_{xl}}{\partial z^2} \right] \\ V_{zl} &= \mu_l \left[\frac{1}{x} \frac{\partial}{\partial x} \left(x \frac{\partial U_{zl}}{\partial x} \right) + \frac{\partial^2 U_{zl}}{\partial z^2} \right] \\ V^*_{zl} &= \mu_l \left[\frac{1}{x} \frac{\partial}{\partial x} \left(x \frac{\partial u^*_{zl}}{\partial x} \right) + \frac{\partial^2 u^*_{zl}}{\partial z^2} \right] \end{aligned} \tag{6.153}$$

The following dimensionless quantities are introduced next:

$$\begin{aligned} \bar{x} &= \frac{x}{a\sqrt{\delta}} \\ \bar{z} &= \delta \frac{z}{a} \\ \bar{U}_{zl} &= \frac{U_{zl}}{U_b} \\ \bar{U}_{xl} &= \frac{U_{xl}}{U_b \delta^4 \sqrt{\delta}} \\ \bar{u}^*_{zl} &= \frac{u^*_{zl}}{U_b \delta} \\ \bar{u}^*_{xl} &= \frac{u^*_{zl}}{U_b \sqrt{\delta}} \\ \bar{p}^* &= \frac{p^*}{\rho_l U_b^2} \end{aligned} \tag{6.154}$$

An order of magnitude analysis then shows that:

$$\begin{aligned} \bar{U}_{xl} &= \frac{3\bar{x}\bar{z}}{(\delta^3 \bar{x}^2 + \bar{z}^2)^{5/2}} \sim 1 \\ \frac{\partial \bar{U}_{xl}}{\partial \bar{x}} &= \frac{3\bar{z}}{(\delta^3 \bar{x}^2 + \bar{z}^2)^{5/2}} \left(1 - \frac{5\delta^3 \bar{x}^2}{\delta^3 \bar{x}^2 + \bar{z}^2} \right) \sim 1 \\ \frac{\partial \bar{U}_{xl}}{\partial \bar{z}} &= \frac{2 - 2\varepsilon^{2/3}}{2 - 3\varepsilon^{2/3} - \varepsilon} \frac{3\bar{x}}{(\delta^3 \bar{x}^2 + \bar{z}^2)^{5/2}} \left(1 - \frac{5\bar{z}^2}{\delta^3 \bar{x}^2 + \bar{z}^2} \right) \sim 1 \\ \\ \bar{U}_{zl} &= -\left(1 + \frac{\delta^3}{(\delta^3 \bar{x}^2 + \bar{z}^2)^{3/2}} + \frac{\delta^6 \bar{x}^2}{(\delta^3 \bar{x}^2 + \bar{z}^2)^{5/2}} \right) \sim 1 \\ \frac{\partial \bar{U}_{zl}}{\partial \bar{x}} &= \frac{\delta^6 \bar{x}}{(\delta^3 \bar{x}^2 + \bar{z}^2)^{5/2}} \left(1 - \frac{5\delta^3 \bar{x}^2 \bar{z}}{\delta^2 \bar{x}^2 + \bar{z}^2} \right) \sim \delta^6 \\ \frac{\partial \bar{U}_{zl}}{\partial \bar{z}} &= \frac{\delta^3 \bar{z}}{(\delta^3 \bar{x}^2 + \bar{z}^2)^{5/2}} \left(3 - \frac{5\delta^3 \bar{x}^2}{\delta^3 \bar{x}^2 + \bar{z}^2} \right) \sim \delta^3 \end{aligned} \tag{6.155}$$

The Navier-Stokes equations can therefore be simplified as indicated below:

$$\begin{aligned}
\frac{\partial \bar{u}^*_{xl}}{\partial \bar{x}} + \frac{\bar{u}^*_{xl}}{\bar{x}} + \delta^2 \frac{\partial \bar{u}^*_{zl}}{\partial \bar{z}} &= 0 && (a)\\
\delta^4 \underbrace{\bar{U}_{xl}}_{\sim 1} \frac{\partial \bar{u}^*_{xl}}{\partial \bar{x}} + \delta^4 \bar{u}^*_{xl} \underbrace{\frac{\partial \bar{U}_{xl}}{\partial \bar{x}}}_{\sim 1} + \delta\sqrt{\delta} \underbrace{\bar{U}_{zl}}_{\sim 1} \frac{\partial \bar{u}^*_{xl}}{\partial \bar{z}} + \delta\sqrt{\delta} \bar{u}^*_{xl} \underbrace{\frac{\partial \bar{U}_{zl}}{\partial \bar{z}}}_{\sim \delta^3} &= -\frac{1}{\sqrt{\delta}} \frac{\partial \bar{p}^*_l}{\partial \bar{x}} + \bar{V}_{xl} + \bar{V}^*_{xl} && (b1)\\
\delta^6\sqrt{\delta} \underbrace{\bar{U}_{xl}}_{\sim 1} \frac{\partial \bar{u}^*_{zl}}{\partial \bar{z}} + \delta\sqrt{\delta} \bar{u}^*_{xl} \underbrace{\frac{\partial \bar{U}_{zl}}{\partial \bar{z}}}_{\sim \delta^3} + \delta^2 \underbrace{\bar{U}_{zl}}_{\sim 1} \frac{\partial \bar{u}^*_{zl}}{\partial \bar{z}} + \delta^2 \bar{u}^*_{zl} \underbrace{\frac{\partial \bar{U}_{zl}}{\partial \bar{z}}}_{\sim \delta^3} &= -\delta \frac{\partial \bar{p}^*_l}{\partial \bar{z}} + \bar{V}_{zl} + \bar{V}^*_{zl} && (b2)
\end{aligned} \tag{6.156}$$

with the viscous terms:

$$\begin{aligned}
\bar{V}_{xl} &= \delta^7\sqrt{\delta} \frac{\partial}{\partial \bar{x}} \left(\frac{1}{\bar{x}} \frac{\partial}{\partial \bar{x}} (\bar{x} \bar{U}_{xl}) \right) + \delta^8 \sqrt{\delta} \frac{\partial^2 \bar{U}_{xl}}{\partial \bar{z}^2}\\
\bar{V}^*_{xl} &= \delta\sqrt{\delta} \frac{\partial}{\partial \bar{x}} \left(\frac{1}{\bar{x}} \frac{\partial}{\partial \bar{x}} (\bar{x} \bar{u}^*_{xl}) \right) + \delta^4 \sqrt{\delta} \frac{\partial^2 \bar{u}^*_{xl}}{\partial \bar{z}^2}\\
\bar{V}_{zl} &= \delta^3 \underbrace{\frac{1}{\bar{x}} \frac{\partial}{\partial \bar{x}} \left(\bar{x} \frac{\partial \bar{U}_{zl}}{\partial \bar{x}} \right)}_{\sim \delta^3} + \delta^4 \frac{\partial^2 \bar{U}_{zl}}{\partial \bar{z}^2}\\
\bar{V}^*_{zl} &= \delta^2 \frac{1}{\bar{x}} \frac{\partial}{\partial \bar{x}} \left(\bar{x} \frac{\partial \bar{u}^*_{zl}}{\partial \bar{x}} \right) + \delta^5 \frac{\partial^2 \bar{u}^*_{zl}}{\partial \bar{z}^2}
\end{aligned} \tag{6.157}$$

Considering $\delta << 1$ and equations (6.155), the Navier-Stokes equations(6.156) simplify to

$$\begin{aligned}
\frac{\partial \bar{u}^*_{xl}}{\partial \bar{x}} + \frac{\bar{u}^*_{xl}}{\bar{x}} &= 0 && (a)\\
\frac{\partial \bar{u}^*_{xl}}{\partial \bar{z}} &= -\frac{1}{\delta^2} \frac{\partial \bar{p}^*_l}{\partial \bar{x}} + \frac{\partial}{\partial \bar{x}} \left(\frac{1}{\bar{x}} \frac{\partial}{\partial \bar{x}} (\bar{x} \bar{u}^*_{xl}) \right) && (b1)\\
\frac{\partial \bar{u}^*_{zl}}{\partial \bar{z}} &= \frac{1}{\bar{x}} \frac{\partial}{\partial \bar{x}} \left(\bar{x} \frac{\partial \bar{u}^*_{zl}}{\partial \bar{x}} \right) && (b2)
\end{aligned} \tag{6.158}$$

The matching procedure with the boundary layer correction leads to :

$$\begin{gathered}
u^*_{zl}\,|_{z=0} = -(6 + 9\bar{\mu})\sqrt{2} U_b \delta \left(\frac{1}{\sqrt{\pi}} e^{-\tau^2} - \tau(1 - \mathrm{erf}(\tau)) \right)\\
\tau = \frac{\bar{x}^2}{4\sqrt{2}} = \frac{x^2}{4\sqrt{2} a^2 \delta}
\end{gathered} \tag{6.159}$$

6.5.3 Force calculation considering boundary layer and wake correction

We can now calculate the forces on the bubble without neglecting the boundary layer. Since pressure in the boundary layer was neglected since a direct integration of the stress will not lead to the correct results, so we can evaluate the dissipation as Moore suggested, using the function Φ (cf. equation (6.100))

$$\begin{aligned}
\Phi &= \mu_l \frac{\partial u_i}{\partial x_j}\left(\frac{\partial u_i}{\partial x_j}+\frac{\partial u_j}{\partial x_i}\right)\\
\Phi &= \Phi_0+\Phi^*+\mu_l\frac{\partial U_i}{\partial x_j}\left(\frac{\partial u_i^*}{\partial x_j}+\frac{\partial u_j^*}{\partial x_i}\right)+\mu_l\frac{\partial u_i^*}{\partial x_j}\left(\frac{\partial U_i}{\partial x_j}+\frac{\partial U_j}{\partial x_i}\right)\\
\Phi &= \Phi_0+\Phi^*+2\mu_l\frac{\partial U_i}{\partial x_j}\frac{\partial u_i^*}{\partial x_j}+2\mu_l\frac{\partial U_j}{\partial x_i}\frac{\partial u_i^*}{\partial x_j}\\
\Phi &= \Phi_0+\Phi^*+2\mu_l\left[\frac{\partial}{\partial x_j}\left(u_i^*\frac{\partial U_i}{\partial x_j}\right)-u_i^*\nabla^2 U_i\right]\\
&\quad +2\mu_l\left[\frac{\partial}{\partial x_j}\left(u_i^*\frac{\partial U_i}{\partial x_j}\right)-u_i^*\frac{\partial}{\partial x_i}\left(\frac{\partial u_j^*}{\partial x_j}\right)\right]
\end{aligned} \tag{6.160}$$

with $\Phi_0=\mu_l\frac{\partial U_i}{\partial x_j}\left(\frac{\partial U_i}{\partial x_j}+\frac{\partial U_j}{\partial x_i}\right)$ and $\Phi^*=\mu_l\frac{\partial u_i^*}{\partial x_j}\left(\frac{\partial u_i^*}{\partial x_j}+\frac{\partial u_j^*}{\partial x_i}\right)$ since u is irrotationnal

$$\begin{gathered}
\Phi=\Phi_0+\Phi^*+4\mu_l\frac{\partial}{\partial x_j}\left(u_i^*E_{ij}\right)\\
\text{with : } E_{ij}=\tfrac{1}{2}\left(\frac{\partial U_i}{\partial x_j}+\frac{\partial U_j}{\partial x_i}\right)
\end{gathered} \tag{6.161}$$

We deduce the drag forces :

$$\begin{aligned}
\vec{f}\vec{U}_b &= \int_V \Phi_0 dV+\int_V \Phi^* dV+4\mu_l\int_V\frac{\partial}{\partial x_j}\left(u_i^*E_{ij}\right)dV\\
\vec{f}\vec{U}_b &= \int_V \Phi_0 dV+\int_V \Phi^* dV+4\mu_l\int_{S_l} n_j u_i^* E_{ij}dA-4\mu_l\int_{S_a} n_j u_i^* E_{ij}dA
\end{aligned} \tag{6.162}$$

where S_a and S_l are the surface area of the sphere of radius a and l, respectively. The integral $\int_V \Phi_0 dV$ was already evaluated in Eqn. (6.100), and $\Phi^*=\Phi^*_{bl}+\Phi^*_w$, where bl and w stand respectively for the boundary layer and the wake :

$$\begin{aligned}
\int_V \Phi^*_{bl}dV &= \mu_l\int_{\varphi=0}^{2\pi}\int_{\theta=0}^{\pi}\int_{r=a}^{l}\left(\left(\frac{1}{r}\frac{\partial u^*_{rl}}{\partial\theta}\right)^2+\left(\frac{\partial u^*_{\theta l}}{\partial r}\right)^2+2\left(\frac{1}{r}\frac{\partial u^*_{rl}}{\partial\theta}\frac{\partial u^*_{\theta l}}{\partial r}\right)\right)r^2\sin\theta d\varphi d\theta dr\\
\int_V \Phi^*_{bl}dV &\simeq 2\pi\mu_l\int_{\theta=0}^{\pi}\int_{r=a}^{l}\left(\frac{\partial u^*_{\theta l}}{\partial r}\right)^2 r^2\sin\theta d\theta dr\\
\int_V \Phi^*_{bl}dV &\simeq 2\pi\mu_l\int_{\theta=0}^{\pi}\int_{r=a}^{l}\left(U_b\sqrt{\frac{2}{Re}}\chi^{1/2}\sqrt{\frac{Re}{8\chi a^2}}F'(\tau)\right)^2 r^2\sin^3\theta d\theta dr\\
\int_V \Phi^*_{bl}dV &\simeq \frac{\pi\mu_l U_b^2 a}{2}\int_{\theta=0}^{\pi}\int_{\tau=0}^{\sqrt{\frac{Re}{8\chi}}\left(\frac{l}{a}-1\right)}\left((6+9\bar{\mu})\mathrm{erfc}(\tau)\right)^2\left(\sqrt{\frac{8\chi}{Re}}\tau+1\right)^2\sin^3\theta\sqrt{\frac{8\chi}{Re}}d\theta d\tau
\end{aligned} \tag{6.163}$$

As $Re\geq\chi$, we can perform the integral to the limit $\tau\to\infty$. However $\chi\to\infty$ as $\theta\to\pi$, because the assumption to construct boundary layer are no longer true (cf. equation 6.149),

we can only integrate until $\pi-\alpha$, with $\alpha^4 = 1/Re$. The previous equation becomes :

$$\begin{aligned}\int_V \Phi^*_{bl} dV &= \pi\mu_l U_b^2 a(6+9\bar{\mu})^2\sqrt{\tfrac{2}{Re}}\int_{\theta=0}^{\pi-\alpha}\int_{\tau=0}^{+\infty}\mathrm{erfc}(\tau)^2\left(\sqrt{\frac{8\chi}{Re}}\tau+1\right)^2\sqrt{\chi}\sin^3\theta d\theta d\tau \\ &= \pi\mu_l U_b^2 a(6+9\bar{\mu})^2\sqrt{\tfrac{2}{Re}}\int_{\theta=0}^{\pi-\alpha}\int_{\tau=0}^{+\infty}\mathrm{erfc}(\tau)^2\left(\frac{8\chi\sqrt{\chi}}{Re}\tau^2+\sqrt{\frac{32}{Re}}\chi\tau+\sqrt{\chi}\right)\sin^3\theta d\theta d\tau\end{aligned} \tag{6.164}$$

The various θ integrals are evaluated as follows :

$$\begin{aligned}\int_{\theta=0}^{\pi-\alpha}\sqrt{\chi}\sin^3\theta d\theta &= \tfrac{2}{15}\left(\sqrt{\cos(\pi-\alpha)+2}\,(\cos^2(\pi-\alpha)-\cos(\pi-\alpha)-6)+6\sqrt{3}\right) \\ &\simeq \tfrac{2}{15}(6\sqrt{3}-2) \\ \int_{\theta=0}^{\pi-\alpha}\chi\sin^3\theta d\theta &= \tfrac{1}{9}\left(-1+4\log(2)+\cos^2(\pi-\alpha)-8\log(\sin(\pi-\alpha))+4\log(1-\cos(\pi-\alpha))\right) \\ &\simeq \tfrac{1}{9}\left(8\log(2)-8\log(\alpha)\right)\simeq\log(Re)\end{aligned}$$

$$\begin{aligned}\int_{\theta=0}^{\pi-\alpha}\chi\sqrt{\chi}\sin^3\theta &= -\tfrac{8}{27\sqrt{2}}\left(\log(\cos(\pi-\alpha)+1)-\log(\cos(\pi-\alpha)+\sqrt{\cos(\pi-\alpha)+2}+3)\right) \\ &-\tfrac{8}{27\sqrt{2}}\left(\log(2+\sqrt{3})+\tfrac{\sqrt{3}}{2}-\tfrac{(\cos^2(\pi-\alpha)-2)\sqrt{\cos(\pi-\alpha)+2}}{3(\cos(\pi-\alpha)+1)}\right) \\ &= -\tfrac{8}{27\sqrt{2}}\left(\log(\tfrac{\alpha^2}{2})+\log\left(\tfrac{2+\sqrt{3}}{3}\right)+\tfrac{\sqrt{3}}{2}-\tfrac{2}{3\alpha^2}\right) \\ &\simeq \tfrac{1}{\alpha^2}\simeq\sqrt{Re}\end{aligned} \tag{6.165}$$

The τ integrals gives :

$$\begin{aligned}\int_{\tau=0}^{+\infty} erfc(\tau)^2 d\tau &\simeq 0.33 \\ \int_{\tau=0}^{+\infty}\tau erfc(\tau)^2 d\tau &\simeq 0.09 \\ \int_{\tau=0}^{+\infty}\tau^2 erfc(\tau)^2 d\tau &\simeq 0.04\end{aligned} \tag{6.166}$$

Finally we deduce :

$$\begin{aligned}\int_V \Phi^*_{bl} dV &= \pi\mu_l U_b^2 a(6+9\bar{\mu})^2\sqrt{\tfrac{2}{Re}}\int_{\theta=0}^{\pi-\alpha}\int_{\tau=0}^{+\infty}\mathrm{erfc}(\tau)^2\left(\frac{8\chi\sqrt{\chi}}{Re}\tau^2+\sqrt{\frac{32}{Re}}\chi\tau+\sqrt{\chi}\right)\sin^3\theta d\theta d\tau \\ &= 0.523\pi\mu_l U_b^2 a(6+9\bar{\mu})^2\tfrac{1}{\sqrt{Re}}\end{aligned} \tag{6.167}$$

For the wake, using equations (6.158) and (6.159), as suggested by Moore, we have :

$$\begin{aligned}
\int_V \Phi_w^* dV &= \pi\rho_l U_b \int_{x=0}^{\infty} z u_{zl}^{*2} \mid_{z=0} dx \\
&= \frac{4\pi\rho_l U_b a^2}{\sqrt{Re}} \int_{\tau=0}^{\infty} u_{zl}^{*2} \mid_{z=0} d\tau \\
&= \frac{4\pi\rho_l U_b a^2}{\sqrt{Re}} \frac{4(6+9\bar{\mu})^2 U_b^2}{Re} \int_{\tau=0}^{\infty} \left(\frac{1}{\sqrt{\pi}} e^{-\tau^2} - \tau(1-\mathrm{erf}(\tau)) \right)^2 d\tau \\
&= \frac{8(6+9\bar{\mu})^2 \pi\mu_l U_b^2 a}{\sqrt{Re}} \int_{\tau=0}^{\infty} \left(\frac{1}{\sqrt{\pi}} e^{-\tau^2} - \tau(1-\mathrm{erf}(\tau)) \right)^2 d\tau \\
&= \frac{0.623(6+9\bar{\mu})^2 \pi\mu_l U_b^2 a}{\sqrt{Re}}
\end{aligned} \tag{6.168}$$

Finally, for the last two terms, we have :

$$\begin{aligned}
-2\mu_l \int_{S_a} n_j u_i^* \left(\frac{\partial U_i}{\partial x_j} + \frac{\partial U_j}{\partial x_i} \right) dA &= -4\mu_l \int_{\theta=0}^{\pi} \int_{\varphi=0}^{2\pi} u_{\theta l}^* \mid_{r=a} \frac{\partial U_\theta}{\partial r} \mid_{r=a} a^2 \sin\theta d\theta d\varphi \\
&= 12\pi a\mu_l U_b \int_{\theta=0}^{\pi} u_{\theta l}^* \mid_{r=a} \sin^2\theta d\theta \\
&= -12\pi a\mu_l U_b^2 (6+9\bar{\mu}) \sqrt{\frac{2}{\pi Re}} \int_{\theta=0}^{\pi} \chi^{1/2} \sin^3\theta d\theta \\
&= -10.7\pi a\mu_l U_b^2 (6+9\bar{\mu}) \frac{1}{\sqrt{Re}}
\end{aligned} \tag{6.169}$$

and

$$2\mu_l \int_{S_l} n_j u_i^* \left(\frac{\partial U_i}{\partial x_j} + \frac{\partial U_j}{\partial x_i} \right) dA = 0 \tag{6.170}$$

Thus,

$$\begin{aligned}
\vec{f}\vec{U}_b &= a\pi\mu_l U_b^2 \left[12(1-\varepsilon^{5/3}) + 1.146(6+9\bar{\mu})^2 \frac{1}{\sqrt{Re}} - 10.7(6+9\bar{\mu}) \frac{1}{\sqrt{Re}} \right] \\
f &= 12\pi a\mu_l U_b \left[1 - \varepsilon^{5/3} - \frac{5.357(1+1.5\bar{\mu}) - 3.439(1+1.5\bar{\mu})^2}{\sqrt{Re}} \right]
\end{aligned} \tag{6.171}$$

we finally deduce for the drag coefficient :

$$\begin{aligned}
C_D &= \frac{48}{Re} \left[1 - \varepsilon^{5/3} - \frac{5.36(1+1.5\bar{\mu}) - 3.44(1+1.5\bar{\mu})^2}{\sqrt{Re}} \right] \\
\text{if } \bar{\mu} = 0, \varepsilon = 0 & \\
C_D &= \frac{48}{Re} \left[1 - \frac{1.9}{\sqrt{Re}} \right]
\end{aligned} \tag{6.172}$$

References

ANSCUTTER, F., BÉGUIN, C., ROSS, A., PETTIGREW, M. and MUREITHI, N. (2006). Two-phase damping and interface surface area in tubes with internal flow. *ASME PVP2006*. 11.

AUTON, T. (1987). The lift force on a spherical body in a rotational flow. *Journal of Fluid Mechanics*, 183, 199–218.

BATCHELOR, G. (1971). *An Introduction to Fluid Dynamics.* Cambridge University Press, seconde édition.

BÉGUIN, C., ÉTIENNE, S., PETTIGREW, M. and MUREITHI, N. (submitted in 2010). A model for bubbly two-phase flow - part II bubble size and pseudo two-phase turbulence. *Journal of fluid mechanic*.

BEYERLEIN, S., COSSMAN, R. and RICHTER, H. (1985). Predicting of bubble concentration profiles in vertical turbulent two-phase flow. *International Journal of Multiphase Flow*, 11, 629–641.

BHAGA, D. and WEBER, W. (1981). Bubbles in visous liquids : shapes, wakes and velocities. *Journal of Fluid Mechanics*, 105, 61–85.

CLIFT, R., GRACE, J. and WEBER, M. (1978). *Bubbles, drops and particles*. Academics Press, New York.

COLLIER, J. and THOME, J. (1996). *Convective boiling and condensation*. Clarendon Press, Oxford University Press, troisième édition.

ETIENNE, S. and PELLETIER, D. (2005). A general approach to sensitivity analysis of fluid-structure interactions. *Journal of fluids and structures*, 21, 169–186.

FEENSTRA, P., WEAVER, D. and JUDD, R. (2000). An improved void fraction model for two-phase cross-flow in horizontal tube bundles. *International Journal of Multiphase flow*, 26, 1851.

HARMATHY, T. (1960). Velocity of large drops and bubbles in media of infinite or restricted extend. *AIChE Journal*, 6, 281.

ISHII, M. and ZUBER, N. (1979). Drag coefficient and relative velocity in bubbly, droplet or particulate flows. *American Institute of Chemical Engineers Journal*, 25, 843–855.

KENDOUSH, A. (2001). Hydrodynamic model for bubbles in a swarm. *Chemical engineering Science*, 56, 235–238.

LEON-BECERRIL, E. and LINÉ, A. (2001). Stability analysis of a bubble column. *Chemical Engineering Science*, 56, 6135–6141.

MEI, R., KLAUSNER, J. and LAWRENCE, C. (1994). A note on the history force on a spherical bubble at finite reynolds number. *Physics of fluids*, 6, 418–420.

MILNE-THOMSON, L. (1968). *Theorical Hydrodynamics*. Macmillan, New York, 5^{th} édition.

MOKEYEV, G. (1977). Effect of particule concentration on their drag and induced mass. *Fluid Mechanics Sov. Res.*, 6, 161.

MOORE, D. (1963). The boundary layer on a spherical gas bubble. *Journal of Fluid Mechanic*, 16, 161–176.

NIGMATULIN, R. (1979). Spatial averaging in the mechanics of heterogeneous and dispersed systems. *International Journal of Multiphase Flow*, 5, 353–385.

OSEEN, C. (1910). über die stokessche formel und überdie verwandte aufgabe in der hydrodynamik. *Arkiv für Mathematik, Astronomi och Fysik*, 6, 29.

PARK, J., DREW, R. and LAHEY, R. (1998). The analysis of void wave propagation in adiabatic monodispersed bubbly two-phase flows using an ensemble-averaged two-fluid model. *International Journal of Multiphase Flow*, 24, 1205–1244.

PETTIGREW, M. and TAYLOR, C. (2004). Damping of heat exchanger tubes in two-phase flow: Review and design guidelines. *ASME Journal of Pressure Vessel Technology*, 126, 523.

SCHENK, O. and GÄRTNER, K. (2004). Solving unsymmetric sparse systems of linear equations with pardiso. *Journal of Future Generation Computer Systems*, 20(3), 475–487.

SCHENK, O. and GÄRTNER, K. (2006). On fast factorization pivoting methods for symmetric indefinite systems. *Electronic Transactions on Numerical Analysis*, 23, 158–179.

TAITEL, Y., BORNEA, D. and A.E., D. (1980). Modelling flow pattern transitions for steady upward gas-liquid flow in vertical tubes. *AIChE Journal*, 26, 345–354.

TAYLOR, T. and ACRIVOS, A. (1964). On the deformation and drag of a falling viscous drop at low reynolds number. *Journal of fluid mechanics*, 18, 466–476.

VAN WIJNGAARDEN, L. (1976). Hydrodynamic interaction between gas bubbles in liquid. *Journal of fluid Mechanics*, 77, 27–44.

VAN WIJNGAARDEN, L. (1991). *Bubble Deformation in Bubbly Liquid and its Effect on the Stability of Voidage Waves*. Mathematical approaches in hydrodynamics, SIAM, Miloh t. édition.

VOINOV, O. (1973). Force acting on a sphere in a homogeneous flow of an ideal incompressible fluid. *Journal of Applied Mechanics and Technology Physics*, 14, 592–594.

ZUBER, N. (1964). On the dispersed two-phase flow in the laminar flow regime. *Chemical Engineering Science*, 19, 897–903.

ZUBER, N. and HENCH, J. (1962). Steady-state and transcient void fraction of bubbling systems and their operating limits, part 1. steady state operation. *General Electric Report 62GL100*.

CHAPITRE 7

A MODEL FOR BUBBLY FLOW TWO-PHASE FLOW - PART II BUBBLE SIZE AND PSEUDO TURBULENCE

La principale conclusion de l'article précédent est que l'écoulement de Stokes représente, de façon très précise, l'écoulement autour des bulles. L'écoulement est laminaire et par conséquent la turbulence ne peut être attribuée à de la turbulence classique. L'écoulement dans la phase continue peut être considéré comme un écoulement de film dans lequel la turbulence classique ne peut se développer. La turbulence diphasique est essentiellement due à des perturbations induites par le passage de bulles. La turbulence diphasique est encore mal comprise. Une étude de celle-ci, aux échelles fondamentales, permet une meilleure compréhension de sa nature à une échelle plus globale.

Cet article est la deuxième partie d'un article en deux parties soumis pour publication dans le *Journal of Fluid Mechanics*. Il propose un modèle pour la pseudo-turbulence (turbulence induite par les particules). Des relations pour le tenseur de Reynolds de la phase continue et dispersée sont proposées en fonction du nombre de Reynolds Re, du taux de vide ε et du rapport de viscosité et de densité entre les deux phases ($\bar{\mu}$ et$\bar{\rho}$). Les implications pour la taille des bulles et les forces induites par la turbulence sur les bulles sont également étudiées.

C. Béguin[1], S. Étienne[2], N.W. Mureithi[1] & M. J. Pettigrew[1]

[1] BWC/AECL/NSERC Chair of Fluid-Structure Interaction

[2] Canada research chair in analysis, characterization and optimization of complex flows,

Department of Mechanical Engineering, École Polytechnique,

P.O.Box 6079, succ.Centre-Ville, Montréal, Quebec, Canada H3C3A7

Abstract

This paper proposes a model for pseudo turbulence (particles induced turbulence) in two-phase flow. Relations for the Reynolds stress tensor for both the dispersed and the continuous phases are proposed depending on Reynolds number Re, void fraction ε and viscosity and density ratios ($\bar{\mu}, \bar{\rho}$). The proposed relations are useful for all fluid-fluid cases. The implications for bubble size and turbulence forces on bubbles are also studied.

The main conclusion is that Stokes flow represents very accurately the flow around bubbles. The flow is consequently laminar leading to the conclusion that two-phase turbulence cannot

be attributed to classical turbulence. The flow in the continuous phase can be viewed as a film flow in which classical turbulence does not develop. Two-phase turbulence is therefore essentially due to perturbations induced by bubble passage commonly named pseudo turbulence. A simple model is proposed in this paper.

Nomenclature

Variables :

a: bubble/drop radius (m)
B_i, C_i, D_i: integration constants
D: tube diameter (m)
f: force (N)
g: gravitational acceleration (m/s^2)
l: inter-bubble distance (m)
P, p: fluid pressure (Pa)
Q: volume flow rate (m^3/s)
U, u, v: velocity (m/s)
V: volume of fluid (m^3)
β: volumetric quality
ε: void fraction
ρ: mass density (kg/m^3)
γ: surface tension (N/m)
μ: viscosity (Pa.s)
r, θ, ϕ : spherical coordinate

Dimensionless numbers :

$Re = \dfrac{2\rho_l U_b a}{\mu_l}$: Reynolds number
$Mo = \dfrac{\mu_l^4 \Delta\rho g}{\rho_l^2 \gamma^3}$: Morton Number
$Bo = \dfrac{4\Delta\rho g a^2}{\gamma}$: Bond Number
$\bar{\rho} = \dfrac{\rho_g}{\rho_l}$: Density ratio
$\bar{\mu} = \dfrac{\mu_g}{\mu_l}$: Viscosity ratio
β: volumetric quality
ε: void fraction
C_D: Drag coefficient

C_L: Lift coefficient
C_M: Added mass coefficient
Subscripts :
$_i$: at the liquid/gas interface
$_w$: at the wall interface
$_k$: phase k
$_l$: liquid/continuous phase
$_g$: gas/inclusion phase
$_{2\phi}$: two-phase
$_{ls}$: superficial liquid (velocity)
$_{gs}$: superficial gas (velocity)
$_{r,\theta,\phi}$: spherical coordinates

Superscripts :
$\langle X \rangle$: Space averaged variable
$\bar{X}$: dimensionless number
X^*: boundary layer correctional term

Other symbols are defined in the text.

Introduction

This paper follows a previous paper Béguin *et al.* (submitted in 2010) concerning drag coefficient of spherical bubbles (or droplets) and discussion about the sphericity assumption. The present paper intends to investigate turbulence induced by spherical bubbles (or droplets). This information is essential to completely characterize bubbly flow, where gas bubbles are present in a continuous liquid phase and in annular flow, where liquid droplets are present in a continuous gas phase. Flow pattern description are presented in Part I (Béguin *et al.* (submitted in 2010)). One classical way to model two-phase flow is by spatial or time averaging of the Navier-Stokes equations, see *e.g.* Ishii and Zuber (1979); Park *et al.* (1998) and Leon-Becerril and Liné (2001). In the process new terms must be determined by closure relations. Some of these terms are turbulence induced by the dispersed phase, commonly named pseudo turbulence.

Previous studies assume potential flow between bubbles (Lance and Bataille (1991); Park *et al.* (1998)). However, as shown in Part I, the terminal bubble/drop velocity (relative

to the continuous phase) is quite small and Stokes flow around the bubble represents the most commonly encountered condition. Moreover the transition from Stokes flow to Euler flow occurs at larger Reynolds numbers with higher void fraction (see Part I Béguin *et al.* (submitted in 2010)). In Stokes approximation, the variation in the boundary condition strongly influences the whole domain. This is why it is essential to consider the effect of surrounding bubbles/droplets.

This paper will explore the turbulence due to spherical inclusions. For simplicity, the bubbles (or droplets) will be named "gas" or "bubbles" and the continuous phase "liquid" with the respective subscripts $_g$ and $_l$. A priori, the turbulence Reynolds tensor ($\tau^{\bar{\bar{R}e}}$) depends on fluid viscosity (μ_l,μ_g), fluid density (ρ_l,ρ_g),"bubbles" size (radius : a), void fraction (ε - ratio of gas volume to total volume) and "bubble" velocity (U_b). Assuming there are no other parameters involved, such as presence of impurities, then according to the Buckingham-π theorem, the turbulence Reynolds stress tensor($\tau^{\bar{\bar{R}e}}$) is a function of four independent dimensionless numbers. We choose:

- $\bar{\mu} = \dfrac{\mu_g}{\mu_l}$
- $\bar{\rho} = \dfrac{\rho_g}{\rho_l}$
- $Re = \dfrac{2\rho_l U_b a}{\mu_l}$
- ε

The purpose of the paper is to find a general relation $\tau^{\bar{\bar{R}e}} = \bar{\bar{F}}(\bar{\mu}, \bar{\rho}, Re, \varepsilon)$. The paper is divided into six sections. The first section will define two-phase parameters, and present a brief literature review on two-phase flow models. The second will propose an analytical solution for the Reynolds stress tensor for Stokes and Euler flows. The third will present a numerical experiment, discuss the results and propose a general relation for the turbulence Reynolds stress tensor for a cloud of spherical bubbles. The fourth section will discuss bubble size models. The fifth section will attempt to deduce the forces on bubbles due to turbulence. In the last section, the main results are summarized and conclusions drawn.

7.1 Two-phase flow considerations

This first section introduces basic definitions and concepts specific to two-phase flows as well as a brief literature review. Some parts of this section will be identical to parts of the first paper Béguin *et al.* (submitted in 2010). However, they are necessary for this paper to be relatively standalone. This is also done for clarity.

7.1.1 Basic definitions

The proportion of gas in a two-phase gas-liquid mixture is characterized either by the void fraction ε or by the volumetric quality β [Collier and Thome (1996)]. The two phase mixture void fraction and volumetric quality in a tube section, of length ΔL, are defined as:

$$\begin{aligned} \varepsilon &= \frac{V_g}{V_g + V_l} = \frac{A_g \Delta L}{A_g \Delta L + A_l \Delta L} = \frac{A_g}{A_g + A_l} \\ \beta &= \frac{Q_g}{Q_g + Q_l} = \frac{A_g U_g}{A_g U_g + A_l U_l} = \frac{A_g}{A_g + A_l \frac{U_l}{U_g}} = \frac{\varepsilon}{\varepsilon + (1-\varepsilon) S_r} \end{aligned} \tag{7.1}$$

where V_g and V_l are the volumes of the gas and liquid phases in the mixture, A_g and A_l are the cross sectional areas of each phase in the tube cross section, Q_g and Q_l are the volume flow rates, and U_g and U_l the phase velocities. The void fraction and volumetric quality are related through the slip ratio, $S_r = U_l/U_g$. The superficial velocities of the phases (U_{gs}, U_{ls}) and the total superficial velocity also named sometimes the homogeneous velocity ($U_{2\phi}$) are defined as:

$$\begin{aligned} U_{gs} &= \frac{Q_g}{A} = \frac{A_g U_g}{A} = \varepsilon U_g = \beta U_{2\phi} \\ U_{ls} &= \frac{Q_l}{A} = (1-\varepsilon) U_l = (1-\beta) U_{2\phi} \\ U_{2\phi} &= \frac{Q_g + Q_l}{A} = U_{gs} + U_{ls} \end{aligned} \tag{7.2}$$

The difference between the gas and liquid velocities denoted as $U_b = U_g - U_l$, represents the velocity of bubbles relative to the liquid (typical magnitude around 0.25 m/s). The higher the homogeneous velocity, the smaller is the difference between ε and β. Indeed, at higher homogeneous velocity, gravity effects which govern U_b become relatively smaller (cf. equation (6.3). The homogeneous model corresponds to zero relative velocity between phases $U_b = 0$ leading to equality between void fraction and volumetric quality, $\varepsilon = \beta$. In this case as well, the homogeneous velocity corresponds to the phase velocities ($U_{2\phi} = U_l = U_g$).

7.1.2 Averaged Navier-Stokes equation

The averaging process of the Navier-Stokes equations uses spatial averaging to allow the solution of the two-phase flow without solving for each phase and inclusions, which require a resolution of the interface location. Such a full resolution will require a very large amount of resources. Averaging the Navier-Stokes equations makes it possible to numerically solve two-phase flow with a reasonable amount of resources.

In the case where gravity is the only body force, the Navier-Stokes equations for each

phase k (k: liquid or gas) are:

$$\begin{aligned} &\frac{\partial \rho_k}{\partial t} + \nabla.(\rho_k \vec{v_k}) = 0 \\ &\frac{\partial \rho_k \vec{v_k}}{\partial t} + \nabla.(\rho_k \vec{v_k} \vec{v_k}) = \rho_k \vec{g} - \nabla P_k + \mu_k \Delta \vec{v_k} \end{aligned} \tag{7.3}$$

with the following boundary conditions (where ^{i} represents the liquid-gas interface):
a) Mass transfer :

$$[\![\rho_k(\vec{v_k} - \vec{v^i}).\vec{n_k^i}]\!] = 0 \tag{7.4}$$

Without mass transfer, the previous condition becomes:

$$\begin{aligned} &\rho_l(\vec{v_l} - \vec{v^i}).\vec{n_l^i} = \rho_g(\vec{v_g} - \vec{v^i}).\vec{n_g^i} = 0 \\ \text{or} \quad &(\vec{v_l} - \vec{v_g}).\vec{n_l^i} = 0 \end{aligned} \tag{7.5}$$

b) Momentum transfer :

$$[\![P_k \vec{n_k^i} + \bar{\bar{\tau}}_k.\vec{n_k^i} - \rho_k \vec{v_k}(\vec{v_k} - \vec{v^i}).\vec{n_k^i}]\!] = \frac{2\gamma}{a}\vec{n_l^i} \tag{7.6}$$

c) Wall condition :

$$\vec{v_k} = 0 \tag{7.7}$$

In order to integrate the equations independently of phase location, the following phase indicator function χ_k is introduced.

$$\chi_k(\vec{x}, t) = \begin{cases} 1, \text{ if phase k is at position } (\vec{x}, t) \\ 0, \text{ if not} \end{cases} \tag{7.8}$$

The derivatives of the function χ_k is zero everywhere except at the interface. The gas-liquid interface is denoted by the superscript ^{i}. The derivative of the indicator function are :

$$\begin{aligned} \frac{\partial \chi_k}{\partial t} &= -\vec{v^i}.\vec{n_k^i}\delta^i \\ \nabla \chi_k &= \vec{n_k^i}\delta^i \end{aligned} \tag{7.9}$$

where δ^i is the Dirac delta function which is non zero at the gas-liquid interface.

The averaging procedure for the quantity φ is defined as[1] :

$$\langle\varphi\rangle(\vec{x}, t) = \frac{1}{L^3}\int_{x^*=x-L/2}^{x+L/2}\int_{y^*=y-L/2}^{y+L/2}\int_{z^*=z-L/2}^{z+L/2}\varphi(\vec{x}^*, t)dx^*dy^*dz^* \tag{7.10}$$

1. Note that some authors use the notation $\langle\varphi\rangle^k = \langle\chi_k\varphi\rangle$

The function χ_k is introduced prior to averaging. The averaging procedure of the Navier-Stokes equations is thus :

$$\begin{aligned}
&\langle \chi_k \frac{\partial \rho_k}{\partial t} \rangle + \langle \chi_k \nabla.(\rho_k \vec{v_k}) \rangle = 0 \\
&\langle \chi_k \frac{\partial \rho_k \vec{v_k}}{\partial t} \rangle + \langle \chi_k \nabla.(\rho_k \vec{v_k} \vec{v_k}) \rangle = \langle \chi_k \rho_k \vec{g} \rangle - \langle \chi_k \nabla P_k \rangle + \langle \chi_k \nabla.\bar{\bar{\tau}}_k \rangle
\end{aligned} \tag{7.11}$$

Noting that :

$$\begin{aligned}
\langle \chi_k \frac{\partial \rho_k}{\partial t} \rangle &= \frac{\partial \langle \chi_k \rho_k \rangle}{\partial t} - \langle \rho_k \frac{\partial \chi_k}{\partial t} \rangle = \frac{\partial \langle \chi_k \rho_k \rangle}{\partial t} + \langle \rho_k \vec{v^i}.\vec{n_k^i} \delta^i \rangle \\
\langle \chi_k \frac{\partial \rho_k \vec{v_k}}{\partial t} \rangle &= \frac{\partial \langle \chi_k \rho_k \vec{v_k} \rangle}{\partial t} - \langle \rho_k \vec{v_k} \frac{\partial \chi_k}{\partial t} \rangle = \frac{\partial \langle \chi_k \rho_k \vec{v_k} \rangle}{\partial t} + \langle \rho_k \vec{v_k} (\vec{v^i}.\vec{n_k^i}) \delta^i \rangle \\
\langle \chi_k \nabla.(\rho_k \vec{v_k}) \rangle &= \nabla.\langle \chi_k \rho_k \vec{v_k} \rangle - \langle \rho_k \vec{v_k}.\vec{n_k^i} \delta^i \rangle \\
\langle \chi_k \nabla.(\rho_k \vec{v_k} \vec{v_k}) \rangle &= \nabla.\langle \chi_k \rho_k \vec{v_k} \vec{v_k} \rangle - \langle \rho_k \vec{v_k} \vec{v_k}.\vec{n_k^i} \delta^i \rangle \\
\langle \chi_k \nabla P_k \rangle &= \nabla \langle \chi_k P_k \rangle - \langle P_k.\vec{n_k^i} \delta^i \rangle \\
\langle \chi_k \nabla.\bar{\bar{\tau}}_k \rangle &= \nabla.\langle \chi_k.\bar{\bar{\tau}}_k \rangle - \langle \bar{\bar{\tau}}_k \vec{n_k^i} \delta^i \rangle
\end{aligned} \tag{7.12}$$

The final averaged equations are :

$$\begin{aligned}
\frac{\partial \langle \chi_k \rho_k \rangle}{\partial t} + \nabla.\langle \chi_k \rho_k \vec{v_k} \rangle &= \langle \rho_k (\vec{v_k} - \vec{v^i}).\vec{n_k^i} \delta^i \rangle \\
\frac{\partial \langle \chi_k \rho_k \vec{v_k} \rangle}{\partial t} + \nabla.\langle \chi_k \rho_k \vec{v_k} \vec{v_k} \rangle &= -\nabla \langle \chi_k P_k \rangle + \langle \chi_k \rho_k \rangle \vec{g} \\
&\quad + \nabla.\langle \chi_k \bar{\bar{\tau}}_k \rangle + \langle (\rho_k \vec{\tilde{v}_k} (\vec{\tilde{v}_k} - \vec{v^i})).\vec{n_k^i} \delta^i \rangle \\
&\quad + \langle P_k.\vec{n_k^i} \delta^i \rangle - \langle \bar{\bar{\tau}}_k \vec{n_k^i} \delta^i \rangle
\end{aligned} \tag{7.13}$$

The same averaging procedure is done for the boundary conditions, yielding, for mass transfer :

$$[\![\langle \rho_k (\vec{v_k} - \vec{v^i}).\vec{n_k^i} \delta^i \rangle]\!] = 0 \tag{7.14}$$

and for momentum transfer :

$$[\![-\langle P_k.\vec{n_k^i} \delta_k^i + \bar{\bar{\tau}}_k \vec{n_k^i} \delta^i - \rho_k \vec{v_k} (\vec{v_k} - \vec{v^i}).\vec{n_k^i} \delta_k^i \rangle]\!] = \langle \frac{2\gamma}{a} \vec{n_l^i} \rangle \tag{7.15}$$

To resolve, the liquid and gas equations, the following averaged quantities are defined :

$$
\begin{aligned}
&\text{Void fraction}\\
\varepsilon &= \langle \chi_g \rangle\\
1-\varepsilon &= \langle \chi_l \rangle\\
&\text{Average densities}\\
\langle \rho_g \rangle &= \langle \chi_g \rho_g \rangle / \varepsilon\\
\langle \rho_l \rangle &= \langle \chi_l \rho_l \rangle / (1-\varepsilon)\\
&\text{Average velocities}\\
\langle \vec{v}_g \rangle &= \frac{\langle \chi_g \rho_g \vec{v}_g \rangle}{\varepsilon \langle \rho_g \rangle}\\
\langle \vec{v}_l \rangle &= \frac{\langle \chi_l \rho_l \vec{v}_l \rangle}{(1-\varepsilon)\langle \rho_l \rangle}\\
&\text{Average pressures}\\
P_g &= \langle \chi_g P_g \rangle / \varepsilon\\
P_l &= \langle \chi_l P_l \rangle / (1-\varepsilon)\\
&\text{Average viscous tensors}\\
\nabla.(\varepsilon \langle \bar{\bar{\tau}}_g \rangle) &= \nabla. \langle \chi_g \bar{\bar{\tau}}_g \rangle\\
\nabla.((1-\varepsilon) \langle \bar{\bar{\tau}}_l \rangle) &= \nabla. \langle \chi_l \bar{\bar{\tau}}_l \rangle\\
&\text{Average forces at interface location}\\
\vec{M}_g^i &= \langle (\rho_g \vec{v}_g (\vec{v}_g - \vec{v^i})).\vec{n}_g^i \delta^i \rangle + \langle P_g . \vec{n}_g^i \delta^i \rangle - \langle \bar{\bar{\tau}}_g \vec{n}_g^i \delta^i \rangle\\
\vec{M}_l^i &= \langle (\rho_l \vec{v}_l (\vec{v}_l - \vec{v^i})).\vec{n}_l^i \delta^i \rangle + \langle P_l . \vec{n}_l^i \delta^i \rangle - \langle \bar{\bar{\tau}}_l \vec{n}_l^i \delta^i \rangle\\
&\text{Turbulence tensor}\\
\nabla.\left(\varepsilon \bar{\bar{\tau}}_g^{Re}\right) &= -\nabla. \langle \chi_g \rho_g \vec{v}_g \vec{v}_g \rangle + \nabla. \varepsilon \langle \rho_g \rangle \langle \vec{v}_g \rangle \langle \vec{v}_g \rangle\\
\nabla.\left((1-\varepsilon) \bar{\bar{\tau}}_l^{Re}\right) &= -\nabla. \langle \chi_l \rho_l \vec{v}_l \vec{v}_l \rangle + \nabla.(1-\varepsilon) \langle \rho_l \rangle \langle \vec{v}_l \rangle \langle \vec{v}_l \rangle\\
&\text{Mass transfer}\\
\Gamma_g &= \langle \rho_g (\vec{v}_g - \vec{v^i}).\vec{n}_g^i \delta^i \rangle\\
\Gamma_l &= \langle \rho_l (\vec{v}_l - \vec{v^i}).\vec{n}_l^i \delta^i \rangle\\
&\text{Surface tension effect}\\
\vec{\kappa} &= \langle \frac{2\gamma}{a} \vec{n}_l^i \rangle
\end{aligned}
\tag{7.16}
$$

With these defined quantities, the averaged gas equations are :

$$
\begin{aligned}
\frac{\partial}{\partial t}\left(\varepsilon \langle \rho_g \rangle\right) + \nabla.\left(\varepsilon \langle \rho_g \rangle \langle \vec{v}_g \rangle\right) &= \Gamma_g\\
\frac{\partial}{\partial t}\left(\varepsilon \langle \rho_g \rangle \langle \vec{v}_g \rangle\right) + \nabla.\left(\varepsilon \langle \rho_g \rangle \langle \vec{v}_g \rangle \langle \vec{v}_g \rangle\right) &= -\nabla(\varepsilon P_g) + \varepsilon \langle \rho_g \rangle \vec{g}\\
&\quad + \nabla.(\varepsilon \langle \bar{\bar{\tau}}_g \rangle) + \vec{M}_g^i + \nabla.\left(\varepsilon \bar{\bar{\tau}}_g^{Re}\right)
\end{aligned}
\tag{7.17}
$$

while for the liquid phase, the equations are :

$$\begin{aligned}
\frac{\partial}{\partial t}\left((1-\varepsilon)\langle\rho_l\rangle\right) + \nabla.\left(\langle(1-\varepsilon)\langle\rho_l\rangle\langle\vec{v}_l\rangle\right) = &\quad \Gamma_l \\
\frac{\partial}{\partial t}\left((1-\varepsilon)\langle\rho_l\rangle\langle\vec{v}_l\rangle\right) + \nabla.\left((1-\varepsilon)\langle\rho_l\rangle\langle\vec{v}_l\rangle\langle\vec{v}_l\rangle\right) = &\quad -\nabla((1-\varepsilon)P_l) + (1-\varepsilon)\langle\rho_l\rangle\vec{g} \\
&\quad +\nabla.\left((1-\varepsilon)\langle\bar{\bar{\tau}}_l\rangle\right) + \vec{M}_l^i \\
&\quad +\nabla\cdot\left((1-\varepsilon)\tau_l^{\bar{\bar{Re}}}\right)
\end{aligned} \tag{7.18}$$

Finally, the equations for the boundary conditions at the interface location are :

$$\begin{aligned}
[\![\Gamma_k]\!] = &\quad 0 \\
[\![\vec{M}_k^i]\!] = &\quad \vec{\kappa}
\end{aligned} \tag{7.19}$$

These equations need closure relations and in particular the average force on the interface, $\vec{M}_k^i$.

The explicit determination of the interface forces can be avoided by considering the mixture equations instead of the separate phase equations. Summing the gas and liquid phase equations (7.17) and (7.18) and applying the boundary conditions at the interface, (see Eq.(7.19) the following averaged mixture equations are obtained. This equations make it possible to avoid modelling the interface condition.

$$\frac{\partial}{\partial t}\left(\varepsilon\langle\rho_g\rangle + (1-\varepsilon)\langle\rho_l\rangle\right) + \nabla\cdot\left(\varepsilon\langle\rho_g\rangle\langle\vec{v}_g\rangle + (1-\varepsilon)\langle\rho_l\rangle\langle\vec{v}_l\rangle\right) = 0$$

$$\begin{aligned}
&\frac{\partial}{\partial t}\left(\varepsilon\langle\rho_g\rangle\langle\vec{v}_g\rangle + (1-\varepsilon)\langle\rho_l\rangle\langle\vec{v}_l\rangle\right) + \nabla\cdot\left(\varepsilon\langle\rho_g\rangle\langle\vec{v}_g\rangle\langle\vec{v}_g\rangle + (1-\varepsilon)\langle\rho_l\rangle\langle\vec{v}_l\rangle\langle\vec{v}_l\rangle\right) = \ldots \\
&-\nabla(\varepsilon P_g + (1-\varepsilon)P_l) + (\varepsilon\langle\rho_g\rangle + (1-\varepsilon)\langle\rho_l\rangle)\vec{g}\ldots \\
&+\nabla\cdot\left(\varepsilon\langle\bar{\bar{\tau}}_g\rangle + (1-\varepsilon)\langle\bar{\bar{\tau}}_l\rangle\right) + \nabla\cdot\left(\varepsilon\tau_g^{\bar{\bar{Re}}} + (1-\varepsilon)\tau_l^{\bar{\bar{Re}}}\right) + \vec{\kappa}
\end{aligned} \tag{7.20}$$

Defining the average mixture density, velocity, pressure, viscous tensor and Reynolds tensor, respectively as :

$$\begin{aligned}
\rho_{2\phi} &= \langle\chi_g\rho_g + \chi_l\rho_l\rangle = \varepsilon\langle\rho_g\rangle + (1-\varepsilon)\langle\rho_l\rangle \\
\vec{v}_{2\phi} &= \langle\chi_g\rho_g\vec{v}_g + \chi_l\rho_l\vec{v}_l\rangle/\rho_{2\phi} = \left(\varepsilon\langle\rho_g\rangle\langle\vec{v}_g\rangle + (1-\varepsilon)\langle\rho_l\rangle\langle\vec{v}_l\rangle\right)/\rho_{2\phi} \\
P_{2\phi} &= \langle\chi_g P_g + \chi_l P_l\rangle = \varepsilon P_g + (1-\varepsilon)P_l \\
\nabla\cdot(\bar{\bar{\tau}}_{2\phi}) &= \nabla\cdot\left(\varepsilon\langle\bar{\bar{\tau}}_g\rangle + (1-\varepsilon)\langle\bar{\bar{\tau}}_l\rangle\right) \\
\nabla\cdot\tau_{2\phi}^{\bar{\bar{Re}}} &= -\nabla\cdot\langle\chi_g\rho_g\vec{v}_g\vec{v}_g + \chi_l\rho_l\vec{v}_l\vec{v}_l\rangle + \nabla\cdot\rho_{2\phi}\vec{v}_{2\phi}\vec{v}_{2\phi}
\end{aligned} \tag{7.21}$$

The mixture equations become :

$$\begin{aligned}
&\frac{\partial \rho_{2\phi}}{\partial t} + \nabla \cdot \rho_{2\phi}\vec{v}_{2\phi} = 0 \\
&\frac{\partial \rho_{2\phi}\vec{v}_{2\phi}}{\partial t} + \nabla \cdot \rho_{2\phi}\vec{v}_{2\phi}\vec{v}_{2\phi} = -\nabla P_{2\phi} + \rho_{2\phi}\vec{g} + \nabla \cdot \bar{\bar{\tau}}_{2\phi} + \vec{\kappa} + \nabla \cdot \bar{\bar{\tau}}^{Re}_{2\phi}
\end{aligned} \tag{7.22}$$

While these equations need fewer closure relations, since the interface boundary conditions do not need to be modelled, we however lose information such as void fraction variation which cannot be captured by this equation. We still need some, albeit fewer, closure relations to be able to solve the mixture equations. In particular a closure relation for the viscous tensor, is proposed in the part I Béguin *et al.* (submitted in 2010).

It is noted that the average velocity weighted by the mass of each phase $\vec{v}_{2\phi}$ is more useful and more representative of the physical phenomena than the homogeneous velocity which is usually used and which is the averaged velocity weighted by the volume of each phase (cf. Eq. 5.4).

In the case we want to solve the equations of both phases, interface forces are needed. To obtain the interface forces, we consider a control volume containing N bubbles. Interface forces M_g^i can be evaluated by summing the individual forces on the n^{th} bubble : $\vec{f_{g_n}^i}$

$$\vec{M_g^i} = \frac{1}{V_0}\sum_{n=1}^{N} \vec{f_{g_n}^i} = \frac{N}{V_0}\langle \vec{f_g^i} \rangle \tag{7.23}$$

The number of bubbles is determined from the volume occupied by the gas which is N times the average volume occupied by one bubble :

$$V_G = \varepsilon V_0 = N\frac{4}{3}\pi\langle a^3 \rangle \tag{7.24}$$

This gives :

$$\vec{M_g^i} = \frac{3\varepsilon}{4\pi\langle a^3 \rangle}\langle \vec{f_g^i} \rangle \tag{7.25}$$

with :

$$\begin{aligned}
\langle \vec{f_g^i} \rangle \;=\; & \left\langle \tfrac{4}{3}\pi\rho_l a^3 C_M \frac{D\vec{U}_b}{Dt} \right\rangle && \text{Added mass} \\
& + \left\langle \pi \tfrac{1}{2}\rho_l a^2 C_D |\vec{U}_b| \vec{U}_b \right\rangle && \text{Drag force} \\
& + \left\langle \tfrac{1}{2}\pi\rho_l a^2 C_L \vec{U}_b \times \nabla \times \vec{U}_b \right\rangle && \text{Lift Force} \\
& + \left\langle \tfrac{4}{3}\pi\Delta\rho a^3 \vec{g} \right\rangle && \text{Buoyancy} \\
& + \left\langle \vec{f_{turb}^i} \right\rangle && \text{Interface force due to turbulence}
\end{aligned} \tag{7.26}$$

or

$$\begin{aligned}\vec{M}_g^i = \quad & \varepsilon\left(\rho_l\frac{\left\langle C_M a^3\frac{D\vec{U}_b}{Dt}\right\rangle}{\langle a^3\rangle}+\frac{3}{8}\rho_l\frac{\left\langle a^2 C_D|\vec{U}_b|\vec{U}_b\right\rangle}{\langle a^3\rangle}+\frac{3}{8}\rho_l\frac{\left\langle\ a^2 C_L\vec{U}_b\times\nabla\times\vec{U}_b\right\rangle}{\langle a^3\rangle}\right)\\ & +\varepsilon\Delta\rho\vec{g}+\varepsilon\frac{\left\langle f_{turb}^{\vec{i}}\right\rangle}{\langle a^3\rangle}\end{aligned} \tag{7.27}$$

where the average for $\langle\vec{f}_g^i\rangle$ and its various component can be modelled as :

$$\begin{aligned}\langle\vec{f}_g^i\rangle \quad = \quad & \left\langle C_M\tfrac{4}{3}\pi\rho_l a^3\tfrac{D\vec{U}_b}{Dt}\right\rangle && \text{Added mass}\\ & +\left\langle\pi\tfrac{1}{2}\rho_l a^2 C_D|\vec{U}_b|\vec{U}_b\right\rangle && \text{Drag force}\\ & +\left\langle\tfrac{1}{2}\pi\rho_l a^2 C_L\vec{U}_b\times\nabla\times\vec{U}_b\right\rangle && \text{Lift Force}\\ & +\left\langle\tfrac{4}{3}\pi\Delta\rho a^3\vec{g}\right\rangle && \text{Buoyancy}\\ & +\left\langle f_{turb}^{\vec{i}}\right\rangle && \text{interface force due to turbulence}\end{aligned} \tag{7.28}$$

The explicit form for the interface forces becomes

$$\begin{aligned}\vec{M}_g^i = \quad & \varepsilon\left(\rho_l\frac{\left\langle C_M a^3\frac{D\vec{U}_b}{Dt}\right\rangle}{\langle a^3\rangle}+\frac{3}{8}\rho_l\frac{\left\langle a^2 C_D|\vec{U}_b|\vec{U}_b\right\rangle}{\langle a^3\rangle}+\frac{3}{8}\rho_l\frac{\left\langle\ a^2 C_L\vec{U}_b\times\nabla\times\vec{U}_l\right\rangle}{\langle a^3\rangle}\right)\\ & +\varepsilon\Delta\rho\vec{g}+\varepsilon\frac{\left\langle f_{turb}^{\vec{i}}\right\rangle}{\langle a^3\rangle}\end{aligned} \tag{7.29}$$

A complete set of the closure relations needs also a model for C_M, C_L. Several values of added mass have presented by previous authors and summarize in Table 7.1 where Z is the sphericity correction factor given by Milne-Thomson (1968)

$$Z = -2\frac{\chi^2 cos^{-1}(\chi^{-1})-\chi^2(\chi^2-1)^{1/2}}{\chi^2 cos^{-1}(\chi^{-1})-(\chi^2-1)^{1/2}} \tag{7.30}$$

And χ the sphericity coefficient defined for an ellipsoid as $\chi = a/b$ where a and b are the two diameter or the generatrix ellipse. *Note : for a sphere (a = b)* $\chi = 1$.. For the lift coefficient we can mention the work of Auton (1987) proposing a lift coefficient of $C_L = 0.5$. Little work consider void fraction effect on lift coefficient. We can mention the work of Beyerlein *et al.* (1985) leading to :

$$C_L = \frac{1.65\times10^{-3}}{\varepsilon^{0.78}} \tag{7.31}$$

Author	Assumption	C_M
Voinov (1973) Nigmatulin (1979)	Spherical bubble in an infinite liquid domain with a potential flow	$\frac{1}{2}$
Zuber (1964)	Non isolated spherical bubbles with a potential flow	$\frac{1}{2}\frac{1+2\varepsilon}{1-\varepsilon} \simeq \frac{1}{2} + 1.5\varepsilon$
Van Wijngaarden (1976)	Non isolated spherical bubbles with a potential flow	$\frac{1}{2} + 1.39\varepsilon$
Van Wijngaarden (1991)	Non isolated Ellipsoidal bubbles with a potential flow	$\frac{1}{2}\left[1 + \left(1 + \frac{2}{Z}\right)\varepsilon\right]$
Mokeyev (1977)	Empirical correlation	$\frac{1}{2} + 2.1\varepsilon$

Table 7.1 Models for added mass coefficient C_M

The previous equation does not agree with Auton (1987)'s work when void fraction approaches to zero. This shows the complexity and difficulty of obtaining good model for the interface forces depending on void fraction. This work will only concentrate on modeling the turbulence due to spherical bubbles. This means developing a closure relations for Reynolds stress tensor and the interface force due to turbulence.

7.1.3 Bubble size in turbulent flow

The equilibrium breakup and coalescence of bubbles in turbulent flow determines the bubble size distribution. Two important parameters, the minimum and maximum bubble radii, a_{max} and a_{min}, can be identified at these conditions (Shinnar (1961); Liu and Li (1999)). There is a high probability of coalescence for bubbles having a radius smaller than a_{min} and a high probability of break up for those having a radius larger than a_{max}.

After the initial contributions by Hinze (1955), bubble break up in turbulent flow has been studied by Levich (1962),Wilkinson *et al.* (1993) and Razzaque *et al.* (2003) among others. All authors agree that the largest stable bubble is determined by the equilibrium between pressure fluctuation due to turbulence and surface tension forces. Hinze (1955) defined a critical Weber number by evaluating this equilibrium obtaining :

$$We_c = \frac{2\tau a_{max}}{\gamma} \tag{7.32}$$

where τ is the dynamic pressure force defined as :

$$\tau = \rho_{2\phi} < U_{2\phi}^2 >= \rho_{2\phi} \left(32 e_{d2\phi}^2 a_{max}^2\right)^{1/3} \tag{7.33}$$

In equation (7.33), $< U_{2\phi}^2 >$ is the average mean square fluctuating velocity, and $e_{d2\phi}$ the average energy dissipation rate per unit mass. According to Liu and Li (1999) we should use :

$$\begin{aligned} e_{d2\phi} &= e_{dl} \left(\frac{\mu_{2\phi}}{\mu_l} \frac{\rho_l}{\rho_{2\phi}} \right)^3 \\ &= \frac{2 f U_{2\phi}^3}{D} \left(\frac{\mu_{2\phi}}{\mu_l} \frac{\rho_l}{\rho_{2\phi}} \right)^3 \end{aligned} \tag{7.34}$$

In equation (7.34), $f = 0.079 Re^{-1/4}$ is the friction factor which is assumed to be adequately represented by the Blasius relation. Liu and Li (1999) recommend using the definition of

Taylor (1932) for both two-phase density and viscosity :

$$\begin{aligned} \rho_{2\phi} &= \varepsilon\rho_g + (1-\varepsilon)\rho_l = \rho_l\left[\varepsilon\bar{\rho} + (1-\varepsilon)\right] \\ \mu_{2\phi} &= \mu_l\left[1 + \varepsilon\tfrac{1+2.5\bar{\mu}}{1+\bar{\mu}}\right] \end{aligned} \tag{7.35}$$

Levich (1962) assumed that a deformed bubble breaks up when the internal pressure force overcomes the surface tension force. Considering a balance between these two forces, he obtained a different critical Weber number,

$$We_c^* = \frac{2\tau\ a_{max}}{\gamma}\left(\frac{\rho_g}{\rho_l}\right)^{1/3} \tag{7.36}$$

Based on the two results (7.32, 7.36) of the critical Weber number, Hesketh *et al.* (1987) derived an equation for the maximum bubble radius a_{max}. If we include the suggestion of Liu and Li (1999) for the dissipation rate and two-phase viscosity, we have :

$$\begin{aligned} \frac{a_{max}}{D} &= 0.69(\,We_c)^{0.6}\frac{Re_{2\phi}^{0.1}}{We_{2\phi}^{0.6}}\left(\frac{1+\varepsilon(\bar{\rho}-1)}{1+\varepsilon\frac{1+2.5\bar{\mu}}{1+\bar{\mu}}}\right)^{1.2} \\ &\text{or} \\ \frac{a_{max}}{D} &= 0.69(\,We_c^*)^{0.6}\frac{Re_{2\phi}^{0.1}}{\bar{\rho}^{0.2}\,We_{2\phi}^{0.6}}\left(\frac{1+\varepsilon(\bar{\rho}-1)}{1+\varepsilon\frac{1+2.5\bar{\mu}}{1+\bar{\mu}}}\right)^{1.2} \end{aligned} \tag{7.37}$$

Most authors use U_l rather than $U_{2\phi}$ but $U_{2\phi}$ seems more appropriate and considering the low slip ratio in internal bubbly flow ($U_{2\phi} \simeq U_l$), the change will have minor consequences. Razzaque *et al.* (2003) suggested that the Levich (1962) formula is the most consistent and suggested $We_c^* = 1.1$; thus,

$$\frac{a_{max}}{D} = 0.73\frac{Re_{2\phi}^{0.1}}{\bar{\rho}^{0.2}\,We_{2\phi}^{0.6}}\left(\frac{1+\varepsilon(\bar{\rho}-1)}{1+\varepsilon\frac{1+2.5\bar{\mu}}{1+\bar{\mu}}}\right)^{1.2} \tag{7.38}$$

compared to the relation proposed by Hinze (1955)

$$\frac{a_{max}}{D} = 0.43\frac{Re_{2\phi}^{0.08}}{We_{2\phi}^{0.6}} \tag{7.39}$$

The experiments of Razzaque *et al.* (2003) were conducted with void fraction up to 0.3% far below the usual conditions in the nuclear industry. The previous relations have only been verify for very low void fraction. When classical turbulence is destroyed by bubbles presence,

and pseudo turbulence becomes larger, no model for bubbles size has been proposed at the knowledge of the authors.

The minimum bubble radius, a_{min}, has been studied by Shinnar (1961) and Liu and Li (1999). The fluctuating turbulent flow forces the bubbles to collide. The trapped liquid film between the bubbles must be drained, before bubbles separate, for coalescence to occur. An analytical solution for the minimum bubble radius, a_{min}, is available only if it is assumed that the bubble surfaces are immobilized by the presence of impurities. If we consider the mobility of the interface only, the numerical study of Liu and Li (1999) proposed the following relation for a_{min}:

$$333.8\frac{\gamma^{1.29}\mu_l^{0.02}B^{0.26}}{E^{1.7}\mu_g^{1.02}\rho_l^{0.55}e_d^{0.7}a_{min}^{2.03}} + 25.2\frac{\gamma^{1.38}B^{0.46}}{E^{0.7}\mu_l\rho_l^{0.84}e_d^{0.89}a_{min}^{3.11}} = 1 \tag{7.40}$$

with E, being the dimensionless radius of curvature of the liquid film between two colliding bubbles given by :

$$E = 12.61 + 2.166\tan^{-1}(2M^{0.8}) \tag{7.41}$$

where M is the interface mobility coefficient given by :

$$M = 0.63\frac{\mu_l}{\mu_g}\left(\frac{\pi\gamma}{\rho_l e_d^{2/3}a_{min}^{5/3}}\right)^{1/2} \tag{7.42}$$

In order to have the simplest model we neglect this effect and choose $a_{min} = 0$. According to Riverin and Pettigrew (2004) the distribution law of bubble diameters follows a Rayleigh distribution. The experimental results of Razzaque *et al.* (2003) leads us to conclude that the bubble size distribution generally follows a similar distribution (log-normal). The Rayleigh

distribution is expressed as follows.

$$
\begin{aligned}
&\mathrm{PDF}(a) = \begin{cases} 0 & ,\text{if } a < a_{min} \\ 10\dfrac{a-a_{min}}{(a_{max}-a_{min})^2} exp\left(-5\left(\dfrac{a-a_{min}}{a_{max}-a_{min}}\right)^2\right) & ,\text{if } a \geq a_{min} \end{cases} \\
&\mathrm{CDF}(a) = \begin{cases} 0 & ,\text{if } a < a_{min} \\ 1 - exp\left(-5\left(\dfrac{a-a_{min}}{a_{max}-a_{min}}\right)^2\right) & ,\text{if } a \geq a_{min} \end{cases} \\
&\mathrm{CDF}(a_{max}) \simeq 99.3\% \\
&< a >= a_{min} + \sqrt{\frac{\pi}{20}}\,(a_{max} - a_{min}) \\
&\text{if } a_{min} = 0 \\
&< a >= \sqrt{\frac{\pi}{20}}\, a_{max} \\
&< a^2 >= \frac{1}{5} a_{max}^2 \\
&< a^3 >= \frac{3}{10}\sqrt{\frac{\pi}{20}}\, a_{max}^3
\end{aligned}
\tag{7.43}
$$

In the equation above, PDF is the probability density function and CDF the cumulative density function. This distribution law is presented on Figure 7.1. This paper will discuss the relation between two-phase flow turbulence and bubble distribution.

7.2 Average Reynolds tensor

In this section, analytical results for a simple model representing one bubble in a bubbly flow are presented. All calculation details are obtained in the Part I (Béguin *et al.* (submitted in 2010)). In order to model the effect of void fraction, in the bubble reference frame, we consider the stationary solution of a gas bubble of radius a centered in a liquid sphere of radius l (cf. Figure 7.5). The void fraction which is the ratio of gas to total volume can be easily calculated in this case as $\varepsilon = a^3/l^3$. We consider an incompressible fluid flow governed by :

$$
\begin{aligned}
\nabla.\vec{u_g} &= 0 \qquad (a) \\
\rho_g \vec{u_g} \nabla \vec{u_g} &= -\nabla P_g + \mu_g \Delta \vec{u_g} \qquad (b)
\end{aligned}
\tag{7.44}
$$

and

$$
\begin{aligned}
\nabla.\vec{u_l} &= 0 \qquad (a) \\
\rho_l \vec{u_l} \nabla \vec{u_l} &= -\nabla P_l + \mu_l \Delta \vec{u_l} \qquad (b)
\end{aligned}
\tag{7.45}
$$

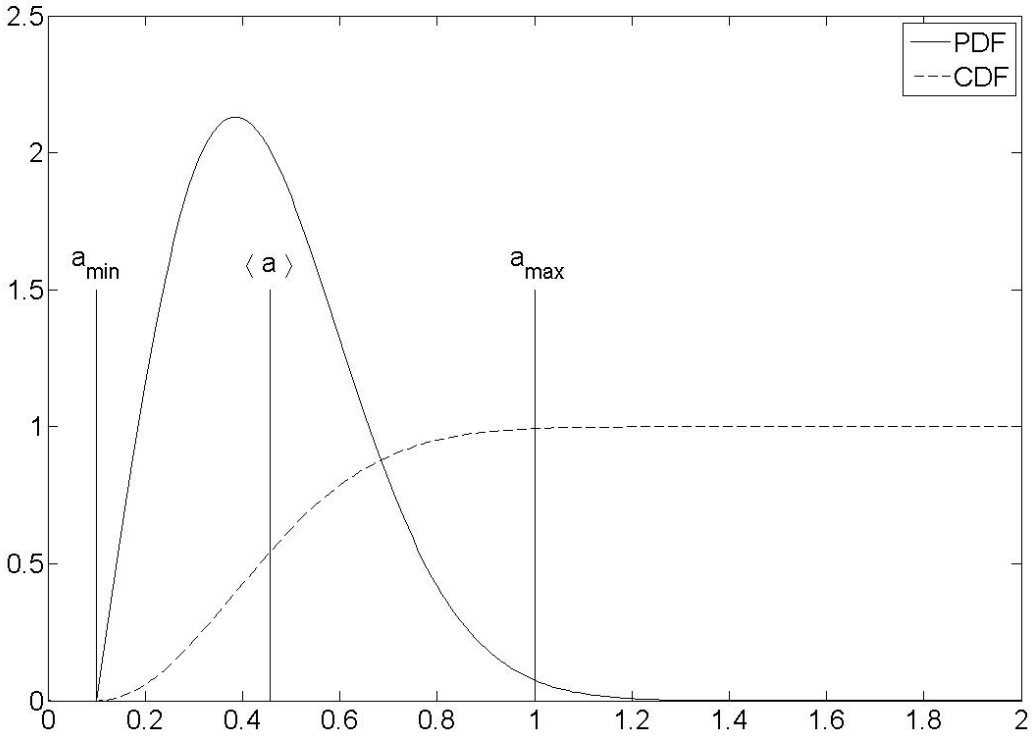

Figure 7.1 Example of a Rayleigh distribution law.

The actual pressure would include a hydrostatic pressure component : $P_l + \rho_l g z$ and $P_g + \rho_g g z$ as well as the equation would include gravity. However, the effect of the hydrostatic pressure results in the well known buoyancy force $\frac{4}{3}\Delta\rho g \pi a^3$. Thus the hydrostatic pressure component effects is already taken into account and does not have to be include explicitly. We consider the following boundary conditions :

$$
\begin{aligned}
&r = l = \frac{a}{\varepsilon^{1/3}} : \\
&\qquad u_{rl} = -U_b(1-\varepsilon)\cos(\theta) && (1)\\
&\qquad u_{\theta l} = U_b(1-\varepsilon)\sin(\theta) && (2)\\
&r = 0 : \quad \text{The condition of existence of a physical solution imposes} \\
&\qquad \text{that } u_{rg} \text{ and } u_{\theta g} \text{ have finite values.} && (3)\\
&r = a : \\
&\qquad u_{\theta l} = u_{\theta g} && (4)\\
&\qquad \mu_l\left(r\frac{\partial}{\partial r}\left(\frac{u_{\theta l}}{r}\right) + \frac{1}{r}\frac{\partial u_{rl}}{\partial \theta}\right) = \mu_g\left(r\frac{\partial}{\partial r}\left(\frac{u_{\theta g}}{r}\right) + \frac{1}{r}\frac{\partial u_{rg}}{\partial \theta}\right) && (5)\\
&\qquad P_l + \rho_l g a\cos\theta - 2\mu_l\frac{\partial u_{rl}}{\partial r} = P_g + \rho_g g a\cos\theta - 2\mu_g\frac{\partial u_{rg}}{\partial r} - \frac{2\gamma}{a} && (6)
\end{aligned}
\tag{7.46}
$$

Conditions (1) and (2) are chosen in order to have $\langle u_l \rangle = U_b$. This is important for the closure relation for space averaged Navier-stokes equation. Indeed, the proposed correct closure relations model is expressed using unknown factors of the averaged Navier-stokes equations. Somes of the unknown factors are the average liquid and gas velocities. Since the problem is solve in the bubble frame we have $\rangle u_g \langle = 0$. In this case, U_b is not necessarily the actual relative velocity of the bubbles but rather is the velocity easily obtained from the unknown factors of averaged Navier-Stokes equation.

The case $l \to \infty$ ($\varepsilon \to 0$) corresponds to the case of a single bubble in an infinite liquid volume. The influence of neighboring bubbles is set through the distance l, which represents the average half distance between the bubbles and its neighbors. Condition (6) in equation (7.46) is never valid because the assumption of a spherical bubble was made. This condition is replaced by $u_{rl} = u_{rg} = 0$. However, the condition (6) is used to verify the validity of the spherical shape assumption. Surface tension contributes to maintain spherical shape against other forces. Condition (6) is used in Part I (Béguin *et al.* (submitted in 2010)) to evaluate if surface tension forces are strong enough to overcome forces that could deform the bubble. We are able to solve this problem analytically only for Stokes or Euler flow. In the case of Euler flow, the analytical solution of the equations cannot satisfy all boundary conditions. Conditions (1) and (2) are therefore replaced by $\langle u_l \rangle = U_b$. As explained before, this is important for closure relation in the space averaged Navier-stokes equations as the considered velocities are averaged velocities.

Because, a Navier-Stokes solution for flow inside the bubble is found, we have to solve only two cases, external Stokes flow ($Re << 1$) and external Euler Flow ($Re >> 1$).

7.2.1 Internal solution

As shown in Part I of the paper, in the case of an internal incompressible flow, a Navier-Stokes solution exists. Using spherical coordinates (r,θ,ϕ), this solution is

$$\begin{aligned} u_{rg} &= 2B_0(r^2-a^2)\cos\theta \\ u_{\theta g} &= -2B_0(2r^2-a^2)\sin\theta \\ P_g &= \underbrace{20B_0\mu_g r\cos\theta}_{\text{Stokes component}} + \underbrace{\rho_g B_0^2\left[(4r^4-6a^2r^2)\sin^2\theta - 2r^4 + 4a^2r^2 + B_1\right]}_{\text{Euler or convective component}} \end{aligned} \tag{7.47}$$

Note that the only difference between the Stokes and Navier-Stokes solutions lies in the pressure expression due to convective terms.

From equations (7.16) and (7.47) the average gas Reynolds tensor is deduced as (all details are presented in Appendix 7.7) :

$$\varepsilon\bar{\bar{\tau}}_g^{Re} = -\frac{\rho_g B_0^2 a^4}{35}\varepsilon\begin{pmatrix} 4 & 0 & 0 \\ 0 & 4 & 0 \\ 0 & 0 & 32 \end{pmatrix} \tag{7.48}$$

with a more general expression, not depending on the coordinate system, being :

$$\varepsilon\bar{\bar{\tau}}_g^{Re} = -\frac{4\rho_g B_0^2 a^4}{35U_b^2}\varepsilon\left((\vec{U}_b.\vec{U}_b)\bar{\bar{I}} + 7\vec{U}_b\otimes\vec{U}_b\right) \tag{7.49}$$

The turbulence in the gas phase will represent the internal kinetic energy of the vortex inside the bubble. This corresponds also to the intensity of the internal vortex. For high viscosity ratio ($\bar{\mu}$) this turbulence term is markedly reduced, the bubble then effectively corresponding to a "solid" drop (*e.g. a water droplet in air*). As the anisotropic gas turbulence is exactly seven times the isotropic turbulence, the Reynolds stress tensors in the gas is presented in Figure 7.2 in terms of isotropic turbulence alone. Depending on the Stokes or Euler assumption for the external flow the values of B_0 will change.

$$\begin{aligned} a^2B_0 &= -\frac{U_b}{2}\frac{1-\varepsilon}{F(\varepsilon)}(2-5\varepsilon+3\varepsilon^{5/3}) \quad \text{Stokes flow} \\ a^2B_0 &= -\frac{3}{4}U_b \quad\quad\quad\quad\quad\quad\quad\quad\quad\quad\quad\quad\quad\quad\quad\quad \text{Euler flow} \end{aligned} \tag{7.50}$$

7.2.2 External Flow

External Stokes Flow ($Re << 1$)

As shown in Part I, in the case of external Stokes flow we have, using spherical coordinates (r,θ,ϕ) :

$$\begin{aligned} u_{rl} &= 2\left(C_0\left(r^2-a^2\right)+C_2\left(\tfrac{1}{r}-\tfrac{1}{a}\right)+C_3\left(\tfrac{1}{r^3}-\tfrac{1}{a^3}\right)\right)\cos(\theta) \\ u_{\theta l} &= -\left(2C_0\left(2r^2-a^2\right)+C_2\left(\tfrac{1}{r}-\tfrac{2}{a}\right)-C_3\left(\tfrac{1}{r^3}+\tfrac{2}{a^3}\right)\right)\sin(\theta) \\ P_l &= \mu_l\left(20C_0 r+\tfrac{2C_2}{r^2}\right)\cos(\theta)+C_4 \end{aligned} \tag{7.51}$$

with

$$\begin{aligned} a^2B_0 &= -\frac{U_b}{2}\frac{1-\varepsilon}{F(\varepsilon)}(2-5\varepsilon+3\varepsilon^{5/3}) \\ a^2C_0 &= \frac{U_b}{2}\frac{1-\varepsilon}{F(\varepsilon)}(2\varepsilon+3\bar{\mu}(\varepsilon-\varepsilon^{5/3})) \\ \tfrac{C_2}{a} &= U_b\frac{1-\varepsilon}{F(\varepsilon)}(2+3\varepsilon^{5/3}+3\bar{\mu}(1-\varepsilon^{5/3})) \\ \tfrac{C_3}{a^3} &= -U_b\frac{1-\varepsilon}{F(\varepsilon)}(\varepsilon+\bar{\mu}(1-\varepsilon)) \end{aligned} \tag{7.52}$$

$$F(\varepsilon) = (1-\varepsilon^{1/3})^3\left((4+6\varepsilon^{1/3}+6\varepsilon^{2/3}+4\varepsilon)+\bar{\mu}(4+3\varepsilon^{1/3}-3\varepsilon^{2/3}-4\varepsilon)\right)$$

The force on the bubble, evaluated from the surface stress integration, and the corresponding drag coefficient and terminal velocity are :

$$\begin{aligned} f &= 4\pi\mu_l U_b a\left[\frac{1-\varepsilon}{(1-\varepsilon^{1/3})^3}\right]\left[\frac{4+6\varepsilon^{5/3}+6\bar{\mu}(1-\varepsilon^{5/3})}{(4+6\varepsilon^{1/3}+6\varepsilon^{2/3}+4\varepsilon)+\bar{\mu}(4+3\varepsilon^{1/3}-3\varepsilon^{2/3}-4\varepsilon)}\right] \\ C_D &= \frac{16}{Re}\left[\frac{1-\varepsilon}{(1-\varepsilon^{1/3})^3}\right]\left[\frac{4+6\varepsilon^{5/3}+6\bar{\mu}(1-\varepsilon^{5/3})}{(4+6\varepsilon^{1/3}+6\varepsilon^{2/3}+4\varepsilon)+\bar{\mu}(4+3\varepsilon^{1/3}-3\varepsilon^{2/3}-4\varepsilon)}\right] \\ U_b &= \frac{1}{3}\frac{a^2\Delta\rho g}{\mu_l}\left[\frac{(1-\varepsilon^{1/3})^3}{1-\varepsilon}\right]\left[\frac{(4+6\varepsilon^{1/3}+6\varepsilon^{2/3}+4\varepsilon)+\bar{\mu}(4+3\varepsilon^{1/3}-3\varepsilon^{2/3}-4\varepsilon)}{4+6\varepsilon^{5/3}+6\bar{\mu}(1-\varepsilon^{5/3})}\right] \end{aligned} \tag{7.53}$$

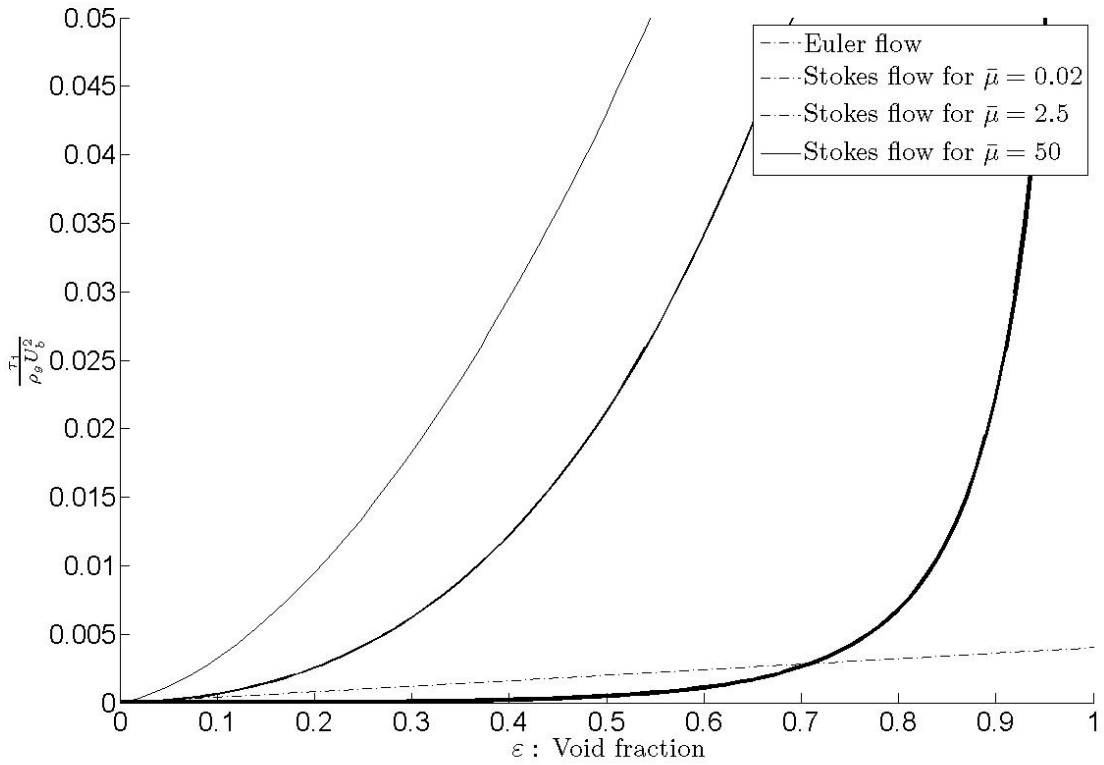

Figure 7.2 Isotropic gas pseudo turbulence in two-phase flow

For a bubble in an infinite liquid domain ($\varepsilon = 0$), these reduce to :

$$\begin{aligned} f &= 4\pi\mu_l U_b a \frac{2+3\bar{\mu}}{2+2\bar{\mu}} \\ U_b &= \frac{1}{3}\frac{\Delta\rho g a^2}{\mu_l}\frac{2+2\bar{\mu}}{2+3\bar{\mu}} \\ C_D &= \frac{16}{Re}\frac{2+3\bar{\mu}}{2+2\bar{\mu}} \end{aligned} \tag{7.54}$$

As shown in Part I, this result is in accordance with equation proposed by Taylor and Acrivos (1964) for $\varepsilon = 0$. Most importantly it should be noted that equation (7.53) extends the expression for C_D to all values of void fraction (ε).

Noting :

$$(1-\varepsilon)\bar{\bar{\tau}}_l^{Re} = -\rho_l \begin{pmatrix} \tau_{Rl} & 0 & 0 \\ 0 & \tau_{Rl} & 0 \\ 0 & 0 & \tau_{Zl} - (1-\varepsilon)U_b^2 \end{pmatrix} \tag{7.55}$$

the Reynolds stress tensor is calculated from equations (7.16), (7.51) and (7.52) giving (all details are presented in Appendix 7.8) :

$$\begin{aligned} \tau_{Rl} &= \frac{\rho_l}{5}\varepsilon^{1/3}\left(-\frac{4}{7}\left(\varepsilon^{8/3}-\varepsilon\right)\frac{a^4 C_0^2}{\varepsilon^2} + \left(\varepsilon^{5/3}-\varepsilon^{1/3}\right)\frac{aC_0C_2}{\varepsilon} + 6\left(\varepsilon^{5/3}-\varepsilon\right)\frac{C_0C_3}{a\varepsilon}\right) \\ &\quad + \frac{\rho_l}{5}\varepsilon^{1/3}\left(-\left(\varepsilon^{2/3}-\varepsilon^{1/3}\right)\frac{C_2^2}{a^2}6\left(\varepsilon^{2/3}-\varepsilon^{4/3}\right)\frac{C_2C_3}{a^4} + 3\left(\varepsilon^{2/3}-\varepsilon^{5/3}\right)\frac{C_3^2}{a^6}\right) \end{aligned} \tag{7.56}$$

and :

$$\begin{aligned} \tau_{Zl} &= \frac{4\rho_l}{5}\left(\frac{43}{7}\varepsilon^{2/3}(1-\varepsilon^{7/3})\frac{a^4C_0^2}{\varepsilon^2} + 10\varepsilon^{1/3}\left(1-\varepsilon^{5/3}\right)\frac{a^2C_0C_1}{\varepsilon}\right) \\ &\quad + \frac{4\rho_l}{5}\left(8\varepsilon^{2/3}\left(1-\varepsilon^{4/3}\right)\frac{aC_0C_2}{\varepsilon} - 2\varepsilon^{4/3}(1-\varepsilon^{2/3})\frac{C_0C_3}{a\varepsilon} + 5(1-\varepsilon)C_1^2\right) \\ &\quad + \frac{4\rho_l}{5}\left(10\varepsilon^{1/3}(1-\varepsilon^{2/3})\frac{C_1C_2}{a} + 7\varepsilon^{2/3}\left(1-\varepsilon^{1/3}\right)\frac{C_2^2}{a^2}\right) \\ &\quad + \frac{4\rho_l}{5}\left(2\varepsilon\left(1-\varepsilon^{1/3}\right)\frac{C_2C_3}{a^4} + \varepsilon\left(1-\varepsilon\right)\frac{C_3^2}{a^6}\right) \end{aligned} \tag{7.57}$$

with a more general expression, not depending on the coordinate system being :

$$(1-\varepsilon)\bar{\bar{\tau}}_l^{Re} = \frac{\rho_l}{U_b^2}\left(\tau_{Rl}(\vec{U}_b.\vec{U}_b)\bar{\bar{I}} + \left(\frac{\tau_{Zl}-\tau_{Rl}}{U_b^2} - 1\right)\vec{U}_b \otimes \vec{U}_b\right) \tag{7.58}$$

Later on, we will use the general notation

$$(1-\varepsilon)\bar{\bar{\tau}}_l^{Re} = \rho_l \left(\tau_1(\vec{U}_b.\vec{U}_b)\bar{\bar{I}} + \tau_2 \vec{U}_b \otimes \vec{U}_b\right) \tag{7.59}$$

where τ_1 is the isotropic turbulence, and τ_2 is the anisotropic turbulence.

External Euler flow without boundary layer correction ($Re >> 1$)

As shown in Part I (Béguin *et al.* (submitted in 2010)), in the case of Euler flow, we have :

$$\begin{aligned} u_{rl} &= -U_b\left(1-\frac{a^3}{r^3}\right)\cos\theta \\ u_{\theta l} &= U_b\left(1+\frac{a^3}{2r^3}\right)\sin\theta \\ P_l &= -\rho_l U_b^2\left[\left(\frac{3a^3}{2r^3}-\frac{3a^6}{8r^6}\right)\sin^2\theta - \frac{a^3}{r^3}+\frac{a^6}{2r^6}+C_1\right] \end{aligned} \tag{7.60}$$

Satisfying solely the condition $\langle u_l \rangle = U_b$ instead of $\vec{u}_l\,|_{r=l} - U_b(1-\varepsilon)\vec{e}_z$, leads to the following velocities at $r = l$

$$\begin{aligned} u_{rl}\,|_{r=l} &= -U_b(1-\varepsilon)\cos\theta \\ u_{\theta l}\,|_{r=l} &= U_b\left(1+\frac{\varepsilon}{2}\right)\sin\theta \end{aligned} \tag{7.61}$$

which are different from a pure vertical flow boundary condition. The difference grows as void fraction increases.

The tangential stress component does not vanish on $r = a$, because a boundary layer (non Euler flow) exists. If we neglect the boundary layer, we deduce the force on the bubble through total dissipation in the liquid domain which needs to be equal to the power of drag forces Batchelor (1971) and deduce force on the bubble :

$$\begin{aligned} f &= 12\pi\mu_l a U_b(1-\varepsilon^{5/3}) \\ U_b &= \frac{1}{9}\frac{\Delta\rho g a^2}{\mu_l}\frac{1}{1-\varepsilon^{5/3}} \\ C_D &= \frac{48}{Re}(1-\varepsilon^{5/3}) \end{aligned} \tag{7.62}$$

This relation is in agreement, for $Re >> 1$ and $\varepsilon = 0$, with the relation of Mei *et al.* (1994).

The following equivalent turbulence tensor is deduced from equation (7.60), where all

details are presented in Appendix 7.8.2.

$$(1-\varepsilon)\bar{\bar{\tau}}_l^{Re} = -\frac{\rho_l U_b^2}{20}\varepsilon(1-\varepsilon)\begin{pmatrix} 3 & 0 & 0 \\ 0 & 3 & 0 \\ 0 & 0 & 4 \end{pmatrix} \tag{7.63}$$

A more general expression, not depending on the coordinate system is :

$$(1-\varepsilon)\bar{\bar{\tau}}_l^{Re} = -\frac{\rho_l}{20}\varepsilon(1-\varepsilon)\left(3(\vec{U}_b.\vec{U}_b)\bar{\bar{I}} + \vec{U}_b \otimes \vec{U}_b\right) \tag{7.64}$$

Park *et al.* (1998), using a probability function and potential flow found :

$$(1-\varepsilon)\bar{\bar{\tau}}_l^{Re} = -\frac{\rho_l}{20}\varepsilon\left(3(\vec{U}_b.\vec{U}_b)\bar{\bar{I}} + \vec{U}_b \otimes \vec{U}_b\right) \tag{7.65}$$

On the other hand, Biesheuvel and Van Wijngaarden (1984) proposed :

$$(1-\varepsilon)\bar{\bar{\tau}}_l^{Re} = -\frac{\rho_l}{20}\varepsilon(1-\varepsilon)^2\left(3(\vec{U}_b.\vec{U}_b)\bar{\bar{I}} + \vec{U}_b \otimes \vec{U}_b\right) \tag{7.66}$$

The three proposed relations are in agreement for low void fraction. These three models are based on different assumptions for the liquid velocity when $r \to \infty$. In the present work, we have chosen to have $U_b = \langle u_l \rangle - \langle u_g \rangle$ in accordance with the assumptions described in Part I. As the calculations are done in the bubble reference frame, we only have $\langle u_l \rangle = U_b$. Biesheuvel and Van Wijngaarden (1984) assumed that the velocity is $U_0 = (1-\varepsilon)\langle u_l \rangle - \varepsilon\langle u_g \rangle$ when $r \to \infty$. Park *et al.* (1998) assumed that the distribution of bubble locations is such that,

$$P(\vec{x};t;\vec{z}) = \frac{dV}{\frac{4}{3}\pi l^3}\left(1 - \vec{x'}\frac{\nabla\varepsilon(\vec{x},t)}{\varepsilon(\vec{x},t)}\right) \tag{7.67}$$

is the probability of finding a bubble in a volume dV surrounding the point $\vec{x}$ at time t where $\vec{x'} = \vec{x} - \vec{z}$. The center of the bubble, $\vec{z}$, can lie anywhere inside the sphere of radius l.

We compare the equations for the Reynolds stress tensor in Stokes flow (7.58) and the Reynolds stress tensor in Euler flow,(7.64), with Park's model (7.65) and Bieusheuvel's model (7.66), in Figures 7.3 and 7.4.

All the models are in agreement with the conclusion of Lance and Bataille (1991). That is, the fluctuating kinetic energy in the liquid is considered as a simple superposition of shear-induced and bubble/droplet-induced turbulence. In conformity with the classical usage we call this bubble/droplet-induced turbulence, pseudo turbulence. The experiments of Lance and Bataille (1991) were done for a range of void fractions from 0% to 3%. They argue that the linear superposition of the shear-induced (classical turbulence) and fluid particle-induced

turbulence (pseudo turbulence) is valid up to a void fraction of ($\varepsilon \sim 1\%$). Above this void fraction only pseudo turbulence is present. The experiments lead to the conclusion that bubble-induced turbulence can be expressed as :

$$\tau \sim \varepsilon \rho_l U_b^2 \tag{7.68}$$

7.3 Numerical Solutions

To validate and improve the new relations to evaluate the Reynolds stress tensor (7.49), (7.58) and (7.64), numerical experiments have been carried out by varying the Reynolds number Re (from 0.01 to 300), the void fraction ε (from 10^{-6} to 0.6), the viscosity ratio $\bar{\mu}$ (from 0.02 to 50) and the density ratio $\bar{\rho}$ (from 10^{-3} to 10^3).

7.3.1 Numerical Solution Strategy

Figure 7.5 shows the geometry of the problem solved both numerically and analytically. Figure 7.6 shows the geometry of a more realistic case of a five bubble train. This problem was solved with two types of boundary condition, first with $u = U_b(1-\varepsilon), v = 0$ for $r = l$ named later on the "Dirichlet case" and secondly with $u =$ "$Free$", $v = 0$ for $r = l$ named later on the "Neumann case". Both cases have for inlet and outlet conditions : $u = U_b(1-\varepsilon), v = 0$. A finite element code has been used to solve the incompressible Navier-Stokes equations in an axisymmetric frame of reference (the central axis of rotation is denoted by a dash-dot line). The numerical method and convergence study are presented in Part I of the paper.

7.3.2 Comparison between Analytical and Numerical Results for a single Bubble

Non dimensionalization allows us to set $a = 0.5$, $U_b = 1$, $\mu_l = 1$, which means : $Re = \rho_l$, $\bar{\rho} = \rho_g/Re$, $\bar{\mu} = \mu_g$ and $\varepsilon = 1/8l^3$ We choose to obtain solutions for the following cases :

- $\bar{\rho} = 10^{-3}, 1, 10^3$
- $\bar{\mu} = 0.02, 0.1, 0.5, 2.5, 12.5, 50$
- $Re = 0.01, 0.1, 1, 10, 100, 300$
- $l = 0.59(60\%), 0.68(40\%), 0.79(25\%), 1(12.5\%),$
  $2.5(0.8\%), 5(0.1\%), 10(0.0125\%), 50(0.0001\%)$

The corresponding void fraction (ε) is indicated in brackets. As confirmed in Part I, the numerical drag coefficient results are in good agreement with the relations of Mei *et al.* (1994) and Taylor and Acrivos (1964). We are therefore confident about the accuracy of the numerical results.

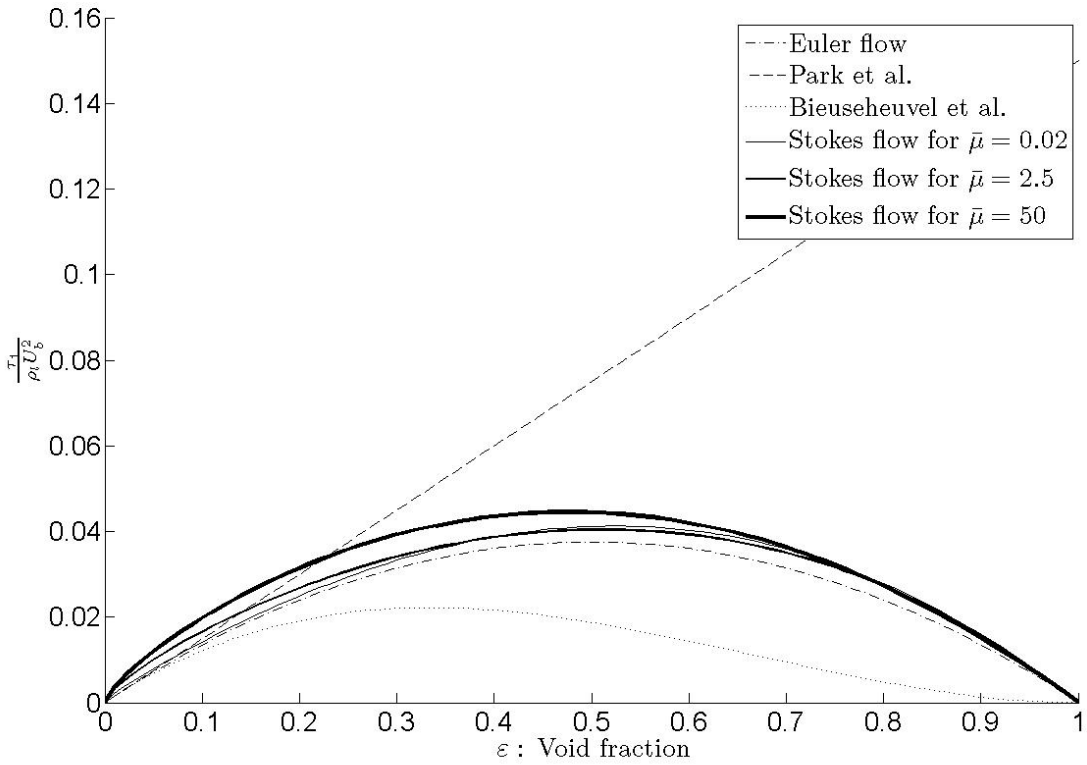

Figure 7.3 Isotropic liquid pseudo turbulence in two-phase flow

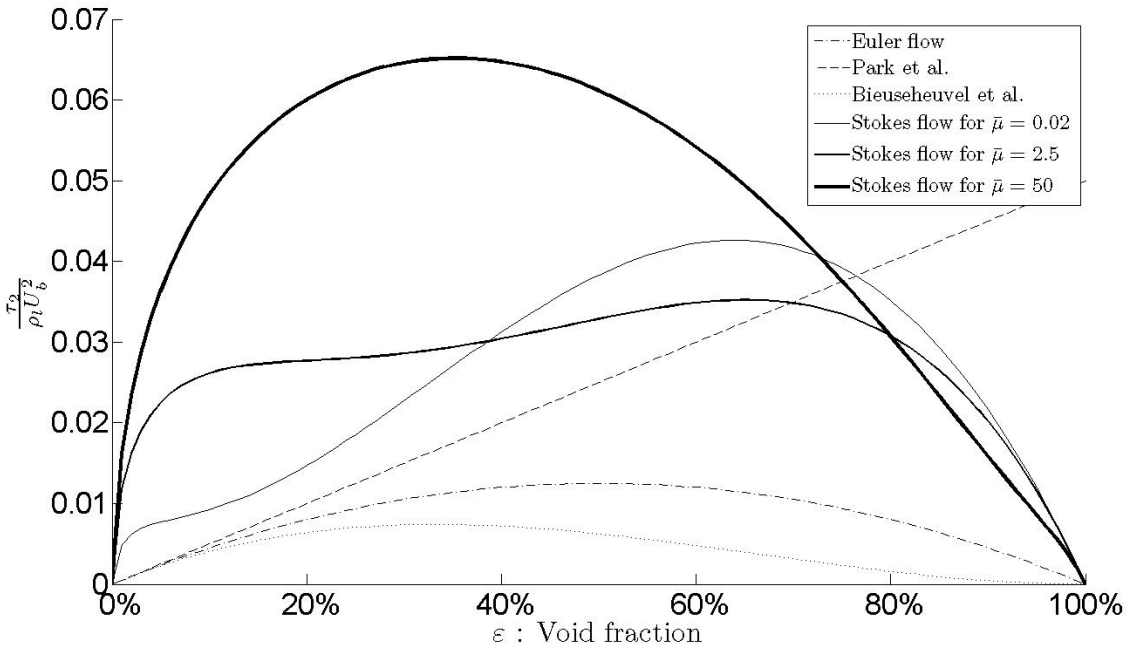

Figure 7.4 Anisotropic liquid pseudo turbulence in two-phase flow

Figures 7.7 and 7.8 compare the computed isotropic and anisotropic pseudo turbulence with the analytical relation. The equations considered are the Euler pseudo turbulence (7.64), Park's model (7.65), Bieusheuvel's model (7.66) and Stokes pseudo turbulence (7.58). For bubble Reynolds numbers (Re) below 100, the agreement is excellent. For low void fraction and high Reynolds numbers, the analytical solution of the anisotropic turbulence overestimates the pseudo turbulence. However, the Reynolds effect remains small and for high void fraction ($\varepsilon = 60\%$) its effects is significantly reduced.

For isotropic turbulence, the simple Euler formulation could be a reasonable choice at least for some parameters. However, for anisotropic turbulence, the relation is far more complex, and the Euler formulation and the potential flow assumption are no longer correct. In this case the Stokes formulation is a far superior choice.

7.3.3 Numerical results for a more realistic case

The agreement between numerical and analytical results for a single bubble gives us confidence in the accuracy of both the numerical and analytical calculations. We can therefore now study more realistic cases. The previous case gives us an analytical solution which does not take into account the wake generated by surrounding bubbles. To investigate this, the

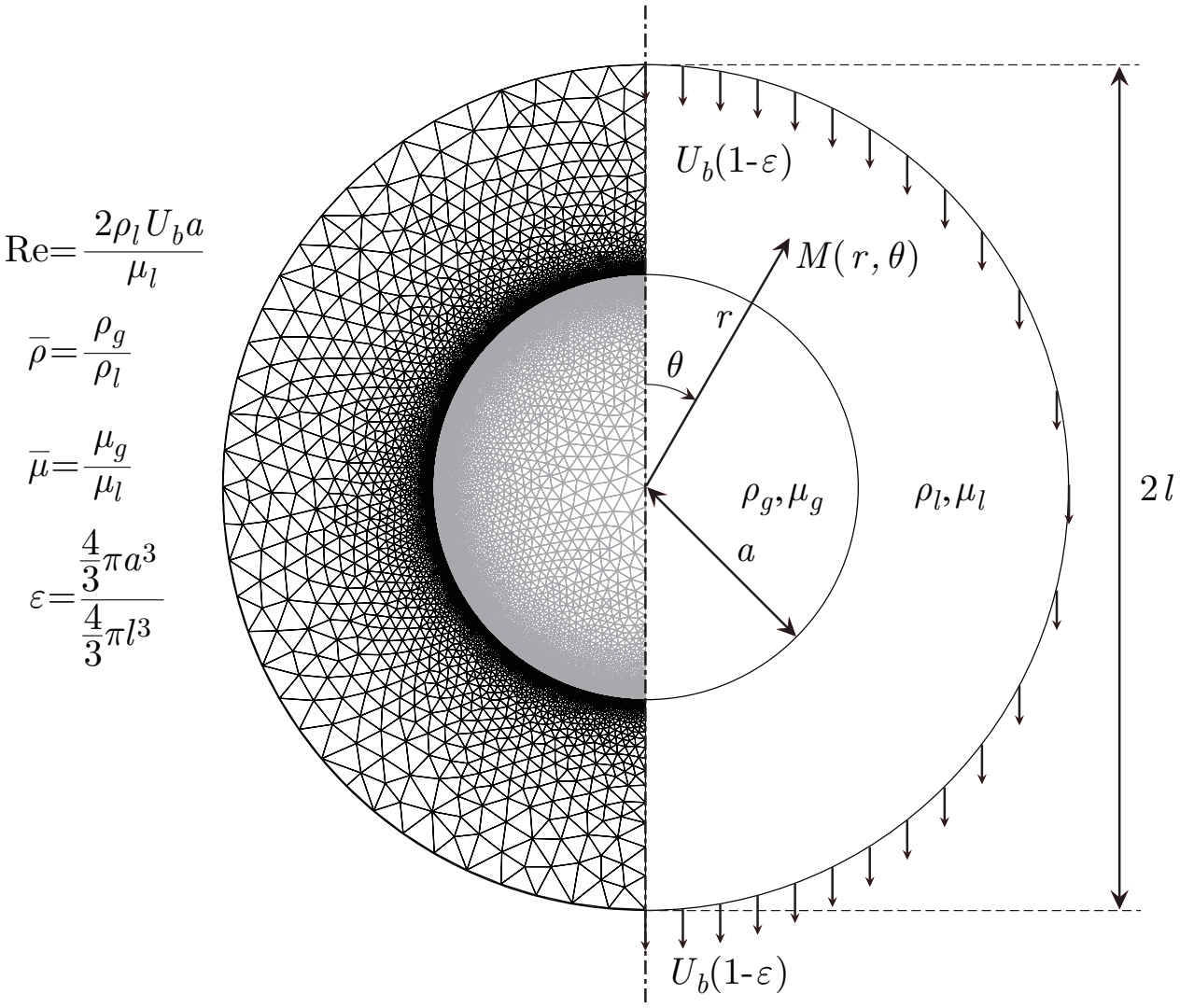

Figure 7.5 Geometry of the Problem of one single bubble.

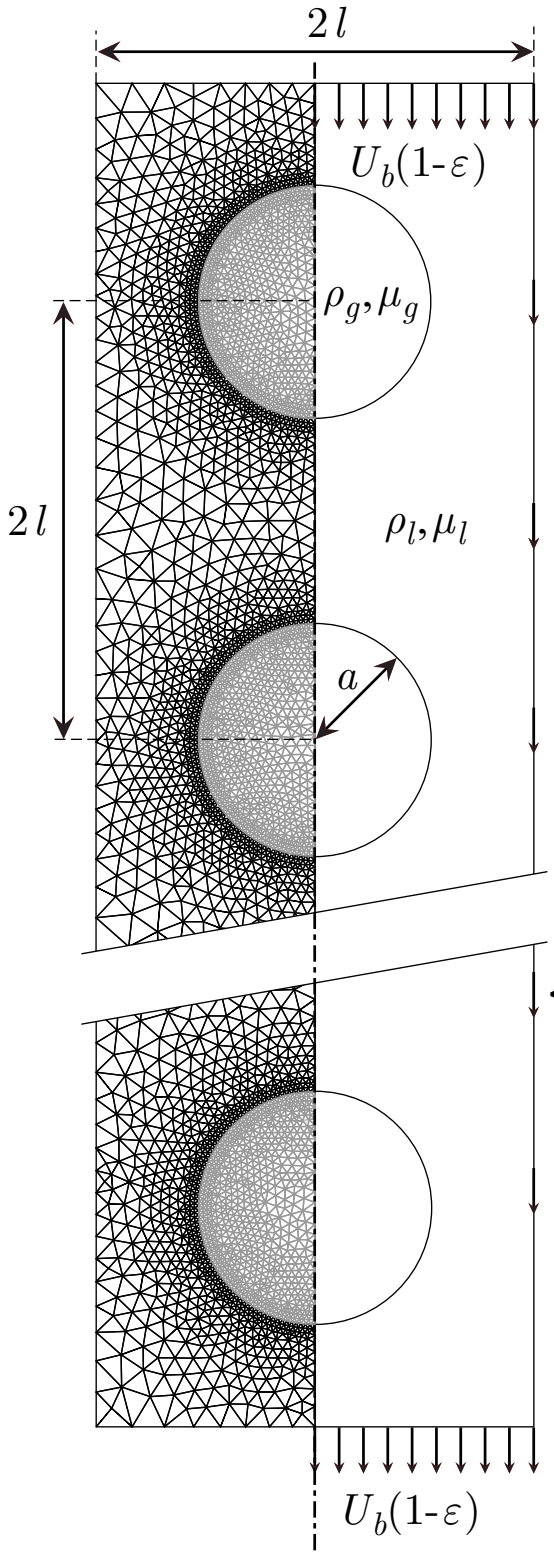

$$\mathrm{Re} = \frac{2\rho_l U_b a}{\mu_l}$$

$$\overline{\rho} = \frac{\rho_g}{\rho_l}$$

$$\overline{\mu} = \frac{\mu_g}{\mu_l}$$

$$\varepsilon = \frac{\frac{4}{3}\pi a^3}{2\pi l^3}$$

Figure 7.6 Geometry of the Problem of a n bubbles train.

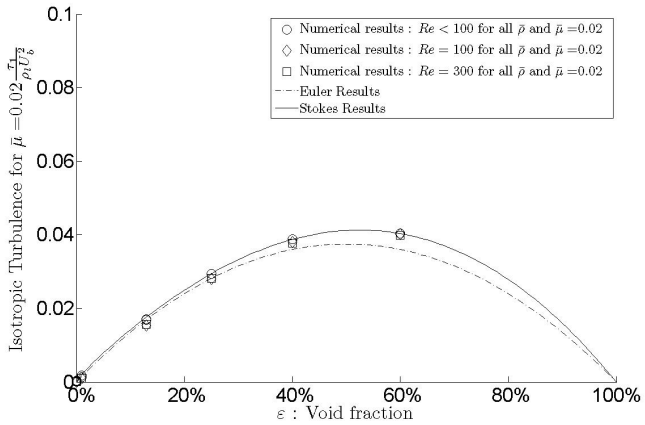

(a) $\bar{\mu}$ = 0.02

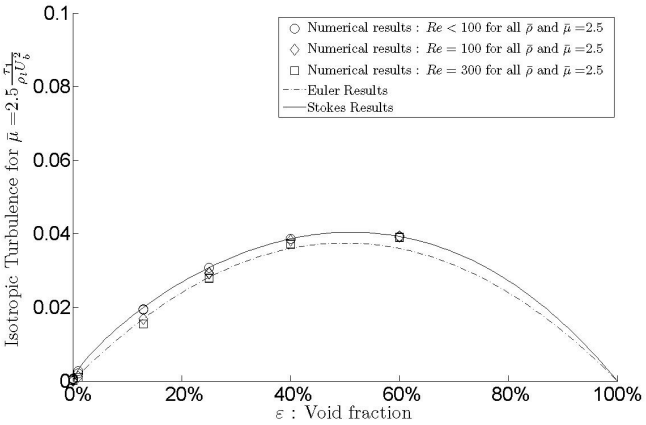

(b) $\bar{\mu}$ = 2.5

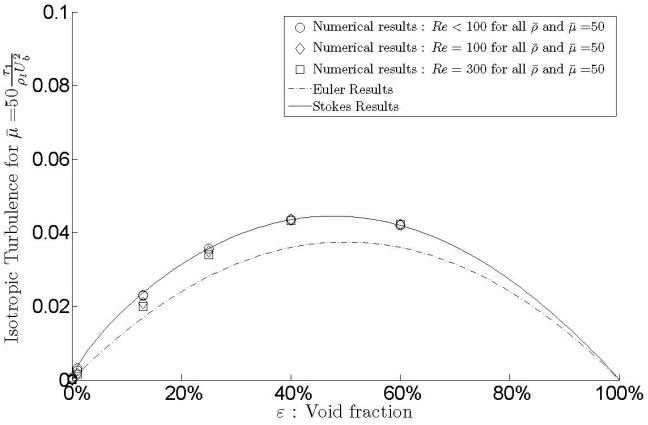

(c) $\bar{\mu}$ = 50

Figure 7.7 Comparison between numerical and analytical results of isotropic turbulence in continuous phase for one bubble.

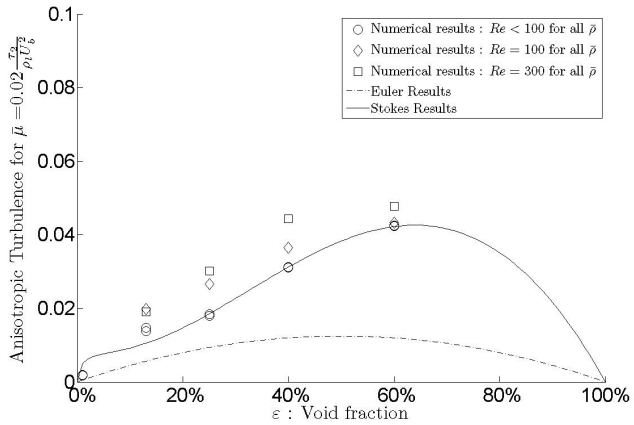

(a) $\bar{\mu}$ = 0.02

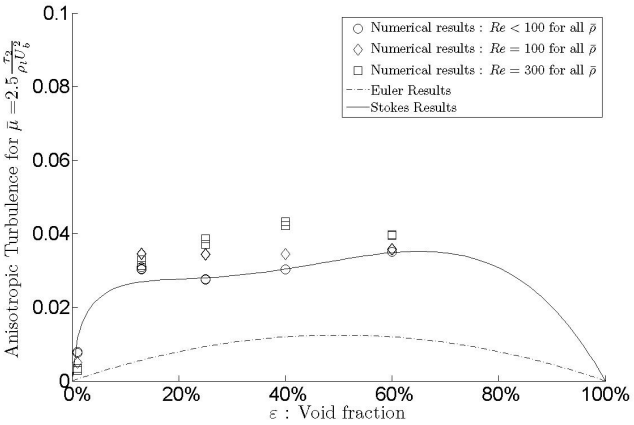

(b) $\bar{\mu}$ = 2.5

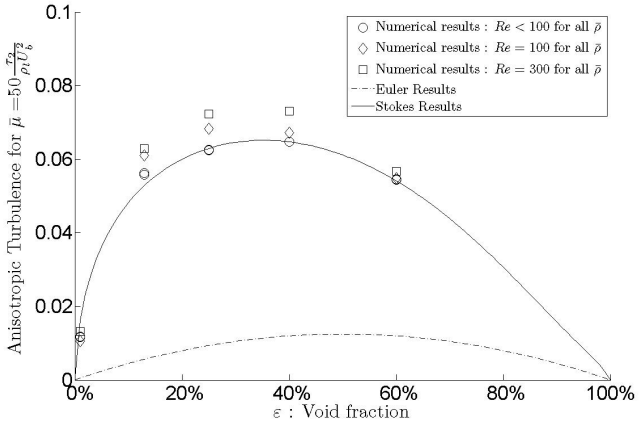

(c) $\bar{\mu}$ = 50

Figure 7.8 Comparison between numerical and analytical results of anisotropic turbulence in continuous phase for one bubble.

problem presented in Figure 7.6 has been solved. The bubbles are separated by a distance $2l$ inside a tube of radius l. Several computations were done varying the number of bubbles in a bubble train. As shown in Part I, a five bubble train was found to be sufficiently long to eliminate any substantial variation in the C_D of the central bubble by addition of more bubbles in the train. Numerical solutions were obtained for the following combination of parameters :

- $\bar{\mu} = 0.02, 0.1, 0.5, 12.5, 25, 50$
- $Re = 0.01, 0.1, 1, 10, 100, 300$
- $\varepsilon = 0, 0001\%, 1\%, 2\%, 5\%, 10\%, 20\%, 30\%, 40\%, 45\%, 50\%$

In Part I, the agreement between numerical results and the following correlation for the C_D, deduced from the analytical relation (7.53), have been shown

$$
\begin{aligned}
C_D &= \frac{16}{Re}\left(1 + \frac{2\left(\dfrac{2+3\bar{\mu}}{2+2\bar{\mu}}\right)^2}{1+\dfrac{Re_c}{Re}}\right)\frac{1-\varepsilon}{(1-\varepsilon^{1/3})^3}\frac{P_1(\varepsilon)+\bar{\mu}P_2(\varepsilon)}{P_3(\varepsilon)+\bar{\mu}P_4(\varepsilon)} \\
&\text{with :} \\
&P_1(\varepsilon) = 4 + 6\varepsilon^{5/3} \\
&P_2(\varepsilon) = 6 - 6\varepsilon^{5/3} \\
&P_3(\varepsilon) = 4 + 6\varepsilon^{1/3} + 6\varepsilon^{2/3} + 4\varepsilon \\
&P_4(\varepsilon) = 4 + 3\varepsilon^{1/3} - 3\varepsilon^{2/3} - 4\varepsilon \\
&Re_c = 33 + 50000\varepsilon
\end{aligned}
\tag{7.69}
$$

The transition between Stokes and Euler flow occurs at the critical Reynolds number Re_c. It has been shown that the transition occurs for higher Reynolds number as the void fraction increases. This explain why the classical turbulence disappears for a such low void fraction as low as 1%. However, since the maximum Reynolds number of the study was $Re = 300$, we can only conclude that the transition from Stokes to Euler Flow occurs for values of Reynolds number larger than 300 for void fraction greater than 0.5%.

As pseudo turbulence is scaled with relative bubble velocity U_b, the values of the drag forces compared to buoyancy forces will be useful to calculate the order of magnitude of pseudo turbulence.

Analytical and numerical results for the Neumann case are both presented on Figures 7.9 and 7.10. If the Stokes approximation of one bubble (solid line) is valid to evaluate multi-bubble drag coefficients, it is not true for pseudo turbulence in liquid. Because Neumann case is closer than the Dirichlet cases to the physical phenomenon, a new correlation for the

Neumann case is proposed (bold solid line) as :

$$
\begin{aligned}
(1-\varepsilon)\tau_l^{\bar{\bar{Re}}} &= \rho_l \left(\tau_1(\vec{U}_b.\vec{U}_b)\bar{\bar{I}} + \tau_2(\vec{U}_b \otimes \vec{U}_b)\right) \\
\tau_1 &= \frac{1}{25}\left(\frac{5+\bar{\mu}}{5+2\bar{\mu}}\right)\varepsilon^{\frac{2+2\bar{\mu}}{3+4\bar{\mu}}}(1-\varepsilon) \\
\tau_2 &= \left(\frac{0.15+0.08\bar{\mu}}{1+0.15\bar{\mu}}\sqrt{\varepsilon}+5\varepsilon^4\right)(1-\varepsilon)
\end{aligned}
\tag{7.70}
$$

As the results show, the anisotropic pseudo turbulence in the continuous phase (τ_2 - Figure 7.10) is much higher than the isotropic pseudo turbulence (τ_1 - Figure 7.9). The wakes have a much stronger effect on pseudo turbulence than on the drag. Indeed, while the drag coefficient does not vary much between single bubble case (without wake) and the five bubble train, it is not the case for pseudo turbulence. This explains the greater role played by viscosity ratio and Reynolds number.

However, the pseudo turbulence remains unchanged for Reynolds number below 100 (represented by circles). Only for high viscosity ratios ($\bar{\mu} > 10$) does the Reynolds number have a significant influence on pseudo turbulence. Moreover for a Reynolds number of 100 ($Re = 100$), its effect decreases for higher void fraction and pseudo turbulence comes closer to that observed at low Reynolds numbers. The critical Reynolds number Re_c, at which transition occurs from Stokes flow to Euler flow, increases with void fraction (cf. Eq. (7.69) or Part I).This leads to the conclusion that Stokes flow represents flow around bubbles, and confirms that classical turbulence cannot developed in two-phase flow as long as the void fraction is sufficiently high.

The computed isotropic turbulence τ_1 is half that predicted by the analytical model (cf. Figure 7.9). Conversely, the anisotropic turbulence τ_2 is ten times higher than expected by the analytical model (cf. Figure 7.10). In other words, the bubble wake creates mostly anisotropic turbulence. As logically expected, anisotropic turbulence is higher for larger viscosity ratios (high viscosity ratio bubbles are relatively closer to solid particles). But even for low viscosity ratios, the pseudo turbulence is still a lot larger than predicted by the theories of Park *et al.* (1998) and Biesheuvel and Van Wijngaarden (1984).

Figure 7.10 shows that at low void fraction, pseudo turbulence increases faster for higher viscosity ratio. This trend was already predicted by the analytical results shown on Figure 7.4. As expected, a higher Reynolds number leads to higher anisotropic turbulence but this effect is only noticeable for Reynolds numbers higher than 100 and high viscosity ratios.

Figure 7.11 presents numerical results for isotropic pseudo turbulence for the Dirichlet case. A higher isotropic turbulence is observed closer to models as the wake is more constrained.

Figure 7.12 presents numerical results for anisotropic pseudo turbulence for the Dirichlet case. same magnitude of turbulence is noticed. For the Dirichlet case, the wake is more constrained and the Reynolds numbers is far less important. But as the isotropic turbulence represents only 10% of the total turbulence (cf. scale of Figures 7.10 and 7.9), the Dirichlet case and the Neumann case present the same magnitude of total turbulence.

Finally for both the Neumann and Dirichlet cases, the density ratio $\bar{\rho}$ has no effect. We do not see any significant difference between the results for $\bar{\rho} = 10^{-3}, 1$ and 10^{3}. In all figures presented before results for all density ratios were presented but the data overlaps each other.

Figure 7.13 presents experimental results of pseudo turbulence by Garnier *et al.* (2002) and 3D numerical prediction by Brunner and Tryggvason (2002). Garnier *et al.* (2002) note relative velocity of the bubble U_R and Brunner and Tryggvason (2002) denote it w_r. Both results are in the same magnitude as ours. For a void fraction of 20%, we predict a dimensionless pseudo turbulence between 0.1 and 0.2 depending on viscosity ratio. Garnier *et al.* (2002) predict a also smaller isotropic turbulence $(U_b'^2 + V_b'^2)/w_r^2$.

While pseudo turbulence in the liquid is not well modelled by Stokes analytical solution, for the pseudo turbulence in gas the analytical results for Stokes flow are in very good agreement as shown in Figure 7.14. This pseudo turbulence inside the bubbles represents the internal kinetic energy magnitude of the internal vortex. The figure shows both isotropic and anisotropic turbulence. As predicted, isotropic turbulence is seven times lower than anisotropic turbulence (cf. eq. 7.49). Indeed, points for $7\tau_1/(\rho_g U_b^2)$ and $\tau_2/(\rho_g U_b^2)$ overlap each other.

As expected, this internal pseudo turbulence decreases with viscosity ratio. Indeed for high viscosity ratio bubbles are closer to solid particles. Reynolds number and density ratio have no effect on this internal turbulence. For the Dirichlet case the internal turbulence is higher than predicted by the analytical results, Figure 7.15, but the order of magnitude and variation are correctly predicted by the theory. Note that for the Dirichlet case, the flow is more constrained and more energy is transfered to the bubbles, which explains the higher magnitude of internal turbulence observed.

7.4 Discussion on bubble size

As explained in the first section, turbulence forces are responsible for bubble breakup and therefore for their size. However, previous models have, to date, used only classical turbulence modelling which is not correct for void fraction greater than 1%. Moreover a statistic knowledge of bubble size is needed for the closure relation for interface forces as shown by equation (7.29).

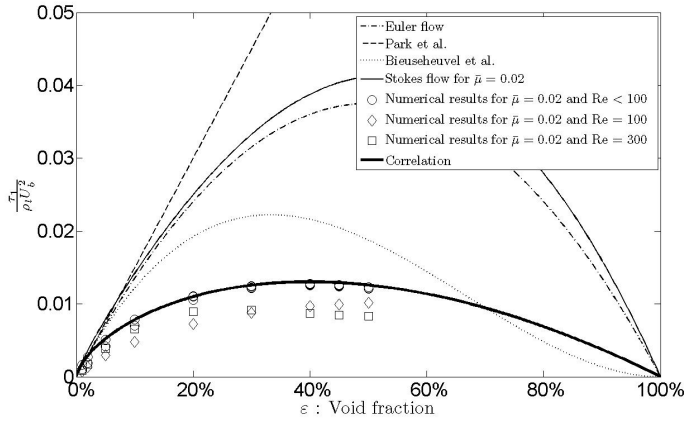

(a) $\bar{\mu}$ = 0.02

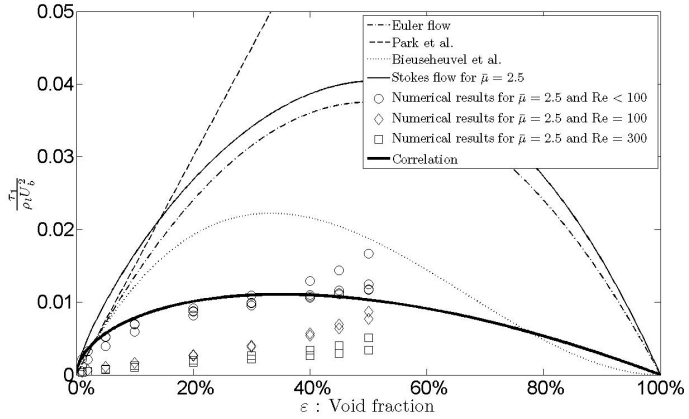

(b) $\bar{\mu}$ = 2.5

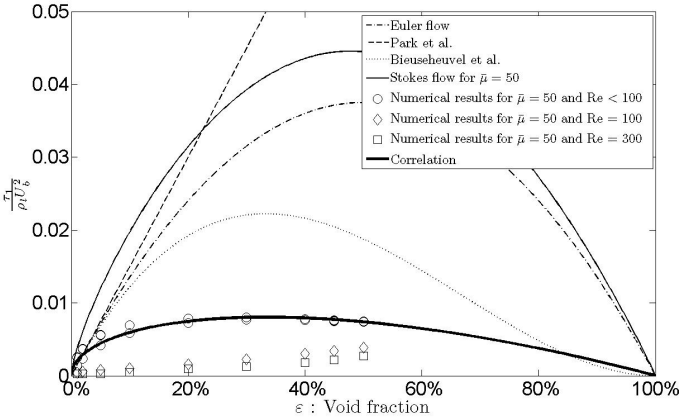

(c) $\bar{\mu}$ = 50

Figure 7.9 Comparison between numerical, analytical results (eq. (7.57,7.56 and 7.64)) and correlation (eq. (7.70)) for isotropic turbulence in continuous phase for Neumann case.

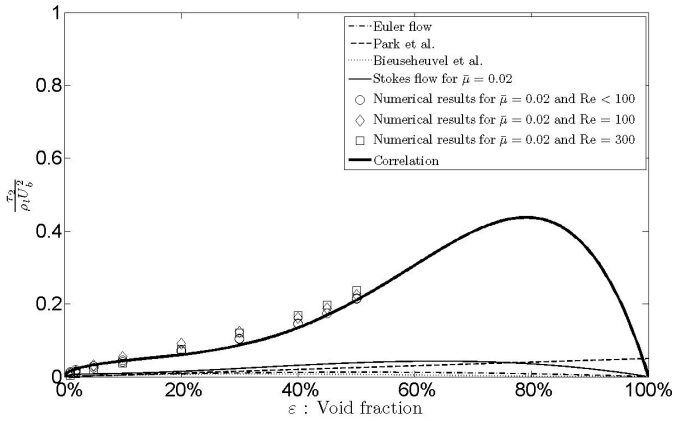

(a) $\bar{\mu} = 0.02$

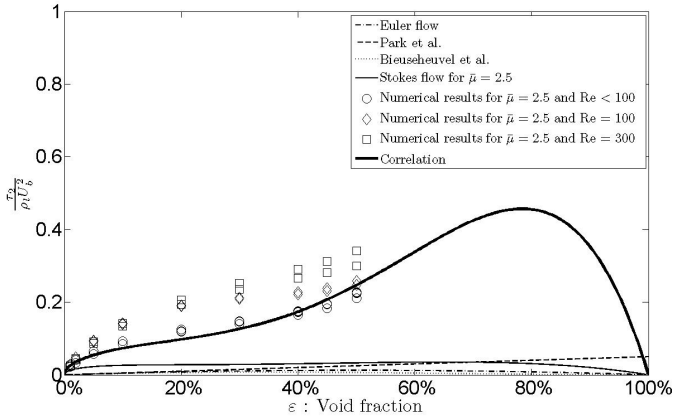

(b) $\bar{\mu} = 2.5$

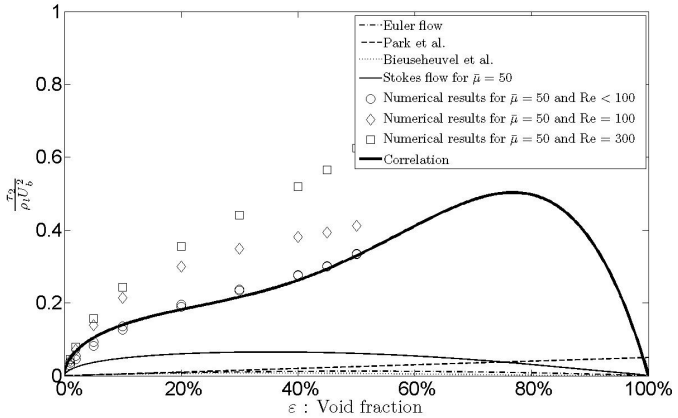

(c) $\bar{\mu} = 50$

Figure 7.10 Comparison between numerical, analytical results (eq. (7.57,7.56 and 7.64)) and correlation (eq. (7.70)) for anisotropic turbulence in continuous phase for Neumann case.

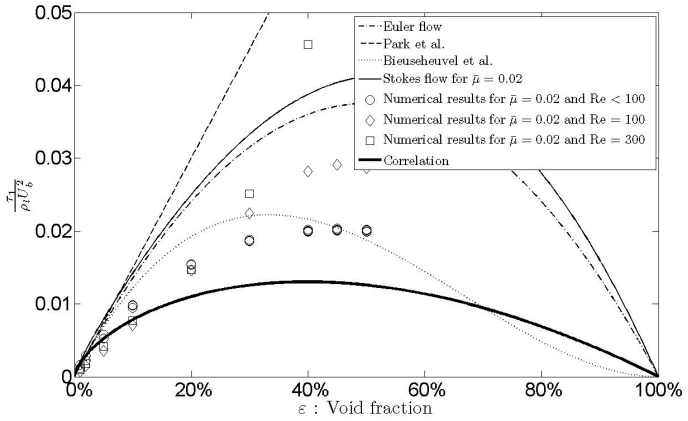

(a) $\bar{\mu} = 0.02$

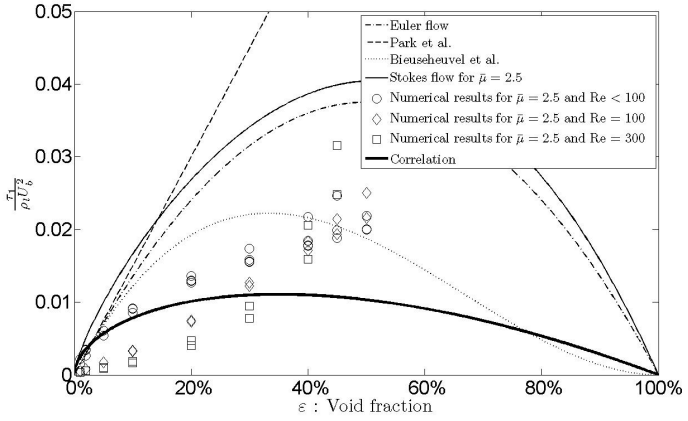

(b) $\bar{\mu} = 2.5$

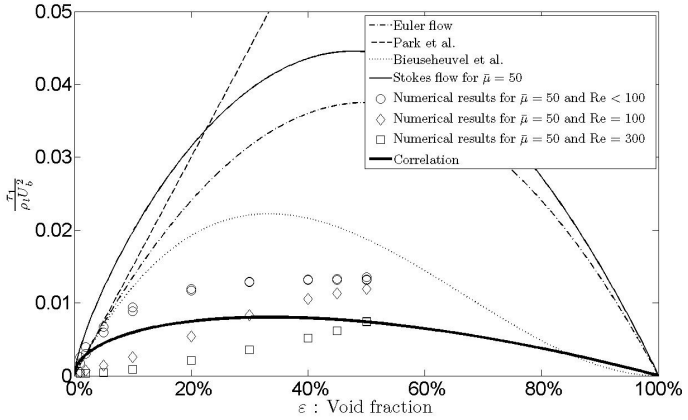

(c) $\bar{\mu} = 50$

Figure 7.11 Comparison between Numerical, analytic results (eq. (7.57,7.56 and 7.64) and Correlation (eq. (7.70)) of isotropic turbulence in continuous phase for Dirichlet case.

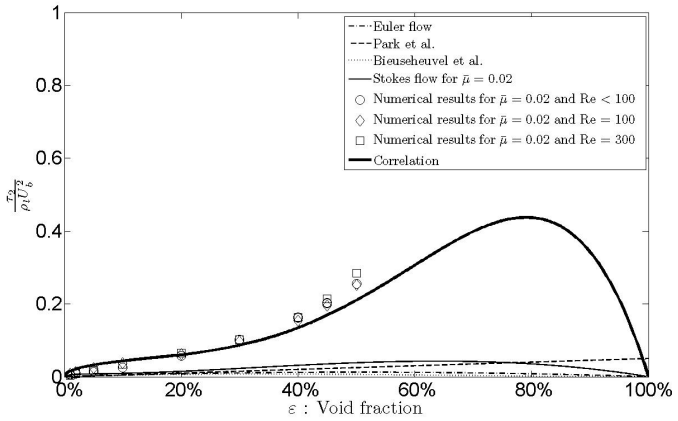

(a) $\bar{\mu} = 0.02$

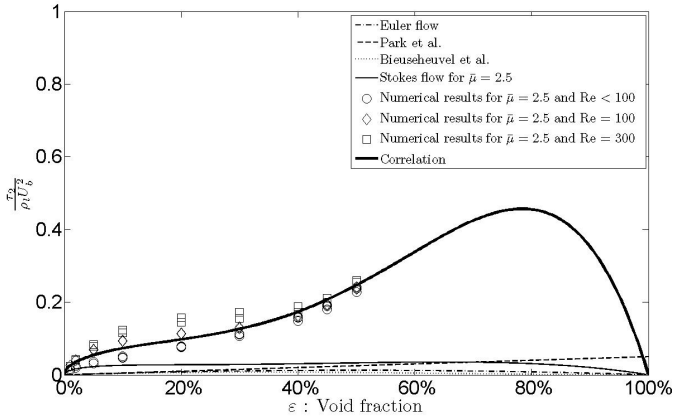

(b) $\bar{\mu} = 2.5$

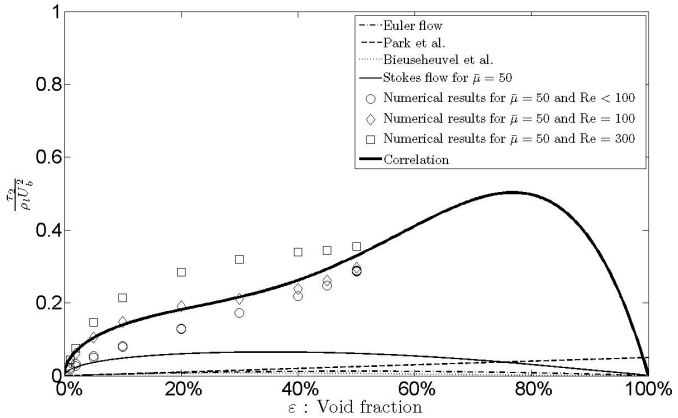

(c) $\bar{\mu} = 50$

Figure 7.12 Comparison between Numerical, analytic results (eq. (7.57,7.56 and 7.64) and Correlation (eq. (7.70)) of anisotropic turbulence in continuous phase for Dirichlet case.

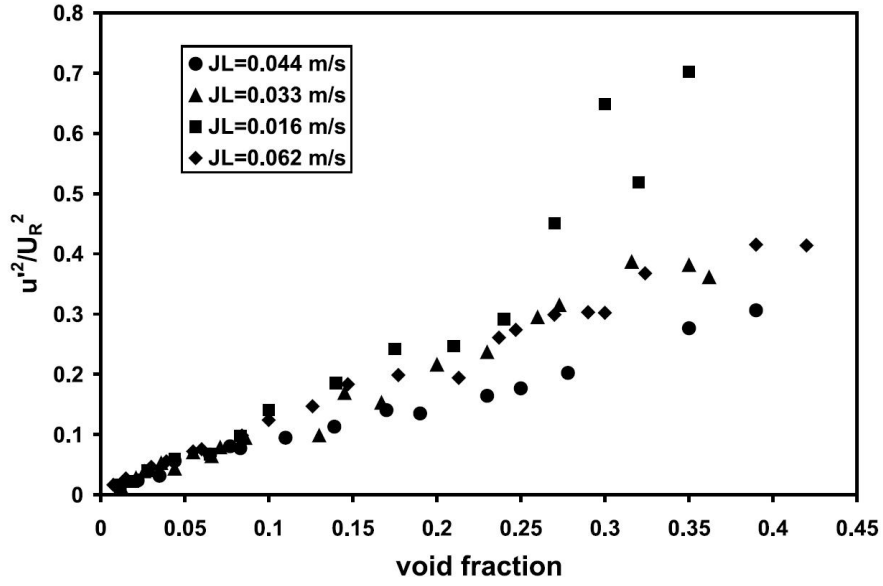

(a) Experimental measurement of velocity fluctuation by Garnier *et al.* (2002)
.

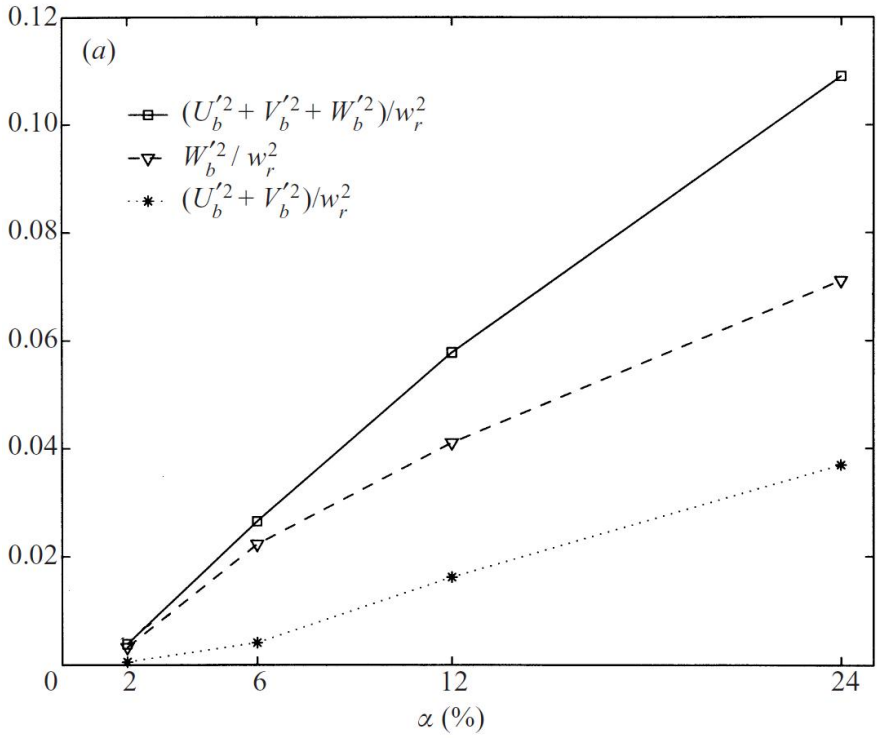

(b) Numerical experiment of velocity fluctuation by Brunner and Tryggvason (2002) with $\bar{\rho} = \bar{\mu} = 0.02$ and Re below 30.

Figure 7.13 Velocity fluctuations results by other authors.

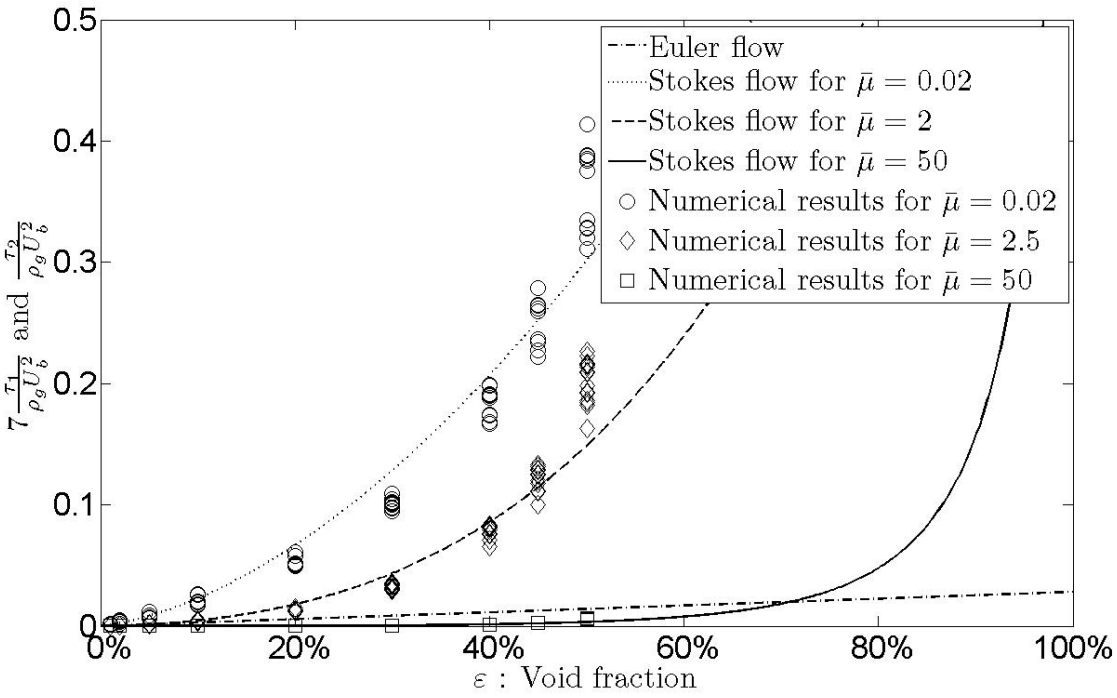

Figure 7.14 Comparison between numerical and analytical results for seven times isotropic pseudo turbulence and anisotropic pseudo turbulence in the dispersed phase for the Neumann case.

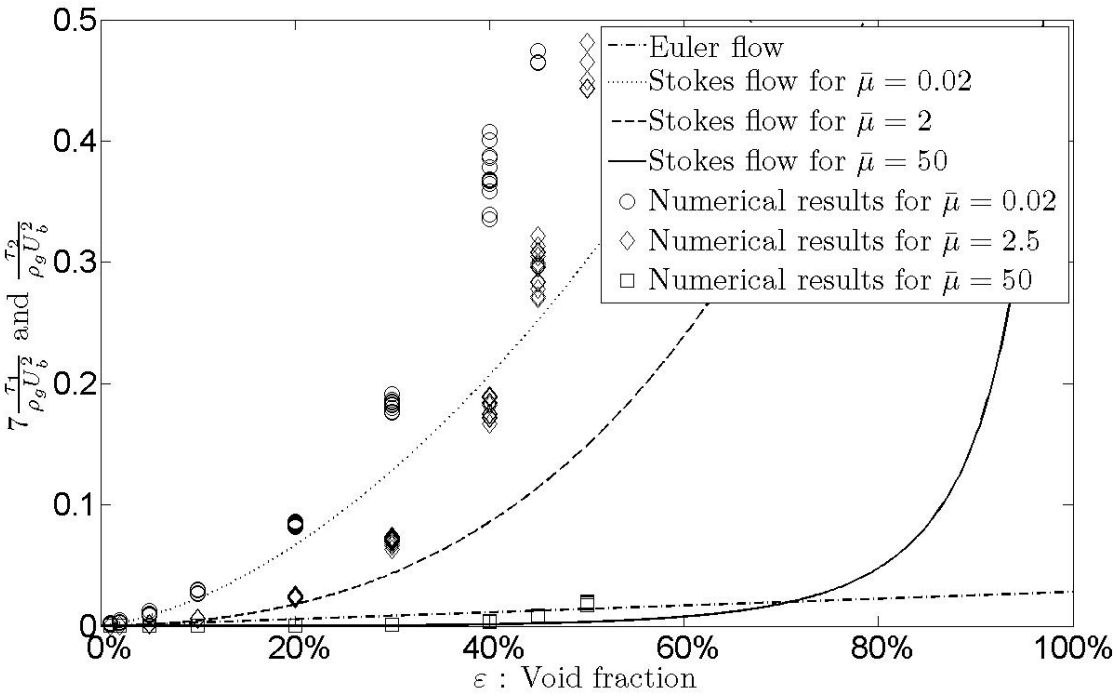

Figure 7.15 Comparison between numerical and analytical results for seven times isotropic pseudo turbulence and anisotropic pseudo turbulence in the dispersed phase for the Dirichlet case.

7.4.1 Bubble size distribution modelling

Pseudo turbulence depends on the relative bubble velocity $U_b = u_g - u_l$. However this relative bubble velocity depends directly on bubble size through the drag coefficient.

Two strategies can be selected to overcome this problem. The first strategy is to solve one equation for each bubble size, and to define void fraction depending on each bubble size arriving at a result of the form ($\varepsilon_{a<0.1\text{mm}}$, $\varepsilon_{0.1<a<0.2\text{mm}}$, etc.). The second strategy is to solve only one equation for the dispersed phase but to take into account the bubble size distribution in the closure relation.

Whatever the strategy chosen, a closure relation is required to model bubble size. If we admit that the bubble size distribution is well represented by a Rayleigh law distribution (cf. Figure 7.1) and considering $a_{min} = 0$, the Rayleigh law is described by the following equation :

$$\begin{aligned}
&\text{PDF}(a) = 10\frac{a}{a_{max}^2} exp\left(-5\left(\frac{a}{a_{max}}\right)^2\right)\\
&\text{CDF}(a) = 1 - exp\left(-5\left(\frac{a}{a_{max}}\right)^2\right)\\
&\text{CDF}(a_{max}) \simeq 99.3\%\\
&< a >= \sqrt{\frac{\pi}{20}} a_{max}\\
&< a^2 >= \frac{1}{5} a_{max}^2\\
&< a^3 >= \frac{3}{10}\sqrt{\frac{\pi}{20}} a_{max}^3
\end{aligned} \tag{7.71}$$

What follows is an example of how to apply this distribution law for the closure relation of the drag forces. According to equation (7.26) and (7.69) we have, for $Re << 1$, the resulting drag forces

$$\begin{aligned}
C_D &= \frac{16}{Re}\frac{1-\varepsilon}{(1-\varepsilon^{1/3})^3}\frac{P_1(\varepsilon) + \bar{\mu}P_2(\varepsilon)}{P_3(\varepsilon) + \bar{\mu}P_4(\varepsilon)}\\
\vec{F_D} &= \frac{3}{8}\rho_l\varepsilon\frac{\left\langle a^2 C_D|\vec{U_b}|\vec{U_b}\right\rangle}{\langle a^3\rangle}\\
\vec{F_D} &= -\frac{3\rho_l\varepsilon}{8\langle a^3\rangle}\left\langle a^2\frac{8\mu_l}{\rho_l a}\vec{U_b}\right\rangle\frac{1-1.5\varepsilon}{(1-(1.5\varepsilon)^{1/3})^3}\frac{P_1(\varepsilon) + \bar{\mu}P_2(\varepsilon)}{P_3(\varepsilon) + \bar{\mu}P_4(\varepsilon)}\\
&= -3\mu_l\varepsilon\frac{\langle a\rangle}{\langle a^3\rangle}\frac{1-\varepsilon}{(1-\varepsilon)^{1/3})^3}\frac{P_1(\varepsilon) + \bar{\mu}P_2(\varepsilon)}{P_3(\varepsilon) + \bar{\mu}P_4(\varepsilon)}\vec{U_b}\\
&= -\frac{10\mu_l\varepsilon}{a_{max}^2}\frac{1-\varepsilon}{(1-\varepsilon^{1/3})^3}\frac{P_1(\varepsilon) + \bar{\mu}P_2(\varepsilon)}{P_3(\varepsilon) + \bar{\mu}P_4(\varepsilon)}\vec{U_b}
\end{aligned} \tag{7.72}$$

7.4.2 Bubble breakup and bubble size model

As suggested by the results presented in Part I and in this paper together with experimental results by Lance and Bataille (1991), the model of Hinze (1955) is not valid for void fractions higher than 1% because classical turbulence cannot take place due to confinement (the liquid can be seen as a film). Turbulence is dominated by bubble induced turbulence which is commonly named pseudo turbulence.

Another hint that pseudo turbulence is dominant for void fractions larger than 1% comes from the common assumption made when the size of the bubbles is larger than the Kolmogorov scale η, Hosokawa *et al.* (2010). The Kolmogorov scale is defined by :

$$\eta = \left(\frac{\mu_{2\phi}^3}{\rho_{2\phi}^3 e_{d2\phi}} \right)^{1/4} \tag{7.73}$$

where $e_{d2\phi}$ is the rate of energy dissipation already defined in equation (7.34). Thus, the previous equation becomes :

$$\frac{\eta}{D} \simeq \frac{1.58}{Re^{0.7}} \tag{7.74}$$

As an example from classical nuclear applications, typical pipe sizes of 10 mm, for Reynolds numbers over 10^6, are commonly encounter. This leads to a typical Kolmogorov scale of η in the order of one micrometer. Typical drops and bubbles normally encountered are of the order of a millimeter, leading to $a >> \eta$. The size of the bubbles is then considerably larger than the Kolmogorov scale η, and hence pseudo turbulence is dominant.

Evidently, the high Reynolds numbers ($\sim 10^6$) encountered in the global flow will generate a turbulent boundary layer at the wall. However, the critical bubble Reynolds number, at which transition from Stokes to Euler flow occurs, increases dramatically with void fraction (cf. Part I). The flow between bubbles is closer to Stokes flow than turbulent flow. This leads us to conclude that wall turbulence will not propagate into the main flow and will instead decrease rapidly, away from the wall, because of the presence of the bubbles. The confinement of the turbulence to the wall region is a good explanation for the huge increase of pressure drop in two-phase flow compared to single phase flow pressure drop for the same Reynolds number.

The experimental work by Hosokawa *et al.* (2010) led them to conclude that the boundary between the linear sublayer and the log region shifts toward the wall by addition of bubbles into the buffer layer. In many practical cases bubbles remain small compared to the typical pipe diameters ($a << D$). We conclude that even for high Reynolds number, pseudo turbulence will dominate classical turbulence and classical turbulence is confined in a thin wall boundary layer.

All this evidence points to the importance of pseudo turbulence, and the fact that it should be used rather than classical turbulence to model bubble size. For void fractions larger than 1%, we can assume that the first assessment of Levich (1962) is still valid except that energy dissipation (τ) should be calculated through bubble induced turbulence. Levich (1962) assumed that a deformed bubble breaks up when the internal pressure force overcomes the surface force. Considering a balance between these two forces, he obtained the following critical Weber number,

$$We_c^* = \frac{2\tau a_{max}}{\gamma}\left(\frac{\rho_g}{\rho_l}\right)^{1/3} \tag{7.75}$$

In the case of bubble induced turbulence we have both isotropic and anisotropic turbulence. If we only consider the larger one, the anisotropic turbulence, which is well modelled by equation (7.70), we deduce :

$$We_c^* = \frac{3\rho_l U_b^2 a_{max}}{10\gamma}\left(\frac{0.15+0.08\bar{\mu}}{1+0.15\bar{\mu}}\sqrt{\varepsilon}+5\varepsilon^4\right)(1-\varepsilon)\left(\frac{\rho_g}{\rho_l}\right)^{1/3} \tag{7.76}$$

Razzaque *et al.* (2003) suggested for the equation of Levich (1962) a critical Weber number of $We_c^* = 1.1$. This relation can be directly used as a closure relation for bubble size when modelling by the averaged Navier-Stokes equation.

Considering the bubble velocity deduced from the equilibrium between the drag and the buoyancy forces (cf. Eq. (7.69), we get :

$$\begin{aligned}
\left\langle \tfrac{1}{2}\pi\rho_l a^2 C_D |\vec{U}_b|\vec{U}_b \right\rangle &= \left\langle \tfrac{4}{3}\pi\Delta\rho g a^3 \right\rangle \\
\left\langle \tfrac{1}{2}\pi\rho_l a^2 \frac{16}{Re}\frac{1-\varepsilon}{(1-\varepsilon^{1/3})^3}\frac{P_1(\varepsilon)+\bar{\mu}P_2(\varepsilon)}{P_3(\varepsilon)+\bar{\mu}P_4(\varepsilon)}U_b^2 \right\rangle &= \tfrac{4}{3}\pi\left\langle a^3\right\rangle\Delta\rho g \\
\frac{1-\varepsilon}{(1-\varepsilon^{1/3})^3}\frac{P_1(\varepsilon)+\bar{\mu}P_2(\varepsilon)}{P_3(\varepsilon)+\bar{\mu}P_4(\varepsilon)}U_b &= \frac{1}{3}\frac{\Delta\rho g\left\langle a^3\right\rangle}{\mu_l\left\langle a\right\rangle} \\
\frac{1-\varepsilon}{(1-\varepsilon^{1/3})^3}\frac{P_1(\varepsilon)+\bar{\mu}P_2(\varepsilon)}{P_3(\varepsilon)+\bar{\mu}P_4(\varepsilon)}U_b &= \frac{1}{10}\frac{\Delta\rho g a_{max}^2}{\mu_l}
\end{aligned} \tag{7.77}$$

defining the size :

$$a_c = \left(\frac{\rho_l(\Delta\rho g)^2}{\gamma\mu_l^2}\right)^{1/5}\left(\frac{\rho_g}{\rho_l}\right)^{1/15} \tag{7.78}$$

from the previous equations (7.76) and (7.77), we deduce :

$$\begin{aligned}\frac{a_{max}}{a_c} &= \sqrt{\frac{Bo\bar{\rho}^{2/15}}{Mo^{1/5}}} \\ &= 5.52\left(\frac{1-\varepsilon}{\left(\frac{0.15+0.08\bar{\mu}}{1+0.15\bar{\mu}}\sqrt{\varepsilon}+5\varepsilon^4\right)\left(1-\varepsilon^{1/3}\right)^6}\right)^{1/5}\left(\frac{P_1(\varepsilon)+\bar{\mu}P_2(\varepsilon)}{P_3(\varepsilon)+\bar{\mu}P_4(\varepsilon)}\right)^{2/5}\end{aligned} \tag{7.79}$$

Equation (7.79) (see Figure 7.16) defines a typical bubble radius a_c which is presented in Table 7.2 for classical two-phase mixtures. Equation (7.79) highlights two opposing effects :

- turbulence induced by bubble increases due to a larger number of bubbles (maximum is obtained for $\varepsilon \sim 75\%$)

- turbulence decreases for lower slip ratio.

Consequently, the minimum bubble size occurs at a void fraction of approximately 5% ($\varepsilon \sim 5\%$). However, as a first order approximation, the maximum bubble size is 20 times the typical bubble radius a_c presented in Table 7.2. We obtain a typical maximum bubble radius of 7 mm, which is quite large. This leads us to conclude that for flows where pseudo turbulence is dominant ($\varepsilon \geq 1\%$ - Lance and Bataille (1991)), no significant break up forces are encountered.

Common experiments use a mixer to mix gas and liquid upstream of the test section. Bubble size is determined by the mixer, depending on mixer properties and velocity inside the mixer. In the test section no more break up process is observed and only coalescence should be observed. With smaller bubbles generated by the mixer, coalescence will be slower. This is why, experiment observed variation of bubble properties due to velocity even if no break up occurs in the test section. All bubbles size depnds on velocity inside the mixer. Das *et al.* (2005) have proposed the model below to predict the maximum stable bubble radius

Mixture	ρ_l	ρ_g	μ_l	μ_g	γ	$a_c(mm)$
Air bubble in water	1000	1	$8.9\,10^{-4}$	$18.6\,10^{-6}$	0.072	0.36
Water droplet in air	1	1000	$18.6\,10^{-6}$	$8.9\,10^{-4}$	0.072	0.63
Steam bubble in water	890	10	$1.2\,10^{-4}$	$18.6\,10^{-6}$	0.05	0.22
Water droplet in steam	10	890	$18.6\,10^{-6}$	$1.2\,10^{-4}$	0.05	0.38

Table 7.2 Typical radius of bubble in two-phase mixture

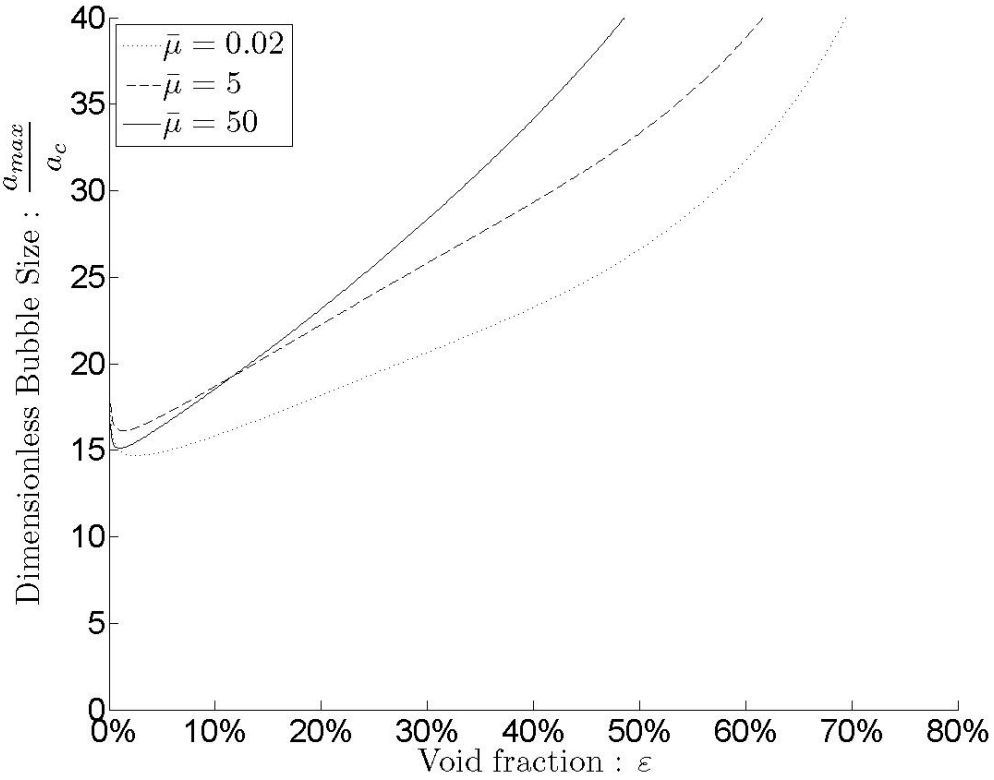

Figure 7.16 Dimensionless bubble size (cf. Eqn 7.79)

a_{max}, at the exit of a static mixer :

$$\begin{gathered}\text{At low Reynolds numbers } Re_p < 20 \\ \frac{a_{max}}{d_p} = \frac{0.38}{Ca_p} \qquad (a) \\ \text{At higher Reynolds numbers } Re_p > 20 \\ \frac{a_{max}}{d_p} = \frac{0.33}{We_p^{0.33}} \qquad (b)\end{gathered} \tag{7.80}$$

where d_p is a typical size of a pore inside the mixer, $Ca_p = \mu_{2\phi} U_p/\gamma$ is the pore capillarity number defined with the pore velocity, and $We_p = \rho_{2\phi} U_p^2 d_p/\gamma$ is the pore Weber number defined using the pore velocity and typical pore size. The pore size d_p is part of the mixer design parameter. The pore velocity U_p, depends on mixer properties and is proportional to $U_{2\phi}$. The mixer properties can be deduced by mixer pressure drop (see explanation of Morencais *et al.* (1999)). The first equation (7.80 (a)) leads to a bubble size proportional to $1/U_{2\phi}$. While the second equation (7.80 (b)) leads to a bubble size proportional to $1/U_{2\phi}^{2/3}$. Their results for a void fraction of 20% ($\varepsilon = 20\%$) are presented in Figures 7.17 and 7.18. This model presents similar trends of model of Hinze (1955) (bubble size proportional to $1/U_{2\phi}^{1.1}$). The difference is explained by the fact that inside the mixer, turbulence does not have time to fully developed. In the mixer, shear turbulence is dominant and controls the bubble size. For higher flow velocities, the mixer will generate smaller and consequently almost solid bubbles. This will reduce coalescence and allow bubbly flow at higher void fractions in the test section downstream of the mixer.

The bubble size model from pseudo turbulence predicts no significant breakup force in pipe, however for higher homogeneous velocities, transition from bubbly to churn or slug flow occurs at higher void fractions (see Taitel *et al.* (1980); Béguin *et al.* (2008)). The usual explanation is that two-phase turbulence inside the pipe produces smaller bubbles, and consequently drives the transition from bubbly to churn flow. However the foregoing arguments suggest that no significant break up forces are present in the pipe. Since no such breakup forces are present, the mixer effect should be considered in two-phase flow pattern transition. A previous study has already shown the effect of initial bubble size on two phase flow pattern transition. Larger initial bubble size leads to transition from bubbly to slug flow at lower void fractions (*c.f.* Cheng *et al.* (2002)).

No significant break up is encountered due to pseudo turbulence. Break up can only occurs in narrow passage such as mixer or very close to the wall.

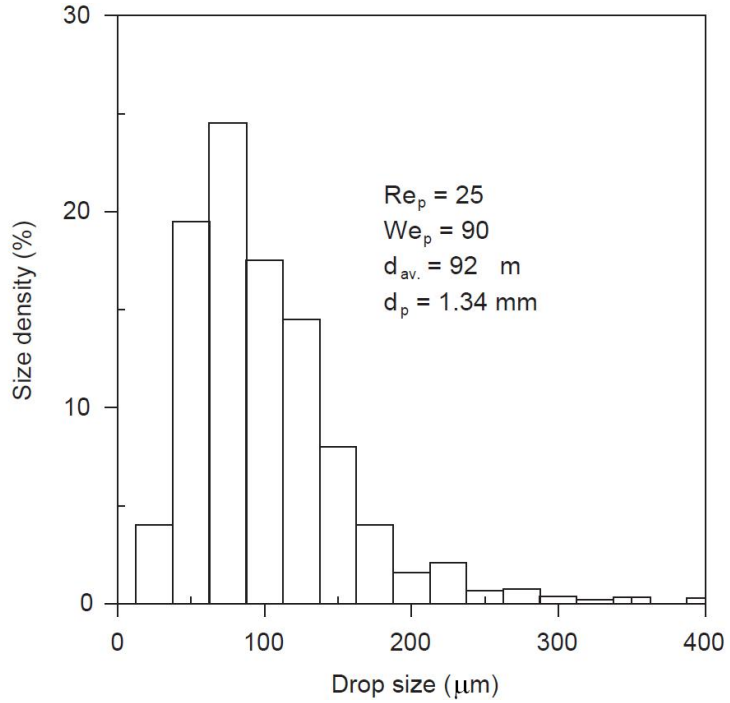

Figure 7.17 Typical bubble size distribution from Das *et al.* (2005) (similar to Rayleigh distribution).

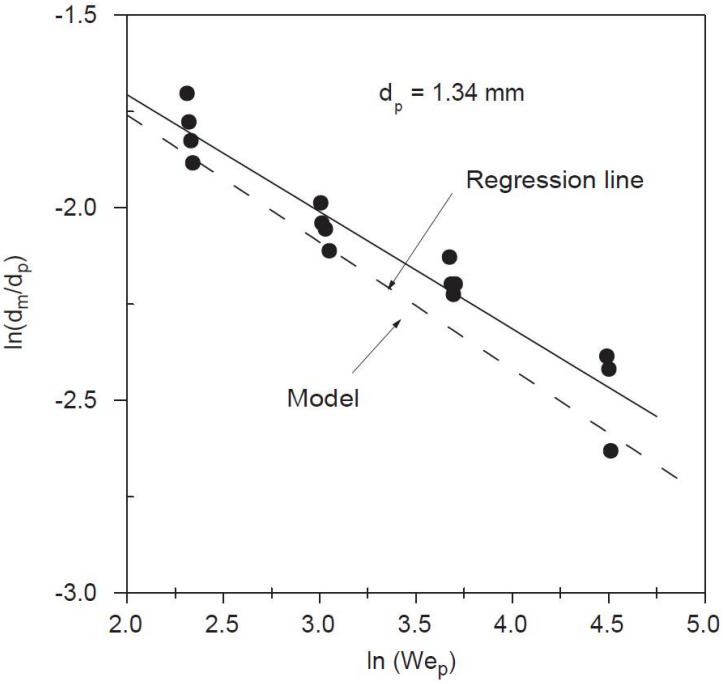

Figure 7.18 Maximum stable bubble size vs Weber number cf. Model equation (7.80 (b)) from Das *et al.* (2005).

7.5 Turbulence Force on Bubble

Since we have a model for the Reynolds stress tensor, we can deduce a closure relation for the turbulence force on bubble. This section will propose such closure relation.

For the same reason that gravity has an effect both on the main equation (hydrostatic pressure) and on the force at interface (Buoyancy forces), turbulence should have an effect on the main equation (Reynolds stress tensor) and the force at the interface (turbulence forces).

Integrating the turbulence Reynolds stress tensor at bubble interface location and considering the divergence of this tensor constant over the volume of a bubble yields :

$$\begin{aligned} \vec{f^i_{Turb}} &= \underset{\substack{\text{Bubble}\\ \text{interface}}}{\iint} \bar{\bar{\tau_l^{Re}}} d\vec{S}^i_l = \underset{\substack{\text{Bubble}\\ \text{volume}}}{\iiint} \nabla . \bar{\bar{\tau_l^{Re}}} dV \\ &= \frac{4}{3}\pi a^3 \nabla \cdot \bar{\bar{\tau_l^{Re}}} \end{aligned} \tag{7.81}$$

As the turbulence tensor is already an averaged quantities, the forces correspond to an averaged value of the force on the bubbles due to turbulence. The exact force is therefore not evaluated only the averaged turbulence forces is modelled.

The Reynolds stress tensor main contribution is anisotropic and varies as $\vec{U_b} \otimes \vec{U_b}$. Consequently turbulence forces on bubbles act like an inertial effect due to the surrounding bubble cloud $\nabla \cdot (\vec{U_b} \otimes \vec{U_b})$. This explains why bubbles have tendency to follow each other; recall that anisotropic turbulence is associated with wake effects.

7.6 Conclusion

This paper proposes a relation for two-phase turbulence induced by spherical bubbles (or droplets) for Reynolds number Re less than 300, void fraction up to 50%, viscosity ratio $\bar{\mu}$ between 0.02 and 50 and density $\bar{\rho}$ between 10^{-3} and 10^3. In practical cases, only solid spheres are able to reach Reynolds number much larger than 1000 while remaining spherical. The following proposed relation for two-phase pseudo turbulence is therefore useful for all fluid-fluid cases :

$$\begin{aligned} (1-\varepsilon)\bar{\bar{\tau_l^{Re}}} &= \rho_l \left(\tau_1 (\vec{U_b}.\vec{U_b}) \bar{\bar{I}} + \tau_2 (\vec{U_b} \otimes \vec{U_b}) \right) \\ \tau_1 &= \frac{1}{25} \left(\frac{5+\bar{\mu}}{5+2\bar{\mu}} \right) \varepsilon^{\frac{2+2\bar{\mu}}{3+4\bar{\mu}}} (1-\varepsilon) \\ \tau_2 &= \left(\frac{0.15+0.08\bar{\mu}}{1+0.15\bar{\mu}} \sqrt{\varepsilon} + 5\varepsilon^4 \right) (1-\varepsilon) \end{aligned} \tag{7.82}$$

In all practical cases of bubbly flows, the flow around the spherical bubbles can be considered as a Stokes flow. The void fraction ε has a major effect on turbulence. The proposed relation can be used to develop a two-phase flow model for bubbly two-phase flow. C_D, C_L, turbulence,

viscous terms, etc. depend on Re, ε, Bo, Mo, $\bar{\rho}$, $\bar{\mu}$ and can be analytically modelled with Stokes flow. Presently, two-phase flow models use the classical relation of Park *et al.* (1998) and Biesheuvel and Van Wijngaarden (1984) which are deduced from Euler (potential) flow around a bubble. While the relations of Park *et al.* (1998) or Biesheuvel and Van Wijngaarden (1984) may be acceptable for isotropic pseudo turbulence, anisotropic turbulence is definitely not accurately modelled. This is particularly important because anisotropic turbulence is in fact ten times larger than isotropic turbulence and hence the primary turbulence effect.

To the authors knowledge, the pseudo turbulence of the dispersed phase is for the first time modelled and accurately represented by the Stokes analytical model

$$\begin{aligned} \varepsilon\bar{\bar{\tau}}_g^{Re} &= -\frac{\rho_g}{35}\frac{\varepsilon(1-\varepsilon)}{F(\varepsilon)}(2-5\varepsilon+3\varepsilon^{5/3})\left(\left(\vec{U}_b.\vec{U}_b\right)\bar{\bar{I}}+7\left(\vec{U}_b\otimes\vec{U}_b\right)\right) \\ \text{where} & \\ F(\varepsilon) &= (1-\varepsilon^{1/3})^3\left((4+6\varepsilon^{1/3}+6\varepsilon^{2/3}+4\varepsilon)+\bar{\mu}(4+3\varepsilon^{1/3}-3\varepsilon^{2/3}-4\varepsilon)\right) \end{aligned} \tag{7.83}$$

Pseudo turbulence of the dispersed phase can also be interpreted via internal kinetic energy.

Using the new turbulence model, we can deduce the forces on a bubble due to two-phase turbulence as :

$$\vec{f^i_{Turb}} = \frac{4}{3}\pi a^3 \nabla\cdot\bar{\bar{\tau}}_l^{Re} \tag{7.84}$$

This forces act like an inertial effect of bubble cloud as its major component is of the form $\nabla\cdot(\vec{U}_b\otimes\vec{U}_b)$.

The present work has shown that Stokes flow very accurately represents flow around bubbles, as no significant change is seen for Reynolds numbers ranging from 0.01 to 300. The only exception occurs for high viscosity ratios, where the Reynolds number has an effect but only for Reynolds number larger than 100. The fact that two-phase turbulence is not classical turbulence and is instead dominated by pseudo turbulence is explained by the fact that the transition from Stokes flow to Euler flow occurs at higher Reynolds number when the void fraction increases. Flow in the continuous phase can in fact be defined as a film flow where classical turbulence cannot develop. Two-phase turbulence is essentially due to bubble passage, and can therefore be modeled. The next step is to include this model in a numerical solver.

Evidently, the high Reynolds numbers encountered in the global flow will generate a turbulent boundary layer at the wall. However, the wall turbulence will not propagate inside the main flow and will instead decrease rapidly, away from the wall, because of the presence of the bubbles. Confinement of the turbulence at the wall is a good explanation for the huge increase in pressure drop in two-phase flow compared to single phase flow pressure drop for the same Reynolds number. More work still needs to be done to model the interaction between

turbulence and walls in two-phase flows; this could, for instance, be done via development of wall functions similarly to the case for single phase flows.

7.7 Internal solution

As shown in Part I, for the case of the internal flow, a solution for the incompressible Navier-Stokes equations exists. Using spherical coordinates (r,θ,ϕ), we obtain :

$$\begin{aligned} u_{rg} &= 2B_0(r^2 - a^2)\cos\theta \\ u_{\theta g} &= -2B_0(2r^2 - a^2)\sin\theta \end{aligned} \tag{7.85}$$

According to equation (7.16), the average gas Reynolds tensor is :

$$\begin{aligned} \varepsilon\bar{\bar{\tau}}_g^{Re} &= \varepsilon\rho_g\langle\vec{u}_g\rangle\otimes\langle\vec{u}_g\rangle - \langle\chi_g\rho_g\vec{u}_g\otimes\vec{u}_g\rangle \\ \langle\chi_g\rho_g\vec{u}_g\otimes\vec{u}_g\rangle &= \rho_g\tfrac{3}{4\pi l^3}\int_{r=0}^{a}\int_{\varphi=0}^{2\pi}\int_{\theta=0}^{\pi}\left(\begin{Bmatrix} u_{Rg}\sin\varphi \\ u_{Rg}\cos\varphi \\ u_{Zg}\end{Bmatrix}\otimes\begin{Bmatrix} u_{Rg}\sin\varphi \\ u_{Rg}\cos\varphi \\ u_{Zg}\end{Bmatrix}\right)r^2\sin\theta d\varphi d\theta dr \end{aligned} \tag{7.86}$$

In this model $\langle\vec{u}_g\rangle = \vec{0}$. Using $u_{Zg} = u_{rg}\cos\theta - u_{\theta g}\sin\theta$ and $u_{Rg} = u_{rg}\sin\theta + u_{\theta g}\cos\theta$, we obtain for the Reynolds stress tensor :

$$\begin{aligned} \varepsilon\bar{\bar{\tau}}_g^{Re} &= -\rho_g\frac{3}{4\pi l^3}\int_{r=0}^{a}\int_{\theta=0}^{\pi}\begin{pmatrix} \pi u_{Rg}^2 & 0 & 0 \\ 0 & \pi u_{Rg}^2 & 0 \\ 0 & 0 & 2\pi u_{Zg}^2\end{pmatrix}r^2\sin\theta d\theta dr \\ &= -\begin{pmatrix} \tau_{Rg} & 0 & 0 \\ 0 & \tau_{Rg} & 0 \\ 0 & 0 & \tau_{Zg}\end{pmatrix} \end{aligned} \tag{7.87}$$

Using $u_{rg} = \frac{2}{r^2}G(r)\cos\theta$ and $u_{\theta g} = -\frac{1}{r}G'(r)\sin\theta$

$$\begin{aligned}
\tau_{Rg} &= \rho_g \frac{3}{4l^3}\int_{r=0}^{a}\int_{\theta=0}^{\pi} u_{Rg}^2 r^2 \sin\theta d\theta dr \\
&= \rho_g \frac{3}{4l^3}\int_{r=0}^{a}\int_{\theta=0}^{\pi} \left(u_{rg}\sin\theta + u_{\theta g}\cos\theta\right)^2 r^2 \sin\theta d\theta dr \\
&= \rho_g \frac{1}{5l^3}\int_{r=0}^{a}\left(\frac{2G}{r} - G'\right)^2 dr \\
\tau_{Zg} &= \rho_g \frac{3}{2l^3}\int_{r=0}^{a}\int_{\theta=0}^{\pi} u_{Zg}^2 r^2 \sin\theta d\theta dr \\
&= \rho_g \frac{3}{2l^3}\int_{r=0}^{a}\int_{\theta=0}^{\pi} \left(u_{rg}^2\cos^2\theta + u_{\theta g}^2\sin^2\theta - 2u_{rg}u_{\theta g}\sin\theta\cos\theta\right) r^2\sin\theta d\theta dr \\
&= \rho_g \frac{3}{2l^3}\int_{r=0}^{a}\int_{\theta=0}^{\pi} \frac{4G^2}{r^2}\cos^4\theta\sin\theta + G'^2\sin^5\theta + \frac{4GG'}{r}\cos^2\theta\sin^3\theta d\theta dr \\
&= \rho_g \frac{4}{5l^3}\int_{r=0}^{a} \frac{3G^2}{r^2} + 2G'^2 + \frac{2GG'}{r} dr
\end{aligned} \tag{7.88}$$

With the previous solution for the Navier-Stokes equation Eq. (7.85), the Reynolds stress tensor is calculated from equation (7.88), yielding,

$$\begin{aligned}
G(r) &= B_0(r^4 - a^2r^2) \\
\tau_{Rg} &= \rho_g \frac{1}{5l^3}\int_{r=0}^{a}\left(\frac{2G}{r} - G'\right)^2 dr \\
&= \frac{\rho_g B_0^2}{5l^3}\int_{r=0}^{a}\left(2(r^3 - a^2r) - (4r^3 - 2a^2r)\right)^2 dr \\
&= \frac{4\rho_g B_0^2 a^4}{35}\varepsilon,
\end{aligned} \tag{7.89}$$

$$\begin{aligned}
\tau_{Zg} &= \rho_g \frac{4}{5l^3}\int_{r=0}^{a} \frac{3G^2}{r^2} + 2G'^2 + \frac{2GG'}{r} dr \\
&= \frac{4\rho_g B_0^2}{5l^3}\int_{r=0}^{a} 3(r^3 - a^2r)^2 + 2(4r^3 - 2a^2r)^2 + 2(r^3 - a^2r)(4r^3 - 2a^2r) dr \\
&= \frac{2\rho_g B_0^2}{5l^3}\int_{r=0}^{a} 86r^6 - 100a^2r^4 + 30a^4r^2 dr \\
&= \frac{32\rho_g B_0^2 a^4}{35}\varepsilon
\end{aligned} \tag{7.90}$$

and finally.

$$\varepsilon\tau_g^{\bar{\bar{R}}e} = -\frac{\rho_g B_0^2 a^4}{35}\varepsilon\begin{pmatrix} 4 & 0 & 0 \\ 0 & 4 & 0 \\ 0 & 0 & 32 \end{pmatrix} \tag{7.91}$$

A more general expression, not depending on the coordinate system is :

$$\varepsilon\tau_g^{\bar{\bar{R}}e} = -\frac{4\rho_g B_0^2 a^4}{35}\varepsilon\left(\bar{\bar{I}} + \frac{7}{U_b^2}\vec{U}_b \otimes \vec{U}_b\right) \tag{7.92}$$

7.8 External Flow

7.8.1 External Stokes Flow ($Re << 1$)

As shown in Part I, for the case of external Stokes flow, using spherical coordinates (r,θ,ϕ), we can derive the velocity field and pressure as

$$\begin{aligned} u_{rl} &= 2\left(C_0\left(r^2-a^2\right)+C_2\left(\tfrac{1}{r}-\tfrac{1}{a}\right)+C_3\left(\tfrac{1}{r^3}-\tfrac{1}{a^3}\right)\right)\cos(\theta) \\ u_{\theta l} &= -\left(2C_0\left(2r^2-a^2\right)+C_2\left(\tfrac{1}{r}-\tfrac{2}{a}\right)-C_3\left(\tfrac{1}{r^3}+\tfrac{2}{a^3}\right)\right)\sin(\theta) \\ P_l &= \mu_l\left(20C_0 r+\tfrac{2C_2}{r^2}\right)\cos(\theta)+C_4 \end{aligned} \tag{7.93}$$

where

$$\begin{aligned} a^2B_0 &= -\frac{U_b}{2}\frac{1-\varepsilon}{F(\varepsilon)}(2-5\varepsilon+3\varepsilon^{5/3}) \\ a^2C_0 &= \frac{U_b}{2}\frac{1-\varepsilon}{F(\varepsilon)}(2\varepsilon+3\bar{\mu}(\varepsilon-\varepsilon^{5/3})) \\ \tfrac{C_2}{a} &= U_b\frac{1-\varepsilon}{F(\varepsilon)}(2+3\varepsilon^{5/3}+3\bar{\mu}(1-\varepsilon^{5/3})) \\ \tfrac{C_3}{a^3} &= -U_b\frac{1-\varepsilon}{F(\varepsilon)}(\varepsilon+\bar{\mu}(1-\varepsilon)) \end{aligned} \tag{7.94}$$

$$F(\varepsilon) = (1-\varepsilon^{1/3})^3\left((4+6\varepsilon^{1/3}+6\varepsilon^{2/3}+4\varepsilon)+\bar{\mu}(4+3\varepsilon^{1/3}-3\varepsilon^{2/3}-4\varepsilon)\right)$$

According to equation (7.16), the average liquid Reynolds stress tensor is :

$$\begin{aligned} (1-\varepsilon)\bar{\bar{\tau}}_l^{Re} &= (1-\varepsilon)\rho_l\langle\vec{u}_l\rangle\otimes\langle\vec{u}_l\rangle-\langle\chi_l\rho_l\vec{u}_l\otimes\vec{u}_l\rangle \\ \langle\chi_l\rho_l\vec{u}_l\otimes\vec{u}_l\rangle &= \rho_l\tfrac{3}{4\pi l^3}\int_{r=a}^{l}\int_{\varphi=0}^{2\pi}\int_{\theta=0}^{\pi}\left(\begin{Bmatrix} u_{Rl}\sin\varphi \\ u_{Rl}\cos\varphi \\ u_{Zl}\end{Bmatrix}\otimes\begin{Bmatrix} u_{Rl}\sin\varphi \\ u_{Rl}\cos\varphi \\ u_{Zl}\end{Bmatrix}\right)r^2\sin\theta d\varphi d\theta dr \end{aligned} \tag{7.95}$$

In this model $\langle\vec{u}_l\rangle=\vec{U}_b$. Using $u_{Zl}=u_{rl}\cos\theta-u_{\theta l}\sin\theta$ and $u_{Rl}=u_{rl}\sin\theta+u_{\theta l}\cos\theta$, we deduce :

$$(1-\varepsilon)\bar{\bar{\tau}}_l^{Re}=(1-\varepsilon)\vec{U}_b\otimes\vec{U}_b-\rho_l\frac{3}{4\pi l^3}\int_{r=a}^{l}\int_{\theta=0}^{\pi}\begin{pmatrix}\pi u_{Rl}^2 & 0 & 0\\ 0 & \pi u_{Rl}^2 & 0\\ 0 & 0 & 2\pi u_{Zl}^2\end{pmatrix}r^2\sin\theta d\theta dr \tag{7.96}$$

We note that $\tau_{Rl} = \rho_l \frac{3}{4l^3} \int_{r=a}^{l} \int_{\theta=0}^{\pi} u_{Rl}^2 r^2 \sin\theta d\theta dr$ and $\tau_{Zl} = \rho_l \frac{3}{2l^3} \int_{r=a}^{l} \int_{\theta=0}^{\pi} u_{Zl}^2 r^2 \sin\theta d\theta dr$ Using $u_{rl} = \frac{2}{r^2} G(r) \cos\theta$ and $u_{\theta l} = -\frac{1}{r} G'(r) \sin\theta$, as previously, we deduce :

$$\begin{aligned} \tau_{Rl} &= \rho_l \frac{1}{5l^3} \int_{r=a}^{l} \left(\frac{2G}{r} - G' \right)^2 dr \\ \tau_{Zl} &= \rho_l \frac{4}{5l^3} \int_{r=a}^{l} \frac{3G^2}{r^2} + 2G'^2 + \frac{2GG'}{r} dr \end{aligned} \tag{7.97}$$

The Reynolds tensor is calculated from equations (7.93), (7.94) and (7.97) giving

$$\begin{aligned} \tau_{Rl} &= \frac{\rho_l}{5l^3} \left(-\frac{4}{7}(a^7 - l^7) C_0^2 + (a^4 - l^4) C_0 C_2 + 6(a^2 - l^2) C_0 C_3 \right) \\ &\quad + \frac{\rho_l}{5l^3} \left(-(a-l) C_2^2 + 6 \left(\frac{1}{a} - \frac{1}{l} \right) C_2 C_3 + 3 \left(\frac{1}{a^3} - \frac{1}{l^3} \right) C_3^2 \right) \\ &= \frac{\rho_l}{5} \varepsilon^{1/3} \left(-\frac{4}{7} \left(\varepsilon^{8/3} - \varepsilon \right) \frac{a^4 C_0^2}{\varepsilon^2} + \left(\varepsilon^{5/3} - \varepsilon^{1/3} \right) \frac{a C_0 C_2}{\varepsilon} + 6 \left(\varepsilon^{5/3} - \varepsilon \right) \frac{C_0 C_3}{a\varepsilon} \right) \\ &\quad + \frac{\rho_l}{5} \varepsilon^{1/3} \left(- \left(\varepsilon^{2/3} - \varepsilon^{1/3} \right) \frac{C_2^2}{a^2} + 6 \left(\varepsilon^{2/3} - \varepsilon^{4/3} \right) \frac{C_2 C_3}{a^4} + 3 \left(\varepsilon^{2/3} - \varepsilon^{5/3} \right) \frac{C_3^2}{a^6} \right) \end{aligned} \tag{7.98}$$

and :

$$\begin{aligned} \tau_{Zl} &= \frac{4\rho_l}{5l^3} \left(-\frac{43}{7}(a^7 - l^7) C_0^2 - 10(a^5 - l^5) C_0 C_1 - 8(a^4 - l^4) C_0 C_2 \right) \\ &\quad + \frac{4\rho_l}{5l^3} \left(2(a^2 - l^2) C_0 C_3 - 5(a^3 - l^3) C_1^2 - 10(a^2 - l^2) C_1 C_2 \right) \\ &\quad + \frac{4\rho_l}{5l^3} \left(-7(a-l) C_2^2 + 2(1/a - 1/l) C_2 C_3 + (1/a^3 - 1/l^3) C_3^2 \right) \\ &= \frac{4\rho_l}{5} \left(\frac{43}{7} \varepsilon^{2/3} (1 - \varepsilon^{7/3}) \frac{a^4 C_0^2}{\varepsilon^2} + 10 \varepsilon^{1/3} \left(1 - \varepsilon^{5/3} \right) \frac{a^2 C_0 C_1}{\varepsilon} + 8 \varepsilon^{2/3} \left(1 - \varepsilon^{4/3} \right) \frac{a C_0 C_2}{\varepsilon} \right) \\ &\quad + \frac{4\rho_l}{5} \left(-2\varepsilon^{4/3} (1 - \varepsilon^{2/3}) \frac{C_0 C_3}{a\varepsilon} + 5(1-\varepsilon) C_1^2 + 10 \varepsilon^{1/3} (1 - \varepsilon^{2/3}) \frac{C_1 C_2}{a} \right) \\ &\quad + \frac{4\rho_l}{5} \left(7\varepsilon^{2/3} \left(1 - \varepsilon^{1/3} \right) \frac{C_2^2}{a^2} + 2\varepsilon \left(1 - \varepsilon^{1/3} \right) \frac{C_2 C_3}{a^4} + \varepsilon (1 - \varepsilon) \frac{C_3^2}{a^6} \right) \end{aligned} \tag{7.99}$$

$$(1-\varepsilon) \tau_l^{\overline{\overline{Re}}} = - \begin{pmatrix} \tau_{Rl} & 0 & 0 \\ 0 & \tau_{Rl} & 0 \\ 0 & 0 & \tau_{Zl} - (1-\varepsilon) U_b^2 \end{pmatrix} \tag{7.100}$$

A more general expression, not depending on the coordinate system is :

$$(1-\varepsilon) \tau_l^{\overline{\overline{Re}}} = \frac{1}{U_b^2} \left(\tau_{Rl} (\vec{U}_b . \vec{U}_b) \overline{\overline{I}} + \left(\frac{\tau_{Zl} - \tau_{Rl}}{U_b^2} - (1-\varepsilon) \right) \vec{U}_b \otimes \vec{U}_b \right) \tag{7.101}$$

Noting that

$$(1-\varepsilon)\bar{\bar{\tau}}_l^{Re} = \rho_l\left(\tau_1(\vec{U}_b.\vec{U}_b)\bar{\bar{I}} + \tau_2\vec{U}_b\otimes\vec{U}_b\right) \tag{7.102}$$

we have :

$$\begin{aligned}\tau_1 &= \frac{1}{5U_b^2}\varepsilon^{1/3}\left(-\frac{4}{7}\left(\varepsilon^{8/3}-\varepsilon\right)\frac{a^4C_0^2}{\varepsilon^2} + \left(\varepsilon^{5/3}-\varepsilon^{1/3}\right)\frac{aC_0C_2}{\varepsilon} + 6\left(\varepsilon^{5/3}-\varepsilon\right)\frac{C_0C_3}{a\varepsilon}\right)\\ &+\frac{\rho_l}{5U_b^2}\varepsilon^{1/3}\left(-\left(\varepsilon^{2/3}-\varepsilon^{1/3}\right)\frac{C_2^2}{a^2} + 6\left(\varepsilon^{2/3}-\varepsilon^{4/3}\right)\frac{C_2C_3}{a^4} + 3\left(\varepsilon^{2/3}-\varepsilon^{5/3}\right)\frac{C_3^2}{a^6}\right)\end{aligned} \tag{7.103}$$

And :

$$\begin{aligned}\tau_2 &= \frac{4}{5U_b^2}\left(\frac{44}{7}\varepsilon^{2/3}(1-\varepsilon^{7/3})\frac{a^4C_0^2}{\varepsilon^2} + 10\varepsilon^{1/3}\left(1-\varepsilon^{5/3}\right)\frac{a^2C_0C_1}{\varepsilon} + \frac{31}{4}\varepsilon^{2/3}\left(1-\varepsilon^{4/3}\right)\frac{aC_0C_2}{\varepsilon}\right)\\ &+\frac{4}{5U_b^2}\left(-\frac{9}{2}\varepsilon^{4/3}(1-\varepsilon^{2/3})\frac{C_0C_3}{a\varepsilon} + 5(1-\varepsilon)C_1^2 + 10\varepsilon^{1/3}(1-\varepsilon^{2/3})\frac{C_1C_2}{a}\right)\\ &+\frac{4}{5U_b^2}\left(\frac{29}{4}\varepsilon^{2/3}\left(1-\varepsilon^{1/3}\right)\frac{C_2^2}{a^2} + \frac{1}{2}\varepsilon\left(1-\varepsilon^{1/3}\right)\frac{C_2C_3}{a^4} + \frac{1}{4}\varepsilon\left(1-\varepsilon\right)\frac{C_3^2}{a^6}\right)\\ &-(1-\varepsilon)\end{aligned} \tag{7.104}$$

7.8.2 External Euler flow without boundary layer correction ($Re >> 1$)

As shown in Part I, in the case of Euler flow, we have :

$$\begin{aligned}u_{rl} &= -U_b\left(1-\tfrac{a^3}{r^3}\right)\cos\theta\\ u_{\theta l} &= U_b\left(1+\tfrac{a^3}{2r^3}\right)\sin\theta\end{aligned} \tag{7.105}$$

We deduce the equivalent turbulence tensor from equation 7.97 and 7.105

$$\begin{aligned}G(r) &= -\tfrac{U_b}{2}\left(r^2-\tfrac{a^3}{r}\right)\\ \tau_{Rl} &= \frac{3\rho_lU_b^2}{20}(1-\varepsilon)\varepsilon\end{aligned} \tag{7.106}$$

and :

$$\tau_{Zl} = \rho_lU_b^2(1-\varepsilon)\left(1+\frac{4}{20}\varepsilon\right) \tag{7.107}$$

$$(1-\varepsilon)\bar{\bar{\tau}}_l^{Re} = -\frac{\rho_lU_b^2}{20}\varepsilon(1-\varepsilon)\begin{pmatrix}3&0&0\\0&3&0\\0&0&4\end{pmatrix} \tag{7.108}$$

A more general expression, not depending on the coordinate system is :

$$(1-\varepsilon)\overline{\overline{\tau_l^{Re}}} = -\frac{\rho_l}{20}\varepsilon(1-\varepsilon)\left(3(\vec{U}_b.\vec{U}_b)\overline{\overline{I}} + \vec{U}_b \otimes \vec{U}_b\right) \tag{7.109}$$

References

AUTON, T. (1987). The lift force on a spherical body in a rotational flow. *Journal of Fluid Mechanics*, 183, 199–218.

BATCHELOR, G. (1971). *An Introduction to Fluid Dynamics.* Cambridge University Press, seconde édition.

BÉGUIN, C., ÉTIENNE, S., PETTIGREW, M. and MUREITHI, N. (submitted in 2010). A model for bubbly two-phase flow - part I drag coefficient. *Journal of fluid mechanic.*

BÉGUIN, C., ROSS, A., PETTIGREW, M. and MUREITHI, N. (2008). Relationship between vibration behavior and two-phase flow regime transition for piping with internal flow. *9th International Conference on Flow-Induced Vibrations.* Institute of Thermomechanics, Academy of Sciences of Czech Republic, Prague, Czech Republic, 619.

BEYERLEIN, S., COSSMAN, R. and RICHTER, H. (1985). Predicting of bubble concentration profiles in vertical turbulent two-phase flow. *International Journal of Multiphase Flow*, 11, 629–641.

BIESHEUVEL, A. and VAN WIJNGAARDEN, L. (1984). Two-phase equations for a dilute dispersion of gas bubble in liquid. *Journal of Fluid Mechanics*, 148, 301–318.

BRUNNER, B. and TRYGGVASON, G. (2002). Dynamic of homogeneous bubbly flows part 2. velocity fluctuations. *Journal of fluid mechanic*, 466, 53–84.

CHENG, H., HILLS, J. and AZZOPARDI, B. (2002). Effects of initial bubble size on flow pattern transitions in a 28.9 mm diameter column. *International Journal of Multiphase Flow*, 28, 1047–1062.

COLLIER, J. and THOME, J. (1996). *Convective boiling and condensation.* Clarendon Press, Oxford University Press, troisième édition.

DAS, P. D., LEGRAND, J., MORANÇAIS, P. and CARNELLE, G. (2005). Drop breakage model in static mixers at low and intermediate reynolds number. *Chemical Engineering Science*, 60, 231–238.

GARNIER, C., LANCE, M. and J.L., M. (2002). Measurement of local flow characteristics in buoyancy-driven bubbly flow at high void fraction. *Experimental Thermal and Fluid Science*, 26, 811–815.

HESKETH, R., RUSSELL, T. and ETCHELLS, A. (1987). Bubble size in horizontal pipelines. *AIChE Journal*, 33, 663.

HINZE, J. (1955). Fundamentals of hydrodynamic mechanism of splitting in dispersion processes. *Chemical Engineering Progress*, 1, 289–295.

HOSOKAWA, S., TAKASHI, S. and TOMIYAMA, A. (2010). Effect of bubbles on turbulence properties in a duct flow. *Multiphase Science and Technology*, 22, 211–232.

ISHII, M. and ZUBER, N. (1979). Drag coefficient and relative velocity in bubbly, droplet or particulate flows. *American Institute of Chemical Engineers Journal*, 25, 843–855.

LANCE, M. and BATAILLE, J. (1991). Turbulence in the liquid phase of uniform bubble air-water flow. *Journal of fluid mechanic*, 222, 95–118.

LEON-BECERRIL, E. and LINÉ, A. (2001). Stability analysis of a bubble column. *Chemical Engineering Science*, 56, 6135–6141.

LEVICH, V. (1962). *Physiochemical Hydrodynamics*. Prentice-Hall Inc, NJ.

LIU, S. and LI, D. (1999). Drop coalescence in turbulent dispersions. *Chemical Engineering Science*, 54, 5667.

MEI, R., KLAUSNER, J. and LAWRENCE, C. (1994). A note on the history force on a spherical bubble at finite reynolds number. *Physics of fluids*, 6, 418–420.

MILNE-THOMSON, L. (1968). *Theorical Hydrodynamics*. Macmillan, New York, 5^{th} édition.

MOKEYEV, G. (1977). Effect of particule concentration on their drag and induced mass. *Fluid Mechanics Sov. Res.*, 6, 161.

MORENCAIS, P., HIRECH, K., CARNELLE, G. and LEGRAND, J. (1999). Friction factor in static mixer and determination of geometric parameters of smx sulzer mixers. *Chemical Engineering Communication*, 171, 77–93.

NIGMATULIN, R. (1979). Spatial averaging in the mechanics of heterogeneous and dispersed systems. *International Journal of Multiphase Flow*, 5, 353–385.

PARK, J., DREW, R. and LAHEY, R. (1998). The analysis of void wave propagation in adiabatic monodispersed bubbly two-phase flows using an ensemble-averaged two-fluid model. *International Journal of Multiphase Flow*, 24, 1205–1244.

RAZZAQUE, M., AFACAN, A., LIU, S., NANDAKUMARA, K., MASLIYAH, J. and SANDERS, R. (2003). Bubble size in coalescence dominant regime of turbulent air-water flow through horizontal pipes. *International Journal of Multiphase Flow*, 29, 1451.

RIVERIN, J. and PETTIGREW, M. (2004). Fluctuating forces in piping elements subjected to internal two-phase flow. *8th International Conference on Flow-Induced Vibrations*. École Polytechnique, Paris, France, 327.

SHINNAR, R. (1961). On the behaviour of liquid dispersions in mixing vessels. *Journal of Fluid Mechanic*, 10, 259.

TAITEL, Y., BORNEA, D. and A.E., D. (1980). Modelling flow pattern transitions for steady upward gas-liquid flow in vertical tubes. *AIChE Journal*, 26, 345–354.

TAYLOR, G. (1932). The viscosity of a fluid containing small drops of another fluid. *Proceedings of the Royal Society of London, Containing Papers of a Mathematical and Physical Character*. vol. 138, 41.

TAYLOR, T. and ACRIVOS, A. (1964). On the deformation and drag of a falling viscous drop at low reynolds number. *Journal of fluid mechanics*, 18, 466–476.

VAN WIJNGAARDEN, L. (1976). Hydrodynamic interaction between gas bubbles in liquid. *Journal of fluid Mechanics*, 77, 27–44.

VAN WIJNGAARDEN, L. (1991). *Bubble Deformation in Bubbly Liquid and its Effect on the Stability of Voidage Waves*. Mathematical approaches in hydrodynamics, SIAM, Miloh t. édition.

VOINOV, O. (1973). Force acting on a sphere in a homogeneous flow of an ideal incompressible fluid. *Journal of Applied Mechanics and Technology Physics*, 14, 592–594.

WILKINSON, P., VAN SCHAYK, A., SPRONKEN, J. and VAN DIERENDONCK, L. (1993). The influence of gas density and liquid properties on bubble breakup. *Chemical engineering science*, 48, 1213.

ZUBER, N. (1964). On the dispersed two-phase flow in the laminar flow regime. *Chemical Engineering Science*, 19, 897–903.

CHAPITRE 8

DISCUSSION GÉNÉRALE ET CONCLUSION

La première partie de cette thèse était consacrée à l'amortissement diphasique. Cet amortissement est important, car il permet d'améliorer la durée de vie des structures en constituant un élément dominant de l'amortissement total dans la tuyauterie transportant des écoulements diphasiques. Cependant, les mécanismes responsables de l'amortissement diphasique ne sont pas encore bien compris et il n'existe pas de modèle pratique disponible pour prévoir cet amortissement. Cela constituait la première étape de mon doctorat.

Dans les écoulements internes, notamment dans un tube encastré encastré, tous les mécanismes d'amortissement autres que l'amortissement structural sont relativement faibles et permettent une mesure directe de l'amortissement diphasique. Des mesures d'amortissement diphasique ont été réalisées en écoulement interne avec différent type de tube (fréquence naturelle et diamètre), ainsi qu'avec différent mélange faisant varier la densité et la viscosité, mais aussi la tension de surface dans une moindre mesure.

Cette étude a fait l'objet de deux articles (*Journal of Fluids and Structures*) et (*International Journal of Multiphase Flow*). Nous sommes arrivés à la conclusion que l'amortissement diphasique en écoulement à bulles est un effet purement inertiel. La viscosité n'a pas d'influence sur le phénomène. L'amortissement diphasique est proportionnel à la surface d'interface. Cependant, l'amortissement diphasique ne peut pas être expliqué par un amortissement engendré par la création de nouvelles surfaces d'interface. La tension de surface joue, cependant, un rôle dans la forme et la taille des bulles et par conséquent sur l'amortissement. L'amortissement diphasique est expliqué par un transfert d'énergie cinétique du tube à la phase continue par l'intermédiaire du mouvement relatif entre la phase dispersée et la phase continue.

En écoulement à bulles, l'amortissement diphasique ne dépend pas fortement de la viscosité du fluide, l'énergie cinétique ajoutée dans le liquide est donc sans doute transportée en dehors du tube avec l'écoulement. De nouvelles hypothèses ont été proposées suggérant deux mécanismes possibles ne faisant pas intervenir la viscosité du liquide. La première suggère l'existence en écoulement oscillant d'une trainée de forme des bulles indépendante de la viscosité du liquide. La seconde suggère que des impacts entre les bulles ou entre les bulles et la structure ou bien encore que le champ de vitesse oscillant créent des vibrations de l'interface permettant d'apporter de l'énergie dans la phase continue. Ces vibrations sont caractérisées par une raideur liée à la tension de surface γ et un effet de masse lié à la différence de densité

des phases $\Delta\rho$. Le nombre de Bond est un paramètre majeur de l'amortissement diphasique. L'amortissement diphasique augmente assez linéairement avec le taux de vide jusqu'à un taux de vide critique. Le taux de vide est directement proportionnel à la masse de gaz et à la surface d'interface. Le taux de vide critique correspond à un changement de comportement de l'amortissement et à une transition de configuration d'écoulement. La transition d'écoulement ne semble dépendre que de la vitesse homogène, cela est expliqué par la présence de forces de fragmentation des bulles (pseudo-turbulence) trop faible et indépendante du diamètre du tube.

L'amortissement diphasique est maximum juste avant la transition de l'écoulement à bulles à l'écoulement à bouchons. Au-delà de la transition, l'amortissement diminue. L'amortissement diphasique augmente avec le diamètre du tube. En écoulement à bouchons, un certain amortissement visqueux est ajouté sans doute à cause du sillage et du film oscillant des bulles de Taylor.

Pour être en mesure de comprendre plus finement les mécanismes de transition en configuration d'écoulement et l'amortissement diphasique, la modélisation des forces d'interface et de l'écoulement autour d'une bulle est clairement apparue comme une nécessité. En effet, peu de travaux ont été consacrés pour comprendre le rôle du taux de vide sur les forces d'interface agissant sur une bulle ainsi que la structure de l'écoulement autour d'elle. Parallèlement, à une étude numérique et analytique sur l'écoulement autour des bulles, la conception du capteur capacitif a été amorcée. Cet instrument de mesure du taux de vide utilise la différence de propriété électrique de l'air et de l'eau. Il est un instrument utile pour étudier la variation spatiale et spectrale du taux de vide. En effet, l'instabilité des ondes de taux de vide est une bonne candidate pour expliquer la transition de l'écoulement à bulles à l'écoulement à bouchons.

L'influence du taux de vide sur l'écoulement autour des bulles et sur les forces d'interface sont le moteur des ondes de taux de vide. L'étude expérimentale des ondes de taux de vide avec capteur de capacité serait un bon moyen de valider les connaissances acquises par les études analytiques et numériques.

Un article en deux parties (*Journal of Fluid Mechanics*) présente le résultat de nos investigations. La Partie I de cet article propose une relation entre le coefficient de traînée de bulles (ou gouttes) sphériques et le nombre de Reynolds Re, le taux de vide ε et les rapports de viscosité et de densité entre les deux phases ($\bar{\mu}$ et$\bar{\rho}$). La limite sous laquelle les bulles restent sphériques a également été étudiée. Cette condition permet d'identifier la limite du modèle.

Nous avons pu prouver que le taux de glissement dans les écoulements à bulles reste en général très faible. Dans presque tous les cas pratiques d'écoulement à bulles, l'écoulement

autour de la bulle peut être considéré comme un écoulement de Stokes. Le taux de vide ε a un effet majeur sur la traînée essentiellement par confinement. L'effet de sillage sur la trainée des bulles est en comparaison plutôt faible. De plus, le taux de vide repousse très vite la transition de Stokes à Euler à des nombres de Reynolds élevés. L'écoulement de Stokes représente, de façon très précise, l'écoulement autour des bulles. L'écoulement est donc laminaire et par conséquent la turbulence ne peut être attribuée à de la turbulence classique. L'écoulement dans la phase continue peut être considéré comme un écoulement de film dans lequel la turbulence classique ne peut se développer. La turbulence diphasique est essentiellement due à des perturbations induites par le passage de bulles. La relation proposée peut être utilisée pour construire un modèle d'écoulement à deux phases pour les écoulements à bulles ou annulaire. Ce travail propose une amélioration sur les relations de la fermeture du coefficient de traînée (C_D) par rapport aux travaux antérieurs.

La Partie II propose un modèle pour la pseudo-turbulence (turbulence induite par les particules). Des relations entre le tenseur de Reynolds de la phase continue et dispersée et le nombre de Reynolds Re, le taux de vide ε et les rapports de viscosité et de densité entre les deux phases ($\bar{\mu}$ et$\bar{\rho}$) ont proposées. Les implications pour la taille des bulles et les forces induites par la turbulence sur les bulles sont également étudiées. Un modèle simple est proposé faisant le lien entre les forces de turbulence sur les bulles et la prédiction de la taille des bulles.

Il est montré que les forces conduisant à la rupture des bulles sont peu présentes dans le conduit. Cela explique que, pour des tubes de taille intermédiaire (11 mm $< D <$ 25 mm), la transition de l'écoulement à bulles à l'écoulement à bouchons ne dépend pas du diamètre du conduit. Par ailleurs, la pseudo-turbulence est fortement anisotropique et elle crée une force d'inertie sur les bulles reliée au mouvement d'ensemble du champ de bulles. Cela explique pourquoi les bulles ont tendance à se suivre. De plus, le comportement des forces turbulentes en écoulement diphasique est complètement différent de celui observé en écoulement monophasique.

CHAPITRE 9

RECOMMANDATIONS

Les étapes suivantes de ce travail sont :

- La modélisation de la masse ajoutée par calcul analytique et numérique afin de proposer une relation de fermeture de la masse ajoutée en fonction du taux de vide.
- De futurs développements des sondes à capacitance afin de réduire significativement le bruit lors de la mesure.
- La mesure des ondes de taux de vide avec les sondes à capacitance et la comparaison avec les ondes de taux de vide prévu avec les relations de fermeture que nous proposons.
- De futures mesures de l'amortissement diphasique en faisant varier entre autres la tension de surface.
- La mesure du mouvement des bulles à la caméra ultra rapide lors de la vibration du tube et la corrélation de ce mouvement avec la modélisation des forces sur les bulles.
- Des mesures de l'amortissement dans des tubes de petit diamètre, afin de comprendre l'amortissement visqueux des écoulements à bouchons. Le film du mouvement des bulles Taylor à la caméra ultra rapide lors de la vibration du tube nous sera utile pour mieux comprendre son origine.

RÉFÉRENCES

ALOUI, F. (1994). *Étude des écoulements monophasiques et diphasiques dans les élargissements brusques axisymétriques et bidimensionnels*. Thèse de doctorat, INPL Nancy.

ANSCUTTER, F., BÉGUIN, C., ROSS, A., PETTIGREW, M. et MUREITHI, N. (2006). Two-phase damping and interface surface area in tubes with internal flow. *ASME PVP2006*. 11.

AUTON, T. (1987). The lift force on a spherical body in a rotational flow. *Journal of Fluid Mechanics*, 183, 199–218.

AZZOPARDI, B. et BAKER, G. (2003). Characteristics of periodic structures in gas/liquid two-phase flow. *Proceedings of UK/Japan Two-Phase Flow Meeting, Guildford, April 14-15*.

BAJ, F. (1998). *Amortissement et instabilité fluide-élastique dus aux écoulements diphasiques à l'interieur d'un tube*. Thèse de doctorat, Paris VI.

BAKER, G. (1954). Simultaneous flow of oil and gas. *Oil and Gas Journal*, 53, 185–189.

BATCHELOR, G. (1971). *An Introduction to Fluid Dynamics.* Cambridge University Press, seconde édition.

BÉGUIN, C., ÉTIENNE, S., PETTIGREW, M. et MUREITHI, N. (submitted in 2010a). A model for bubbly two-phase flow - part I drag coefficient. *Journal of fluid mechanic*.

BÉGUIN, C., ÉTIENNE, S., PETTIGREW, M. et MUREITHI, N. (submitted in 2010b). A model for bubbly two-phase flow - part II bubble size and pseudo two-phase turbulence. *Journal of fluid mechanic*.

BÉGUIN, C., ROSS, A., PETTIGREW, M. et MUREITHI, N. (2008). Relationship between vibration behavior and two-phase flow regime transition for piping with internal flow. *9th International Conference on Flow-Induced Vibrations*. Institute of Thermomechanics, Academy of Sciences of Czech Republic, Prague, Czech Republic, 619.

BÉGUIN, C., WEHBE, J., ROSS, A., PETTIGREW, M. et MUREITHI, N. (2009). Influence of viscosity, density and surface tension on two-phase damping. *Proceedings of ASME 2009 Pressure Vessels & Piping Conference*. ASME, Prague, Czech Republic, PVP2009 77423.

BEYERLEIN, S., COSSMAN, R. et RICHTER, H. (1985). Predicting of bubble concentration profiles in vertical turbulent two-phase flow. *International Journal of Multiphase Flow*, 11, 629–641.

BHAGA, D. et WEBER, W. (1981). Bubbles in visous liquids : shapes, wakes and velocities. *Journal of Fluid Mechanics*, 105, 61–85.

BIESHEUVEL, A. et GORISSEN, W. (1990). Void fraction disturbances in a uniform bubbly fluid. *International Journal of Multiphase Flow*, 16, 211–231.

BIESHEUVEL, A. et VAN WIJNGAARDEN, L. (1984). Two-phase equations for a dilute dispersion of gas bubble in liquid. *Journal of Fluid Mechanics*, 148, 301–318.

BRODKEY, R. (1967). *The Phenomena of Fluid Motions.* Addison-Wesley Press.

BRUNNER, B. et TRYGGVASON, G. (2002). Dynamic of homogeneous bubbly flows part 2. velocity fluctuations. *Journal of fluid mechanic*, 466, 53–84.

CARLUCCI, L. (1980). Damping and hydrodynamic mass of a cylinder in two-phase flow. *ASME Journal of Mechanical Design*, 102, 597–602.

CARLUCCI, L. et BROWN, J. (1983). Experimental studies of damping and hydrodynamic mass of a cylinder in confined two-phase flow. *ASME Journal of Vibration, Acoustics, Stress, and Reliability in Design*, 105, 83–89.

CHEN, S. (1987). *Flow-induced Vibration of Cylindrical Structures.* Hemisphere Publishing,New York,.

CHENG, H., HILLS, J. et AZZOPARDI, B. (1998). A study of the bubble-to-slug transition in vertical gas-liquid flow in columns of different diameters. *International Journal of Multiphase Flow*, 24, 431–452.

CHENG, H., HILLS, J. et AZZOPARDI, B. (2002). Effects of initial bubble size on flow pattern transitions in a 28.9 mm diameter column. *International Journal of Multiphase Flow*, 28, 1047–1062.

CLANET, C., BÉGUIN, C., RICHARD, D. et QUÉRÉ, D. (2004). Maximal deformation of an impacting drop. *Journal of Fluid Mechanics*, 517, 199–208.

CLIFT, R., GRACE, J. et WEBER, M. (1978). *Bubbles, drops and particles.* Academics Press, New York.

COLLIER, J. et THOME, J. (1996). *Convective boiling and condensation.* Clarendon Press, Oxford University Press, troisième édition.

COMITI, J. et MAURICE, R. (1989). A new model for determining mean structure parameters of fixed beds from pressure drop measurements : application to beds packed with parallelepipedal particles. *Chemical Engineering Science*, 40, 1539–1545.

COSTIGAN, G. et WHALLEY, P. (1996). Slug flow regime identification from dynamic void fraction measurement in vertical air-water flows. *International Journal of Multiphase Flow*, 23, 263–282.

DAS, P. D., LEGRAND, J., MORANÇAIS, P. et CARNELLE, G. (2005). Drop breakage model in static mixers at low and intermediate reynolds number. *Chemical Engineering Science*, 60, 231–238.

DAS, R. et PATTANAYAK, S. (1994). Measurement of void fraction in different flow regime of a vertical gas-liquid flow through narrow tube. *Measurement Science Technology*, 5, 1538–1545.

DE LANGRE, E. (2001). *Fluides et solides*. Edition de l'École Polytechnique, Paris.

DREW, D. et LAHEY, R. J. (1983). Mathematical modeling of two-phase flow. *Annual Reviews of Fluid Mechanics*, 15, 261–291.

DUNCAN, D., TRABOLD, T., MOHR, C. et BERETT, M. (1993). Measurement of local void fraction at elevated temperature and pressure. 3^{rd} *World Conference on Experimental Heat Transfer, Fluid Mechanics and Thermodynamics, Honolulu*.

ELKOW, K. et REZKALLAH, K. (1996). Void fraction measurements in gas - liquid flows using capacitance sensors. *Measurement Science Technology*, 7, 1153–1163.

ERGUN, S. (1952). Fluid flow through packed columns. *Chemical Engineering Prog.*, 48, 89–94.

ESPINOSA-PAREDES, G. (2001). Theoretical derivation of the interaction effects with an eccentric cell model and void fraction propagation in two-phase flow. *Annals of Nuclear Energy*, 28, 659–688.

ETIENNE, S. et PELLETIER, D. (2005). A general approach to sensitivity analysis of fluid-structure interactions. *Journal of fluids and structures*, 21, 169–186.

FARRIS, S. C., BUGG, J. D. et GABRIEL, K. S. (2004). The motion of bubbles in a sinusoidally oscillating liquid in microgravity. *Microgravity Science and Technology*, 15, 28–35.

FEENSTRA, P., WEAVER, D. et JUDD, R. (2000). An improved void fraction model for two-phase cross-flow in horizontal tube bundles. *International Journal of Multiphase flow*, 26, 1851.

GARNIER, C., LANCE, M. et J.L., M. (2002). Measurement of local flow characteristics in buoyancy-driven bubbly flow at high void fraction. *Experimental Thermal and Fluid Science*, 26, 811–815.

GRANT, I. (1975). Flow and pressure drop with single-phase and two-phase flow in the shell-side of segmentally baffled shell-and-tube heat exchangers. *Report NEL-590, National Engineering Laboratory*.

GRANT, I. et MURRAY, I. (1972). Pressure-drop on the shell-side of a segmentally baffled shell-and-tube heat exchanger with vertical two-phase flow. *Report NEL-500, National Engineering Laboratory*.

GRAVELLE, A., ROSS, A., PETTIGREW, M. et MUREITHI, N. (2007). Damping of tubes due to internal two-phase flow. *Journal of Fluids and Structures*, 23, 447.

HAHNE, E., SPINDLER, K., CHEN, Q. et WINDISCH, R. (1990). Local void fraction measurements in finned tube bundles. *Proceedings of the Ninth International Conference on Heat Transfer, Jerusalem, Israel*, 6, 41–45.

HAN, Y. (1999). *Two-phase flow pattern identification from fluctuating signals of pressure and void fraction*. Mémoire de maîtrise, École Polytechnique de Montréal.

HARA, F. (1985). Review of damping of two-phase flows. *ASME, Pressure Vessels and Piping Division (Publication) PVP*, 256, 87–101.

HARA, F. et KOHGO, O. (1993). A theory for a vibrating circular rod damping in two-phase bubbly fluid. *Transactions JSME*, 51, 143–148.

HARMATHY, T. (1960). Velocity of large drops and bubbles in media of infinite or restricted extend. *AIChE Journal*, 6, 281.

HESKETH, R., RUSSELL, T. et ETCHELLS, A. (1987). Bubble size in horizontal pipelines. *AIChE Journal*, 33, 663.

HEWITT, G. (1978). *Measurement of two-phase flow parameters*. London :Academic Press.

HEWITT, G. et ROBERTSON, D. (1969). Studies of two-phase flow patterns by simultaneous x-ray and flash photography. *AERE-M2159, UKAEA, Harwell*.

HINZE, J. (1955). Fundamentals of hydrodynamic mechanism of splitting in dispersion processes. *Chemical Engineering Progress*, 1, 289–295.

HOSOKAWA, S., TAKASHI, S. et TOMIYAMA, A. (2010). Effect of bubbles on turbulence properties in a duct flow. *Multiphase Science and Technology*, 22, 211–232.

ISHII, M. (1975). *Thermo-Fluid Dynamic Theory of Two-Phase Flow*. Eyrolles, Paris.

ISHII, M. et ZUBER, N. (1979). Drag coefficient and relative velocity in bubbly, droplet or particulate flows. *American Institute of Chemical Engineers Journal*, 25, 843–855.

JAWOREK, A. et KRUPA, A. (2004). Gas/liquid ratio measurements by rf resonance capacitance sensor. *Sensors and Actuators*, 113, 133–139.

JONES, A. et PROSPERETTI, A. (1985). On the stability of first order differential models for two-phase flow prediction. *International Journal of Multiphase Flow*, 11, 133–148.

JONES, O. et ZUBER, N. (1975). The interrelation between void fraction fluctuations and flow patterns in two-phase flow. *International Journal of Multiphase Flow*, 2, 273–306.

KENDOUSH, A. (2001). Hydrodynamic model for bubbles in a swarm. *Chemical engineering Science*, 56, 235–238.

KONDO, M. et NAKAJIMA, K.-I. (1980). Experimental investigation of air-water upflow across horizontal tube bundles 1.flow pattern and void fraction. *Bulletin of the JSME*, 23, 365–393.

KRISHNA, R. et VAN BATEN, J. (1999). Simulating the motion of gas bubbles in a liquid. *Nature*, 398, 208.

LANCE, M. et BATAILLE, J. (1991). Turbulence in the liquid phase of uniform bubble air-water flow. *Journal of fluid mechanic*, 222, 95–118.

LEON-BECERRIL, E. (2001). *Analyse de stabilité et simulation numérique des colonnes à bulles*. Thèse de doctorat, INSA Toulouse.

LEON-BECERRIL, E. et LINÉ, A. (2001). Stability of a bubble column. *Chemical Engineering Science*, 56, 6135–6141.

LEON-BECERRIL, E. et LINÉ, A. (2001). Stability analysis of a bubble column. *Chemical Engineering Science*, 56, 6135–6141.

LEVICH, V. (1962). *Physiochemical Hydrodynamics*. Prentice-Hall Inc, NJ.

LIU, S. et LI, D. (1999). Drop coalescence in turbulent dispersions. *Chemical Engineering Science*, 54, 5667.

MC QUILLAN, K.W.AND WHALLEY, P. (1985). Flow patterns in vertical two- phase flow. *International Journal of Multiphase Flow*, 11, 161–175.

MEI, R., KLAUSNER, J. et LAWRENCE, C. (1994). A note on the history force on a spherical bubble at finite reynolds number. *Physics of fluids*, 6, 418–420.

MERILO, M., DECHENE, R. et CICOWLAS, W. (1977). Void fraction measurement with a rotating electric field conductance gauge. *Journal of Heat Transfer*, 99, 330–331.

MILNE-THOMSON, L. (1968). *Theorical Hydrodynamics*. Macmillan, New York, 5^{th} édition.

MOKEYEV, G. (1977). Effect of particule concentration on their drag and induced mass. *Fluid Mechanics Sov. Res.*, 6, 161.

MOORE, D. (1963). The boundary layer on a spherical gas bubble. *Journal of Fluid Mechanic*, 16, 161–176.

MORANCAIS, P., HIRECH, K., CARNELLE, G. et LEGRAND, J. (1999). Friction factor in static mixer and determination of geometric parameters of smx sulzer mixers. *Chemical Engineering Communication*, 171, 77–93.

MORENCAIS, P., HIRECH, K., CARNELLE, G. et LEGRAND, J. (1999). Friction factor in static mixer and determination of geometric parameters of smx sulzer mixers. *Chemical Engineering Communication*, 171, 77–93.

MORRIS, D., TEYSSEDOU, A., LAPIERRE, J. et TAPUCU, A. (1987). Optical fiber probe to measure local void fraction profiles. *Applied Optics*, 26, 4660–4664.

NIGMATULIN, R. (1979). Spatial averaging in the mechanics of heterogeneous and dispersed systems. *International Journal of Multiphase Flow*, 5, 353–385.

NOGHREKAR, G., KAWAJI, M. et CHAN, A. (1999). Investigation of two-phase flow rehimes in tube bundles under cross-flow conditions. *International Journal of Multiphase Flow*, 25, 857–874.

OSEEN, C. (1910). über die stokessche formel und überdie verwandte aufgabe in der hydrodynamik. *Arkiv für Mathematik, Astronomi och Fysik*, 6, 29.

PARK, J., DREW, R. et LAHEY, R. (1998). The analysis of void wave propagation in adiabatic monodispersed bubbly two-phase flows using an ensemble-averaged two-fluid model. *International Journal of Multiphase Flow*, 24, 1205–1244.

PAUCHON, C. et BANERJEE, S. (1986a). Interphase momentum interaction effects in the averaged multifield model. part ii : Kinematic waves and interfacial drag in bubbly flows. *International Journal of Multiphase Flow*, 14, 253–264.

PAUCHON, C. et BANERJEE, S. (1986b). Interphase momentum interaction effects in the averaged multifield model. part i :void propagation in bubbly flow. *International Journal of Multiphase Flow*, 12, 559–573.

PAUCHON, C. et SMEREKA, S. (1992). Momentum interactions in disperse flow qn averaging and a variational approach. *International Journal of Multiphase Flow*, 18, 65–87.

PETTIGREW, M. et TAYLOR, C. (1994). Two-phase flow-induced vibration : an overview. *ASME Journal of Pressure Vessel Technology*, 116, 233–253.

PETTIGREW, M. et TAYLOR, C. (2003). Vibration analysis of shell-and-tube heat exchangers : An overview - part 1 : Flow, damping, fluidelastic instability. *Journal of Fluids and Structures*, 18, 469–483.

PETTIGREW, M. et TAYLOR, C. (2004). Damping of heat exchanger tubes in two-phase flow : Review and design guidelines. *ASME Journal of Pressure Vessel Technology*, 126, 523.

PETTIGREW, M., TAYLOR, C. et KIM, B. (1988). Vibration of tube bundles in two-phase cross-flow : part 1 - hydrodynamic mass and damping. *International Sympsium on Flow Induced Vibration, Noise Flow Induced Vibration, Cylinder Arrays Cross Flow*, 79–103.

RAZZAQUE, M., AFACAN, A., LIU, S., NANDAKUMARA, K., MASLIYAH, J. et SANDERS, R. (2003). Bubble size in coalescence dominant regime of turbulent air-water flow through horizontal pipes. *International Journal of Multiphase Flow*, 29, 1451.

RICHARD, D. et QUÉRÉ, D. (2000). Bouncing water drops. *Europhysics Letters*, 50, 769–775.

RIVERIN, J. et PETTIGREW, M. (2004). Fluctuating forces in piping elements subjected to internal two-phase flow. *8th International Conference on Flow-Induced Vibrations*. École Polytechnique, Paris, France, 327.

SCHENK, O. et GÄRTNER, K. (2004). Solving unsymmetric sparse systems of linear equations with pardiso. *Journal of Future Generation Computer Systems*, 20(3), 475–487.

SCHENK, O. et GÄRTNER, K. (2006). On fast factorization pivoting methods for symmetric indefinite systems. *Electronic Transactions on Numerical Analysis*, 23, 158–179.

SCOTT, A., GREEN, R. et SERAI, K. (1985). Comparison of the use of internal and external electrodes for the measurement of the capacitance and conductance of fluids in pipes. *Journal Phys. E : Sci. Instrum.*, 18, 587–592.

SHINNAR, R. (1961). On the behaviour of liquid dispersions in mixing vessels. *Journal of Fluid Mechanic*, 10, 259.

SONG, J. et ISHII, M. (2001). On the stability of a one-dimensional two-fluid model. *Nuclear Engineering and Design*, 204, 101–115.

SUN, B., WANG, R., ZHAO, X. et YAN, D. (2002). The mechanism for the formation of slug flow in vertical gas liquid two-phase flow. *Solid-State Electronics*, 46, 2323–2329.

TAITEL, Y., BORNEA, D. et A.E., D. (1980). Modelling flow pattern transitions for steady upward gas-liquid flow in vertical tubes. *AIChE Journal*, 26, 345–354.

TAITEL, Y. et DUKLER, A. (1976). A model for predicting flow regime transition in horizontal and near horizontal gas-liquid flow. *AIChE Journal*, 22, 47–55.

TAYLOR, G. (1932). The viscosity of a fluid containing small drops of another fluid. *Proceedings of the Royal Society of London, Containing Papers of a Mathematical and Physical Character*. vol. 138, 41.

TAYLOR, T. et ACRIVOS, A. (1964). On the deformation and drag of a falling viscous drop at low reynolds number. *Journal of fluid mechanics*, 18, 466–476.

TEYSSEDOU, A. (2005). *Thermohydraulique des systèmes diphasiques*. Recueil de notes du cours ENE6002, École Polytechnique de Montréal, automne 2005 édition.

TEYSSEDOU, A., AUBE, F. et CHAMPAGNE, P. (1992). Void fraction measurement system for high temperature flows. *Measurement science & technology*, 3, 485–494.

TEYSSEDOU, A., TAPUCU, A. et LORTIE, M. (1988). Impedance probe to measure local void fraction profiles. *Review of Scientific Instruments*, 59, 631–638.

THOM, J. (1968). Prediction of pressure drop during forced circulation boiling of water. *International Journal of Heat Mass Transfer*, 7, 709–724.

TOLLEFSEN, J. et HAMMER, A. (1998). Capacitance sensor design for reducing errors in phase concentration measurements. *Flow Measurement and Instrumentation*, 9, 5–32.

TUTU, N. (1982). Pressure fluctuation and flow pattern recognition in vertical two phase gas-liquid flow. *International Journal of Multiphase Flow*, 8, 443–447.

UENO, T., LEUNG, W. et ISHII, M. (1995). Local measurement in two-phase flow across a horizontal tube bundle. *Proceedings of the 2nd International Conference on Multiphase Flow*, 89–95.

ULBRICH, R. et MEWES, D. (1994). Vertical, upward gas/liquid two-phase flow across a tube bundle. *International Journal of Multiphase Flow*, 20, 249–272.

VAN WIJNGAARDEN, L. (1976). Hydrodynamic interaction between gas bubbles in liquid. *Journal of fluid Mechanics*, 77, 27–44.

VAN WIJNGAARDEN, L. (1991). *Bubble Deformation in Bubbly Liquid and its Effect on the Stability of Voidage Waves*. Mathematical approaches in hydrodynamics, SIAM, Miloh t. édition.

VINCE, M. et LAHEY, R. (1982). On the development of an objective flow regime indicator. *International Journal Multiphase Flow*, 8, 93–124.

VOINOV, O. (1973). Force acting on a sphere in a homogeneous flow of an ideal incompressible fluid. *Journal of Applied Mechanics and Technology Physics*, 14, 592–594.

WALLIS, G. (1969). *One-dimensional two-phase flow*. Mathematical approaches in Hydrodynamics, New York, McGraw-Hill édition.

WILKINSON, P., VAN SCHAYK, A., SPRONKEN, J. et VAN DIERENDONCK, L. (1993). The influence of gas density and liquid properties on bubble breakup. *Chemical engineering science*, 48, 1213.

ZUBER, N. (1964). On the dispersed two-phase flow in the laminar flow regime. *Chemical Engineering Science*, 19, 897–903.

ZUBER, N. et HENCH, J. (1962). Steady-state and transcient void fraction of bubbling systems and their operating limits, part 1. steady state operation. *General Electric Report 62GL100*.